CLIMATE SENSITIVITIES OF POLYTHERMAL ICE SHEET, ICE CAP, AND ALPINE ICE DYNAMICS AND RELATED EPISODIC EROSION ON CUMBERLAND PENINSULA, BAFFIN ISLAND, NUNAVUT

by

Annina Margreth

Submitted in partial fulfilment of the requirements
for the degree of Doctor of Philosophy

at

Dalhousie University
Halifax, Nova Scotia
April 2015

To my mom, who could not witness this thesis coming to completion.

Thank you for your unconditional support and love.

TABLE OF CONTENTS

LIST OF TABLES

LIST OF FIGURES

ABSTRACT

The sensitivity of glaciers to climate and the resulting landscape changes has not been fully evaluated because of difficulties in extracting records of glacial advance, comparing sensitivities of different glacier types (ice sheets, ice caps, and alpine ice) for the same location, and measuring rates of episodic processes, which are common to glacial systems. This thesis applied innovative strategies to Cumberland Peninsula, Baffin Island, Arctic Canada, to achieve these objectives by i) radiocarbon dating currently exhuming, subfossilized bryophytes to test the sensitivity of cold-based ice cap growth to short-lived Holocene cooling events; ii) analysing the climate-sensitivities of all three glacier types by mapping and comparing their coeval ice margin extents during three short-lived but significant post-Last Glacial Maximum (LGM) climate changes (Heinrich Event-1, Younger Dyras, and the cooling associated with the regionally extensive Cockburn moraines); iii) quantifying the landscape evolution of upland plateaus by a novel approach, which couples the measurement of two cosmogenic radionuclides in pairs of tor surfaces to a Monte Carlo method to establish long-term rates of subglacial episodic erosion.

The radiocarbon results indicate that cold-based ice caps advanced instantaneously (within years) of major volcanic eruptions and also suggest that bryophytes may re-grow after thousands of years of ice entombment. The high-resolution ice-margin map coupled with the first glacial chronology through the interior of the peninsula, reveal that the three glacier types responded differently to post-LGM climate changes. Asymmetric retreat pattern of alpine glaciers indicates a first-order control by precipitation, possibly as a manifestation of sea-ice cover extent. Except for narrow, high-elevation coastal ridges, upland surfaces were covered by cold-based ice during Pleistocene glaciations that caused lowering of the landscape at an-order-of-magnitude slower rates than adjoining glacially-deepened valleys.

The results suggest that most of the peninsula was covered by a relatively climate-sensitive polythermal alpine glacier system, while the Laurentide Ice Sheet was restricted to the westernmost part of the peninsula where it coalesced with an expanded Penny Ice Cap. This and the quantification of episodic erosion rates provide a significant improvement of the conceptual model of paleo-ice dynamics on Cumberland Peninsula and the resulting Quaternary landscape evolution.

LIST OF ABBREVIATIONS AND SYMBOLS USED

ABBREVIATIONS:

AD	Anno Domini
AMS	Accelerator Mass Spectrometry
AO	Atlantic Oscillation
BP	Before Present
CAMS	Center for Accelerator Mass Spectrometry
CSIS	Cumberland Sound Ice Stream
DEM	Digital Elevation Model
DGC	Dalhousie Geochronology Center
ELA	Equilibrium Line Altitude
GEM	Geo-mapping for Energy and Minerals
GSC	Geological Survey of Canada
H – 1	Heinrich Event 1
HTO	Holocene Thermal Optimum
ICP-MS	Inductively Coupled Plasma Mass Spectrometry
ICP-OES	Inductively Coupled Plasma Optical Emission Spectrometry
LGM	Last Glacial Maximum
LIS	Laurentide Ice Sheet
LLNL	Lawrence Livermore National Laboratory
LSD	Lifton, Sato, Dunai
MC	Monte Carlo
MWP	Medieval Warm Period
NAO	North Atlantic Osciallation
OIS	Oxygen Isotope Stage
OSL	Optically Stimulated Luminescence
PDF	Probability Density Function
PIC	Penny Ice Cap
RSL	Relative Sea Level
SLHL	Sea Level High Latitude

TCN	Terrestrial Cosmogenic Nuclides
YD	Younger Dryas

SYMBOLS:

ε	cm a^{-1}	erosion rate
f	-	fraction of ice-free time
Inh_{wth}	atoms g^{-1}	inherited nuclide concentration of weathered surface
Inh_{frh}	atoms g^{-1}	inherited nuclide concentration of fresh surface
N_{int}	atoms g^{-1}	Nuclide concentration at the end of interglacials
N_{glc}	atoms g^{-1}	Nuclide concentration at the end of glacials
λ	a^{-1}	decay constant
Λ_i	g cm^{-2}	attenuation length for fast neutron, fast or negative muons
P_i	atoms g^{-1} a^{-1}	Production rate for fast neutron, fast or negative muons
ρ_{ice}	g cm^{-3}	density of ice
ρ_r	g cm^{-3}	bulk density of rock
t_c	a	duration of glacial-interglacial cycles
t_{sp}	a	time since plucking
χ^2	-	chi-square value
z_{ice}	cm	thickness of ice
z_r	cm	thickness of joint block

ACKNOWLEDGMENTS

First and foremost I have to thank my supervisor John Gosse for his guidance and support over the last few years. It was at times a bumpy road, but it was our common interest in science which allowed us successfully navigating around all potholes. Everything I know about cosmogenic nuclide exposure dating I owe to John, but I have also grown as a person over the last few years thanks to his supervision. Equally, I would like to thank Art Dyke, who has introduced me to the incredible landscape of Cumberland Peninsula and opened my eyes for the rich history inscribed in glacial deposits, tors, felsenmeer, cirques and beaches of an area as large as my home country! Thank you for the extra bar of Coffee Crisp you always carried with you in the field.

My committee member, Lawrence Plug, was always available for discussion of data and modelling approaches throughout my time at Dalhousie University. Although it was not included in my thesis, I learned a great deal from Keith Taylor while working on experiments in the *in-situ* ^{14}C laboratory. I own a big thank you to Guang Yang, our laboratory supervisor, for her guidance and help inside and outside of the lab. Thank you for providing delicious homemade food when I was most in need of it.

I would like also to thank the faculty and staff at the Earth Science Department at Dalhousie University for their support and help whenever I needed it. Whether it was questions about administration or research, I always found someone who was willing to help. I especially would like to thank Martin Gibling, Barrie Clarke and Marcos Zentilli for their kind words and support during a difficult time and the common interest in classical music.

I have to thank my fellow graduate students at Dalhousie University for making sure that I left the concrete cube without windows - called office - from time to time. Particularly, I would like to thank Alan Hidy and Paul Mattern for their patience while teaching me the basics of Matlab; Léa Braschi, Gabe Creason, and Tom Lakeman, who brought a lot of life to the cosmo group and who became good friends over the last few years. Olivia, Sofie, Dawn, Konstanze, Julie, Niel, Joanna, Matthias, Louise, Carl, Holly, Alessandro, Kelsey, Omid, Jared, Fred, Zhihai, Janice, Harold, Tanya, Bertha, Kyle, Stefanie, Glenn, Sam, Jocelyn, Ricardo, Anne, Charlie, and anyone I forgot to mention, who made it very enjoyable to be a grad student at Dal.

I also would like to express gratitude to Christian Schlüchter, my former Diploma thesis advisor, who taught me to look through geological goggles in the first place and who ever since supported me throughout my diverse geological adventures; to the Quaternary Geology team at the Norwegian Geological Survey for their patience and encouragement while finishing my thesis, especially Ola Fredin and Alexandra Jarnà for their help and interest in landscape classification of Cumberland Peninsula.

Last but certainly not least, I would like to thank my family and partner for their support throughout this adventure, although they did not really understand why I had to go all the way to Canada for my PhD. My partner, Stefan, had to miss me for a far too long time and my siblings, Flurina and Armon, got married and had their first child while I was in Canada. I know that my dad is very proud of what a farmer's daughter has achieved, but I am equally proud of you how you managed and what you learned in the last year! Lastly, I need to thank my mom, who could not witness this thesis coming to completion, for all her love and support. I know you have helped me finish this thesis although you are not with us anymore: grazcha fich per tout cha tü as fat per nus!

CHAPTER 1 – Introduction

1.1 MOTIVATION

The last two and a half million years of Earth's climate history have had a major impact on the Arctic for two reasons. First, owing to the steepening of the latitudinal temperature gradient during ice ages, the Arctic has a much greater sensitivity to small changes in global climate (Cite Ballantyne 2010 Geology paper). Second, the Pleistocene glacier system has significantly altered the Arctic landscape, but in a complex way because of the different styles of glaciations (ice sheets, ice caps, and alpine systems). The implications of higher sensitivity and complex effects of glacierization range from complete repopulation of terrestrial biota in glaciated regions, intensification of topographic relief, and transfer of sediment to the ocean. To quantify these impacts of glaciation in the Arctic three datasets are needed: (i) maps with clear distinction of glacier style operating throughout the Arctic linked to regional paleoclimate through estimates of paleo-glacier mass balance, (ii) precise glacial chronologies linking advances, still-stands, and retreat rates to climate time series and other forcing mechanisms, and (iii) analyses of Quaternary erosion rates of valleys and summits from interior plateaus to coastal fiords. Thus, the motivation of this thesis is to evaluate the broad contributions of decades of previous Arctic studies and to provide new data for a representative Arctic region, to help inform societal policy in Arctic regions and offer the boundary conditions needed for the application of the new generation of sophisticated numerical landscape evolution models for the Arctic.

1.2 GLACIAL PROCESSES AND ARCTIC LANDSCAPE RESPONSE TO CLIMATE CHANGE

High-latitude regions are more susceptible to the currently ongoing change in global climate than any other region on earth (Serreze and Francis, 2006; Miller et al., 2010; Serreze and Barry, 2011). This sensitivity to climate change is not only exemplified by the significant reduction of sea ice (Nghiem et al., 2007; Stroeve et al., 2007; Wang and Overland, 2009), accelerated melting of glaciers and ice caps (Gardner et al., 2011; Nghiem et al., 2012), and increased thawing of permafrost (Payette et al., 2004; Lawrence and Slater, 2005; Plug et al., 2008), but also the effects of these changes on the ecosystems (Oechel et al., 1993; Hinzman et al., 2005; Post et al., 2009) and the local people (Berkes and Jolly, 2002), who rely largely on hunting and finishing. Through feedbacks within the coupled ice-ocean-atmosphere system (Curry et al., 1995; Serreze and Francis, 2006; Miller et al., 2012), changes in the Arctic may have profound global impacts (McGuire et al., 2006; Anisimov, 2007). One way to better understand these current and future changes in the Arctic is to improve our knowledge of past responses of glaciers and ice caps to climate perturbations.

Over the last million years, climate has periodically shifted from longer cold periods (glacials) to warmer intervals (interglacials) causing large changes in global glacier volume (Lisiecki and Raymo, 2005) and glacier dynamics in the Arctic. It has been shown that these climate shifts are primarily linked to changes in the Earth's orbit around the Sun (e.g., Huybers, 2006; Elderfield et al., 2012; Rial et al., 2013; Rybczynski et al., 2013). The resulting waxing and waning of glaciers and ice sheets led to an increase of erosion (Hallet et al., 1996; Glasser and Hall, 1997; Schaller et al., 2002) and consequent increase in sediment flux to adjacent ocean basins (Aksu and Piper, 1987;

Ottesen et al., 2009). However, whether Quaternary glaciations led to an increase of global erosion and sediment production is debated (Molnar, 2004; Willenbring and von Blanckenburg, 2010a; Hidy et al., 2014). Glacial erosion shaped the present landscape, likely exploiting a pre-existing drainage system (Sugden, 1978; Andrews and Miller, 1979; England, 1986). Deepening and widening of pre-existing valleys by glacial erosion is becoming better understood (e.g., Harbor and Wheeler, 1992; Harbor, 1995; Montgomery, 2002), and rates of active glacier erosion have either been directly measured (e.g., Briner and Swanson, 1998; Colgan et al., 2002; Staiger et al., 2005) or indirectly inferred from sediment volumes deposited in ocean basins during the Quaternary (e.g., Aksu and Piper, 1987; Dowdeswell et al., 2010; Steer et al., 2012). The basic processes governing glacial erosion have been assessed experimentally (Hallet, 1979, 1996) and with numerical models (MacGregor et al., 2009; Anderson, 2014). Feedbacks between glacial erosion and topography have been investigated (Marquette et al., 2004; Pelletier, 2004; Staiger et al., 2005; Stern et al., 2005; Briner et al., 2008; Kessler et al., 2008; Champagnac et al., 2014) and the correlation between climate, tectonic forcing and changes in topography due to glacial erosion have been debated (Molnar and England, 1990; Raymo and Ruddiman, 1992; Whipple et al., 1999; Montgomery et al., 2001; Grujic et al., 2006; Pelletier, 2008; Champagnac et al., 2012).

Despite these concerted contributions to our understanding of how climate controls the principle mechanisms, rates, and large-scale effects of glacial erosion and glacial dynamics, many processes in glacial geology have not yet been fully evaluated or quantified. The interaction of continental ice sheets with alpine glacier systems has not been investigated widely, particularly differences in response time to climate forcing

(Oerlemans and Fortuin, 1992). Although the surface area of the world's continental ice sheets is increasingly better known for the last and also previous glaciations (e.g., Dyke, 2004; Roy et al., 2004; Balco and Rovey, 2010; Hidy et al., 2013), the vertical extent of former ice sheets is less well constrained. The vertical extent of ice sheets has major implications for estimates of global glacier volume, ice dynamics and basal thermal conditions, as well as conceptual models for ice inception and evolution of ice sheets. For instance, two early opposing models were proposed for the inception and evolution of the Laurentide Ice Sheet (LIS) throughout the Quaternary (Flint, 1943; Ives, 1957). Numerical ice sheet models constrained by relative sea data have improved our understanding of ice flow and climate responses on a continental scale (e.g., ICE-5G, Peltier and Fairbanks, 2006; Simpson et al., 2009), but the relatively coarse resolution of these models make it difficult to test hypotheses of glacial geology at regional scales that are imperative for field geologists. These hypotheses regard the presence of ice-free enclaves for biologic refugia (Fernald, 1925; Belland and Brassard, 1988; Abbott et al., 2000; Waltari et al., 2004), the distribution of cold (frozen to substrate) and warm (wet, sliding) glacier basal thermal regime (Staiger et al., 2006), and the evolution of glacial landscapes through the Quaternary (Staiger et al., 2005; Briner et al., 2006). While the spatial distribution of the intensity of glacial erosion related to changes in basal thermal conditions has been investigated (Staiger et al., 2005; Briner et al., 2006), the long-term rate of glacial erosion under predominately cold-based conditions is not well constrained. In particular, rates of episodic erosion processes, such as sporadic plucking by cold-based ice, have been difficult to measure over the timescale of multiple glacial-interglacial

intervals, but may be a first-order control on the long-term landscape evolution of high latitude plateaus.

1.3 OBJECTIVES

This thesis aims to test different hypotheses regarding the origin and extent of ice cover in the eastern Canadian Arctic: (1) the instantaneous glacierization model (Ives, 1957; Ives et al., 1975) suggesting rapid expansion of permanent snowfields and plateau ice caps during snowline lowering, (2) the Nunatak Hypothesis (Ives, 1974; Ives et al., 1975) postulating that coastal summits remained ice-free during glaciations, (3) the Goldilocks model of intermediate ice sheet extent in the eastern Canadian Arctic (Miller et al., 2002), (4) the climate sensitivity idea suggesting that smaller glaciers respond faster to climate change than larger continental ice sheets (Oerlemans and Fortuin, 1992), and (5) the concept of selective linear erosion (Sugden, 1968, 1978) proposing enhanced glacial erosion by warm-based, sliding glaciers in fiords and valleys, while weakly erosive, cold-based ice protetcted upland plateaus.

1.3.1 General Thesis Objectives

In order to test these hypotheses, the following long-term objectives were proposed:

Objective 1: Establish a high-resolution record of Holocene glacier responses to regional or hemispheric atmospheric changes. While moraines provide evidence for *ice retreat*, records of *glacier advances* are difficult to establish on land in most regions. Furthermore, moraines are often obliterated by subsequent ice advances, so that they present an incomplete proxy for changes in glacier extent related to climate variation (Gibbons et al., 1984). Based on previous observations of preservation of fragile plant

remains beneath cold-based ice caps on Baffin Island (Falconer, 1966), the numerous thin plateau ice caps at various elevations on Cumberland Peninsula offer the potential of establishing a high-resolution record of ice cap expansion. The data allows testing of the hypothesis that small Arctic glaciers respond with sufficient sensitivity to record short-term climate perturbations caused by large volcanic eruptions proposed from contemporary work elsewhere on Baffin Island (Miller et al., 2012).

Objective 2: Examine the dynamics of different glacier types and test their sensitivity to late Pleistocene and Holocene climate change. By studying the interaction and retreat of LIS, polythermal alpine glaciers, and expanded local ice caps in an area where all three glacial styles coexist, it is possible to investigate differences in response to climate variation. The reconstruction of ice dynamics permits testing the hypothesis that small (alpine) glaciers respond more sensitively to climate change than larger (LIS) ice masses (Oerlemans and Fortuin, 1992).

Objective 3: Evaluate long-term rates of episodic erosion and determine the timing of last glacial plucking on upland plateaus. The timing of the last glacial plucking provides maximum-limiting constraint for the timing of ice coverage on plateaus in a historically well-scrutinized area, where the vertical extent of ice sheets has intensely been debated. Long-term rates of episodic erosion offer insights into landscape evolution on shorter timescales than provided by thermochronometry and establish the sources and rates of sediment-flux to the oceans.

1.4 RATIONALE FOR CHOSEN APPROACH

Cumberland Peninsula, the easternmost extent of Baffin Island, is an ideal location for these objectives because of the diversity of glacier type and basal thermal regimes, a rich history of glacial geology and geomorphology study by Europeans, Americans, and Canadians, and an opportunity of logistical support during two summer field seasons with the Geological Survey of Canada Geo-mapping for Energy and Minerals (GSC-GEM) program on Cumberland Peninsula. The short-term objectives required to attain the long-term goals outlined above are based on well-established and new geochronological techniques.

1.4.1 Short-Term Thesis Objectives

The short-term goals for General Objective 1 are: (1) Determine if bryophytes provide a reliable radiocarbon dating media for ice cap expansion and if they are affected by regrowth during intervening ice-free periods. (2) Test a hypothesis relating Little Ice Age glacier expansion to volcanism that was based on a bryophyte radiocarbon dataset in a different Arctic region (Miller et al., 2012) by determining if their bryophyte chronology is reproducible elsewhere. (3) Expand the existing record of glacier growth and decay further back in time to investigate the onset of renewed ice growth in the mid-Holocene.

The short-term goals for General Objective 2 are: (1) Provide new geochronological constraint for deglaciation in the interior of Cumberland Peninsula, Baffin Island, where previous age control was largely restricted to the coast. (2) Establish the paleo-flow pattern during the Last Glacial Maximum (LGM) and early deglaciation to examine complexities related to the interaction of an ice sheet and

associated marine-based ice stream with coalescent local fiord and alpine glaciers. (3) Map the deglaciation pattern of different glacier types (ice sheet, alpine glaciers, ice caps) at high-resolution throughout the Cumberland Peninsula to forecast past ice marginal positions throughout the region and establish patterns in retreat rates that can be compared to climate variation. (4) With new high-resolution maps of ice margins, reconstruct paleo-equilibrium line altitudes (ELA) for the entire peninsula at critical time periods (Heinrich Event 1, Younger Dryas, and Cockburn Moraine cooling event) to reveal the impact of local climate changes on the mass balance and dynamics of the three different glacier types.

The short-term goals for General Objective 3 are: (1) Develop a new approach to model complex cosmic ray exposure histories involving recurring burial by ice, gradual subaerial erosion, and episodic subglacial erosion. (2) Estimate the rate of episodic erosion by glacial quarrying and the timing of the last plucking event based on cosmogenic nuclides with a Monte Carlo method constrained by a proxy record of global ice volume change. (3) Associate the derived episodic erosion rates and timing of last plucking with local variation in bedrock characteristics and local and regional topography.

The following sections provide the rationale for using the chosen chronometers to address these objectives and the justification for returning to a well-studied location in the eastern Canadian Arctic.

1.4.2 Geochronometers

Radiocarbon dating is a well established and widely used geochronometer (Lowell, 1995; Guilderson et al., 2005), but in the Arctic it can only be applied scarcely, because typically only glacio-marine deposits are fossiliferous (e.g., Dyke, 1979). However, a unique archive of past climate change is preserved at the base of thin ice caps, which are frozen to the ground, thus protecting its substrate (Falconer, 1966; Carrara and Andrews, 1972; Miller et al., 2012). Delicate, sub-fossilized, in-situ rooted bryophytes and liverworts are currently being melted out along the rapidly receding margins of cold-based ice caps located on broad interfiord upland plateaus. Owing to the harsh environmental conditions on the wind-exposed plateaus, the fragile, weakly rooted material is quickly swept away destroying a unique record of former expansion of cold-based ice caps. The extraordinary warm summer temperatures in 2009 facilitated collection of organic matter at the margins of these ice caps for radiocarbon dating (*Chapter 2*) complementing only few previous studies (Anderson et al., 2008; Miller et al., 2012; Lowell et al., 2013; Miller et al., 2013b). Therefore, *Chapter 2* provides an independent dataset to test the results of previous studies in a different region of high-latitude North Atlantic coastal areas.

The scarcity of radiocarbon datable material in the Arctic and the short half-life of ^{14}C has limited the establishment of firm ages of glacial deposits. In many places, moraines and other glacial landforms have been correlated to each other by relative criteria based on cross-cutting relationships, geomorphic position, or differences in the degree of weathering of boulders and bedrock surfaces, and associated with global or regional climate records on the basis of these relative correlations. The glacial

stratigraphy can be better resolved with terrestrial cosmogenic nuclides (TCN, e.g., Lal, 1991; Gosse and Phillips, 2001). TCN analyses are widely applied to determine the age of surfaces or deposits using different approaches (e.g., depth profiles (Anderson et al., 1996; Braucher et al., 2009; Hidy et al., 2010) or burial dating (Nishiizumi et al., 1991; Granger and Muzikar, 2001; Hidy et al., 2013; Rybczynski et al., 2013)). They are also used to estimate average erosion rates (e.g., Lal, 1991; Nishiizumi et al., 1991; Briner and Swanson, 1998; Cockburn et al., 1999; Staiger et al., 2006; Belmont et al., 2007; Hidy et al., 2014). While in many glaciated regions (e.g., New Zealand, Schaefer et al., 2009) the TCN method provides the same precision as radiocarbon dating, in polar regions with cold-based glaciation, the lack of sufficient erosion to reset the cosmogenic nuclide clock causes exposure dating to overestimate the actual age. Nevertheless, in the absence of suitable material for radiocarbon and other Quaternary dating methods, it is the only technique available to help fill the gap of glacial chronology in interior regions.

Different TCN techniques are used in *Chapter 3* to constrain the deglaciation history of the LIS, the expanded Penny Ice Cap (PIC), and independent, polythermal alpine glaciers, thus broadening the previously available age control to the interior of Cumberland Peninsula. The new and previously published age constraints are then combined with a high-resolution map of ice margin positions to derive a conceptual model of glaciation of Cumberland Peninsula. The dynamics of different ice masses are assessed for three different phases during deglaciation in response to late glacial and early Holocene climate change. Reconstruction of paleo-ELA at the three different time intervals reveal the change in environmental conditions during deglaciation.

Despite the significant advances in TCN dating over the last few decades, the assessment of former coverage by cold-based ice is still ambiguous in eastern Arctic Canada (e.g., Steig et al., 1998; Bierman et al., 1999; Marquette et al., 2004; Staiger et al., 2005; Gosse et al., 2006). While the former existence of cold-based ice coverage can be revealed by measuring two radionuclides with differing decay rates (Nishiizumi et al., 1991; Bierman et al., 1999; Gosse et al., 2006), the duration and timing of individual burial events cannot be resolved. Tors are prominent outcrops of weathered bedrock protruding through felsenmeer, regolith or till cover, which have been attributed to differential weathering during warmer pre-Quaternary climate and preservation under predominately cold-based ice (e.g., Stroeven et al., 2002; Gosse et al., 2006; Goodfellow et al., 2014). Besides coverage by cold-based ice, tors are also affected by gradual subaerial and episodic subglacial erosion. *Chapter 4* presents a new TCN approach, which is used to quantify the timing and rate of sporadic plucking of weathered bedrock block. Constrained by a proxy for global ice volume (Lisiecki and Raymo, 2005), a Monte Carlo method computes complex histories of exposure, burial, and episodic plucking events to derive probability density functions of average ice-free time, total duration of complex exposure history, gradual subaerial erosion rates and, most significantly, episodic erosion rates by glacial plucking. Timing and rates of episodic erosion events have been difficult to determine (Macchiaroli, 1995; Phillips et al., 2006; Jansen et al., 2013; Fujioka et al., 2015); *Chapter 4* thus presents a valuable contribution in understanding episodic erosion processes, particularly on weathered plateaus that have often been assumed to represent relict, ancient landscapes.

1.4.3 Study Area

The GSC-GEM project provided the logistical and financial support for fieldwork during two summers (2009 and 2010) on Cumberland Peninsula. Mineral exploration in Arctic regions is confronted with high risks, one of which are meagre knowledge of bedrock geology in remote glacier- and drift-covered regions and limited information about past ice-flow directions that would allow tracing anomalies in till geochemistry to their source. A second risk regards the difficulty in establishing the Cenozoic sediment flux to basins with petroleum potential such as Baffin Bay. An improved knowledge of sediment flux to the oceans will provide essential constraints for basin models simulating the reservoirs and maturing history of potential hydrocarbon sources. The helicopter support provided by the GSC-GEM project facilitated sample collection for this thesis throughout the high-latitude mountainous region with a relief similar to the Alps, hence enabling access to glacier margins and glacial deposits in the interior of the peninsula, as well as on upland plateaus (Fig. 1.1a). The diverse landscapes and rich assemblage of glacial deposits on Cumberland Peninsula have previously been studied to understand the increase of weathering degree with altitude (Boyer and Pheasant, 1974; Birkeland, 1978; Watts, 1979), to decipher the dynamics of ice cover (Miller, 1973; Dyke, 1979; Locke, 1987; Steig et al., 1998; Marsella et al., 2000), and to investigate the spatial variation of glacial erosion (Andrews and Dugdale, 1971; Sugden and Watts, 1977; Anderson, 1978; Bierman et al., 1999; Kaplan et al., 2001).

The previous research on Cumberland Peninsula provided the foundation for many theoretical models of glacier dynamics and basal thermal conditions. These models include the concept of selective linear erosion by polythermal ice cover (Sugden and

Watts, 1977; Sugden, 1978) or the notion of attitudinally distinct zonation of weathering degree (Ives, 1966; Boyer and Pheasant, 1974; Ives, 1975; Dyke, 1979). Recognition of glacial modification of tors on the northeastern coast of Cumberland Peninsula led Sugden and Watts (1977) to propose that the area had been selectively eroded with enhanced erosion occurring in troughs, which were occupied by sliding, warm-based outlet glaciers, and restricted erosion on upland plateaus that were protected beneath thin, cold-based ice caps. The increase of weathering degree of bedrock surfaces and boulders with altitude was either interpreted to indicate longer duration of subaerial exposure (Boyer and Pheasant, 1974; Dyke, 1979; Watts, 1979) or, alternatively, interpreted to signify non-uniform glacial erosion related to basal thermal conditions of the former ice cover (Sugden, 1968; 1978 Sugden and Watts, 1977). The differing interpretations of altitudinal weathering zones had implications for models of the extent of the LIS in the eastern Canadian Arctic. Longer subaerial exposure at higher elevations was related to successively more restricted ice cover, thus supporting a minimum ice sheet model for the last glaciation (Fig. 1.1b, Ives, 1978). This minimum model challenged a previous, widely accepted maximum model postulating an enormous LIS completely covered Cumberland Peninsula (and other coastal areas on Baffin Island) and extended onto the continental shelf (Flint, 1943). In contrast to the maximum model, the minimum ice sheet paradigm suggested that many high-elevation areas had never been ice covered, and thus may have served as refugia for biota during glacial intervals (evident from disjunct species populations, Fernald, 1925; Belland and Brassard, 1988; Abbott et al., 2000; Waltari et al., 2004). Evidence for more extensive ice in fiords and tributary valleys emerged from TCN dating of boulders and bedrock, which was reconciled with

indications of ice-free conditions on intervening plateaus by a newly proposed intermediate ice sheet model (Fig. 1.1b). The so-called Goldilocks model proposes that low-gradient, warm-based outlet glaciers occupied fiords and valleys, while plateaus remained ice-free along the coast and were covered by thin, cold-based ice caps further inland (Miller et al., 2002).

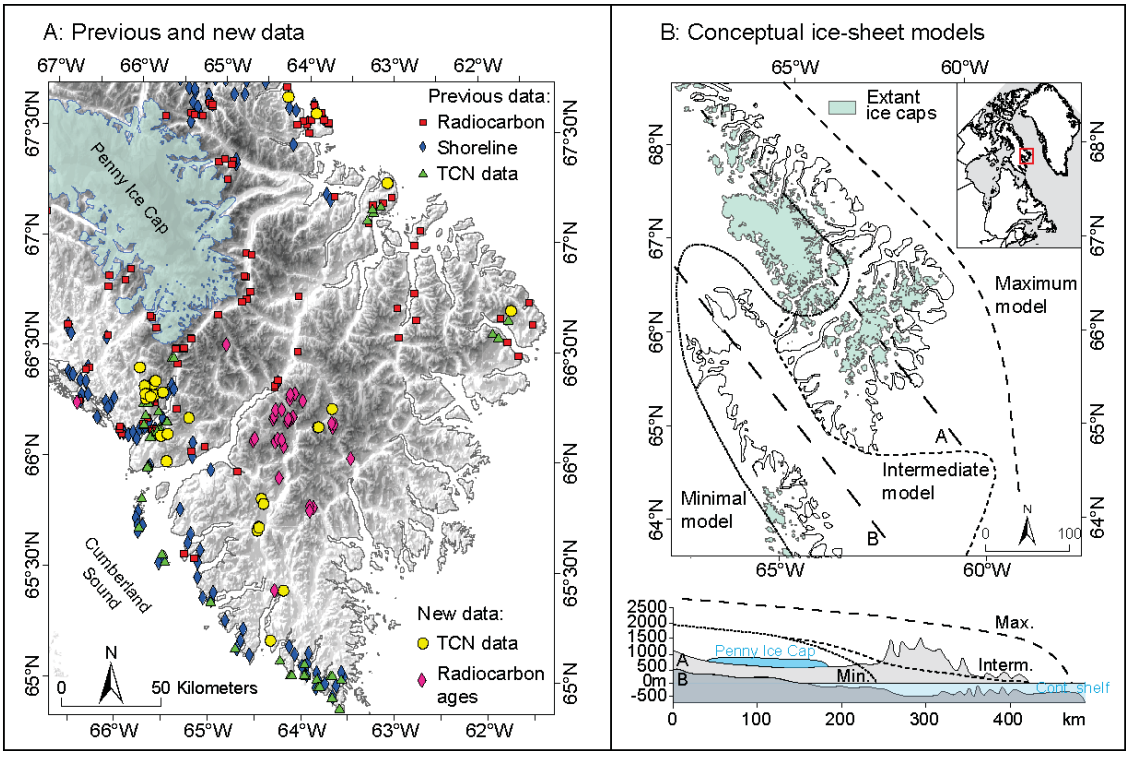

Fig. 1.1 Location of Cumberland Peninsula in Eastern Canadian Arctic and sites of previous glacial research. **A.** Digital elevation map of Cumberland Peninsula displaying the location of previous and new glacial geochronology. **B.** Schematic illustration of the three major conceptual ice-sheet models: Maximum model (Flint, 1943), Intermediate model (Miller et al., 2002), and Minimal model (Ives, 1978). Red box in inset shows location of Cumberland Peninsula in northeastern Canada. Approximate locations of elevation-profiles A and B for the vertical section are indicated with dashed lines. Vertical cross-section showing two elevation-profiles is adapted from (Miller et al., 2002).

1.5 ORGANISATION OF THESIS

In *Chapter 2*, the most recent history of renewed ice cap growth following the early to middle Holocene climate optimum is investigated by radiocarbon dating of bryophytes and faunal fossils collected within a metre of rapidly receding cold-based ice caps (Objective 1). The radiocarbon ages indicate when the organic material was covered by the expanding ice cap providing a distinctive measure of deteriorating climate conditions in the Arctic. The age distribution reveals discrete phases of ice cap growth that are shown to be related to both lower solar activity and decreased air temperatures associated with multiple successive volcanic eruptions. The striking similarity of the presented age distribution with previous data suggests that the climate change was at least of regional extent, if not globally significant. The manuscript of *Chapter 2* has been published in *Quaternary Science Reviews* (May 2014).

The interaction of three different glacier systems that influenced Cumberland Peninsula is unraveled by detailed mapping of moraines and meltwater channels throughout the peninsula (Dyke, 2011a-f; 2013a-c). The conceptual model of ice cover and paleo-ice flow at LGM is presented in *Chapter 3* (Objective 2). New glacial chronology is obtained from TCN exposure ages of boulders collected on selected moraines and near meltwater channels that record a continuous retreat sequence in a major alpine valley from the southwestern coast to the interior of the peninsula. The interaction of LIS and local fiord ice is investigated in a valley, in which a lake was concurrently dammed by outlet glaciers of both ice masses. The new chronological control is combined with previous data to derive the retreat pattern of the polythermal alpine glacier system based on the high-resolution map of ice margin positions. From

maps of ice extent during three distinct readvance phases (Heinrich Event 1, Younger Dryas and Cockburn-equivalent), retreat rates are inferred for independent alpine outlet glaciers, outlet glaciers of the PIC, and the land-based LIS. The dynamics of the different glacier types are compared with climate variability during deglaciation. Changes in paleo-ELA reveal the variation of environmental conditions during the late Pleistocene and early Holocene. Additionally, a TCN depth profile is used to resolve a middle Wisconsinan radiocarbon age from a mollusc shell, which was in disagreement with the morphostratigraphic correlation of the marine delta. The manuscript of *Chapter 3* is currently being prepared for submission to *Quaternary Research*.

In *Chapter 4,* the rate of episodic erosion and the timing of last plucking are determined for tors on weathered upland plateaus (Objective 3). The rate of episodic erosion has been difficult to estimate, although it might be significantly higher than gradual erosion rates (Small et al., 1997; Muzikar, 2008, 2009). Estimating the total depth of glacial erosion of upland plateaus during the Quaternary is important, because even low erosion rates may contribute significantly to the sediment flux to the adjacent oceans, owing to the relatively large surface area of the plateaus (Dowdeswell et al., 2010; Steer et al., 2012). The new approach presented in *Chapter 4* has been developed to reduce the degrees of freedom in a complex system of alternating exposure intervals with subaerial gradual erosion and burial intervals with gradual or episodic subglacial erosion. Reduction of degrees of freedom is achieved by measuring the concentration of two radioisotopes with differing decay rates (^{10}Be, $t_{½}$ = 1.38 Ma and ^{26}Al, $t_{½}$ = 0.72 Ma) in adjacent plucked and not-recently plucked surfaces. The timing of plucking can be constrained using three different depth functions (concentrations of both ^{10}Be and ^{26}Al,

plus their relative abundances $^{26}Al/^{10}Be$). Long-term rates of episodic plucking of weathered bedrock blocks are determined with a Monte Carlo method that computes complex exposure histories constrained with a proxy record of global ice volume. Variation of episodic erosion rates is shown to be associated with both the location of the sampled tor in the landscape and local differences in fracture spacing of the bedrock. The results of *Chapter 4* suggest that weathered plateaus are lowered by a slow rate (1 - 8 mm ka^{-1}), which is a magnitude lower than in adjacent, glacially-deepened valleys, but that the contribution to the sediment flux to the oceans cannot be neglected owing to the relative large surface area of high-elevation interfluves. A manuscript of this chapter is being prepared for submission to *Quaternary Science Reviews*.

The major contributions and implications of all manuscripts are summarized in *Chapter 5*. In light of the new data presented in this thesis, previous glacial geology and geomorphology work on Cumberland Peninsula is reviewed. Future research directions are discussed, which propose numerical modelling of late Wisconsinan ice dynamics on Baffin Island constrained by the new data presented in this thesis. Second, a strategy is presented to constrain the timing of regolith stripping from upland plateaus. Finally, the long-term evolution of the landscape of Cumberland Peninsula is considered with discussion of an approach to classify fragments of old surfaces from digital elevation models. Reconstruction of the former topography and improved understanding of the formation of, for instance, glacial cirques throughout the Quaternary would shed light onto the evolution of the current alpine landscape on Cumberland Peninsula.

The appendices include the methodological and chemical details of all chemistry and AMS experiments, so that they may be appropriately reproduced. They contain all of

the information required to recalculate the exposure ages, as TCN production rates and scaling routines are updated and nuclear cross-sections and half-lives are revised. Complete code scripts and selected modeling outputs are included to supplement the outputs provided in the manuscripts. Also included in the appendices are additional field photos and graphics that provide information for specific locations that were sampled or studied. The electronic supplementary file constrains a hand-coloured map of ice margin positions during deglaciation, which were inferred from a high-resolution map of ice margins derived from airphoto interpretation combined with new and previous geochronological constraint in the interior and along the coast.

CHAPTER 2 - Neoglacial Ice Expansion and Late Holocene Cold-Based Ice Cap Dynamics on Cumberland Peninsula, Baffin Island, Arctic Canada

Paper published in *Quaternary Science Review*, doi: 10.1016/j.quascirev.2014.02.005

Annina Margreth[1*], Arthur S. Dyke[2], John C. Gosse[1], Alice M. Telka[3]

[1]Department of Earth Sciences, Dalhousie University, Halifax, Nova Scotia B3H 4R2, Canada

[2]Geological Survey of Canada, 601 Booth Street, Ottawa, Ontario K1A 0E8, Canada

[3]PALEOTEC Services, Ottawa, Ontario, Canada

2.1 ABSTRACT

Radiocarbon dating of fossil flora and fauna collected along receding cold-based ice caps and cold-based sections of polythermal glaciers on Cumberland Peninsula reveal insights into Neoglacial ice expansion and late Holocene ice dynamics. The taphonomic advantages of subfossilized moss were exploited to precisely document regional expansions of ice caps through the late Holocene. When compared with climate proxies and records of volcanic eruptions, the moss radiocarbon age distributions indicate i) onset of Neoglaciation shortly after 5 ka, concomitant with increased sea ice cover, ii) intensification of ice expansion between 1.9 – 1.1 ka, followed by halt of ice growth, or ice recession during the Medieval Warm Period, and iii) renewed ice expansion after 0.8 ka, in response to cooling related to a combination of large volcanic eruptions and low solar activity. Overall, the observations support a model of near-instantaneous glacial response to regional climate controls and that these responses were synchronous throughout eastern Canadian Arctic and possibly eastern Greenland.

[*]Corresponding author: Email address: annina.margreth@dal.ca

2.2 INTRODUCTION

Small ice caps provide a useful archive of local paleoclimate because they are more responsive than larger, more sluggish and complex ice sheets or alpine glacier compounds (Paterson, 1994). Subfossil plant material collected in growth position along the margins of receding, small, cold-based ice caps provide a high-resolution record of ice cap expansion phases. Anderson et al. (2008) and Miller et al. (2012) associated the distribution of radiocarbon ages of moss collected from similar ice margins in northern Baffin Island (Fig. 2.1a) with decreases in solar irradiance and the impact of large volcanic eruptions. Miller et al. (2012) observed non-cyclic, sub-millennial, high-amplitude signals in their summed probability distribution of calibrated radiocarbon ages, and hypothesized that individual pulses of ice cap expansion during the Little Ice Age (LIA, AD 1100-1850, 750-100 yr BP, where yr BP refers to years before AD 1950) were triggered by large volcanic eruptions and concomitant positive sea-ice climate feedbacks.

To independently test the hypothesis proposed by Miller et al. (2012) that volcanism, solar irradiance, sea ice variability, and changes in regional atmospheric and paleoceanographic circulation are collectively the dominant primary controls on glacial responses in the eastern Canadian Arctic, we collected relict organic material along cold-based ice caps in a different region of Baffin Island (Cumberland Peninsula, Fig. 2.1). The new subfossil flora and fauna radiocarbon chronologies document the time of ice expansion from margins that were at least as retracted as they are today. Subfossilized, weakly rooted bryophytes are rapidly comminuted by winds and precipitation once uncovered by the receding ice margin. Therefore mosses are unlikely to be reworked. Unlike moraines which mark times of glacial maxima or retreat, recently exhumed

subfossil bryophytes provide precise maximum-limiting ages of ice cap expansion at that location. Our results support the hypothesis of Miller et al. (2012) and further reveal that late Holocene cold-based ice cap growth is in phase with both the general decrease in insolation and higher frequency (decadal- to century-scale) climate perturbations over the eastern Canadian Arctic. We also demonstrate the advantage of using subfossil plant materials which can be found in growth position and survive for only a few summers owing to their vulnerability to erosional processes once exhumed from cold-based glacial cover.

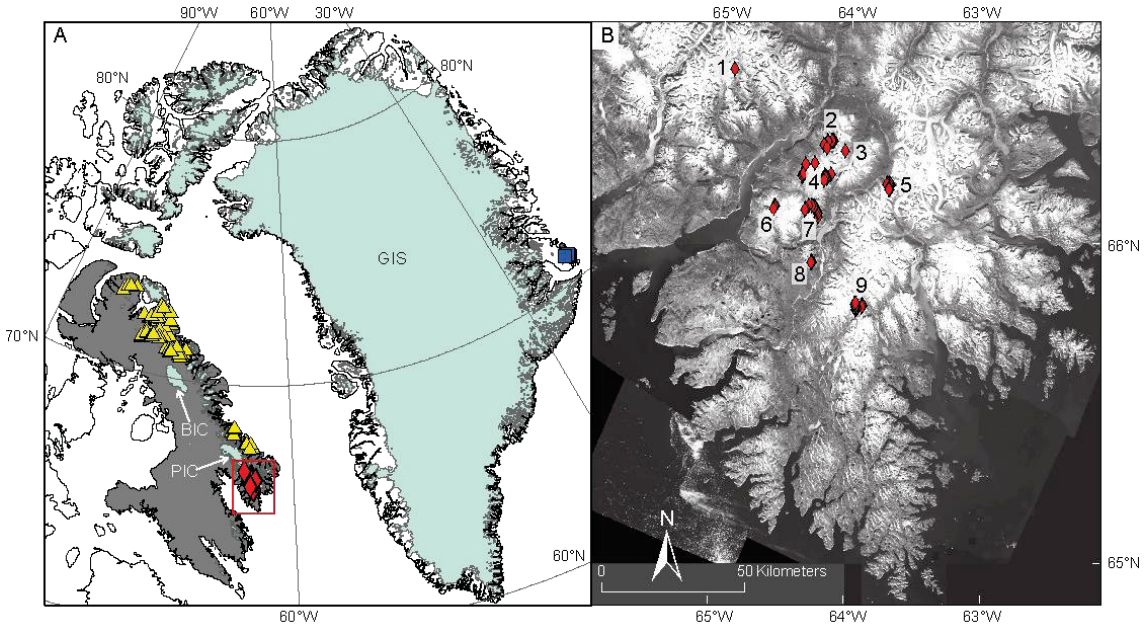

Fig. 2.1. A. Baffin Island and Greenland with locations of previous radiocarbon dates on fossil vegetation and new samples on Cumberland Peninsula: Anderson et al. (2008), Miller et al. (2012; 2013b) yellow triangle, Lowell et al. (2013) blue square, this study red diamond. GIS = Greenland Ice Sheet, BIC = Barnes Ice Cap, PIC = Penny Ice Cap. **B.** Southern part of Cumberland Peninsula with location of radiocarbon dated relict flora and fauna, collected along nine individual ice caps marked with red diamonds.

2.3 BACKGROUND

The uncovering of subfossilized flora from under a receding cold-based glacier has been previously documented in the Canadian Arctic (Falconer, 1966; Carrara and Andrews, 1972; Anderson et al., 2008; Miller et al., 2012). If the flora died as a result of ice cover, its chronology is related to the growth of the ice cap that entombed it. The chronological record of glacial advances can be further optimized by selecting flora that have a low probability of survival once re-exposed by a retreating ice margin. Delicate, in situ, rooted bryophytes on wind-swept, stony, polar desert sites have minimal preservation potential when uncovered. This taphonomic advantage avoids the drawbacks related to reworking of the fossil material, which is common for woody plants or faunal remains. In some instances, other flora (leaves, branches) or fauna (caribou bones, antler, and hides) are preserved, but the cause of death and the association with a precise contemporaneous ice margin position is usually undeterminable.

Areas with restricted lichen and other plant growth—recognized from aerial photos and in the field by their relatively light-tone—were interpreted to delimit the extent of permanent snow and ice cover during the last few centuries (Ives, 1962; Falconer, 1966; Carrara and Andrews, 1972). The absence of evidence for glacial erosion and subglacial drainage suggested that the ice caps were cold-based (Ives, 1962). The protective nature of cold-based glaciers was further revealed by the emergence of undisturbed patterned ground underneath a rapidly receding ice cap in northern Baffin Island (Tiger Ice Cap, 71° 20’ N, 78° 45’ W), where patches of dead moss were found near the ice margin (Falconer, 1966). A radiocarbon age of 330 ± 75 years (I-1204, uncalibrated, on *Polytrichum juniperinum* moss fragments; Falconer, 1966) suggested more widespread ice cover than today, which was corroborated by a similar radiocarbon age of 330 ± 90

years (Gak-3099, uncalibrated) on fossil moss and lichen collected below a lichen-kill trimline immediately in front of the Boas Glacier on Cumberland Peninsula (Carrara and Andrews, 1972).

Over the following decades, increasing evidence for more extensive LIA ice caps was found throughout the eastern Canadian Arctic (Andrews et al., 1976a; Locke and Locke, 1977; Williams, 1978). The light-toned areas were more precisely attributed to erosion of dead lichen, killed under permanent snow cover associated with the LIA. The previous ice margin positions, as observed in the field and from remotely sensed imagery (Fig. 2.2, Wolken et al., 2008) reveal that the LIA glaciation threshold and paleo-ELA were 200 – 300 m lower than present. Lowering of the ELA was attributed to reduction of the mean summer temperature by 1 - 3 °C (Locke and Locke, 1977; Williams, 1978).

In recent years, systematic sampling of moss emerging from receding cold-based ice caps has shown that widespread ice cap expansion occurred at 670 yr BP and intensified 500 years ago (Anderson et al., 2008; Miller et al., 2012). An absence of moss ages between 950 and 700 yr BP was interpreted to be related to reduced ice cover during the Medieval Warm Period (MWP, AD 950 – 1250, 1000 – 700 yr BP), known as a period of milder climate in Europe and elsewhere (Lamb, 1965; Bradley et al., 2003; Mann et al., 2009). Note that the interpretation of gaps in the moss chronology is an indication of lack of ice cover to kill the moss, *not* that there were no mosses living because of ice cover. This assumption can only be tested by showing (i) that there is independent evidence of warming or moisture-starvation during the moss age gaps, and (ii) that the gaps occur elsewhere in the region and are not just a local phenomena related to glacial dynamics. Individual peaks in the moss age probability distribution coincide

with large volcanic aerosol loading in the stratosphere, as well as reduced solar irradiance causing summer cooling and initiating ice cap expansion (Anderson et al., 2008). Simulations using global circulation models suggested that sea-ice and oceanic feedback systems sustained the initial cooling caused by shielding of solar radiance through stratospheric volcanic sulfur loadings (Miller et al., 2012). Thus, the main contribution of this work is to obtain an independent record from Anderson et al. (2008) and Miller et al. (2012, our sites are more than 600 km from most of theirs).

2.4 METHODS

2.4.1 Field Methodology

The southwestern part of Cumberland Peninsula is characterized by weathered upland plateaus intersected by glacially eroded valleys and fiords. The plateaus range in elevation from 400 to 900 m above sea level (asl) at the southwestern coast, increase to 1200 - 1900 m asl at the Penny Ice Cap and decrease again to 300 – 600 m asl toward the northwestern coast. Dyke et al. (1982) described in detail the major landforms and landscape elements of the region; five surficial maps at a scale of 1:100,000 (Dyke, 2011a-f) established new insights into the history of Holocene deglaciation. The extent of Neoglacial polythermal ice cover is defined by moraines along previous margins of warm-based ice lobes, and lichen-kill zones along previous cold-based ice margins. Margins of extant cold-based and polythermal plateau ice caps are indicated for AD 1958, mapped from air photos, superimposed by the marginal position at AD 2009, mapped from satellite images (Fig. 2.2). Besides plateau ice caps, the region exhibits other types of glacial systems including warm-based outlet glaciers descending from the plateaus and small cirque glaciers. The largest extant glacier is the Penny Ice Cap which

covers 6000 km^2 of Auyuittuq National Park. Ice from the north-easternmost extent of the Wisconsinan Laurentide Ice Sheet is preserved at the base of the Penny Ice Cap (Fisher et al., 1998).

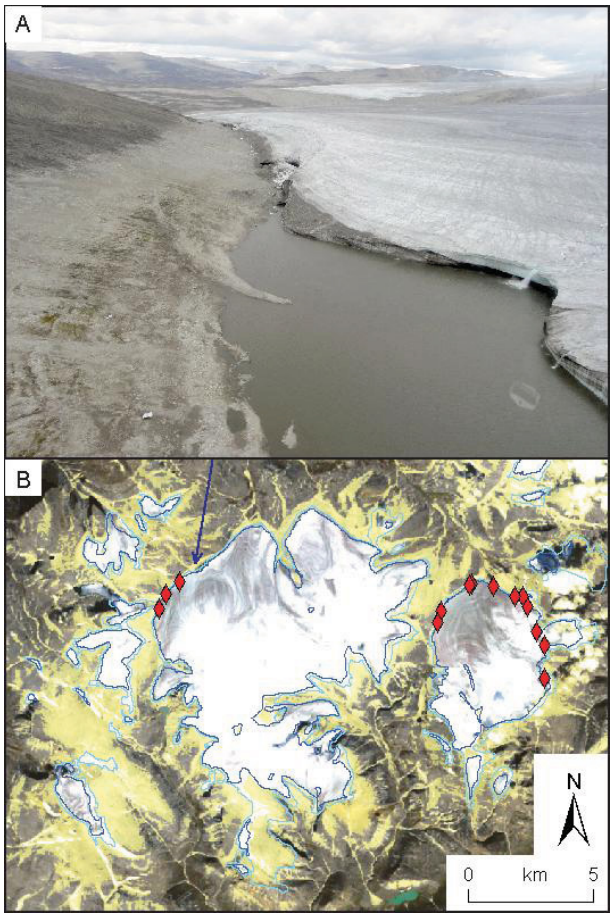

Fig. 2.2. A. Light-toned lichen kill zone surrounding cold-based ice cap on Cumberland Peninsula. Lichen kill zone in the picture is approximately 250 m wide. Note the sharp trimline between the lichen-free area and the dark outside area with mature lichen cover. Location of picture is indicated by blue arrow in map below. **B.** Lichen-kill map derived from satellite imagery showing the ice cap extent AD 2009 in blue and the ice margin mapped from air photos from AD 1958 in light blue. Red diamonds mark location of fossil vegetation collected around two of the shown cold-based ice caps (number 6 and 7 in Fig. 2.1b and Fig. 2.3). Lichen-kill zones, shown in yellow, have been mapped by classifying high reflectance areas on Landsat 7 images after elimination of ice, water, and vegetation through thresholding respective sensitive bands.

Nine cold-based ice caps or cold-based zones of polythermal ice caps were targeted for sampling of recently emerged subfossil organic matter (Fig. 2.3). We chose ice caps at different elevations and of different sizes to examine the topographic influence on ELA lowering and the regional extent of ice expansion in response to climate deterioration.

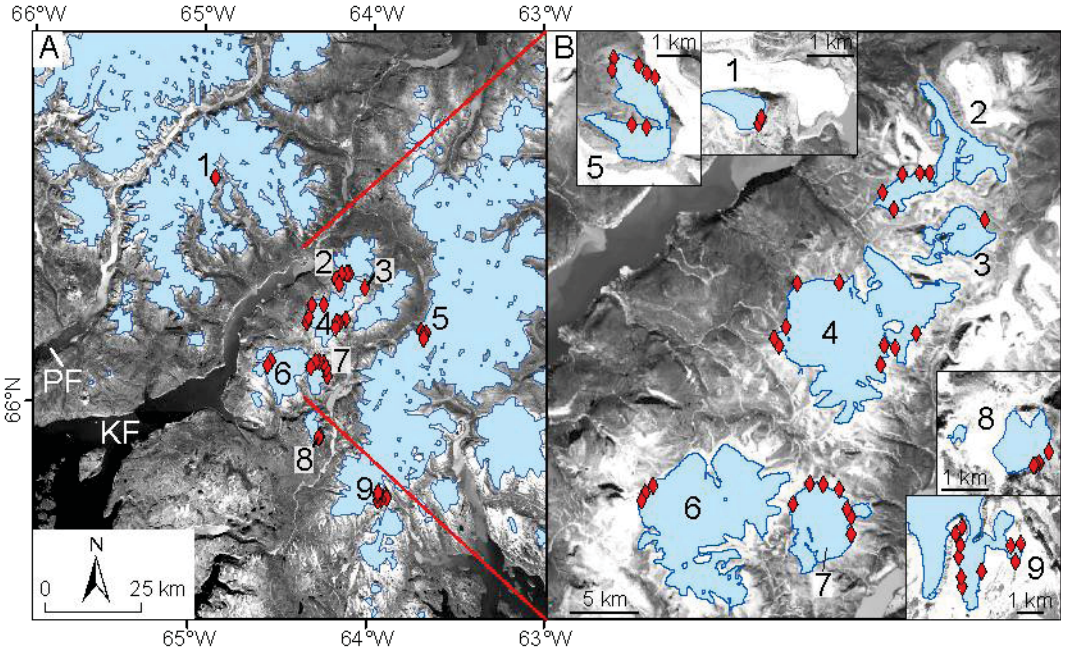

Fig. 2.3. Sample sites on Cumberland Peninsula from nine different ice caps. **A.** Overview of all sample sites at the head of Kingnait Fiord (KF); extant ice cover is shown in blue, PF = Pangnirtung Fiord. **B.** Enlargement of central part of map shown in A, and inset maps of smaller peripheral ice caps with ice margins from AD 2009.

Samples of in situ rooted dead moss (typically hand-sized clumps) and other fossil vegetation were collected during transects along ice cap margins (Fig. 2.4). We examined most closely the recently deglaciated zone within 1 m of the ice margin. Each sample was inspected for modern plant growth or re-growth, water and sediment were gently removed, and samples were placed into an air-tight Ziploc freezer bag and kept in a freezer before and after shipment from the field.

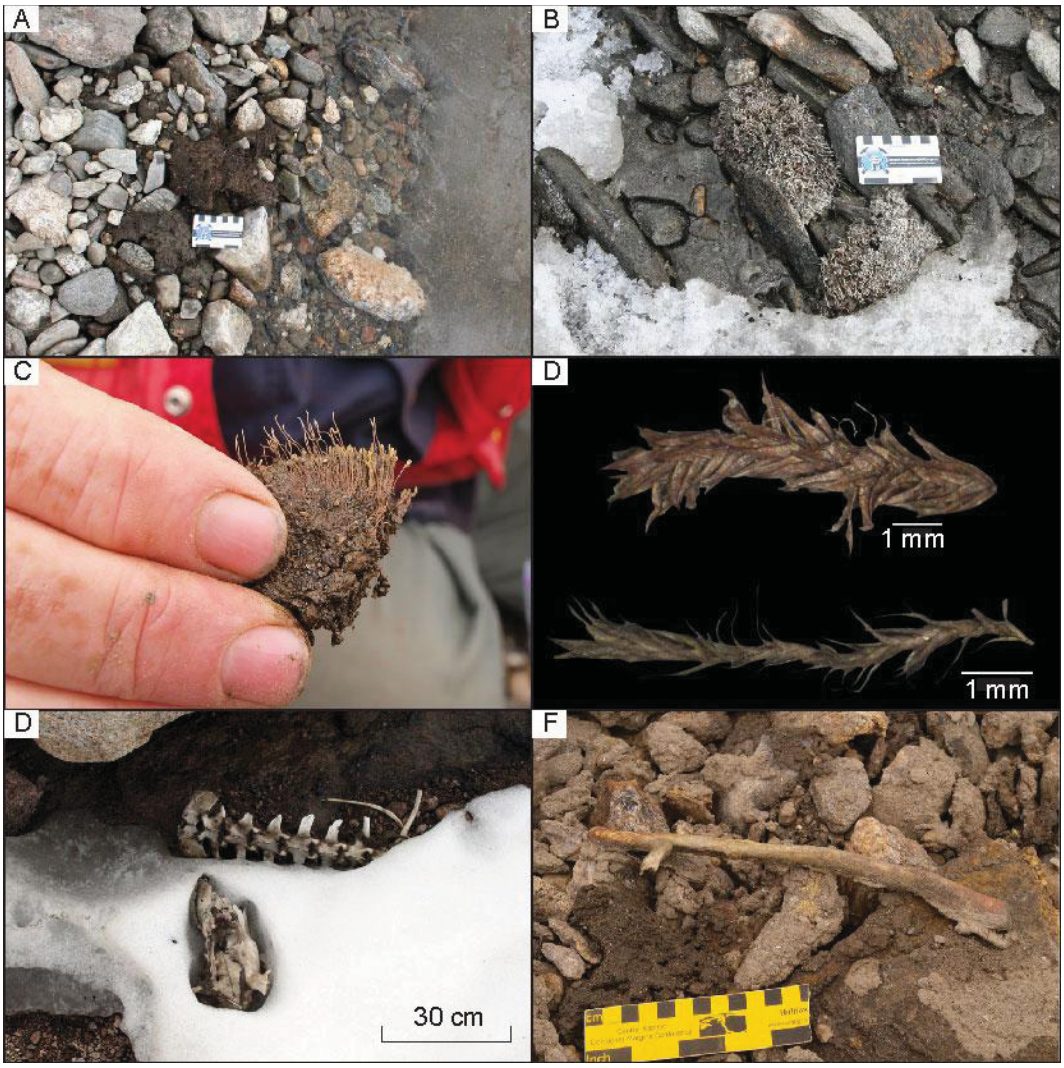

Fig. 2.4. Preservation of fossil flora and fauna beneath receding cold based ice-caps. **A.** and **B.** Moss (samples 09SRB-K085A-01 and 09SRB-K057A-01, respectively) found in-situ on soil and gravel within 5-10 cm of the current ice margin (pictures: K. Kosar). **C.** Detail of a collected moss clump (09SRB-A387A-01, UCIAMS-77686, mode 1.56 ka, Table 2.1). **D.** Moss fragments of two samples submitted for AMS radiocarbon analysis above: *Racomitrium lanuginosum* (UCIAMS 77695, mode 0.17 ka), below *Andreaea blyttii* (UCIAMS 83969, mode 3.24 ka). **E.** Remains of a caribou backbone and skull (09SRB-A266A-01, UCIAMS-78110, mode 3.24 ka) emerging beneath a retreating ice margin (picture: K. Kosar). **F.** Caribou antler and organic material (09SRB-A383A-01, UCIAMS-78111, mode 1.7 ka) found within 1m of extant ice margin.

2.4.2 Sample Characterization and Analysis

In total, 64 organic samples were collected in the field and afterwards characterized and separated according to the type of material. Isolation of macrofossils followed standard procedures of wet sieving in water using Canadian Standard Tyler series sieves with mesh openings of 0.85 mm (20 mesh) and 0.425 mm (40 mesh). All material greater than 0.425 mm was examined using a binocular microscope. The coarse organic residue (>0.85 mm) comprised a tangled mass of a few types of mosses and liverworts, interspersed with lichens. For each sample, mosses and liverworts were separated microscopically and placed in containers according to type. Some of the dated mosses and liverworts were identified by fossil bryologist Jan Janssens, Lambda-Max Ecological Research, Minneapolis, Minnesota and by bryologist Jennifer Doubt, Canadian Museum of Nature, Ottawa. Monospecific plant fragments or individual, similarly preserved moss and liverwort macrofossils were selected for dating. In preparation for dating, all rhizoids (roots) were removed. Fifty macrofossil sub-samples comprising tundra mosses (44), liverworts (3), rooted wood rush (*Luzula* sp.) (1), snowbed willow leaves (*Salix herbacea*) (2) and three fossil sub-samples of caribou (bone, antler and molar) were radiocarbon dated (Table 2.1). Twenty-six macrofossils were further analyzed with eleven species of mosses and one species of liverwort identified (Table 2.2).

Table 2.1. *(Next page)* Details of all radiocarbon dated samples. Calibration of conventional ^{14}C ages was done with the downloaded version of the Calib 6.1.0 program (Stuiver and Reimer, 1993) using the Northern Hemisphere IntCal09 curve (Reimer et al., 2009). Calibrated ages are given for full age ranges including multiple individual age ranges. Median and mode are based on the probability distribution function. Ages are given as ka or as before AD 1950. Last column indicates the affiliation of each sample to an age group discussed in the text: Group 1 = 4.7 – 3.3 ka, Group 2 = 1.9 – 1.2 ka, and Group 3 = 0.74 – 0.17 ka.

Ice cap	Sample No.	Lat.	Long.	Elevation	Organic material used for radiocarbon dating	Distance from ice margin	UCI AMS No.	$\delta^{13}C$	conventional ^{14}C age (1σ error)	calibrated ^{14}C age 1σ range	2σ range	median probability	modal probability	Age group
		d.d	d.d	m asl		cm		‰	a	a	a	ka	ka	
1	09SRB-A266A-01	66.54	-64.92	1469	caribou molar	0	78110	-20.5 ± 0.1	3015 ± 25	3164 - 3318	3082 - 3333	3.23	3.24	1
	09SRB-A265A-01	66.54	-64.92	1461	tundra moss	200	83969	-17.1 ± 0.1	3385 ± 20	3588 - 3642	3577 - 3689	3.63	3.64	1
2	09SRB-Q013A-01	66.29	-64.04	1000	caribou bone		78112	-19.7 ± 0.1	385 ± 25	335 - 501	324 - 506	0.46	0.48	3
3	09SRB-K082A-01	66.32	-64.14	1419	tundra moss	100	83979	-24.7 ± 0.1	1280 ± 20	1182 - 1266	1178 - 1275	1.23	1.20	2
	09SRB-K080A-01	66.32	-64.13	1514	liverwort	30	83977	-24.9 ± 0.1	1290 ± 20	1184 - 1274	1178 - 1282	1.24	1.20	2
	09SRB-K086A-01	66.30	-64.19	1115	liverwort	5	83980	-23.7 ± 0.1	1705 ± 20	1565 - 1687	1548 - 1693	1.61	1.58	2
	09SRB-K081A-01	66.32	-64.14	1423	tundra moss	30	83978	-19.5 ± 0.1	1735 ± 20	1613 - 1694	1569 - 1706	1.65	1.66	2
4	09SRB-K049A-01	66.25	-64.34	892	tundra moss	<50	77694	-26.7 ± 0.1	-1860 ± 20					
	09SRB-K051A-01	66.25	-64.27	1045	tundra moss	<50	77695	-22.1 ± 0.1	185 ± 20	-1 - 284	-2 - 287	0.18	0.17	3
	09SRB-K047A-01	66.22	-64.37	959	rooted wood rush	<50	77693	-26.2 ± 0.1	165 ± 25	-1 - 281	-2 - 285	0.18	0.20	3
	09SRB-K048A-01	66.22	-64.36	998	tundra moss	<50	118700	-26.2 ± 0.1	165 ± 15	-1 - 275	-2 - 282	0.19	0.20	3
	09SRB-K098A-01	66.20	-64.20	1199	tundra moss	30	83984	-19.6 ± 0.1	365 ± 20	332 - 483	320 - 497	0.44	0.35	3
	09SRB-K094A-01	66.21	-64.19	1309	tundra moss	10	83982	-22.8 ± 0.1	405 ± 20	476 - 504	335 - 510	0.49	0.50	3
	09SRB-K092A-01	66.20	-64.18	1153	tundra moss	30	118703	-21.4 ± 0.1	625 ± 15	561 - 650	556 - 656	0.60	0.64	3
	09SRB-K045A-01	66.21	-64.37	1158	tundra moss	20	77692	-20.7 ± 0.1	1200 ± 20	1081 - 1170	1063 - 1176	1.12	1.16	2
	09SRB-K095A-01	66.21	-64.20	1340	tundra moss	30	83983	-19.7 ± 0.1	1530 ± 20	1375 - 1505	1353 - 1516	1.41	1.41	2
	09SRB-K096A-01	66.20	-64.19	1266	tundra moss	40	118704	-19.8 ± 0.1	1620 ± 15	1424 - 1544	1418 - 1555	1.52	1.53	2
	09SRB-K090A-01	66.22	-64.15	1455	tundra moss	1	83981	-20.6 ± 0.1	3520 ± 20	3726 - 3840	3719 - 3864	3.78	3.80	1
5	09SRB-K136A-01	66.19	-63.71	903	snowbed willow leaves	1	83935		-185 ± 30					
	09SRB-K136A-01-moss	66.19	-63.71	903	tundra moss	1	118706	-22.7 ± 0.1	1245 ± 20	1155 - 1257	1087 - 1265	1.21	1.22	2
	09SRB-K138A-01	66.19	-63.71	911	liverwort	5	118707		1250 ± 15	1174 - 1255	1144 - 1265	1.22	1.22	2
	09SRB-K139A-01	66.18	-63.70	1153	tundra moss	5	118708	-25.7 ± 0.1	1680 ± 15	1548 - 1603	1536 - 1685	1.58	1.56	2
	09SRB-K133A-01	66.19	-63.68	1055	tundra moss	10	118705	-25.2 ± 0.1	1940 ± 15	1872 - 1920	1829 - 1928	1.89	1.89	2
	09SRB-K131A-01	66.19	-63.68	1048	tundra moss	1	83985	-23.9 ± 0.1	3155 ± 20	3362 - 3395	3347 - 3442	3.38	3.38	1
	09SRB-K131A-01-fresh	66.19	-63.68	1048	tundra moss	1	135210		1830 ± 100[a]	1625 - 1877	1536 - 1988	1.76	1.76	2
	09SRB-K131A-01-fresh bu	66.19	-63.68	1048	tundra moss	1	135211		1895 ± 20	1824 - 1867	1742 - 1893	1.85	1.83	2
	09SRB-K134A-01	66.19	-63.69	1086	tundra moss	1	83986	-24.3 ± 0.1	3090 ± 20	3269 - 3359	3259 - 3367	3.33	3.34	1
	09SRB-K141A-01	66.17	-63.70	1134	tundra moss	30	83988	-24.3 ± 0.1	3795 ± 20	4103 - 4232	4093 - 4239	4.18	4.22	1
	09SRB-K141A-01-fresh	66.17	-63.70	1134	tundra moss	30	135208		3685 ± 20	3981 - 4080	3931 - 4088	4.04	4.08	1
	09SRB-K141A-01-fresh bu	66.17	-63.70	1134	tundra moss	30	135209		3645 ± 25	3909 - 4057	3888 - 4080	3.99	3.98	1
	09SRB-K140A-01	66.17	-63.69	1191	tundra moss	30	83987	-22.1 ± 0.1	4170 ± 20	4649 - 4822	4624 - 4827	4.72	4.71	1
6	09SRB-E265A-01	66.11	-64.59	1037	tundra moss	<50	77690	-21.6 ± 0.1	155 ± 20	-1 - 274	-2 - 282	0.18	0.19	3
	09SRB-E266A-01	66.10	-64.59	1014	tundra moss	<50	77691	-20.3 ± 0.1	255 ± 25	158 - 309	-1 - 426	0.30	0.30	3
	09SRB-E263A-01	66.12	-64.57	939	snowbed willow leaves	10	77688		245 ± 30	154 - 308	-1 - 427	0.29	0.30	3
	09SRB-E263A-01-moss	66.12	-64.57	939	tundra moss	10	118699	-19.9 ± 0.1	255 ± 15	293 - 305	157 - 309	0.30	0.30	3
	09SRB-E264A-01	66.11	-64.58	970	tundra moss	20	77689	-21.2 ± 0.1	405 ± 20	476 - 504	335 - 510	0.49	0.50	3
7	09SRB-K064A-01	66.11	-64.34	956	tundra moss	<50	83972	-22.8 ± 0.1	200 ± 20	-1 - 288	-1 - 296	0.17	0.17	3
	09SRB-K059A-01	66.11	-64.27	1025	tundra moss	<50	83971	-25.0 ± 0.1	715 ± 20	664 - 677	656 - 686	0.67	0.67	3
	09SRB-K058A-01	66.11	-64.26	1066	tundra moss	10	77697	-20.5 ± 0.1	845 ± 20	731 - 773	698 - 789	0.75	0.74	3
	09SRB-K053A-01	66.08	-64.24	1227	tundra moss	<50	77696	-25.5 ± 0.1	1640 ± 25	1450 - 1592	1418 - 1610	1.54	1.54	2
	09SRB-K055A-01	66.10	-64.25	1318	tundra moss	<50	83970		1820 ± 20	1717 - 1811	1710 - 1818	1.76	1.73	2
8	09SRB-A385A-01	65.94	-64.28	1172	tundra moss	40	77685	-18.8 ± 0.1	1510 ± 20	1368 - 1407	1341 - 1506	1.39	1.39	2
	09SRB-A387A-01	65.94	-64.29	1171	tundra moss	100	77686	-23.8 ± 0.1	1675 ± 20	1542 - 1603	1529 - 1686	1.57	1.56	2
	09SRB-A388A-01	65.94	-64.29	1159	tundra moss	300	77687	-25.0 ± 0.1	1685 ± 20	1551 - 1608	1534 - 1689	1.59	1.57	2
	09SRB-A383A-01	65.94	-64.28	1153	caribou antler	100	78111	-17.0 ± 0.1	1740 ± 25	1615 - 1697	1569 - 1710	1.65	1.66	2
9	09SRB-K073A-01	65.79	-63.94	877	tundra moss	2	77699	-22.4 ± 0.1	405 ± 25	467 - 506	333 - 513	0.48	0.50	3
	09SRB-K074A-01	65.80	-63.94	924	tundra moss	10	83975	-19.6 ± 0.1	750 ± 20	672 - 688	667 - 722	0.68	0.67	3
	09SRB-K076A-01	65.81	-63.95	1024	tundra moss	30	118701	-25.3 ± 0.1	1450 ± 15	1314 - 1348	1306 - 1370	1.34	1.34	2
	09SRB-K078A-01	65.81	-63.94	972	tundra moss	30	118702	-24.9 ± 0.1	1470 ± 15	1338 - 1376	1314 - 1387	1.36	1.35	2
	09SRB-K068A-01	65.81	-63.90	962	tundra moss	20	83973	-21.8 ± 0.1	1470 ± 20	1335 - 1379	1310 - 1392	1.36	1.35	2
	09SRB-K069A-01	65.81	-63.89	886	tundra moss	50	77698	-23.3 ± 0.1	1505 ± 25	1358 - 1405	1329 - 1508	1.38	1.39	2
	09SRB-K071A-01	65.80	-63.90	889	tundra moss	10	83974	-20.1 ± 0.1	1635 ± 20	1520 - 1557	1419 - 1602	1.54	1.53	2
	09SRB-K077A-01	65.81	-63.95	1035	tundra moss	5	83976	-22.1 ± 0.1	3390 ± 20	3591 - 3686	3581 - 3690	3.64	3.64	1

[a] large uncertainty due to very small sample size (single macrofossil measured)

Bryophyte identifications	Sub-sample
Mosses:	
Andreaea rupestris Hedw.	09SRB-E264A-01
	09SRB-A385A-01
	09SRB-K055A-01
	09SRB-E264A-01
	09SRB-K064A-01
Andreaea blyttii Schimp.	09SRB-A265A-01
	09SRB-E265A-01
	09SRB-K090A-01
Pohlia obtusifolia (Brid.) L.F. Koch	09SRB-A387A-01
	09SRB-K068A-01
Bryum sp.	09SRB-K073A-01
Pohlia nutans (Hedw.) Lindb.	09SRB-K077A-01
Pohlia sp.	09SRB-K140A-01
Pogonatum urnigerum (Hedw.) P. Beauv.	09SRB-K053A-01
Pogonatum dentatum (Menzies ex Brid.) Brid.	09SRB-K094A-01
Polytrichum juniperinum Hedw.	09SRB-K141A-01
Polytrichum juniperinum Hedw., *Pogonatum dentatum* (Menzies ex Brid.) Brid. and *Pogonatum urnigerum* (Hedw.) P. Beauv.	09SRB-K049A-01
Racomitrium lanuginosum (Hedw.) Brid.	09SRB-K051A-01
	09SRB-K060A-01[a]
	09SRB-K062A-01[a]
	09SRB-K083A-01[a]
	09SRB-K084A-01[a]
	09SRB-K085A-01[a]
Psilopilum laevigatum (Wahlenb.) Lindb.	09SRB-K069A-01
Liverwort:	
Acolea concinnata (Lightf.) Dumort.	09SRB-K080A-01
	09SRB-K086A-01

[a]not dated

Table 2.2 Characterization of 26 sub-samples with eleven species of mosses and one species of liverwort identified by fossil bryologists Jan Janssens, Lambda-Max Ecological Research, Minneapolis, Minnesota, and by bryologist Jennifer Doubt, Canadian Museum of Nature Ottawa.

Recently it has been reported that bryophytes exhumed beneath the cold-based ice margin of Teardrop Glacier in central Ellesmere Island show signs of re-growth and that it is possible to regenerate several moss species in growth chamber experiments (in vitro, La Farge et al., 2013). This differential preservation of macrofossils was not evident in field collection but noted under microscopic examination of the material. With microscopy, a few moss samples were observed to contain dissimilarly preserved bryophytes of one type suggesting regeneration or re-growth of modern or younger bryophytes (Fig. 2.5). Younger-looking fragments have rounded cross-sections and preserve mm-long fibrous white awns (supplementary file, Fig. A1.1). In the field it may be possible to see these features under a powerful hand-lens. To test whether these

dissimilarly preserved macrofossils yield younger ages due to the mixing of modern and fossil ^{14}C, we radiocarbon dated both flattened macrofossils and younger-looking macrofossils from two samples.

All radiocarbon measurements were performed at the Keck Carbon Cycle AMS Laboratory at the University of California, Irvine, CA. The radiocarbon ages were corrected for measured carbon isotope fractionation. Calibration of the radiocarbon ages was done with the Calib 6.1.0 program (Stuiver and Reimer, 1993) using the Northern Hemisphere IntCal09 calibration curve (Reimer et al., 2009).

Fig. 2.5 Moss fragments from the same sample (09SRB-K141A-01 above, 09SRB-K131A-01 below) showing dissimilar preservation. **A.** Flattened *Polytrichum juniperinum* radiocarbon dated to 4.22 ka (mode, UCIAMS-83988, Table 2.1). **B.** A single fragment of younger-looking *Polytrichum juniperinum* with remnant white awns, which was initially excluded for dating and later dated to 4.08 ka (mode, UCIAMS-135208). **C.** Flattened moss fragment (*Polytrichum/Pogonatum*) radiocarbon dated to 3.38 ka (mode, UCIAMS-83985). **D.** A single fragment of younger-looking moss fragments (*Polytrichum/Pogonatum*) was initially excluded for dating and later dated to 1.76 ka (mode, UCIAMS-135210).

2.5 RESULTS

The calibrated ages are reported as 1σ and 2σ ranges of the age distribution (cal ka BP, reported as ka or a), as well as the median and the mode of the probability distribution (Table 2.1). We prefer to consider the full 2σ age ranges of a dated moss, but if a point estimate of the calibrated ages range is required for a particular statistical analysis, we use the mode of the probability distribution to represent the best estimate of the true age (Michczynski, 2007). For comparison with paleoclimate proxies, we use summed probability plots, despite the possible amplification of individual peaks through the calibration process (supplementary file, Fig. A1.2 - A1.4, Chiverrell et al., 2011; Bamforth and Grund, 2012; Williams, 2012; Armit et al., 2013).

To test the reproducibility of the AMS analysis, we radiocarbon dated different organic material from two samples. Snow bed willow (*Salix herbacea*) leaves and *Andreaea* sp. moss fragments (UCIAMS - 77688 and - 118699, respectively) from one sample yielded indistinguishable radiocarbon ages within 1σ error (mode of both calibrated age ranges is 0.3 ka, Table 2.1). However, for the second sample snow bed willow leaves yielded a modern (post-bomb) radiocarbon activity (UCIAMS - 83935), while *Pohlia* sp. moss fragments returned an older radiocarbon age (UCIAMS -118706, mode 1.22 ka). Reworked willow leaves are easily transported by wind and may have blown into sample site. We are uncertain of the cause of the modern radiocarbon activities measured for *Polytrichum* sp. and *Pogonatum* sp. moss fragments (UCIAMS-77694). However, preservation of these moss macrofossils is nearly perfect including intact white awns suggesting that this sample may originate from modern moss (supplementary file, Fig. A1.1).

To test the differences in preservation of macrofossils from the same moss type within one sample, we radiocarbon dated dissimilarly preserved macrofossils under the assumption they may represent different generations of moss growth (with time). Two measurements of younger-looking fragments retaining remnants of white awns of *Polytrichum juniperinum* (UCIAMS -135208 and -135209, modes 4.08 and 3.98 ka, respectively) yielded slightly younger radiocarbon ages than flattened *Polytrichum juniperinum* fragments (UCIAMS- 83988, mode 4.22 ka) from the same sample (Fig. 2.5 a-b, Table 2.1). The calibrated age ranges of the three measurements nearly overlap indicating that these fragments originate from the same plant growth generation (Fig. 2.6a). However, younger-looking fragments of *Polytrichum/Pogonatum* (UCIAMS -135210 and -135211, modes 1.76 and 1.83 ka, respectively) from the other sample returned consistent, yet younger radiocarbon ages than the flattened *Polytrichum/Pogonatum* macrofossils (UCIAMS- 83985, mode 3.38 ka, Fig. 2.5 c-d, Table 2.1). Corresponding bimodal radiocarbon ages were measured on two samples (UCIAMS -118705 and -83986, modes 1.89 and 3.34 ka, respectively) located along the same ice margin in close proximity to this sample suggesting different generations of moss growth (Fig. 2.6 b-c). This interpretation is supported by field evidence that this sample was collected along an ice margin resting against a steep ridge protecting the sampling site from strong wind or precipitation (Fig. 2.6d). In this specific location, subfossil organic material covered during an earlier ice expansion phase was preserved throughout an interim period of ice recession. During this interval new moss was growing that was again covered by a subsequent ice advance event.

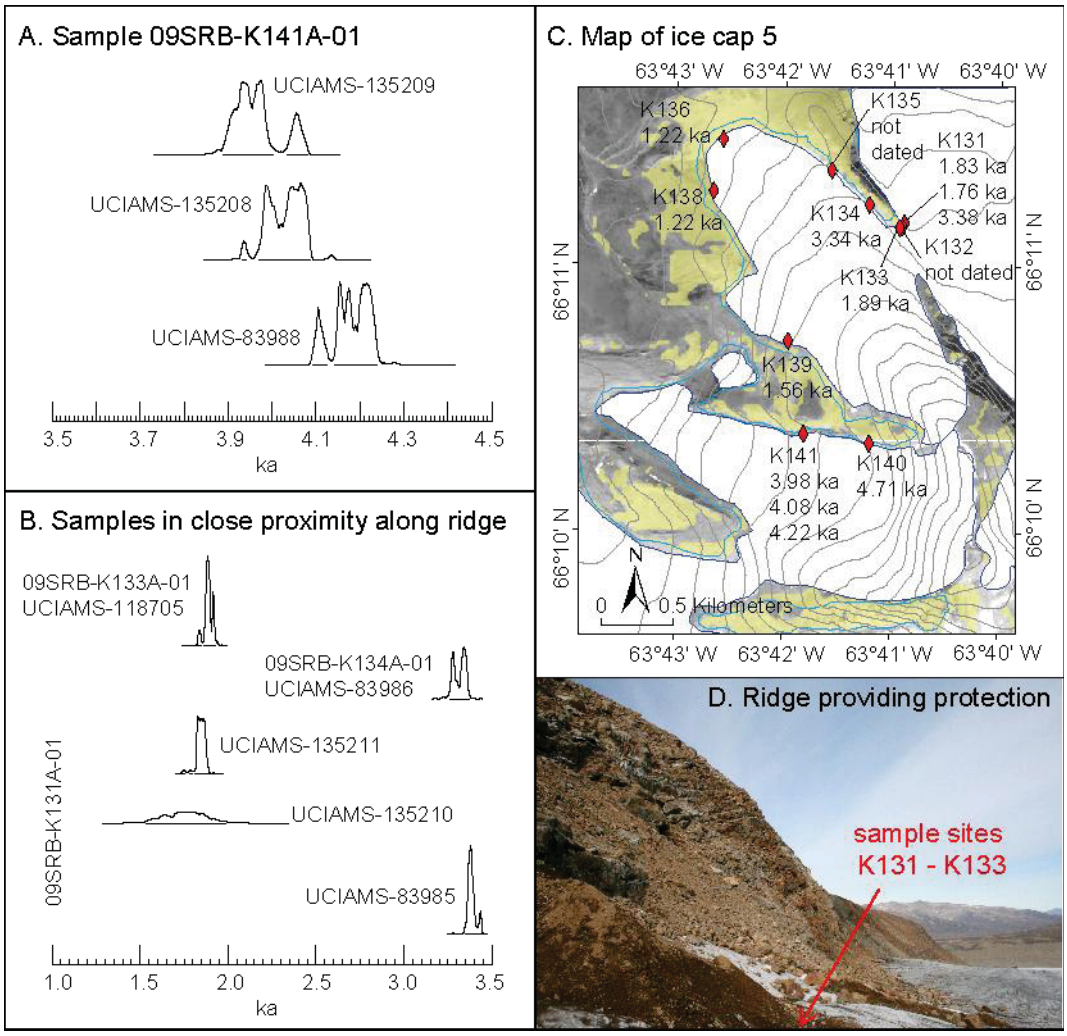

Fig. 2.6 Calibrated age ranges and sampling location of samples containing dissimilarly preserved macrofossils. **A.** Probability density functions of younger-looking macrofossils (UCIAMS-135208 and -135209, modes 4.08 and 3.98 ka, respectively) and flattened macrofossils (UCIAMS-83988, mode 4.22 ka) of sample 09SRB-K141A-01. **B.** Probability density functions of samples collected in close proximity along a steep ridge displaying a bimodal age distribution indicating two generations of moss growth. Older generation: flattened macrofossils of sample 09SRB-K131A-01 (UCIAMS-83985, mode 3.38 ka) and sample 09SRB-K134A-01 (UCIAMS- 83986, mode 3.34 ka); younger generation: younger-looking macrofossils of sample 09SRB-K131A-01 (UCIAMS-135210 and -135211, modes 1.76 and 1.83 ka, respectively) and sample 09SRB-K133A-01 (UCIAMS-118705, mode 1.89 ka). **C.** Map of ice cap 5 showing sample locations along ice margin with the mode of the calibrated radiocarbon ages (sample numbers have been shortened for clarity). Blue = ice cap extent AD 2009, light blue = ice extent AD 1958, grey = topographic contours, yellow = lichen-kill zones as mapped in Fig. 2.2b. **D.** Steep ridge (approximately 10 m high) at sampling locations 09SRB-K131A-01, 09SRB-K132A-01 (not dated), and 09SRB-K133A-01providing protection of the sample sites from high wind speeds and slope wash.

The analyzed samples, collected at elevations between 890 and 1510 m asl, yielded calibrated ages ranging from 4.7 to 0.17 ka (modes) defining three distinct age groups (Fig. 2.7). The oldest grouping (group 1) is defined by only nine dates dating between 4.7 - 3.3 ka, with minimal overlap (Table 2.1, Fig. 2.7d). The largest number of dates (n = 23) delineate age group 2, ranging continuously between 1.9 – 1.2 ka except for one small gap. Group 3 is defined by 16 samples ranging nearly continuously between 0.74 – 0.17 ka, apart from a short gap (50 a) separating the oldest four samples. Owing to the large variation in radiocarbon activity over the past 300 years, calibration of the youngest seven samples yielded large uncertainties extending their age range to modern times but there is no reason to suspect that they are truly modern (e.g., they lack bomb ^{14}C).

Although we focused on moss chronology, the opportunistic fauna dates allow a comparison of an ice-marginal chronology independent from the fragile bryophyte records. The three caribou samples differ significantly in age and each date is concurrent with at least one moss sample, albeit not always collected at the same site. The caribou molar sample was collected from a carcass resting on regolith and just emerging from the ice margin, with the head and neck (with tissue) exposed (Fig. 2.4e). The age of the caribou molar (UCIAMS -78110, mode 3.24 ka) is slightly younger than a moss sample collected nearby (UCIAMS -83969, mode 3.64 ka) suggesting that the caribou died on the ice cap or close to an ice margin during a phase of ice cap expansion. Because the association between death of the caribou and ice growth is uncertain (i.e., the caribou may have died several years before incorporation into the ice cap due to its higher preservation potential) these samples are not included in the summed probability plots

(Fig. 2.7c). However, for comparison they are included in the summed probability plots of individual ice caps in the supplementary file (supplementary file, Fig. A1.5).

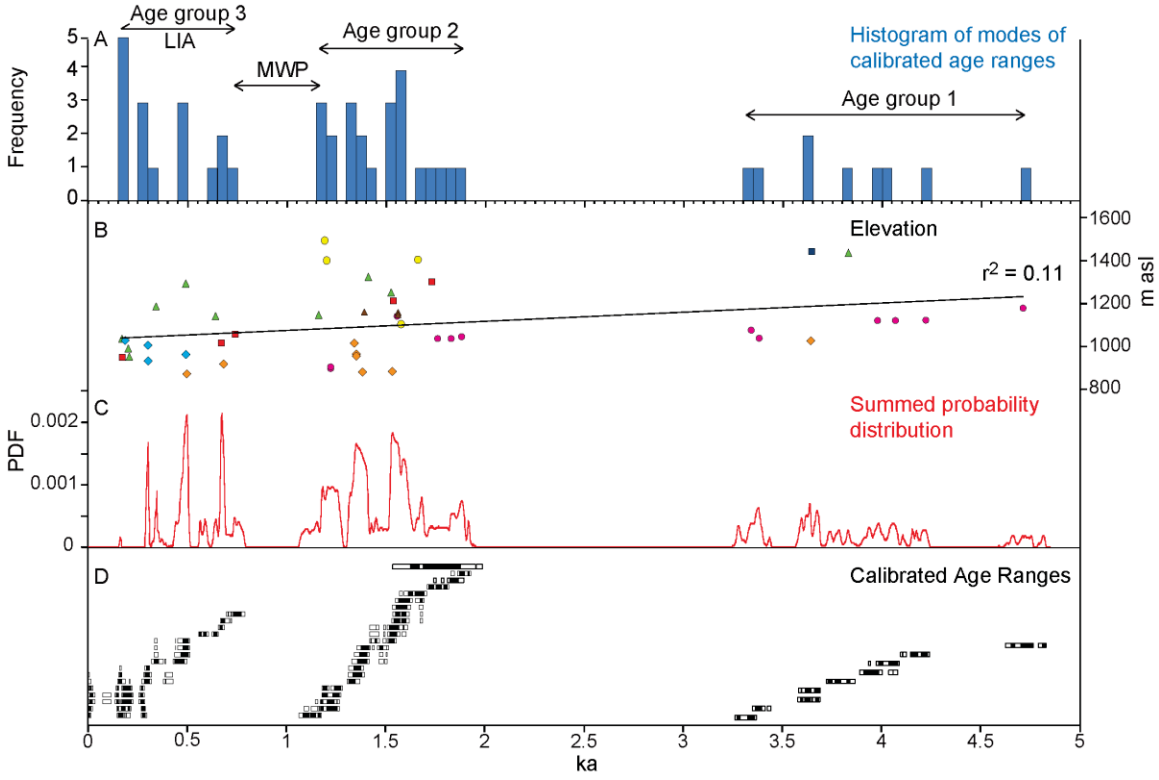

Fig. 2.7 Calibrated ages of all vegetation samples collected on Cumberland Peninsula (excluding three caribou ages). A. Histogram of mode of calibrated ages in 50 year bins. **B.** Elevation of each sample plotted against the mode of the calibrated age, different shapes and colours of points mark samples from individual ice caps: 1 = blue square, 2 = yellow circle, 4 = green triangle, 5 = pink circle, 6 = blue diamond, 7 = red square, 8 = brown triangle, 9 = orange diamond, 3 = not shown. C. Summed probability distribution excluding youngest seven dates yielding calibrated ages ranging from modern to 460 a. **D.** Block diagrams of all calibrated age ranges. Large uncertainty of one sample due to small small size (single macrofossil measured).

2.6 DISCUSSION

2.6.1 Cumberland Peninsula Moss Data

Assuming that ice cover was responsible for moss death, we relate the moss ages to periods of ice advance. At most sampling locations, exhumation of subfossil vegetation during interim ice recession phases permitted rapid erosion of the dead, weakly-rooted mosses by a combination of wind, slope wash, or precipitation impact. Therefore, these sites are inferred to have been continuously covered by cold-based ice (and to have been exposed within weeks of our sampling). A gap in the moss age distribution means that we did not field collected mosses that died during the age gap. However, it does not imply that the ice caps completely melted during that time, because continuous ice cover was required to preserve the subfossil moss covered during earlier expansion phases. In rare circumstances, subfossil moss fragments have the potential to be preserved in wind sheltered locations allowing for recolonization of mosses during an interim recession phase. On ice cap 5, bryophytes re-grew either through regenerative processes (asexual or vegetative reproduction) or colonized sexually by spore production at the collection site. The site was subsequently covered by renewed ice advance retaining organic material from two different expansion events.

The Group 1 expansion phase marks the regional onset of Neoglaciation, which is documented by nine dates collected along four different ice caps at elevations between 1035 – 1461 m asl. Despite the few samples contained in this age group, their distribution across different ice caps indicates that this early expansion phase is at least regional in extent, which has been recently corroborated by similar radiocarbon ages on rooted tundra vegetation in northern Baffin Island (Fig. 2.8, Miller et al., 2013b). A more precise timing of the onset of Neoglaciation might have been attained if higher elevations

had been sampled. It is unclear from our limited dataset if the summits were completely ice free prior to Neoglaciation. However, Miller et al. (2013b) obtained pre-Holocene ages on rooted vegetation from four small plateau ice caps on northern Cumberland Peninsula, suggesting that the Penny Ice Cap is not the only extant ice cap to persist from the late Wisconsinan (Fisher et al., 1998). Due to the limited sample size, it is impossible to infer uninterrupted expansion between 4.7 and 3.3 ka nor halt of ice growth after 3.3 ka, but it is certain that the majority of these sites had to remain ice covered since their entombment. Hence, these ice caps persisted throughout the gap between 3.3 and 1.9 ka, followed by renewed ice expansion documented by the younger moss radiocarbon ages at similar or lower elevations (groups 2 and 3).

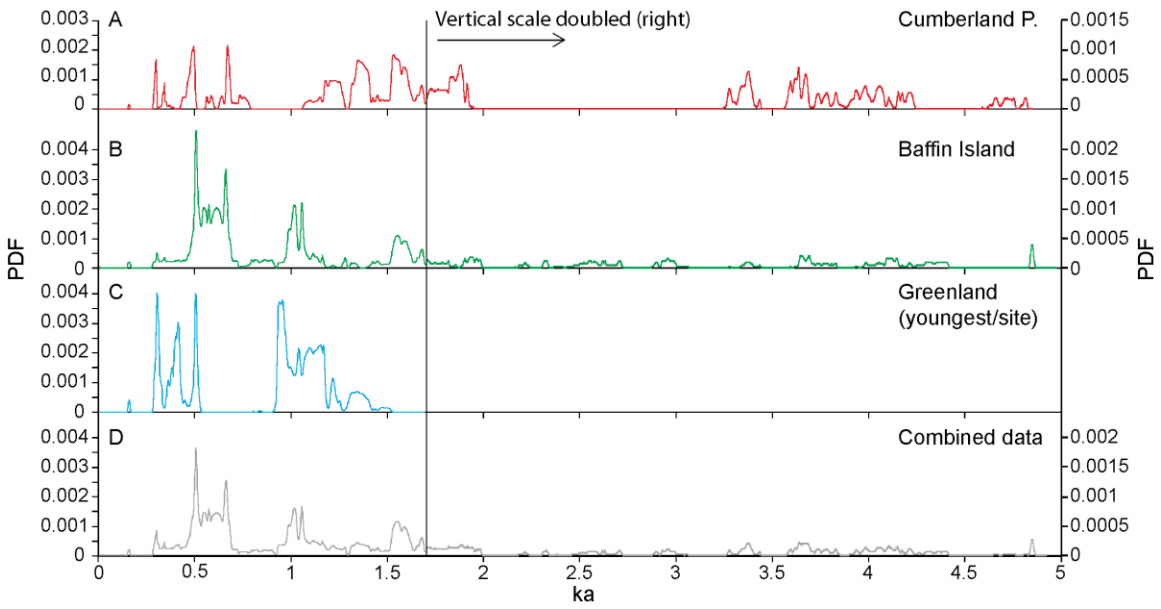

Fig. 2.8 Comparison of summed probability distributions of new and previously published fossil plant data. **A.** Cumberland Peninsula (n = 40). **B.** Baffin Island (n = 135, Anderson et al., 2008; Miller et al., 2012; 2013b). **C.** Greenland: only youngest age at each sample site is shown (n = 12, Lowell et al., 2013). **D.** Summed probability plot of all datasets combined. Note: the summed probability plots are normalised, so that the amplitude of the peaks of different probability plots cannot directly be compared to each other, because of different size of sample numbers in each dataset. Vertical scale of probability density function > 1.7 ka is doubled (scale to the right) for better readability.

Because of the limited number of samples in group 1, it is difficult to infer causes for the gap in age distribution between 3.3 and 1.9 ka. Potentially, no plants were preserved during this interval due to oscillating or retreating ice margins. However, deglaciation could not have been complete, since ice must have persisted at most sites with older radiocarbon ages. At one unique sample location organic material from both ice advances just prior and just after the age gap was preserved indicating that the ice margin had retreated during the age gap (Fig. 2.6b). Because of the high elevation of the ELA in the early Neoglacial, local factors had a larger influence in ELA change leading to more spatially variable ice marginal dynamics. Therefore, the observed similarity of sample elevations of the following ice expansion phase (group 2) might be attributed to these variable ice margin dynamics.

Intensified ice expansion is inferred from the tight suite of radiocarbon ages measured on 23 samples (group 2) ranging between 1.9 and 1.2 ka. These samples were collected along six different ice caps at elevations (1024 - 1423 m asl) equivalent to or below the elevation of the early Neoglacial samples (group 1). The clustering of samples between 1.58 – 1.53 ka (mode, n = 7), 1.41 – 1.34 ka (n = 6), and 1.22 – 1.16 ka (n = 5) suggests three discrete pulses of ice growth within this expansion interval (Fig 2.7a and 2.7c).

The second gap in radiocarbon ages (1.1 – 0.74 ka) corresponds largely to the MWP. This interval of oscillating or retreating ice margins must have been regional in extent, as no samples of this age were preserved, supporting our assumption that in general, dead moss does not survive long unless covered by ice. The tight clustering of samples before and after this hiatus gives us some assurance that, while more samples

would provide a greater confidence in our interpretations, well-dated independently-recognized climate changes are clearly apparent in the existing dataset.

Age group 3 indicates renewed ice advance during the LIA documented at four different ice caps at elevations between 877 and 1309 m asl (n = 16 samples). In the Northern Hemisphere, the LIA was the largest glacier expansion during the last 5 ka, accounting for the conspicuous lichen-kill zones around ice caps. Three clusters of ages ranging between 0.74 – 0.64 ka (n = 4), 0.50 – 0.48 ka (n = 3), and 0.35 – 0.17 ka (n = 9) are observed, including the youngest seven samples (Fig. 2.7a). We note that the amplitude of the corresponding sharp peaks in the summed probability distribution (excluding the youngest seven samples) appear to be exaggerated due to risers (steep slopes) in the ^{14}C calibration curve (Reimer et al., 2009) compared to the peaks in the preceding expansion interval (Fig. 2.7c, supplementary file, Fig. A1.2 – A1.4). The complex structure of the moss age distribution, suggesting several periods of intensified ice advance each persisting for several decades or a century, is supported by earlier notions of a tripartite or more complex model of ELA cooling (Bradley and Jonest, 1993; Bradley, 2000; Wanner et al., 2008).

We interpret both hiatuses, having a total duration of 1.7 ka (or 30% of the last 5 ka), as evidence for retracted or oscillating ice cap margins. Conversely, net expansion of ice cap margins is inferred from the abundant radiocarbon ages corresponding to the remaining intervals of the last 5 ka. The general decrease in both sample age and elevation with time since the onset of Neoglaciation supports an interpretation that long-term average ice expansion was caused by general lowering of the ELA related to declining summer temperatures over the past 5 ka (Fig. 2.7b). A rough estimate of

temperature change can be obtained from a linear regression line (r^2 = 0.11) fitted through all sample points (n = 48, including the seven youngest samples). The average ELA was at around 1261 m asl at the onset of the Neoglacial and dropped to about 1040 m asl at the end of LIA (inferred from the intercept of regression line at 5 and 0 ka, respectively) resulting in a rate of decrease of 44 ± 19 m per millennium. Using a lapse rate of 4.9 ± 0.4 °C per 1000 m measured at the surface of several Arctic Ice Caps (Gardner et al., 2009), we calculate a long term decrease in temperature of 1.1 ± 0.5 °C over the past 5 ka on Cumberland Peninsula, and an average rate of temperature change of -0.22 ± 0.09 °C ka^{-1}. As mentioned above the early Neoglacial ELA lowering was probably affected more strongly by local factors. At this stage ice expansion mainly occurred through lateral growth by winter snow, which survived summer melt. During the LIA, on the other hand, ice expansion was mainly controlled by persistent regional ELA lowering. Ice caps during the LIA also consisted increasingly of polythermal ice margins, which maybe were affected by a time-delay between ELA depression and ice advance through internal creep.

It is noteworthy that the elevation vs. time correlation is much tighter for individual ice caps (correlation coefficient ranging between 0.41 and 0.98 for four ice caps) yielding similar estimates of cooling (supplementary file, Fig. A1.5). The variability in the observed cooling rate (slope of the regression line) can be attributed to local factors affecting the ELA at each ice cap. These additional influences are based on prevailing wind directions, regional precipitation patterns, solar exposure, and other glaciological factors, such as response time, hypsometry and ice dynamics. The retreat of the ice margin may be affected differentially by the same factors, leading to dissimilar patterns

of ice retreat compared to the expansion phase. This discrepancy between ice advance and retreat patterns may also explain the smaller sample size of the earlier expansion phase (group 1), as these sites had to retain their ice covers through several retreat phases. A mean temperature decrease (-2.4 ± 0.5 °C) over the past 5 ka and cooling rate (-0.47 ± 0.09 °C ka^{-1}) calculated by averaging the values for the individual ice caps thus only represents a minimum value of the long-term, regional temperature change. This cooling rate is about twice the estimate based on linear regression through all samples (see above), which also has a lower coefficient of variance. Therefore, this larger estimate is considered to be more representative, which is comparable to the cooling rate calculated by Miller et al. (2013b) over the same time interval. It is important to note that these estimates do not account for potentially higher elevations of ELA at the onset of Neoglaciation or for lower elevations reached during the maximum of the LIA, as evident by the widespread lichen-kill trimlines.

The calculated drop in temperature is comparable to the estimated increase of temperature of 1 – 3 °C since the LIA, inferred from exposed lichen-free zones (Locke and Locke, 1977; Williams, 1978). Retreat rates of cold-based ice caps accelerated during the last three decades, suggesting that the modern warming is the greatest seen at any sample sites since at least 5 ka (Gardner et al., 2011). Modelling the sensitivity of snow extent to temperature change revealed that a consistent lowering of the perennial snowline can occur within one melt season, with amplification of the temperature perturbation by positive sea ice-ocean feedbacks (Berdahl and Robock, 2013). Most of the plateaus on Baffin Island are in a critical elevation range that are affected by widespread changes of snow and ice cover in response to small temperature changes.

This sensitivity of ice cap initiation to small temperature changes supports the instantaneous glacierization hypothesis proposed by Ives (1957; 1975), suggesting that inception of continental ice sheets occurred over high-elevation plateaus with subsequent advance and merging in lower-lying areas. On the other hand, this sensitivity also implies that slight increases in temperature can cause immediate withdrawal of ice margins at varying elevations due to local controlling factors, hence explaining the complex response of the ice caps to recent warming. Extant ice caps are currently undergoing wholesale retreat at all elevations, exposing subfossilized moss of widely different ages.

2.6.2 Comparison With Other Vegetation Data

Our interpretation of the age distribution of moss collected along extant ice margins is consistent with the model proposed by Anderson et al. (2008) and Miller et al. (2012; 2013b). They interpreted radiocarbon ages of rooted tundra vegetation to date the last time the collection site was ice free and related the death of the organic material to the inception of permanent ice cover at each location. The frequency of radiocarbon ages (specifically peaks and gaps on a summed probability diagram) of their Baffin Island dataset is very similar to our Cumberland Peninsula results (Fig. 2.8). However, a different interpretation of fossil plant data has recently been proposed by Lowell et al. (2013), who investigated the late Holocene expansion of a local ice cap in eastern Greenland using multiple proxies, including sediment cores from a threshold lake (Fig. 2.1a). Based on multiple lines of evidence, they interpret the radiocarbon age distribution to mark times of restricted ice and absence of radiocarbon ages to indicate intervals of ice growth. Lowell et al. (2013) mostly dated woody parts of dwarf shrubs

(*Salix arctica* and *Dryas octopetala*) that have a longer potential residence time on the surface before being buried beneath a cold-based ice cap. Moreover, Arctic willow (*Salix arctica*) is a long-lived, slow growing decumbent shrub that can live to be a hundred years old or more (Raup, 1965). Therefore, their radiocarbon ages may not reflect the timing of ice growth as accurately as would a chronology based on mosses that have much shorter life cycles. Lowell et al. (2013) suggest that the plant death is caused by deteriorating environmental conditions resulting in expansion of snow cover, but that widespread ice expansion only began during the hiatus in their plant ages, concurrent with the onset of glacial sedimentation in the threshold lake located outside of the LIA glaciation limit.

Interestingly, the plant data of Lowell et al. (2013) embrace the same time intervals as the age distributions on Baffin Island (Anderson et al., 2008; Miller et al., 2012; 2013b, and this paper, Fig. 2.8). In Fig. 2.8c we include the only youngest age at each sampling location of Lowell et al. (2013) to reduce the possibility that death of the plant may have occurred before the ice margin advanced at the sample site. All three data sets indicate synchronized ice expansion pulses in the LIA and all three show paucity of dates during the preceding MWP. We note that the MWP appears to have had a later onset in eastern Greenland and in northern Baffin Island than on Cumberland Peninsula. This discrepancy may be attributed to an insufficient number of samples in the Cumberland Peninsula dataset, or it may indicate that ice caps on Cumberland Peninsula are more sensitive to other mass balance forcings. For example, the large peninsula may have been affected by reduced sea-ice cover in the surrounding water bodies (Cumberland Sound, Davis Strait, and Baffin Bay) at the onset of the MWP (see discussion below). The

Cumberland Peninsula dataset also reveals additional ice extension phases before 1.4 ka, which are not as well documented in the aforementioned studies, but have recently been confirmed by Miller et al. (2013b) in an enlarged dataset from Baffin Island.

This overall agreement among different north Atlantic Arctic regions suggests a common cause for ice growth most likely related to pan-Arctic, if not global, climate changes. The same conclusion was also drawn by Miller et al. (2013a) who discuss in detail the differing interpretation of relict vegetation data and demonstrate how the Greenland dataset (Lowell et al., 2013) can be brought to conformity with the North Baffin dataset (Anderson et al., 2008; Miller et al., 2012), and by inference the Cumberland Peninsula moss dates.

2.6.3 Climate Forcing

Following a maximum at 11 ka, summer insolation steadily decreased in polar and mid-latitudes in the Northern Hemisphere throughout the Holocene (Huybers, 2006), inducing declining temperatures in the Arctic. Colder summer temperatures initiated renewed glacier advances following widespread ice withdrawal during the early to middle Holocene thermal optimum (8 - 5 ka; Kaufman et al., 2004). Early Holocene warm temperatures and onset of Neoglaciation at around 4.5 ka have been documented on northern Cumberland Peninsula from paleoclimate records obtained from lake sediments (Wolfe and Härtling, 1996; Wolfe et al., 2000; Kerwin et al., 2004; Miller et al., 2005; Francis et al., 2006; Frechette et al., 2006). High concentrations of exotic pollen in lake sediments during the Holocene thermal optimum have been related to prevailing southerly winds (Miller et al., 1999). Ice expansion during Neoglaciation is recorded by large ice-cored moraines on Cumberland Peninsula. These are dated by

lichenometry (Miller, 1973; Davis, 1985), based on the rate of lichen growth on boulders since stabilization of the moraine following initial ice retreat (Miller and Andrews, 1972). Although the moraine record is generally incomplete due to obliteration of older moraines by subsequent more extensive advances (e.g., Gibbons et al., 1984), good agreement between moraine stabilization and ice expansion phases can be seen throughout Neoglaciation. Taking into account the large uncertainties intrinsic to lichenometry (generally larger than 20%, Miller and Andrews, 1972), our early ice expansion phase (4.7 – 3.3 ka) correlates well with the oldest moraine stabilization at around 3.8 – 3.6 ka and 3.3 ka (Miller, 1973; Davis, 1985). The following moraine building events at 2.4 – 2.2 ka and 2 – 1.9 ka are not represented in the moss data set (hiatus between 3.3 – 1.9 ka), but the subsequent moraine stabilization phase at 1.15 – 0.9 ka corresponds to the transition into the MWP. The youngest lichenometric dates at 0.65 – 0.5 ka , 0.4 – 0.2 ka, and after 0.1 ka document short-term ice recession and moraine stabilization during the LIA and match well with the three ice expansion pulses recorded in our moss data (0.74 – 0.64 ka, 0.50 – 0.48 ka, and 0.35 – 0.17 ka).

Although declining air temperatures related to gradually decreasing summer insolation is also documented in the delta ^{18}O record from Penny Ice Cap, no consistent correlation between ice expansion phases and intensification of temperature decrease can be seen throughout the Neoglacial (supplementary file, Fig. A1.6c; Fisher et al., 1998). Similar gradually declining delta ^{18}O trends are apparent in other Arctic and Greenland ice cores (supplementary file, Fig. A1.6), with additional variation evident in the temperature and accumulation reconstructions of the GRIP and GISP2 ice cores (Dahl-

Jensen et al., 1998; Alley, 2000). In addition to the long-term cooling trend, the moss datasets and the other paleoclimate proxies reveal higher-frequency climate variations.

Changes in oceanic circulation affecting sea surface temperature and extent of sea ice influence terrestrial climate on centennial to millennial timescales, especially in coastal regions. Minimum sea-ice conditions prevailed in the early and middle Holocene (11.5 - 6 ka), with subsequent increase of sea ice in the northwest North Atlantic inducing changes in albedo and the regional heat budget (de Vernal and Hillaire-Marcel, 2006; Fisher et al., 2006). These changes in oceanic circulation are associated with prevailing atmospheric circulation patterns, with negative phases of the Arctic Oscillation (AO) and the North Atlantic Oscillation (NAO) favoring colder conditions in the Eastern Canadian Arctic (Hurrell et al., 2001). During the late Holocene, a short-lived swing to positive NAO phase, in association with higher solar irradiance and less active tropical volcanism, has been proposed to explain the warmer conditions during the MWP (Mann et al., 2009; Trouet et al., 2009). Besides atmospheric circulation patterns, variability in solar irradiance and multiple volcanic eruptions occurring within few successive years also affect climate on decadal timescales, and can therefore induce atmospheric perturbations favourable for ice cap expansion. For instance, the last intensive phase of LIA has been related to a prolonged sunspot minimum, the Maunder minimum, lasting from AD 1630 – 1715 (320 - 235 yr BP, Eddy, 1976; Wanner et al., 2008). While short-term variations (2 – 3 years) in air temperature have been noticed subsequent to large explosive volcanic eruptions, it has been proposed that a series of eruptions over a short time can induce decadal-scale cooling (Robock, 2000).

The high-precision radiocarbon ages obtained from the fossil organic material reveal sub-centennial ice cap expansion pulses during the past 2 ka that can be compared to proxy records for solar irradiance and volcanism. Although the amplitude of some peaks in the summed probability distribution are exaggerated through the calibration process due to risers (steep parts) in the calibration curve, their occurrences still reflect real structure in the data (supplementary file, Fig. A1.2 – A1.4).

Past solar activity can be estimated from variation of ^{10}Be concentration measured in ice cores (Steinhilber et al., 2009) or atmospheric ^{14}C activity changes recorded in the radiocarbon calibration curves (Vieira et al., 2011). Differences in these solar irradiance reconstructions are related to diverse uncertainties intrinsic to either method (Fig. 2.9a). Large explosive volcanic eruptions inject large amounts of aerosols and sulfur gases into the stratosphere, where they are transformed into sulfur aerosols (Robock, 2000). Therefore, volcanic sulfate deposits in polar ice cores are used as proxies of past volcanic activity, and the global extent of the stratospheric sulfur loading can be inferred using several ice cores from both hemispheres (Gao et al., 2008). Sulfate concentrations measured in a single ice core provide higher resolved records of past volcanic eruptions for the past 2 ka (Sigl et al., 2013) and are also available for the entire Holocene (Zielinski et al., 1994; Zielinski and Mershon, 1997). Although the Northern Hemisphere index of stratospheric volcanic sulfate injection (Gao et al., 2008) shows a strong correlation with individual peaks in moss radiocarbon age distribution during the LIA (supplementary file, Fig. A1.2), we primarily use the high-resolution, single-core proxy records for comparison with our fossil moss dataset (Fig. 2.9b). It is important to note that both timescales of the volcanic eruption proxies and the solar activity record based

on the ^{10}Be concentration in ice cores (Steinhilber et al., 2009) are independent of the radiocarbon dating method used to date the fossil flora and fauna and the atmospheric ^{14}C-based solar irradiance proxy (Vieira et al., 2011). The timescale for the volcanic activity archives is based on cross-reference with well-dated ice cores established from a combination of annual accumulation layers and measurement of multiple parameters with strong seasonal variability pinned to known volcanic time markers (Sigl et al., 2013).

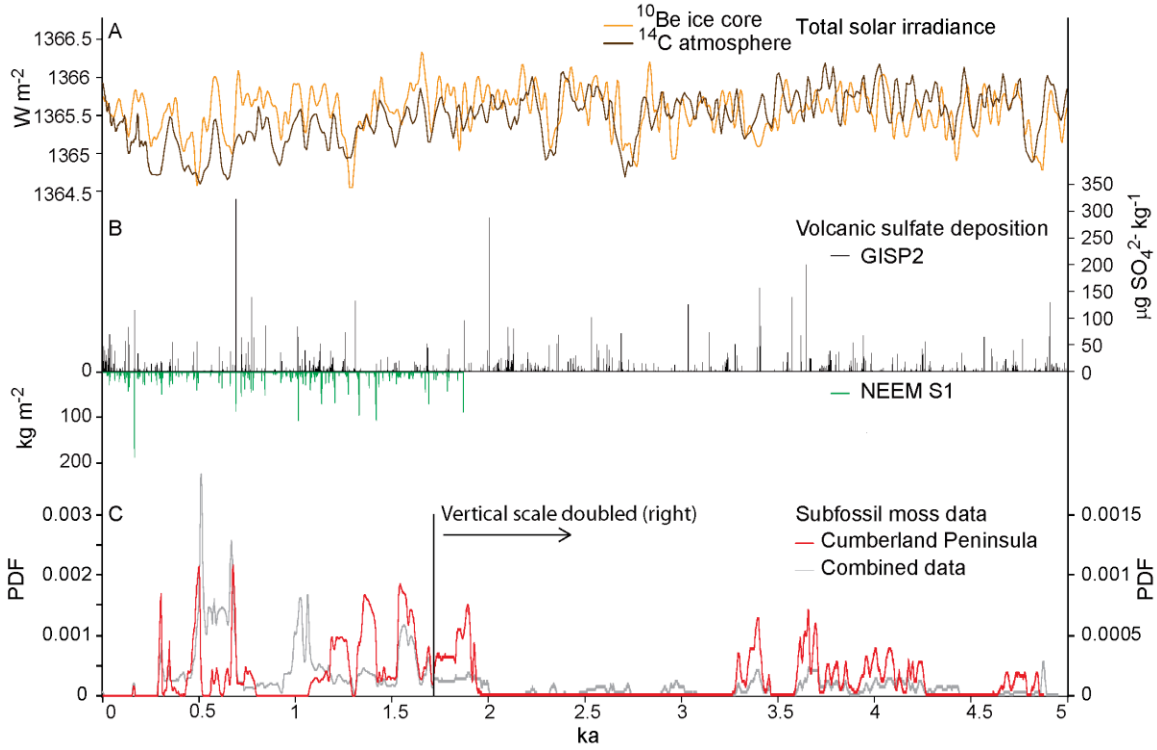

Fig. 2.9 Comparison of moss radiocarbon age distribution with proxies of climate forcing. **A.** Solar irradiance calculated from ^{10}Be ice core record (Steinhilber et al., 2009) and atmospheric ^{14}C variation (IntCal04, Vieira et al., 2011). **B.** Atmospheric sulfate aerosol loading: volcanic sulfate deposition in GISP 2 ice core over the last 5 ka (black, axis to the right, Zielinski and Mershon, 1997) and high-resolution record based on NEEM S1 ice core for the last 2 ka (green, axis to the left, Sigl et al., 2013). **C.** Summed probability distributions for all previously published fossil plant data (gray; youngest/site, Lowell et al., 2013; Miller et al., 2013b; this paper), and the Cumberland Peninsula dataset on its own (red). Vertical scale of probability density function > 1.7 ka is doubled (scale to the right) for better readability.

Again, in agreement with northern Baffin Island results (Anderson et al., 2008; Miller et al., 2012), we find a strong correlation between peaks in the Cumberland Peninsula moss age distribution and both large volcanic eruptions and low solar activity over the past 800 years. In addition to the observed strong correlation between inception (675 – 650 a) and intensification (520 – 450 a) of ice cap expansion during the LIA in northern Baffin Island, we find further links between volcanic activity and ice cap expansion in the later part of the LIA just prior to the Maunder minimum (320 – 235 a). Continued ice cap growth throughout the LIA was facilitated by sustained high volcanic activity and generally low solar activity (Fig. 2.9). The agreement between the moss radiocarbon age distribution and volcanism or low solar irradiance is less convincing further back in time, possibly because of the decreasing resolution of the volcanic record and underlying influences of the calibration process on the moss age distribution (see supplementary file, Fig. A1.2 – A1.4). Nevertheless, there are possibly meaningful correlations between moss dates and volcanic eruptions at about 1.65 ka (Cumberland peak), 1.42 ka (riser of Cumberland distribution), 1.35 ka (peak in Cumberland moss distribution,), 1.25 ka (riser in Cumberland distribution), as well as 1.05 ka and 1.01 ka (Baffin Island moss data). The few samples comprising group 1 impede a clear correlation with the volcanic eruption record. However, tentative associations of clusters of volcanic eruptions with moss radiocarbon ages can be seen at around 4.25 ka, 3.8 ka, 3.65 ka, and 3.4 ka, supported by both the Cumberland Peninsula record and the extended Baffin Island database (Miller et al., 2013b). As explored by Miller et al. (2012), short-term climate perturbation might be sustained and amplified by positive sea ice-ocean-atmosphere climate feedbacks enhancing climate variability in the Arctic.

2.7 CONCLUSION

In many Arctic regions with polythermal ice coverage, records of past ice cap expansion preserved in dead vegetation are currently being exposed along rapidly receding cold-based ice margins. The dead vegetation is composed of delicate subfossilized mosses, liverworts, willow leaves, and lichens, which are quickly eroded by wind and slope wash. Therefore, records of early expansion phases are generally eradicated during recession phases and only sites that remained continually covered by ice until today reveal the onset of Neoglaciation. Potentially, even older organic material is still buried under ice at higher elevations.

The age distribution of subfossil moss collected on Cumberland Peninsula indicates that the middle to late Holocene climate was more variable than what might be expected from the monotonic decrease of insolation and, therefore, climate was additionally influenced by high-frequency forcings. The discrete pulses of ice expansion inferred from the peaks in moss age distribution after 2 ka indicate sudden lowerings of ELA in response to intensified coolings superimposed on a general trend of declining summer temperatures throughout the middle to late Holocene. Preservation of subfossil moss samples older than 3 ka generally required permanent ice cover until the year of collection (AD 2009), and thus document that sporadic periods of oscillating or retreating ice margins were insufficient in magnitude to expose these sites. In rare circumstances, older organic material may be preserved during ice recession in protected locations and such sites should be sampled with caution. Overall, the ice expansion record accords with evidence of moraine stabilization inferred from lichenometry, both suggesting a complex structure to LIA cooling.

The complex structure of the LIA glacier record and other late Holocene ice advances signifies the importance of short-term climate perturbations resulting from large explosive volcanic eruptions and solar irradiance variability. As suggested by Miller et al. (2012), positive internal ocean-atmosphere feedbacks may have sustained and amplified these atmospheric perturbations. Changes in sea-ice coverage related to oceanic circulation dynamics affect climate on centennial to millennial timescale and are thought to have initiated ice expansion during the onset of the Neoglaciation. A hiatus in subfossil moss age distributions observed in northern Baffin Island and in this study coincides with changes in the mode of atmospheric circulations patterns (NAO and AO) was well as with higher solar irradiance and less active tropical volcanism inferred for the MWP.

A general decrease in elevations of samples with time (Fig. 2.7b) indicates that ice expansion was caused by lowering of ELA due to decreasing temperatures or increasing precipitation. Based on regression lines fitted to four individual ice caps, a mean temperature decrease of 2.4 ± 0.5 °C is inferred for the past 5 ka, which is associated with irregular lowering of the ELA throughout Neoglaciation culminating in the LIA. The accelerated retreat of cold-based ice caps in recent decades suggests that the current warming exceeds temperatures experienced in the Arctic over the past 5 ka. Additional samples from other ice caps over wider elevation ranges and different Arctic regions are required to i) more closely define the regional onset of Neoglaciation and better constrain the early ice expansion phases, ii) test the synchronicity of ice growth throughout the North Atlantic Arctic as suggested by Miller et al. (2013a) and this study, and iii) to

better understand the association between short-term atmospheric perturbations and persistent climate deterioration through internal ocean-atmosphere feedback mechanisms.

2.8 ACKNOWLEDGEMENTS

We thank Mary Sanborn-Barrie and Mike Young, project leaders for the Geo-mapping for Energy and Minerals (GEM) program on Cumberland Peninsula (Geological Survey of Canada and Canada- Nunavut Geoscience Office), for support of fieldwork. Kevin Kosar assisted in sample collection, Lars G. Hedenäs aided in the identification of the moss samples, and Jon A. Shaw provided moss reference material. Olivia Brown and Tracy Lynds developed the procedure for mapping the lichen-kill zones form satellite imagery. John Southon and the staff at the Keck Carbon Cycle facility at University of California produced the radiocarbon ages and discussed issues involved in the radiocarbon calibration process. Funding for AMS dating was provided by the Climate Change Program of the Geological Survey of Canada and by an NSERC Discovery Grant and NSERC Northern Research Supplement to JCG. We thank the two anonymous reviewers for their thoughtful comments, which helped improve the paper.

CHAPTER 3 – Wisconsinan Glacial Dynamics of Cumberland Peninsula, Baffin Island, Arctic Canada

Manuscript in preparation for submission to *Quaternary Research*

Annina Margreth[1], John C. Gosse[1], Arthur S. Dyke[1]

[1]Department of Earth Sciences, Dalhousie University, Halifax, Nova Scotia B3H 4R2, Canada

3.1 ABSTRACT

The interaction of the Laurentide Ice Sheet with an expanded local Penny Ice Cap and an extensive polythermal alpine glacier complex covering most of Cumberland Peninsula is the most studied but still poorly understood dynamical glacier system in Arctic Canada. The first high-resolution mapping of glacial deposits of the entire peninsula is here combined with new cosmogenic nuclide and radiocarbon chronological constraints to reconstruct ice margin positions of all three glacier types for the most prominent late glacial cooling events (Heinrich Event 1, Younger Dryas, and Cockburn-equivalent). From these maps we derive post-Last Glacial Maximum ice retreat rates. While the retreat rates for the thinner alpine complex are more responsive to north Atlantic temperature changes than the neighbouring ice cap and ice sheet, a north-south asymmetry in alpine glacier retreat rates is apparent. The distribution of paleo-equilibrium line altitudes, now available for the three cooling intervals, reveals a pattern similar to the retreat history, and suggests that the alpine complex on Cumberland Peninsula was significantly controlled by sea-ice limitations to winter moisture since the Last Glacial Maximum.

3.2 INTRODUCTION

Cumberland Peninsula on Baffin Island is in an interesting location with respect to late Pleistocene glacial history and one of the most studied regions in Arctic Canada for ice dynamics and glacial landscape evolution. Part of the fascination with the peninsula resides in the fortuitous interaction during the Wisconsin Glaciation of three independent glacier systems: The northeastern fringe of the Laurentide Ice Sheet (LIS), the expanded Penny Ice Cap (PIC) (still one of the largest extant ice caps in Arctic Canada, >6,000 km^2, Fig. 3.1), and an expanded alpine glacier complex, the remnants of which cover about a third of the eastern part of the peninsula with valley and cirque glaciers (some reaching tidewater) and summit ice caps. Cumberland Sound, which defines the southern coast of the peninsula, was occupied by LIS ice, which for much of its history produced a prominent ice stream (Cumberland Sound Ice Stream, CSIS) that extended across the continental shelf during the Last Glacial Maximum (LGM, Jennings, 1993; Jennings et al., 1996).

Despite the significant amount of geomorphic and glacial geologic work on Cumberland Peninsula during the last five decades (Fig. 3.1a, e.g., Miller, 1973; Andrews et al., 1976b; Sugden and Watts, 1977; Dyke, 1979; Dyke et al., 1982; Locke, 1987; Wolfe, 1994; Steig et al., 1998; Bierman et al., 1999; Wolfe et al., 2000; Miller et al., 2002), previous analysis of the paleo-ice dynamics was restricted by limited access other than to some segments of the coast. In 2009 and 2010, the Geomapping for Energy and Minerals (GEM) project for Cumberland Peninsula provided a remote camp in the interior of the peninsula and helicopter support to map most of the peninsula at an uniformly higher resolution (scale 1:100,000, Dyke 2011a-f; 2013a-c).

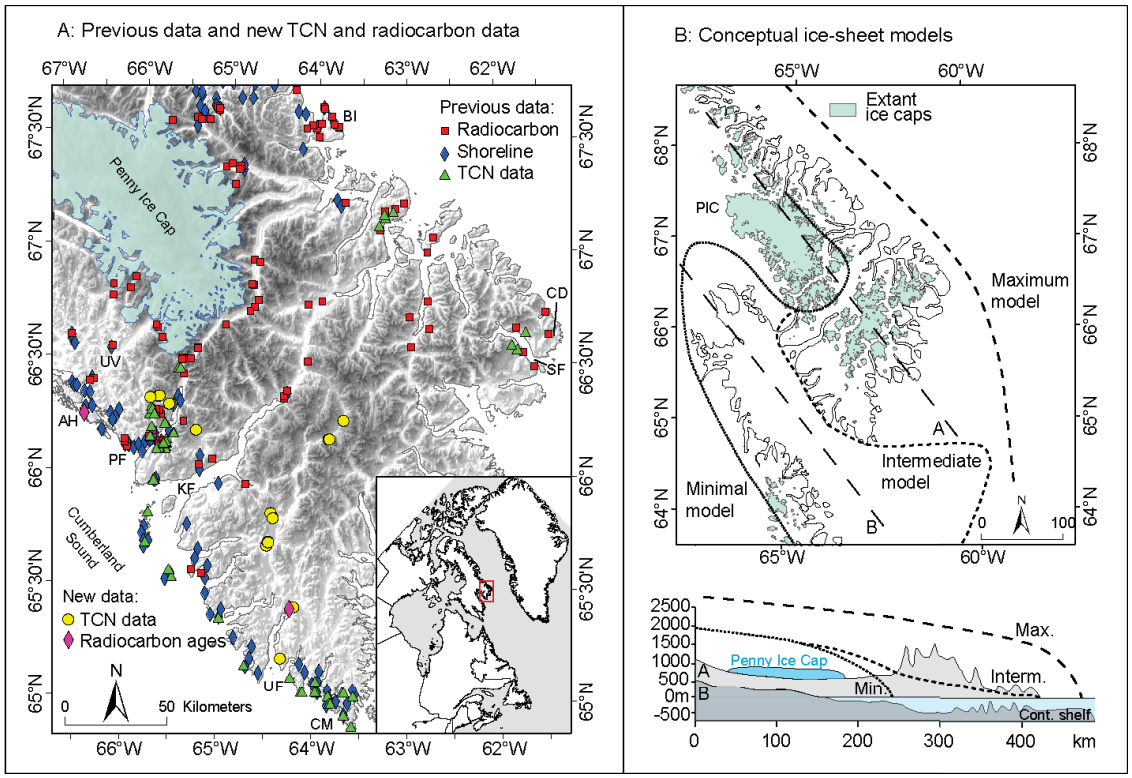

Fig. 3.1 **A.** Digital elevation map of Cumberland Peninsula with previous sample locations (squares: radiocarbon dating, diamonds: shoreline measurements, triangles: terrestrial cosmogenic nuclide (TCN) data), new TCN sample locations (circles), and new radiocarbon ages (pink diamonds). Location of Cumberland Peninsula in the Eastern Canadian Arctic is shown in inset map. BI: Broughton Island, CD: Cape Dyer, SF: Sunneshine Fiord, CM: Cape Mercy, UF: Ujuktuk Fiord, KF: Kingnait Fiord, PF: Pangnirtung Fiord, AH: American Harbour, UV: Usualuk Valley. **B.** Schematic illustration of the three major conceptual ice-sheet models: Maximum model (Flint, 1943), Intermediate model (Miller et al., 2002), and Minimal model (Ives, 1978). Approximate locations of elevation-profiles A and B for the vertical section are indicated with dashed lines. Vertical cross-section showing two elevation-profiles is adapted from (Miller et al., 2002).

The overall objectives of the research included i) to analyse the glacial dynamics among the different ice systems on the peninsula during and since the LGM, and ii) to relate any observed differences and trends in the dynamics to paleoclimate and glaciological controls. An additional goal was to revisit sites with records that had previously generated tenuous or problematical interpretations or led to debates regarding the regional ice dynamics. In particular, the improved pattern of deglaciation presented

in this paper provides constraints on the dynamics of the CSIS, which is an important element of the northeastern sector of the LIS. To achieve these objectives, we obtained the first chronology for glacial deposits throughout the interior of the peninsula. The new age control is combined with published chronologies and new high-resolution maps of glacial deposits (Dyke, 2011a-f; Dyke, 2013a-c) are used to locate and interpolate ice marginal positions for three major late-glacial cooling events corresponding to the end of a composite Heinrich Event 1 (H-1, ~20 - 14.6 ka, Stanford et al., 2011), to the end of the Younger Dryas (YD, 12.9 – 11.7 ka, Rasmussen et al., 2006) and the Cockburn moraines of the LIS (9.5 - 8.5 ka, Miller and Dyke, 1974; Andrews and Ives, 1978; Briner et al., 2009). Reconstruction of paleo-equilibrium line altitudes (ELA) for these time intervals offers insights into the spatial variation of glacier response to late glacial cooling and warming and together with retreat rate patterns reveal that precipitation is a likely first order control on the alpine ice dynamics.

3.3 BACKGROUND

Conceptual ice sheet models for the Eastern Canadian Arctic have changed considerably over the last half century (Fig. 3.1b) and Cumberland Peninsula was one of the main stages where the debates were played out. The idea of a single-dome ice sheet (Flint, 1943) that completely covered northeastern Canada was eventually dismissed on the basis of observations that highly weathered upland plateaus lacked any evidence of glacial erosion or deposition (Ives, 1966), the occurrence of disjunct species populations in high latitude coastal highlands of Baffin Island and Labrador (Fernald, 1925), and the inference of multiple dispersion centres for the LIS (Dyke and Prest, 1987). A minimum ice sheet model was proposed on Cumberland Peninsula and elsewhere in eastern Canada

to accommodate ice-free conditions on upland plateaus that served as refugia for fauna and flora (Ives, 1974; Ives, 1978). The minimum ice sheet model and associated 'Nunatak Hypothesis' received further support from subsequent detailed fieldwork throughout the eastern Canadian Arctic and especially on Cumberland Peninsula (Miller, 1973; Dyke, 1979; Locke, 1987). However, the occasional occurrence of erratic blocks and subtle glacial modification of tors on upland plateaus of Cumberland Peninsula indicated extensive coverage at higher elevation areas by cold-based ice (Sugden and Watts, 1977), challenging the Nunatak Hypothesis. Thus, several first-order conundrums could not be explained with a single simple ice cover model, partly owing to the limited mapping resolution, limited available chronology, and non-uniqueness of interpretations of the same datasets.

Attempts to reconcile mapped ice volumes with those inferred from marine oxygen isotopes records have been challenged by an overall dearth of ice marginal chronology, sparse controls on vertical ice limits, and difficulties in interpreting both. Evidence for an extensive LIS during the Late Wisconsinan was retrieved from sediment cores obtained from the floor of Cumberland Sound (Jennings, 1993) and on the adjacent continental shelf and slope (Jennings et al., 1996). Foraminiferal assemblages and radiocarbon dating indicated that ice occupied Cumberland Sound until ~13.4 ^{14}C ka revealing that the marine-based LIS extended onto the continental shelf for a significantly longer period relative to more southern regions (Jennings, 1993). Later, Jennings et al. (1996) postulated that the CSIS advanced twice to the continental shelf, once approximately between 34 and 21 ^{14}C ka followed by recession and re-advance during the Younger Dryas at around ~11 ^{14}C ka (radiocarbon ages are indicated here consistent with how they

were stated by A. Jennings). TCN exposure dating of boulders and bedrock along the southwestern coast also suggested that fiords and intervening plateaus were ice covered during the last glaciation (Bierman et al., 1999; Marsella et al., 2000; Kaplan et al., 2001). Samples collected from boulders on the Duval Moraines above Pangnirtung Fiord yielded a bimodal age distribution with peaks at ~22 ka and ~10 ka (Fig. 3.1a, Marsella et al., 2000). Terrestrial cosmogenic nuclide (TCN) concentrations in bedrock surfaces above these moraines revealed complex exposure histories that were interpreted to indicate cold-based ice cover during the last glaciation (Bierman et al., 1999; Kaplan et al., 2001). Kaplan's recognition of a trimline delineating weathered bedrock on the highlands and scoured rock in valleys and fiords suggested that the CSIS had a low-gradient along the outer half of the sound (Fig. 3.1a). The geometry and dynamics of the CSIS was simulated in a numerical ice sheet model (Kaplan et al., 1999).

Detailed mapping of the increase in rock weathering with altitude (Boyer and Pheasant, 1974; Dyke, 1979; Watts, 1979) and reconstructions of relative sea level histories based on radiocarbon dating of shells from ice marginal deltas (England and Andrews, 1973; Dyke, 1979; Locke, 1987) suggested that the late Wisconsinan ice extent around Cumberland Peninsula was more restricted than previously thought. These field studies were synthesized into a map depicting the early and late Foxe (Wisconsinan) glacial limits at a scale of 1:500,000 (Dyke et al., 1982) indicating that large areas of the peninsula remained ice-free during the last glaciation (Nunataks, Fig. 3.1b, Ives, 1974; 1978). Additionally, it was recognized that local cirque glaciers and ice caps advanced independently from the LIS and occupied fiords and valleys in eastern and northeastern Cumberland Peninsula (Fig. 3.1a, Miller, 1973; Hawkins, 1985; Locke, 1987), a

significant departure from the assumption of ice sheet glaciation first, followed by Holocene alpine systems during deglaciation. Further evidence for restricted ice cover was recovered from sediment cores obtained from tarns located on the interfluves of coastal fiords (Wolfe and Härtling, 1996; Steig et al., 1998). The stratigraphy and radiocarbon dating of the cores indicated continuous sedimentation since the last interglaciation (Wolfe et al., 2000), which was corroborated by the lack of till deposits in the lake basins. This conclusion was augmented by TCN dating of boulders on moraines down slope of one of the lakes revealing that actively eroding ice remained below the lake elevations (Steig et al., 1998).

The concept of selective linear erosion (Sugden, 1977, 1978) offered a possible solution for the conundrum by proposing that wet, sliding, warm-based ice eroded the substrate and dry cold-based ice frozen to the bed protected the weathered upland plateaus. Altitudinal weathering contrasts were thus interpreted to indicate changes in subglacial erosion related to basal thermal conditions. This notion led to a new conceptual model of ice extent in the eastern Canadian Arctic which seemingly reconciled many of the conflicting interpretations (Goldilocks model, Miller et al., 2002). Their conceptual model proposed an intermediate LIS extent (Fig. 3.1b) with fast-moving, low-gradient outlet glaciers occupying marine embayments and fiords, while slow-moving ice that was frozen to the bed covered the intervening upland plateaus. Because slow-moving ice has steeper surface gradients, it was proposed that it terminated inland from the coast, so that high-elevation coastal terrain remained ice free during the last glaciation (Miller et al., 2002). Although the Goldilocks model provided a framework that was consistent with many of the observations, the LGM ice model was

based on limited field evidence from the interior of the peninsula. Therefore, high-resolution maps depicting the different ice masses that covered Cumberland Peninsula and additional geochronology data, particularly from the interior, are required to test the Goldilocks model, to address the remaining conundrums regarding the anomalous readvance of the CSIS during the YD, and to investigate the variation of ice dynamics in response to post-LGM climate changes.

3.4 METHODS

3.4.1 Geochronology

The principal targets for chronology included selected ice marginal positions from coast to interior and a glaciolacustrine subaqueous fan in a lake that was dammed at one end by the LIS and at the other end by local valley ice. We also needed to resolve the significance of a new date of 43.1 ± 0.4 cal ka BP (cal ka BP is used for re-calibrated radiocarbon ages with BP indicating time before the year 1950), on mollusc shell from a glaciomarine delta that appeared to have been deposited during the current interglacial. The abundance of quartz in boulders on moraines and erratics near meltwater channels allowed us to use cosmogenic ^{10}Be. Samples for TCN exposure dating were collected from large flat-topped boulders that consisted of Proterozoic fine- to medium-grained metatonalities or medium- to coarse-grained gneisses and granodiorites with 8% to 30% quartz (Fig. 3.2, Table A2.1). Most samples were obtained by cutting 2 - 3 cm deep grooves with a gas-powered diamond-blade cutoff saw and removing 2 - 4 cm wide by 8 - 10 cm long blocks of rock by chisel and hammer. Where joint planes were suitable, thin chips of rock were knocked off by hammer and chisel from the surface of the boulders. Thickness of the sample, surface inclination, boulder geometry, landscape

position, and condition of the sampled surface (weathering degree, type of weathering, lichen cover, lithology and grain-size) were noted. No samples had topographic shielding and shielding by snow cover was minimised by selecting wind-exposed sites and the highest boulders possible (correction for the effect of snow cover will increase the ages by a few percent at most). Approximately 2 kg of rock were collected from the centre of near-horizontal top surfaces (<10° inclination) of large boulders (>1 m height). Lichen and loose minerals were removed with a wire brush, and the rock pieces were crushed in a jaw crusher and disk pulverizer, and dry sieved for separation of grain size fraction 350 – 500 μm.

Two cosmogenic nuclide depth profiles (e.g., Hidy et al., 2010) were collected from pits dug into the surface of glacio-lacustrine and glacio-marine deposits. The raised glaciomarine delta is situated on the southern coast of Cumberland Peninsula (65.42 °N, 64.25 °W, 20.5 m asl, Ujuktuk Fiord, Fig. 3.3a), and the glaciolacustrine deposit is located in Nacsac Valley (here referred to as Moon Valley, as in previous publications) north of Pangnirtung connecting the west coast of Pangnirtung Fiord with the Kolik River valley (66.35°N, 65.73 °W, 574 m asl, Fig. 3.3b). The pits were excavated by hand in locations that appeared to be stable, i.e., lacking conspicuous cryoturbation features and away from gulley edges, or other evidence of post-depositional modification. The stratigraphy of the deposits was described before collection of samples (Fig. 3.4, supplementary file, Table A2.1, Fig. A2.5). The profiles consisted of five 2-kg coarse sand samples, each collected from an approximately 5 cm thick swath at depths ranging between 35 and 150 cm below the mixing zone (mixing was caused by cryoturbation and in places bioturbation, and can be easily distinguished from unmixed sediment on the

basis of sedimentary structure). The sand samples were rinsed, dried, and dry sieved to separate the 350 – 500 μm size fraction. For one of the profiles, the sieved size fraction was increased to 250 – 500 μm, and larger clasts were crushed and sieved for size fraction 350 – 500 μm to obtain enough quartz mass. The sieved and crushed material were purified separately, and purified quartz of both batches were combined in equal proportions for each depth profile sample (20% sieved : 80% crushed) based on the relative mass of available purified quartz in both batches.

For all TCN samples, quartz purification was achieved by a combination of physical (magnetic separation, sand abrasion) and chemical (aqua regia, HF etching, and multiple cycles of dilute HF ultrasonication) procedures (Kohl and Nishiizumi, 1992). For rock samples, 35 g of quartz were spiked with 200 mg of ^{9}Be-carrier solution (produced by J. Klein from a shielded beryl crystal extracted from the Homestake Gold Mine, the carrier has 1015 μg Be g^{-1} and a long-term average $^{10}Be/^{9}Be$ of 4×10^{-15} at Lawrence Livermore National Lab) before dissolution in a mixture of hydrofluoric and perchloric acid. For the depth profiles, considering the potential short exposure time and low production rate with depth, 100 – 150 g of quartz was dissolved after addition of 200 mg carrier. Extraction of Be was completed by a combination of ion chromatography and pH-controlled precipitations of Be- hydroxides, followed by evaporation and ignition to BeO using a Bunsen burner. Be-oxides were mixed with high purity niobium (1:1 by volume) and sent to Lawrence-Livermore National Lab for accelerator mass spectrometry (AMS) analysis. AMS measurements were completed in three separate runs in April 2010 and October 2011 using standard 07KNSTD3110 ($^{10}Be/^{9}Be$ 2.85 x 10^{-12}) and yielding a 1-σ precision of <3% for most samples (except for two, with 7.4 and 9.3%

precision). Process blanks for the three AMS runs ranged between 4.9 x 10^{-15} to 1.7 x 10^{-14}, which were used for subtraction of background concentrations that were <1% for all samples. Total uncertainty of calculated ^{10}Be concentrations includes AMS measurement error, blank correction error, and 2% uncertainty for chemistry processing, added in quadrature (Table 3.1). Exposure ages were calculated with the CRONUS KU online calculator version 1.0 (http://web1.ittc.ku.edu:8888/) using the new ^{10}Be production rate (Borcher et al., in press) and time-variant, nuclide-specific scaling scheme of Lifton et al. (2014), and assuming a low subaerial erosion rate of 1 mm ka^{-1} (*Chapter 4*). The depth profiles were modeled with a geologically-constrained Monte Carlo approach (Hidy et al., 2010) that allows simultaneously solving for exposure ages and inheritance with constraints on erosion rates. Solutions for the depth profiles were found at 1σ confidence level (supplementary file, Table A2.3, Fig. A2.3 and A2.5 – A2.6).

Previously published studies provide additional chronological constraint in other parts of Cumberland Peninsula. However, the previous data were calculated assuming a higher production rate and using a different half-life for ^{10}Be decay. These two effects cause 10-15 % younger ages than those calculated with the new, lower production rate (Borcher et al., in press), and the revised ^{10}Be half-life (Chmeleff et al., 2010; Korschinek et al., 2010). Because essential information required for re-calculation of exposure ages was not stated in the original publication, we cannot currently correct the previous data for the change in ^{10}Be half-life and productions rates.

Hiatella arctica shells collected in a 3.5 m thick foreset package at the top of a 15 m thick ice-marginal, glaciomarine delta at the head of Ujuktuk Fiord, and shells of

Mytillus edilus collected in the upper section of a 30 m thick sandy marine terrace at American Harbour (Fig. 3.1) were radiocarbon dated at the Keck Carbon Cycle AMS Laboratory at the University of California, Irvine, CA. Calibration of these two ages has been completed with the Calib 7.0.2 program (Stuiver and Reimer, 1993) using the marine 13 calibration curve (Reimer et al., 2013) with an additional ΔR correction of 140 a or a total ΔR of 540 a as applied for this region in recent studies (Table 3.3, Dyke, 2004; McNeely et al., 2006). Previously published radiocarbon dates on marine shells referred to below are similarly calibrated, but for samples measured at the Geological Survey of Canada (GSC) radiocarbon laboratory 'normalized corrected' radiocarbon ages were used (McNeely and Brennan, 2005). Previously published dates on terrestrial materials are calibrated using the Northern Hemisphere IntCal09 calibration curve (supplementary file, Table A2.4, Reimer et al., 2009).

3.4.2 Surficial Deposits

Surficial mapping was completed by airphoto interpretation at a scale of 1:60,000 followed by field verification during the summers of 2009 and 2010. Raised marine deposits were visited for measurements of the marine limit with a Wallace and Tiernan surveying altimeter as well as sample collection for radiocarbon dating and TCN depth profiles. Mapped moraines were searched for boulders suitable for TCN dating (>1m high to limit the effects of rolling, snow cover, and exhumation from under till by frost heave or moraine erosion), and glacier paleoflow directions were measured opportunistically on striated bedrock (multifaceted and lee-side surfaces where available) in order to assess the validity of ice flow features mapped from airphotos. The revised

field maps were then compiled into nine map sheets published at a scale of 1:100,000 (Dyke 2011a-f; 2013a-c).

A map of ice margin positions depicting the retreat of glaciers throughout the peninsula was compiled from the mapped moraines and lateral meltwater channels through topographic correlation. Field and airphoto measurements of ice flow directions were combined with interpretations from the ice margin map. A database of over 200 previously available dates (radiocarbon, TCN, and optical stimulated luminescence (OSL)) and the new TCN ages presented here was used to provide numerical chronology for the mapped ice margin positions. Based on this chronological control, the extent of three distinct ice advances (moraine building) was mapped throughout the peninsula. From these maps, a minimum estimate for paleo-ELA was inferred using the highest elevation of lateral moraines (Meierding, 1982; Porter, 2000). The interpolated isolines of paleo-ELA were corrected for isostatic rebound inferred from relative sea level data (Dyke, 1979; Kaplan and Miller, 2003; Cowan, 2015; Hughes Clarke et al., 2015) and estimated eustatic sea level for the specific time interval (supplementary file, section A2.4, Miller et al., 2011). While eustatic sea level does not account for gravitational rise of sea level due to the mass of ice in the region, the uncertainty related to the simplified approach used here is within the uncertainty for estimation of the elevation of lateral moraines and interpolation of relative sea level data. Therefore, inferred changes in ELA through time should be interpreted with caution, but they reveal general patterns in temperature and precipitation change in the region.

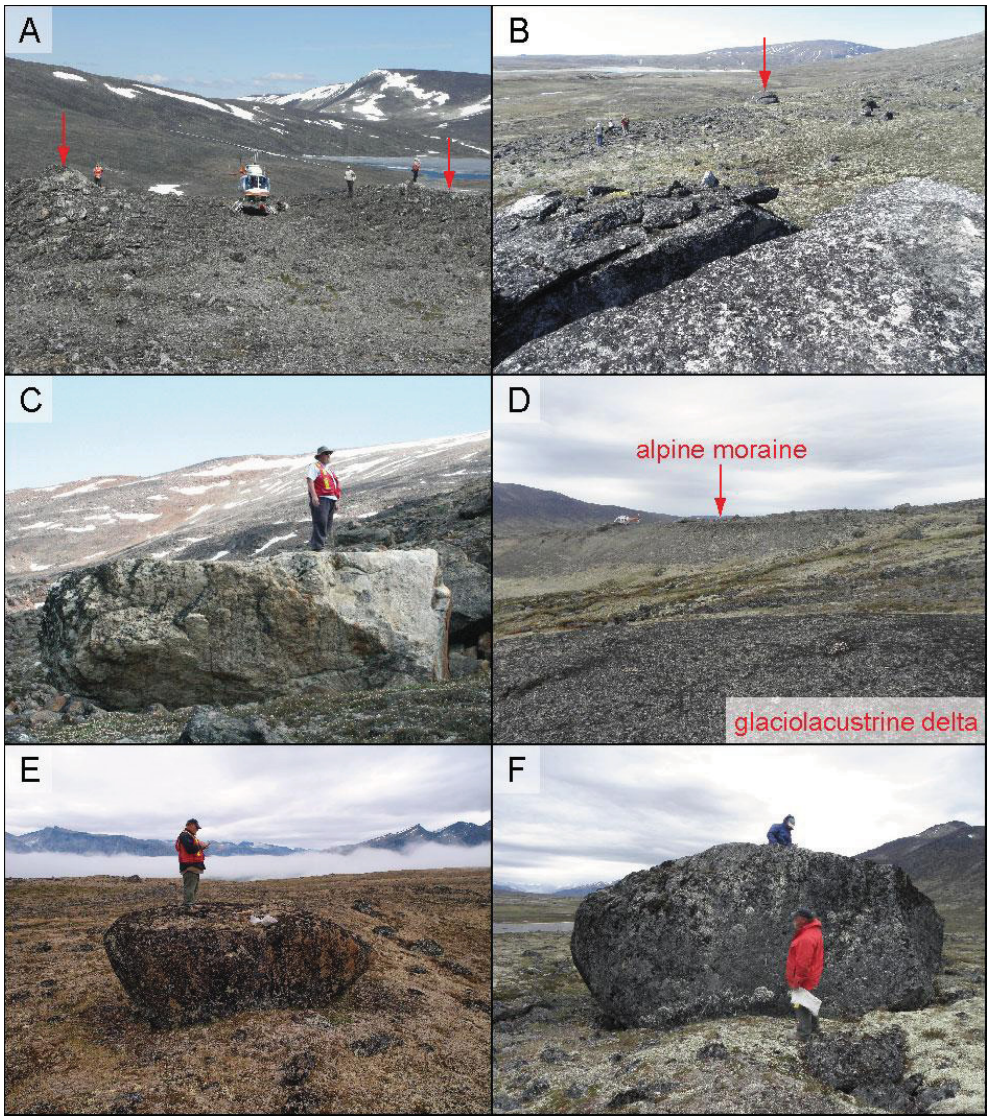

Fig. 3.2 Examples of moraines and erratic selected for exposure dating (see Table 3.1 and Fig. 3.3 for locations). **A.** Double crested lateral moraine (indicated by red arrows) near the mouth of the fiord on the southwestern coast of Cumberland Peninsula, where samples E025 - E027 were collected. **B.** Surface of sample E039 looking towards sample E040 (marked by red arrow) located in a broad part of the valley. C**.** Sample E002 on lateral moraine in the interior of the peninsula. **D.** Glaciolacustrine delta (depth profile of samples E282A-01 to -05) dammed simultaneously by LIS and Pangnirtung Fiord ice cross-cutting an alpine moraine (indicated by red arrow). **E.** Sample A353 on the second recession moraine deposited by Pangnirtung Fiord ice. **F.** Sample E284A-02 on LIS recession moraine.

	Sample ID[a]	Latitude (d.d)	Longitude (d.d)	Elevation (m)	Bouder height (cm)	^{10}Be concentration[b] (10^5 atom g^{-1})	^{10}Be age[c] (1 mm ka^{-1}) (ka)	Weighted mean (ka)
'central valley'	E092A-01	66.25	-63.70	764	150	1.86 ± 0.05	*20.6 ± 1.7*	
	E002A-01[d]	66.17	-63.86	539	200			
	E003A-01	66.17	-63.85	552	50	0.76 ± 0.03	10.3 ± 0.9	10.0 ± 0.4
	E004A-01	66.17	-63.85	558	80	0.72 ± 0.02	9.7 ± 0.8	
	E041A-01	65.84	-64.47	555	120	2.11 ± 0.20	*29.3 ± 3.7*	
	E052A-01	65.82	-64.45	392	100	1.21 ± 0.09	*19.2 ± 2.1*	
	E059A-01	65.71	-64.49	318	130	1.36 ± 0.04	*23.0 ± 2.0*	11.7 ± 0.9
	E060A-01	65.71	-64.49	298	140	0.68 ± 0.02	11.7 ± 0.9	
	E039A-01	65.70	-64.51	290	300	1.17 ± 0.04	*20.8 ± 1.7*	
	E040A-01[d]	65.70	-64.51	295	180			
	E025A-01[d]	65.20	-64.34	199	160			
	E026A-01	65.20	-64.34	204	50	0.73 ± 0.02	14.1 ± 1.2	14.3 ± 0.8
	E027A-01	65.20	-64.34	207	60	0.75 ± 0.03	14.6 ± 1.3	
Moon Valley	A167A-01	-65.31	-65.31	472	120	0.87 ± 0.03	11.1 ± 0.9	
	A167A-02	-65.31	-65.31	472	150	1.03 ± 0.03	*13.2 ± 1.1*	11.1 ± 0.9
	A167A-03	-65.31	-65.31	472	100	1.49 ± 0.05	*19.1 ± 1.6*	
	A351A-01	66.31	-65.61	477	150	0.69 ± 0.02	10.1 ± 0.9	
	A352A-01	66.31	-65.61	470	130	0.72 ± 0.03	10.6 ± 0.9	10.2 ± 0.3
	A353A-01	66.31	-65.61	470	130	0.69 ± 0.02	10.1 ± 0.9	
	E284A-01	66.34	-65.82	482	200	0.76 ± 0.02	11.2 ± 0.9	
	E284A-02	66.34	-65.82	482	350	0.78 ± 0.02	11.3 ± 1.0	11.2 ± 0.4
	E284A-03	66.34	-65.82	482	200	1.07 ± 0.03	*15.7 ± 1.3*	
	E223A-01	66.34	-65.74	559	150	1.06 ± 0.03	14.6 ± 1.2	
	E223A-02[d]	66.34	-65.74	559	150			14.6 ± 1.2
	E223A-03[e]	66.34	-65.74	559	300	0.79 ± 0.02	*10.7 ± 0.9*	
	E283A-01	66.35	-65.72	578	150	1.71 ± 0.06	*23.0 ± 2.0*	
	E224A-01	66.34	-65.73	563	150	1.37 ± 0.04	18.8 ± 1.6	
	E224A-02[e]	66.34	-65.73	563	100	0.64 ± 0.02	*8.6 ± 0.8*	18.8 ± 1.6
	E224A-03	66.34	-65.73	563	80	2.51 ± 0.07	*35.0 ± 3.0*	

[a] abbreviated sample ID for clarity, full sample ID in Table A2.1

[b] 1σ external uncertainty includes random error associated with the concentration measurement, and systematic error associated with production rate and decay constants

[c] CRONUS KU online calculator, verion 1.0, accessed 15.11.2014. 1σ error includes uncertainty in nuclide concentrations, production rates and decay constants. Ages are calculated for a subaerial erosion rate of 1 mm ka^{-1}, considering the depth of sample, using an attenuation lenghts of 150 g cm^{-2}, and assuming full exposure to cosmic ray flux (2π). Ages in italics are interpreted to be statistical outliers considering their stratigraphic position and relationship to other ages on the same landform. They may be too old owing to an inherited TCN component, or too young because of post-depositional processes including exhumation from a till cover, overturning by cryoturbation, periodic burial by a very thick or dense snow cover, or unrecognized erosion (see footnote e).

[d] samples yielded too low current during AMS measurement

[e] too-young ages for morpho-stratigraphic position

Table 3.1 TCN data chronology for boulders collected in the 'central valley' and in Moon Valley.

	Sample ID[a]	Depth to top of sample swath (cm)	Sample swath thickness (cm)	^{10}Be concentration[b] (10^5 atom g^{-1})	Deposition age[c] (ka)
'central valley'	E140A-06	35	5	0.50 ± 0.02	
	E140A-05	65	5	0.42 ± 0.01	12.4 - 1.0 + 2.8
	E140A-04	90	5	0.36 ± 0.01	
	E140A-03	125	5	0.34 ± 0.01	
	E140A-02	150	5	0.36 ± 0.01	
Moon Valley	E282A-05	48	6	1.38 ± 0.04	
	E282A-04	63	8	1.29 ± 0.04	14.7 - 1.6 + 2.5
	E282A-03	80	7	1.20 ± 0.03	
	E282A-02	98	8	1.11 ± 0.03	
	E282A-01	117	7	1.10 ± 0.03	

[a] abbreviated sample ID for clarity, full sample ID in Table A2.1

[b] 1σ error includes AMS measurement uncertainty, weighted blank correction, and 2%

[c] computed using the depth profile calculator by Hidy et al. 2010, stated is 1σ uncertainty

Table 3.2 TCN chronology for two depth profiles. **Top:** Raised glacio-marine delta, capped by a glacio-lacustrine layer (sampled) in the 'central valley' (Lat. 65.42, Long. -64.25, 20.5 m asl). Depositional age is determined for the four uppermost samples (see text and Fig. 3.4). **Bottom:** Glaciolacustrine delta deposited in ice-dammed lake in Moon Valley (Lat. 66.35, Long. -65.73, 574 m asl; see supplementary file, Fig. A2.5).

UCIAMS Lab ID	Sample ID	Latitude (d.d)	Longitude (d.d)	Elevation [a] (m)	Material	$d^{13}C$ (‰)	fraction Modern	$D^{14}C$ (‰)	14C age (BP)	Calibrated age [b] (cal ka BP)
77704	09SRB-A027	65.42	-64.25	20.5	*Hyatella arctica*	1.71 ± 0.1	0.0071 ± 0.0004	-992.95 ± 0.43	39800 ± 490	43.1 ± 0.4
77705	09SRB-K015	66.25	-66.54	32.0	*Mytilus edulis*	-0.78 ± 0.1	0.3837 ± 0.0009	-616.30 ± 0.91	7695 ± 20	8.0 ± 0.1

[a] measured with a Wallace and Tierman surveying altimeter

[b] calculated with Calib 7.0.2 (Stuiver and Reimer, 1993) using marine 13 calibration curve (Reimer et al., 2013), 1σ uncertainty stated

Table 3.3 New radiocarbon data on marine shells collected from raised marine deltas in 2009. Sample locations are indicated in Fig. 3.1.

3.5 GEOCHRONOLOGY RESULTS AND INTERPRETATION

3.5 1 Boulder Exposure Ages

While samples were collected at various targeted and opportunistic locations throughout the peninsula (high boulder height was a limiting factor), two dynamical systems received greater focus: retreat history of alpine ice from Cumberland Sound back to cirque sources, and the separation of the LIS from locally sourced fiord ice in the western portion of the Peninsula.

The TCN data for 29 boulders and two depth profiles are presented in Tables 3.1 and 3.2 and summarized in Figure 3.3. Three samples yielded insufficient currents during AMS analysis to measure $^{10}Be/^{9}Be$ ratios, likely caused by incomplete purification of quartz in quartz-poor samples. Calculated exposure ages of the other samples range from 8.6 ± 0.8 to 35 ± 3 ka (Table 3.1, Fig. 3.3, all error ranges are stated with 1σ confidence level throughout the paper). The spread in ages has significantly reduced the confidence and precision of the chronology at any location. However, by using stratigraphic constraints (end moraine ages decrease upvalley) and comparison with other available radiocarbon and exposure dating chronology, it is possible to provide an interpretation of the age distribution. Most of this variation is interpreted to be related to a number of exposure ages that appear to be too old relative to the neighbouring ages or for their stratigraphic position. The anomalously old exposure ages may be best

explained by inherited TCN concentrations from exposure prior to their final deposition, signifying insufficient erosion during glacial transport. This explanation is consistent with the interpretations by others for similar positive-tail distributions in the exposure ages in TCN datasets on Baffin Island (e.g., Davis et al., 1999; Marsella et al., 2000; Briner et al., 2006). The most probable average inheritance for the amalgamated sand grains in the top of the delta at the head of Ujuktuk Fiord is 2.5 x 10^4 atoms g^{-1} (supplementary file Table A2.3), corresponding to an exposure age of 5.7 ± 0.6 ka (assuming a time-averaged site production rate of 4.1 atoms g^{-1} a^{-1}, supplementary file Table A2.2). Likewise, the estimated average inheritance for the amalgamated sand grains in the glaciolacustrine delta in Moon Valley is 8.8 x 10^4 atoms g^{-1} (supplementary file Table A2.3), which corresponds to an exposure age of 12 ± 1.1 ka (assuming a time-averaged site production rate of 7.0 atoms g^{-1} a^{-1}, supplementary file Table A2.2). These high inheritance concentrations are a rough indication of the average TCN concentrations throughout the subglacial catchment that fed the deltas. It is also apparent that locations exhibiting the greatest range in exposure ages tend to be in the interior of the peninsula, whereas replicate boulder exposure ages on coastal and deep valley sites reproduced better (Fig. 3.3). This correlation supports the interpretation that inheritance has caused much of the scatter in ages, because the fiord ice should be more erosive than the summit ice that tends to be cold-based (*Chapter 4,* Briner et al., 2014).

Two boulders yielded ages that are too young for their respective morpho-stratigraphic positions. These could be related to exhumation through till that was not apparent at time of collection, overturning of boulders by cryoturbation, toppling of boulders early in the exposure history so that differences in lichen patterns are

indistinguishable, or significantly greater snow cover than assumed. While there is no apparent correlation between boulder height and exposure age that would support this interpretation (supplementary file Fig. A2.1), these are the most logical explanations (Briner et al., 2005; Applegate et al., 2010; Heyman et al., 2011; Applegate et al., 2012). We rule out unrecognized problems with the chemistry or AMS analyses because the depth profile concentrations can be explained with exposure histories that fit within their 1σ measurement precisions (supplementary file Fig. A2.3 and A2.5). Because inheritance can cause ages to be too old by a factor of 2 or more, whereas the effect of post-depositional processes will only change the ages by a few percent, we chose the youngest date(s) (indicated in red in Fig. 3.3) on a set of moraines to represent the age of the deposition (in italics, Fig. 3.3). However, we note that the presented TCN data could also be interpreted in other ways, if different processes are assumed to cause the spread of calculated exposure ages. The exposure ages that remain after culling the youngest exposure ages at each site provide chronological control on the deglaciation history of an alpine outlet glacier in a major central alpine valley, which we refer to as 'central valley' in the following sections (Fig. 3.3a) and the timing of initial separation of the LIS and local fiord ice in Moon Valley (Fig. 3.3b).

The chronology established from boulder exposure ages in the 'central valley' reveals that the alpine outlet glacier retreated from the coast at 14.3 ± 0.8 ka (weighted mean is stated if two or more ages are available at one location, samples E026 and E027, Table 3.1). A prominent sequence of moraines and meltwater channels in a wider area of the main valley are dated to 11.7 ± 0.9 ka (sample E060, Table 3.1) by one of six boulders collected on the associated till deposit. Final retreat to the interior is constrained

by two boulders collected on one of the innermost recessional moraines (close to modern glaciers) that are dated to 10.0 ± 0.4 ka (samples E003 and E004, Table 3.1).

In Moon valley, the outermost LIS moraine was deposited at 14.6 ± 1.2 ka based on one of three boulders (sample E223A-01, Table 3.1), and the next younger LIS moraine is dated to 11.2 ± 0.4 ka based on two out of three boulders (samples A284A-01 and -02, Table 3.1). While the maximum position of Pangnirtung Fiord ice could not be dated because of a lack of suitably large boulders, the recessional moraine, part of the Duval moraine system, yielded an age of 10.2 ± 0.3 ka (samples A351 – A 353, Table 3.1). The alpine moraine deposited by ice flowing southward from a cirque was most likely deposited at 18.8 ± 1.6 ka (middle age of three boulders, sample E224A-01, Table 3.1), because the cross-cutting relationship with the glacio-lacustrine delta indicates that it has to be older than the formation of the lake.

The ages of the recessional moraines of both LIS and Pangnirtung Fiord ice are comparable to the younger mode established previously for the Duval moraines along Pangnirtung Fiord (modes ~22 ka and ~10 ka, Marsella et al., 2000). Except for the alpine moraine in Moon Valley, we have not found ages corresponding to the older Duval moraine mode. Surmising from the high number of boulders we measured that incurred inheritance, it would be reasonable to suggest that the older mode (~22 ka) is also an artifact of inherited concentrations. However, the close agreement of a half dozen of the previously published samples with ages of 18.9 ± 1.4 to 25.3 ± 1.3 ka is difficult to explain solely by inheritance, since inherited concentration should yield a more dispersed age distribution (Marsella et al., 2000). The older mode may correlate with the initial

advance of the CSIS postulated by Jennings et al. (1996) to have occurred between ~34 ^{14}C ka and ~21 ^{14}C ka. A lack of ages corresponding to the older mode elsewhere along the southwestern coast might be attributed to the complete confluence of alpine outlet glaciers and Cumberland Sound ice stream, during which no ice marginal moraines were deposited.

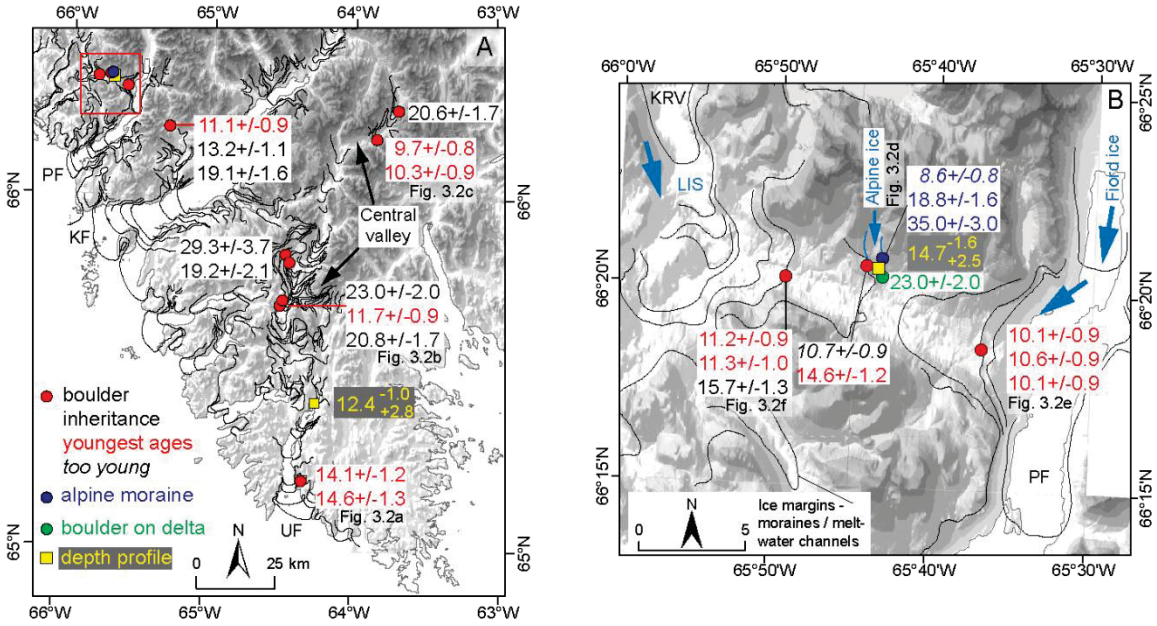

Fig. 3.3 New TCN data and indication of locations of pictures shown in Fig. 3.2. **A.** Ice recession in the 'central valley' occupied by an alpine outlet glacier. Red box indicates location of Moon Valley shown in detail in B. PF: Pangnirtung Fiord, KF: Kingnait Fiord, UF: Ujuktuk Fiord. **B.** Moon Valley west of Pangnirtung Fiord (PF), where a lake was concurrently dammed by the LIS and local fiord ice. A glaciolacustrine delta deposited at the margin of the lake, which cross-cuts a moraine deposited by a preceding advance of an alpine glacier on the northern slope of the valley, was dated with a TCN depth profile and a boulder deposited on the delta. Exposure ages shown are calculated for a subaerial erosion rate of 1 mm ka^{-1}. KRV: Kolik River Valley.

3.5.2 Depth Profile Chronologies

Ujuktuk Fiord glaciomarine delta. The glaciomarine delta on the south coast has a depth profile exposure age of 12.4 $^{-1.0}/_{+2.8}$ ka calculated using only the four shallowest samples (Fig. 3.4, Table A2.3, Fig. A2.3). The deepest sample of this depth profile has a

significantly higher TCN concentration than the next deepest sample, suggesting that the lowest sediment has a higher inheritance. The deepest sample was collected just above a shell-bearing zone (Fig. 3.4). As seen in the adjacent gully section and coastal scarp, the shells are contained in a 3.5 m thick foreset package at the top of a 15 m thick ice-marginal, glaciomarine delta that is capped by a 1.5 m thick glaciofluvial topset layer. It is possible that part of the deepest TCN sample included some of the foreset sediments, hence a different initial TCN concentration. A *Hiatella arctica* shell collected in the shell-rich area with several well preserved species on the wind-eroded scarp of the delta has been radiocarbon dated to 43.1 ± 0.4 cal ka BP (Table 3.3, see section below) indicating the possibility of an unconformity within the depth profile that is dated to 12.4 $^{-1.0}/_{+2.8}$ ka (separating the four shallow samples from the deepest sample). The top of the delta is wind eroded (Fig. A2.5) with scattered cobbles and boulders on the topset surface; they may represent a combination of eolian lag, outwash flood deposits, and ice rafted debris. At the location of the depth profile, net erosion of the glaciofluvial topset layer was estimated to range between 30 and 100 cm. This estimate of net eroded thickness was used in the depth profile calculator to constrain the age and inheritance of the depth profile (Table 3.2, Table A2.2 – A2.3). If less net erosion is assumed, calculated exposure ages are too young to fit into the morpho-stratigraphic moraine sequence based on the new chronology (Fig. 3.3a).

Moon Valley fan constraint on LIS glacial maximum position. Besides the boulder exposure age of 14.6 ± 1.2 ka (samples E223A-01, Table 3.1) obtained for the outermost LIS moraine, the intial retreat of the LIS is also constrained by a TCN depth profile collected from a glacio-lacustrine delta deposited in a small lake that was dammed

between the LIS margin and the local ice occupying Pangnirtung Fiord. The age of 14.7 $^{-1.6}/_{+2.5}$ ka obtained from the depth profile (Fig. A2.5) agrees closely with the boulder exposure age for the moraine damming the lake.

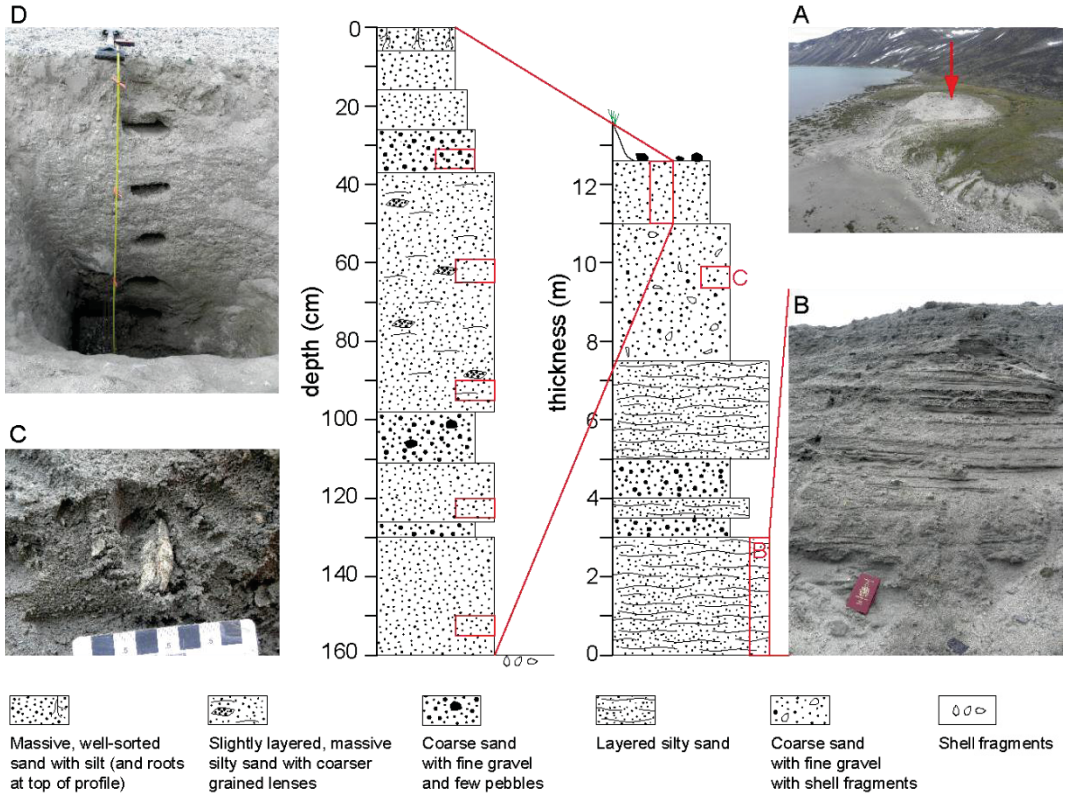

Fig. 3.4 Stratigraphic description of the raised glacio-marine and glacio-lacustrine complex delta (right column) and detail of uppermost 1.6 m (left column), in which samples for a TCN depth profile (red squares) were collected. **A.** Oblique air photograph of the delta (view NE taken in 2010) near the head of Ujuktuk Fiord at the southwestern coast of Cumberland Peninsula (see Fig. 3.3a for location). Location of depth profile on the delta is marked by red arrow. **B.** Photo viewing E showing the lowest section of the exposed horizontal finely bedded silty sand with gravelly lenses. **C.** Shells of *Hiatella arctica* in growth position in upper section of glaciomarine foreset sequence (scale shows cm), which is capped by glaciofluvial topsets. **D.** Depth profile in the uppermost 1.6 m of the glaciofluvial portion of the raised delta.

3.5.3 Radiocarbon Chronologies

The *Hiatella arctica* shell collected in the topset layer of the glacio-marine delta at the head of Ujuktuk Fiord (Fig. 3.3a) yielded a calibrated radiocarbon age of 43.1 ± 0.4

cal ka BP (Table 3.3). This age is significant, because this delta is the only OIS-3 marine deposit known from the Cumberland Sound area and it implies that minimum OIS-3 ice recession was at least about a third of the OIS-2 recession (from the coast to the interior). Furthermore, it indicates that crustal depression caused by ice cover during OIS-4 was not completely compensated during that part of OIS-3, and the shell age provides a maximum-limit for the timing of ice advance to LGM.

The *Mytilus edulis* shell sample, collected from a raised marine deposit (32 m asl) at American Harbour northwest of Pangnirtung Fiord (Fig. 3.1, Fig. A2.1h), yielded a calibrated radiocarbon age of 8.0 ± 0.1 cal ka BP (Table 3.3). This age is in agreement with previous chronology obtained from a nearby raised marine deposit below a terrace at 28 m (DIC-334, *Hiatella arctica*, calibrated age 8.3 ± 0.1 cal ka BP, Dyke, 1979, Table S2.4). It provides a minimum age for LIS recession. However, better minimum limiting ages for ice recession through Cumberland Sound have been obtained previously in Pangnirtung Fiord and Usualuk Valley northeast of our sample site (Fig. 3.1, see discussion below, Dyke, 1979, LeBlanc et al., 2011). The significance of the newly obtained date is that *Mytilus edulis* is regarded as a thermophile in this region and Cumberland Sound is near its geographic limit on the Canadian side of Baffin Bay (Aitken and Gilbert, 1989). The new 8.0 ± 0.1 cal ka BP date thus provides a minimum limiting age for incursion of subarctic waters into an ice free Cumberland Sound.

3.6 ICE FLOW AT LGM

Streamlined glacial bedforms mapped from airphotos and striae on bedrock surfaces were the primary ice flow indicators used. Care was taken to avoid measuring striae that may be affected by small-scale topographical anomalies. Cross-cutting striae

and striae on lee-side surfaces protected from the primary ice flow were sought to provide directions and relative timing of ice flow from a slightly different direction, but none were observed. Small scale (nail-head striae, cresentic gouges, stoss-lee features) and large-scale bedrock erosional features (roches moutonnées and other glacially streamlined bedrock forms) were used to infer dominant ice flow direction. Moraine shape (concave up ice), lateral moraine dip, and orientation of lateral meltwater channels also helped constrain glacier geometry and dominant ice flow direction during deglaciation.

Although the highest plateaus near Cape Mercy at the southern tip of the peninsula (Fig. 3.5) are mantled with felsenmeer showing no sign of glacial erosion, somewhat lower plateaus just north of there are glacially scoured and inscribed by a set of eastward trending bedforms that cross the width of the landmass. Because these bedforms originate in onshore flow from Cumberland Sound, they indicate that the CSIS inundated the southernmost tip of the peninsula. The sharp inland limit of this flowset indicates that the ice stream lateral margin was up to 18 km north of Cape Mercy at its widest, and the elevation of the scoured terrain indicates that the ice stream surface was >300 m above present sea level as it exited onto the continental shelf in Davis Strait. West of this flowset, there is no onshore bedform evidence of the CSIS east of Pangnirtung Fiord. We infer, therefore, that the boundary between the CSIS and alpine outlet glaciers lay outside of the coast within the sound.

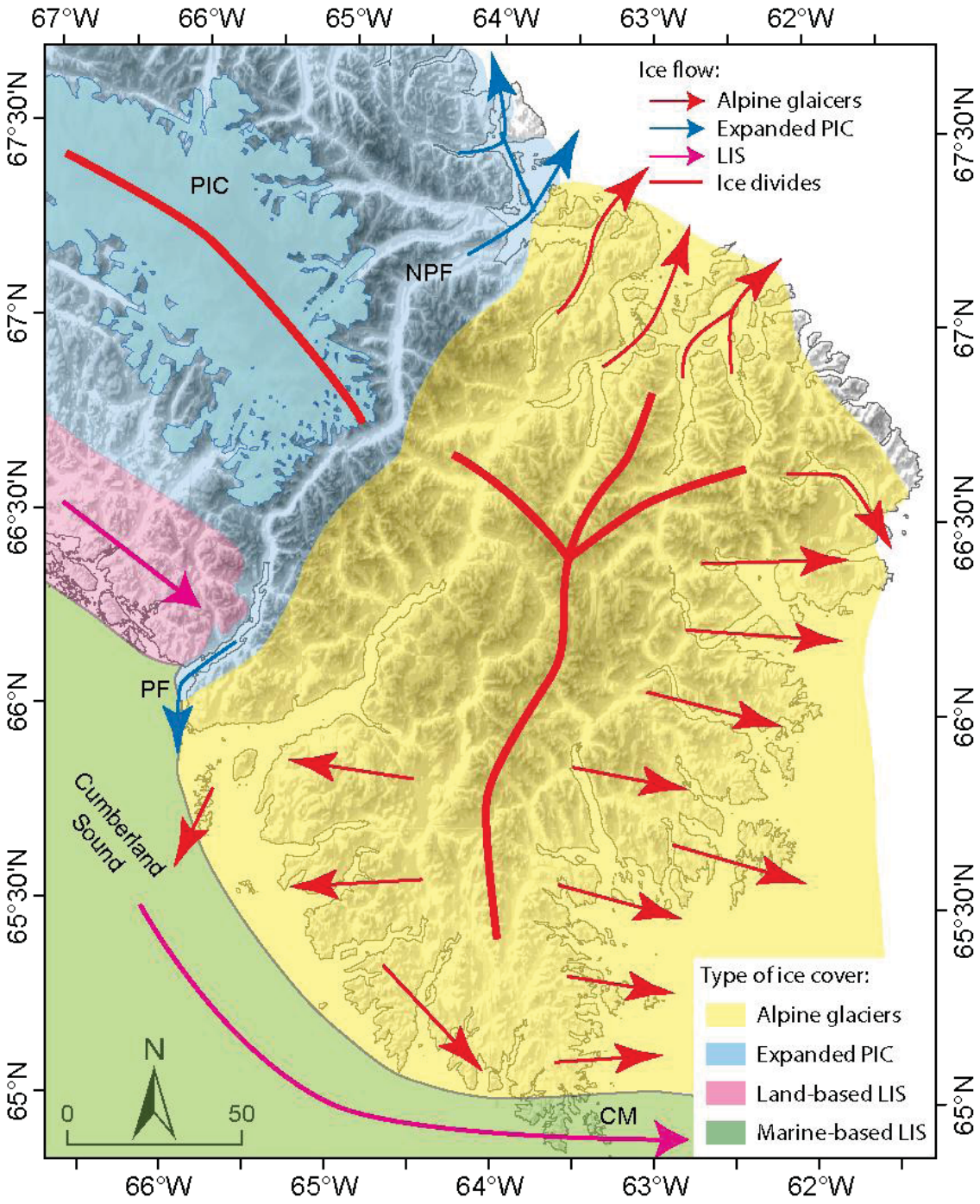

Fig. 3.5 Generalized ice flow at LGM: Most of the peninsula is covered by polythermal alpine glaciers (yellow shading). The land-based LIS (pink shading) only extended to west of Pangnirtung Fiord (PF), while the marine-based LIS (green shading) occupied Cumberland Sound causing deflection of the alpine ice flow at the southwestern coast of the peninsula. The expanded PIC coalesced with the LIS to the southwest, whereas the eastern PIC margin remained dynamically independent. CM: Cape Mercy, NPF: North Pangnirtung Fiord.

Abundant and well preserved bedforms and striae in scoured terrain farther north along the southeastern coast demonstrate persistent west to east flow, which is oblique to many NW-SE orientated valleys and fiords. This persistent flow pattern requires ice thicker than the topographic relief. However, along the southwest coast, ice flow directions vary but the overall flow direction was to the west and southwest, opposite to any flow that might possibly be related to an over-riding LIS. We interpret the ages of the ice flow indicators to represent the LGM ice configuration (Fig. 3.5), because there is only one set of striae preserved at each location visited, the striae and small- and large-scale landforms yield accordant directions, and the flow directions are consistent at nearby sites. Based on the opposing flow patterns, an alpine ice divide is inferred to have extended from the northeastern to the southwestern coast, generally setting atop the highest mountain ranges. Thus almost all of Cumberland Peninsula east of the PIC was covered by an alpine glacier system during the last glaciation. The highest plateaus and summits in this region, including many adjacent to extant glaciers, show no obvious sign of glacial scouring and instead are mantled by felsenmeer. The rest of the terrain is glacially scoured and (or) till covered. Hence, we infer that the alpine glacier complex was polythermal, thick enough to cover (almost) all of the topography but too thin to attain a warm base on the highest parts. The alpine ice divide funneled ice through most valleys and fiords of the peninsula, except for Pangnirtung and North Pangnirtung Fiords (Fig. 3.5). These fiords and fiords north of North Pangnirtung Fiord were filled by outlet glaciers of an expanded PIC that coalesced with the LIS on its western side, but remained dynamically independent on its eastern margin. The land-based LIS only extended onshore to the west of Pangnirtung Fiord, where it coalesced with the expanded PIC to

the north. Despite dedicated searches for ice flow indicators or provenance-indicating lithologies, there is no evidence for the LIS east of 65.74 °W. This interpretation is based on ice flow direction and the lack of high concentrations of calcium, magnesium or inorganic carbon in tills collected throughout the peninsula for geochemical analysis (Gammon et al., 2011). Elevated calcium concentrations would indicate origin of ice flow in the Foxe Basin, which is underlain by Paleozoic sediments. Limited land-based LIS extent on Cumberland Peninsula is corroborated by previous observation of dispersal of limestone erratics on Baffin Island (Andrews and Miller, 1979). Kaplan (1999) found a single dolomite erratic along the southeast coast of Cumberland Peninsula within the area we inferred was overridden by LIS, but two days of helicopter sampling of till adjacent to the head of Cumberland Sound by us failed to turn up a single carbonate erratic. While the land-based LIS did not cross the peninsula during the LGM, the CSIS impinged the southernmost tip of the Cumberland Peninsula at Cape Mercy (described above) causing eastwards deflection of ice flow from the fiords along the Cumberland Sound coastline (Fig. 3.5). Extension of the CSIS onto the continental shelf is supported by radiocarbon ages offshore (Jennings, 1993; Jennings et al., 1996).

3.7 DISCUSSION

3.7.1 Regional Deglacial Ice Dynamics

Based on moraines, lateral meltwater channels, and ice-contact deltas, over 100 ice margins have been mapped from air photos and field observations (Fig. 3.6). The new deglacial geochronology (Fig. 3.3) complemented by previously published TCN data (Steig et al., 1998; Marsella et al., 2000; Kaplan et al., 2001; Miller et al., 2002) and radiocarbon data (England and Andrews, 1973; Miller, 1973; Dyke, 1979; Dyke et al.,

1982; Brigham, 1983; Locke, 1987; Jennings, 1993; Miller et al., 2002; LeBlanc et al., 2011), and geomorphic position permit the correlation of three prominent ice marginal positions throughout the peninsula (Fig. 3.7 – 3.9). Ice marginal positions (moraines) are interpreted to represent re-advances of alpine ice at the end of H-1 at ~14.6 ka (Fig. 3.7), shortly after retreat of the CSIS from the outer part of the Sound (Jennings, 1993; Jennings et al., 1996; Kaplan et al., 2001), then at the end of the YD cold interval at ~11.7 ka (Fig. 3.8), and finally during the Cockburn substage, when the widespread Cockburn moraines were deposited by the LIS at ~9.5 ka (Fig. 3.9, Miller and Dyke, 1974; Andrews and Ives, 1978; Briner et al., 2009). Retreat rates for the intervening interstadials are inferred from these maps (Fig. 3.10) as well as the change in ELA through deglaciation (Fig. 3.11).

3.7.2 Heinrich Event 1 Re-Advance

At 14.6 ka, most of Cumberland Peninsula was still covered by alpine ice, the PIC extended to the northwestern coast, and the land-based LIS terminated in Moon Valley just west of Pangnirtung Fiord (Fig. 3.7). The CSIS had retreated through the deepest section of the Sound and the ice margin probably was located just west of the mouth of Pangnirtung Fiord adjacent to a prominent Laurentide recessional moraine onshore. Along most of the coast, ice was located at the mouths of embayments, fiords and valleys, but between Touak Fiord and Cape Mercy alpine ice still extended onto the (modern) continental shelf. This position is consistent with a closer proximity of the ice divide to the coast (Fig. 3.7) at this time relative to the younger readvances. We assume that parts of the northeastern coast between Cape Dyer and Reid Bay remained ice free at and after the LGM (see discussion below).

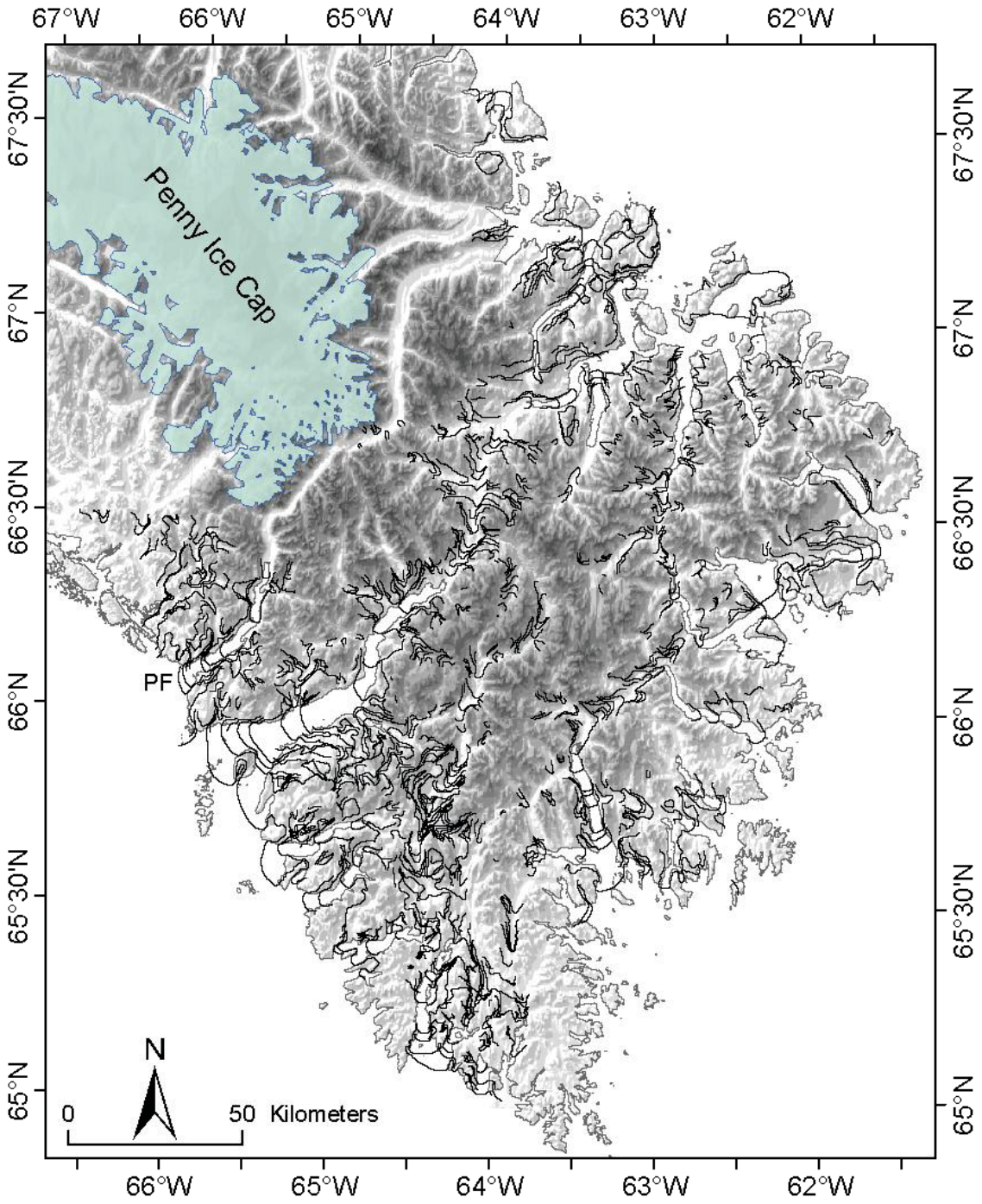

Fig. 3.6 Ice margin positions, inferred from mapped moraines and meltwater channels, are shown as black lines. The ice margins depict the retreat of outlet glaciers of the predominant polythermal glacier system, the PIC, and the land-based LIS west of Pangnirtung Fiord (PF).

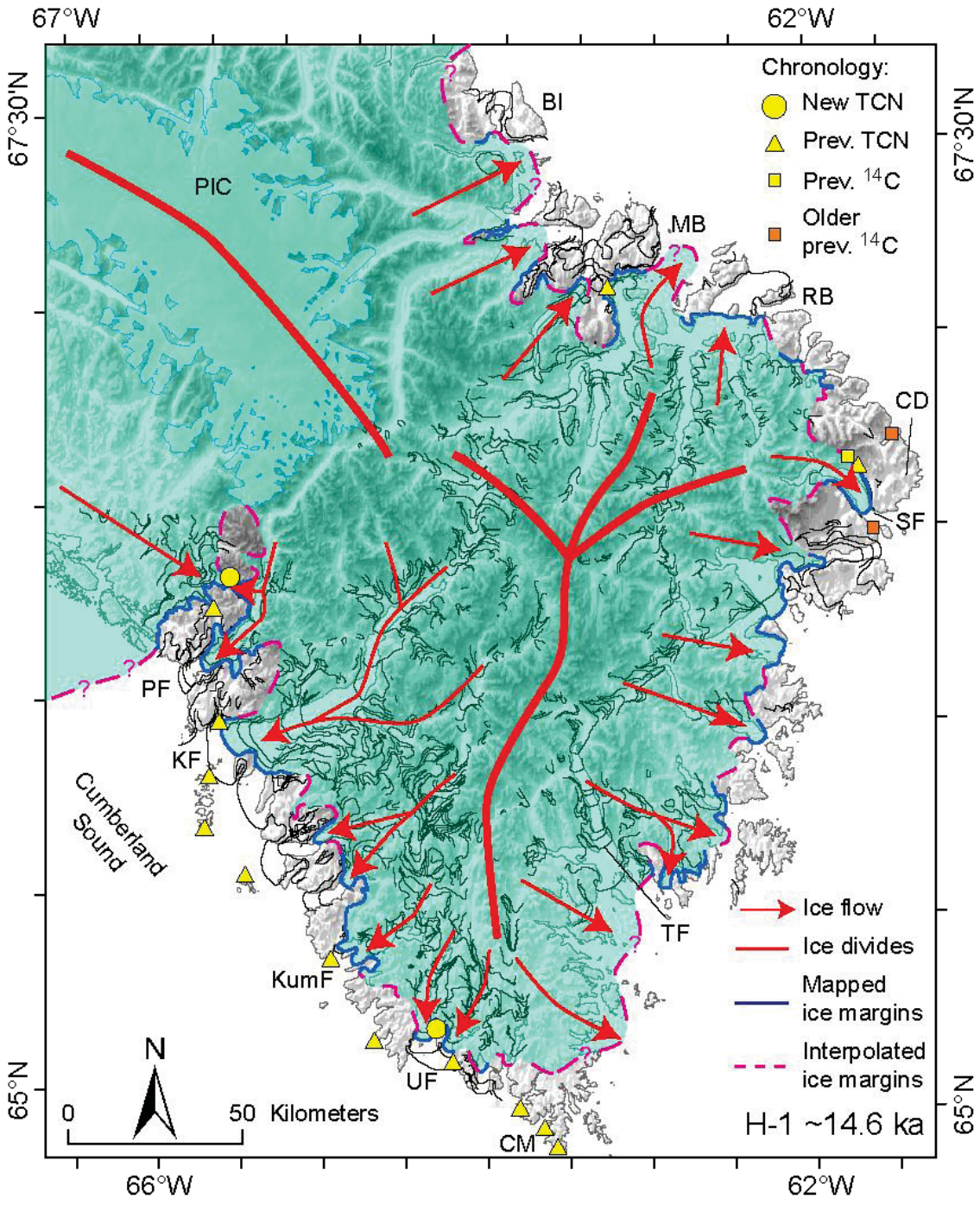

Fig 3.7 Early deglacial ice extent at ~14.6 ka. Yellow circles indicate new chronological constraint, yellow triangles indicate previous TCN data, and yellow square indicates previous radiocarbon data used to infer ice extent. BI: Broughton Island, MB: Merchants Bay, RB: Reid Bay, CD: Cape Dyer, SF: Sunneshine Fiord, TF: Touak Fiord, CM: Cape Mercy, UF: Ujuktuk Fiord, KumF: Kumlien Fiord, PF: Pangnirtung Fiord.

Recession of the CSIS through the deepest section of the sound is inferred from previous data indicating that Cape Mercy and the outermost areas of the southwestern coast were deglaciated between 12.4 – 14.4 ka (Kaplan et al. 2001, adjusted to ~14 – 16 ka with new production rate and lower ^{10}Be half-life). Considering relative sea-level data, Kaplan and Miller (2003) proposed that the ice stream rapidly retreated from the outer sound, followed by slower retreat through the narrowest part of the sound (between Ujuktuk and Kumlien Fiord), with subsequent fast retreat through the deepest section of the sound to Kingnait Fiord (Fig. 3.7). Prior retreat of the CSIS is required for the formation of moraines, meltwater channels, and raised marine deposits at the mouth of fiords and major valleys along the southwestern coast of Cumberland Peninsula. This retreat pattern of the CSIS, inferred from terrestrial data, is largely consistent with radiocarbon dating of marine sediment cores indicating that initial retreat from the continental shelf occurred no later than 15.9 ± 2.2 cal ka BP followed by retreat of the CSIS through the deepest section at around 12.1 ± 0.4 cal ka BP (Table A2.4, BETA-7405 and AA-3939, respectively, Jennings, 1993). The older age was derived from correction of an even older radiocarbon age of bulk organic matter (Jennings, 1993). Calibrating the uncorrected radiocarbon date yields an age of 23.6 ± 2.2 cal ka BP (Table A2.4, BETA-7405 orig.), which agrees better with the later interpretation that the CSIS initially advanced between 34 and 21 ^{14}C ka followed by ice recession and subsequent re-advance during the Younger Dryas at ~11 ^{14}C ka (see discussion below, Jennings et al., 1996).

The land-based LIS and local ice stood at their oldest recessional moraines in Moon Valley west of Pangnirtung Fiord, where outlet glaciers of both ice masses

simultaneously dammed a lake, as indicated by concordant ages obtained for the depth profile in the glaciolacustrine delta ($14.7\ ^{-1.6}/_{+2.5}$ ka) and a boulder exposure age on the oldest LIS moraine (14.6 ± 1.2 ka). Because all ice marginal features suggest that higher ground emerged earlier from the ice, we conclude that the plateaus adjacent to Moon Valley were deglaciated at about 16 - 18 ka (Fig. 3.7). That conclusion contradicts previous work indicating continuous sedimentation in tarns on these plateaus (Wolfe, 1994; Wolfe and Härtling, 1996). Wolfe and Härtling (1996) suggested that the unconsolidated lake sediments would have been eroded by covering ice, and thus concluded that the lake basins remained ice-free throughout the last glaciation. However, new and previous TCN data (*Chapter 4,* Bierman et al., 1999) indicate that the plateaus were covered by weakly erosive, cold-based ice caps during the last glaciation. These TCN results favour the subsequent reinterpretation of the lake record as a deglacial sequence followed by Holocene organic deposition, which are separated by a depositional hiatus from the underlying organic sediments (Frechette et al., 2006). Interestingly, Wolfe and Härtling (1996) had already considered this interpretation as one of three possible explanation of their radiocarbon data, but disregarded it as unlikely in favour of the ice-free interpretation.

In the Merchants Bay region (Fig. 3.7), previous TCN exposure dating of a series of moraines revealed successively younger ages with lower elevation (Steig et al., 1998) indicating diminishing ice extent since OIS-3. Ice-free conditions on the plateaus beyond the highest moraine ridge are supported by radiocarbon and OSL dating of lake sediments demonstrating continuous sedimentation on the plateaus since the last interglacial (Wolfe et al., 2000). Previous research on Broughton Island also suggested that ice covered only

the lower-lying areas of the island during the early Wisconsin, and was restricted to the channel between Broughton Island and Cumberland Peninsula during a re-advance in OIS-2 following significant retreat in the middle Wisconsinan (OIS-3, England and Andrews, 1973; Andrews et al., 1976b; Brigham, 1983). Because we do not have additional age constraints on the northeastern coast, we assume that the H-1 ice margin (Fig. 3.7) corresponds to the lowest moraine dated by Steig et al. (1998) and that ice did not extend across Broughton Island. Contrary to the Goldilocks paradigm, we believe that the plateaus on Broughton Island and in the Merchants Bay region were covered during the last glaciation, albeit by thin, weakly erosive, cold-based ice (*Chapter 4*). Therefore, we suggest that the unconsolidated lake sediments were protected beneath perennial ice ceasing sedimentation during glacial stages.

Moraines along Sunneshine Fiord in the Cape Dyer area (Fig. 3.7) have been previously assigned to the early Wisconsinan and an older glaciation based on relative weathering data augmented with radiocarbon and amino acid recrimination dating of marine shells collected from raised marine deltas (Locke, 1987). TCN exposure dating of boulders deposited on the moraines revealed that the moraines may be associated with ice margins of the early and late Wisconsinan (Miller et al., 2002). Following Miller et al. (2002), we place the Late Wisconsinan ice margin on the inner two moraine ridges, which is further supported by an age of 15.0 ± 0.2 cal ka BP for an aquatic moss in basal sediments of Donard Lake located just outside of the Sunneshine Fiord moraines (Table A2.4, CAMS-23554, Moore et al., 2001). However, we cannot preclude the possibility that the entire nested moraine sequence was formed during the Late Wisconsinan. In this scenario, the infinite radiocarbon age (≥57 ^{14}C ka, CAMS-11337, Table A2.4, Miller et

al. 2002) on paired mollusc valves in a raised marine delta associated with the outermost moraine would need to have been preserved beneath the late Wisconsinan ice advance (see discussion in following section). Approximately 20 km NW of the Sunneshine Fiord delta, however, it appears that the ice did not advance during the LGM to a raised marine delta which has been dated to 41.1 ± 0.8 cal ka BP (Table A2.4, QL-979, Miller, 1979; Locke, 1987). The mollusc shells on this delta are fragile and well preserved (including internal mother-of-pearl (nacre)) so the date seems viable. Field observations of that delta confirmed that there is no overlying till or boulder scatter and no evidence of deformation or truncation of the delta. Therefore, we support the previous interpretation that the coastal stretch between Cape Dyer and Reid Bay, including outer Sunneshine Fiord, remained ice-free during OIS-2 (Fig. 3.7).

Preservation of a raised marine delta deposited during middle Wisconsinan ice retreat is also documented by the newly acquired finite 43.1 ± 0.4 cal ka BP radiocarbon age on *Hiatella arctica* collected from a marine terrace in Ujuktuk Fiord along the southwestern coast of Cumberland Peninsula (Table 3.3, Fig. 3.3a). The marine terrace is capped by glacio-fluvial deposits dated to 12.4 $^{-1.0}/_{+2.8}$ ka by a TCN depth profile. These sands are indistinguishable from the underlying marine sequence (Table 3.2, Fig. 3.4). Despite the vulnerable location of the delta at the head of a large fiord, the outlet glacier advancing to the mouth of the fiord during OIS-2 did not erode the entire delta indicating that basal thermal conditions may have varied spatially.

3.7.3 Younger Dryas Re-Advance

By the end of the Younger Dryas cold stage, wide stretches (40 – 60 km) of the coastline remained ice-free and glaciers were limited to fiords (Merchants Bay region and

Touak Fiord area), the head of the fiords (southeastern coast) or further inland (southwestern coast, Fig. 3.8). In the Pangnirtung Fiord area ice (partly fed by PIC) still stood within the Duval moraine system with only minor recession of the ice margin (3 - 5 km in Moon Valley).

Jennings et al. (1996) postulated that the CSIS re-advanced to the continental shelf during the Younger Dryas cold period based on evidence for a dolomite-rich detrital carbonate layer in a sediment core from the Labrador sea. In particular, the high dolomite concentration of this detrital carbonate layer compared to previous layers in the same core, and the recognition of a similar layer in a core from Sunnehine Fiord in the Cape Dyer area (Andrews et al., 1996), led Jennings et al. (1996) to conclude that it correlated with an ice advance in Cumberland Sound. However, Jennings et al. (1996) also proposed an alternate interpretation based on the high fraction of shelf-dwelling foraminifera in the detrital carbonate layer, which suggested that the layer could also be deposited by a gravity flow caused by failure of the continental shelf that was overloaded with glacial sediments. Onshore, despite targeted searches, we did not find any evidence for a re-advance of CSIS during the YD, thus supporting Jennings et al. (1996) alternate interpretation that the dolomite-rich layer did not mark an ice-marginal position. Furthermore, it is unlikely that the marine-based LIS re-advanced >300 km through the Cumberland Sound, while the terrestrial LIS margin simultaneously retreated ~3 km by 11.2 ± 0.4 ka, as indicated by the new chronological control obtained from the second recession moraine.

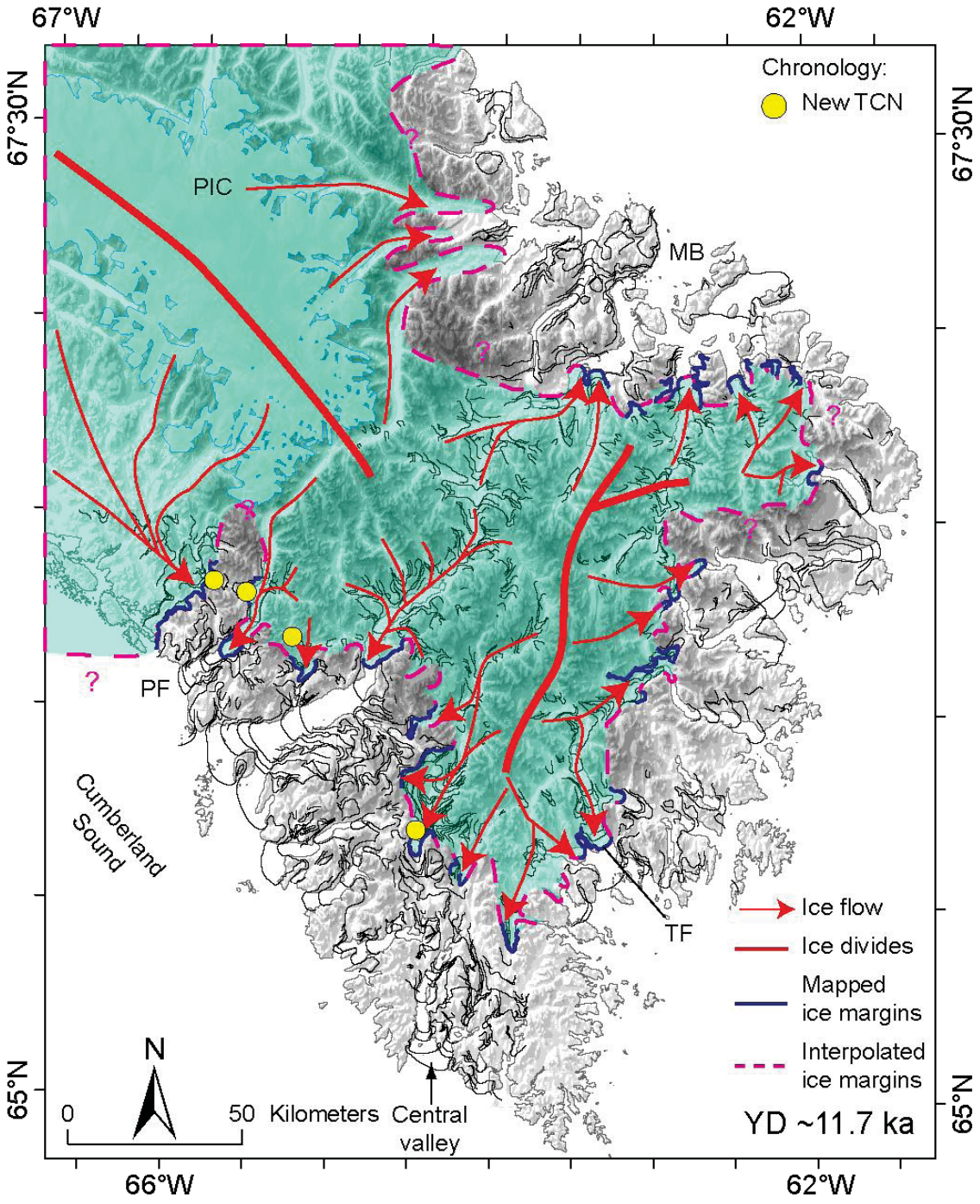

Fig 3.8 Ice extent at the end of the YD cold interval (~11.7 ka). Yellow circles indicate locations of age constraint for the interpreted ice extent. BI: Broughton Island, MB: Merchants Bay, TF: Touak Fiord, PF: Pangnirtung Fiord.

At the northeastern margin of the PIC, outlet glaciers still extended to the mouth of fiords and coastal valleys, as indicated by a minimum limiting age of 11.4 ± 1.3 cal ka BP obtained from a *Mya truncata* shell collected in the bottomset silts overlain by deltaic foresets of a raised glacio-marine deposits in the middle of Narpaing Fiord (just north of Fig. 3.8, Table A2.4, GaK-2574, Dyke et al., 1982). In the 'central valley' ice advanced in the broadest part of the valley during the Younger Dryas cold interval. Subsequent ice recession left a remarkable set of nested moraines and meltwater channels, possibly indicating annual ice margin positions. In the intervening area between Kingnait Fiord and Pangnirtung Fiord, the youngest age of three erratic boulders deposited on a till plain indicates that the area deglaciated shortly after the YD cold interval (11.1 ± 0.9 ka, Table 3.1, Fig. A2.2g). Local ice occupying Pangnirtung Fiord retreated only a short distance (~5 km) from its H-1 position by 10.2 ± 0.3 ka (Fig. 3.3a). This age obtained for the recessional moraine approximately agrees with the younger mode of the bimodal age distribution previously determined for the Duval moraine and equivalent moraine ridges (discussed above, Marsella et al., 2000).

3.7.4 Cockburn-Equivalent Re-Advance

In most areas, the innermost pre-Neoglacial moraine ridges can be correlated with the prominent Cockburn moraines, which were deposited along the northeastern and northern margins of the LIS (Miller and Dyke, 1974; Andrews and Ives, 1978). Cockburn moraines are primarily dated by fossiliferous ice-marginal glaciomarine deposits ranging in age from 9.5 to 8.5 cal ka BP (Miller and Dyke, 1974; Andrews and Ives, 1978; Briner et al., 2009). The moraines wrap around the heads of fiords in a nearly continuous line paralleling the outer coast of Baffin Island from Bernier Bay in the

northwest to Forbisher Bay in the south. The Ranger moraine, at the head of Cumberland Sound and on westernmost Cumberland Peninsula, is the local member of the Cockburn moraine system. It extends almost continuously from the mouth of Clearwater Fiord to the western lobe of the PIC, which is presently over-riding it (inset in Fig. 3.9, Dyke, 1979; Dyke et al., 1982). Outlet glaciers of the PIC still occupied valleys along its northeastern and southwestern margin, but in places the PIC had retreated to or behind its present day margin, as illustrated by the cross-cutting mentioned above (Miller, 1973; Dyke, 1979; Dyke et al., 1982). East of the PIC, the Cockburn-equivalent re-advance was restricted to the interior of Cumberland Peninsula, where the alpine glacier system had separated in several smaller ice masses (Fig. 3.9).

In the 'central valley' ice had retreated to the highest part of the valley. Two boulders on the most distal of a set of end moraines that are only a few kilometres beyond the LIA moraines of cirque glaciers provide a maximum limiting age for recession to this point (10.0 ± 0.4 ka, Table 3.1). We thus infer that the youngest Pre-Neoglacial moraines here are likely of Cockburn age.

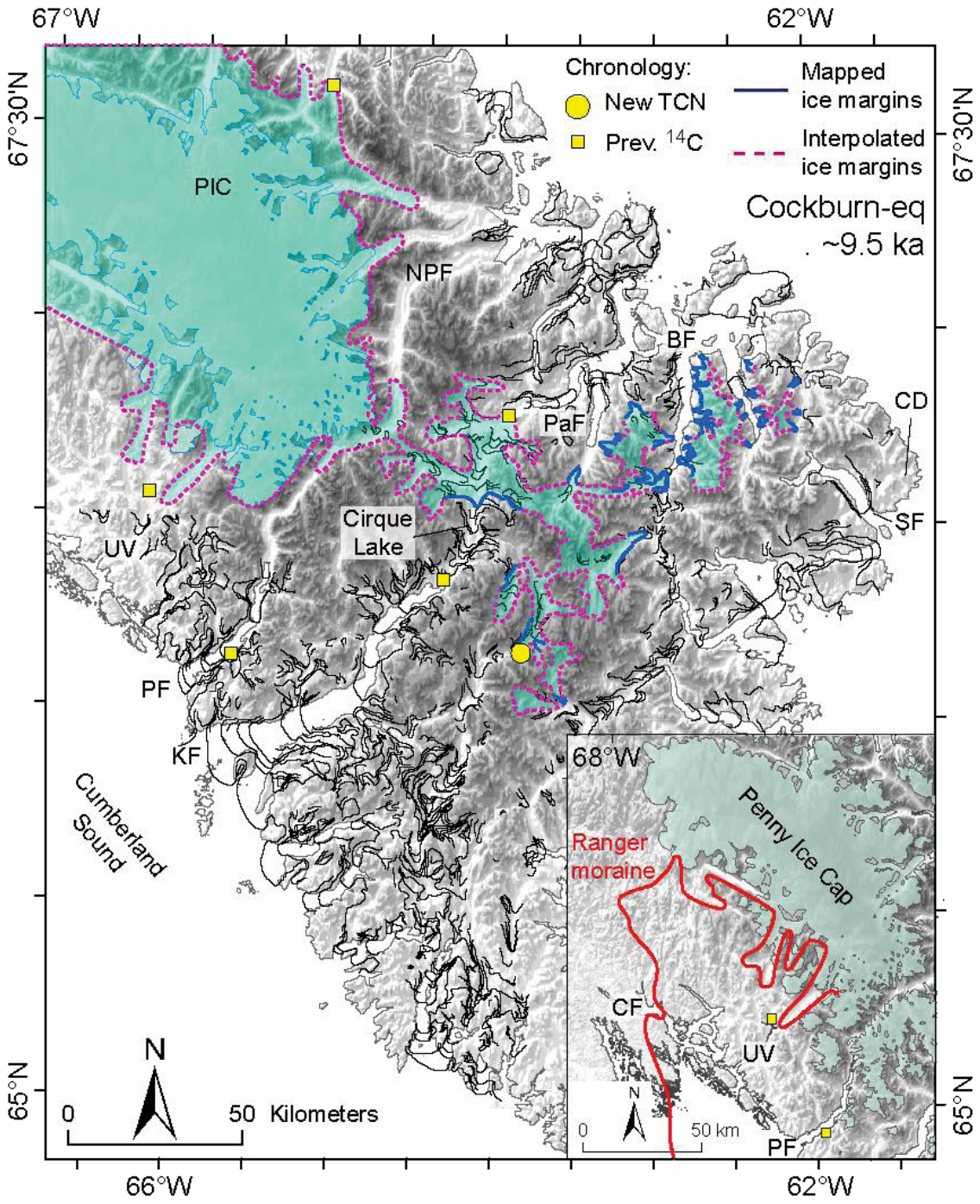

Fig 3.9 Cockburn-equivalent ice extent (<10 ka). Yellow circles indicate locations of age constraint for the interpreted ice extent. NPF: North Pangnirtung Fiord, PaF: Padle Fiord, BF: Boas Fiord, CD: Cape Dyker, SF: Sunneshine Fiord, PF: Pangnirtung Fiord, UV: Usualuk Valley, CF: Clearwater Fiord.

Farther north, the alpine glacier system had retreated towards the late ice dispersal centre at the heads of Padle Fiord and Boas Fiord (Fig. 3.9). Because the fiords were ice free during cooling associated with these moraines, local cirque glacier complexes were free to expand into the sides of fiords on the northeastern coast to form some of the best developed and well preserved Holocene lateral and end moraines on the peninsula. Because of their exceptional development (Dyke 2013 b; c), we correlate them with the Cockburn moraines, as have others (Hawkins, 1985). By Cockburn time, the most dominant alpine glacier system probably had just retreated to a position north of Cirque Lake (pass between Kingnait Fiord and Padle Fiord) and south of Akvaqiak Lake (near the head of Padle Fiord), where basal lake sediments are dated at 9.5 ± 0.1 cal ka BP (Table A2.4, NSRL-10139, Frechette and de Vernal, 2009) and to Pangnirtung Pass (Fig. 3.9).

Additional constraint for ice extent during this interval is provided by previous radiocarbon dating of mollusc shells at various locations (Fig. 3.9). At the northeastern margin of the PIC, outlet glaciers still occupied valleys and as indicated by both *Mya truncata* ages of 10.0 ± 0.2 cal ka BP at the head of Quajon Fiord (shown in Fig. 3.9, Table A2.4, GaK-5479, Dyke et al., 1982) and 9.2 ± 0.2 cal ka BP in Okoa Bay in ice-contact sediment (just north of Fig. 3.9, Table A2.4, St-3816, Miller, 1973; Dyke et al. 1982). At the head of Kingnait Fiord, the minimum-limiting age for ice recession prior to readvance during the Cockburn-equivalent cold interval is given by *Mya truncata* shells collected in bottomset clayey silts below foresets terminating at a terrace at 16 m asl (GSC-2083, calibrated to 9.4 ± 0.4 cal ka BP, Table A2.4, Dyke, 1979; McNeely and Brennan, 2005). Near the Pangnirtung airstrip, two radiocarbon ages on *Mya truncata*

and other shells collected from a bulldozer cut and a borehole drilled into the 50 m asl marine-limit delta signify ice recession of the PIC outlet glacier by 9.6 ± 0.1 cal ka BP (Table A2.4, UCIAMS-85913, LeBlanc et al., 2001; GSC-2001, Dyke, 1979). At the same time, PIC outlet glaciers occupied Usualuk Valley and an adjacent valley as indicated by a radiocarbon age of 9.6 ± 0.1 cal ka BP obtained from *Portlandia arctica* collected in badland sandy silts of a raised marine-limit delta (GSC-2183, Table A2.4, Dyke, 1979; McNeely and Brennan, 2005). By implication, the LIS had withdrawn to the Ranger moraine by this time (Dyke, 1979). The LIS then separated from the western margin of the PIC, which subsequently re-advanced to form the outer PIC moraines. The marine-based LIS prevailed at the mouth of Clearwater Fiord at the head of Cumberland Sound until 6.4 ± 0.1 cal ka BP (inset map Fig. 3.9, Table A2.4, DIC-334, Dyke, 1979; McNeely and Brennan, 2005), implying slow retreat of LIS from the Ranger moraine.

3.7.5 Deglacial Retreat Rates

Retreat of the alpine glacier system was previously documented along the coast west of Broughton Island (Miller, 1973) and in the Cape Dyer area (Fig. 3.1, Locke, 1987; Miller et al., 2002). Ice occupied the fiords west of Broughton Island until approximately 11.4 ± 1.3 cal ka BP (Table A2.4, GaK-2574, Dyke et al. 1982), followed by rapid deglaciation of the fiords between 7 - 6 ka and final withdrawal to the current northwestern margin of the PIC by 5.8 ± 0.1 cal ka BP (Table A2.4, GaK-3273, Dyke et al. 1982). Miller (1973) estimated average ice retreat rates of 15 - 20 m a^{-1} for the PIC outlet glaciers in this region.

The newly mapped ice marginal positions and recession pattern derived in the preceding sections permits more precise calculations of retreat rates for withdrawal of the alpine glacier system, outlet glaciers of the PIC, and the land-based LIS. Figures 3.7 – 3.9 show that the alpine glacier system retreated asymmetrically with fastest withdrawal along the southwestern coast and slowest retreat along the northeastern coast. This asymmetry of recession displaced the ice dispersal centre from an LGM ice divide system located over the mountain ridges to final centres near the heads of Padle and Boas Fiords. Intermediate ice retreat presumably occurred along the lower southeastern coast, where the ice margin extended onto the continental shelf during the LGM.

Retreat rates can be calculated for the 'central valley', where we have the tightest chronological control (Fig. 3.3a). Here, ice initially retreated through Ujuktuk Fiord at an average rate of 20 m a^{-1} (recession from 14.3 ± 0.8 ka to 11.7 ± 0.9 ka) during the Bølling-Allerød interstadial (14.6 – 12.9 ka, Rasmussen et al., 2006). Final retreat to the interior is correlated with the Preboreal interstadial (11.7 – 9.5 ka, Rasmussen et al., 2006; 2007) and occurred at an average rate of approximately 30 m a^{-1} (11.7 ± 0.9 ka – 10.0 ± 0.4 ka). Based on the ice margin positions shown in Figures 3.7 – 3.9, retreat rates from the northeastern coast are estimated to vary between 12 - 15 m a^{-1} for ice withdrawal from the coast (Merchants Bay region) to the fiord mouth during the Bølling-Allerød interstadial, and 15 - 25 m a^{-1} for ice recession through the fiords during the Preboreal interstadial. Retreat rates at the southeastern coast (Touak Fiord) can only be estimated for the Preboreal interstadial averaging about 15 – 20 m a^{-1} for final retreat to the interior of Cumberland Peninsula (Table 3.4).

In comparison, ice retreated more slowely through Pangnirtung Fiord with initial retreat approximating 1 m a^{-1} (14.6 ± 1.2 ka – 10.2 ± 0.3 ka, Fig. 3.3b) and subsequent withdrawal to Pangnirtung Pass with an estimated rate of 18 – 23 m a^{-1}, which is comparable with the retreat rates inferred for the alpine glacier system (Fig. 3.8 – 3.9). This initial slow rate of ice withdrawal is consistent with the requirement that the Pangnirtung Fiord ice was at least partly, if not wholly, sourced by the PIC. Owing to its greater volume and fewer tidewater outlets, the PIC response to the Bølling-Allerød warming is expected to be more sluggish than the smaller alpine systems. Additionally, during 1.3 ka of this period, the YD ice advance would have temporarily reversed and ceased ice recession, causing the retreat rates to appear even slower. For similar reasons, the land-based LIS initially only retreated with an approximate rate of 1.2 m a^{-1} (14.6 ± 1.2 ka – 11.2 ± 0.4 ka, Fig. 3.3b) before accelerated withdrawal to the Ranger moraine during the following Preboreal interstadial with an average rate of ~60 m a^{-1} (11.2 ± 0.4 ka – 9.6 ± 0.1 ka, Dyke, 1979).

Climate variation	Time ka	Ice mass	Retreat rate m a^{-1}	Time constraint ka
Bølling - Allerød	14.7 - 12..9	Alpine SW coast, initial retreat through fiord	20	14.6 - 11.7
		Alpine NE coat	12 - 15	~14.6 - ~11.7
		Pangnirtung (PIC)	1	14.6 - 10.2
		Land-based LIS	1.2	14.6 - 11.2
Younger Dryas	12.9 - 11.7	moraine building phase		
Pre-boreal	11.7 - 9.5	Alpine SW coast	30	11.7 - 10.0
		Alpine NE coat	12 - 25	~11.7 - ~10.0
		Alpine SE coast	12 - 20	~11.7 - ~10.0
		Pangnirtung (PIC)	18 - 23	10.6 - ~10.0
		Land-based LIS	~60	11.3 - 9.6
Cockburn and Ranger	9.5 - 9.2	moraine building phase		

Table 3.4 Association of retreat rates of the different ice masses on Cumberland with late glacial and early Holocene climate variation. Yellow shading: alpine glacier system, blue shading: PIC outlet glacier, red shading:land-based LIS.

In summary, the variation of retreat rates for the different sectors of the alpine glacier system, outlet glaciers of the PIC in Pangnirtung Fiord, and the LIS appear to coincide with distinct late glacial and early Holocene climate events seen in Greenland ice cores (Fig. 3.10 top, Table 3.4). The initial retreat of alpine outlet glaciers from the coast occurred during the Bølling-Allerød interstadial (Rasmussen et al., 2006). During the following YD cold interval, ice margins re-advanced to the mouths of many fiords along the northeastern coast, while a prominent sequence of moraines and meltwater channels was formed in the broadest section of the 'central valley' (Fig. 3.8). Average retreat rates of the alpine glacier system during the following Preboreal interstadial are of the same magnitude than for the earlier Bølling-Allerød interstadial (Fig. 3.10 bottom). The last moraine building phase can be associated with a brief cold interval between 9.5 and 9.2 ka (Fig. 3.10, Vinther et al., 2006; Rasmussen et al., 2007; Axford et al., 2009). Apparently very few cirque glaciers along the northeastern coast re-advanced during the last major cold interval (8.2 ka event, Fig. 3.10, Axford et al., 2009; Young et al., 2012). However, closer dating of the putative Cockburn correlatives, especially where they are multi-crested, may reveal moraines of this age. During the subsequent Holocene thermal optimum (8 - 5 ka, Kaufman et al., 2004; Gajewski, 2015), many (all?) of the alpine glaciers possibly vanished. The most interesting results of the spatial and temporal variations in retreat rates is that, in general, ice retreat appears to have been slower on the northern sloping alpine glaciers than the southern sloping alpine glaciers. Generally, the smaller alpine systems were initially more responsive to climate warming than the larger PIC and LIS (Fig. 3.10 bottom left). However, once the LIS margin retreated, ice recession occurred much faster than the PIC or alpine glacier system (Fig. 3.10 bottom

right). Similar results have been observed globally (Oerlemans and Fortuin, 1992), and further insight in the spatial asymmetry may be gained by an analysis of the post-LGM ELAs throughout the peninsula.

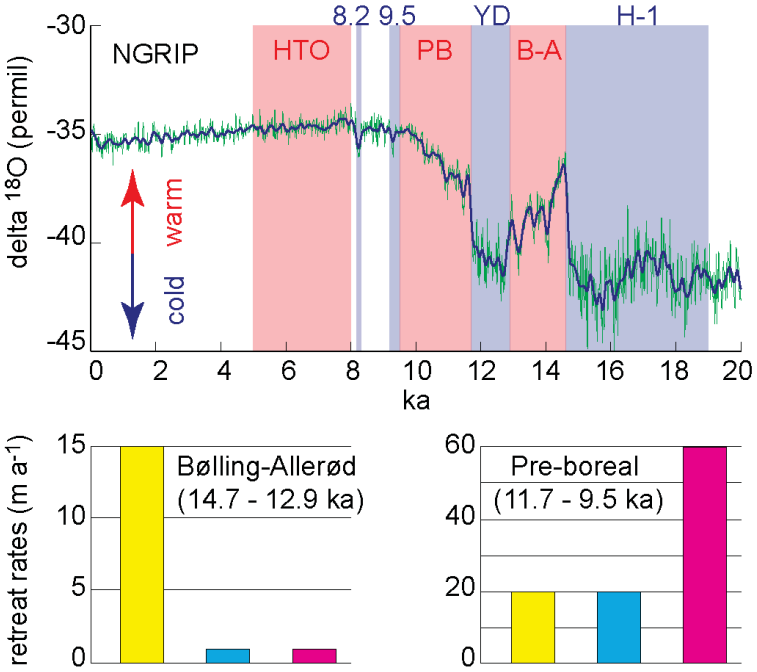

Fig 3.10 **Top.** Palaeoclimatology inferred from NGRIP (green: measured 20 year averages, blue: slight smoothing, Vinther et al., 2006) Blue shading = cold intervals: composite Heinrich Event 1 (H-1, Stanford et al., 2011), Younger Dryas (YD, Rasmussen et al., 2006), 9.5 and 9.2 ka (9.2, Vinther et al., 2006; Rasmussen et al., 2007; Axford et al., 2009), 8.2-ka event (8.2, Young et al., 2012). Red shading = warm intervals: Bølling-Allerød (B-A, Rasmussen et al., 2009), Pre-boreal (PB, Rasmussen et al., 2006; 2007), Holocene thermal optimum (HTO, Kaufman et al., 2004; Gajewski, 2015). **Bottom.** Inferred average retreat rates for the Bølling-Allerød interstadial (left) and the Pre-boreal interstadial (right). Note different vertical axis. Yellow: alpine glacier system, blue: PIC outlet glacier, magenta: land-based LIS.

3.7.6 Paleo-ELA Reconstructions

Maps of paleo-ELA distribution throughout the peninsula were derived from the maximum elevation of lateral moraines assigned to the three specific time intervals (supplementary file, Fig. A2.7 – A2.9). Owing to erosion or non-deposition of the upper reaches of lateral moraines, the inferred paleo-ELAs are minimum estimates (Meierding,

1982; Porter, 2000). Large uncertainties also arise from the available elevation data, particularly in the interior of the peninsula where topographic data is only available at a scale of 1:250,000 with contour intervals of 100 m. Along the coast, topographic data are available at a scale of 1:50,000 with contour intervals of 40 m. Furthermore, current elevations of lateral moraines need to be corrected for isostatic rebound of the area since deposition of the moraines (supplementary file, section A2.4). Available sea-level data (Dyke, 1979; Kaplan and Miller, 2003; Cowan, 2015; Hughes Clarke et al., 2015) were combined with an estimate of eustatic sea level (Miller et al., 2011) at each time interval to infer the magnitude of isostatic rebound, which may contribute up to 50 m of uncertainty for a given region and time. Correction for eustatic sea level during deglaciation is debated (Osmaston, 2006; Hanson and Hooke, 2011), but it is required on Cumberland Peninsula to attain enough separation of reconstructed paleo-ELA gradients (Fig. 3.11, supplementary file, section A2.4). While the paleo-ELA of a specific location may not be precise, the patterns of ELA-change during deglaciation are significant and can be linked to associated changes in temperature and precipitation (Fig. 3.11).

Contours of paleo-ELA inferred for the three different time intervals during deglaciation show declining ELA towards all three coasts of the peninsula (Fig. 3.11, supplementary file Fig. A2.7 – A2.10). Concurrent with the withdrawal of ice toward the northeastern coast, ELA contours shift northeastward. Paleo-ELAs for the Cockburn-equivalent time slice are only extracted for alpine moraines, so that contours are centred on the high elevation alpine topography in the interior of the Peninsula. This pattern differs markedly from modern ELA contours that are centred on the PIC, which were derived from the lowest elevation of extant cirque glaciers (Fig. A2.11, Andrews and

Miller, 1972). Interestingly, the modern ELA contours resemble more closely the paleo-ELA pattern for the YD cold stage than the later Cockburn-equivalent cold interval. Since extant glaciers are not in equilibrium with current climate, the inferred modern ELA might be too low and as such may be more closely related to climate conditions during the Little Ice Age (Andrews and Miller, 1972). Paleo-ELAs have been previously inferred for late Foxe moraines in the Merchants Bay area, which was essentially synonymous with the Cockburn stage (Hawkins, 1985) accordant to the assignment in this paper (Fig. 3.9, Dyke, 2013b, c). Our inferred paleo-ELA distribution for this time interval again bears a closer resemblance to the modern ELAs of Hawkins (1985) and not his late Foxe paleo-ELAs, which are approximately 200 – 300 m below the modern ELAs. Some of the discrepancy between the previous studies and our data might be related to the more precise elevation data available today. To evaluate the asymmetry between the north and south sloping glaciers observed in the glacier retreat rates, the paleo-ELA trends were plotted on a topographic profile along the former alpine ice divide (Fig. 3.5), which coincides approximately with the longer axis of the elliptical pattern of paleo-ELA contours (Fig. 3.10). At the southwestern coast, paleo-ELA increased approximately 60 m between the end of H-1 (14.6 ka) and the end of the YD (11.7 ka) time intervals. This increase in ELA corresponds to roughly 0.3 °C warming based on a lapse rate of 4.9° C km^{-1} (Gardner et al., 2009). However, at the northeastern coast, paleo-ELAs first decrease between the end of H-1 and the end of the YD but increase again during the Cockburn-equivalent cold stage, particularly further inland over the high alpine topography (Fig. 3.10). This pattern is consistent with glacier volumes attaining equilibrium during the longer duration of the YD relative to the short-lived and

less intense Cockburn event. Instead of a temperature signal, the drop in ELA during the YD might indicate higher precipitation along the northeastern coast, in relation perhaps to decreasing sea ice cover offshore. Currently, the Cape Dyer region receives twice as much precipitation as Pangnirtung (Moore et al., 2001), which is also reflected by the modern ELA pattern (Fig. A2.11, Andrews and Miller, 1972). Reduced sea ice cover after 13 ka has been inferred from dinocyst assemblages in a sediment core from Labrador Sea and after 10 ka from a sediment core in northern Baffin Bay (de Vernal and Hillaire-Marcel, 2006). The increased moisture source provided by less sea ice and orographic effect on precipitation could have led to lowering of ELA during the YD cold stage, which is also supported by evidence for slower retreat of alpine glaciers in this region compared to the southwestern coast. Warming during the following Preboreal interstadial led to an increase of ELAs in the interior and steepening of the ELA profile towards the coast.

3.8 CONCLUSIONS

New radiocarbon and TCN chronology and a new high-resolution map of ice margin positions have made it possible to analyse differences in the ice dynamics of an extensive alpine glacier system, the PIC, and the LIS. Measurements of ice flow indicators and large-scale bedrock erosional landforms reveal that the majority of Cumberland Peninsula was covered by an independent alpine glacier system with only the southernmost tip being overridden by the CSIS and the land-based LIS merely encroaching the part west of Pangnirtung Fiord.

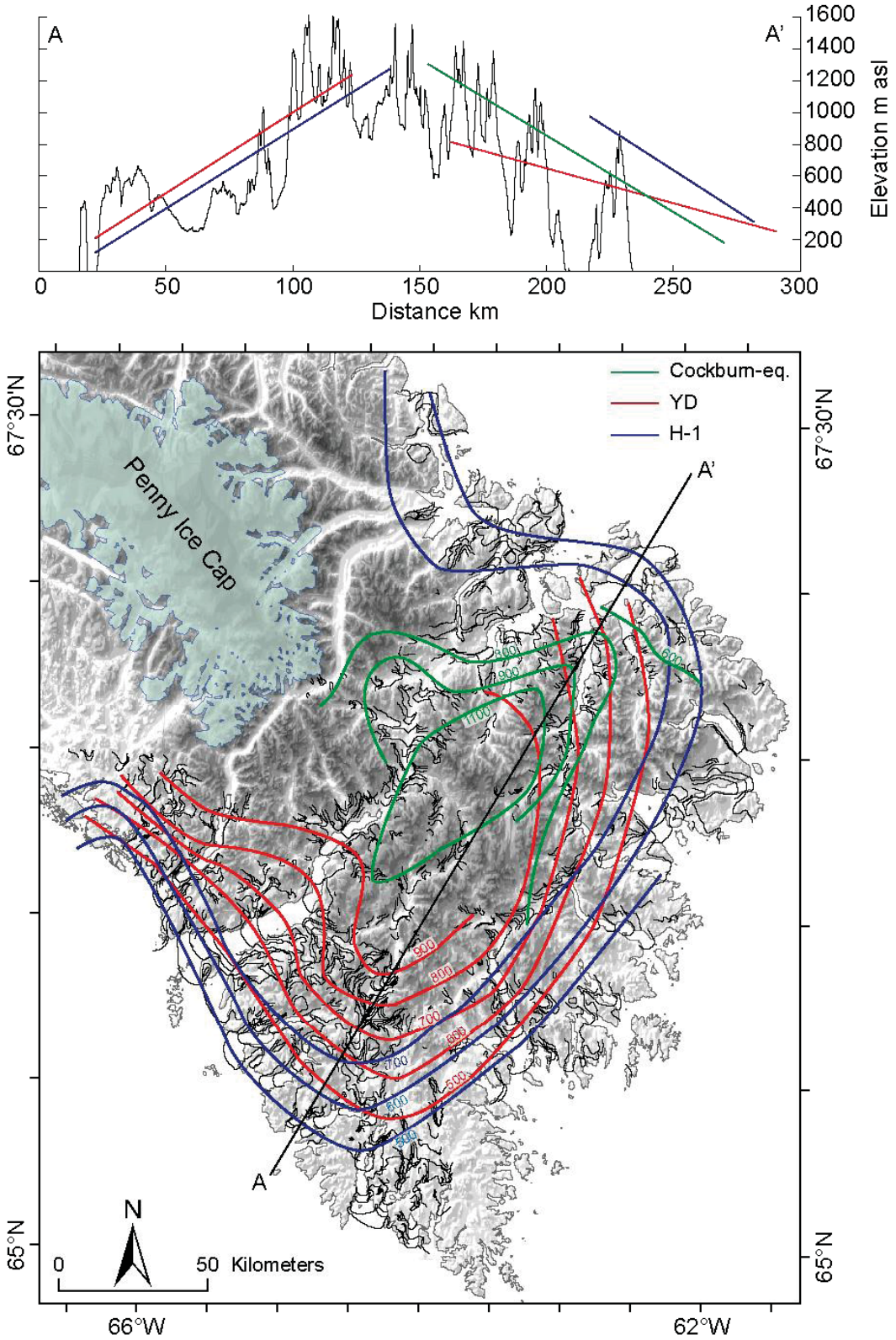

Fig. 3.10 Reconstruction of paleo-ELA for three time intervals during deglaciation shown along profile A-A' from the southwestern to the northeastern coast of Cumberland Peninsula and in plain view.

Response time of the different ice masses to late Pleistocene and early Holocene climate changes varied considerably. Initial sluggish retreat of LIS and PIC outlet glaciers (1 - 2 m a^{-1} between 14.6 – 11.7 ka) contrasted with an order of magnitude faster retreat rate for the alpine system over the same time period. Retreat rates of the land-based LIS accelerated considerably during the Preboreal interstadial (~60 m a^{-1} for LIS), while the PIC outlet glacier and the alpine glacier system continued retreating at similar rates (~20 m ka^{-1}). Whereas the alpine glacier system reacted more sensitively to late Pleistocene warming, there was a large variation among rates for different regions of the peninsula. In general however, outlet glaciers quickly receded from the southwestern coast with average rates 20 – 30 m a^{-1}, while glaciers retracted more slowly along the northeastern coast (12 - 25 m a^{-1}). This slower retreat may be linked to increased precipitation at the northeastern coast related to reduction in sea ice cover in the adjacent marine basins as suggested by decreasing paleo-ELAs in that region. At the southwestern coast paleo-ELAs increased slightly between 14.6 and 11.7 ka implying that air temperatures increased approximately 0.3°C during this time interval.

Preservation of unconsolidated glacio-marine sediments deposited during an intervening ice withdrawal in the middle Wisconsinan interstadial by a re-advancing outlet glacier is revealed by radiocarbon dating of mollusc shells and a TCN depth profile indicating that basal thermal conditions may have varied spatially. The interpretation that most sampled boulders contain inherited TCN concentrations suggests either ice-free or cold-based ice conditions in the source area of the boulders and insufficient erosion during glacial transport. The spatial pattern of the inherited concentrations is consistent with valley and fiord ice being warm-based and more erosive than the highland plateau

regions. The pronounced difference in weathering degree of freshly scoured valleys and regolith mantled plateaus together with evidence for ice coverage of upland areas denote the polythermal character of the alpine ice cover. This conclusion suggests that ice cover was comparatively thin on plateaus, which deglaciated before recession of outlet glaciers in adjacent valleys.

3.9 ACKNOWLEDGEMENTS

This research benefited from funding from the NRCan-GEM project for Cumberland Peninsula (through AD, GSC; project led by Mary Sanborne-Barrie and Mike Young), logistical support from the Polar Continental Shelf Program, and NSERC-DG, NSERC-NRS, CFI-Operating Fund (to JCG) for radiocarbon and TCN chronologies. AM was trained by G. Yang at the Dalhousie Geochronology Centre and prepared many of the BeO and Al_2O_3 targets. AMS analysis at LLNL-CAMS were conducted by S. Zimmerman and R. Finkel.

CHAPTER 4 – New Approach for Quantification of Subaerial and Subglacial Erosion Rates on High Latitude Upland Plateaus: Cumberland Peninsula, Baffin Island, Arctic Canada

Manuscript in preparation for submission to *Quaternary Science Reviews*

Annina Margreth[1], John C. Gosse[1], Arthur S. Dyke[1]

[1]Department of Earth Sciences, Dalhousie University, Halifax, Nova Scotia B3H 4R2, Canada

4.1 ABSTRACT

Rates of episodic quarrying of weathered bedrock blocks by cold-based ice and the timing of the last plucking event have been determined for tors on weathered plateaus on Cumberland Peninsula. By measuring terrestrial cosmogenic nuclide concentrations in bedrock surfaces of different surface weathering degrees at the same tor, we demonstrate how to determine the complex exposure and erosion history involving recurring cold-based ice cover. Average durations of ice cover and total complex (burial plus exposure) histories are estimated based on a simple model of periodic glacial-interglacial cycles. The nature and rate of subaerial and subglacial erosion are assessed with a Monte Carlo approach that computes plausible exposure histories based on a proxy record of global ice volume. Parameters defining the exposure history have to fit for all surfaces sampled at the same site, while parameters defining the exhumation of the surfaces through occasional plucking of overlying bedrock blocks are modelled for each sample individually. Constant subaerial erosion rates by abrasion are limited to low values (<3 mm ka^{-1}), corroborated by nuclide concentrations measured on two tors located on coastal ridge crests that have never been glaciated. Subglacial erosion of tors by plucking of fractured bedrock blocks usually exceeds abrasion, indicating prevailing cold-based

ice conditions on the summit plateaus. Rates of episodic quarrying (1 – 7 mm ka^{-1}) vary between differentially weathered surfaces at the same site as well as between tors exhibiting different degrees of glacial modification. Variation of episodic erosion rates is associated with topographic position of the sampled tors and fracture density of the bedrock. With the exception of two coastal summits that appear to never have been glaciated, all summits were covered by cold-based ice during LGM, but many of the tors were last modified in pre-ultimate glaciations. Tors that exhibit the smallest degree of glacial modification were last plucked >400 ka ago and most probably >1 Ma ago. Tors that are most glacially modified were last plucked prior to LGM and most probably 200-250 ka ago. Despite late Pleistocene intervals of ice cover, tor-studded landscapes of Cumberland Peninsula are of considerable antiquity.

4.2 INTRODUCTION

The erosion history of both upland surfaces and valleys must be known to determine temporal and spatial variability in rates of relief generation, sediment flux to oceans, and isostatic uplift over 10^3 to 10^6-year timescales. For high-latitude dissected coastal plateaus, the large area of upland plateaus suggests that even slow erosion of these surfaces may be significant (Dowdeswell et al., 2010; Steer et al., 2012) owing to polythermal ice and periglacial processes during glaciations and extensive regolith development during warm periods (von Blanckenburg, 2005). In these regions, rates and styles of valley incision by streams and glaciers has been relatively well analysed (e.g., Davis et al., 1999; Briner et al., 2008; Kessler et al., 2008). However, determining the exhumation rates of upland plateaus at timescales shorter than those determined from thermochronometry has been difficult because the rates are slow and the controlling

processes do not operate continuously in a changing climate. Because episodic erosion rates may significantly exceed gradual erosion rates (Small et al., 1997; Muzikar, 2008, 2009), determining rates of sporadic erosion is crucial for constraining rates of landscape lowering and the evolution of high-latitude highland plateaus.

The concentration and ratio of terrestrial cosmogenic nuclides (TCN) vary predictably with depth below bedrock surfaces and can be used to measure episodic rates of erosion. By using twin or triplet samples from adjacent bedrock surfaces that share an exposure history (ice cover, subaerial erosion), climate, and similar lithological properties but exhibit contrasting degrees of weathering because of plucking, it is possible to determine the long-term average total erosion rate (episodic and constant gradual erosion) from glacial and other processes. In this paper, we describe a new approach using TCN data from such differentially weathered surfaces to examine the nature and determine the rates of subaerial and subglacial erosion that prevail on weathered upland plateaus. For this purpose, we collected samples from tors — conspicuous towers of coarsely fractured bedrock protruding metres to decametres above blockfields, regolith cover, and till plains. The differentially plucked tors provide an opportunistic means to collect samples at different depths without the need for drilling, and to use the TCN concentrations and ratios to establish the most probable timing of last plucking and therefore maximum limiting age of last ice cover. Constrained by a climate time-series, a Monte Carlo method is used to generate variable histories of ice cover, fracture densities (thickness of joint blocks), subaerial erosion rate, and timing of subglacial plucking, with which the TCN data can be modelled to provide a probability distribution for episodic erosion rates. The results are used to relate the rate of plucking (i.e., sudden removal of a joint block at

the base of a glacier used here synonymously with quarrying), abrasion, and subaerial history on different summits to the extent and style of glacierization, variation in bedrock properties, and regional and local topography. The inferred rate of total erosion is compared with long-term sediment flux to the ocean and exhumation histories determined by low-temperature thermochronology. The measured TCN concentrations reveal that episodic subglacial erosion by quarrying is slow yet amounts to a tenth of the erosion rates incising fiords and valleys over the Quaternary.

4.3 PREVIOUS STUDIES OF EPISODIC EROSION

Geomorphic processes are often dominated by episodic erosion events that are controlled by climate, tectonic processes, lithology, or autogenic cyclicities (e.g., Womack and Schumm, 1977). It is difficult to quantify the long-term rate of erosion attributed to episodic events, although they may exceed steady rates (Small et al., 1997; Muzikar, 2008, 2009). For instance, landscapes dominated by wasting processes have infrequent but high-volume erosion events that equal or exceed incremental bedrock and soil denudation rates over longer timescales (Kirchner et al., 2001; Antinao Rojas, 2009).

Glacial plucking is an episodic process, which has been shown to be primarily controlled by fracture spacing and the roughness of the glacier bed (Anderson, 2014). Smaller blocks are more likely to be quarried, so that landscapes with higher fracture density are lowered more rapidly (Dühnforth et al., 2010). With additional knowledge or assumptions of the glacial history, the rate of plucking has been estimated using TCN in bedrock surfaces (Macchiaroli, 1995; Phillips et al., 2006; Jansen et al., 2013; Fujioka et al., 2015). For instance, the rate of glacial quarrying was first determined assuming that a single plucking event occurred during the last glaciation (Macchiaroli, 1995). Most of

the previous studies focussed on quarrying and abrasion by warm-based valley glaciers or ice sheets (Briner and Swanson, 1998; Davis et al., 1999; Colgan et al., 2002). But on surfaces with low erosion rates (Nishiizumi et al., 1991; Small et al., 1997; Phillips et al., 2006) TCN concentrations are a mixed signal of exposure during interglacial intervals, shielding during one or more glaciations, episodic plucking of bedrock blocks during some glaciations, and gradual erosion of the surface by subglacial abrasion or subaerial processes. Quantification of low erosion rates on plateaus is important, because low-relief, high-elevation surfaces are often used as reference points for estimates of total glacial erosion in adjacent valleys assuming that the plateaus remained nearly unaltered throughout the Quaternary (Small and Anderson, 1998).

4.4 GLACIAL DYNAMICS OF THE STUDY AREA

Cumberland Peninsula on Baffin Island has been the locus for numerous studies of bedrock weathering, extent of past ice cover, and amount of glacial erosion (Andrews and Dugdale, 1971; Miller, 1973; Boyer and Pheasant, 1974; Miller and Dyke, 1974; Andrews et al., 1976b; Sugden and Watts, 1977; Anderson, 1978; Dyke, 1979; Watts, 1979; Dyke et al., 1982; Steig et al., 1998; Bierman et al., 1999; Davis et al., 1999; Marsella et al., 2000; Kaplan et al., 2001; Miller et al., 2002). The peninsula provides a detailed record of past ice cover by the northeastern fringe of the Laurentide Ice Sheet (LIS), the expanded Penny Ice Cap, and alpine-type polythermal glaciers throughout the cirque-scalloped terrain that forms the core of the eastern half of the peninsula (Fig. 4.1). The extent of ice cover on weathered plateaus during the last (Wisconsinan) glaciation has been extensively debated (Sugden and Watts, 1977; Dyke et al., 1982; Steig et al., 1998; Bierman et al., 1999; Bierman et al., 2001; Wolfe et al., 2001). The debate was

temporarily subdued by a proposal by Miller et al. (2002) that reconciled the previous contradictory maximum (Flint, 1943) and minimum (Ives, 1978) ice cover models with an intermediate level of ice cover. A 'Goldilocks' conceptual model recognizes the preservation of undisturbed pre-Wisconsinan sediments in tarns (Wolfe, 1996; Wolfe and Härtling, 1996; Wolfe et al., 2000) and the advanced weathering degree of plateaus suggested ice-free conditions for at least the last glaciation in some regions. The model is also consistent with glacial modification of tors (Sugden and Watts, 1977; Watts, 1979) and TCN concentrations measured on erratic boulders scattered on the plateaus and on weathered bedrock surfaces of tors (Bierman et al., 1999; Marsella et al., 2000), which indicate coverage by predominately cold-based ice during the last glaciation. However, although coverage of tors at some time by cold-based ice could be revealed by measuring the concentration of two radionuclides with differing decay rates (Bierman et al., 1999; Marsella et al., 2000; Kaplan et al., 2001), the exact timing of the last ice cover could not be uniquely determined from these data alone. A revision to the Miller et al. (2002) glacial dynamical interpretation has developed from recent and higher resolution mapping of glacial geology (Dyke, 2011a-f; Dyke, 2013a-c) and improved deglacial chronology in the interior of the peninsula (Margreth et al., 2014; *Chapter 3*). An estimate of the most probable timing of ice cover on the plateau summits is necessary, and a quantitative assessment of what controls the rate of glacial modification is required to quantify the landscape response to climate change.

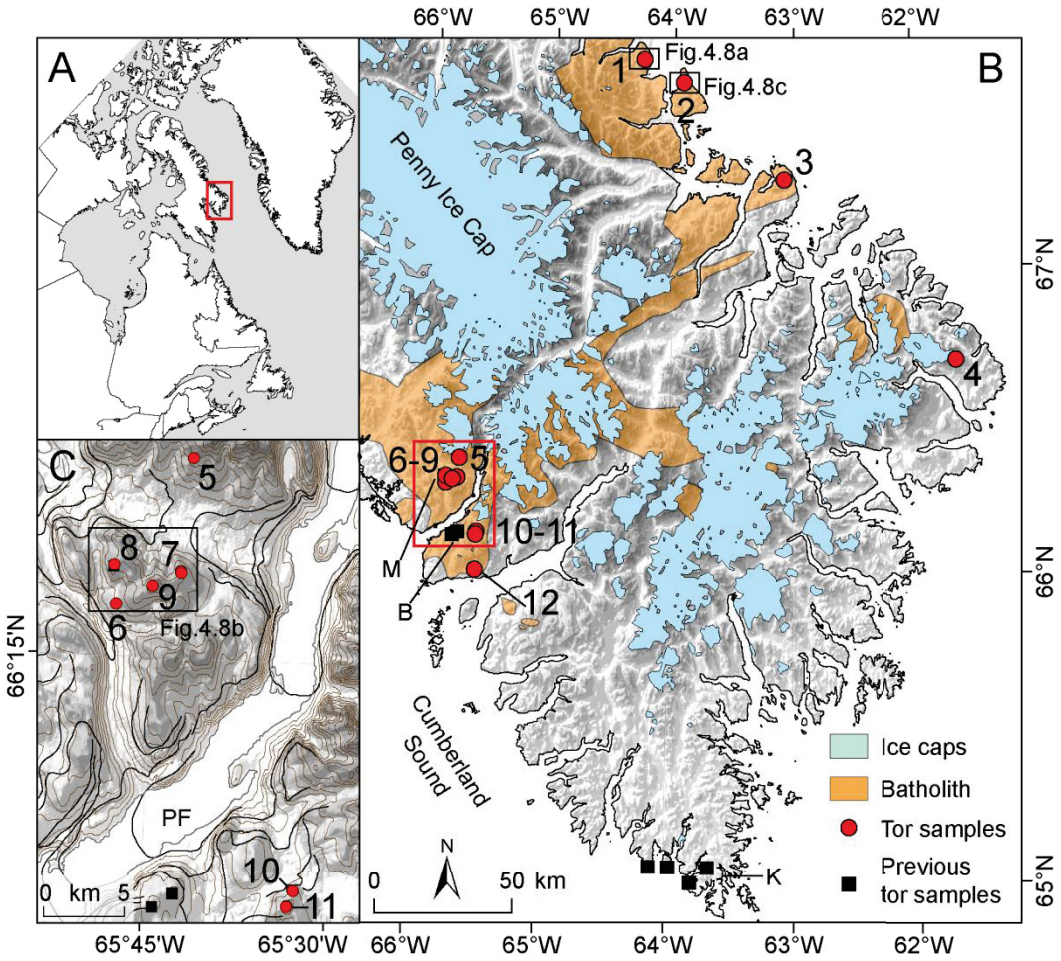

Fig. 4.1 Cumberland Peninsula with locations of sampled tor sites. **A.** Map of eastern Canada and Greenland with location of Cumberland Peninsula indicated by red box. **B.** Shaded relief map of Cumberland Peninsula showing previous sample locations of tors (black squares, B = Bierman et al., 1999; M = Marsella et al., 2000; K = Kaplan et al., 2001) and new sample locations (red circles, sites numbered from 1 – 12 from north to south). Extant ice caps are shown in blue and the occurrence of the Paleoproterozoic Qikiqtarjuaq plutonic suite is indicated in orange (adapted from Sanborn-Barrie et al., 2011). Locations of detailed relief maps shown in Fig. 4.8 are marked by black squares. **C.** Detailed map of red box shown in B with sample locations around Pangnirtung Fiord (PF). Location of detailed relief map shown in Fig. 4.8 is marked by black square. Mapped ice margins (Dyke, 2013b) are shown as black lines.

4.5 METHODS

The new approach to determine the rate of episodic quarrying and the timing of last plucking are based on TCN concentrations measured in nearby differentially weathered bedrock surfaces. Although it has been specifically developed for tors on weathered plateaus, the method could also be applied to interglacial scarp retreat during felsenmeer development on highland summits. In addition, parts of the method could be adapted for studying other episodic erosion processes, such as rockfall, toppling, and coastal cliff retreat of medium to coarsely fractured rock. In general, the question of timing of last plucking or long-term rate of erosion requires multiple parametric constraints for which limited or no data are available. The challenge is to reduce the degrees of freedom in the system. One approach is to use more than two TCN with different production mechanisms and half-lives. Another solution, as we adopted, is to use two nuclides measured at different depths, with the benefit of knowledge of cosmic ray attenuation through mass (ca. 100 to 1000 g cm^{-2}).

Before describing the new approach in section 4.6, we provide details of sample collection, preparation and accelerator mass spectrometry (AMS) analysis in sections 4.5.1 and 4.5.2 (supplementary file sections A3.1 – A3.2). In order to interpret the TCN concentrations, we describe the exposure histories (i.e., cycles of cosmic ray exposure interrupted by cold-based ice cover) in terms of TCN production, decay, gradual subaerial erosion, and episodic plucking of bedrock blocks (section 4.6). We first derive the pertinent equations using a simple cyclic ice-cover model with constant relative durations of ice-free and ice-cover intervals (section 4.6.1, supplementary file section A3.3 – A3.4) and then apply realistic ice cover histories based on global or regional

climate time series (section 4.6.2). Then we employ a Monte Carlo approach to determine the timing of last glacial plucking and episodic erosion rates (section 4.6.3, supplementary file section A3.5).

4.5.1 Sample Collection

On Cumberland Peninsula we have collected samples from twelve strategically-located tor sites over a variety of elevations, coastline proximity, and landscape position (Fig. 4.1). On four sites we sampled two or more differentially weathered surfaces. The pairs and triplets of samples consist of at least one clearly weathered surface and one much fresher surface (e.g., Fig. 4.2 a-b). Significantly, the samples at a given site were in close proximity and apparently lithologically similar, which allows the assumption of a *shared* exposure history from the point of view of cosmic ray flux, atmospheric and ice shielding, interglacial subaerial erosion rates over $>10^3$ year timescales, and long-term (10^6 year) landscape evolution. The weathered surfaces have slightly higher granular relief, subrounded to rounded edges, and often exhibit 30 - 45 cm wide weathering pits (samples were taken at a distance from the pits). The fresh surfaces have a relatively smooth relief, sharper edges, and weathering pits are absent. We assume that the fresher surfaces were plucked most recently based on these weathering differences. At one location, besides three samples from weathered bedrock surfaces, three additional samples were collected from large (1-4 m high) erratic blocks of a slightly different lithology from the underlying bedrock. For all samples, approximately 2 kg of orthogneiss or metasediment were obtained either by chisel and hammer exploiting weakened joint planes or exfoliation layers or, more typically, by cutting four or more 2 cm-deep grooves with a gas-powered diamond blade cutoff saw and removing bars of

sample by chisel and hammer. Site location, sample thickness, inclination of the surface, condition of the sampled surface (weathering degree, type of weathering, lichen cover, lithology and grain-size), and shielding of the sample surface by surrounding topography, sediment, and snow were recorded or estimated. The majority of samples had 2π exposure and were from flat and horizontal surfaces, more than 30 cm from an edge.

4.5.2 Sample Preparation and AMS Analysis

The specific sample processing and chemistry procedures for preparation of ^{10}Be and ^{26}Al oxide targets at the Dalhousie Geochronology Centre for these samples are summarised in supplementary file section A3.1, which also presents the chemical data for the samples. A total of 26 samples were processed for ^{10}Be and ^{26}Al from quartz. Before dissolution of 35 g of pure quartz, 180 - 200 mg of ^{9}Be carrier solution was added (produced by J.Klein from a shielded beryl crystal extracted from the Homestake Gold Mine that has 1015 μg Be g^{-1} at the time of sample preparation and a long-term average ^{10}Be/^{9}Be of 4×10^{-15} atom/atom at Lawrence Livermore National Lab). Owing to the <40 g masses of quartz dissolved, and depending on the estimated native Al concentration, varying masses of ^{27}Al carrier solution was added (0 – 2800 mg, plasma standard solution, from Alfa Aesar, 1000 μg Al g^{-1}). AMS was completed at Lawrence-Livermore National Lab in 3 runs between June 2010 and October 2011, against standards 07KNSTD3110 (^{10}Be/^{9}Be) and KNSTD10650 (^{26}Al/^{27}Al). Average precisions of the sample measurements were 2% for ^{10}Be and 3% for ^{26}Al. Three samples with higher Al-AMS uncertainty (>7%) have been re-analysed after additional quartz purification. Blank corrections were <1% except for three low-concentration samples yielding a higher correction of up to 4%. Total reported error includes the following

sources, added in quadrature: weighted uncertainty in process blank, a 2% error for chemistry processing and Be carrier concentration, uncertainty in Al measurement for ^{26}Al samples (5% reproducibility was reported for all samples analysed with ICP-MS by MAXXAM Inc., Halifax, and <2% for ICP–OES at the Dalhousie Geochronology Centre). Total errors are <3% for ^{10}Be concentrations and <6% for ^{26}Al concentrations.

4.6 PRINCIPLES OF THE TCN APPROACH FOR EPISODIC EROSION

The cosmic ray flux is attenuated with mass causing the spallogenic and muogenic TCN production to decrease in a predictable way below a rock surface (Fig. 4.2, Gosse and Phillips, 2001) The new approach is based on cosmogenic ^{26}Al and ^{10}Be produced in quartz, because their half-lives (^{26}Al = 0.72 Ma, Nishiizumi, 2004; ^{10}Be = 1.378 Ma, Chmeleff et al., 2010; Korschinek et al., 2010) and production rates are suitable for revealing recurring burial by weakly erosive ice over timescales of 10^4 to 10^6 a. Spallogenic production by fast neutrons dominates in <1000 g cm^{-2} rock mass depth (density times thickness) and ^{26}Al is produced 6.75 times faster than ^{10}Be (Nishiizumi et al., 1989; Balco et al., 2008) at the surface. Because relative production of ^{26}Al to ^{10}Be is larger for negative and fast muons, which are weakly attenuated compared to fast neutrons (Heisinger et al., 2002a; 2002b; Braucher et al., 2003; 2011), the relative abundances of ^{26}Al to ^{10}Be increase predictably with greater depth (Fig. 4.2). Therefore, three separate TCN-depth functions (concentrations of ^{10}Be and ^{26}Al, and their ratios) can be used to infer the timing of last plucking (supplementary file section A3.3, section 4.6.1) and subglacial episodic erosion rate (section 4.6.3) reducing the degrees of freedom (i.e., the number of variable parameters).

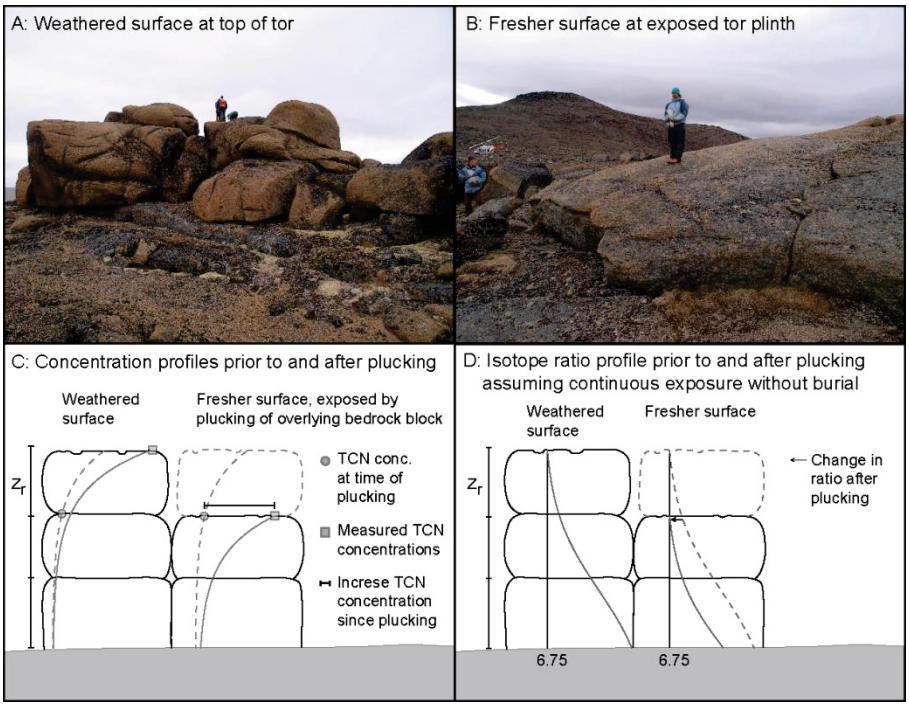

Fig 4.2 Schematic illustration of variation of TCN concentrations and ratios with depth, which is employed to determine the timing of plucking on a relatively less weathered surface sampled along with a more weathered surface at the same tor (illustrated here for site 10, Fig. 4.1, oblique aerial view shown in Fig. A3.2d). **A.** Sampling of a weathered surface (A355, Table 4.2) at the top of the tor. Note the rounded edges of the bedrock blocks and enhanced weathering along horizontal and vertical joint planes. Weathering pits up to 50 cm wide and 20 cm deep occur on these blocks (Fig. 4.4e). **B.** Fresher surface (A356, Table 4.2) on the eastern margin of the tor. The exposed tor plinth has sharp edges and no weathering pits. **C.** Decrease of TCN concentration with depth. At the time of plucking, the TCN concentration (gray circles and dashed lines) in the newly exposed surface is equivalent to the concentration below the weathered surface at depth z_r (here approximately 1 m). New depth profiles (gray solid lines) develop following plucking, but the difference between the measured concentrations (gray squares) of the fresher and weathered surface (extrapolated to depth z_r) is indicative of the time since plucking. **D.** Ratio depth profiles for continuous exposure without intermittent burial. The freshly exposed surface initially has a slightly higher ratio that decreases to the spallogenic production ratio after the plucking event. The ratio depth profile is significantly affected by intermittent burial by ice (see text, supplementary file Fig. A3.5).

The basic concepts of the new approach is illustrated for the example of a granite with wide spacing of horizontal and vertical fractures. If one block z_r (g cm^{-2}) thick is plucked, the TCN concentrations at the newly plucked surface are predictably less than

the concentrations of the adjacent non-plucked surface, and the newly plucked surface has a higher $^{26}Al/^{10}Be$ (Fig. 4.2). Immediately after the plucking event, the concentrations and ratio of the plucked surface are the same as a rock at z_r depth below the non-plucked surface. However, after subaerial exposure the TCN concentrations below the plucked surface increase faster than in the non-plucked rock shielded at depth z_r, and the $^{26}Al/^{10}Be$ of the plucked surface decreases toward 6.75. The difference between the TCN concentrations and ratios on the plucked surface and below the unplucked surface (at depth z_r) are proportionate to exposure time. Therefore, the time since plucking and long-term episodic erosion rate can be estimated by measuring two TCN in a pair of plucked and non-plucked surfaces (supplementary file section A3.3).

4.6.1 Considering a Non-Constant Burial History

While it is possible to apply the strategy we use in non-glaciated regions, we specifically treat the glaciated setting as our interest lies in the measurement of long-term episodic erosion rates on high latitude summit plateaus. In such areas, the concentration and ratio variation with depth is complicated by (i) shielding of the bedrock surfaces by ice, (ii), episodic subglacial plucking, (iii) and subglacial abrasion, in addition to subaerial (interglacial) erosion. Burial by glacial ice of sufficient thickness (>4500 g cm^{-2}, i.e., >45 m of water-equivalent ice) can effectively shield the plucked and non-plucked surfaces from cosmic rays (i.e., only 0.2% of subaerial production will occur at the rock surface below 50 m of ice), so that TCN concentrations and $^{26}Al/^{10}Be$ decrease during ice cover intervals as a result of radioactive decay. We use the term 'complex exposure history' to describe the exposure history of a rock that endures alternating periods of exposure and burial or partial burial with gradual and episodic erosion over its

total history. Burial implies a surface has been previously exposed, and is distinct from simple shielding, which may or may not be constant. Because deep muogenic TCN produced during ice-free intervals in rocks that are exhuming upwards may still record a complex exposure history over long periods of time (> 1 Ma), it is important to establish a similarly long proxy for the glacial-interglacial history.

In a simple first approximation, we consider a periodic sequence of alternating ice-free and ice-cover episodes, each with constant ice thickness $z_{ice.}$ Assuming an instantaneous change in ice thickness and subaerial erosion rate, as well as an invariant ratio of ice-free to ice-cover duration (e.g., 20:80), the equations for TCN concentration in quartz at the rock surface for alternating exposure and burial intervals can be written as:

$$N_{int_k} = \frac{P_i}{\lambda_i'} + e^{-\lambda_i' * f * t_c} * [N_{glc_{k-1}} - \frac{P_i}{\lambda_i'}] \qquad eq(1)$$

$$N_{glc_k} = \frac{P_i}{\lambda_i} * e^{\left(-\frac{z_{ice} * \rho_{ice}}{\Lambda_i}\right)} + e^{-\lambda_i * (1-f) * t_c} * [N_{int_k} - \frac{P_i}{\lambda_i} * e^{\left(-\frac{z_{ice} * \rho_{ice}}{\Lambda_i}\right)}] \qquad eq(2)$$

with $$\lambda_i' = \lambda + \frac{\varepsilon * \rho_r}{\Lambda_i} \qquad eq(3)$$

where N_{int} and N_{glc} (atoms g^{-1}) are the concentrations at the end of the interglacial and glacial of the k'th cycle of duration t_c (a) with f the fraction of ice-free time (i.e., 0.2). P_i (atoms g^{-1} a^{-1}) is the production rate and Λ_i (g cm^{-2}) is the attenuation lengths for fast neutrons and fast or negative muons. λ (a^{-1}) is the decay constant, ε (cm a^{-1}) is the constant subaerial erosion rate during ice free intervals, ρ_r (g cm^{-3}) is the bulk rock density, and z_{ice} (cm) and ρ_{ice} (g cm^{-3}) are the thickness and density of ice (Table 4.1).

During ice cover, the concentration lost to decay is large compared to the meagre muogenic production beneath 50 m of ice.

Complex exposure history model:

Parameters:	Symbol:	Values:	References / Notes:
Reference ^{10}Be production rate neutron spallation	$P_{Be,n}$	4 atoms g^{-1} a^{-1}	Borcher et al., in press.
Reference production ratio of ^{26}Al/^{10}Be	R_n	6.75	Balco et al., 2008; based on Nishiizumi et al., 1989
Reference production rate fast muons (% tot prod.)	$P_{\mu f}$	0.5% for ^{10}Be, 0.6% for ^{26}Al	Lifton et al., 2014; following Heisinger et al., 2002a-b
Reference production rate negative muons (% tot prod.)	$P_{\mu n}$	1.5% for ^{10}Be, 1.8% for ^{26}Al	Lifton et al., 2014; following Heisinger et al., 2002a-b
attenuation lenght for neutron spallation	Λ_{sp}	150 g cm^{-2}	Balco et al., 2008; Gosse and Phillips, 2001
attenuation lengths for fast muons	$\Lambda_{\mu f}$	4320 g cm^{-2}	Heisinger et al., 2002a; Braucher et al., 2011
attenuation lengths for negative and fast muons	$\Lambda_{\mu -}$	1500 g cm^{-2}	Heisinger et al., 2002a; Braucher et al., 2011
half-life for ^{10}Be	λ_{Be}	1.378 Ma	Chmeleff et al., 2010; Korschinek et al., 2010
half-life for ^{26}Al	λ_{Al}	720 ka	Nishiizumi, 2004
constant subaerial erosion rate	ε	i.e., 1 mm ka^{-1} = m Ma^{-1}	MC method: uniform variation between 0 - 4 mm ka^{-1}
rock density	ρ_r	2.65 g cm^{-3}	
ice density	ρ_{ice}	0.9 g cm^{-3}	
complete burial by ice (equivalent to 17m of rock overburden)	z_{ice}	5000 cm	based on ice surface elevations of ice sheet model constrained by relative sea-level data
duration of last ice-free interval (deglaciation time)	t_{deglac}	i.e., 15 ka	based on timing of deglaciation determined for region (*Chapter 3*)
thickness of shielding bedrock block	z_r	i.e., 60 cm	MC method: lognormal distribution (mean 76 cm, variance 38 cm)
duration of periodic glacial-interglacial cycles (orbital pacing)	t_c	i.e., 100 ka, 10 ka or 1 ka	
Cyclic ice cover variables (different for each sample):			
ratio of ice-free time and ice-cover time	f	i.e., 22%	dependent on assumed subaerial erosion rate
total duration of complex history	t_{tot}	i.e., 600 ka	dependent on assumed subaerial erosion rate
MC method variables:			
durations of individual exposure and burial intervals	δ^{18}O	i.e., 4 permil	uniform variation between 3.5 - 4.5 ppm in 0.5 ppm steps
total duration of complex history	t_{tot}	i.e., 2.15 Ma	variation between 0.9 - 3 Ma depending on value of δ^{18}O
number of plucking events	n	i.e., 8 Ma	randomly chosen between one and max number of burial events
occurrence of plucking events	t_{plk}	i.e., 220 ka	occuring at the end of the burial events, randomly chosen amongst burial events
MC method sensitvity tests:			
plucking of tor block during last glacial cycle	z_r	50 cm	effect on estimate of episodic erosion rate
ice thickness	z_{ice}	700 cm	
deglaciation time	t_{degl}	20 or 11 ka	
thickness of plucked bedrock block	z_r		uniform variation betweeen 10 - 200 cm

Table 4.1 List of parameters used to calculate complex exposure histories. References for chosen values are listed where applicable. Scaling of production rates to the sample location follows Lifton et al. (2014) using the particle-specific flux spectra given in Sato et al. (2008). Calculation of site-specific production rates by fast and negative muons is also based on Lifton et al. (2014) following Heisinger et al. (2002a; 2002b). Variables for cyclic ice cover history are determined for each sample individually (Table 4.2). Variation of variables for Monte Carlo (MC) method are listed separately or given in the last column where applicable. Variables changed for sensitivity test are given at the bottom.

TCN accumulation in a 'surface' under a bedrock block of thickness z_r is given by:

$$N_{int_k}^{z_r} = \frac{P_i}{\lambda_i'} * e^{\left(-\frac{z_r * \rho_r}{\Lambda_i}\right)} + e^{-\lambda_i' * f * t_c} * \left[N_{int_k} - \frac{P_i}{\lambda_i'} * e^{\left(-\frac{z_r * \rho_r}{\Lambda_i}\right)}\right] \quad \textit{eq(4)}$$

$$N_{glc_k}^{z_r} = \frac{P_i}{\lambda_i} * e^{\left(-\frac{z_{ice} * \rho_{ice} + z_r * \rho_r}{\Lambda_i}\right)} + e^{-\lambda_i * (1-f) * t_c} * \left[N_{glc_k} - \frac{P_i}{\lambda_i} * e^{\left(-\frac{z_{ice} * \rho_{ice} + z_r * \rho_r}{\Lambda_i}\right)}\right] \quad \textit{eq(5)}$$

These equations (*eq(1-5)*) describe a saw-tooth trajectory for a given bedrock surface represented in an $^{26}Al/^{10}Be$ vs. ^{10}Be burial plot (Fig. 4.3) after multiple glaciations. For long continuous exposures, the $^{26}Al/^{10}Be$ ratio gradually decreases until secular saturation of both isotopes is reached depending on subaerial erosion rate (green erosion island in Fig. 4.3, Lal, 1991). In the case of repeated exposure and burial episodes, the ratio decreases rapidly during burial and increases again during exposure, defining a saw-tooth path within the burial field (blue trajectories, Fig. 4.3). The location of the trajectory within the burial field is most strongly controlled by the relative duration of ice-free and ice-cover intervals (f) and subaerial erosion rate (ε). Decreasing the relative duration of interglacial exposure (smaller f) deflects the trajectory to the left, while increasing the relative exposure duration shifts the trajectory closer to the continuous exposure line (red top line, Fig. 4.3a). Including a gradual subaerial erosion rate deflects the trajectory to the left and a higher transient saturation ratio (end of trajectory) is reached for long cyclic ice cover histories (>4 Ma, Fig. 4.3b). Although not included in *eqs (1-5)*, steady glacial erosion (abrasion) would deflect the trajectory even farther to the left and further increase the transient saturation ratio (Fig. 4.3b). Note that the total duration of each glacial-interglacial cycle (t_c) only affects the amplitude of the oscillations with shorter t_c narrowing the saw-teeth (cf., Bierman et al., 1999). A $t_c = 1$

ka trajectory can be viewed as a 'time-integrated' production rate approximating the TCN accumulation and decay through longer cycles (Fig. 4.3a). The TCN concentrations in a subsurface rock parcel (*eqs (4-5)*) evolve in a similar manner, but the trajectory is deflected to the left at a distance controlled by z_r (Fig. 4.3c). For a sampled surface that had been glacially plucked, the TCN concentrations initially follow a trajectory for a surface shielded at a depth equivalent to the total rock overburden. After a plucking event, the trajectory for the plucked surface starts to shift to the right to reach the trajectory of the remaining rock overburden. Following the final plucking event, the trajectory again shifts to the right reaching the trajectory of an exposed surface (dark blue line in Fig. 4.3c represents two plucking events, marked by the star symbols, each removing 50 cm thick blocks).

The trajectory, which passes through the measured TCN concentration, provides an approximation for the average exposure history of the sampling site (i.e., average ice-free time f for an assumed gradual subaerial erosion rate ε, Fig. 4.3d), if it can be assumed that the last plucking event occurred long enough ago so that the TCN concentrations have reached the trajectory of an exposed surface (0 cm thickness, Fig. 4.3c). The best fitting trajectory for an assumed ε is found using a chi-square approach simultaneously solving for f and the total duration of complex history t_{tot} (distance along the trajectory from zero ^{10}Be concentration to the measured sample, Fig. 4.3d). The values of t_{tot} determined with this approach only provide a minimum estimate of total complex history (sum of alternating burial and exposure durations), because plucking is not yet taken into account (see section 4.6.3). We can constrain the maximum limit of ε based on field evidence and independent TCN data (see section 4.7). However, larger assumed ε would require larger

f and would increase t_{tot}. Uncertainty in estimated f and t_{tot} are derived from the 1σ range of the probability density function based on the calculated chi-squared values.

4.6.2 Ice Cover History Model

The cyclic ice cover model introduced in section 4.6.1 is oversimplified, but it allows assessing the dependencies of the complex exposure model on the value and range of input variables. The results of the cyclic ice cover models are also used for comparison with the results based on a proxy record for ice cover. A more realistic ice cover history can be derived by assuming orbital pacing of glacial cycles, with obliquity driven 41-ka cycles dominating before the transition to longer eccentricity-based 100-ka cycles at 900 ka (Fig. 4.3c, Elderfield et al., 2012; Rial et al., 2013). An accurate ice history model is important because the TCN concentrations and ratios are particularly sensitive to the duration of more recent exposures, especially the current ice-free period. We considered using local climate records that would provide precise proxies of ice cover history. However, these records only extend to the last interglacial interval (Penny Ice Cap core, Fisher et al., 1998), the last glacial cycle (NGRIP, Andersen et al., 2006; Rasmussen et al., 2006; Vinther et al., 2006; Svensson et al., 2008), and the penultimate glaciation (GRIP, Dansgaard et al., 1993). Therefore, we use the globally-stacked marine core record LR04 from Lisiecki and Raymo (2005), which provides a >5 Ma long record of past global ice history, and we presume that past ice cover on Cumberland Peninsula scaled with global ice volume change. Continued cooling during the Pleistocene is reflected by generally decreasing durations of interglacials, so that the f decreases over time (supplementary file section A3.5, Fig. S3.10). Production of TCN during the Pliocene should not be significant owing to decay and the relatively increased production

as the rock exhumes. Simple sensitivity tests verify that time series > 3 Ma do not alter the timing or rate calculations.

4.6.3 Monte Carlo Method for Estimation of Episodic Erosion Rate

We use a Monte Carlo (MC) method (Rubinstein and Kroese, 2011) to (i) estimate the rate of episodic erosion by plucking and (ii) constrain the timing of last glacial plucking at the sampled tor sites on Cumberland Peninsula. The MC method is necessary to compute production and decay for all possible ice cover and plucking histories, to accommodate the various controls on concentration (e.g. ε, f, z_r) and to test the sensitivity to other variables (e.g., z_{ice} and t_{degl}). The MC method consists of an outer loop defining the environmental variables applying to all samples from the same location, and an inner loop determining the plucking variables for each sample individually.

In the outer loop, environmental parameters f, ε and t_{tot} are randomly varied within pre-defined constraints (Table 4.1). The LR04 record is divided into ice-free and ice-cover intervals by choosing different values of $\delta^{18}O$ ranging from 3.5 to 4.5 permil stepped through in 0.05 permil steps (arbitrarily chosen but reasonable boundaries and step size). Subaerial erosion rates are selected from an uniform distribution ranging from 0 to 4 mm ka^{-1} based on observations of grain-scale grusification and height of protruding quartz veins (Bierman et al., 1999; Margreth, 2015). The duration of total complex history is limited to 3 Ma, but it is varied for each model run (Table 4.1) and many runs require less than 2 Ma to explain the measured TCN concentrations. In the inner loop, a wide range of combinations of number and timing of plucking events and of plucked thicknesses are tested for the more weathered surface (tor tops) until a solution lies within the 1σ error range of the measured nuclide concentrations. We have restricted the model

to one plucking event per glaciation based on the generally advanced weathering degree of the sampled tors indicating limited modification in the past. Once the TCN data measured on the more weathered surface can be explained, then different sets of plucking variables (within the limits of environmental variables accepted for the weathered surface) are tested for the fresher surface until an accepted solution is found. The inner loop is broken if no solution is found for a maximum number of attempts (i.e., 500 sets of plucking variables) and a new set of environmental variables is generated until a pre-defined total number of solutions is obtained (i.e., 10,000 accepted solutions). The total number of Quaternary plucking events ranges randomly from one to the number of glaciations and the occurrence of the events is randomly chosen amongst the glaciations. The thickness of plucked bedrock blocks is derived from a log-normal distribution based on the horizontal joint spacing observed in the region. Additional parameters, such as frequency of plucking events or the rate of episodic erosion can be computed for both samples (weathered and fresh). The frequency of plucking is calculated by dividing the number of plucking events by the total duration of complex history for each model run. Taking the thicknesses of all removed bedrock blocks into account, a rate of landscape lowering attributed to episodic plucking of bedrock blocks can be calculated.

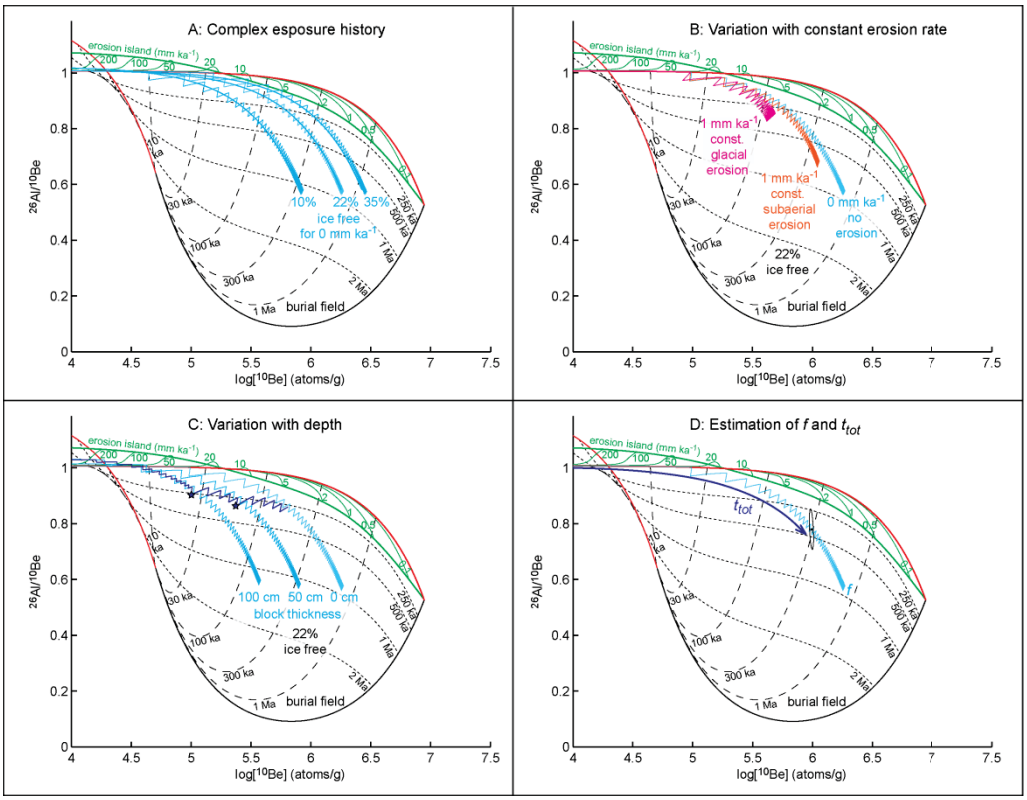

Fig 4.3 Normalised burial plot with cyclic ice cover model shown for a burial depth derived from multiplying the constant ice thickness by the fraction of total time the site is covered by ice ($[z_{ice} * \rho_{ice} * (1-f) * t_c] / t_c$). The right, solid red line defines continuous exposure with no erosion and solid green lines represent continuous exposure with varying erosion rates (defining the green erosion island). The left, solid red line indicates continuous burial, and the lower black line defines the decay path of a buried saturated surface. Black sub-vertical lines (longer dashes) indicate minimum duration of exposure and black sub-horizontal lines (shorter dashes) indicate minimum duration of continuous burial. **A.** Saw-tooth trajectory of a cyclic ice cover model shown for different ratios of ice-free to ice-cover time (percentage of ice-free time in the total duration of a glacial-interglacial cycle). Constant subaerial erosion rate is 0 mm ka^{-1}. Larger oscillations represent invariant 100 ka glacial cycles; amplitude of 1 ka glacial cycle oscillation decreases to a line. **B.** Trajectory for 22% ice-free time and no constant subaerial erosion (light blue), 1 mm ka^{-1} subaerial erosion (orange), and additional 1 mm ka^{-1} constant glacial erosion (abrasion, magenta). Transient saturation (end of trajectory) is reached at higher ratios for larger total constant erosion. **C.** Trajectory for 22% ice-free time and no constant subaerial erosion shown for 0, 50 and 100 cm of rock overburden (light blue). Trajectory for a surface that has been exposed by plucking of two bedrock blocks of each 50 cm is shown in dark blue (22 glacial-interglacial intervals of initially 41-ka duration and 100-ka duration for the last 9 intervals) with plucking events marked by dark blue stars. **D.** Measured concentrations and 1σ error ellipse of sampled surface, through which a trajectory with no constant subaerial erosion is fitted yielding an estimate of average ice-free time (*f*) at the site and a minimum estimate of total complex history (t_{tot}).

To obtain a continuous probability distribution of all tested parameters, the weighted chi-squared value (χ^2, Taylor, 1997) is computed for each set of plucking variables. For the environmental parameters, the weighted chi-squared values of all samples collected at the same site are summed ($\Sigma\chi^2$), from which the maximum is saved if the same set of environmental variables is considered multiple times. For the sample-specific parameters, the largest weighted chi-squared value is saved for a particular set of plucking variables.

To test the sensitivity of the results obtained from the chosen assumptions, we have varied the constant ice thickness, used different distributions of plucked block thicknesses, and altered the duration of the last ice-free interval (Table 4.1). On Cumberland Peninsula, we have not determined the deglaciation time of weathered uplands plateaus directly, but we have based our estimate on geomorphic evidence that the plateaus were deglaciated before the adjacent valleys and fiords (*Chapter 3*).

4.7 RESULTS

4.7.1 TCN Sample Site Characterization

The location of the twelve sampled tors ranges from narrow high-elevation coastal ridges to broad interior plateaus and low-elevation coastal plateaus (Fig. 4.1, Table 4.2). Except for one sample location (site 4, Fig. 4.1), the sampled tors occur in medium- to coarse-grained quartzo-feldspathic plutonic rocks (granodiorites, tonalites and quartz-diorites of the Paleoproterozoic Qikiqtarjuaq suite, Fig. 4.1, Sanborn-Barrie et al., 2011; Sanborn-Barrie and Young, 2013; Sanborn-Barrie et al., 2013b; Jackson and Sanborn-Barrie, 2014). Site 4 is located in silimanite-bearing semipelite (Fig. 4.4a) of the Paleoproterozoic Hoare Bay Group (Sanborn-Barrie et al., 2013a). The sampled tors

range from true tors (Andre, 2004; Hall and Phillips, 2006) consisting of towers of weathered bedrock blocks including nearly detached corestones (Fig. 4.4 a-b), to tor-like features, which are reduced to a few layers of bedrock blocks above a solid bedrock plinth (Fig. 4.4 c-d). The sampled surfaces are differentially weathered, with some surfaces exhibiting gnammas up to 20 - 50 cm deep and 50 - 80 cm wide and protruding quartz veins (Fig. 4.4 e-f, Fig. 4.2a), while other surfaces are smooth and hardly affected by grusification (Fig. 4.4d, Fig. 4.2b). Following the model of glacial modification of granite tors developed by Hall and Phillips (2006), we have classified the sampled tor sites into five stages of progressive modification (Table 4.2). Stage 1 tors (sites 1 & 4, Fig. 4.1, Fig. 4.4 a-b) preserve delicate weathering features indicating no glacial modification (Hall and Phillips, 2006). Removal of corestones on stage 2 tors (sites 8 & 9, Fig. 4.1) suggest slight glacial modification. The majority of our sites (sites 5-7 & 10-12, Fig. 4.1, Fig. 4.4c) are stage 2-3, 3, and 3-4 tors, from which weathered tor blocks have been removed and the tor plinth is exposed on the margins (e.g., Fig. 4.2 a-b). Tor plinths are largely exposed on two sites (2 & 3, Fig. 4.1, Fig. 4.4d), classified as stage 4-5 tors. At site 3 we noted a rounded cobble of a distinctively different granitic lithology (supplementary file, Fig. A3.2g), and at site 5, we collected samples from two weathered erratic blocks and a large, less weathered, angular erratic block (supplementary file, Fig. A3.2 h-i). While we interpret them all as glacial erratics, the rounded cobble may have been a corestone from an overlying lithological unit that has since been eroded.

Tor site #	Latitude (d.d)	Longitude (d.d)	Elevation (m)	Glacial modification[a]	Lithology[b]	Site descriptipn	Sample description	Sample ID
1	67.67	-64.26	1030	Stage 1	medium-grained granodiorite	narrow ridge with highly-weathered tor at summit, individual towers of well-rounded blocks separated by >1 m wide weathered vertical joints, horizontal joints weathered, so that uppermost blocks nearly detached, joint spacing 1-1.5 m, enhanced granular disintegration (grusification), largest gnammas 60 cm wide, 30 cm deep, also on bottom of horizontal joints	weathered tor surface at southern end of outcrop, eight 40 cm wide gnammas, surface crumbly	E065A-01
							weathered tor surface at northern end of outcrop, no gnammas, slightly more solid surface than E065	E066A-01
2	67.60	-63.93	373	Stage 5	medium-grained granodiorite	E-W oriented ridge of three tor-like outcrops, ridge seems to be streamlined from W to E (whaleback), sampled middle outcrop of a single layer of rounded blocks 0.5-0.8 m thick, joint spacing narrow 0.3-0.5 m, blocks tilted to the east on eastern edge of outcrop	sampled moderately rounded block 0.8 m above plinth, vertical joints show incipient widening and deepening	E064A-01
3	67.28	-63.08	570	Stage 4-5	foliated, coarse-grained monzogranite (Charnockite)	2m tall tor-like ridge of rounded blocks on summit of broad plateau, joint spacing 0.5-0.8 m, few vertical joints widened and deepend, ridge drops off at vertical joints on northern end, mm- to cm-thick exfoliation layers, gnammas 40 cm wide, 15 cm deep, one erratic cobble perched on regolith nearby tor ridge	rounded block at top of tor ridge, block 50-80 cm wide, limited by widened and deepended vertical joints	E042A-01
4	66.70	-61.66	1314	Stage 1	layered, silimite-bearing semipelite	few 1.5-2 m tall and 6-8 m wide tor ridgeds at edge of plateau falling off towards a steep cliff, highly-strained tonalite, cavernous weathering, on lower-lying parts of regolith-covered plateau lichen-kill zones related to permanent snowfields during Little Ice Age	sampled weethered surface on top of tallest tor ridge, horizontal joint spacing narrow 0.3-0.5 m, no gnammas	E074A-01
5	66.36	-65.70	1038	Stage 3	medium-grained granodiorite; erratic blocks with 4 cm long kalifeldspar phenocrysts	broad bevel midslope, scattered large, highly rounded weathered blocks, overall outcrop seems to be streamlined by ice flowing from W to E, joint spacing variable ranging from 0.5 to >1.5 m, largest gnammas 20 cm wide, 10 cm deep	large, rounded bedrock block >2 m above ground, gnammas 10 cm wide, 5 cm deep	E222A-01
							large, angular to slightly rounded block, partly embedded in regolith, large feldspar-phenocrysts	E222A-02
							large, rounded bedrock block >1 m above ground, gnammas 20 cm wide, 10cm deep	E222A-03
							mid-sized, angular to slightly rounded block, partly embedded in regolith	E222A-04
						few, only slightly rounded blocks of slightly different lithology resting on or inbetween rounded blocks, one 3.5 m tall angular block	large, rounded bedrock block >2 m above ground, gnammas 20 cm wide, 5 cm deep, 10 cm protruding quartz veins	E222A-05
							huge, angular block, largest block on site, surface appears fresher than other sampled surfaces	E222A-06
6	66.28	-65.80	765	Stage 3	medium-grained quartz-diorite/tonalite	5-8 m tall ridge at SW edge of broad plateau, lowest elevation of a series of tor ridges, joint spacing 1-2 m, vertical joints 1.5 m deep and 0.5 m wide, largest gnammas 25 cm wide, 15 cm deep	large, rounded block on top of tor ridge, no gnammas, granular disintegration (grusification)	E304A-01
7	66.30	-65.71	975	Stage 3-4	medium-grained quartz-diorite and tonalite	5-10 m tall ~NW-SE orientated ridge at the edge of a broad summit plateau (highest elevation 1150 m asl), joint spacing irregular, but mostly 0.5 - 1.6 m, vertical joints partly widened; largest wth pit 40 cm wide, 20 cm deep, exfoliation layers <10 cm thick	mid-sized, rounded block, on top of tor ridge, gnammas 20 cm wide, 10 cm deep	A346A-01
							mid-sized, rounded block, ~1 m above solid plinth at SE end of tor ridge, no gnammas	A347A-01
							large, rounded block on top of tor ridge, gnammas 30 cm wide, 15 cm deep, exfoliation layers 5 cm thick	A348A-01
8	66.30	-65.81	1000	Stage 2	medium-grained quartz-diorite and tonalite	~5 m tall tor ridge on broad plateau, local summit 1km away from highest summit, large, rounded blocks, separated by deeply weathered and widened vertical joints, joint spacing varied, at sample site ~1.5-2 m, largest gnammas 50 cm wide, 30 cm deep, prodruding quartz veins 2-4 cm	sampled prodruding quarz veins on wth surface of large tor block	E020A-01
							sampled prodruding quarz veins on wth surface of large tor block	E021A-01
9	66.29	-65.75	1150	Stage 2	medium-grained quartz-diorite and tonalite	~4 m tall tor ridge at highest elevation of broad plateau, well rounded blocks, largely deepened and widened vertical joints; joint spacing mostly 0.5-1 m, granular disintegration (grusification), no gnammas, but delicate weathering features (mushroom-shaped boulders) preserved	sampled large bedrock block at highest point of tor ridge	E022A-01
10	66.12	-65.54	665	Stage 3-4	medium-grained quartz-diorite and tonalite	5-8 m tall ~NE-SW orientated ridge at the edge of plateau, irregular joint spacing, on average ~1.2 m, vertical joints widened and deeply weathered, largest gnammas 50 cm wide, 20 cm deep	large, rounded block on top of tor ridge, no gnammas, block surrounded by deeply weathered and widened joints	A355A-01
							solid bedrock slab (plinth) at SW end of tor ridge, no gnammas, surface much fresher than on tor top	A356A-01
11	66.11	-65.55	825	Stage 2-3	medium-grained quartz-diorite and tonalite	two tor ridges separated by extensive bedrock slab (plinth) at the summit of a broad plateau, northern tor ridge 2 m high with horizontal joint spacing 0.5-0.8 m, southern tor ridge consisting of 5 blocks 1.5-3 m high, dissected by weathered vertial joints (>1.5 m wide), joint spacing generally large, largest gnammas 3m wide, 50cm deep filled with grus on basal platform (plinth) separating both tor ridges	sampled in the middle of the extensive basal platform, less grussified than tor ridges, plinth partly covered by grus	A186A-01
							well rounded block at top of northern tor ridge, no gnammas, but few loose, smaller blocks scattered on and around tor ridge	A187A-01
							largest, well rounded block at southern tor ridge, gnammas ~60 cm wide, 40 cm deep, granular disintegration (grusification)	A188A-01
12	66.00	-65.54	830	Stage 3-4	medium-grained quartz-diorite and tonalite	E-W orientated ridge of vertically dissected blocks at southern end of broad plateau, irregular joint spacing ranging between 0.5 - 2 m,vertical joints 10-20 cm wide and deeply weathered, rounded blocks, largest wth pit 50 cm wide, 30 cm deep	well rounded block >2 m above ground, gnammas 20 cm wide, 10 cm deep	E221A-01
							smaller, moderately rounded block, 0.8 m above plintth, no gnammas	E221A-02
							smaller, slightly rounded block, 0.8 m above plinth, no gnammas	E221A-03

[a] according Hall and Phillips (2006)

[b] according Sanborn-Barrie et al., 2011; Sanborn-Barrie and Young, 2013; Sanborn-Barrie et al., 2013b; Jackson and Sanborn-Barrie, 2014

Table 4.2 Detailed geomorphic description of tor sites and sampled surfaces.

Fig. 4.4 Representative pictures of sampled tor sites. **A.** Stage 1 tor (site 4) in silimanite-bearing semipelite. Note difference in appearance of weathering compared to other tors located in the plutonic Qikiqtarjuaq suite (B, D, E granodiorite; C, F quartz-diorite – tonilite). **B.** Stage 1 tor (site 1) capped with nearly detached corestones and well-rounded weathered bedrock blocks. **C.** Stage 3 tor (site 7) where corestones have been removed. **D.** Stage 5 tor (site 2) where most upstanding weathered bedrock blocks have been eliminated and the tor plinth is largely exposed. **E.** Typical weathering pit on a stage 3 tor surface (site 10). Samples have been collected at a distance to gnammas. **F.** Protruding quartz vein on stage 2 tor surface (site 8). Samples collected at this site consist of these quartz veins.

4.7.2 TCN Results

Measured ^{10}Be concentrations range between 2 and 82 x 10^5 atoms g^{-1}, while ^{26}Al concentrations range between 10 and 425 x 10^5 atoms g^{-1} (Table 4.3). These concentrations are higher than those measured on boulders on late glacial moraines throughout Cumberland Peninsula (0.7 and 1.5 x 10^5 ^{10}Be atoms g^{-1}, Margreth 2015). Discordance between apparent exposure ages calculated from the ^{10}Be and ^{26}Al concentrations (supplementary file Table A3.1) and low ^{26}Al/^{10}Be ratios (Table 4.3) for a given ^{10}Be concentration indicate that most samples experienced at least one period of burial that interrupted the exposure history of a sampled surface. All samples have apparent exposure durations that predate the last deglaciation of the summits (ca. 15 ka, Margreth, 2015), and most samples have apparent ages that exceed 100 ka. While the entire dataset appears broadly scattered on a burial plot (Fig. 4.5), consideration of their geographic position, intensity of weathering, and degree of glacial modification explains all of this variability.

Three samples, collected from the two sites classified as stage 1 tors (sites 1 & 4), have the highest concentrations and relatively high ratios (5.2 – 6.6, Table 4.3). Their apparent ^{10}Be ages are 0.4, 0.6, and 1.0 Ma (Table A3.1). These samples (purple error ellipses, Fig. 4.5), plotting close to the continuous exposure line or within the constant erosion island, were collected from high-elevation narrow ridges along the northeastern coast of Cumberland Peninsula (Fig. 4.1 & 4.4 a-b) where glacial cover is unlikely. The advanced weathering features observed on these ridges corroborate long subaerial exposure with relatively little, if any, burial by ice. Assuming these samples have reached secular equilibrium, the measured concentrations imply long-term steady

subaerial erosion rates of 0.8 – 1.6 mm ka^{-1} (Table A3.1). If saturation has not yet been reached, the inferred erosion rates are maximum estimates. This calculated range of erosion rates provides a good approximation for an interglacial steady erosion rate occurring at the other sites with similar lithologies.

Tor site #	Sample ID [a]	Measured concentrations			Concentrations normalized to SLHL [c]	
		^{10}Be concentration [b] (10^5 atom g^{-1})	^{26}Al concentration [b] (10^5 atom g^{-1})	^{26}Al/^{10}Be (-)	^{10}Be concentration [b] (10^5 atom g^{-1})	^{26}Al concentration [b] (10^5 atom g^{-1})
1	E065A-01	50.15 ± 1.05	329.35 ± 19.14	6.57 ± 0.41	20.08 ± 0.42	133.31 ± 7.75
	E066A-01	37.51 ± 0.84	225.37 ± 12.92	6.01 ± 0.37	15.07 ± 0.34	91.53 ± 5.25
2	E064A-01	6.35 ± 0.18	40.14 ± 2.72	6.32 ± 0.46	4.51 ± 0.13	28.65 ± 1.94
3	E042A-01	6.71 ± 0.19	40.58 ± 2.72	6.05 ± 0.44	4.00 ± 0.11	24.35 ± 1.63
4	E074A-01	82.32 ± 1.80	424.74 ± 16.91	5.16 ± 0.23	26.00 ± 0.57	136.03 ± 5.42
5	E222A-01	22.35 ± 0.51	126.18 ± 7.59	5.65 ± 0.36	8.89 ± 0.20	50.73 ± 3.05
	E222A-02	3.21 ± 0.09	12.36 ± 0.56	3.85 ± 0.21	1.28 ± 0.04	4.97 ± 0.23
	E222A-03	17.29 ± 0.38	100.80 ± 5.78	5.83 ± 0.36	6.88 ± 0.15	40.53 ± 2.32
	E222A-04	4.62 ± 0.13	19.89 ± 1.05	4.30 ± 0.26	1.84 ± 0.05	8.00 ± 0.42
	E222A-05	20.57 ± 0.45	121.17 ± 6.95	5.89 ± 0.36	8.18 ± 0.18	48.72 ± 2.79
	E222A-06	1.95 ± 0.05	9.49 ± 0.69	4.86 ± 0.38	0.78 ± 0.02	3.82 ± 0.28
6	A346A-01	14.52 ± 0.44	81.84 ± 4.98	5.64 ± 0.38	6.09 ± 0.18	34.69 ± 2.11
	A348A-01	10.33 ± 0.28	63.92 ± 3.81	6.19 ± 0.41	4.34 ± 0.12	27.17 ± 1.62
	A347A-01 [d]		18.03 ± 2.55	3.86 ± 0.56		
	A347A-01 [e]	4.67 ± 0.13	26.26 ± 1.23	5.62 ± 0.31	1.97 ± 0.05	11.17 ± 0.52
7	E304A-01	14.06 ± 0.40	78.74 ± 4.99	5.60 ± 0.39	7.07 ± 0.20	39.90 ± 2.53
8	E020A-01	23.97 ± 0.65	124.80 ± 7.14	5.21 ± 0.33	9.81 ± 0.27	51.63 ± 2.95
	E021A-01	28.63 ± 0.61	140.86 ± 8.58	4.92 ± 0.32	11.75 ± 0.25	58.42 ± 3.56
9	E022A-01	13.67 ± 0.35	68.56 ± 4.26	5.02 ± 0.34	4.95 ± 0.13	25.11 ± 1.56
10	A355A-01	15.70 ± 0.40	89.65 ± 5.24	5.71 ± 0.36	8.57 ± 0.22	49.26 ± 2.88
	A356A-01	5.75 ± 0.17	35.67 ± 2.40	6.20 ± 0.46	3.16 ± 0.10	19.75 ± 1.33
11	A186A-01	13.59 ± 0.42	73.63 ± 4.31	5.42 ± 0.36	6.47 ± 0.20	35.38 ± 2.07
	A188A-01	17.77 ± 0.45	92.20 ± 5.44	5.19 ± 0.33	8.48 ± 0.21	44.38 ± 2.62
	A187A-01	12.37 ± 0.32	73.00 ± 4.27	5.90 ± 0.38	5.90 ± 0.15	35.14 ± 2.05
12	E221A-01 [d]		50.57 ± 4.45	7.15 ± 0.67		
	E221A-01 [e]	7.07 ± 0.21	37.02 ± 2.03	5.23 ± 0.33	3.36 ± 0.10	17.74 ± 0.98
	E221A-01 [d]		50.57 ± 4.45	7.15 ± 0.67		
	E221A-02 [e]	12.61 ± 0.34	57.14 ± 2.02	4.53 ± 0.20	5.99 ± 0.16	27.39 ± 0.97
	E221A-03	9.66 ± 0.27	59.09 ± 3.40	6.12 ± 0.39	4.59 ± 0.13	28.32 ± 1.63

[a] abbreviated sample ID, full sample ID is given in supplementary material Table A3.1

[b] 1σ error includes AMS measurement uncertainty, weighted blank correction, 2% sample preparation uncertainty, and for ^{26}Al uncertainty for native Al measurement (5% ICP-MS and <2% ICP-OES)

[c] normalization to sea-level, high-latitude (SLHL) location 66.50°N, 65.20°W, 0 m above sea level

[d] AMS Al uncertainty >7% possibly related to large native Al concentration (Table A3.1)

[e] AMS Be analysis might be affected by impurities in quartz, samples not further discussed

Table 4.3 TCN data. Measured concentrations and concentrations normalized to a sea-level, high-latitude (SLHL) location at 66.50°N, 65.20°W.

The three sampled erratic blocks, collected near a stage 3 tor (site 5), yielded the lowest TCN concentrations, as well as some of the lowest ratios (3.9 - 4.9, Table 4.3; gray error ellipses, Fig. 4.5) suggesting that they had been buried for >750 ka and exposed for a comparatively short time (Table A3.1). This scenario is unlikely since it does not match the burial histories of all other sites. Alternatively, the TCN concentrations can be interpreted as indicating surfaces that had been continuously exposed for a long time (> 1 Ma) at a rock depth of >2.5 m (no subaerial erosion is required for at least one block, Fig. A3.3) and subsequently flipped (Fujioka et al., 2015). A third interpretation of these samples is recent overturning of a weathered tor block that had periodically been shielded by ice (>1.4 m blocks, <5 ka since overturning). However, the slightly different lithology (~cm-sized feldspar phenocrysts) indicates an origin of the blocks from a different location, for which the TCN production parameters and glacial history are unknown. The low ratios may also be due to high concentrations of native Al in the quartz, which affected the AMS measurements. The same problem may apply to three bedrock surfaces (one sample at site 6, two samples at site 12) that yielded relatively low ^{10}Be concentrations and ratios (orange error ellipses, Fig. 4.5, supplementary file section A3.1) and plot outside a cluster constituted by most other sampled tor surfaces.

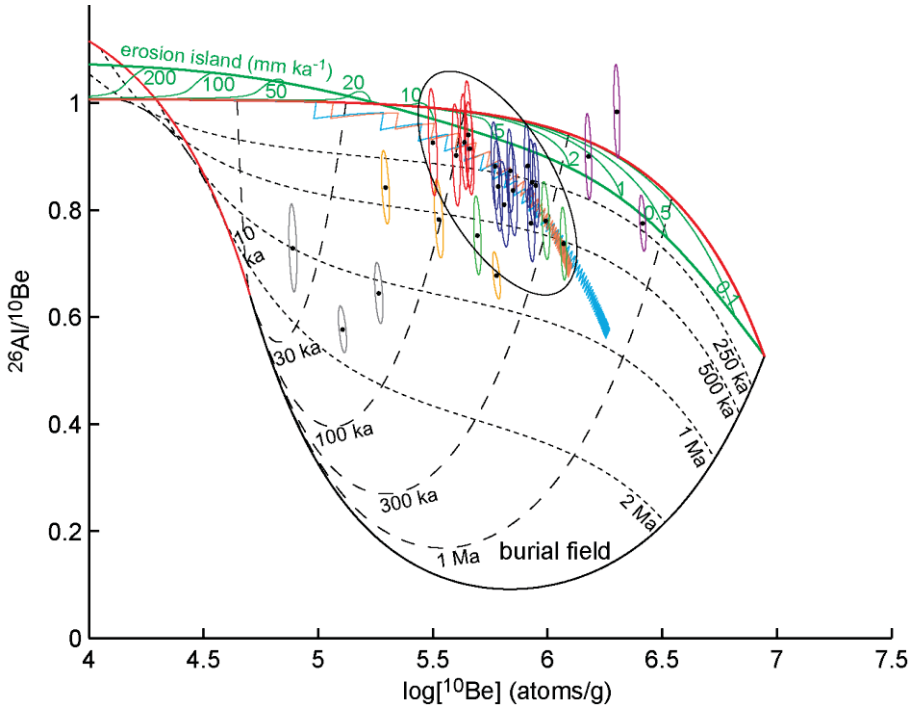

Fig. 4.5 Normalised burial plot with all 26 samples collected on the 12 tors on Cumberland Peninsula. Burial plot is shown for a trajectory of 22% ice-free time (light blue) assuming no constant subaerial erosion rate and a constant ice thickness of 50 m during burial intervals. A trajectory for 27% ice-free time and 1 mm ka^{-1} subaerial erosion rate is shown in orange. Details of burial plots as in Fig. 4.3. Samples are shown for the normalised concentrations (black dots) and 1σ measurement uncertainties (coloured ellipses). Continuously exposed surfaces (purple) plot close to the erosion island. Three erratic blocks (gray) have low concentrations and low ratios. Three samples (yellow) may be affected by impurities in the quartz and are not further discussed. Samples plotting within the large black ellipse are interpreted to have experienced complex exposure histories (section 4.6.1). Green samples are classified as stage 2 tors and the most weathered surface on the stage 2-3 tor that have only slightly been glacially modified. Blue samples comprise sites classified as stage 3, weathered surfaces of stage 3-4 tors, and fresher surfaces on the stage 2-3 tor. The fresher surfaces of stage 3-4 tors are shown in red, together with the samples classified as stage 4-5 tors.

All remaining samples plot in an elongated cluster in the burial field (black ellipse, Fig. 4.5). These samples can be interpreted to have experienced a complex exposure history that can either be approximated by periodic recurring ice cover (section 4.6.1) or by a proxy record for global ice volume (LR04, section 4.6.3). In this section, the results derived from the simple, periodic ice cover history (section 4.6.1) are discussed (Table

4.4 middle panel), while the results derived from the MC method using LR04 are discussed in the next section 4.7.3 (Table 4.4 right panel).

By fitting a trajectory for 1-ka cycles through each sample point (approximating time-integrated production, section 4.6.1), we can estimate the fraction of ice-free time f and minimum duration of total complex history t_{tot} for each sampled bedrock surface (Table 4.4). One sample (site 9, stage 2 tor) plotting slightly below and to the left of the cluster (green ellipse farthest to the left, Fig. 4.5) yields the lowest fraction of ice-free time ($10.9\ ^{-1.1}/_{+4.6}$ %, for 1 mm ka^{-1} subaerial erosion rate, Table 4.4). The values of ice-free time calculated for all other samples of the elongated cluster (sites 2, 3, 5 bedrock surfaces, 6-8, 10-12) ranges from $18.8\ ^{-1.5}/_{+20.8}$ % to $38.6\ ^{-4.2}/_{+41.9}$ % with an average of 27% (Table 4.4). Despite the considerable range of measured TCN concentrations and ratios (including overlap with the continuous exposure line at 1σ for many of the samples), the clustering of these samples implies that these sites experienced similar glacial histories. Note that the estimated values of ice-free time vary for different bedrock surfaces sampled at a given site, but they are still within the estimated 1σ error range, which are quite large, particularly for the higher side (Table 4.4). Additional processes, for instance plucking of overlying bedrock blocks, would explain some of this variation. Considering the effect of plucking, (Fig. 4.3c) the average value of 27% would be a minimum estimate of ice-free time for these surfaces.

The duration of total complex history t_{tot}, equivalent to the distance along the trajectory fitted to each sample, ranges from 330 ka to 2.45 Ma (for 1 mm ka^{-1} subaerial erosion based on the saturated samples at sites 1 & 4, Table 4.4). As indicated in section 4.6.1, these estimates should be interpreted as a minimum duration because plucking of

overlying bedrock blocks has not been taken into account in this simple model (the MC approach will, section 4.7.3). The complex history durations determined with this approach (e.g., 1015 ka, sample A304, Table 4.4) are twice as long as the estimates of minimum durations of a single (e.g., 192 ka, sample A304, Table A3.1) exposure interval followed by a single (e.g., 295 ka, sample A304, Table A3.1) burial interval (Fig. A3.1). Recurring intervals of exposure and burial require longer total complex histories to reach the same TCN concentrations and ratios than a much simpler burial history of a continuous first exposure interval followed by a continuous single burial interval.

Tor site #	Sample ID [a]	Cyclic ice cover history [b]: fraction ice-free time (*f*) (%)	(-%)	(+%)	total complex exposure history (ka)	(-ka)	(+ka)	MC simulation results [c]: occurrence of last plucking event (ka)	(-ka)	(+ka)	episodic erate (mm ka^{-1})	(-mm ka^{-1})	(+mm ka^{-1})	$\delta^{18}O$ (per mil)	(-per mil)	(+per mil)	subaerial erosion rate (mma ka^{-1})	(-mm ka^{-1})	(+mm ka^{-1})	t_{tot} (Ma)	(-Ma)	(+Ma)
1	E065A-01	nd			nd			nd			nd			nd			nd			nd		
	E066A-01	nd			nd			nd			nd											
2	E064A-01	36.4	6.7	49.1	333	91	564	250	93	423	3.5	1.5	6.6	4.25	0.42	0.12	1.2	0.7	2.0	1	0.4	0.9
3	E042A-01	20.3	0.0	60.0	550	225	547	250	102	431	3.3	1.2	7.5	3.85	0.13	0.48	1.3	0.8	1.9	1	0.4	1.1
4	E074A-01	nd			nd			nd			nd			nd			nd			nd		
5	E222A-01	33.1	3.0	37.1	971	291	696	500	183	620	1	0.0	4.8									
	E222A-02	nd			nd			nd			nd											
	E222A-03	29.4	2.1	44.4	748	257	493	400	176	260	3.0	1.1	4.9	4.25	0.32	0.07	0.2	0.0	1.5	1	0.2	1.1
	E222A-04	nd			nd			nd			nd											
	E222A-05	38.6	4.2	41.9	696	226	514	500	213	343	2.5	1.1	4.0									
	E222A-06	nd			nd			nd			nd											
6	A346A-01	21.2	1.2	40.6	940	308	614	300	76	825	1.0	0.0	6.8	3.9	0.11	0.36	0.3	0.0	2.5	1	0.2	1.2
	A348A-01	29.1	1.9	54.5	408	152	466	250	88	265	5.5	2.6	6.4									
	A347A-01	nd			nd			nd			nd			nd			nd			nd		
7	E304A-01	23.9	1.6	38.5	1015	319	716	500	246	665	1.0	0.0	6.0	3.85	0.04	0.41	0.1	0.0	2.2	1.5	0.6	0.7
8	E020A-01	26.9	2.5	13.6	1620	142	nd	1000	599	483	1.3	0.3	4.7	3.85	0.06	0.34	0.0	0.0	1.4	0	1.1	2.5
	E021A-01	28.9	2.2	8.9	2451	nd	nd	1250	672	430	0.5	0.0	3.5									
9	E022A-01	10.9	1.1	4.6	1726	341	1361	100	0	1749	1.0	0.0	5.4	3.60	0.07	0.19	0.0	0.0	2.8	2.4	0.7	0.2
10	A355A-01	32.8	2.8	38.9	919	287	627	500	195	731	1.0	0.0	4.9	4.25	0.34	0.10	0.0	0.0	1.8	1	0.2	1.1
	A356A-01	20.3	0.0	62.5	412	167	541	200	162	12	7.3	3.0	8.4									
11	A186A-01	18.8	1.5	20.8	1220	336	726	500	245	528	3.3	1.3	5.4									
	A188A-01	22.1	2.1	11.0	1608	258	nd	1000	614	550	1.0	0.1	4.9	3.80	0.05	0.24	0.0	0.0	1.7	1.9	0.5	0.6
	A187A-01	26.4	1.3	49.5	682	250	493	500	240	394	3.8	1.1	6.4									
12	E221A-01	nd			nd			nd			nd			nd			nd			nd		
	E221A-02	nd			nd			nd			nd			nd			nd			nd		
	E221A-03	27.1	1.1	54.8	472	182	459	250	86	506	3.3	1.4	6.4	4.10	0.29	0.25	0.7	0.2	2.5	1	0.4	0.9

[a] abbreviated sample ID, full sample ID is given in supplementary material Table A3.1

[b] calculated assuming a consant subaerial erosion rate of 1 mm ka^{-1}, 1σ error includes concentration measurement uncertainty

[c] values derived from probability density functions based on maximum weighted chi square values

nd = not determined

Table 4.4 Estimated values using a cyclic ice cover history (section 4.6.1) and generated by the Monte Carlo (MC) method (section 4.6.3). Error ranges are given for 1σ confidence level based on the concentration measurement uncertainty, which in turn considers AMS measurement uncertainty, weighted blank correction, 2% chemistry procedure error, and, for ^{26}Al, native Al concentration measurement uncertainty.

TCN concentrations and ratios, as well as total complex history and estimates of minimum burial durations, appear to vary systematically with sample elevation (Fig. 4.6). This correlation has previously been observed in other regions and was the basis of supporting the Nunatak Hypothesis (Brook et al., 1996; Steig et al., 1998; Gosse et al., 2006). TCN concentrations increase and ratios decrease with altitude. The correlation is strongest if only the most weathered surfaces at each site are considered. The scatter can be attributed to plucking, which exposes deep surfaces with lower TCN concentrations but higher ratios (section 4.6.1). Likewise, estimates of total complex history and minimum burial durations increase with elevation considering only the most weathered surfaces at each site (the exposure history of fresher surfaces is more strongly controlled by the timing of last major erosion event and not elevation).

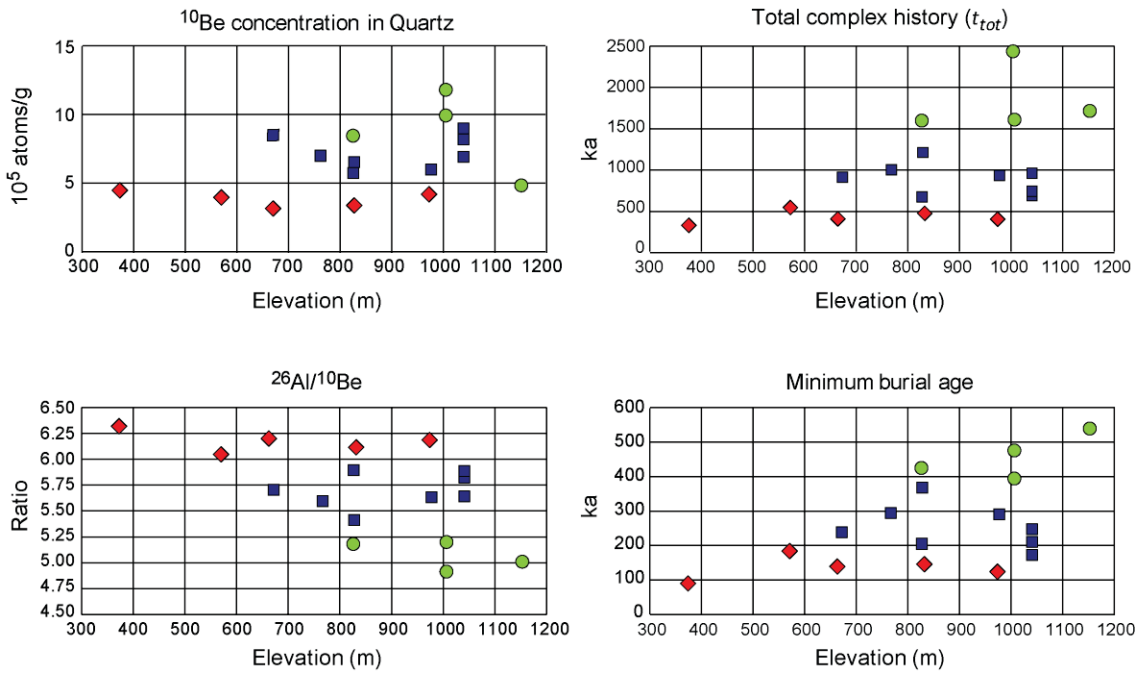

Fig. 4.6 Variation of selected TCN data and derived values with elevation of sampled tor sites. ^{10}Be concentrations are normalized to a sea-level, high-latitude location at 66.50°N, 65.20°W. Green circles: stage 2 tors and most weathered surface on stage the 2-3 tor. Blue squares: stage 3 tor, weathered surfaces of stage 3-4 tors, and fresher surfaces of stage the 2-3 tor. Red diamonds: Stage 4-5 tors and fresher surfaces on stage 3-4 tors.

4.7.3 Timing of Last Plucking and Rate of Episodic Erosion

The results in the previous two sections have ignored the effect of plucking. The estimates of f and t_{tot} derived above are based on a simple periodic ice cover model assuming a constant subaerial erosion rate. To accommodate multiple plucking events with varying block thicknesses, we use the MC method described in section 4.6.3. Since it is based on a globally-stacked marine oxygen proxy for past ice volume change (Lisiecki and Raymo, 2005), the MC method provides an opportunity to study the nature of subaerial weathering and former glacial conditions including sporadic plucking events. The timing of deglaciation is based on published and new deglacial chronology for the region (summarized in Margreth, 2015). Several consistency checks can test the sensitivity of the MC method. For instance, the MC model yields shorter ice-free intervals (equivalent to lower f values in the cyclic ice cover model) in runs where the transition between glaciations and interglaciations is set at lower $\delta^{18}O$ values (colder climate, the value of $\delta^{18}O$ is uniformly varied between 3.5 to 4.5 permil with a stepsize of 0.05 permil). When pairs or triplets of samples are analysed simultaneously, the environmental parameters ($\delta^{18}O$ value, ε, and t_{tot}) are most strongly influenced by the most weathered surface (Table 4.4, note that t_{tot} determined with the MC method is considerably longer than estimated in section 4.7.2). Stage 2 tors require the longest total histories with decreasing durations for more progressively modified sites (stages 3-5). Furthermore, after numerous runs of the MC method with different parameter ranges, the results clearly reveal that variation in subaerial erosion rate at each site is not significant, because the rates are consistently slow (all are <3 mm ka^{-1}). This finding agrees with the low steady state erosion rates determined from the continuously exposed sites 1 and 4

(Table A3.1). Therefore, contrasts in weathering and TCN concentrations within and among tor sites can be attributed to the degree of glacial modification and the location of the tor within the glaciated landscape.

The most important outcomes of the MC method are (i) constraints for the fraction of time the summits were ice free, (ii) estimates for the timing of the last plucking event at a tor site, and (iii) the long-term average episodic erosion rate due to plucking for each sampled bedrock surface (Table 4.4). Compared to the simple cyclic ice cover model (section 4.6.1 and 4.7.2), the MC method yields longer average ice-free time that depends on the $\delta^{18}O$ exposure and burial interval transition value (supplementary file section A3.5). This discrepancy is caused by relatively longer exposure intervals during the early Pleistocene before continued cooling led to increasing durations of glacials (Fig. A3.10).

For most sites, the timing of last glacial plucking is not well constrained (Fig. 4.7) owing to a strong dependence on the thickness of the plucked bedrock block, subaerial erosion rate, and fraction of ice-free time ($\delta^{18}O$ value, supplementary file section A3.5, Fig. A3.12). Low rates of subaerial erosion limit the timing of last plucking, while relatively longer ice-free time is required for more recent plucking (Fig. A3.12). The range of possible timing of last plucking is largest for stage 2 tors and the most weathered surface of the stage 2-3 tor (0.4 – 1.9 Ma, 1σ error range, Fig. 4.7, Table 4.4); intermediate for stage 3 tors, weathered surfaces on stage 3-4 tors, and fresher surfaces on the stage 2-3 tor (0.2 – 1.2 Ma); and narrowest for stage 4-5 tors and the fresher surfaces at the margins of stage 3-4 tors (40 – 680 ka). This pattern is expected because the parts of the tor sites that appear fresher were probably those that were plucked more recently than the more weathered surfaces. The mode of the probability distribution functions

(pdfs) is >1 Ma for stage 2 tors and the most weathered surface of the stage 2-3 tor. It is between 300 and 500 ka for stage 3 tors, weathered surfaces of stage 3-4 tors, and fresher surfaces of the stage 2-3 tor. The mode decreases to 200 - 250 ka for stage 4-5 tors and fresher surfaces of stage 3-4 tors. The climate time series used for the MC method necessitates that summit plateaus were ice covered during all middle and late Pleistocene glaciations. Calculating the TCN concentrations that would have been measured in the sampled surfaces prior to continuous exposure since oxygen isotope stage 3 (OIS-3, i.e., 60 ka, Fig. A3.4) reveals that some surfaces would have required prolonged burial before re-exposure during OIS-3. However, prolonged burial since OIS-4 is difficult to reconcile with the periodic climate shifts in the Quaternary. This result is particularly valuable for summits where no erratics are available for exposure dating, or where erratics have high TCN inheritances.

The range of episodic erosion rates, computed by dividing the total thickness of all plucked bedrock blocks by the total duration of simulated complex history for a given MC method run, is insensitive to the value of subaerial erosion rate or the value of $\delta^{18}O$ dividing LR04 in glacial and interglacial intervals (supplementary file section A3.5). Episodic erosion rates range between 0.5 and 6.5 mm ka^{-1} (1σ range) for stage 2 tors and the most weathered surface of the stage 2-3 tor. It increases to 1.0 – 10.2 mm ka^{-1} for stage 3 tors, weathered surfaces on stage 3-4 tors, and fresher surfaces of the stage 2-3 tor. Episodic erosion rates range between 2.0 – 15.7 mm ka^{-1} for stage 4-5 tors and fresher surfaces on stage 3-4 tors (Fig. 4.8, Table 4.3). The mode of the probability distribution functions ranges between 0.5 – 1.3 mm ka^{-1} for stage 2 tors and the most weathered surface of the stage 2-3 tor. It increases slightly to 1.0 – 3.8 mm ka^{-1} for stage

3 tors, weathered surfaces on stage 3-4 tors, and fresher surfaces of the stage 2-3 tor. The mode increases to 3.5 – 7.3 mm ka^{-1} for stage 4-5 tors and fresher surfaces on stage 3-4 tors (Fig. 4.8, Table 4.4). Larger episodic erosion rates determined for the fresher surfaces is corroborated by the most recent timing of last glacial plucking calculated for these samples, whereas the weathered surfaces require plucking to have occurred a longer time ago (Fig. 4.7).

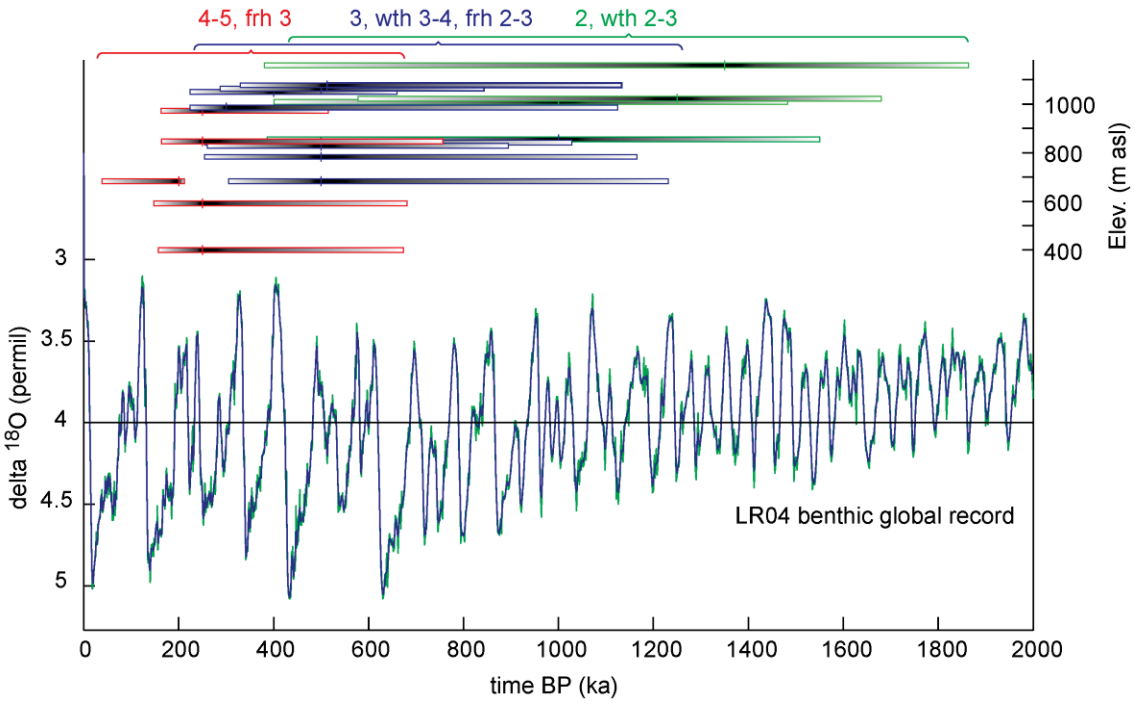

Fig 4.7 Comparison of timing since last glacial plucking with the stacked marine benthic $\delta^{18}O$ record (Lisiecki and Raymo, 2005). **Bottom:** LR04 is shown with reversed vertical axis, so that cold intervals are pointing down (green original data, blue slight smoothing used for MC method). The record is divided in ice-free and ice-cover intervals for a $\delta^{18}O$ value of 4 permil. **Top:** Timing since last glacial plucking plotted against elevation of sampled tor site (multiple samples are slightly offset for better visibility). Green: stage 2 tors and most weathered (wth) surface on stage the 2-3 tor, blue: stage 3 tor, weathered surfaces of stage 3-4 tors, and fresher (frh) surfaces of the stage 2-3 tor, and red: stage 4-5 tors and fresher surfaces of stage 3-4 tors.

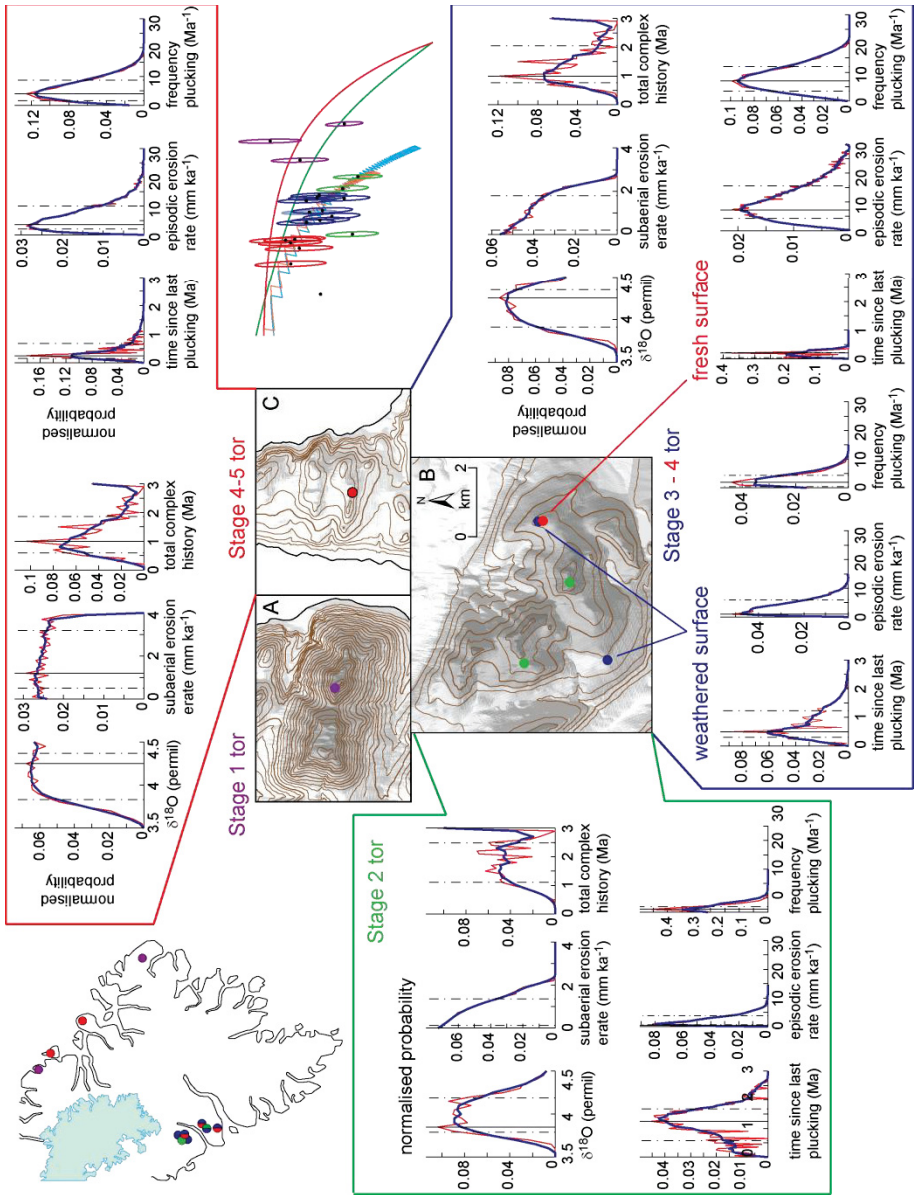

Fig 4.8 Correlation of Monte Carlo (MC) method results with topographic location of sampled tor sites. **Centre:** Shaded-relief maps and contours (40 m intervals) showing examples of **A.** narrow coastal ridge (stage 1 tor), **B.** broad interior plateau (stage 2, 2-3, and 3-4 tors), and **C.** low-elevation coastal plateaus (stage 4-5 tors). Locations of maps are indicated in Fig. 4.1. **Periphery:** Probability density functions (pdfs) of values derived from the MC method (red calculated probability, blue smoothed probability, solid black line mode, and dashed black lines 1σ error ranges). Environmental parameters: $\delta^{18}O$, subaerial erosion rate, total duration of complex history; sample-specific parameters: timing of last glacial plucking, episodic erosion rate, plucking frequency. Note that the horizontal axis is the same for similar pdfs. Simplified burial plot displays variation of TCN concentration and simplified map indicates location of individual samples, which are colour coded according the classification of glacial modification (stage 1 purple, stage 2 green, stage 2-3 blue/green, stage 3 blue, stage 3-4 red/blue, stage 4-5 red).

4.8 DISCUSSION

The TCN data and MC method provide constraints on rates of subaerial weathering as well as broad constraints on rates of episodic subglacial erosion of weathered plateaus on Cumberland Peninsula (Fig. 4.8). It is also possible to distinguish and quantify both the subaerial erosion rate and the steady subglacial erosion rate (abrasion). On a continuously exposed surface, higher subaerial erosion rates shift the saturation point to increasingly higher ratios (erosion island endpoints, Lal, 1991; section 4.6.1, Fig. 4.3). Similarly, slow rates of steady subglacial abrasion (i.e., 1 mm ka^{-1}, Fig. 4.3b) shift the transient saturation point of complex exposure trajectories to higher ratios. Because most of the summits were ice covered 70 – 80 % of the time over the Quaternary (average f = 0.27 for 1 mm ka^{-1} subaerial erosion rate determined with cyclic ice cover model, Table 4.3), TCN ratios measured at most sites require extremely slow or zero subglacial abrasion. This finding is consistent with the notion of weakly erosive cold-based ice cover of the highland plateaus. Only the samples with the highest ratios (stage 4-5 tors and fresher surfaces on stage 3-4 tors, red ellipses Fig. 4.5) would permit discernable rates of subglacial abrasion. Steady subglacial erosion must be negligible for stage 3-4 tors because of the relatively low ratios measured for the weathered surfaces. Therefore, only stage 4-5 tors may have been affected by glacial abrasion, although the rate even there must have been <2 mm ka^{-1}. In comparison, glacial abrasion rates of >100 mm ka^{-1} have been estimated in predominately warm-based valleys (Hallet et al., 1996; Briner and Swanson, 1998; Davis et al., 1999; Staiger et al., 2005).

The range of calculated episodic erosion rates (1 - 16 mm ka^{-1}, 1σ error range of all probability distributions, Table 4.3) always exceeds the range of subaerial erosion rates

for a given site (Fig. 4.8). This finding supports previous notions that, over longer timescales, sporadic erosion involving higher volumes of material (e.g., plucked bedrock blocks of sufficient thickness, or deep-seated landslides) outpaces steady erosion for a given system (Kirchner et al., 2001). Computed episodic erosion rates are influenced by the time since last plucking, particularly for the freshest surfaces sampled (supplementary file section A3.5, Fig. A3.13). This effect is comparable to measurements of basin-wide erosion rates, which yield higher erosion rates following large landsliding events (i.e., triggered by an earthquake) with subsequent progressive decrease to values of background steady erosion rates (Niemi et al., 2005; Antinao Rojas, 2009).

The TCN concentrations and MC results are related to the extent of glacial modification, topographic position, and lithological properties of the sampled tor sites. These relationships are based on a limited dataset, but are consistent with previously reported observed or inferred relationships. Episodic erosion rate, and hence degree of glacial modification, is controlled by the location of the tor in the landscape and fracture density of the bedrock. As demonstrated previously (Dühnforth et al., 2010; Anderson, 2014), glacial plucking is increased with narrower joint spacing, which is corroborated by our MC results. For instance, at site 11 (stage 2-3 tor) large weathered tor blocks (2-4 m tall, Fig. A3.2a, Table 4.2) stand above an exposed plinth opposite a ridge composed of multiple layers of bedrock blocks 0.5 – 1 m thick (Fig. A3.2b). The sample obtained from one of the large tor blocks (most weathered surface) yields lower episodic erosion rates than the two samples collected from the exposed plinth and from the top of the layered tor ridge (Table 4.4). This difference suggests that the large tor blocks (with higher rock mass strengths due to fewer fractures) withstood plucking while smaller

blocks (lower rock mass strengths due to higher fracture density) were more frequently removed from the layered ridge. Both stage 4-5 tors (sites 3 & 4) have comparatively small joint spacing (0.5 – 0.8 m) making them more susceptible to plucking.

The importance of local topography is revealed by tors on high narrow coastal interfluves along the northeastern coast of Cumberland Peninsula that remained ice-free throughout the Quaternary (sites 1 & 4, Fig. 4.1). The ridges are too narrow and wind-exposed to permit significant snow accumulation and ice cap formation (Fig. 4.8a). This conclusion is corroborated by ice sheet models that are constrained by relative sea level data. The models project the coastal ridges above the paleo-ice surface (Staiger et al., 2005; Tarasov et al., 2012). Continuous cosmic ray exposure is supported by the high TCN concentrations (Table 4.3) that can be explained with gradual steady-state erosion rates of 0.8 – 1.6 mm ka^{-1} (Fig. 4.5, Table A3.1). These two sites are of special interest in light of the long debate in this region about the existence of ice-free (and potentially botanically viable) terrain during glacial maxima. Although such terrain was evidently much more limited than previously thought (cf, Dyke et al., 1982), the fact that we included two such sites in a sample of 12 sites means that it is worthwhile prospecting similar sites along eastern Baffin Island for comparable TCN concentrations.

Episodic erosion is also controlled by the topographic position of the sampled tor within a given plateau (Fig. 4.8b). Stage 2 tors (sites 8-9) are located at or close to local summits (~2 km apart) of broad plateaus (>60 km^2, NW section shown in Fig. 4.8b). The samples collected at these high elevation sites, together with the most weathered surface of the stage 2-3 tor (site 11), have relatively high TCN concentrations but low ratios indicating prolong burial by ice and long total complex histories (Fig. 4.6). A history of

long durations of ice cover is also supported by low f values determined with the cyclic ice cover model (section 4.6.1, Fig. 4.3) and relatively lower glacial-interglacial transition values of $\delta^{18}O$ favoured by the MC method (Table 4.3). This result suggests that ice caps initiated at higher elevations as soon as the regional equilibrium line altitude (ELA) descended below the summits (Margreth et al., 2014). Owing to divergent ice flow at the summit and generally thin ice cover, the ice remained cold-based, which limited the glacial modification of stage 2 tors. Minimal glacial modification is supported by the calculated low episodic erosion rates (0.5 – 1.3 mm ka^{-1}, 1σ error range, 0.5 – 6.5 mm ka^{-1}, range of modes, Fig. 4.8) and the requirement for an earlier last plucking event (0.4 – 1.9 Ma, 1σ error range, >1 Ma, modes, Fig. 4.7). At site 11, the low episodic erosion rate and early last plucking derived for the most weathered surface are attributed to the large size of the sampled tor block (Fig. A3.2a)

Sites with stage 3 & 3-4 tors (5-7, 10-12, Fig.4.1) are located on the rims of broad plateaus (Fig. 4.8b) or on a large bevel on a gentle valley slope. These sites were likely covered later by the descending ice caps in response to further lowering of the regional ELA, which is supported by generally longer ice-free times derived for the cyclic ice cover model and the higher $\delta^{18}O$ glacial-interglacial transition values favoured by the MC calculations (Table 4.3). Changes in ice dynamics (and perhaps a shift from cold-based to temporary warm-based conditions) at the slope break of the plateaus facilitated more frequent plucking, which more efficiently exposed the bedrock plinth at the margin of those tors. More intense glacial modification, inferred from field observation, is corroborated by higher episodic erosion rates (2.9 - 11.9 mm ka^{-1}, 1σ error range, 5.5 – 7.3 mm ka^{-1}, range of modes, Table 4.4), as well as lower TCN concentrations and higher

ratios determined for the samples collected on the tor plinth (Fig. 4.6 & 4.8). Meanwhile, the samples obtained from the weathered bedrock blocks at the centre of the same tor have higher TCN concentrations but lower ratios (Fig. 4.6) and yield smaller episodic erosion rates (2.9 – 7.8 mm ka^{-1}, 1σ error range, 1.0 mm ka^{-1}, modes, Table 4.4) indicating relatively less frequent plucking than on the plinth (Fig. 4.8).

Stage 4 and 5 tors (sites 2 & 3, Fig. 4.1) are located on small low-elevation plateaus along the northeastern coast of Cumberland Peninsula (Fig. 4.8c). Thickening of outlet glaciers in adjacent fiords may have caused longer periods of warm-based ice conditions at these sites, so that most highly weathered bedrock blocks have been eroded, exposing the root of the tors. The enhanced glacial modification observed in the field, and first brought to our attention by Sugden and Watts (1977), is supported by higher episodic erosion rates (2.0 – 10.8 mm ka^{-1}, 1σ error range, 3.3 – 3.5 mm ka^{-1}, range of modes, Table 4.4) similar to the values obtained for the tor plinth on stage 3-4 tors and equally low TCN concentrations and high ratios (Fig. 4.6). A white quartzite cobble observed on site 3 indicates glacial entrainment and transport of this distinctive erratic to the tor.

Increasing glacial modification of tors from the summits to the edges of plateaus has been previously recognised on Cumberland Peninsula (Sugden and Watts, 1977; Watts, 1979), as well as in the Cairngorms in Scotland (Hall and Phillips, 2006). Sugden and Watts (1977) proposed a continuum of alteration of tors from essentially unmodified at summits to increasingly higher modification towards the fiords. However, the MC method results suggest that most tor modification occurred prior to the last glaciation, hence implying that tor modification cannot be used to infer basal ice conditions during LGM. For instance, the broad plateau shown in Figure 4.8b may have been influenced by

the LIS during earlier glaciations (probably inducing temporary warm-based conditions at the edges of the plateau), but during the last glaciation the LIS only reached the valley just north of the plateau (Fig. 4.1, Dyke, 2011b; Dyke, 2013b; Margreth, 2015). More intense glacial modification of tors at the edge of the plateaus may also be caused by higher basal shear stresses related to topographically-influenced steeper slopes of the glacier bed and ice surface. Pedersen et al. (2014) showed theoretically that glacial erosion increases at the edge of a plateau-like landscape due to increased basal shear stress, while low basal shear stresses limit glacial erosion at the centre of the plateau independently of the prevailing basal thermal conditions.

While our results reveal faster rates for episodic erosion for weathered plateaus compared to subaerial erosion, total erosion of summits on Cumberland Peninsula is small compared to glacial deepening of adjacent valleys throughout the Quaternary. The total plateau lowering of 5 – 50 m (based on a combined 2 – 18 mm ka^{-1} of subaerial weathering and episodic erosion (total 1σ error range) during the Quaternary determined with our approach is comparable to values inferred from TCN data of bedrock and till in other polar landscapes (Andre, 2004; Marquette et al., 2004; Briner et al., 2006; Phillips et al., 2006; Staiger et al., 2006). Our total lowering depth is a minimum estimate for the entire Cumberland highland because tors are by nature the slower-eroding remnants of a lowering landscape. However, the tors are only a few metres above the average local ground level suggesting that the overall lowering depth of the plateaus may be only slightly greater. The low subaerial and episodic erosion rates signify the long-term stability of the plateaus, while relatively fast flowing, warm-based ice rapidly deepened the valleys previously carved by Mesozoic and Paleogene fluvial drainage (Briner et al.,

2006; Staiger et al., 2006). The plateaus have therefore been interpreted as the last vestige of a pre-Quaternary landscape (Dyke, 1993; Kleman and Stroeven, 1997; Fabel et al., 2002; Hattestrand and Stroeven, 2002; Stroeven et al., 2002; Briner et al., 2003; Fjellanger et al., 2006) that can be used as 'geomorphic markers' (Anderson, 2002) to infer the total amount of glacial erosion and induced isostatic uplift in response to erosional unloading during the Quaternary (Small and Anderson, 1998; Steer et al., 2012). While our results indicate that the tors have been exhumed during the Quaternary, the dissected plateau landscape may have been inherited from a previous episode of deep weathering (Krabbendam and Bradwell, 2014). Although episodic and subaerial erosion of the plateaus are an order of magnitude lower than glacial erosion in adjoining valleys and fiords, the plateaus may have contributed a significant amount of sediment throughout the Quaternary due to the relatively large area of upland regions. On Cumberland Peninsula, low-relief plateaus constitute approximately 15% of the total surface area (based on discrimination of high-elevation areas from trend surfaces fitted to digital elevation maps of the peninsula combined with discrimination of low slope <12° areas), while glacially deepened valleys comprise 30% of the surface area. By comparing offshore sediment volumes with total amount of glacial erosion, Steer et al. (2012) estimated that high-altitude, low-relief surfaces were lowered by 100 – 150 m during the Pleistocene in western Norway. They suggested that the majority of erosion on the plateaus occurred during the Pliocene and early Quaternary, followed by a shift of glacial erosion to lower elevations deepening the fiords and valleys during the late Pleistocene. Such bimodal distribution of Quaternary glacial erosion has been supported by recent numerical modelling (Herman et al., 2011; Pedersen et al., 2014). However, our MC

results suggest that plucking of tor blocks continued throughout the middle and late Pleistocene (Fig. 4.7)

Estimates of late Quaternary sedimentation rates in Baffin Bay vary between 2 – 10 cm ka^{-1}, from which maximum denudation rates of 1.7 cm ka^{-1} for Canadian Shield areas are deduced (Aksu and Piper, 1987). This denudation rate lies at the higher end of estimates of long-term exhumation of 7 – 20 m Ma^{-1} determined from low-temperature thermochronology for Baffin Island (McGregor et al., 2013; Creason, 2015). The total lowering rate of 2 – 18 mm ka^{-1} (1σ error range of subaerial weathering plus episodic erosion) obtained for the weathered plateaus is comparable to the thermochronologically-derived exhumation rate suggesting that denudation of the summit plateaus remained steady over much of the Cenozoic.

4.9 CONCLUSIONS

With new approaches we have shown that it is possible to constrain the episodic and steady subaerial and subglacial erosion rates of summit plateaus by measuring TCN concentrations on adjacent bedrock surfaces exhibiting different degrees of weathering. The MC-based approach provides estimates of the fraction of ice-free time during a glacial-interglacial cycle, the probable last time of subglacial plucking for a sampled surface, and total thickness loss due to a combination of episodic and steady erosion processes. The resolution of the output can be improved with independent constraints of boundary conditions such as climate over the past few million years, timing of the last deglaciation of the site, and average fracture density of material that has been eroded.

Adding episodic and steady erosion mechanisms, summits on Cumberland Peninsula have been eroding at rates between 2 - 18 mm ka^{-1} over the Quaternary, with the highest rates on sites located at the edges of plateaus (stage 3-4 tors) as well as at the tor tops on low-elevation coastal plateaus (stage 4-5 tors). Constant subglacial erosion (abrasion) is sufficiently slow relative to plucking that it can be excluded for most sampled tors with only the two sites from the low-elevation coastal plateaus recording discernable but low rates of abrasion during short intervals of warm-based ice conditions. Slow subaerial weathering rates of <3 mm ka^{-1} are determined from TCN concentrations measured in bedrock surfaces on non-glaciated high coastal ridge tors and corroborated by the results of the MC method. Timing of last glacial plucking is consistently more recent for fresher appearing surfaces and tors with higher degree of glacial modification.

Our results indicate that long-term denudation of summit plateaus is (i) slow but not negligible, since erosion on the summits notably contribute to the Quaternary sediment flux to the oceans similarly to Norway, (ii) slower than valley incision, but similar to thermochronologically-derived exhumation rates 7 - 20 m Ma^{-1}, and (iii) indicate that cold-based ice cover is capable of eroding the landscape by episodic entrainment of weathered bedrock blocks.

Our constraints on ice-free time over the Quaternary and the timing of last ice plucking provide (i) reconciliation of previous dilemmas in published TCN results for Cumberland Peninsula, which are explained by the notion that a depressed $^{26}Al/^{10}Be$ does not necessarily imply burial during the last glaciation, (ii) refinements of the most recent conceptual model of ice volume and extent throughout the entire peninsula (previous studies were mostly coastal), and (iii) enhancement of our understanding of ice dynamics

in regions where ice sheets, valley glacier systems, and independent ice caps interact. Although the methods have been developed for the specific case of episodic plucking of weathered bedrock blocks by predominately cold-based ice, some elements of our approach are transferable to other episodic processes, for instance, to determine the timing and rates of coastal cliff retreat and rockfall or toppling events.

4.10 ACKNOWLEDGEMENTS

Funding for this research was provided by NRC-GEM project through AD (then at Geological Survey of Canada; project managed by Mary Sanborne-Barrie and Mike Young), NSERC-DG, NSERC-NRS, CFI-Operating Fund, and PCSP support to JCG, and SHELL Self grant to AM. G. Yang at the Dalhousie Geochronology Centre trained AM and prepared many of the BeO and Al_2O_3 targets. D. Rood, S. Zimmerman, and R. Finkel provided the AMS analysis at LLNL-CAMS. A. Hidy and P. Mattern assisted with the development of the Matlab codes.

CHAPTER 5 – CONCLUSIONS AND FUTURE WORK

The new insights into the surficial geology of the entire area of Cumberland Peninsula derived from detailed mapping, new geochronological constraints and an innovative approach to interpret cosmic-ray isotope data presented in this thesis provide the necessary information to constrain numerical landscape evolution models that may help understanding unresolved problems of Arctic glacial geology. These problems concern i) the existence of ice-free enclaves for biota, ii) the interaction and dynamics of different ice masses on a regional scale, iii) the influence of progressive glacial erosion of the landscape on the dynamics of successive glaciations, and iv) the long-term evolution of Arctic glaciated landscapes that selectively preserve fragments of former topography during excavation of a distinctively alpine landscape.

The preceding chapters describe the approaches used and results obtained from addressing the objectives of this thesis stated in *Chapter 1*. Taken together, *Chapters 2 – 4* provide a comprehensive review of the Quaternary geology of Cumberland Peninsula augmenting previous research, which was mainly focused on selected regions along the coast. This thesis examines the dynamics of different glacial styles (ice sheet, alpine glaciers, and ice caps) that influenced the area during different time intervals (Holocene – *Chapter 2*, Wisconsinan – *Chapter 3*, Pleistocene – *Chapter 4*). By considering the entire peninsula, a conceptual model of the glaciation on Cumberland Peninsula could be established based on high-resolution maps of surficial deposits and new geochronological constraints obtained for the interior and higher elevation areas that had little previous age control, owing to the inaccessibility of the mountainous terrain.

5.1 MAJOR CONCLUSIONS OF THESIS AND IMPLICATIONS

The following sections summarize the key findings of *Chapters 2 – 4* and relate them to the long-term objectives introduced in *Chapter 1*. For two chapters, new geochronological approaches were developed or improved. These approaches include 1) radiocarbon dating of delicate, subfossilized mosses that are currently melting out along margins of receding cold-based ice caps, and 2) modelling of complex terrestrial cosmogenic nuclide (TCN) exposure histories to fit measured concentrations of two radioisotopes with differing decay rates collected from differentially weathered bedrock surfaces at the same tor. In addition to the development of new and improved geochronological methods, a combination of surface and subsurface exposure dating and radiocarbon dating was used to establish the chronology of deglaciation since the Last Glacial Maximum (LGM) and infer changes in paleo-equillibrium line altituedes (ELA) on Cumberland Peninsula.

5.1.1 Radiocarbon Dating of Moss

Subfossilized, weakly rooted tundra vegetation, which is currently melting out along quickly retracting cold-based ice margins, presents a unique archive of past climate change. The low probability of preservation of such delicate material on the wind-swept stony polar dessert plateaus suggests that the sampling locations remained ice covered since entombment of the plants. Therefore, we interpret the radiocarbon ages obtained from the organic matter as maximum-limiting ages of the expansion of ice caps from positions that were at least as retracted as they are today. Distinct peaks in the radiocarbon age distribution occur at 1.58 – 1.53 ka (n = 7 samples), 1.41 – 1.34 ka (n = 6), 1.22 – 1.16 ka (n = 5), and during the Little Ice Age at 0.74 – 0.64 ka (n = 4), 0.5 –

0.48 ka (n = 3), and 0.35 – 017 ka (n = 9). The results of *Chapter 2* are important because of the difficulty of obtaining a record of ice advance in areas where few lake records are available (Objective 1).

Because the retreat pattern of ice caps differed from the pattern of ice advance, mosses of different ages are concurrently melting out along withdrawing ice margins. The correlation of peaks (and risers) in the age distribution with the timing of large volcanic eruptions confirms a previous hypothesis (Miller et al., 2012) and reveals the sensitivity of thin, cold-based ice caps to short-term, low-amplitude climate perturbations. Through amplification by positive sea-ice – ocean – atmosphere feedbacks (Miller et al., 2012), these kind of climate forcings can cause extensive ice expansion, particularly on plateaus that lie in the critical elevation range with respect to the modern ELA (above which there is positive snow balance and glacier growth), so that a small lowering of ELA can cause an instantaneous widespread glacierization of the region. Extrapolating these findings to Milankovitch orbital-forcing timescales of 10^4 years, this instantaneous glacierization process could also have initiated the growth of continental ice sheets or a polythermal alpine glacier system, as previously proposed by Ives (1957; 1975).

The new dataset from Cumberland Peninsula extends the correlation between ice cap expansion and short-term atmospheric perturbation caused by large volcanic eruptions during the last 2 ka. Exhumation of subfossilized organic material that was covered by expanding ice caps nearly 5 ka ago and remained ice covered until shortly before sample collection suggests that the current warming is the largest seen or longest sustained since the early to middle Holocene thermal optimum, or potentially, since the

last interglacial (Miller et al., 2013b). The close agreement between the new dataset for Cumberland Peninsula and previous datasets from another region of Baffin Island (Anderson et al., 2008; Miller et al., 2012; Miller et al., 2013b) and eastern Greenland (Lowell et al., 2013) demonstrates the reproducibility of the approach and suggests a common cause for ice cap expansion in the North Atlantic Arctic region. Additional data are required to confirm the established relation between ice advance and short-term climate perturbations for the middle Holocene and to find supplementary links to other climate forcings, as for instance changes in atmospheric or oceanic circulation. Additional data could be obtained in the future from collection of organic material along the same ice caps and from ice caps with a broader range of elevation, which should release older ages along individual flow lines by further ice margin retreat.

Finally, the study provides a significant contribution to others who may attempt this moss-dating approach. Regrowth of bryophytes after millennia of entombment was documented by radiocarbon dating of dissimilarly preserved macrofossils from the same moss type collected at the same location. The younger-looking fragments (with remnants of white awns) yielded consistent younger ages than a flattened fragment of the same moss type, indicating re-growth during a brief, intervening ice-recession phase. The re-grown bryophytes may contaminate the ^{14}C from the dead portions of the moss, as suggested at another location, where younger-looking fragments yielded slightly younger but overlapping (within 1σ) calibrated age ranges than flattened macrofossils. Regrowth of bryophytes may also explain the presence of two samples in our dataset that were shown to be isotopically modern. Therefore, sample sites and individual samples should be carefully screened in the field to minimize the slight potential of re-growth of older

organic material during brief ice-recession phases. Samples should be kept dark, cold, and dry, and processing should be completed as soon as possible to reduce the opportunities for regrowth. Contamination of older organic material with re-grown bryophytes can also be detected during sample preparation by noticing dissimilar preservation of macrofossils. Reliable ages for ice cap expansion can be obtained by careful selection of similarly preserved (flattened or old-looking) macrofossils for radiocarbon dating. The notion of dissimilar preservation of macrofossils also supports the growing number of observations that refute the ice age refugium concept and Nunatak Hypothesis, if mosses are able to regenerate after thousands of years of ice cover. Regeneration of several species of subfossilized bryophytes, collected from a cold-based ice cap on Ellesmere Island, succeeded recently in *in-vitro* growth chamber experiments (La Farge et al., 2013). These experiments, showing that bryophytes can be revitalized following millennia of cryogenic suspension, indicate that subglacial plant refugia may be more significant than refugia on Nunataks to explain disjunct species populations.

5.1.2 Wisconsinan Ice Dynamics

Detailed mapping at a scale of 1:100,000 of most of Cumberland Peninsula (Dyke, 2011a-f; Dyke, 2013a-c) provides the basis for a conceptual model of Wisconsinan glaciation and deglaciation in the region. The peninsula was influenced by three different ice masses: Laurentide Ice Sheet (LIS), expanded Penny Ice Cap (PIC), and polythermal alpine glaciers. During the last glaciation, alpine glaciers thickened to form a major ice divide system over the main mountain ranges, which were beyond the reach of other ice masses. New TCN exposure ages, obtained from boulders and depth profiles in ice marginal deltas, are applied to the morphostratigraphic sequence of moraines and

meltwater channels in a major alpine valley ('central valley') from the oldest moraines near the southwestern coast to the youngest moraines in interior of the peninsula close to modern glacier termini. Additional age constraint was established in a valley, where LIS and local fiord ice concurrently dammed a lake, revealing the timing of separation of the two ice masses. The new chronological control, combined with previous geochronology, allows mapping of ice extent for three different re-advance phases during deglaciation: the end of a composite Heinrich Event (H-1, ~20 - 14.6 ka, Stanford et al., 2011), the end of the Younger Dryas (YD, 12.9 – 11.7 ka, Rasmussen et al., 2006), and Cockburn-equivalent cold intervals (9.5 – 9.2 ka, Rasmussen et al., 2007). Based on these maps, retreat rates for the different glacier types were inferred revealing the sensitive response of smaller ice masses (alpine glaciers) to the Bølling-Allerød warm interval (average rates 12 – 20 m a^{-1} between 14.6 to 12.9 ka, Rasmussen et al., 2006) compared with the initial sluggish retreat of both the land-based LIS and an outlet glacier of the PIC (1 – 2 m a^{-1}). But the LIS withdrew more quickly (~60 m a^{-1}) during the subsequent Preboreal warm period (11.7 – 9.5 ka, Rasmussen et al., 2006; 2007) than the PIC and alpine outlet glaciers (12 – 30 m a^{-1}) suggesting rapid destabilization of the northeastern margin of the LIS. Reconstruction of paleo-ELA for the three different time intervals offers insight into the cause of asymmetric retreat pattern of the alpine glacier system. While paleo-ELA rose approximately 60 m along the southwestern coast between the H-1 and YD cold intervals (equivalent to a temperature increase of 0.3°C using a lapse rate of 4.9 °C km^{-1} (Gardner et al., 2009)), paleo-ELAs decreased along the northeastern coast in the same time interval. Decreasing ELAs might be caused by increasing precipitation perhaps

related to a reduction of sea ice cover in the marine basins east of Cumberland Peninsula (de Vernal et al., 2008).

Surprising was the discovery of the composite age of an ice-marginal raised delta located at the head of a fiord on the southwestern coast of Cumberland Peninsula. A radiocarbon age of 43.2 ± 0.4 ka obtained from *Hiatella arctica* shells seemed to be in disagreement with the morphostratigraphic position of the delta within the established retreat sequence in the 'central valley'. A TCN depth profile obtained from the uppermost 1.6 m of the delta revealed an unconformity between the four shallower samples, which were used to constrain an exposure age of $12.4\ ^{-1.0}/_{+2.8}$ ka, and the deepest sample, which has a higher TCN concentration than the sample above. The lowest sample in the profile was collected just above the shell-bearing zone suggesting that the lower part of the profile, and hence the lower part of the delta, was deposited during a middle Wisconsinan interval of ice recession. Protection of the delta during the following re-advance of an outlet glacier to the mouth of the fiord is documented by TCN exposure ages from boulders on a lateral moraine and the TCN depth profile from the top layer of the delta. Preservation of a large raised marine delta under thin, cold-based ice has previously been reported for the northeastern coast of Baffin Island (Davis et al., 2006). But the case reported here is on a lower inner fiord wall, where preservation is less likely. Nevertheless, it illustrates that during some glacial cycles even fiord glaciers were minimally erosive, at least locally. The notion of buried soils in two ~1 m deep profiles dug into a marine delta near the mouth of Kingnait Fiord (Birkeland, 1978) indicates that this prominent glaciomarine deposit may also have been formed in multiple

phases suggesting that the late Wisconsinan age assigned by TCN dating of boulders on its surface (Marsella et al., 2000) may only date the last stage of delta formation.

The high percentage of large boulders, deposited on moraines or near meltwater channels, that contain significant inherited TCN concentrations signifies the long subaerial exposure or limited erosion due to predominately cold-based cover in the source area of the boulders. To circumvent the problem of inheritance, cosmogenic ^{14}C produced in the surface of rocks could be measured (Jull et al., 1994; Lifton et al., 2001; Naysmith et al., 2004). Owing to the short half life of 5,730 years (Godwin, 1962), any inherited inventory of *in-situ* ^{14}C accumulated during previous exposure intervals quickly decays under ice cover. An ultra-high vacuum system for extraction of *in-situ* ^{14}C is currently being built at the Dalhousie Geochronology Centre (DGC). For many samples analysed for ^{10}Be, enough purified quartz is available for additional measurement of the *in-situ* ^{14}C concentration. Additionally, samples of boulders collected from moraines documenting the further retreat of the LIS and the subsequent separation from the western margin of the PIC are available for *in-situ* ^{14}C analysis. Analysing the *in-situ* ^{14}C content of these samples would further constrain the late glacial and early Holocene retreat rates of the LIS enabling more detailed comparison of the dynamics of the different ice masses on Cumberland Peninsula and inferring their sensitivity to climate variation.

5.1.3 Quaternary Complex Exposure Histories

Rates of episodic erosion have been difficult to estimate, owing to the numerous parameters that control the cosmic-ray exposure histories of surfaces affected by episodic erosion events. The new approach presented in *Chapter 4* uses the concentration of two

radionuclides with differing decay rates (^{10}Be, $t_{1/2}$ = 1.38 Ma and ^{26}Al, $t_{1/2}$ = 0.72 Ma) measured in adjacent plucked and non-plucked surfaces of tors in order to reduce the degrees of freedom of the multiple parameter system. The timing of last plucking is derived from three different depth functions (concentrations of both ^{10}Be and ^{26}Al, and their relative abundances ^{26}Al/^{10}Be) that are calculated based on a simple, periodic ice cover history. To estimate the rate of episodic erosion, a Monte Carlo (MC) method had to be developed that computes complex cosmic exposure histories involving multiple plucking events. Constrained by a proxy-record of global glacier volume (Lisiecki and Raymo, 2005), the MC method provides probability density functions of (i) the total duration of complex histories (exposure + burial), (ii) gradual subaerial erosion rates, (iii) rates of episodic plucking of weathered bedrock blocks, and (iv) the timing of last glacial plucking.

Estimates of the total duration of complex histories give minimum-limiting ages for the formation of tors, thus signifying the antiquity of the landscape that has been modified during Pleistocene glaciations (Marquette et al., 2004; Gosse et al., 2006; Krabbendam and Bradwell, 2014). Among the twelve sampled tors, two sites located on narrow, high-elevation, coastal ridges are shown to have never been glaciated. The TCN concentrations measured on these sites indicate that bedrock is eroding at low constant rates (0.8 – 1.6 mm ka^{-1}), which is corroborated by low values (<3 mm ka^{-1}) for subaerial erosion rates derived by the MC method. For the remaining tor sites, predominately cold-based ice cover is inferred based on the relatively high TCN concentrations and concurrent low ^{26}Al/^{10}Be that restrict subglacial abrasion to much lower rates than estimated for sugblacial erosion by episodic plucking. Episodic erosion rates and the

timing of last glacial plucking correlate well with the classification of tors according to the degree of glacial modification established from field observations (Hall and Phillips, 2006). Furthermore, the variation of episodic erosion rate between different tor sites and different surfaces at the same tor can be related to the topographic position of the tors and local differences in bedrock joint spacing. Tors located at the summits of broad interior plateaus require the longest complex histories (1.5 – 2.4 Ma), yield the lowest episodic erosion rates (0.5 – 1.3 mm ka^{-1}, range of modes), and have last been plucked more than 1 Ma ago (range of modes). Tors located at the edge of the same plateaus have last been plucked more recently (300 – 500 ka, range of modes), yield higher episodic erosion rates (1.0 – 3.8 mm ka^{-1}, range of modes) and require shorter complex histories (~1 Ma) indicating larger modification during Pleistocene glaciations. The highest episodic erosion rates (3.5 – 7.3 mm ka^{-1}, range of modes), most recent last plucking (200 – 250 ka, range of modes), and shortest complex histories (<1 Ma) are inferred for bedrock surfaces at the margin of tors located at the edge of broad plateaus as well as for tors located on low-elevation coastal plateaus. High episodic erosion rates determined for tors on low-elevation coastal plateaus corroborate the notion of strongest glacial modification signifying the possibility for short-term, warm-based thermal conditions at these locations. Tors with relatively small block thicknesses yield higher episodic erosion rates and more recent last plucking supporting previous notions that narrower joint spacing facilitates plucking (Dühnforth et al., 2010; Anderson, 2014). The timing of last glacial plucking provides maximum-limiting constraints for the timing of last ice cover, but the new approach presented in *Chapter 4* suggests that the sampled plateaus, with the exception of the two narrow, coastal ridges, were covered by cold-based ice

during the LGM. This result is important, because of the long-lasting debate on Cumberland Peninsula about the vertical extent of ice cover during the late Wisconsinan and the existence of biological refugia.

The estimated episodic erosion rates are generally larger than the inferred rates of gradual subaerial erosion indicating that episodic erosion rates are significant for the long-term evolution of dissected high-latitude landscapes. Since tors are the slowest eroding parts of the landscape, total erosion of upland plateaus amounts to at least 5 – 25 m over the Quaternary. While the estimated total erosion rate of 2 – 8 mm ka^{-1} is an order of magnitude lower than rates for adjacent, glacially carved valleys (Davis et al., 1999; Staiger et al., 2005) and glacial cirques (Anderson, 1978), the erosion of upland plateaus may significantly contribute to the sediment flux to the oceans, owing to the relatively large surface area.

The estimate for the timing of last glacial plucking can be considerably improved, if the thickness of the plucked bedrock block can be inferred from field observations. Therefore, fracture spacing should be measured while sampling differentially weathered surfaces at the same tor. Ideally, the relationship between both surfaces (i.e., the number and thicknesses of blocks that once covered the fresher surface) should be known. Ice coverage at the LGM can be confirmed or rejected by measuring *in-situ* ^{14}C concentrations in the leftover purified quartz from the sampled bedrock surfaces. If the tors were covered by ice during the LGM, then the *in-situ* ^{14}C concentrations would reveal the precise timing of deglaciation. On the other hand, if the tors were ice-free at the LGM, then the *in-situ* ^{14}C concentrations should be saturated providing accurate estimates for rapid, gradual subaerial erosion rates. The new approach presented in

Chapter 4 has been specifically developed for estimation of episodic glacial plucking of tor on weathered upland plateaus, but parts of the approach could be adapted to assess other geomorphic processes, as for instance lateral retreat of plateau escarpments, sporadic rockfall from glaciated valley slopes, and toppling in medium to coarsely fractured rock.

5.2 FUTURE WORK

While implications for future work are stated at the end of each of the previous section, more general prospective research directions are now considered. First, the improved understanding of the dynamics and interaction of different glacier types presented in this thesis (*Chapters 2 - 4*) and other research accomplished over the last decade (e.g., Briner et al., 2006; Davis et al., 2006; Staiger et al., 2006; Kessler et al., 2008; Briner et al., 2009) provide additional constraints for numerical ice sheet models of the evolution of ice cover on Cumberland Peninsula and on Baffin Island. Second, since the episodic erosion rates estimated in *Chapter 4* do not account for stripping of regolith (layer of unconsolidated, residual material above solid bedrock) at the beginning of the Pleistocene glaciations, the Regolith Hypothesis (Clark and Pollard, 1998; Clark et al., 2006) is discussed followed by the presentation of possible approaches to constrain the timing of regolith stripping on Cumberland Peninsula. Third, the long-term evolution of the alpine landscape of Cumberland Peninsula is considered with future work attempting to discern fragments of the previous topography by semi-automatic classification of the landscape from digital elevation models (DEM, Drăguţ and Eisank, 2012; Jarnà, 2014).

5.2.1 Numerical Ice Sheet Models

Previously published constraints for the late Wisconsinan ice dynamics on Baffin Island (e.g., Briner et al., 2006; Davis et al., 2006; Staiger et al., 2006; Kessler et al., 2008; Briner et al., 2009) and *Chapter 3* of this thesis have focused on the LGM deglacial record. However, the inception of ice sheets and subsequent expansion and coalescence of different ice masses are not well understood. Geologically-constrained numerical models have been used to investigate the evolution and dynamics of ice sheets on a continental scale (Peltier and Fairbanks, 2006; Tarasov et al., 2012), but the relatively coarse resolution of these models makes it difficult to investigate glacial dynamics of smaller areas, such as Cumberland Peninsula (~42,000 km^2). Although promising results have been obtained for modelling of specific regions to address particular problems (Kaplan et al., 1999; Staiger et al., 2005; 2006), the evolution of ice cover on Cumberland Peninsula during the last glaciation has not been studied with a numerical model. New sophisticated ice sheet models with dynamical nesting of high resolution areas are now able to model polythermal ice cover in selected regions within the framework of a larger scale simulation of a sector of a continental ice sheet (e.g., Roberts et al., 2009; Simpson et al., 2009; Stokes et al., 2012; Tarasov et al., 2012; Lecavalier et al., 2014). The boundary conditions of these models are constrained by glacial geological data for relative sea level or deglaciation. In the case of Cumberland Peninsula, this thesis now provides not only the deglacial record for three different ice masses (*Chapter 3*), but also a proxy for ice cap expansion in response to atmospheric cooling (*Chapter 2*) and estimates of long-term episodic erosion rates on upland plateaus (*Chapter 4*) offering further constraints for the sensitivity and dynamics of cold-based parts of glacier systems.

Furthermore, new TCN data from detrital quartz in till could confirm the distribution of basal thermal regime and intensity of glacial erosion (e.g., Staiger et al., 2006) and the development of a polythermal alpine glacier system on Cumberland Peninsula.

Other objectives that could be addressed with numerical ice sheet models include the Nunatak Hypothesis (Ives, 1957; 1974) and the flow of the LIS across Baffin Island. The distribution and extent of ice-free areas (Nunataks) could be assessed with a numerical ice sheet model, which would help resolving interdisciplinary questions such as what areas were available for biological refugia during the LGM. The results of *Chapter 4* indicate that Nunataks on Baffin Island may were probably much more restricted than previously hypothesized (Ives, 1957; 1974). However, the documentation of dissimilarly preserved bryophyte macrofossils presented in *Chapter 2* provides an alternate explanation for the occurrence of disjunct species in the Arctic. Revitalization of bryophytes after millennia of cryogenic suspension (La Farge et al., 2013) suggests that cold-based ice caps offered refugium for flora during glaciations thus not requiring ice-free areas with favourable environmental conditions for plant growth. The occurrence of ice-free areas along the coast of Cumberland Peninsula (*Chapter 4*) might also be attributed to the particular location of the area with respect to the flow of LIS from Foxe Basin. Considering the major conduits of LIS across Baffin Island (Fig. 5.1), it is intriguing that the LIS was capable of covering the high-elevation topography northwest of Home Bay and Clyde Fiord, but it failed to invade Cumberland Peninsula. Reasons for this flow pattern might be the expansion of the local PIC obstructing the LIS flow in the region and the proximity of a topographic trough (Cumberland Sound) that funneled the majority of LIS flow past the peninsula. The dynamics of LIS and relative

importance of ice conduits on Baffin Island could be addressed by numerical ice sheet models that are constrained by previously published data for relative sea level and deglaciation patterns augmented with the new chronological constraint presented in this thesis. The model could be tuned with available data on ice streams occupying Hudson Strait (Andrews and MacLean, 2003; Andrews et al., 2012) and other ice streams on Baffin Island (De Angelis and Kleman, 2007; Margold et al., 2014).

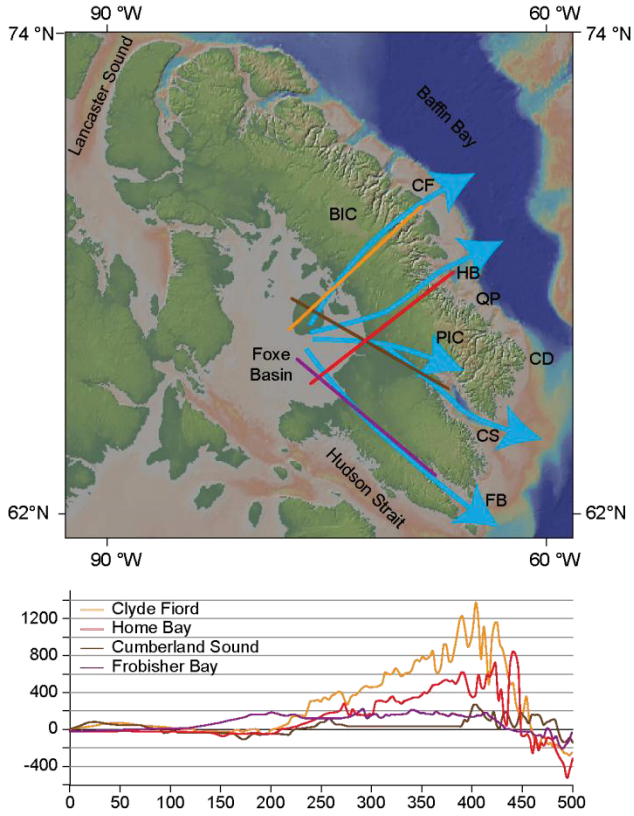

Fig. 5.1 **Top:** Digital elevation model of Baffin Island indicating the major flow directions of LIS from the Foxe Dome and the locations of topographic profiles displayed below. BIC: Barnes Ice Cap, PIC: Penny Ice Cap, CF: Clyde Fiord, HB: Home Bay, QP: Quivitu Peninsula, CD: Cape Dyer, CS: Cumberland Sound, FB: Frobisher Bay. **Bottom:** Topographic profiles along the flow directions of LIS across Baffin Island from Foxe Basin (left) to Baffin Bay or Davis Strait (right). Map and Profiles have been retreived from GeoMapApp.

5.2.2 The Regolith Hypothesis

A thick mantle of regolith (loose residual autochthonous material weathered from local bedrock) presumably covered most areas of the Baffin Island landscape after the warm weathering conditions of the mid Pliocene warm period (Marquette et al., 2004; Staiger et al., 2006; Hidy et al., 2013; Rybczynski et al., 2013). The Regolith Hypothesis postulates that the thick regolith mantle was stripped during successive warm-based glaciations in the early Pleistocene, thus gradually exhuming the fresher bedrock. Higher basal shear stresses over the exhumed bedrock (compared to lower basal shear stresses over a clay-rich regolith with smoother surface) are invoked to explain the transition from 41-ka to 100-ka long glacial cycles during the middle Pleistocene transition in absence of apparent changes in the Earth's orbital parameters (Clark and Pollard, 1998; Clark et al., 2006) Although the stripping of regolith at the beginning of the Pleistocene glaciations would not significantly affect the results presented in *Chapter 4,* constraining the timing of regolith stripping would provide additional information about the preservation of ancient landscapes and their subsequent glacial modification (Sugden and Watts, 1977; Dyke, 1993; Stroeven et al., 2002; Marquette et al., 2004; Staiger et al., 2005; Gosse et al., 2006; Krabbendam and Bradwell, 2014), the formation of tors (e.g., Goodfellow et al., 2014), and changes in the dynamics of ice cover in the eastern Canadian Arctic (e.g., Clark and Pollard, 1998; Refsnider and Miller, 2010). Minimal erosion by cold-based ice cover on weathered summit plateaus has been confirmed by measurements of TCN concentrations in bedrock surfaces (Stroeven et al., 2002; Gosse et al., 2006).

Preservation of relict pre-Quaternary landscapes, despite Pleistocene modification by glacial and periglacial processes, has been recognized in many polar glaciated areas

(Andrews et al., 1972; Sugden and Watts, 1977; Dyke, 1993; Marquette et al., 2004; Gosse et al., 2006; Staiger et al., 2006; Krabbendam and Bradwell, 2014). The most direct evidence for preservation of ancient landscapes was presented by Andrews et al. (1972) from Paleogene palynomorphs found in a thin limestone cover of Precambrain bedrock on northern Baffin Island. Sugden and Watts (1977) and Dyke (1993) described subtle modification of the landscapes of Arctic Islands by cold-based ice cover. Marquette et al. (2004) and Staiger et al. (2005) revealed the persistence of ancient material under cold-based ice by measuring the concentration of weathering products and TCN in soils and till covering upland plateaus. Based on detailed investigation of the geomorphology and bedrock structure, Krabbendam and Bradwell (2014) concluded that the typical 'cnoc-and-lochan' (knoll and lake) landscape of northwestern Scottland actually represents the etch-surface (weathering front) from a former period of intense weathering that had been modified by glacial erosion.

Related to the preservation of relict landscapes is the discussion of the formation process of tors (Linton, 1955; Palmer and Neilson, 1962; Dahl, 1966; Ives, 1966). The two-stage formation model postulates that tors were formed under a thick mantel of regolith during a period of warmer and more humid climate and subsequently exhumed by stripping of the regolith early in the Quaternary (Linton, 1955). Conversely, the one-stage model invokes progressive emergence of tors from a thin regolith cover throughout the Quaternary (Palmer and Neilson, 1962) implying that tors are much younger than proposed for the two-stage model.

Major changes in the dynamics of ice sheets during the middle Pleistocene transition have been inferred from the spatial distribution of chemically altered

weathering products in tills on northeastern Baffin Island. Refsnider and Miller (2010) related the preservation of tills that contained high amounts of weathering products on upland plateaus to the gradual exhumation of bedrock by stripping of regolith in adjacent valleys. The stripping of regolith in valleys caused a persistent alteration of the flow of ice leading to the dynamic decoupling of thin, ice cover on plateaus from fast-flowing ice in troughs. Additional evidence for stripping of regolith has been inferred from the chemical variation of sediments in Baffin Bay that were related to changes in the source area of the glacially transported material on the adjacent mainland (Thiébault et al., 1989; Andrews, 1993).

Different techniques have been used to constrain the timing of regolith stripping and assess the origin of weathered plateaus: chemical fingerprinting of weathering products in tills and remnants of saprolite (Marquette et al., 2004; Roy et al., 2004; Refsnider and Miller, 2010; Ebert et al., 2012), measurement of in-situ ^{10}Be and ^{26}Al concentrations in tills (Staiger et al., 2006), and analysis of meteoric ^{10}Be in till, saprolite, or glacigenic deposits on coastal lowlands (Ebert et al., 2012; Refsnider and Miller, 2013). The chemical analyses of till and bedrock samples from Cumberland Peninsula (Gammon et al., 2011; Whalen et al., 2012) provide the data required to calculate indices of chemical alteration (Nesbitt and Young, 1982; Brimhall and Dietrich, 1987; Chadwick et al., 1990; Riebe et al., 2001; Riebe et al., 2003), which may reveal spatial variations in the incorporation of weathered material in tills. Unprocessed till samples could be used for additional determinations of *in-situ* ^{10}Be and ^{26}Al concentrations and meteoric ^{10}Be content, that could be compared with similar analyses of marine and glacial sequences of the Quivitu Peninsula (Fig. 5.1, located slightly further north of the study area of this

thesis, Nelson, 1980; 1981; 1982). These analyses could reveal the antiquity of tills and the source of the glacial sequences deposited on the Quivitu Peninsula, which could potentially disclose the timing of regolith stripping on Cumberland Peninsula. Likewise *in-situ* produced ^{10}Be, the meteoric ^{10}Be content of till or saprolite is a measure of the antiquity of the deposits. Meteoric ^{10}Be is produced in the atmosphere through interaction of secondary cosmic radiation with oxygen isotopes, transferred to the ground by precipitation, and retained in soil or till through tight attachment to clay- and silt-sized particles (Willenbring and von Blanckenburg, 2010b). The meteoric ^{10}Be content of deposits thus indicates the duration of ^{10}Be deposition from the atmosphere, which is retained when the material is re-deposited by, for instance, glacial transport. Therefore, early glacigenic deposits on coastal lowlands have higher meteoric ^{10}Be content disclosing their origin from weathered regolith. Subsequent glacier advances increasingly exhumed unweathered bedrock, so that the meteoric ^{10}Be signal from weathered regolith is diluted by fresh material with low (or no) ^{10}Be content.

5.2.3 Long-Term Landscape Evolution

The distinct position of Cumberland Peninsula with respect to the northeastern margin of the LIS led to the formation of an exceptional alpine landscape carved by local cirque glaciers. Some of the cirques are presently glaciated while many are currently ice-free (Andrews and Dugdale, 1971). At the outer coast of Cumberland Sound, submerged cirques indicate that they were formed during several periods of lower relative sea level (Fig. 5.2a). To better understand the formation of these coastal cirques as well as cirques at higher elevations in the interior of the peninsula, the long-term evolution of the alpine landscape has to be examined. For the analysis of long-term landscape evolution, the

former topography of Cumberland Peninsula has to be reconstructed. As indicated in *Chapter 4*, many upland plateaus have only been slightly modified during the Quaternary (maximum lowering by 25 m) preserving fragments of the pre-Quaternary landscape. These plateaus have been mapped as 'Residuum' of pre-Wisconsinan landscape (Wv map unit, Fig. 5.2c) and the now available maps (Dyke, 2011a, f, e, d, b, c; Dyke, 2013b, a, c) indicate that such areas occur throughout the peninsula. Interestingly, some of the best preserved plateaus coincide with the area of submerged cirques along the outer coast of Cumberland Sound (Fig. 5.2).

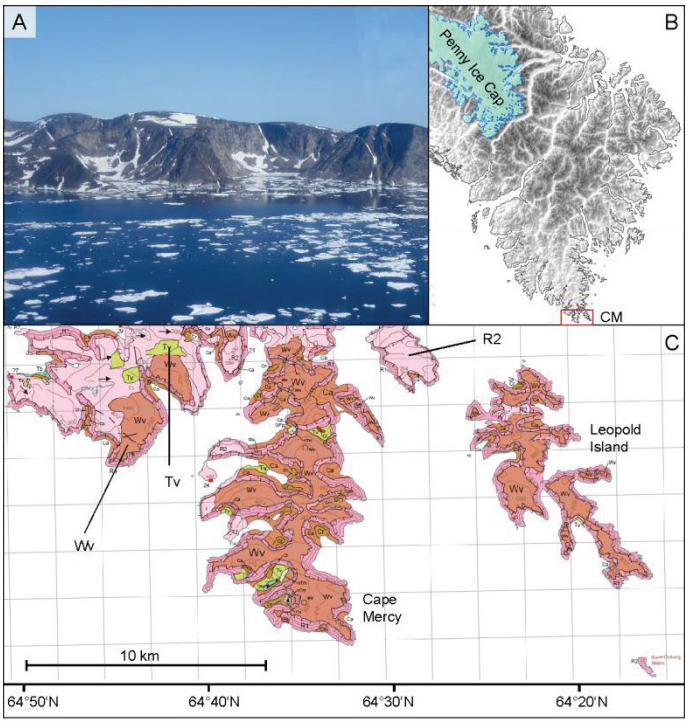

Fig. 5.2 Submerged cirques and weathered upland plateaus mapped as 'Residuum' of a pre-Wisconsinan landscape. **A.** Cirques on Leopold Island with the floors lying below sea level (pictures taken to the east showing cirques on the western coast of Leopold Island). **B.** Location of the snapshot of surficial map shown in C at Cape Mercy (CM) is marked by the red box. **C.** Surficial map of Cape Mercy and Leopold Island (Dyke, 2011a), where weathered upland plateaus (map units Wv) occur concurrently with submerged cirques that were formed during intervals of lower relative sea level. Tv: Till veneer (0.5 – 2 m thick till cover), R2: Glacially scoured rock.

Semi-automatic classification of paleic surfaces (low-relief surfaces at high-elevation that escaped glacial scouring) in Norway from DEMs shows the potential for discerning fragments of former landscapes (Jarnà, 2014). This classification is based on parameters derived from the DEM, such as slope, roughness (the standard deviation of slope), and elevation. Testing of a similar program that classifies landscapes from DEMs (Drăguţ and Eisank, 2012) yielded encouraging results for coastal areas of Cumberland Peninsula (Fig. 5.3). For instance, areas mapped as 'Residuum' (Wv unit, Fig.5.2c) are generally classified at rough low hills with the exception of the plateaus described in *Chapter 4* that are classified as smooth low hills. Besides these plateaus, glacially-scoured area, in places covered by a patches of till veneer (0.5 – 2 m), are as well classified as smooth low hills suggesting that the program can distinguish between less intensively glacially modified areas (i.e., Wv units along the coast) and more strongly glacially modified plateaus (i.e., broad interior plateaus also mapped as Wv units, *Chapter 4*). Glacial valleys with thick till cover (till blanket 2 – 10 m thick, Dyke, 2011a) and extensive areas with continuous till veneer cover are classified as irregular plains. Of course, some locations are classified inconsistently; in particular in areas with small-scale spatial changes in geomorphology. Further alteration of the program for the specific characteristics of the landscape on Cumberland Peninsula is required to refine the results of this approach. For instance, the method could potentially distinguish between different generations of preserved landscape fragments (peneplains) that could provide insights into the long-term evolution of the alpine landscape on Cumberland Peninsula.

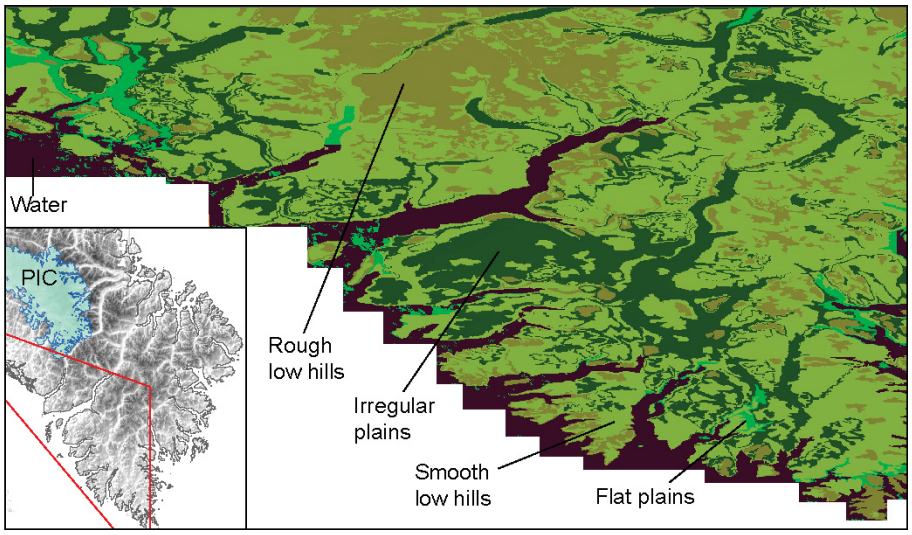

Fig. 5.3 Semi-automatic landscape classification of the southwestern coast of Cumberland Peninsula (area approximately indicated by red polygon in inset map). The area blanked by the white area yielded unreasonable results by the classification algorithm, but the classification of rough low hills, smooth low hills, irregular plains, and flat plains show promising results, which can be refined by further tuning of the program.

The presented future research directions evolve from the work presented in this thesis. Field evidence for the spatial distribution of ice dynamics and basal thermal conditions can be better understood from modelling of glacial processes with sophisticated numerical ice sheet models. The distribution of areas predominately influenced by cold-based ice offer important targets for analyses of geochemical composition as well as *in-situ* and meteoric ^{10}Be concentrations that could reveal the timing of the stripping of an old weathering mantle. Finally, the classification of landscapes from DEMs may help unraveling the long-term evolution of the alpine landscape of Cumberland Peninsula, and by inference many areas of the eastern Canadian Arctic.

REFERENCES

Abbott, R., Smith, L., Milne, R., Crawford, R., Wolff, K., Balfour, J., 2000. Molecular analysis of plant migration and refugia in the Arctic. Science 289, 1343-1346.

Aitken, A.E., Gilbert, R., 1989. Holocene nearshore environments and sea-level history in Pangnirtung Fiord, Baffin Island, N.W.T., Canada. Arctic and Alpine Research 21, 34-44.

Aksu, A.E., Piper, D.J.W., 1987. Late Quaternary sedimentation in Baffin Bay. Canadian Journal of Earth Sciences 24, 1833-1846.

Alley, R.B., 2000. The Younger Dryas cold interval as viewed from central Greenland. Quaternary Science Reviews 19, 213-226.

Andersen, K.K., Svensson, A., Johnsen, S.J., Rasmussen, S.O., Bigler, M., Röthlisberger, R., Ruth, U., Siggaard-Andersen, M.L., Peder Steffensen, J., Dahl-Jensen, D., 2006. The Greenland ice core chronology 2005, 15-42 ka. Part 1: constructing the time scale. Quaternary Science Reviews 25, 3246-3257.

Anderson, L.W., 1978. Cirque glacier erosion rates and characteristics of Neoglacial tills, Pangnirtung Fiord area, Baffin Island, N.W.T., Canada. Arctic and Alpine Research 10, 749-760.

Anderson, R.K., Miller, G.H., Briner, J.P., Lifton, N.A., DeVogel, S.B., 2008. A millennial perspective on Arctic warming from ^{14}C in quartz and plants emerging from beneath ice caps. Geophysical Research Letters 35, L01502.

Anderson, R.S., Repka, J.L., Dick, G.S., 1996. Explicit treatment of inheritance in dating depositional surfaces using in situ ^{10}Be and ^{26}Al. Geology 24, 47-51.

Anderson, R.S., 2002. Modeling the tor-dotted crests, bedrock edges, and parabolic profiles of high alpine surfaces of the Wind River Range, Wyoming. Geomorphology 46, 35-58.

Anderson, R.S., 2014. Evolution of lumpy glacial landscapes. Geology, 42, 679-682.

Andre, M.F., 2004. The geomorphic impact of glaciers as indicated by tors in North Sweden (Aurivaara, 68 N). Geomorphology 57, 403-421.

Andrews, J., Miller, G., 1972. Quarternary history of northern Cumberland Peninsula, Baffin Island, NWT, Canada: Part IV: Maps of the present glaciation limits and lowest equilibrium line altitude for North and South Baffin Island. Arctic and Alpine Research 4, 45-59.

Andrews, J., Davis, P., Wright, C., 1976a. Little Ice Age permanent snowcover in the eastern Canadian Arctic: Extent mapped from Landsat-1 satellite imagery. Geografiska Annaler 58, 71-81.

Andrews, J., Ives, J., 1978. " Cockburn" Nomenclature and the Late Quaternary History of the Eastern Canadian Arctic. Arctic and Alpine Research 10, 617-633.

Andrews, J.T., Dugdale, R.E., 1971. Quaternary history of northern Cumberland Peninsula, Baffin Island, N.W.T.: Part V: Factors afflecting corrie glacierization in Okoa Bay. Quaternary Research 1, 532-551.

Andrews, J.T., Ives, J.D., Guennel, G.K., Wray, J.L., 1972. An early tertiary outcrop in north-central Baffin Island, Northwest Territories, Canada: environment and significance. Canadian Journal of Earth Sciences 9, 233-238.

Andrews, J.T., Feyling-Hanssen, R.W., Miller, G.H., Schluchter, C., Stuiver, M., Szabo, B.J., 1976b. Alternative models of early and middle-Wisconsin events, Broughton Island, Northwest Territories, Canada; toward a Quaternary chronology; Quaternary glaciations in the Northern Hemisphere. International Geological Correlation Programme, Project 73/1/24, Report, 28.

Andrews, J.T., Miller, G.H., 1979. Glacial erosion and ice sheet divides, northeastern Laurentide Ice Sheet, on the basis of the distribution of limestone erratics. Geology 7, 592-596.

Andrews, J.T., 1993. Changes in the silt- and clay-size mineralogy of sediments at Ocean Drilling Program site 645B, Baffin Bay. Canadian Journal of Earth Sciences 30, 2448-2452.

Andrews, J.T., Osterman, L.E., Jennings, A.E., Syvitski, J.P.M., Miller, G.H., Weiner, N., 1996. Abrupt changes in marine conditions, Sunneshine Fiord, eastern Baffin Island, NWT during the last deglacial transition: Younger Dryas and H-0 events. Geological Society, London, Special Publications 111, 11-27.

Andrews, J.T., MacLean, B., 2003. Hudson Strait ice streams: a review of stratigraphy, chronology and links with North Atlantic Heinrich events. Boreas 32, 4-17.

Andrews, J.T., Barber, D.C., Jennings, A.E., Eberl, D.D., Maclean, B., Kirby, M.E., Stoner, J.S., 2012. Varying sediment sources (Hudson Strait, Cumberland Sound, Baffin Bay) to the NW Labrador Sea slope between and during Heinrich events 0 to 4. Journal of Quaternary Science 27, 475-484.

Anisimov, O., 2007. Potential feedback of thawing permafrost to the global climate system through methane emission. Environmental Research Letters 2, 045016.

Antinao Rojas, J.L., 2009. Quaternary landscape evolution of the southern Central Andes of Chile quantified using landslide inventories, beryllium-10 and chloride-36 cosmogenic isotopes and uranium-thorium/helium thermochronology. Earth Sciences, PhD Thesis. Dalhousie University, Halifax, p. 253.

Applegate, P.J., Urban, N.M., Laabs, B.J.C., Keller, K., Alley, R.B., 2010. Modeling the statistical distributions of cosmogenic exposure dates from moraines. Geoscientific Model Development 3, 293-307.

Applegate, P.J., Urban, N.M., Keller, K., Lowell, T.V., Laabs, B.J.C., Kelly, M.A., Alley, R.B., 2012. Improved moraine age interpretations through explicit matching of geomorphic process models to cosmogenic nuclide measurements from single landforms. Quaternary Research 77, 293-304.

Armit, I., Swindles, G.T., Becker, K., 2013. From dates to demography in later prehistoric Ireland? Experimental approaches to the meta-analysis of large ^{14}C data-sets. Journal of Archaeological Science 40, 433-438.

Axford, Y., Briner, J.P., Miller, G.H., Francis, D.R., 2009. Paleoecological evidence for abrupt cold reversals during peak Holocene warmth on Baffin Island, Arctic Canada. Quaternary Research 71, 142-149.

Balco, G., Stone, J.O., Lifton, N.A., Dunai, T.J., 2008. A complete and easily accessible means of calculating surface exposure ages or erosion rates from ^{10}Be and ^{26}Al measurements. Quaternary Geochronology 3, 174-195.

Balco, G., Rovey, C.W., 2010. Absolute chronology for major Pleistocene advances of the Laurentide Ice Sheet. Geology 38, 795-798.

Bamforth, D.B., Grund, B., 2012. Radiocarbon calibration curves, summed probability distributions, and early Paleoindian population trends in North America. Journal of Archaeological Science 39, 1768-1774.

Belland, R., Brassard, G., 1988. The bryophytes of Gros Morne National Park, Newfoundland, Canada: ecology and phytogeography. Lindbergia 14, 97-118.

Belmont, P., Pazzaglia, F.J., Gosse, J.C., 2007. Cosmogenic ^{10}Be as a tracer for hillslope and channel sediment dynamics in the Clearwater River, western Washington State. Earth and Planetary Science Letters 264, 123-135.

Berdahl, M., Robock, A., 2013. Baffin Island snow extent sensitivity: Insights from a regional climate model. Journal of Geophysical Research 118, 1-14.

Berkes, F., Jolly, D., 2002. Adapting to climate change: social-ecological resilience in a Canadian western Arctic community. Conservation ecology 5, 18.

Bierman, P., Marsella, K., Patterson, C., Davis, P., Caffee, M., 1999. Mid-Pleistocene cosmogenic minimum-age limits for pre-Wisconsinan glacial surfaces in southwestern Minnesota and southern Baffin Island: a multiple nuclide approach. Geomorphology 27, 25-39.

Bierman, P., Marsella, K., Davis, P., Caffee, M., 2001. Reply to comment on" Mid-Pleistocene cosmogenic minimum-age limits for pre-Wisconsinan glacial surfaces in southwestern Minnesota and southern Baffin Island: a multiple nuclide approach. Geomorphology 39, 255-261.

Birkeland, P.W., 1978. Soil development as an indication of relative age of Quaternary deposits, Baffin Island, N.W.T., Canada. Arctic and Alpine Research 10, 733-747.

Borcher, B., Marrero, S.M., Balco, G., Caffee, M., Goehring, B., Gosse, J., Kurz, M.D., Lifton, N., Nishiizumi, K., Phillips, F., Schaefer, J., Stone, J.O.H., in press. Geological calibration of spallation production rates for terrestrial cosmogenic nuclides in the CRONUS-Earth Project. Quaternary Geochronology CRONUS-Earth Special Issue.

Boyer, S., Pheasant, T., DR, 1974. Delimitation of weathering zones in the fiord area of eastern Baffin Island, Canada. Geological Society of America Bulletin 85, 805-810.

Bradley, R., 2000. 1000 years of climate change. Science 288, 1353-1355.

Bradley, R.S., Jonest, P.D., 1993. 'Little Ice Age' summer temperature variations: Their nature and relevance to recent global warming trends. The Holocene 3, 367-376.

Bradley, R.S., Hughes, M.K., Diaz, H.F., 2003. Climate in Medieval time. Science 302, 404-405.

Braucher, R., Brown, E.T., Bourlès, D.L., Colin, F., 2003. In situ produced ^{10}Be measurements at great depths: implications for production rates by fast muons. Earth and Planetary Science Letters 211, 251-258.

Braucher, R., Del Castillo, P., Siame, L., Hidy, A.J., Bourlés, D.L., 2009. Determination of both exposure time and denudation rate from an in situ-produced ^{10}Be depth profile: A mathematical proof of uniqueness. Model sensitivity and applications to natural cases. Quaternary Geochronology 4, 56-67.

Braucher, R., Merchel, S., Borgomano, J., Bourlès, D.L., 2011. Production of cosmogenic radionuclides at great depth: A multi element approach. Earth and Planetary Science Letters 309, 1-9.

Brigham, J., 1983. Stratigraphy, amino acid geochronology, and correlation of Quaternary sea-level and glacial events, Broughton Island, Arctic Canada. Canadian Journal of Earth Sciences 20, 577-598.

Brimhall, G.H., Dietrich, W.E., 1987. Constitutive mass balance relations between chemical composition, volume, density, porosity, and strain in metasomatic hydrochemical systems: Results on weathering and pedogenesis. Geochimica et Cosmochimica Acta 51, 567-587.

Briner, J., Miller, G., Davis, P., Bierman, P., Caffee, M., 2003. Last Glacial Maximum ice sheet dynamics in Arctic Canada inferred from young erratics perched on ancient tors. Quaternary Science Reviews 22, 437-444.

Briner, J.P., Swanson, T.W., 1998. Using inherited cosmogenic ^{36}Cl to constrain glacial erosion rates of the Cordilleran ice sheet. Geology 26, 3-6.

Briner, J.P., Miller, G.H., Davis, P., Finkel, R.C., 2005. Cosmogenic exposure dating in arctic glacial landscapes: implications for the glacial history of northeastern Baffin Island, Arctic Canada. Canadian Journal of Earth Sciences 42, 67.

Briner, J.P., Miller, G.H., Davis, P.T., Finkel, R.C., 2006. Cosmogenic radionuclides from fiord landscapes support differential erosion by overriding ice sheets. Geological Society of America Bulletin 118, 406-420.

Briner, J.P., Miller, G.H., Finkel, R., Hess, D.P., 2008. Glacial erosion at the fjord onset zone and implications for the organization of ice flow on Baffin Island, Arctic Canada. Geomorphology 97, 126-134.

Briner, J.P., Bini, A.C., Anderson, R.S., 2009. Rapid early Holocene retreat of a Laurentide outlet glacier through an Arctic fjord. Nature Geoscience 2, 496-499.

Briner, J.P., Davis, P.T., Miller, G.H., 2009. Latest Pleistocene and Holocene glaciation of Baffin Island, Arctic Canada: key patterns and chronologies. Quaternary Science Reviews 28, 2075-2087.

Briner, J.P., Lifton, N.A., Miller, G.H., Refsnider, K., Anderson, R., Finkel, R., 2014. Using in situ cosmogenic ^{10}Be, ^{14}C, and ^{26}Al to decipher the history of polythermal ice sheets on Baffin Island, Arctic Canada. Quaternary Geochronology 19, 4-13.

Brook, E.J., Nesje, A., Lehman, S.J., Raisbeck, G.M., Yiou, F., 1996. Cosmogenic nuclide exposure ages along a vertical transect in western Norway: Implications for the height of the Fennoscandian ice sheet. Geology 24, 207-210.

Carrara, P., Andrews, J., 1972. The Quaternary history of northern Cumberland Peninsula, Baffin Island, NWT Part I: The late-and neoglacial deposits of the Akudlermuit and Boas glaciers. Canadian Journal of Earth Sciences 9, 403-414.

Chadwick, O.A., Brimhall, G.H., Hendricks, D.M., 1990. From a black to a gray box — a mass balance interpretation of pedogenesis. Geomorphology 3, 369-390.

Champagnac, J.-D., Molnar, P., Sue, C., Herman, F., 2012. Tectonics, climate, and mountain topography. Journal of Geophysical Research: Solid Earth 117, B02403.

Champagnac, J.-D., Valla, P.G., Herman, F., 2014. Late-Cenozoic relief evolution under evolving climate: A review. Tectonophysics 614, 44-65.

Chiverrell, R.C., Thorndycraft, V.R., Hoffmann, T.O., 2011. Cumulative probability functions and their role in evaluating the chronology of geomorphological events during the Holocene. Journal of Quaternary Science 26, 76-85.

Chmeleff, J., von Blanckenburg, F., Kossert, K., Jakob, D., 2010. Determination of the ^{10}Be half-life by multicollector ICP-MS and liquid scintillation counting. Nuclear Instruments and Methods in Physics Research Section B: Beam Interactions with Materials and Atoms 268, 192-199.

Clark, P.U., Pollard, D., 1998. Origin of the Middle Pleistocene Transition by ice sheet erosion of regolith. Paleoceanography 13, 1-9.

Clark, P.U., Archer, D., Pollard, D., Blum, J.D., Rial, J.A., Brovkin, V., Mix, A.C., Pisias, N.G., Roy, M., 2006. The middle Pleistocene transition: characteristics, mechanisms, and implications for long-term changes in atmospheric pCO_2. Quaternary Science Reviews 25, 3150-3184.

Cockburn, H.A.P., Seidl, M.A., Summerfield, M.A., 1999. Quantifying denudation rates on inselbergs in the central Namib Desert using in situ–produced cosmogenic ^{10}Be and ^{26}Al. Geology 27, 399-402.

Colgan, P.M., Bierman, P.R., Mickelson, D.M., Caffee, M., 2002. Variation in glacial erosion near the southern margin of the Laurentide Ice Sheet, south-central Wisconsin, USA: Implications for cosmogenic dating of glacial terrains. Geological Society of America Bulletin 114, 1581-1591.

Cowan, B., 2015. Shorelines beneath the sea: Geomorphology and characterization of the postglacial sea-level lowstand, Cumberland Peninsula, Baffin Island, Nunavut. Department of Geography, MSc Thesis. Memorial University of Newfoundland, St. John's.

Creason, G., 2015. Exhumation history of Hall Peninsula, Baffin Island, from apatite and zircon low temperature thermochronology. Earth Sciences, MSc. Dalhousie University, Halifax.

Curry, J.A., Schramm, J.L., Ebert, E.E., 1995. Sea ice-albedo climate feedback mechanism. Journal of Climate 8, 240-247.

Dahl-Jensen, D., Mosegaard, K., Gundestrup, N., Clow, G.D., Johnsen, S.J., Hansen, A.W., Balling, N., 1998. Past temperatures directly from the Greenland Ice Sheet. Science 282, 268-271.

Dahl, R., 1966. Block fields, weathering pits and tor-like forms in the Narvik Mountains, Nordland, Norway. Geografiska Annaler. Series A, Physical Geography 48, 55-85.

Dansgaard, W., Johnsen, S., Clausen, H., Dahl-Jensen, D., Gundestrup, N., Hammer, C., Hvidberg, C., Steffensen, J., Sveinbjörnsdottir, A., Jouzel, J., 1993. Evidence for general instability of past climate from a 250-kyr ice-core record. Nature 364, 218-220.

Davis, P.T., 1985. Neoglacial moraines on Baffin Island, In: Andrews, J.T. (Ed.), Quaternary Environments: Eastern Canadian Arctic, Baffin Bay and Western Greenalnd. Allen and Unwind, Boston, p. 682-718.

Davis, P.T., Bierman, P., Marsella, K., Caffee, M., Southon, J.R., 1999. Cosmogenic analysis of glacial terrains in the eastern Canadian Arctic a test for inherited nuclides and the effectiveness of glacial erosion. Annals of glaciology 28, 181-188.

Davis, P.T., Briner, J.P., Coulthard, R.D., Finkel, R.W., Miller, G.H., 2006. Preservation of Arctic landscapes overridden by cold-based ice sheets. Quaternary Research 65, 156-163.

De Angelis, H., Kleman, J., 2007. Palaeo-ice streams in the Foxe/Baffin sector of the Laurentide Ice Sheet. Quaternary Science Reviews 26, 1313-1331.

de Vernal, A., Hillaire-Marcel, C., 2006. Provincialism in trends and high frequency changes in the northwest North Atlantic during the Holocene. Global and Planetary Change 54, 263-290.

de Vernal, A., Hillaire-Marcel, C., Solignac, S., Radi, T., Rochon, A., 2008. Reconstructing sea ice conditions in the Arctic and sub-Arctic prior to human observations.Arctic Sea ice decline: observations, projections, mechanisms, and implications. . In: Weaver, E. (Ed.), Geohpysical Monograph Series, 180, p. 27-45.

Dowdeswell, J.A., Ottesen, D., Rise, L., 2010. Rates of sediment delivery from the Fennoscandian Ice Sheet through an ice age. Geology 38, 3-6.

Drăguţ, L., Eisank, C., 2012. Automated object-based classification of topography from SRTM data. Geomorphology 141–142, 21-33.

Dühnforth, M., Anderson, R.S., Ward, D., Stock, G.M., 2010. Bedrock fracture control of glacial erosion processes and rates. Geology 38, 423-426.

Dyke, A., 1979. Glacial and sea-level history of southwestern Cumberland Peninsula, Baffin Island, NWT, Canada. Arctic and Alpine Research 11, 179-202.

Dyke, A., Andrews, J., Miller, G., 1982. Quaternary geology of Cumberland Peninsula, Baffin Island, District of Franklin. Geological Survey of Canada, Memoir, 403, p. 32.

Dyke, A.S., Prest, V.K., 1987. Late Wisconsinan and Holocene retreat of the Laurentide ice sheet. Geological Survey of Canada, "A" Series Map 1702A.

Dyke, A.S., 1993. Landscapes of cold-centred Late Wisconsinan ice caps, Arctic Canada. Progress in Physical Geography 17, 223-247.

Dyke, A.S., 2004. An outline of North American deglaciation with emphasis on central and northern Canada. Developments in Quaternary Sciences 2, 373-424.

Dyke, A.S., 2011a. Surficial geology, Hoare Bay–Abraham Bay north, Baffin Island, Nunavut. Canadian Geoscience Map 15, prelim.

Dyke, A.S., 2011b. Surficial geology, Pangnirtung south, Baffin Island, Nunavut. Canadian Geoscience Map 19, prelim.

Dyke, A.S., 2011c. Surficial geology, Cape Dyer south, Baffin Island, Nunavut. Canadian Geoscience Map 20, prelim.

Dyke, A.S., 2011d. Surficial geology, Clearwater Fiord–Pangnirtung south, Baffin Island, Nunavut. Canadian Geoscience Map 18, prelim.

Dyke, A.S., 2011e. Surficial geology, Hoare Bay north, Baffin Island, Nunavut. Canadian Geoscience Map 17, prelim.

Dyke, A.S., 2011f. Surficial geology, Abraham Bay north, Baffin Island, Nunavut. Canadian Geoscience Map 16, prelim.

Dyke, A.S., 2013a. Surficial geology, Broughton Island-Padloping Island, Baffin Island, Nunavut, NTS 16-M, NTS 16-N, and parts of NTS 26-P. Canadian Geoscience Map 23, prelim.

Dyke, A.S., 2013b. Surficial geology, Pangnirtung north, Baffin Island, Nunavut, NTS 26-I northeast and NTS 16-L northwest. Canadian Geoscience Map 21, prelim.

Dyke, A.S., 2013c. Surficial geology, Cape Dyer North, Baffin Island, Nunavut, NTS 16-L northeast and NTS 16-K northwest. Canadian Geoscience Map 22, prelim.

Ebert, K., Willenbring, J., Norton, K.P., Hall, A., Hättestrand, C., 2012. Meteoric ^{10}Be concentrations from saprolite and till in northern Sweden: Implications for glacial erosion and age. Quaternary Geochronology 12, 11-22.

Eddy, J.A., 1976. The Maunder Minimum. Science 192, 1189-1202.

Elderfield, H., Ferretti, P., Greaves, M., Crowhurst, S., McCave, I.N., Hodell, D., Piotrowski, A.M., 2012. Evolution of Ocean Temperature and Ice Volume Through the Mid-Pleistocene Climate Transition. Science 337, 704-709.

England, J., Andrews, J., 1973. Broughton Island–a reference area for Wisconsin and Holocene chronology and sea level changes on eastern Baffin Island. Boreas 2, 17-32.

England, J., 1986. Glacial erosion of a high Arctic valley. Journal oJ Glaciology 32, 60-64.

Fabel, D., Stroeven, A.P., Harbor, J., Kleman, J., Elmore, D., Fink, D., 2002. Landscape preservation under Fennoscandian ice sheets determined from in situ produced 10Be and 26Al. Earth and Planetary Science Letters 201, 397-406.

Falconer, G., 1966. Preservation of vegetation and patterned ground under a thin ice body in northern Baffin Island, NWT. Geographical Bulletin 8, 194-200.

Fernald, M.L., 1925. Persistence of plants in unglaciated areas of boreal America. Memoirs of the American Academy of Arts and Sciences 15, 241-342.

Fisher, D., Dyke, A., Koerner, R., Bourgeois, J., Kinnard, C., Zdanowicz, C., de Vernal, A., Hillaire-Marcel, C., Savelle, J., Rochon, A., 2006. Natural variability of Arctic sea ice over the Holocene. Eos, Transactions American Geophysical Union 87, 273-275.

Fisher, D.A., Koerner, R.M., Bourgeois, J.C., Zielinski, G., Wake, C., Hammer, C.U., Clausen, H.B., Gundestrup, N., Johnsen, S., Goto-Azuma, K., Hondoh, T., Blake, E., Gerasimoff, M., 1998. Penny Ice Cap Cores, Baffin Island, Canada, and the Wisconsinan Foxe Dome connection: Two states of Hudson Bay ice cover. Science 279, 692-695.

Fjellanger, J., Sorbel, L., Linge, H., Brook, E.J., Raisbeck, G.M., Yiou, F., 2006. Glacial survival of blockfields on the Varanger Peninsula, northern Norway. Geomorphology 82, 255-272.

Flint, R., 1943. Growth of North American ice sheet during the Wisconsin age. Bulletin of the Geological Society of America 54, 325-362.

Francis, D.R., Wolfe, A.P., Walker, I.R., Miller, G.H., 2006. Interglacial and Holocene temperature reconstructions based on midge remains in sediments of two lakes from Baffin Island, Nunavut, Arctic Canada; Glacial-interglacial climate of the past 160,000 years; new insights from data and models. Palaeogeography, Palaeoclimatology, Palaeoecology 236, 107-124.

Frechette, B., Wolfe, A.P., Miller, G.H., Richard, P.J.H., de Vernal, A., 2006. Vegetation and climate of the last interglacial on Baffin Island, Arctic Canada; Glacial-interglacial climate of the past 160,000 years; new insights from data and models. Palaeogeography, Palaeoclimatology, Palaeoecology 236, 91-106.

Frechette, B., de Vernal, A., 2009. Relationship between Holocene climate variations over southern Greenland and eastern Baffin Island and synoptic circulation pattern. Climate of the Past 5, 347-359.

Fujioka, T., Fink, D., Nanson, G., Mifsud, C., Wende, R., 2015. Flood-flipped boulders: In-situ cosmogenic nuclide modeling of flood deposits in the monsoon tropics of Australia. Geology 43, 43-46.

Gajewski, K., 2015. Quantitative reconstruction of Holocene temperatures across the Canadian Arctic and Greenland. Global and Planetary Change 128, 14-23.

Gammon, P., Dyke, A., Sanborn-Barrie, M., Young, M., 2011. Geochemistry and physical properties of till samples collected in 2009 from Cumberland Peninsula, Nunavut. Geological Survey of Canada, Open File 6763.

Gao, C., Robock, A., Ammann, C., 2008. Volcanic forcing of climate over the past 1500 years: An improved ice core-based index for climate models. Journal of Geophysical Research: Atmospheres 113, D23111.

Gardner, A.S., Sharp, M.J., Koerner, R.M., Labine, C., Boon, S., Marshall, S.J., Burgess, D.O., Lewis, D., 2009. Near-surface temperature lapse rates over Arctic glaciers and their implications for temperature downscaling. Journal of Climate 22, 4281-4298.

Gardner, A.S., Moholdt, G., Wouters, B., Wolken, G.J., Burgess, D.O., Sharp, M.J., Cogley, J.G., Braun, C., Labine, C., 2011. Sharply increased mass loss from glaciers and ice caps in the Canadian Arctic Archipelago. Nature 473, 357-360.

Gibbons, A.B., Megeath, J.D., Pierce, K.L., 1984. Probability of moraine survival in a succession of glacial advances. Geology 12, 327-330.

Glasser, N.F., Hall, A.M., 1997. Calculating Quaternary glacial erosion rates in northeast Scotland. Geomorphology 20, 29-48.

Godwin, H., 1962. Half-life of Radiocarbon. Nature 195, 984-984.

Goodfellow, B.W., Skelton, A., Martel, S.J., Stroeven, A.P., Jansson, K.N., Hättestrand, C., 2014. Controls of tor formation, Cairngorm Mountains, Scotland. Journal of Geophysical Research: Earth Surface, 2013JF002862.

Gosse, J., Bell, T., Gray, J., Klein, J., Yang, G., Finkel, R., 2006. Using cosmogneic isotopes to interpret the landscape record of glaciation: nunataks in Newfoundland?, In: Knight, P. (Ed.), Glacier science and environmental change. Blackwell Publishing, Malden, MA; Oxford, p. 442-446.

Gosse, J.C., Phillips, F.M., 2001. Terrestrial in situ cosmogenic nuclides: theory and application. Quaternary Science Reviews 20, 1475-1560.

Granger, D.E., Muzikar, P.F., 2001. Dating sediment burial with in situ-produced cosmogenic nuclides: theory, techniques, and limitations. Earth and Planetary Science Letters 188, 269-281.

Grujic, D., Coutand, I., Bookhagen, B., Bonnet, S., Blythe, A., Duncan, C., 2006. Climatic forcing of erosion, landscape, and tectonics in the Bhutan Himalayas. Geology 34, 801-804.

Guilderson, T.P., Reimer, P.J., Brown, T.A., 2005. The boon and bane of radiocarbon dating. Science 307, 362-364.

Hall, A.M., Phillips, W.M., 2006. Glacial modification of granite tors in the Cairngorms, Scotland. Journal of Quaternary Science 21, 811-830.

Hallet, B., 1979. A theoretical model of glacial abrasion. Journal of Glaciology 23, 39-50.

Hallet, B., 1996. Glacial quarrying: A simple rheoretical model. Annals of glaciology 22, 1-8.

Hallet, B., Hunter, L., Bogen, J., 1996. Rates of erosion and sediment evacuation by glaciers: A review of field data and their implications. Global and Planetary Change 12, 213-235.

Hanson, B., Hooke, R.L., 2011. Effect of sea-level lowering on ELA depression during the LGM. Quaternary Research 75, 406-410.

Harbor, J.M., Wheeler, D.A., 1992. On the mathematical description of glaciated valley cross sections. Earth Surface Processes and Landforms 17, 477-485.

Harbor, J.M., 1995. Development of glacial-valley cross sections under conditions of spatially variable resistance to erosion. Geomorphology 14, 99-107.

Hattestrand, C., Stroeven, A.P., 2002. A relict landscape in the centre of Fennoscandian glaciation: Geomorphological evidence of minimal Quaternary glacial erosion. Geomorphology 44, 127-143.

Hawkins, F.F., 1985. Equilibrium-line altitudes and paleoenvironment in the Merchants Bay area, Baffin Island, NWT, Canada. Journal of Glaciology 31, 205-213.

Heisinger, B., Lal, D., Jull, A., Kubik, P., Ivy-Ochs, S., Knie, K., Nolte, E., 2002a. Production of selected cosmogenic radionuclides by muons: 2. Capture of negative muons. Earth and Planetary Science Letters 200, 357-369.

Heisinger, B., Lal, D., Jull, A., Kubik, P., Ivy-Ochs, S., Neumaier, S., Knie, K., Lazarev, V., Nolte, E., 2002b. Production of selected cosmogenic radionuclides by muons:: 1. Fast muons. Earth and Planetary Science Letters 200, 345-355.

Herman, F., Beaud, F., Champagnac, J.-D., Lemieux, J.-M., Sternai, P., 2011. Glacial hydrology and erosion patterns: A mechanism for carving glacial valleys. Earth and Planetary Science Letters 310, 498-508.

Heyman, J., Stroeven, A.P., Harbor, J.M., Caffee, M.W., 2011. Too young or too old: Evaluating cosmogenic exposure dating based on an analysis of compiled boulder exposure ages. Earth and Planetary Science Letters 302, 71-80.

Hidy, A.J., Gosse, J.C., Pederson, J.L., Mattern, J.P., Finkel, R.C., 2010. A geologically constrained Monte Carlo approach to modeling exposure ages from profiles of cosmogenic nuclides: An example from Lees Ferry, Arizona. Geochemistry Geophysics Geosystems 11, Q0AA10.

Hidy, A.J., Gosse, J.C., Froese, D.G., Bond, J.D., Rood, D.H., 2013. A latest Pliocene age for the earliest and most extensive Cordilleran Ice Sheet in northwestern Canada. Quaternary Science Reviews 61, 77-84.

Hidy, A.J., Gosse, J.C., Blum, M.D., Gibling, M.R., 2014. Glacial–interglacial variation in denudation rates from interior Texas, USA, established with cosmogenic nuclides. Earth and Planetary Science Letters 390, 209-221.

Hinzman, L., Bettez, N., Bolton, W.R., Chapin, F.S., Dyurgerov, M., Fastie, C., Griffith, B., Hollister, R., Hope, A., Huntington, H., Jensen, A., Jia, G., Jorgenson, T., Kane, D., Klein, D., Kofinas, G., Lynch, A., Lloyd, A., McGuire, A.D., Nelson, F., Oechel, W., Osterkamp, T., Racine, C., Romanovsky, V., Stone, R., Stow, D., Sturm, M., Tweedie, C., Vourlitis, G., Walker, M., Walker, D., Webber, P., Welker, J., Winker, K., Yoshikawa, K., 2005. Evidence and Implications of Recent Climate Change in Northern Alaska and Other Arctic Regions. Climatic Change 72, 251-298.

Hughes Clarke, J.E., Muggah, J., Renoud, W., Bell, T., Forbes, D.L., Cowan, B., Kennedy, J., 2015. Reconnaissance seabed mapping around Hall and Cumberland peninsulas, Nunavut: opening up southeastern Baffin Island to nearshore geological investigations, Summary of Activities 2014. Canada-Nunavut Geoscience Office, p. 133–144.

Hurrell, J.W., Kushnir, Y., Visbeck, M., 2001. The North Atlantic Oscillation. Science 291, 603-605.

Huybers, P., 2006. Early Pleistocene glacial cycles and the integrated summer insolation forcing. Science 313, 508-511.

Ives, J., 1957. Glaciation of the Torngat Mountains, northern Labrador. Arctic 10, 66-87.

Ives, J., 1962. Indications of recent extensive glacierization in north-central Baffin Island, NWT. Journal of Glaciology 4, 197-205.

Ives, J.D., 1966. Block fields, associated weathering forms on mountain tops and the Nunatak Hypothesis. Geografiska Annaler. Series A, Physical Geography 48, 220-223.

Ives, J.D., 1974. Biological refugia and the nunatak hypothesis, In: Ives, J.D., Barry, R.G. (Eds.), Arctic and alpine environments. Methuen London United Kingdom, p. 605-636.

Ives, J.D., 1975. Delimitation of surface weathering zones in eastern Baffin Island, Northern Labrador and Arctic Norway: A discussion. Geological Society of America Bulletin 86, 1096-1100.

Ives, J.D., Andrews, J.T., Barry, R.G., 1975. Growth and decay of the Laurentide Ice Sheet and comparisons with Fenno-Scandinavia. Naturwissenschaften 62, 118-125.

Ives, J.D., 1978. The maximum extent of the Laurentide Ice Sheet along the east coast of North America during the last glaciation. Arctic, 24-53.

Jackson, G.D., Sanborn-Barrie, M., 2014. Geology, Pangnirtung Fiord, Baffin Island, Nunavut. Canadian Geoscience Map 4, prelim.

Jansen, J.D., Nanson, G.C., Cohen, T.J., Fujioka, T., Fabel, D., Larsen, J.R., Codilean, A.T., Price, D.M., Bowman, H.H., May, J.H., Gliganic, L.A., 2013. Lowland river responses to intraplate tectonism and climate forcing quantified with luminescence and cosmogenic 10Be. Earth and Planetary Science Letters 366, 49-58.

Jarnà, A., 2014. Geomorphology of glacial- and non-glacial landscapes in mountain regions; testing of formation processes using GIS characterization. Faculty of Mining and Geology, Institute of Geoinformatics, MSc Thesis. Technical University of Ostrava, Ostrava, p. 68.

Jennings, A.E., 1993. The Quaternary history of Cumberland Sound, southeastern Baffin Island: the marine evidence. Géographie physique et Quaternaire 47, 21–42.

Jennings, A.E., Tedesco, K.A., Andrews, J.T., Kirby, M.E., 1996. Shelf erosion and glacial ice proximity in the Labrador Sea during and after Heinrich events (H-3 or 4 to H-0) as shown by foraminifera. Geological Society, London, Special Publications 111, 29-49.

Jull, A.J.T., Lifton, N., Phillips, W.M., Quade, J., 1994. Studies of the production rate of cosmic-ray produced 14C in rock surfaces. Nuclear Instruments and Methods in Physics Research Section B: Beam Interactions with Materials and Atoms 92, 308-310.

Kaplan, M., 1999. The last glaciation of the Cumberland Sound region, Baffin Island, Canada, based on glacial geology, cosmogenic dating, and numerical modeling. PhD Thesis. University of Colorado, Boulder, p. 206.

Kaplan, M., Pfeffer, W., Sassolas, C., Miller, G., 1999. Numerical modelling of the Laurentide Ice Sheet in the Baffin Island region: The role of a Cumberland Sound ice stream. Canadian Journal of Earth Sciences 36, 1315-1326.

Kaplan, M., Miller, G., Steig, E., 2001. Low-gradient outlet glaciers (ice streams?) drained the Laurentide ice sheet. Geology 29, 343-346.

Kaplan, M., Miller, G., 2003. Early Holocene delevelling and deglaciation of the Cumberland Sound region, Baffin Island, arctic Canada. Geological Society of America Bulletin 115, 445-462.

Kaufman, D.S., Ager, T.A., Anderson, N.J., Anderson, P.M., Andrews, J.T., Bartlein, P.J., Brubaker, L.B., Coats, L.L., Cwynar, L.C., Duvall, M.L., Dyke, A.S., Edwards, M.E., Eisner, W.R., Gajewski, K., Geirsdóttir, A., Hu, F.S., Jennings, A.E., Kaplan, M.R., Kerwin, M.W., Lozhkin, A.V., MacDonald, G.M., Miller, G.H., Mock, C.J., Oswald, W.W., Otto-Bliesner, B.L., Porinchu, D.F., Rühland, K., Smol, J.P., Steig, E.J., Wolfe, B.B., 2004. Holocene thermal maximum in the western Arctic (0–180°W). Quaternary Science Reviews 23, 529-560.

Kerwin, M.W., Overpeck, J.T., Webb, R.S., Anderson, K.H., 2004. Pollen-based summer temperature reconstructions for the eastern Canadian boreal forest, subarctic, and Arctic. Quaternary Science Reviews 23, 1901-1924.

Kessler, M., Anderson, R., Briner, J., 2008. Fjord insertion into continental margins driven by topographic steering of ice. Nature Geoscience 1, 365-369.

Kirchner, J.W., Finkel, R.C., Riebe, C.S., Granger, D.E., Clayton, J.L., King, J.G., Megahan, W.F., 2001. Mountain erosion over 10 yr, 10 k.y., and 10 m.y. time scales. Geology 29, 591-594.

Kleman, J., Stroeven, A.P., 1997. Preglacial surface remnants and Quaternary glacial regimes in northwestern Sweden. Geomorphology 19, 35-54.

Kohl, C., Nishiizumi, K., 1992. Chemical isolation of quartz for measurement of in-situ-produced cosmogenic nuclides. Geochimica et Cosmochimica Acta 56, 3583-3587.

Korschinek, G., Bergmaier, A., Faestermann, T., Gerstmann, U.C., Knie, K., Rugel, G., Wallner, A., Dillmann, I., Dollinger, G., von Gostomski, C.L., Kossert, K., Maiti, M., Poutivtsev, M., Remmert, A., 2010. A new value for the half-life of ^{10}Be by Heavy-Ion Elastic Recoil Detection and liquid scintillation counting. Nuclear Instruments and Methods in Physics Research Section B: Beam Interactions with Materials and Atoms 268, 187-191.

Krabbendam, M., Bradwell, T., 2014. Quaternary evolution of glaciated gneiss terrains: pre-glacial weathering vs. glacial erosion. Quaternary Science Reviews 95, 20-42.

La Farge, C., Williams, K.H., England, J.H., 2013. Regeneration of Little Ice Age bryophytes emerging from a polar glacier with implications of totipotency in extreme environments. Proceedings of the National Academy of Sciences 110, 9839-9844.

Lal, D., 1991. Cosmic ray labeling of erosion surfaces: in situ nuclide production rates and erosion models. Earth and Planetary Science Letters 104, 424-439.

Lamb, H.H., 1965. The early medieval warm epoch and its sequel. Palaeogeography, Palaeoclimatology, Palaeoecology 1, 13-37.

Lawrence, D.M., Slater, A.G., 2005. A projection of severe near-surface permafrost degradation during the 21st century. Geophysical Research Letters 32, L24401.

LeBlanc, A., Allard, M., Carbonneau, A., Oldenborger, G., L'Hérault, E., Sladen, W., Gosselin, P., Mate, D., 2011. Assessing permafrost conditions and landscape hazards in support of climate change adaptation in Pangnirtung, Nunavut. Geological Survey of Canada Open File 6868, p. 59.

Lecavalier, B.S., Milne, G.A., Simpson, M.J.R., Wake, L., Huybrechts, P., Tarasov, L., Kjeldsen, K.K., Funder, S., Long, A.J., Woodroffe, S., Dyke, A.S., Larsen, N.K., 2014. A model of Greenland ice sheet deglaciation constrained by observations of relative sea level and ice extent. Quaternary Science Reviews 102, 54-84.

Lifton, N., Sato, T., Dunai, T.J., 2014. Scaling in situ cosmogenic nuclide production rates using analytical approximations to atmospheric cosmic-ray fluxes. Earth and Planetary Science Letters 386, 149-160.

Lifton, N.A., Jull, A., Quade, J., 2001. A new extraction technique and production rate estimate for in situ cosmogenic ^{14}C in quartz. Geochimica et Cosmochimica Acta 65, 1953-1969.

Linton, D.L., 1955. The problem of tors. The Geographical Journal 121, 470-487.

Lisiecki, L.E., Raymo, M.E., 2005. A Plio-Pleistocene stack of 57 globally distributed benthic ^{18}O records. Paleoceanography 20, 522–533.

Locke, C.W., Locke, W.W.I., 1977. Little Ice Age snow-cover extent and paleoglaciation thresholds: North-central Baffin Island, N.W.T., Canada. Arctic and Alpine Research 9, 291-300.

Locke, W., 1987. The late Quaternary geomorphic and paleoclimatic history of the Cape Dyer area, easternmost Baffin Island, NWT. Canadian Journal of Earth Sciences 24, 1185-1198.

Lowell, T.V., 1995. The application of radiocarbon age estimates to the dating of glacial sequences: an example from the Miami sublobe, Ohio, USA. Quaternary Science Reviews 14, 85-99.

Lowell, T.V., Hall, B.L., Kelly, M.A., Bennike, O., Lusas, A.R., Honsaker, W., Smith, C.A., Levy, L.B., Travis, S., Denton, G.H., 2013. Late Holocene expansion of Istorvet ice cap, Liverpool Land, east Greenland. Quaternary Science Reviews 63, 128-140.

Macchiaroli, P.E., 1995. Resolving aspects of past glaciations by dating exposed rock surfaces using aluminum-26 and beryllium-10 produced in situ: Wright Valley, Southern Victoria Land, Antarctica and the southeasternmost ridge of the Appalachian mountains, northeast United States. PhD Thesis. University of Pennsylvania, p. 161.

MacGregor, K., Anderson, R., Waddington, E., 2009. Numerical modeling of glacial erosion and headwall processes in alpine valleys. Geomorphology 103, 189-204.

Mann, M.E., Zhang, Z., Rutherford, S., Bradley, R.S., Hughes, M.K., Shindell, D., Ammann, C., Faluvegi, G., Ni, F., 2009. Global signatures and dynamical origins of the Little Ice Age and Medieval Climate Anomaly. Science 326, 1256-1260.

Margold, M., Stroeven, A.P., Clague, J.J., Heyman, J., 2014. Timing of terminal Pleistocene deglaciation at high elevations in southern and central British Columbia constrained by ^{10}Be exposure dating. Quaternary Science Reviews 99, 193-202.

Margreth, A., Dyke, A.S., Gosse, J.C., Telka, A.M., 2014. Neoglacial ice expansion and late Holocene cold-based ice cap dynamics on Cumberland Peninsula, Baffin Island, Arctic Canada. Quaternary Science Reviews 91, 242-256.

Margreth, A., 2015. Geochronological approaches for quantification of polythermal glacier dynamics and subglacial episodic erosion on high-latitude highland plateaus, Cumberland Peninsula, Baffin Island, Nunavut. Earth Sciences, PhD. Dalhousie University, Halifax.

Marquette, G.C., Gray, J.T., Gosse, J.C., Courchesne, F., Stockli, L., Macpherson, G., Finkel, R., 2004. Felsenmeer persistence under non-erosive ice in the Torngat and Kaumajet mountains, Quebec and Labrador, as determined by soil weathering and cosmogenic nuclide exposure dating. Canadian Journal of Earth Sciences 41, 19-38.

Marsella, K., Bierman, P., Davis, P., Caffee, M., 2000. Cosmogenic ^{10}Be and ^{26}Al ages for the last glacial maximum, eastern Baffin Island, Arctic Canada. Geological Society of America Bulletin 112, 1296-1312.

McGregor, E.D., Nielsen, S.B., Stephenson, R.A., Petersen, K.D., MacDonald, D.I.M., 2013. Long-term exhumation of a Palaeoproterozoic orogen and the role of pre-existing heterogeneous thermal crustal properties: a fission-track study of SE Baffin Island. Journal of the Geological Society 170, 877-891.

McGuire, A.D., Chapin, F.S., Walsh, J.E., Wirth, C., 2006. Integrated Regional Changes in Arctic Climate Feedbacks: Implications for the Global Climate System*. Annual Review of Environment and Resources 31, 61-91.

McNeely, R., Brennan, J., 2005. Geological Survey of Canada revised shell dates. Geological Survey of Canada, Open File 5019, p. 530.

McNeely, R., Dyke, A.S., Southon, J.R., 2006. Canadian marine reservoir ages, preliminary data assessment. Geological Survey of Canada, Open File 5049, p. 3.

Meierding, T.C., 1982. Late pleistocene glacial equilibrium-line altitudes in the Colorado Front Range: A comparison of methods. Quaternary Research 18, 289-310.

Michczynski, A., 2007. Is it possible to find a good point estimate of a calibrated radiocarbon date? Radiocarbon 49, 393-401.

Miller, G., Andrews, J., 1972. Quaternary history of northern Cumberland Peninsula, east Baffin Island, NWT, Canada Part VI: Preliminary lichen growth curve for Rhizocarpon geographicum. Geological Society of America Bulletin 83, 1133-1138.

Miller, G., 1973. Late Quaternary glacial and climatic history of northern Cumberland Peninsula, Baffin Island, NWT, Canada. Quaternary Research 3, 561-583.

Miller, G., Dyke, A., 1974. Proposed extent of late Wisconsin Laurentide ice on eastern Baffin Island. Geology 2, 125-130.

Miller, G., 1979. Radiocarbon date list IV, Baffin Island, NWT, Canada. University of Colorado, Institute of Arctic and Alpine Research Occasional Paper, 29, p. 61.

Miller, G.H., Mode, W.N., Wolfe, A.P., Sauer, P.E., Bennike, O., Forman, S.L., Short, S.K., Stafford, T., 1999. Stratified interglacial lacustrine sediments from Baffin Island, Arctic Canada: Chronology and paleoenvironmental implications. Quaternary Science Reviews 18, 789-810.

Miller, G.H., Wolfe, A.P., Steig, E.J., Sauer, P.E., Kaplan, M.R., Briner, J.P., 2002. The Goldilocks dilemma; big ice, little ice, or "just-right" ice in the eastern Canadian Arctic; Ice sheets and sea level of the last glacial maximum. Quaternary Science Reviews 21, 33-48.

Miller, G.H., Wolfe, A.P., Briner, J.P., Sauer, P.E., Nesje, A., 2005. Holocene glaciation and climate evolution of Baffin Island, Arctic Canada; Quaternary land-ocean correlation; a tribute to Professor David Q. Bowen. Quaternary Science Reviews 24, 1703-1721.

Miller, G.H., Alley, R.B., Brigham-Grette, J., Fitzpatrick, J.J., Polyak, L., Serreze, M.C., White, J.W.C., 2010. Arctic amplification: Can the past constrain the future? Quaternary Science Reviews 29, 1779-1790.

Miller, G.H., Geirsdóttir, Á., Zhong, Y., Larsen, D.J., Otto-Bliesner, B.L., Holland, M.M., Bailey, D.A., Refsnider, K.A., Lehman, S.J., Southon, J.R., Anderson, C., Björnsson, H., Thordarson, T., 2012. Abrupt onset of the Little Ice Age triggered by volcanism and sustained by sea-ice/ocean feedbacks. Geophysical Research Letters 39, L02708.

Miller, G.H., Briner, J.P., Refsnider, K.A., Lehman, S.J., Geirsdóttir, Á., Larsen, D.J., Southon, J.R., 2013a. Substantial agreement on the timing and magnitude of Late Holocene ice cap expansion between East Greenland and the eastern Canadian Arctic: a commentary on Lowell et al., 2013. Quaternary Science Reviews 77, 239-245.

Miller, G.H., Lehman, S.J., Refsnider, K.A., Southon, J.R., Zhong, Y., 2013b. Unprecedented recent summer warmth in Arctic Canada. Geophysical Research Letters 40, 1-7.

Miller, K.G., Mountain, G.S. , Wright, J.D., Browning, J.V., 2011. A 180-million-year record of sea level and ice volume variations from continental margin and deep-sea isotopic records. Oceanography 24, 40-53.

Molnar, P., England, P., 1990. Late Cenozoic uplift of mountain ranges and global climate change: Chicken or egg? Nature 346, 29-34.

Molnar, P., 2004. Late Cenozoic increase in accumulation rates of terrestrial sediment: How might climate change have affected erosion rates? Annual Review of Earth and Planetary Sciences 32, 67-89.

Montgomery, D.R., Balco, G., Willett, S.D., 2001. Climate, tectonics, and the morphology of the Andes. Geology 29, 579-582.

Montgomery, D.R., 2002. Valley formation by fluvial and glacial erosion. Geology 30, 1047-1050.

Moore, J., Hughen, K., Miller, G., Overpeck, J., 2001. Little Ice Age recorded in summer temperature reconstruction from vared sediments of Donard Lake, Baffin Island, Canada. Journal of Paleolimnology 25, 503-517.

Muzikar, P., 2008. Cosmogenic nuclide concentrations in episodically eroding surfaces: Theoretical results. Geomorphology 97, 407-413.

Muzikar, P., 2009. General models for episodic surface denudation and its measurement by cosmogenic nuclides. Quaternary Geochronology 4, 50-55.

Naysmith, P., Cook, G., Phillips, W., Lifton, N., Anderson, R., 2004. Preliminary results for the extraction and measurement of cosmogenic in situ C-14 from quartz. Radiocarbon 46, 201-206.

Nelson, A., 1981. Quaternary glacial and marine stratigraphy of the Qivitu Peninsula, northern Cumberland Peninsula, Baffin Island, Canada: summary. Geological Society of America Bulletin 92, 512-518.

Nelson, A., 1982. Aminostratigraphy of Quaternary marine and glaciomarine sediments, Qivitu Peninsula, Baffin Island. Canadian Journal of Earth Sciences 19, 945-961.

Nelson, A.R., 1980. Chronology of Quaternary landforms, Qivitu Peninsula, northern Cumberland Peninsula, Baffin Island, N.W.T., Canada. Arctic and Alpine Research 12, 265-286.

Nesbitt, H., Young, G., 1982. Early Proterozoic climates and plate motions inferred from major element chemistry of lutites. Nature 299, 715-717.

Nghiem, S.V., Rigor, I.G., Perovich, D.K., Clemente-Colón, P., Weatherly, J.W., Neumann, G., 2007. Rapid reduction of Arctic perennial sea ice. Geophysical Research Letters 34, L19504.

Nghiem, S.V., Hall, D.K., Mote, T.L., Tedesco, M., Albert, M.R., Keegan, K., Shuman, C.A., DiGirolamo, N.E., Neumann, G., 2012. The extreme melt across the Greenland ice sheet in 2012. Geophys. Res. Lett. 39, L20502.

Niemi, N.A., Oskin, M., Burbank, D.W., Heimsath, A.M., Gabet, E.J., 2005. Effects of bedrock landslides on cosmogenically determined erosion rates. Earth and Planetary Science Letters 237, 480-498.

Nishiizumi, K., Winterer, E.L., Kohl, C.P., Klein, J., Middleton, R., Lal, D., Arnold, J.R., 1989. Cosmic ray production rates of ^{10}Be and ^{26}Al in quartz from glacially polished rocks. Journal of Geophysical Research: Solid Earth 94, 17907-17915.

Nishiizumi, K., Kohl, C.P., Arnold, J.R., Klein, J., Fink, D., Middleton, R., 1991. Cosmic ray produced ^{10}Be and ^{26}Al in Antarctic rocks: exposure and erosion history. Earth and Planetary Science Letters 104, 440-454.

Nishiizumi, K., 2004. Preparation of 26Al AMS standards. Nuclear Instruments and Methods in Physics Research Section B: Beam Interactions with Materials and Atoms 223–224, 388-392.

Oechel, W.C., Hastings, S.J., Vourlrtis, G., Jenkins, M., Riechers, G., Grulke, N., 1993. Recent change of Arctic tundra ecosystems from a net carbon dioxide sink to a source. Nature 361, 520-523.

Oerlemans, J., Fortuin, J.P.F., 1992. Sensitivity of glaciers and small ice caps to greenhouse warming. Science 258, 115-117.

Osmaston, H.A., 2006. Should Quaternary sea-level changes be used to correct glacier ELAs, vegetation belt altitudes and sea level temperatures for inferring climate changes? Quaternary Research 65, 244-251.

Ottesen, D., Rise, L., Sletten Andersen, E., Bugge, T., Eidvin, T., 2009. Geological evolution of the Norwegian continental shelf between 61° N and 68° N during the last 3 million years. Norwegian Journal of Geology/Norsk Geologisk Forening 89, 251-265.

Palmer, J., Neilson, R.A., 1962. The origin of granite tors on Darmoor, Devonshire. Proceedings of the Yorkshire Geological and Polytechnic Society 33, 315-340.

Paterson, W., 1994. The physics of glaciers. Oxford Press, Butterworth-Heinemann.

Payette, S., Delwaide, A., Caccianiga, M., Beauchemin, M., 2004. Accelerated thawing of subarctic peatland permafrost over the last 50 years. Geophysical Research Letters 31, L18208.

Pedersen, V.K., Huismans, R.S., Herman, F., Egholm, D.L., 2014. Controls of initial topography on temporal and spatial patterns of glacial erosion. Geomorphology 223, 96-116.

Pelletier, J.D., 2004. Estimate of three-dimensional flexural-isostatic response to unloading: Rock uplift due to late Cenozoic glacial erosion in the western United States. Geology 32, 161-164.

Pelletier, J.D., 2008. Glacial erosion and mountain building. Geology 36, 591-592.

Peltier, W.R., Fairbanks, R.G., 2006. Global glacial ice volume and Last Glacial Maximum duration from an extended Barbados sea level record. Quaternary Science Reviews 25, 3322-3337.

Phillips, W.M., Hall, A.M., Mottram, R., Fifield, L.K., Sugden, D.E., 2006. Cosmogenic 10Be and 26Al exposure ages of tors and erratics, Cairngorm Mountains, Scotland: timescales for the development of a classic landscape of selective linear glacial erosion. Geomorphology 73, 222-245.

Plug, L.J., Walls, C., Scott, B.M., 2008. Tundra lake changes from 1978 to 2001 on the Tuktoyaktuk Peninsula, western Canadian Arctic. Geophysical Research Letters 35, L03502.

Porter, S.C., 2000. Snowline depression in the tropics during the Last Glaciation. Quaternary Science Reviews 20, 1067-1091.

Post, E., Forchhammer, M.C., Bret-Harte, M.S., Callaghan, T.V., Christensen, T.R., Elberling, B., Fox, A.D., Gilg, O., Hik, D.S., Høye, T.T., Ims, R.A., Jeppesen, E., Klein, D.R., Madsen, J., McGuire, A.D., Rysgaard, S., Schindler, D.E., Stirling, I., Tamstorf, M.P., Tyler, N.J.C., van der Wal, R., Welker, J., Wookey, P.A., Schmidt, N.M., Aastrup, P., 2009. Ecological dynamics across the Arctic associated with recent climate change. Science 325, 1355-1358.

Rasmussen, S.O., Andersen, K.K., Svensson, A., Steffensen, J.P., Vinther, B.M., Clausen, H.B., Siggaard-Andersen, M., Johnsen, S.J., Larsen, L.B., Dahl-Jensen, D., 2006. A new Greenland ice core chronology for the last glacial termination. Journal of Geophysical Research 111, 1-16.

Rasmussen, S.O., Vinther, B.M., Clausen, H.B., Andersen, K.K., 2007. Early Holocene climate oscillations recorded in three Greenland ice cores. Quaternary Science Reviews 26, 1907-1914.

Raup, H.M., 1965. The Flowering Plants and Ferns of the Mesters Vig District, Northeast Greenland. Meddelelser om Gronland 166, p. 119.

Raymo, M., Ruddiman, W.F., 1992. Tectonic forcing of late Cenozoic climate. Nature 359, 117-122.

Refsnider, K.A., Miller, G.H., 2010. Reorganization of ice sheet flow patterns in Arctic Canada and the mid-Pleistocene transition. Geophysical Research Letters 37, L13502.

Refsnider, K.A., Miller, G.H., 2013. Ice-sheet erosion and the stripping of Tertiary regolith from Baffin Island, eastern Canadian Arctic. Quaternary Science Reviews 67, 176-189.

Reimer, P.J., Baillie, M.G.L., Bard, E., Bayliss, A., Beck, J.W., Blackwell, P.G., Ramsey, C.B., Buck, C.E., Burr, G.S., Edwards, R.L., Friedrich, M., Grootes, P.M., Guilderson, T.P., Hajdas, I., Heaton, T.J., Hogg, A.G., Hughen, K.A., Kaiser, K.F., Kromer, B., McCormac, F.G., Manning, S.W., Reimer, R.W., Richards, D.A., Southon, J.R., Talamo, S., Turney, C.S.M., van der Plicht, J., Weyhenmeyer, C.E., 2009. IntCal09 and Marine09 radiocarbon age calibration curves, 0-50,000 years cal BP. Radiocarbon 51, 1111-1150.

Reimer, P.J., Bard, E., Bayliss, A., Beck, J.W., Blackwell, P.G., Bronk Ramsey, C., Buck, C.E., Cheng, H., Edwards, R.L., Friedrich, M., Grootes, P.M., Guilderson, T.P., Haflidason, H., Hajdas, I., Hatté, C., Heaton, T.J., Hoffmann, D.L., Hogg, A.G., Hughen, K.A., Kaiser, K.F., Kromer, B., Manning, S.W., Niu, M., Reimer, R.W., Richards, D.A., Scott, E.M., Southon, J.R., Staff, R.A., Turney, C.S.M., van der Plicht, J., 2013. IntCal13 and Marine13 Radiocarbon Age Calibration Curves 0–50,000 Years cal BP. Radiocarbon 55, 1869-1887.

Rial, J.A., Oh, J., Reischmann, E., 2013. Synchronization of the climate system to eccentricity forcing and the 100,000-year problem. Nature Geosci 6, 289-293.

Riebe, C.S., Kirchner, J.W., Granger, D.E., 2001. Quantifying quartz enrichment and its consequences for cosmogenic measurements of erosion rates from alluvial sediment and regolith. Geomorphology 40, 15-19.

Riebe, C.S., Kirchner, J.W., Finkel, R.C., 2003. Long-term rates of chemical weathering and physical erosion from cosmogenic nuclides and geochemical mass balance. Geochimica et Cosmochimica Acta 67, 4411-4427.

Roberts, D.H., Long, A.J., Schnabel, C., Davies, B.J., Xu, S., Simpson, M.J.R., Huybrechts, P., 2009. Ice sheet extent and early deglacial history of the southwestern sector of the Greenland Ice Sheet. Quaternary Science Reviews 28, 2760-2773.

Robock, A., 2000. Volcanic eruptions and climate. Reviews of Geophysics 38, 191-219.

Roy, M., Clark, P.U., Raisbeck, G.M., Yiou, F., 2004. Geochemical constraints on the regolith hypothesis for the middle Pleistocene transition. Earth and Planetary Science Letters 227, 281-296.

Rubinstein, R.Y., Kroese, D.P., 2011. Simulation and the Monte Carlo method. John Wiley & Sons.

Rybczynski, N., Gosse, J.C., Harington, C.R., Wogelius, R.A., Hidy, A.J., Buckley, M., 2013. Mid-Pliocene warm-period deposits in the High Arctic yield insight into camel evolution. Nature communications 4, 1550.

Sanborn-Barrie, M., Young, M., Whalen, J., 2011. Geology, Kingnait Fiord, Nunavut. Canadian Geoscience Map 22, prelim.

Sanborn-Barrie, M., Young, M., 2013. Geology, Padle Fiord, Baffin Island, Nunavut. Canadian Geoscience Map 37, prelim.

Sanborn-Barrie, M., Young, M., Keim, R., Hamilton, B., 2013a. Geology, Sunneshine Fiord, Baffin Island, Nunavut. Canadian Geoscience Map 6, prelim.

Sanborn-Barrie, M., Young, M., Whalen, J.B., 2013b. Geology, Qikiqtarjuaq, Baffin Island, Nunavut. Canadian Geoscience Map 39, prelim.

Sato, T., Yasuda, H., Niita, K., Endo, A., Sihver, L., 2008. Development of PARMA: PHITS-Based Analytical Radiation Model in the Atmosphere. Radiation Research 170, 244-259.

Schaefer, J.M., Denton, G.H., Kaplan, M., Putnam, A., Finkel, R.C., Barrell, D.J.A., Andersen, B.G., Schwartz, R., Mackintosh, A., Chinn, T., Schlüchter, C., 2009. High-Frequency Holocene Glacier Fluctuations in New Zealand Differ from the Northern Signature. Science 324, 622-625.

Schaller, M., von Blanckenburg, F., Veldkamp, A., Tebbens, L.A., Hovius, N., Kubik, P.W., 2002. A 30 000 yr record of erosion rates from cosmogenic 10Be in middle European river terraces. Earth and Planetary Science Letters 204, 307-320.

Serreze, M., Francis, J., 2006. The Arctic Amplification Debate. Climatic Change 76, 241-264.

Serreze, M.C., Barry, R.G., 2011. Processes and impacts of Arctic amplification: A research synthesis. Global and Planetary Change 77, 85-96.

Sigl, M., McConnell, J.R., Layman, L., Maselli, O., McGwire, K., Pasteris, D., Dahl-Jensen, D., Steffensen, J.P., Vinther, B., Edwards, R., Mulvaney, R., Kipfstuhl, S., 2013. A new bipolar ice core record of volcanism from WAIS Divide and NEEM and implications for climate forcing of the last 2000 years. Journal of Geophysical Research: Atmospheres 118, 1-19.

Simpson, M.J.R., Milne, G.A., Huybrechts, P., Long, A.J., 2009. Calibrating a glaciological model of the Greenland ice sheet from the Last Glacial Maximum to present-day using field observations of relative sea level and ice extent. Quaternary Science Reviews 28, 1631-1657.

Small, E.E., Anderson, R.S., Repka, J.L., Finkel, R., 1997. Erosion rates of alpine bedrock summit surfaces deduced from in situ ^{10}Be and ^{26}Al. Earth and Planetary Science Letters 150, 413-425.

Small, E.E., Anderson, R.S., 1998. Pleistocene relief production in Laramide mountain ranges, western United States. Geology 26, 123-126.

Staiger, J., Gosse, J., Johnson, J., Fastook, J., Gray, J., Stockli, D., Stockli, L., Finkel, R., 2005. Quaternary relief generation by polythermal glacier ice. Earth Surface Processes and Landforms 30, 1145-1159.

Staiger, J., Gosse, J., Little, E., Utting, D., Finkel, R., Johnson, J., Fastook, J., 2006. Glacial erosion and sediment dispersion from detrital cosmogenic nuclide analyses of till. Quaternary Geochronology 1, 29-42.

Stanford, J.D., Rohling, E.J., Bacon, S., Roberts, A.P., Grousset, F.E., Bolshaw, M., 2011. A new concept for the paleoceanographic evolution of Heinrich event 1 in the North Atlantic. Quaternary Science Reviews 30, 1047-1066.

Steer, P., Huismans, R.S., Valla, P.G., Gac, S., Herman, F., 2012. Bimodal Plio-Quaternary glacial erosion of fjords and low-relief surfaces in Scandinavia. Nature Geosci 5, 635-639.

Steig, E.J., Wolfe, A.P., Miller, G.H., 1998. Wisconsinan refugia and the glacial history of eastern Baffin Island, Arctic Canada: Coupled evidence from cosmogenic isotopes and lake sediments. Geology 26, 835-838.

Steinhilber, F., Beer, J., Fröhlich, C., 2009. Total solar irradiance during the Holocene. Geophysical Research Letters 36, L19704.

Stern, T.A., Baxter, A.K., Barrett, P.J., 2005. Isostatic rebound due to glacial erosion within the Transantarctic Mountains. Geology 33, 221-224.

Stokes, C.R., Tarasov, L., Dyke, A.S., 2012. Dynamics of the North American Ice Sheet Complex during its inception and build-up to the Last Glacial Maximum. Quaternary Science Reviews 50, 86-104.

Stroeve, J., Holland, M.M., Meier, W., Scambos, T., Serreze, M., 2007. Arctic sea ice decline: Faster than forecast. Geophysical Research Letters 34, L09501.

Stroeven, A.P., Fabel, D., Hättestrand, C., Harbor, J., 2002. A relict landscape in the centre of Fennoscandian glaciation: cosmogenic radionuclide evidence of tors preserved through multiple glacial cycles. Geomorphology 44, 145-154.

Stuiver, M., Reimer, P.J., 1993. Extended ^{14}C data base and revised CALIB 3.0 ^{14}C age calibration program. Radiocarbon 35, 215-230.

Sugden, D., 1968. The selectivity of glacial erosion in the Cairngorm Mountains, Scotland. Transactions of the Institute of British Geographers, 79-92.

Sugden, D., 1977. Reconstruction of the morphology, dynamics, and thermal characteristics of the Laurentide Ice Sheet at its maximum. Arctic and Alpine Research 9, 21-47.

Sugden, D., Watts, S., 1977. Tors, felsenmeer, and glaciation in northern Cumberland Peninsula, Baffin Island. Canadian Journal of Earth Sciences 14, 2817-2823.

Sugden, D., 1978. Glacial erosion by the Laurentide ice sheet. Journal of Glaciology 20, 367-391.

Svensson, A., Andersen, K.K., Bigler, M., Clausen, H.B., Dahl-Jensen, D., Davies, S., Johnsen, S.J., Muscheler, R., Parrenin, F., Rasmussen, S.O., 2008. A 60 000 year Greenland stratigraphic ice core chronology. Climate of the Past 4, 47-57.

Tarasov, L., Dyke, A.S., Neal, R.M., Peltier, W.R., 2012. A data-calibrated distribution of deglacial chronologies for the North American ice complex from glaciological modeling. Earth and Planetary Science Letters 315–316, 30-40.

Taylor, J., 1997. Introduction to error analysis: the study of uncertainties in physical measurements, 2nd ed. Univ. Sci. Books, Mill Valley, Calif.

Thiébault, F., Cremer, M., Debrabant, P., Foulon, J., Nielsen, O., Zimmerman, H., 1989. Analysis of sedimentary facies, clay mineralogy, and geochemistry of the Neogene-Quaternary sediments in Site 645, Baffin Bay. Proc. Ocean Drill. Program Sci. Results, 105, p. 83-100.

Trouet, V., Esper, J., Graham, N.E., Baker, A., Scourse, J.D., Frank, D.C., 2009. Persistent positive North Atlantic Oscillation mode dominated the Medieval Climate Anomaly. Science 324, 78-80.

Vieira, L.E.A., Solanki, S.K., Krivova, N.A., Usoskin, I., 2011. Evolution of the solar irradiance during the Holocene. Astronomy & Astrophysics 531, A6-A16.

Vinther, B., Clausen, H., Johnsen, S., Rasmussen, S., Andersen, K., Buchardt, S., Dahl-Jensen, D., Seierstad, I., Siggaard-Andersen, M., Steffensen, J., 2006. A synchronized dating of three Greenland ice cores throughout the Holocene. Journal of Geophysical Research 111, D13102.

von Blanckenburg, F., 2005. The control mechanisms of erosion and weathering at basin scale from cosmogenic nuclides in river sediment. Earth and Planetary Science Letters 237, 462-479.

Waltari, E., Demboski, J., Klein, D., Cook, J., 2004. A molecular perspective on the historical biogeography of the northern high latitudes. Journal of Mammalogy 85, 591-600.

Wang, M., Overland, J.E., 2009. A sea ice free summer Arctic within 30 years? Geophysical Research Letters 36, L07502.

Wanner, H., Beer, J., Bütikofer, J., Crowley, T.J., Cubasch, U., Flückiger, J., Goosse, H., Grosjean, M., Joos, F., Kaplan, J.O., Küttel, M., Müller, S.A., Prentice, I.C., Solomina, O., Stocker, T.F., Tarasov, P., Wagner, M., Widmann, M., 2008. Mid- to Late Holocene climate change: an overview. Quaternary Science Reviews 27, 1791-1828.

Watts, S.H., 1979. Some observations on rock weathering, Cumberland Peninsula, Baffin Island. Canadian Journal of Earth Sciences 16, 977-983.

Whalen, J.B., Sanborn-Barrie, M., Young, M., 2012. Geochemical data from Archean and Paleoproterozoic plutonic and volcanic rocks of Cumberland Peninsula, eastern Baffin Island, Nunavut. Geological Survey of Canada, Open File 6933.

Whipple, K.X., Kirby, E., Brocklehurst, S.H., 1999. Geomorphic limits to climate-induced increases in topographic relief. Nature 401, 39-43.

Willenbring, J.K., von Blanckenburg, F., 2010a. Long-term stability of global erosion rates and weathering during late-Cenozoic cooling. Nature 465, 211-214.

Willenbring, J.K., von Blanckenburg, F., 2010b. Meteoric cosmogenic Beryllium-10 adsorbed to river sediment and soil: Applications for Earth-surface dynamics. Earth-Science Reviews 98, 105-122.

Williams, A.N., 2012. The use of summed radiocarbon probability distributions in archaeology: A review of methods. Journal of Archaeological Science 39, 578-589.

Williams, L.D., 1978. The Little Ice Age glaciation level on Baffin Island, Arctic Canada. Palaeogeography, Palaeoclimatology, Palaeoecology 25, 199-207.

Wolfe, A., 1994. Late Wisconsinan and Holocene diatom stratigraphy from Amarok Lake, Baffin Island, N.W.T., Canada. Journal of Paleolimnology 10, 129-139.

Wolfe, A., Steig, E., Kaplan, M., 2001. An alternative model for the geomorphic history of late Wisconsinan surfaces on eastern Baffin Island: A comment on Bierman et al.(1999). Geomorphology 39, 251-254.

Wolfe, A.P., 1996. Wisconsinan refugial landscapes, eastern Baffin Island, Northwest Territories. Canadian Geographer 40, 81-87.

Wolfe, A.P., Härtling, J.W., 1996. The late Quaternary development of three ancient tarns on southwestern Cumberland Peninsula, Baffin Island, Arctic Canada: paleolimnological evidence from diatoms and sediment chemistry. Journal of Paleolimnology 15, 1-18.

Wolfe, A.P., Frechette, B., Richard, P.J.H., Miller, G.H., Forman, S.L., 2000. Paleoecology of a >90,000-year lacustrine sequence from Fog Lake, Baffin Island, Arctic Canada. Quaternary Science Reviews 19, 1677-1699.

Wolken, G.J., Sharp, M.J., England, J.H., 2008. Changes in late-Neoglacial climate inferred from former equilibrium-line altitudes in the Queen Elizabeth Islands, Arctic Canada. The Holocene 18, 629-641.

Womack, W.R., Schumm, S.A., 1977. Terraces of Douglas Creek, northwestern Colorado: An example of episodic erosion. Geology 5, 72-76.

Young, N.E., Briner, J.P., Rood, D.H., Finkel, R.C., 2012. Glacier extent during the Younger Dryas and 8.2-ka event on Baffin Island, Arctic Canada. Science 337, 1330-1333.

Zielinski, G.A., Mayewski, P.A., Meeker, L.D., Whitlow, S., Twickler, M.S., Morrison, M., Meese, D.A., Gow, A.J., Alley, R.B., 1994. Record of volcanism since 7000 B.C. from the GISP2 Greenland Ice Core and implications for the volcano-climate system. Science 264, 948-952.

Zielinski, G.A., Mershon, G.R., 1997. Paleoenvironmental implications of the insoluble microparticle record in the GISP2 (Greenland) ice core during the rapidly changing climate of the Pleistocene–Holocene transition. Geological Society of America Bulletin 109, 547-559.

APPENDIX A1 - Supplementary File for Margreth et al. (2014): Neoglacial Ice Expansion and Late Holocene Cold-Based Ice Cap Dynamics on Cumberland Peninsula, Baffin Island, Arctic Canada

A1.1 DISSIMILAR PRESERVATION OF MACROFOSSILS

During sample characterisation and separation of individual macrofossils for radiocarbon dating, it became apparent that some macrofossils displayed near perfect preservation whereas other moss fragments were less preserved with flattened or discoloured leaves. In particular, preservation of *Polytrichum/Pogonatum* mosses in sample 09SRB-K049A-01, which yielded a modern radiocarbon activity (UCIAMS-77694, Table 2.1, main text), are pristine with intact, long, white awns at the leaf tips (Fig. A1.1 a-b). The white awns on the moss leaves are complete in length to a fine tip and most are in growth position (straight up). Other moss types in this sample, e.g., *Pohlia* sp., which were not submitted for dating, are green in colouration indicating chlorophyll-retaining mosses of modern age. Sample 09SRB-K049A-01 is a modern contaminant of a windswept mat of mosses with intact roots deposited at the collection site.

In selecting macrofossils for radiocarbon dating from other samples that contained this moss type (*Polytrichum/Pogonatum*), the pristine, modern aged mosses in sample 09SRB-K049A-01 were used as reference material for comparison. For example, the awns of *Polytrichum juniperinum* macrofossils in sample 09SRB-K141A-01 vary in length (mostly shorter), are often bent, and are absent on many of the leaf tips (Fig. A1.1c). These macrofossil moss fragments have been radiocarbon dated to 4.08 ka (mode, UCIAMS-135208, on a single moss fragment) and 3.98 ka (mode, UCIAMS-

135209, including five moss fragments). The similarity in ages (within 1σ AMS error) among these two measurements indicate that the ages indeed represent the time when the sample site was covered by ice or snow causing death of the organic material.

Another sample that contained dissimilarly preserved macrofossils of *Polytrichum/ Pogonatum* is sample 09SRB-K131A-01 (Fig. 2.5 c-d in main text). For AMS analysis, macrofossils of similar preservation with flattened moss depicted in Fig. 2.5c (main text) were dated to 3.38 ka (mode, UCIAMS-83985, Table 2.1, main text). Two more dates from this sample on younger-looking mosses with remnant, incomplete or absent awns (Fig. 2.5d, main text) yielded ages of 1.76 and 1.83 ka (mode, UCIAMS-135210 (on single moss fragment) and -135211 (on few moss fragments), respectively) indicating two generations of moss growth at this site. These aliquots were all from a single sample that was collected from the base of a long steep bedrock ridge (Fig. 2.6, main text). The older-appearing 3.38 ka old sample is interpreted to be subfossil organic material that was covered and killed during an earlier ice expansion phase, but preserved throughout an interim period of ice recession, possibly because it was slightly sheltered from wind. During this ice free interval, *Polytrichum/Pogonatum* re-grew either through regenerative processes (asexual, vegetative reproduction) or by spore production (sexual reproduction). Sexual reproduction is favoured since both genera are prolific spore producers. Both the old and new growth was subsequently entombed by a later ice advance event and exhumed from the retreating ice margin in AD 2009.

Fig. A1.1 Dissimilarly preserved macrofossils of *Polytrichum/Pogonatum* mosses. **A. & B.** Pristine moss fragments of sample 09SRB-K049A-01 with complete white awns in upright growth position yielded a modern radiocarbon activity (UCIAMS-77694). **C.** Moss fragments of sample 09SRB-K141A-01 with missing or incomplete awns with some being bent. A single macrofossil (fifth from the top) has been dated to 4.08 ka (mode, UCIAMS-135208) and the five other macrofossils yielded a radiocarbon age of 3.98 ka (mode, UCIAMS-135209).

A1.2 EFFECTS OF CALIBRATION PROCESS ON SUMMED PROBABILITY PLOTS

Plateaus and risers (steeper slopes) of the Holocene calibration curve (measured ^{14}C vs. treering calibrated age, IntCal09 (Reimer et al., 2009)) are mostly related to short-term variations in solar activity and Earth's magnetic field strength (Stuiver et al., 1991). The effect of the shape of the calibration curve on calibrated age probability distributions has been previously recognized (e.g., Bartlein et al., 1995) and recently has gained more attention owing to a more widespread use of summed probability plots (Chiverrell et al., 2011; Bamforth and Grund, 2012; Williams, 2012; Armit et al., 2013).

Some of the peaks in our summed probability plot are related to risers and some low probability areas coincide with plateaus in the calibration curve (Fig. A1.2). Not all peaks or low probability areas in the moss age probability distribution correspond to risers or plateaus in the calibration curve. Vice versa, not all plateaus or risers in the calibration curve are represented as low probability areas or peaks in the moss age

probability distribution. However, it is interesting to explore the effect of plateaus and risers in the calibration curve on summed probability plots of radiocarbon ages to increase the confidence in the observed moss age probability distribution. Plateaus tend to smooth the summed probability distribution while risers condense several hundred years of measured radiocarbon ages into a small range of calibrated ages. The amplitude of the sharp narrow peaks is thus amplified through superimposition of multiple radiocarbon dates (Williams, 2012). Interestingly, during the Little Ice Age (LIA, AD 1100 - 1850, 750 - 100 yr BP) these peaks are also concurrent with high volcanic activity (Gao et al., 2008; Sigl et al., 2013). Representative radiocarbon ages were generated for each recorded large volcanic eruption using the R_simulate function of OxCal 4.2 (Bronk Ramsey, 2009) and calibrated in the same manner as was the relict moss data using Calib 6.1.0 (Stuiver and Reimer, 1993). In particular, the volcanism reconstruction by Gao et al. (2008) displays peaks that are synchronous with the peaks in the relict moss age distribution, whereas peaks are more subdued for the Sigl et al. (2013) volcanism record, which is based on a single Greenland ice core (Fig. A1.2b).

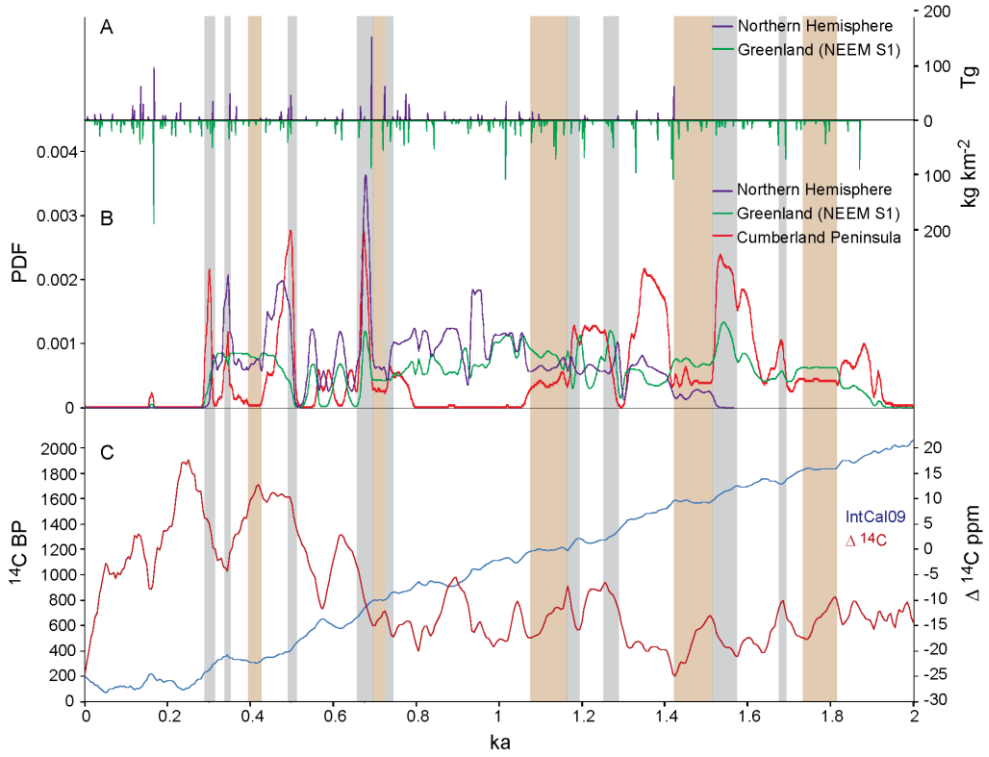

Fig. A1.2 Correspondence of some risers (steep slopes, grey shading) and some plateaus (brown shading) of the calibration curve to some peaks and some troughs in summed probability distributions. **A.** Volcanic activity reconstructed from multiple ice cores in the Northern Hemisphere (purple, volcanic stratospheric sulfate aerosol loading (Tg), Gao et al. 2008) and based on a single Greenland ice core (green, volcanic sulfate deposition (kg km^{-2}), Sigl et al. 2013). **B.** Summed probability distributions of Cumberland Peninsula moss data for the last 2 ka (red, excluding the youngest seven samples and two caribou samples) and both volcanic activity records (colours as above, excluding eruptions < 250 a). **C.** IntCal09 (blue) calibration curve and past variation of ^{14}C concentration in the atmosphere (Δ^{14}C, red).

Different methods have been proposed to account for the influence of the shape of the calibration curve on summed probability distributions. All of these methods are based on a summed probability distribution generated from a simulated dataset of equally distributed radiocarbon dates (50-year interval starting at 275 years up to 1975 years, n = 35, Fig. A1.3a, Chiverrell et al., 2011; Bamforth and Grund, 2012; Armit et al., 2013). The simulated radiocarbon dataset is calibrated using Calib 6.1.0 after assigning a 1σ error to each radiocarbon date (Fig. 1.3b-c). Simple approaches include subtraction of

the simulated summed probability anomalies (i.e., from evenly spaced radiocarbon dates) from the actual summed probability (moss data) for each calibrated year (one year interval) or the division of the latter by the former (Fig. A1.3d, Chiverrell et al., 2011). We have derived a different method using the maximum probability of the simulated radiocarbon dataset (i.e., the highest peak in the simulated probability distribution) to normalise the measured summed probability distribution (moss data) for each calibrated year (one year bin) according to following equation:

$$P(\text{normalised})_{\text{cal yr}} = P(\text{measured})_{\text{cal yr}} * ((P(\text{simulated})_{\text{max}} - P(\text{simulated})_{\text{cal yr}} * f) / P(\text{simulated})_{\text{max}})$$

Where $P(\text{normalised})_{\text{cal yr}}$ is the normalised probability in a particular calibrated year
$P(\text{measured})_{\text{cal yr}}$ is the measured probability in the same calibrated year
$P(\text{simulated})_{\text{max}}$ is the maximum probability of the simulated dataset
$P(\text{simulated})_{\text{cal yr}}$ is the simulated probability in the same calibrated year
f is a scaling factor

The maximum probability of the simulated radiocarbon dataset was chosen to minimise the residual effect of the calibration on the measured summed probability distribution. With this approach the amplitude of peaks in the actual summed probability distribution are scaled according to the simulated radiocarbon dataset, whose summed probability distribution is primarily a function of the shape (risers and plateaus) of the calibration curve (Fig. A1.2c). Interestingly, when simulating equally spaced (50-year interval starting at 275 years up to 1975 years, n = 35, Fig. A1.4a) calendar years, which were then transferred into representative radiocarbon ages using R_simulate function of OxCal 4.2 (Fig. A1.4b) and re-calibrated using Calib 6.1.0 (Fig. 1.4c), the resulting probability density function appears fairly smooth without large troughs or peaks (Fig. 1.4d).

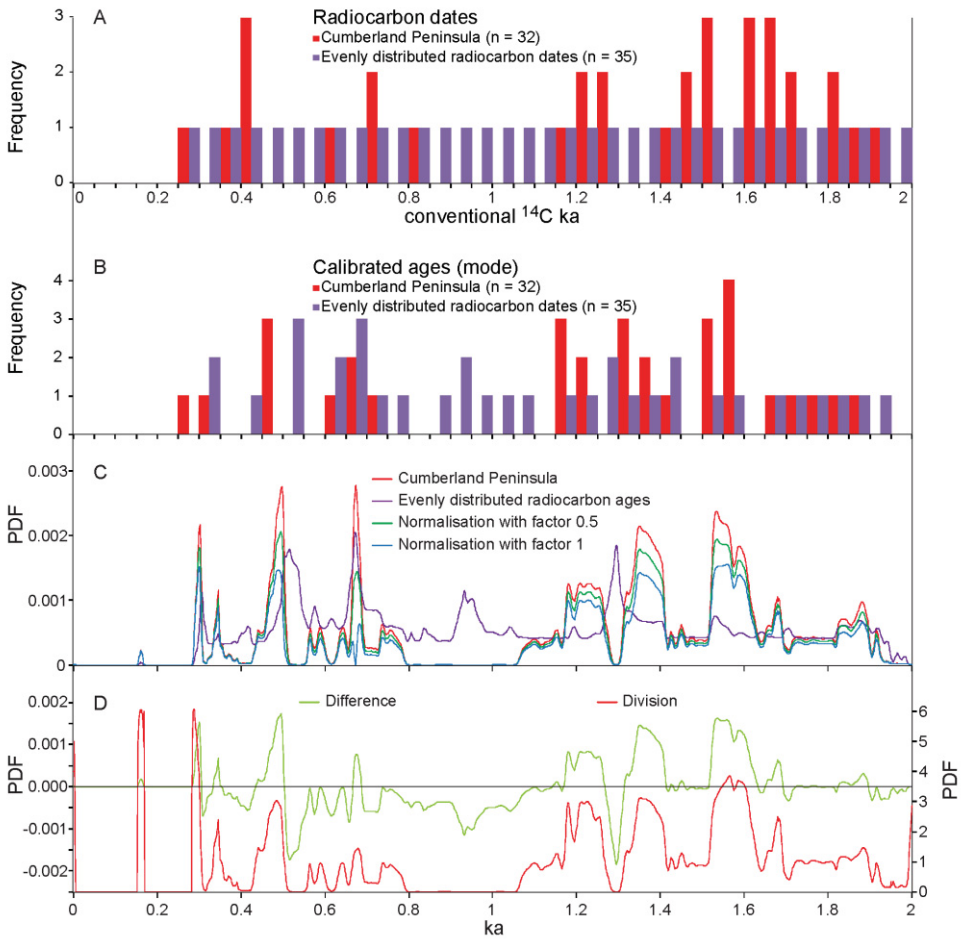

Fig. A1.3 Approaches to normalizing summed probability distributions. **A.** Histogram of measured radiocarbon ages from relict moss samples for the last 2 ka in 50 year bins (red, excluding youngest seven samples and two caribou samples, n = 32) and simulated dataset of evenly spaced radiocarbon dates of similar size (n = 35, purple) shown on a conventional ^{14}C ka timescale. **B.** Histogram of calibrated ages of both datasets shown above: modal probability of calibrated age ranges of moss samples (red), and modal probability of calibrated age ranges of simulated radiocarbon dates (purple), to which a 1σ error of 20 years was assigned before calibration (comparable to the average error of the moss radiocarbon ages). **C.** Summed probability plot of moss samples (red) and simulated dataset (purple), as well as a new approach derived to reduce the amplitude of individual peaks using the maximum probability of the simulated dataset (blue, scaling factor f = 1 (full scaling), green, f = 0.5 (half scaling)). **D.** Two previously used methods (Chiverrell et al. 2011), in which the simulated probability is subtracted from the measured probability for each calibrated year (light green, vertical axis to the left), and division of the latter by the former (red, vertical axis to the right).

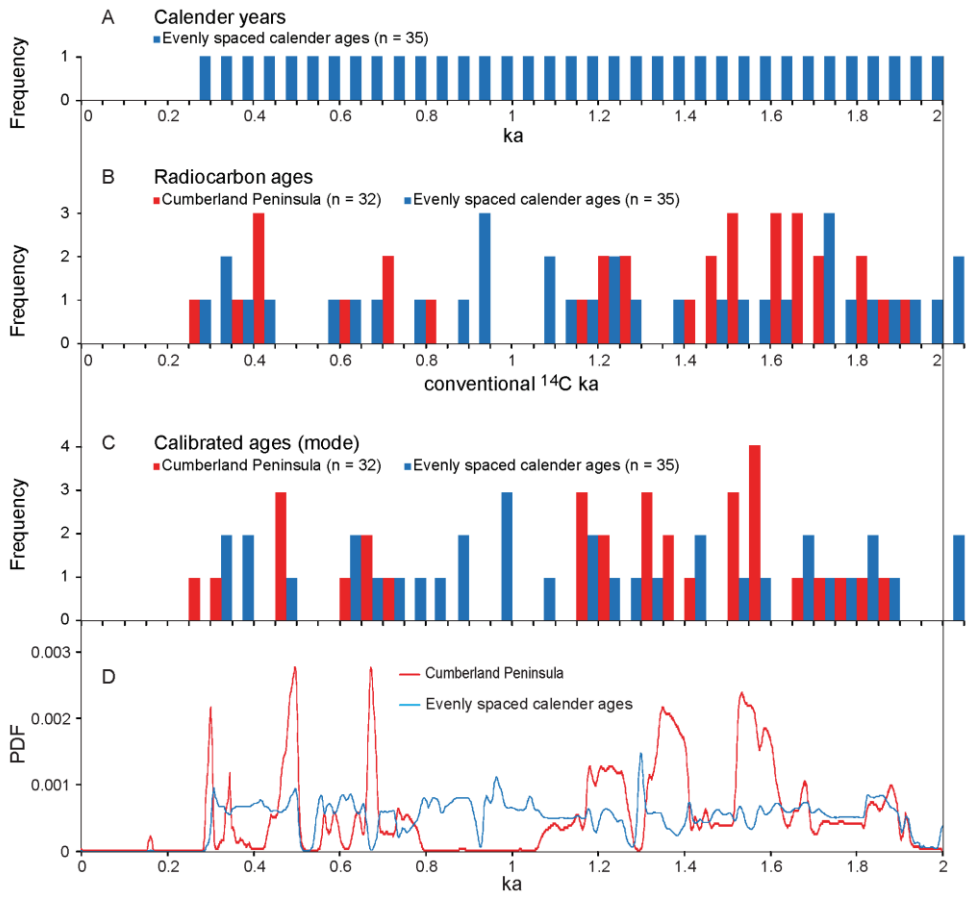

Fig. A1.4 Comparison of Cumberland Peninsula moss data with a simulated dataset of equally spaced calendar ages of similar size. **A.** Histogram of simulated dataset of equally spaced calendar ages shown on a 'real' (calendar) timescale (blue, n = 35). **B.** Histogram of radiocarbon dates for simulated calendar age dataset (blue) and measured radiocarbon ages of moss samples for the last 2 ka (red, n = 32, excluding seven youngest samples and two caribou samples), both shown on a conventional radiocarbon timescale. **C.** Histogram of (re-) calibrated simulated dataset (blue, modal probability of calibrated age ranges) and calibrated moss data (red, modal probability of calibrated age ranges). **D.** Summed probability distributions of both dataset (colour coding as above).

A1.3 LOWERING OF REGIONAL ELA

The general trend of decreasing elevation of sample sites with time is more obvious if individual ice caps are considered (Fig. A1.5). Assuming that the organic material was killed due to ice advance related to a drop of the regional ELA, the change in elevation of sample sites with time can be used to approximate the drop in temperature with time. Using four ice caps, for which the fossil moss ages span more than 1 ka, we can estimate

the lowering of the regional ELA from the difference of the highest and the lowest sample elevation or the regression line fitted through the sample points (Table A1.1). The corresponding decline in temperature can be calculated using a temperature lapse rate of 4.9 ± 0.4 °C per 1000 m (Gardner et al., 2009). This approach, of course, assumes that ELA changes were not influenced by changes in amounts or seasonality of precipitation.

The calculated net temperature changes range from -0.8 to -2.4 °C, which occur over time intervals of 1.6 to 3.6 ka (Table A1.1a). The rate of net temperature change varies between -0.20 ± 0.10 to -1.12 ± 0.14 °C ka^{-1} with comparable values calculated using both methods (difference of highest and lowest sample elevation vs. slope of regression line) for each ice cap. Ice cap 9, located furthest south, yielded the lowest rate of temperature change. For ice cap 4, two different values were calculated using the highest and lowest sample elevation difference, once including the youngest samples with non-unique calibrated age ranges and once excluding these samples. The rate of temperature change obtained using the slope of the regression line yielded a value in between the two former estimates. The range of values of the rate in temperature change obtained from different ice caps reflects the influence of local topographic conditions on ice expansion and may also be affected by the small number of samples collected at each site. Calculating the pooled mean of all slopes of the regression lines fitted through the individual ice caps, yield an overall cooling rate of -0.47±0.09 °C ka^{-1} and a temperature decrease of -2.4 ± 0.5 °C over the past 5 ka. These estimates are roughly twice the values inferred from the regression line fitted through all collected samples (see main text: temperature change -0.22 ± 0.09°C ka^{-1}, temperature decline of -1.1 ± 0.5 °C over the

past 5 ka). The former value based on the regression fitted for individual ice caps is also comparable to the estimate for Neoglacial cooling (-2.7 ± 0.7 °C over 5 ka) obtained by Miller et al. (2013) from radiocarbon dated fossil vegetation collected along cold-based ice caps on Baffin Island (see main text for further discussion).

These values provide a rough minimum estimate of regional temperature change during Neoglaciation because we have likely not captured the full range in elevation (i.e., older ages at higher elevation) and we did not reconstruct ELA during the maximum ice extent indicated by the lichen-kill trimlines. The inferred rate of temperature change may have been reversed during intervals of ice recession as indicated by the hiatuses in the moss data. The actual rate of short term temperature change was probably higher than the net rates determined here.

Table A1.1 Estimates of Neoglacial temperature change calculated from a) the highest and lowest elevation of individual moss samples and b) the regression line fitted through all sample points at a particular ice cap. A temperature lapse rate of 4.9 ± 0.4 °C per 1000 m was used to infer changes in temperature from elevation differences or from the slope of the regression lines (Gardner et al., 2009).

	a) Individual sample locations				b) Regression line		
Ice cap	Δ Elev.	Δ Time	Δ Temp	Rate	Slope	Rate	Δ Temp
	m	ka	°C	°C ka^{-1}	m a^{-1}	°C ka^{-1}	°C in 5 ka
4	496[a]	3.6	-2.4±0.2	-0.68±0.06	0.11±0.03	-0.54±0.16	-2.7±0.8
	302[b]	3.2	-1.5±0.1	-0.46±0.04			
5	288	3.5	-1.4±0.1	-0.40±0.04	0.05±0.01	-0.25±0.08	-1.2±0.4
7	362	1.6	-1.8±0.2	-1.11±0.10	0.23±0.02	-1.12±0.14	-5.6±0.7
9	158	3.2	-0.8±0.1	-0.24±0.04	0.04±0.02	-0.20±0.10	-1.0±0.5
	Pooled mean of all regression line slopes:				0.097±0.017	-0.47±0.09	-2.4±0.5

[a]including youngest samples with non-unique calibrated age ranges
[b]excluding these youngest samples

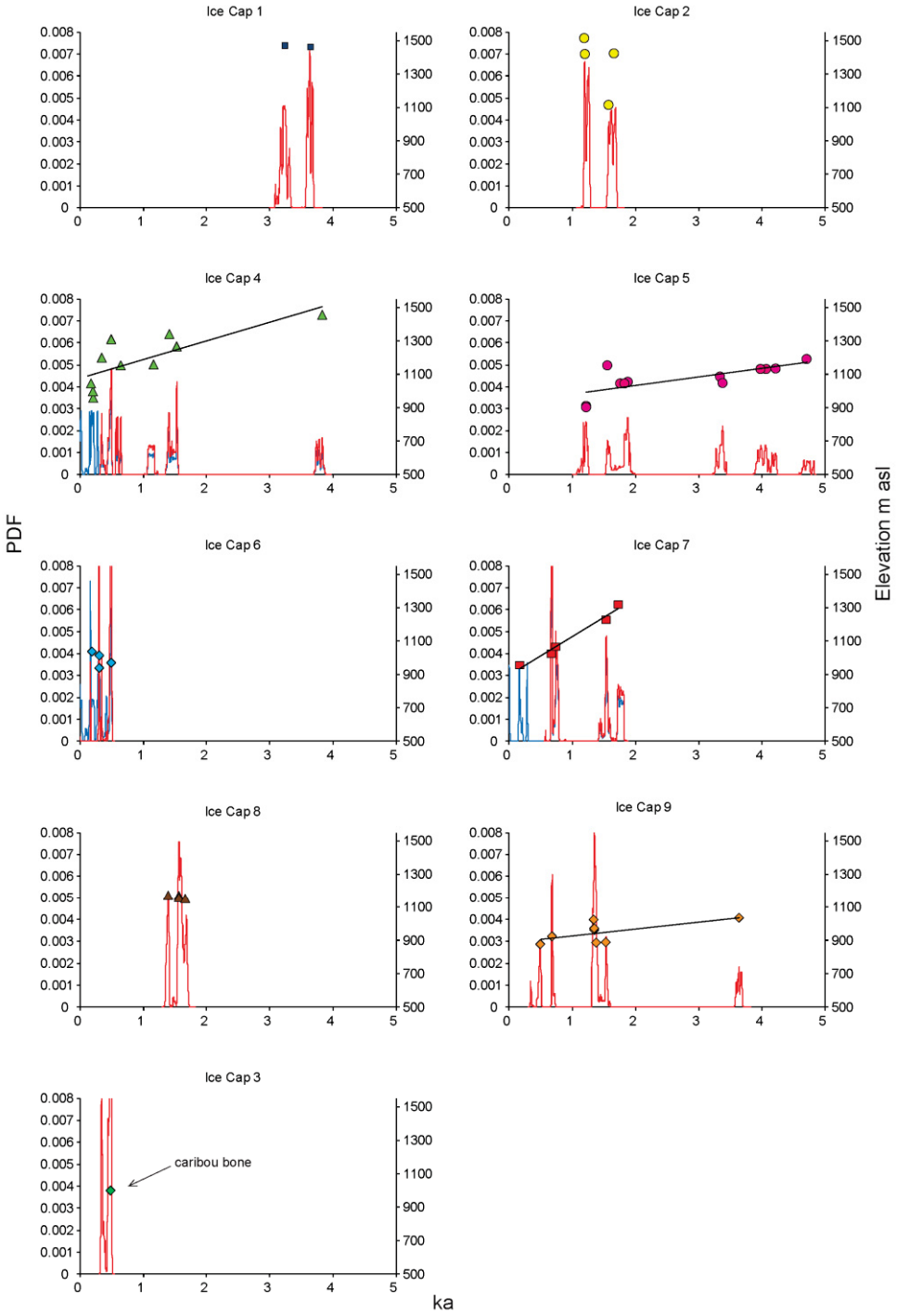

Fig. A1.5 Elevation vs. age plots for all sampled ice caps (for location see Fig. 2.3 in main text). For each ice cap the summed probability age distribution is shown in red excluding the youngest samples with non-unique calibrated age ranges and in blue for all samples. Elevations are plotted against the mode of the calibrated age distribution of the samples. Note: the caribou samples have been included in the summed probability plots and their occurrence is indicated in the individual plots. Colours and shapes of elevation vs. age points are the same than used in Fig. 2.7b (in main text).

A1.4 PALEOCLIMATE PROXIES

In addition to the paleoclimate proxies discussed in Margreth et al., we have compared our moss age distribution with several other paleoclimate datasets (Fig. A1.6). However, none of these additional datasets showed clear correlations with peaks in the moss radiocarbon age distribution. We thus concluded that volcanism and changing solar activity were the most influential climate forcing on ice cap expansion on decadal to centennial timescales, prior to accelerated ice recession observed in recent years related to anthropogenic greenhouse gas emissions. It seems that short-term atmospheric perturbations caused by large volcanic eruptions and varying solar irradiance are well documented in the Arctic fossil record owing to the sensitive response of cold-based ice caps to eruption-induced cooling. The same signal appears to be attenuated and possibly blended with regional climate effects in ice cores. The gradual decrease of summer insolation at high latitudes induced steadily declining temperatures and increased seasonality in the Arctic (Fig. A1.6b). This gradual decrease in temperature is documented by generally decreasing delta ^{18}O values observed in many Arctic ice cores (Penny, Devon and Agassiz ice caps) over the last 5 ka (Fig. A1.6 c-e, Fisher, 1979; Fisher et al., 1983; 1995; 1998; Vinther et al., 2008). In the Devon ice core delta ^{18}O values decline after reaching a pre-industrial maximum shortly before 4.5 ka. A similar smooth decline of delta ^{18}O is observed in the NGRIP ice core (Fig. A1.6f, Vinther et al., 2006), whereas temperature reconstructions derived from the GRIP (Dahl-Jensen et al., 1998) and GISP2 (Alley, 2000) ice cores show slightly larger variation over the last 5 ka (Fig. A1.6 g-i). In particular, lower temperatures during the LIA and relatively warmer temperatures during the Medieval Warm Period (MWP, AD 950 – 1250, 1000 – 750 yr BP) are noticeable, but no more precise correlation can be seen between the Cumberland

Peninsula moss radiocarbon age distribution (Fig. A1.6a) and temperature or precipitation changes recorded in the Greenland ice cores (Fig. A1.6 f-i).

A varve record interpreted as summer temperature has been obtained from sediments at Donard Lake on Cumberland Pensinula (Fig. A1.7a, Moore et al., 2001). Annual couplets of light-coloured, coarser-grained layers and thin, dark-coloured, fine-grained layers (varves) are visible for the last 1.2 ka. The thickness of the coarser-grained layers reflects changes in average summer temperature affecting melting of the Caribou Glacier, which provided the main source of sediment. For calibration of varve thickness to summer temperatures, instrumental data from the Cape Dyer DEW Line radar site was used. Over the instrumental record a good agreement between varve thickness and June, July and August temperatures was seen, however with an additional variance probably related to spatial heterogeneity of climate variability (Moore et al., 2001). This spatial heterogeneity might also be the case when comparing the summer temperature record from Donard Lake with the fossil moss radiocarbon age distribution documenting ice cap expansion on upland plateaus approximately 150 km distant from Cape Dyer (Fig. A1.7b). Some of the peaks in the moss radiocarbon age distribution during the LIA seem to correlate with cold summer temperatures recorded at Donard Lake, but the varve thickness record shows a high variability from year to year and no clear trend in summer temperature change can be seen over the last 1.2 ka. In order to capture the response of plateau ice caps to the high-frequency climate variability recorded in the Donard Lake varve record, a larger moss sample size (hundreds) would be required. Moreover, different response times to climate change between cold-based ice

caps and warm-based glaciers could account for some differences between the moss data and the summer temperature record based on varve thickness.

Fig. A1.6 *(Next page)* Selected paleoclimate records are compared to moss age distribution over the last 5 ka. **A.** Cumberland Peninsula moss data (red, excluding youngest seven samples and three caribou samples; blue, only excluding three caribou samples). **B.** Integrated summer insolation at 65 °N (Huybers, 2006). **C.** Delta ^{18}O values of Penny Ice Cap core (Fisher et al., 1998). **D.** Devon ice cap delta ^{18}O record shown as 50 year averages (blue) and 5 year averages for the last 2.7 ka (blue, Fisher, 1979; Fisher et al., 1983). **E.** Agassiz ice cap delta ^{18}O record (20 year averages, Vinther et al., 2008). **F.** NGRIP delta ^{18}O record (20 year averages, Vinther et al., 2006). **G.** GRIP temperature record (Dahl-Jensen et al., 1998). **H.** GISP2 temperature record (Alley, 2000). **I.** GISP2 accumulation record (Alley, 2000).

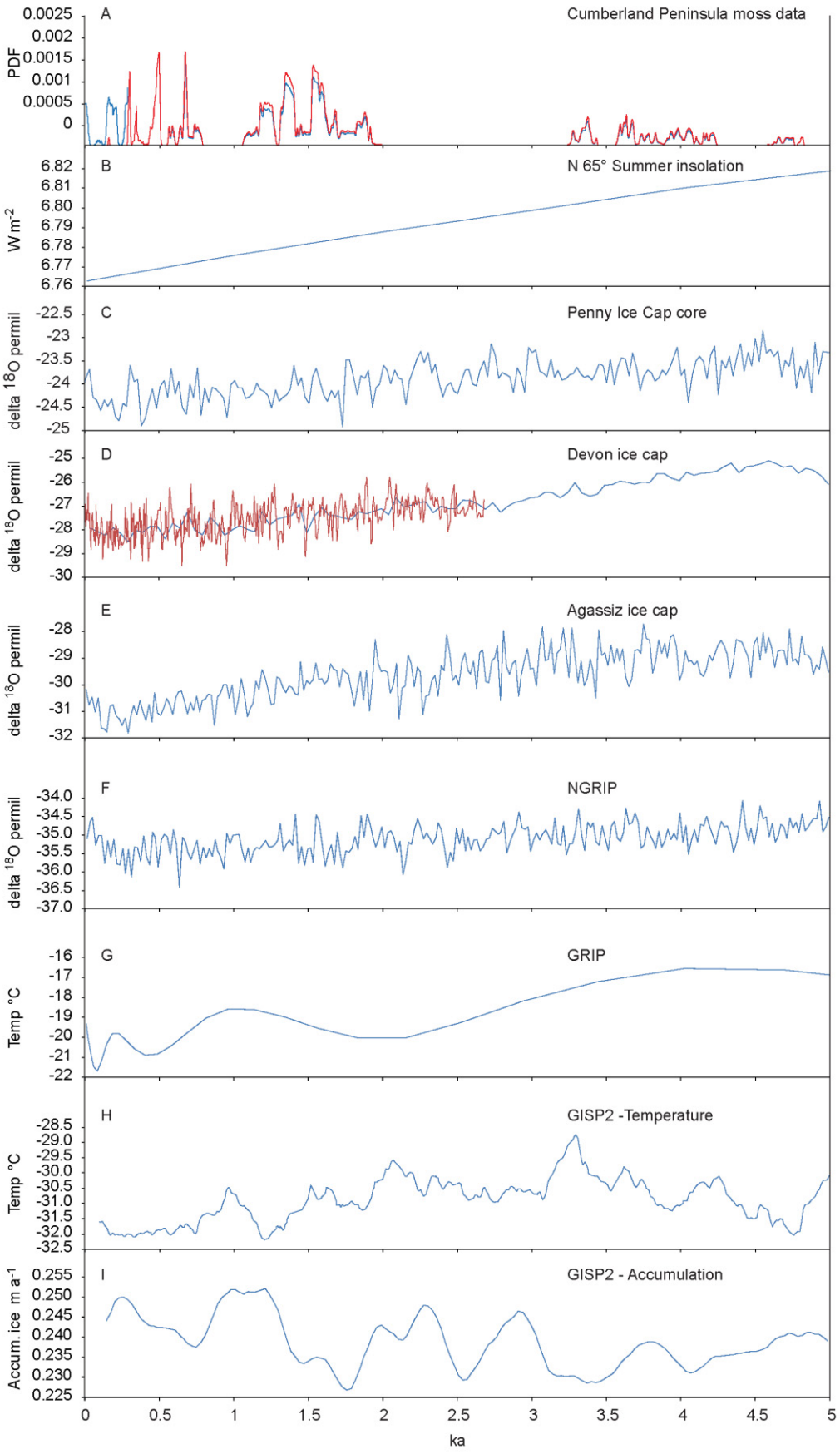
A
Cumberland Peninsula moss data
PDF
0.0025
0.002
0.0015
0.001
0.0005
0
B
N 65° Summer insolation
W m-2
6.82
6.81
6.80
6.79
6.78
6.77
6.76
C
Penny Ice Cap core
delta 18O permil
-22.5
-23
-23.5
-24
-24.5
-25
D
Devon ice cap
delta 18O permil
-25
-26
-27
-28
-29
-30
E
Agassiz ice cap
delta 18O permil
-28
-29
-30
-31
-32
F
NGRIP
delta 18O permil
-34.0
-34.5
-35.0
-35.5
-36.0
-36.5
-37.0
G
GRIP
Temp °C
-16
-17
-18
-19
-20
-21
-22
H
GISP2 -Temperature
Temp °C
-28.5
-29.0
-29.5
-30.0
-30.5
-31.0
-31.5
-32.0
-32.5
I
GISP2 - Accumulation
Accum. ice m a-1
0.255
0.250
0.245
0.240
0.235
0.230
0.225
0
0.5
1
1.5
2
2.5
3
3.5
4
4.5
5
ka

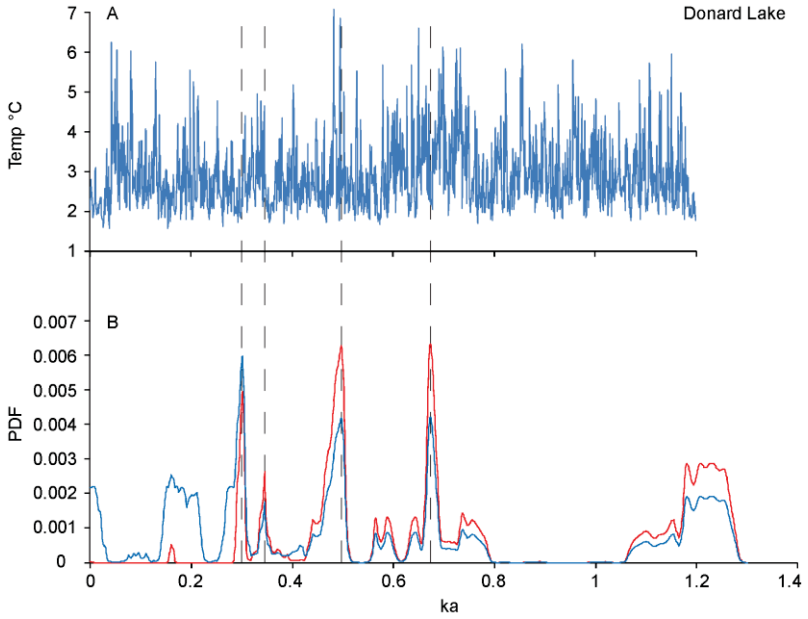

Fig. A1.7 Donard Lake summer temperature record compared to the last 1.3 ka of Cumberland Peninsula moss age distribution. **A.** Summer temperatures inferred from varve thickness at Donard Lake (66° 40' N, 61° 21' W; Moore et al., 2001); **B.** Cumberland Peninsula summed probability distributions for the last 1.3 ka (red, excluding seven youngest samples and one caribou sample; blue, excluding only one caribou sample).

A1.5 REFERENCES FOR A1

Alley, R.B., 2000. The Younger Dryas cold interval as viewed from central Greenland. Quaternary Science Reviews 19, 213-226.

Armit, I., Swindles, G.T., Becker, K., 2013. From dates to demography in later prehistoric Ireland? Experimental approaches to the meta-analysis of large ^{14}C data-sets. Journal of Archaeological Science 40, 433-438.

Bamforth, D.B., Grund, B., 2012. Radiocarbon calibration curves, summed probability distributions, and early Paleoindian population trends in North America. Journal of Archaeological Science 39, 1768-1774.

Bartlein, P.J., Edwards, M.E., Shafer, S.L., Barker Jr, E.D., 1995. Calibration of radiocarbon ages and the interpretation of paleoenvironmental records. Quaternary Research 44, 417-424.

Bronk Ramsey, C., 2009. Bayesian Analysis of Radiocarbon Dates. Radiocarbon 51, 337-360.

Chiverrell, R.C., Thorndycraft, V.R., Hoffmann, T.O., 2011. Cumulative probability functions and their role in evaluating the chronology of geomorphological events during the Holocene. Journal of Quaternary Science 26, 76-85.

Dahl-Jensen, D., Mosegaard, K., Gundestrup, N., Clow, G.D., Johnsen, S.J., Hansen, A.W., Balling, N., 1998. Past temperatures directly from the Greenland Ice Sheet. Science 282, 268-271.

Fisher, D.A., 1979. Comparison of 105 years of oxygen isotope and insoluble impurity profiles from the Devon Island and Camp Century ice cores. Quaternary Research 11, 299-305.

Fisher, D.A., Koerner, R.M., Paterson, W.S.B., Dansgaard, W., Gundestrup, N., Reeh, N., 1983. Effect of wind scouring on climatic records from ice-core oxygen-isotope profiles. Nature 301, 205-209.

Fisher, D.A., Koerner, R.M., Reeh, N., 1995. Holocene climatic records from Agassiz Ice Cap, Ellesmere Island, NWT, Canada. The Holocene 5, 19-24.

Fisher, D.A., Koerner, R.M., Bourgeois, J.C., Zielinski, G., Wake, C., Hammer, C.U., Clausen, H.B., Gundestrup, N., Johnsen, S., Goto-Azuma, K., Hondoh, T., Blake, E., Gerasimoff, M., 1998. Penny Ice Cap Cores, Baffin Island, Canada, and the Wisconsinan Foxe Dome connection: Two states of Hudson Bay ice cover. Science 279, 692-695.

Gao, C., Robock, A., Ammann, C., 2008. Volcanic forcing of climate over the past 1500 years: An improved ice core-based index for climate models. Journal of Geophysical Research: Atmospheres 113, D23111.

Gardner, A.S., Sharp, M.J., Koerner, R.M., Labine, C., Boon, S., Marshall, S.J., Burgess, D.O., Lewis, D., 2009. Near-surface temperature lapse rates over Arctic glaciers and their implications for temperature downscaling. Journal of Climate 22, 4281-4298.

Huybers, P., 2006. Early Pleistocene glacial cycles and the integrated summer insolation forcing. Science 313, 508-511.

Miller, G.H., Lehman, S.J., Refsnider, K.A., Southon, J.R., Zhong, Y., 2013. Unprecedented recent summer warmth in Arctic Canada. Geophysical Research Letters 40, 1-7.

Moore, J., Hughen, K., Miller, G., Overpeck, J., 2001. Little Ice Age recorded in summer temperature reconstruction from vared sediments of Donard Lake, Baffin Island, Canada. Journal of Paleolimnology 25, 503-517.

Reimer, P.J., Baillie, M.G.L., Bard, E., Bayliss, A., Beck, J.W., Blackwell, P.G., Ramsey, C.B., Buck, C.E., Burr, G.S., Edwards, R.L., Friedrich, M., Grootes, P.M., Guilderson, T.P., Hajdas, I., Heaton, T.J., Hogg, A.G., Hughen, K.A., Kaiser, K.F., Kromer, B., McCormac, F.G., Manning, S.W., Reimer, R.W., Richards, D.A., Southon, J.R., Talamo, S., Turney, C.S.M., van der Plicht, J., Weyhenmeyer, C.E., 2009. IntCal09 and Marine09 radiocarbon age calibration curves, 0-50,000 years cal BP. Radiocarbon 51, 1111-1150.

Sigl, M., McConnell, J.R., Layman, L., Maselli, O., McGwire, K., Pasteris, D., Dahl-Jensen, D., Steffensen, J.P., Vinther, B., Edwards, R., Mulvaney, R., Kipfstuhl, S., 2013. A new bipolar ice core record of volcanism from WAIS Divide and NEEM and implications for climate forcing of the last 2000 years. Journal of Geophysical Research: Atmospheres 118, 1-19.

Stuiver, M., Braziunas, T.F., Becker, B., Kromer, B., 1991. Climatic, solar, oceanic, and geomagnetic influences on late-glacial and holocene atmospheric $^{14}C/^{12}C$ change. Quaternary Research 35, 1-24.

Stuiver, M., Reimer, P.J., 1993. Extended ^{14}C data base and revised CALIB 3.0 14C age calibration program. Radiocarbon 35, 215-230.

Vinther, B., Clausen, H., Johnsen, S., Rasmussen, S., Andersen, K., Buchardt, S., Dahl-Jensen, D., Seierstad, I., Siggaard-Andersen, M., Steffensen, J., 2006. A synchronized dating of three Greenland ice cores throughout the Holocene. Journal of Geophysical Research 111, D13102.

Vinther, B.M., Clausen, H.B., Fisher, D.A., Koerner, R.M., Johnsen, S.J., Andersen, K.K., Dahl-Jensen, D., Rasmussen, S.O., Steffensen, J.P., Svensson, A.M., 2008. Synchronizing ice cores from the Renland and Agassiz ice caps to the Greenland Ice Core Chronology. Journal of Geophysical Research: Atmospheres 113, D08115.

Williams, A.N., 2012. The use of summed radiocarbon probability distributions in archaeology: A review of methods. Journal of Archaeological Science 39, 578-589.

APPENDIX A2 - Supplementary File for Wisconsinan Glacial Dynamics of Cumberland Peninsula, Baffin Island, Arctic Canada

A2.1 TCN CHEMISTRY DATA AND ADDITIONAL FIELD PICTURES

		Sample ID	Mass of quartz dissolved	Mass of Be carrier [a]	$^{10}Be/^{9}Be$ AMS		Lithology	Quatz content	Description
			(g)	(g)	(-)	(-)		(%)	
boulders	'central valley'	09SRB-E092A-01	35.3615	0.1975	5.04E-13 ±	9.52E-15	medium-grained meta-tonalite	15	boulder on lateral moraine ridge (Fig. 3.2c)
		09SRB-E002A-01 [b]	35.0875	0.2023			Pegmatie	30	
		09SRB-E003A-01	35.7158	0.2003	2.09E-13 ±	6.50E-15	medium-grained gneis	30	boulder near mealtwater channel
		09SRB-E004A-01	35.4866	0.1906	2.08E-13 ±	4.65E-15	medium-grained gneis with quartz veins	20	
		09SRB-E041A-01	35.4114	0.1933	5.85E-13 ±	5.36E-14	medium-grained meta-tonalite	15	boulder on lowest moraine crest
		09SRB-E052A-01	11.1915	0.1821	1.19E-13 ±	8.21E-15	quartz vein	80	boulder just below lowest meltwater channel (Fig. A2.1d)
		09SRB-E059A-01	36.1225	0.2014	3.72E-13 ±	7.11E-15	coarse-grained tonalite	25	boulder inside lateral moraine complex (Fig. A2.1c)
		09SRB-E060A-01	27.2192	0.1938	1.50E-13 ±	3.16E-15	medium-grained gneis	15	
		09SRB-E039A-01	36.0183	0.1932	3.33E-13 ±	7.67E-15	medium-grained meta-tonalite	15	large boulder split in two segments (Fig. 3.2b)
		09SRB-E040A-01 [b]	36.2254	0.2046			medium-grained meta-tonalite	15	boulder inside lateral moraine complex (Fig. 3.2b)
		09SRB-E025A-01 [b]	35.0693	0.2129			medium-grained meta-tonalite	25	on inner crest of double-crested lateral moraine (Fig. 3.2a and A2.1 a-b)
		09SRB-E026A-01	35.8344	0.1939	2.08E-13 ±	3.92E-15	medium-grained meta-tonalite	25	
		09SRB-E027A-01	35.5406	0.1932	2.14E-13 ±	8.52E-15	medium-grained meta-tonalite	25	
	Moon Valley	09SRB-A167A-01	40.5384	0.1924	2.81E-13 ±	6.44E-15	coarse-grained granite	30	boulder on till veneer
		09SRB-A167A-02	37.1910	0.1909	3.08E-13 ±	7.23E-15	coarse-grained granite	30	boulder on ridge
		09SRB-A167A-03	36.6939	0.1964	4.22E-13 ±	9.65E-15	coarse-grained granite	30	boulder
		09SRB-A351A-01	35.3900	0.2087	1.80E-13 ±	4.59E-15	medium-grained granodiorite	30	
		09SRB-A352A-01	35.0260	0.2040	1.88E-13 ±	5.90E-15	medium-grained granodiorite	30	boulders on Pangnirtung Fiord Ice recession moraine
		09SRB-A353A-01	36.2615	0.2274	1.68E-13 ±	3.94E-15	medium-grained granodiorite	30	
		09SRB-E284A-01	36.7188	0.2055	2.11E-13 ±	5.21E-15	coarse-grained granodiorite	30	
		09SRB-E284A-02	37.1511	0.2015	2.21E-13 ±	3.86E-15	coarse-grained granodiorite	30	boulders on LIS recession moraine
		09SRB-E284A-03	36.6987	0.1970	3.04E-13 ±	6.96E-15	coarse-grained granodiorite	30	
		09SRB-E223A-01	36.2755	0.2037	2.90E-13 ±	6.63E-15	coarse-grained granodiorite	30	
		09SRB-E223A-02 [b]	37.0617	0.2025			coarse-grained granodiorite	30	boulders on oldest LIS moraine, cross-cutting alpine moraine
		09SRB-E223A-03	37.6230	0.1994	2.28E-13 ±	4.51E-15	coarse-grained granodiorite	30	
		09SRB-E283A-01	38.3565	0.2011	4.94E-13 ±	1.30E-14	coarse-grained granodiorite	30	boulder on sandy to gravelly glacio-fluvial delta (Fig. A2.1e-f)
		09SRB-E224A-01	37.3268	0.1938	4.01E-13 ±	8.16E-15	coarse-grained granodiorite	30	boulders on alpine moraine ridge, cut by oldes tLIS moraine and glacio-fluvial delta
		09SRB-E224A-02	37.5235	0.2005	1.86E-13 ±	5.61E-15	coarse-grained granodiorite	30	
		09SRB-E224A-03	36.5319	0.2047	6.76E-13 ±	1.38E-14	coarse-grained granodiorite	30	
depth profiles	'central valley'	10SRB-E140A-06	97.3646	0.1941	3.90E-13	9.16E-15	Raised marine delta, 12 - 15 m horizontal bottomset silts overlain by sand and thin gravel, shell fragments and few paired samples in upper part of section in massiv, silty sand with few pebbles; front edge of terrace surface wind-eroded, covered with scattered cobbles and boulders, at sample location approximately 30 - 100 cm eroded relative to vegetated terrace remnant, alitmeter reading 20.5 m (within 5 min readings)		
		10SRB-E140A-01	130.8439	0.1854	4.64E-13	1.07E-14			
		10SRB-E140A-02	150.0270	0.1797	4.70E-13	9.12E-15			
		10SRB-E140A-03	150.1752	0.1886	4.19E-13	7.78E-15			
		10SRB-E140A-02	150.0810	0.1884	4.45E-13	1.24E-14			
	Moon valley	09SRB-E282A-05	112.4853	0.2136	1.09E-12 ±	2.09E-14	sandy to gravelly glaciolacustrine delta deposited in lake damed by LIS lobe to the west and Pangnirtung Fiord ice lobe to the east; cross-cutting moraine of local alpine outlet glacier descending from northern slope; terrace surface horizontal and flat, fully vegetated indicating stability, scattered with few boulders; mixing zone on top approximately 18 cm thick with vertical clasts indicating cryoturbation		
		09SRB-E282A-04	130.3569	0.2086	1.21E-12 ±	2.74E-14			
		09SRB-E282A-03	130.1105	0.2030	1.15E-12 ±	2.19E-14			
		09SRB-E282A-02	135.7612	0.2048	1.11E-12 ±	2.29E-14			
		09SRB-E282A-01	130.7309	0.2085	1.04E-12 ±	2.34E-14			

[a] carrier produced from an Ural Mountain phenacite, Carrier Be31 has 1015µg Be g^{-1} and $^{10}Be/^{9}Be$ below 1 x 10^{-16} at Lawrence Livermore National Lab

[b] samples yielded to low current during AMS measurement

Table A2.1 TCN chemistry data for boulders and depth profiles including detailed sample description.

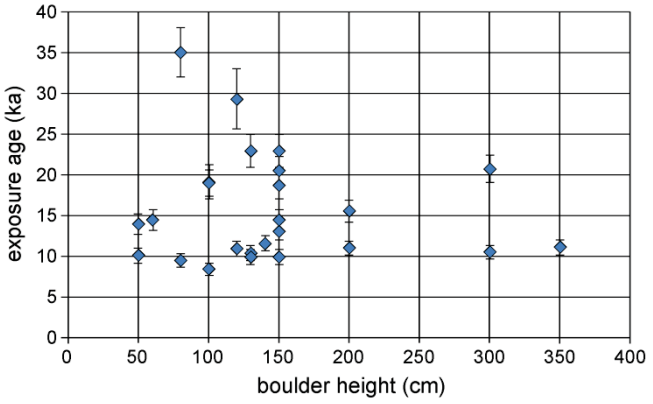

Fig. A2.1 Variation of exposure age with boulder height.

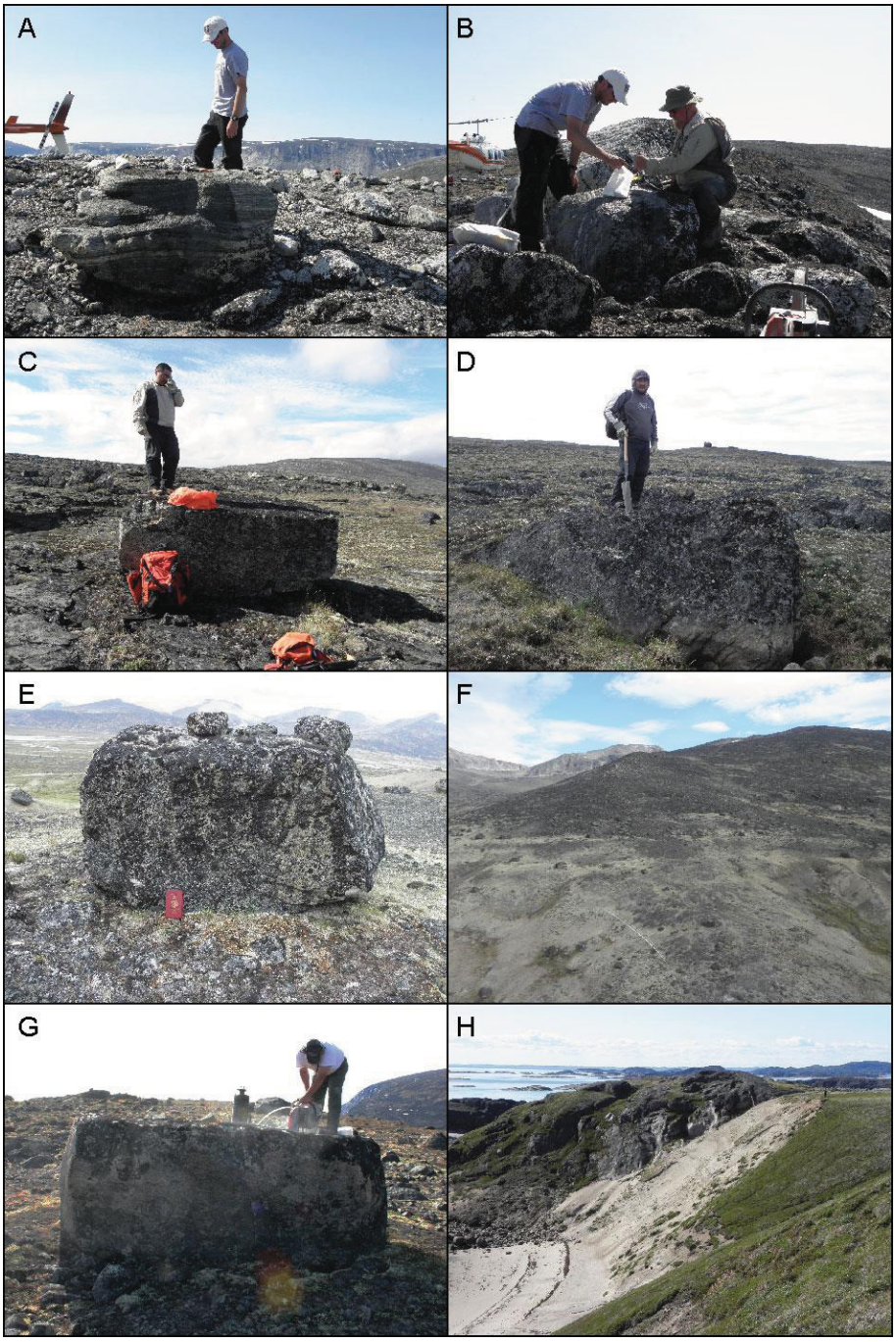

Fig. A2.2 Additional field pictures. **A - B.** Samples E027 (A) and E026 (B) on double-crested lateral moraine at the mouth of Ujuktuk Fiord (Fig. 3.3a). **C - D.** Samples E060 (C) and E052 (D) near meltwater channels and moraines in the broadest part of 'central valley' (Fig. 3.3a). **E.** Sample A283, boulder on glaciofluvial delta in Moon Valley (Fig. 3.3b). **F.** Glaciofluvial delta cross-cutting alpine moraine descending from northern slope of Moon Valley (Fig. 3.3b). **G.** Sample A167A-01 deposited on till veneer in the intervening area between Pangnirtung and Kingnait Fiords. **H.** Raised marine deposit at American Harbour on the coast to Cumberland Sound containing *Mytilus edilus* shells.

A2.2 DEPTH PROFILE CALCULATIONS

A2.2.1 Input and Output Files for Depth Profile Calculator

		'central valley'	Moon Valley	Uncertainty
Site production rate spallation [a]	(atoms g^{-1} a^{-1})	3.95	6.78	5%
Muon production (depth 5 m) [b]	(atoms g^{-1} a^{-1})	0.18	0.22	10%
Half-life	(Ma)	1.387	1.387	10%
Attenuation length spallation	(g cm^{-2})	150	150	±5
Shielding factor		1	1	
Density range (const. with depth)	(g cm^{-3})	1.9 - 2.1	1.9 - 2.1	uniform
Age range	(ka)	8 - 20	10 - 20	uniform
Erosion rate range	(cm ka^{-1})	2 - 8	0 - 2	uniform
Net erosion range	(cm)	30 - 100	0 - 20	uniform
Inheritance	(10^4 atoms g^{-1})	2 - 3	7 - 10	uniform
number of runs		100,000	500,000	
confidence level	σ	1	1	

[a] obtained from CRONUS KU calculator, version 1.0, accessed 19.11.2014

[b] half values of Heisinger et al. (2002a-b) scaling scheme used

Table A2.2 Input variables for depth profile calculator (Hidy et al., 2010).

	Statistic	Age (ka)	Inheritance (10^4 atoms g^{-1})	Erosion rate (cm ka^{-1})
'central valley'	mean	13.7	2.45	4.7
	median	13.6	2.45	4.8
	mode	12.4	2.45	5.6
	min χ^2	12.3	2.54	3.7
	χ^2 2σ upper	17.9	2.65	6.5
	χ^2 2σ lower	10.4	2.23	2.5
	Bayesian optimum	12.8	2.48	5.2
	Bayesian 2σ upper	17.8	2.77	6.9
	Bayesian 2σ lower	9.7	2.14	2.7
Moon Valley	mean	15.1	8.73	0.8
	median	15.0	8.74	0.8
	mode	14.7	8.82	1.3
	min χ^2	14.2	8.95	0.1
	χ^2 2σ upper	19.6	9.49	1.9
	χ^2 2σ lower	11.5	7.84	0.0
	Bayesian optimum	14.4	8.89	1.0
	Bayesian 2σ upper	21.4	10.27	1.9
	Bayesian 2σ lower	8.0	7.29	0.0

Table A2.3 Model output values for depth profiles.

A2.2.2 'Central Valley' Depth Profile

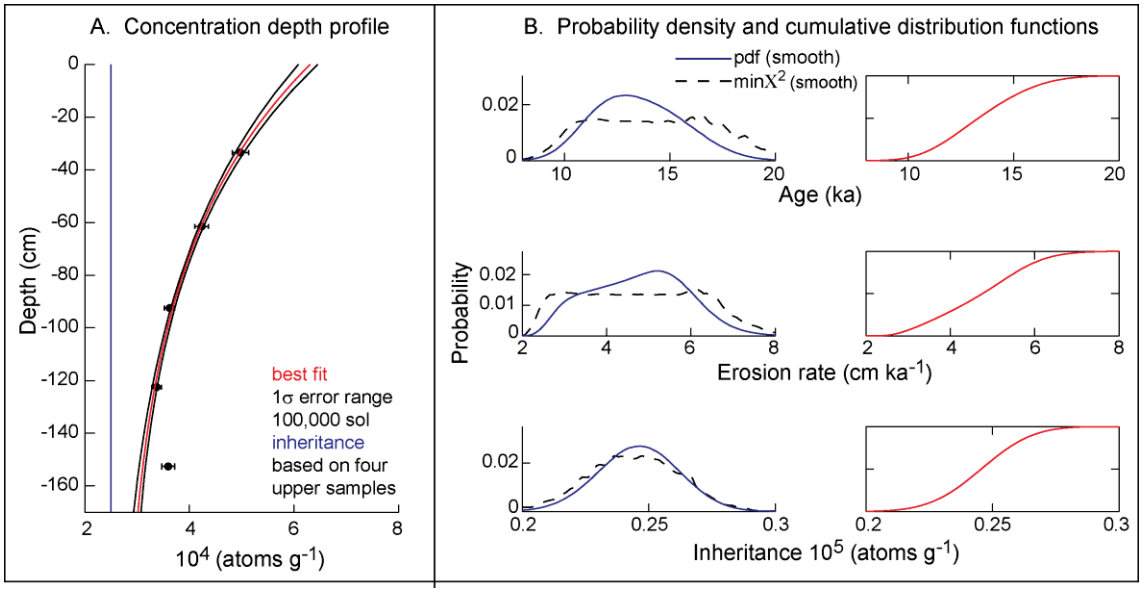

Fig. A2.3 'Central valley' depth profile. **A.** Modelled concentration depth profile using four upper samples. Deepest sample, collected 5 cm above a shell-bearing zone, has a higher concentration than the next deepest sample. **B.** Probability density functions (left) and cumulative distribution functions (right) of modelled parameters.

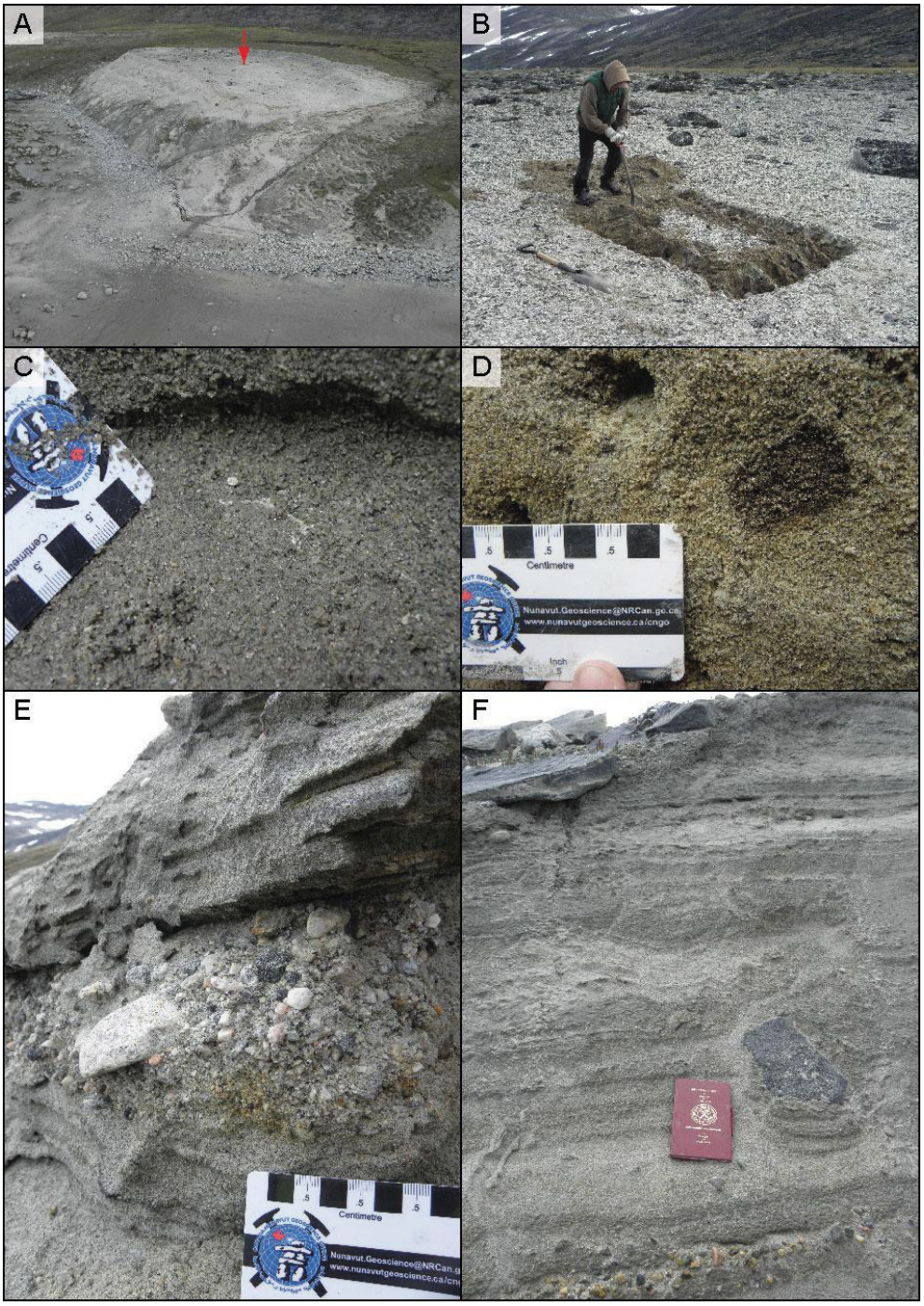

Fig. A2.4 Additional field pictures from depth profile in 'central valley'. **A.** Composite delta at the head of Ujuktuk Fiord (Fig. 3.3a). Location of depth profile is indicated by red arrow. **B.** The vertical distance between the boulder lag deposit in the background and the location of the depth profile is approximately 30 – 100 cm, which is used as an estimate for net surface erosion (Table A2.2). **C.** Shell in frozen layer at the bottom of the depth profile. **D.** Completely weathered clast at 120 cm depth. **E.** Sandy gravel layer (5 – 10 cm thick) within layered silty sand in lower part of the delta. **F.** Dropstone within layered sand sand with coarser grained lenses.

A2.2.3 Moon Valley Depth Profile

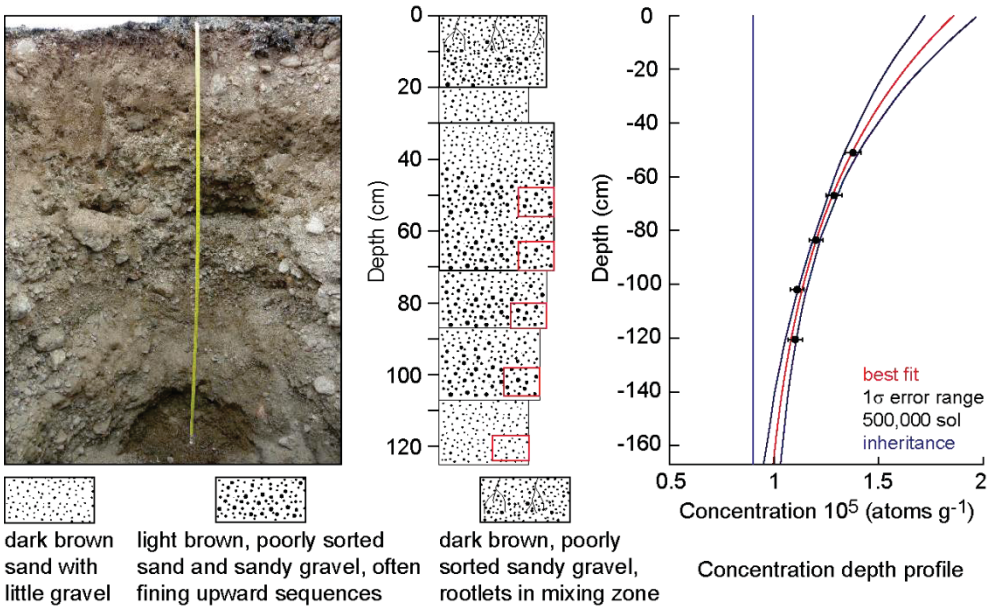

Fig.A2.5 Stratigraphic description and modelled TCN concentrations of depth profile in Moon Valley.

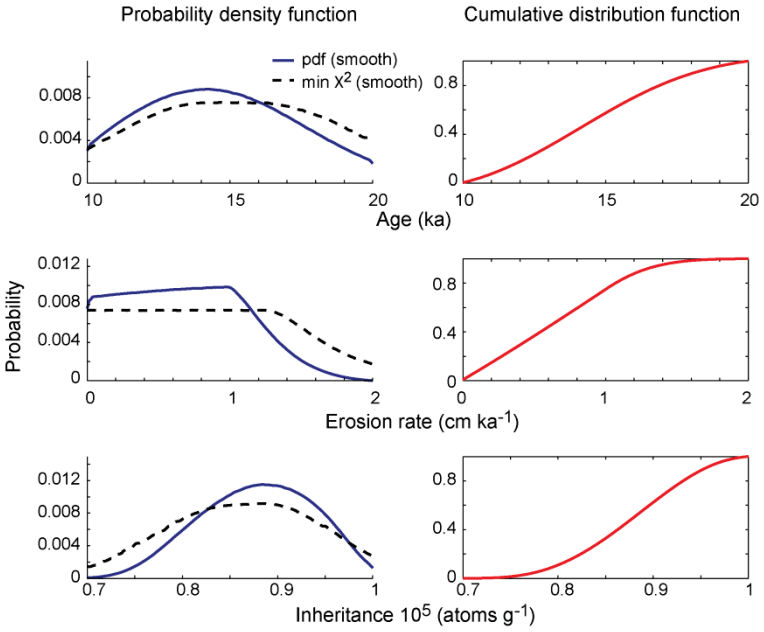

Fig. A2.6 Probability density and cumulative distribution functions of calculated values.

A2.3 CALIBRATION OF PREVIOUS RADIOCARBON DATA

	Lab ID	Latitude (d.d)	Longitude (d.d)	Elevation (m)	Material	^{14}C age [a] (BP)	Calibrated age [b] (ka)	Location	Reference
Northeastern coast	GaK-3723	67.78	-66.45	17	*Mya truncata*	5600 ± 100	5.8 ± 0.1	Nedlukseak Fiord, head east arm, in situ shells in fine sand and silt in river bank	Dyke et al., 1982; pers. comm.
	St-3816	67.95	-65.77	27	*Mya truncata*	8760 ± 350	9.2 ± 0.5	Okoa Bay, outer east side, local marine limit 27 m asl, ice-contact sediment	Miller, 1973; Dyke et al., 1982
	NSRL-10139	66.78	-63.95	17	macroflora	8560 ± 100	9.5 ± 0.1	basal sediment in Akvaqiak lake, head of western branch of Padle Fiord	Fréchette et al., 2009
	GaK-5479	67.62	-65.17	34	*Mya truncata*	9380 ± 180	10.0 ± 0.2	Quajon Fiord head, easternmost valley, marine limit 34 m asl on distal side of moraine	Dyke et al., 1982; pers. comm.
	GaK-2574	67.79	-65.62	2	*Mya truncata*	10400 ± 1000	11.4 ± 1.3	Middle Narpaing Fiord, bottomset silts overlain by deltaic foresets, terrace at 26 m asl	Dyke et al., 1982; pers. comm.
Cape Dyer	CAMS-23554	66.67	-61.78	450	aquatic moss	12600 ± 60	15.0 ± 0.2	basal sediment in Donard Lake, Cape Dyer	Moore et al., 2001,
	QL-979	66.73	-61.45	18	marine shells	37200 ± 800	41.1 ± 0.8	raised marine delta at Uga't, NW Cape Dyer	Miller, 1979; Locke, 1987
	CAMS-11337	66.49	-61.59		marine shells	57000		raised marine delta at Sunneshine Fiord, Cape Dyer	Miller et al., 2002
Southwestern coast	DIC-335	66.63	-67.93	1	marine shells	6110 ± 80	6.4 ± 0.1	Head of Clearwater Fiord	Dyke, 1979; pers. comm.
	DIC-334	66.26	-66.55	28	*Hiatella arctica*	8010 ± 65	8.3 ± 0.1	American Harbour	Dyke, 1979; pers. comm.
	GaK-4837	66.35	-64.35		*Mya truncata*	8390 ± 170	8.8 ± 0.2	Head of Kingnait Fiord, shells from silt forming prominent terrace at 16 m asl	
	GSC-2083	66.36	-64.35	16	*Mya truncata*	8880 ± 270	9.4 ± 0.4	Head of Kingnait Fiord, shells in bottomset clay-silt below foresets terminating at 16 m terrace	Dyke, 1979; McNeely and Brennan, 2005
	CAMS-85913			20	marine shells	9015 ± 25	9.5 ± 0.1	Pangnirtung, borehole SDH08 north of airstrip at depth 2.37 - 2.47 m	LeBlanc et al., 2011
	GSC-2001	66.14	-65.73	39	*Mya truncata*	9110 ± 90	9.7 ± 0.1	Pangnirtung, bulldozer cut near airstrip, 50 m marine limit	Dyke, 1979; McNeely and Brennan, 2005
	GSC-2183	66.56	-66.27	70	*Portlandia arctica*	9060 ± 110	9.6 ± 0.1	Usualuk Valley, marine limit site with silts exposed in badland silts	Dyke, 1979; McNeely and Brennan, 2005
Cumberland Sound	BETA-7405	66.42	-62.43		benthic foraminifera	13823 1700	15.9 2.2	Core 82034-041 on continental shelf off Cumberland Sound at depth 280-298 cm	Jennings, 1993
	BETA-7405 orig.					20180 295	23.6 2.2		
	AA-3939	66.39	-65.43		bulk organic matter	10920 250	12.1 0.4	Core 82027-031 in deepest section of Cumberland Sound at depth 278 - 285 cm	Jennings, 1993

[a] 'conventionally normalized' dates, previously reported data were not normalized to $\delta^{13}C$ = -25 ppm and were often corrected for resevoir ages

[b] calculated with Calib 7.0.2 (Stuiver and Reimer, 1993) using marine 13 calibration curve (Reimer et al., 2013) for marine samples and the Northern Hemisphere IntCal09 calibration curve (Reimer et al., 2009) for terrestrial samples, 1σ uncertainty stated

Table A2.4 Calibration of previous radiocarbon data. Calibration is completed using the Calib 7.0.2 program (Stuiver and Reimer, 1993) with the marine calibration curve (Reimer et al., 2013) and an additional ΔR correction of 140 a for a total ΔR correction 540 a. For samples measured at the Geological Survey of Canada (GSC) radiocarbon laboratory 'normalized corrected' radiocarbon ages were used for calibration (McNeely and Brennan, 2005). References for radiocarbon data is listed in the last column (Miller, 1973; Dyke, 1979; Miller, 1979; Dyke et al., 1982; Frechette and de Vernal., 2009; Locke, 1987; Jennings, 1993; Moore et al., 2001; LeBlanc et al., 2011).

A2.4 PALEO-ELA RECONSTRUCTION

Contours of paleo-ELA are constructed from measured maximum elevations of lateral moraines assigned to a specific time interval during deglaciation. The distribution of lateral moraines at each time interval is not equal throughout Cumberland Peninsula introducing significant uncertainty into the reconstruction of paleo-ELA contours. For instance, no lateral moraines for the Heinrich Event 1 (H-1, 14.6 ka) time interval are available along the lower southeastern coast or between Cape Dyer and the Merchants Bay area (Fig. A2.7). For the Younger Dryas (YD, 11.7 ka) time interval no moraines are available north of the Merchants Bay area (Fig. A2.8). Finaly, for the Cockburn-equivalent (9.5 ka) time interval lateral moraines are only available for the alpine glacier system leading to an elliptical shape of paleo-ELA contours (Fig. A2.9).

At each time interval, contours of relative sea level (rsl) are interpolated from previously published data of raised (Dyke, 1979; Kaplan and Miller, 2003) and submerged (Cowan, 2015; Hughes Clarke et al., 2015) marine deltas (lighter coloured lines in Fig. A2.7 – A2.9). In addition to rsl, an estimate of the eustatic sea level stand is required at each time interval (Miller et al., 2011) to correct for isostatic rebound since deposition of the lateral moraines. The gradients of isostatic rebound and paleo-ELA are constructed for two different profiles that are nearly perpendicular to each other (Fig. A2.10). These profiles were chosen to assess the change in paleo-ELA through time at different coastal sections of Cumberland Peninsula. The paleo-ELA gradients based on the measured maximum elevations of lateral moraines (dashed dark lines in Fig. A2.10) are corrected by subtracting the amount of isostatic rebound (bright lines in Fig. A2.10)

to receive the elevation of lateral moraines at the time of deposition (solid dark lines in Fig. A2.10).

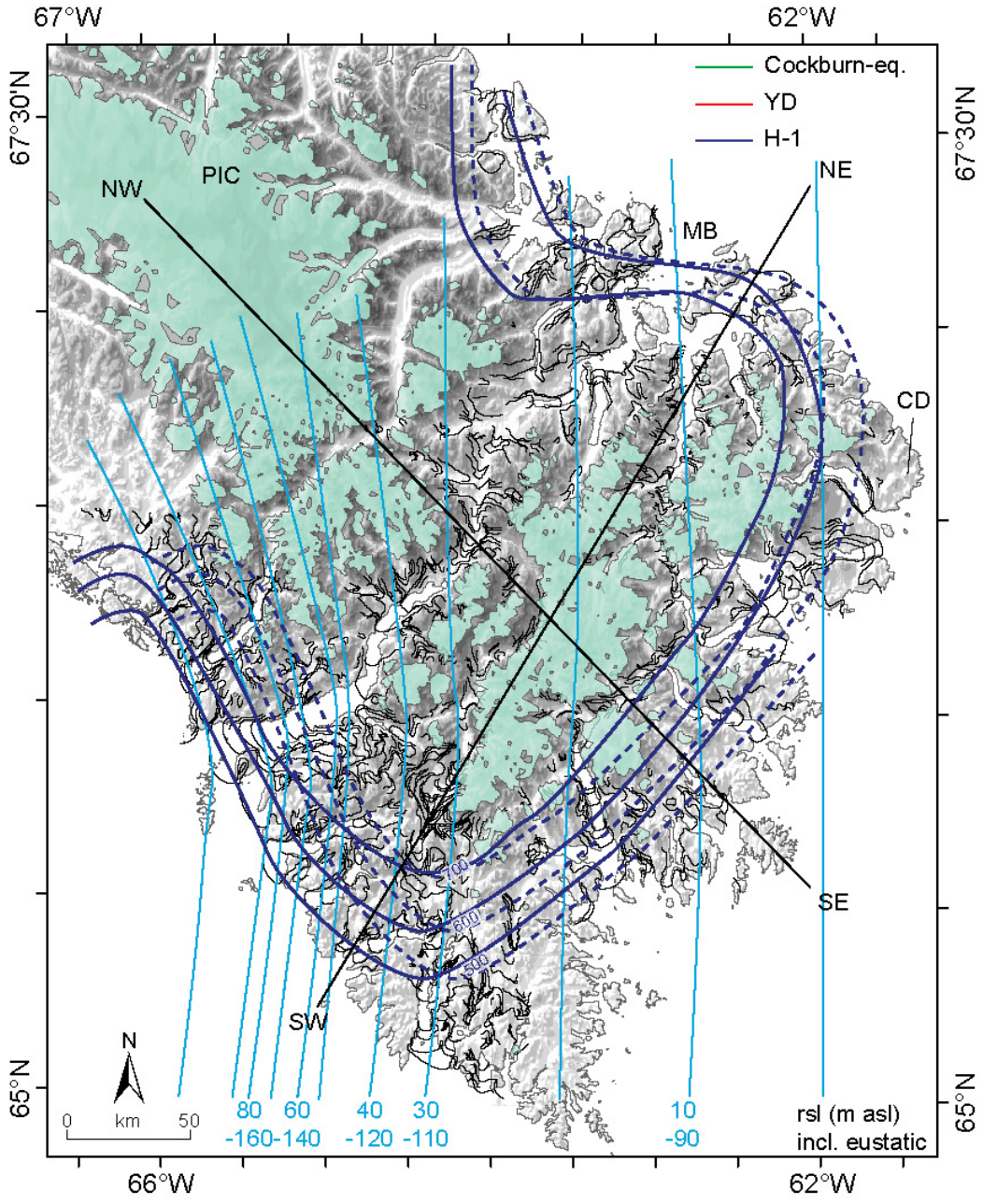

Fig. A2.7 Paleo-ELA (dark blue) and rsl contours (light blue) for H-1 time interval. Dashed paleo-ELA contours indicate measured maximum elevations of lateral moraines and solid paleo-ELA show contours corrected for isostatic rebound since deposition of the lateral moraines. Eustatic sea level was at approximately 80 m below present sea level at this time interval (Miller et al., 2011). MB: Merchants Bay area, CD: Cape Dyer.

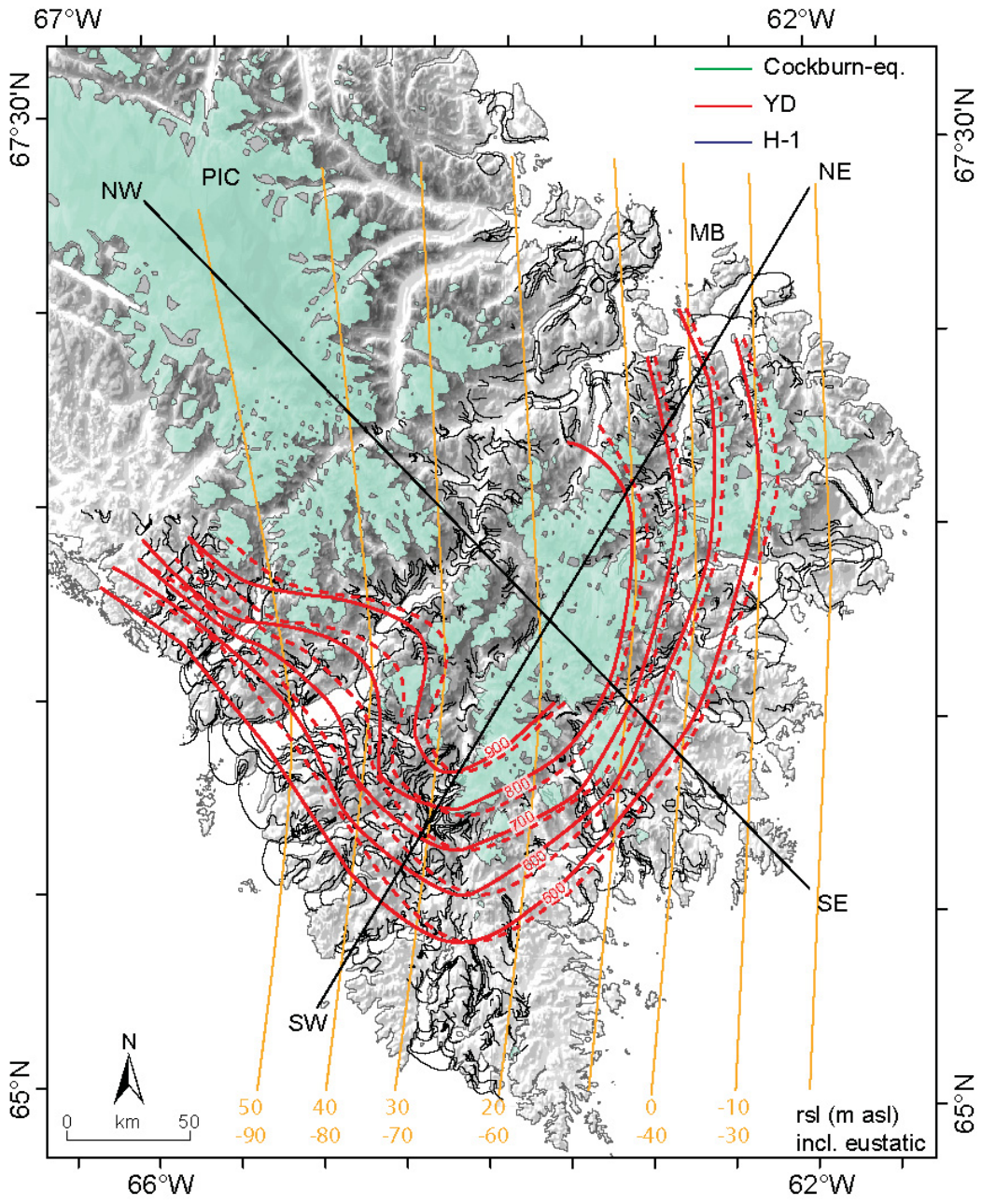

Fig. A2.8 Paleo-ELA (red) and rsl contours (orange) for YD time interval. Dashed paleo-ELA contours indicate measured maximum elevations of lateral moraines and solid paleo-ELA show contours corrected for isostatic rebound since deposition of the lateral moraines. Eustatic sea level was at approximately 40 m below present sea level at this time interval (Miller et al., 2011). MB: Merchants Bay.

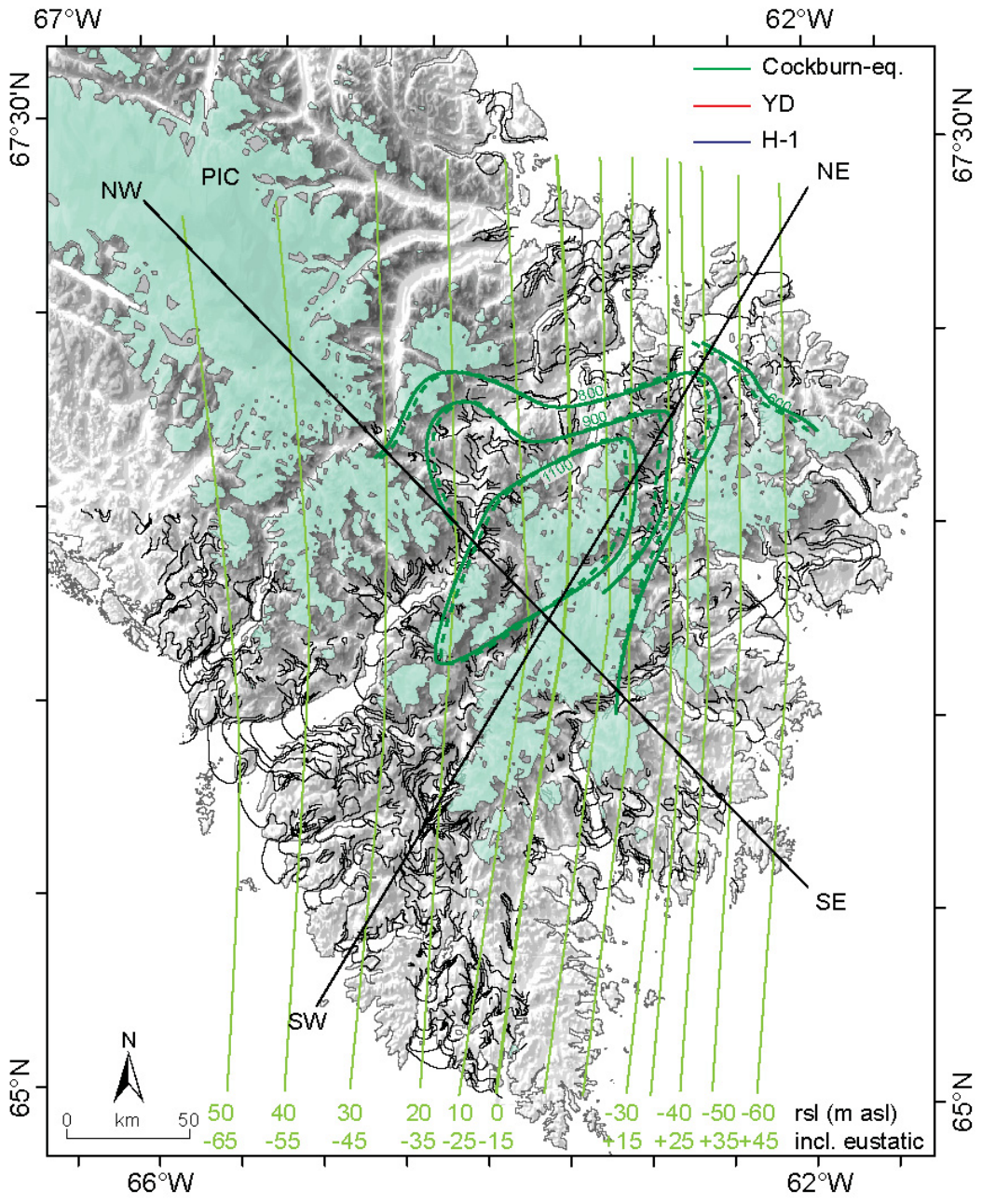

Fig. A2.9 Paleo-ELA (dark green) and rsl contours (light green) for Cockburn-equivalent time interval. Dashed paleo-ELA contours indicate measured maximum elevations of lateral moraines and solid paleo-ELA show contours corrected for isostatic rebound since deposition of the lateral moraines. Eustatic sea level was at approximately 15 m below present sea level at this time interval (Miller et al., 2011).

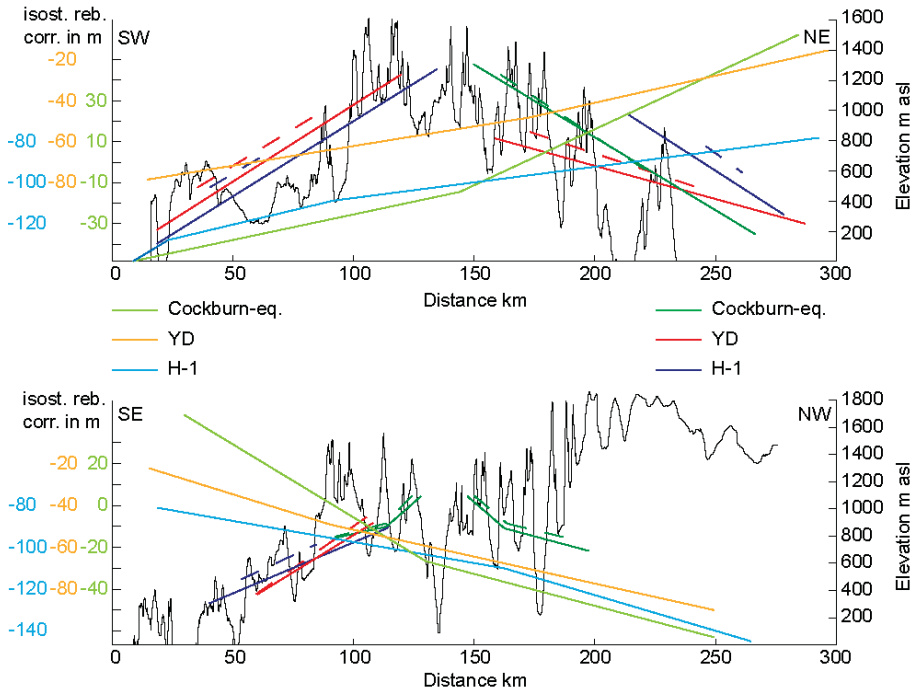

Fig. A2.10 Profiles shown in Fig. A2.7 – A2.9 displaying uncorrected paleo-ELA gradients (dashed dark lines, axis to the right), corrected paleo-ELA gradients (solid dark lines, axis to the right), and gradients of isostatic rebound (solid bright lines, axis to the left). For correction of isostatic rebound the amount of relative sea level plus eustatic sea level stand at each time interval is subtracted from the measured maximum elevation of lateral moraines.

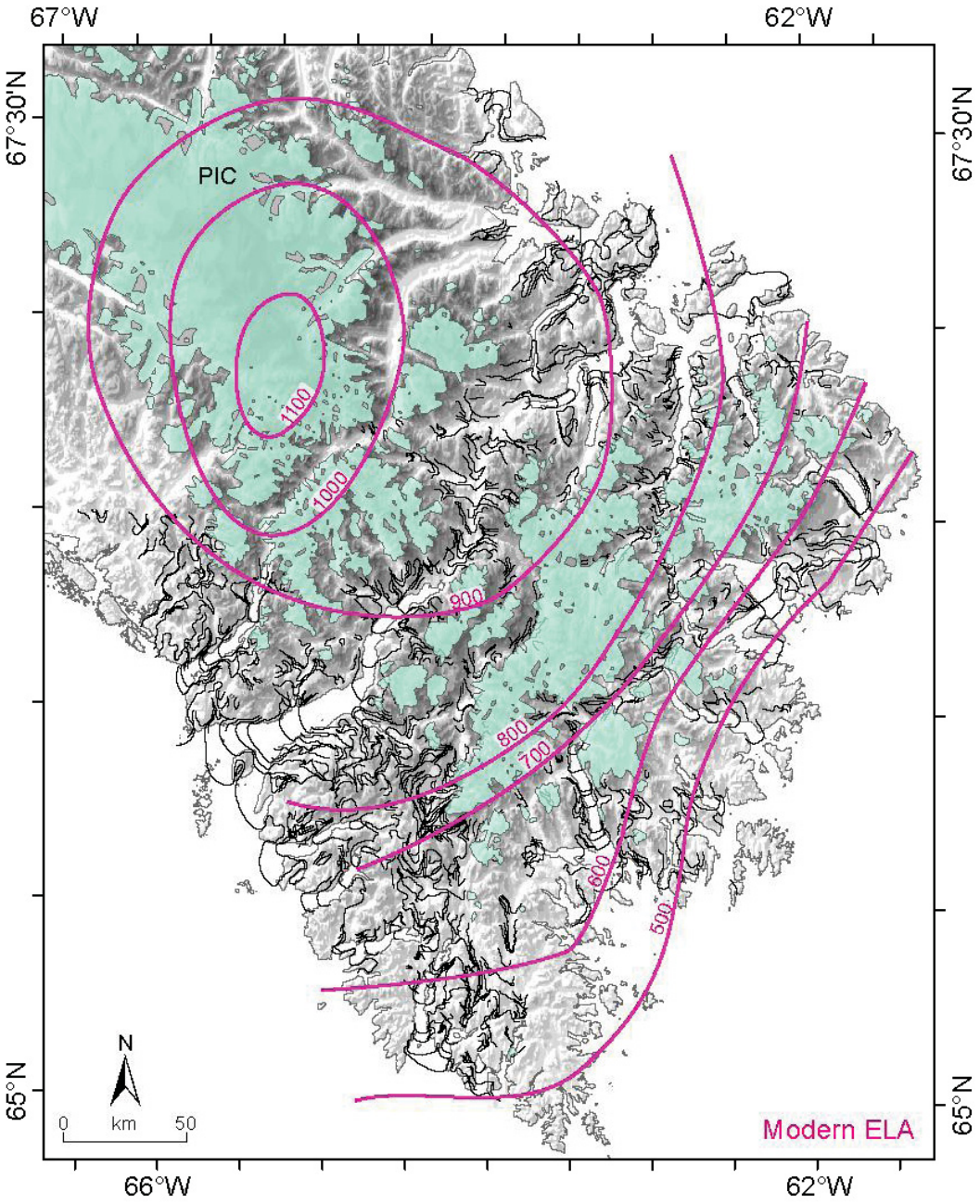

Fig. A2.11 Modern ELA distribution on Cumberland Peninsula inferred from the lowest corrie glacier elevations (adapted from Andrews and Miller, 1972).

A2.5 REFERENCES FOR A2

Andrews, J., Miller, G., 1972. Quarternary history of northern Cumberland Peninsula, Baffin Island, NWT, Canada: Part IV: Maps of the present glaciation limits and lowest equilibrium line altitude for North and South Baffin Island. Arctic and Alpine Research 4, 45-59.

Cowan, B., 2015. Shorelines beneath the sea: Geomorphology and characterization of the postglacial sea-level lowstand, Cumberland Peninsula, Baffin Island, Nunavut. Department of Geography, MSc thesis. Memorial University of Newfoundland, St. John's.

Dyke, A., 1979. Glacial and sea-level history of southwestern Cumberland Peninsula, Baffin Island, NWT, Canada. Arctic and Alpine Research 11, 179-202.

Dyke, A., Andrews, J., Miller, G., 1982. Quaternary geology of Cumberland Peninsula, Baffin Island, District of Franklin. Geological Survey of Canada, Memoir, 403, p. 32.

Frechette, B., de Vernal, A., 2009. Relationship between Holocene climate variations over southern Greenland and eastern Baffin Island and synoptic circulation pattern. Climate of the Past 5, 347-359.

Hidy, A.J., Gosse, J.C., Pederson, J.L., Mattern, J.P., Finkel, R.C., 2010. A geologically constrained Monte Carlo approach to modeling exposure ages from profiles of cosmogenic nuclides: An example from Lees Ferry, Arizona. Geochemistry Geophysics Geosystems 11, Q0AA10.

Heisinger, B., Lal, D., Jull, A., Kubik, P., Ivy-Ochs, S., Knie, K., Nolte, E., 2002a. Production of selected cosmogenic radionuclides by muons: 2. Capture of negative muons. Earth and Planetary Science Letters 200, 357-369.

Heisinger, B., Lal, D., Jull, A., Kubik, P., Ivy-Ochs, S., Neumaier, S., Knie, K., Lazarev, V., Nolte, E., 2002b. Production of selected cosmogenic radionuclides by muons:: 1. Fast muons. Earth and Planetary Science Letters 200, 345-355.

Hughes Clarke, J.E., Muggah, J., Renoud, W., Bell, T., Forbes, D.L., Cowan, B., Kennedy, J., 2015. Reconnaissance seabed mapping around Hall and Cumberland peninsulas, Nunavut: opening up southeastern Baffin Island to nearshore geological investigations, Summary of Activities 2014. Canada-Nunavut Geoscience Office, p. 133–144.

Jennings, A.E., 1993. The Quaternary history of Cumberland Sound, southeastern Baffin Island: the marine evidence. Géographie physique et Quaternaire 47, 21–42.

Kaplan, M., Miller, G., 2003. Early Holocene delevelling and deglaciation of the Cumberland Sound region, Baffin Island, arctic Canada. Geological Society of America Bulletin 115, 445-462.

LeBlanc, A., Allard, M., Carbonneau, A., Oldenborger, G., L'Hérault, E., Sladen, W., Gosselin, P., Mate, D., 2011. Assessing permafrost conditions and landscape hazards in support of climate change adaptation in Pangnirtung, Nunavut. Geological Survey of Canada, Open File 6868, p. 59.

Locke, W., 1987. The late Quaternary geomorphic and paleoclimatic history of the Cape Dyer area, easternmost Baffin Island, NWT. Canadian Journal of Earth Sciences 24, 1185-1198.

McNeely, R., Brennan, J., 2005. Geological Survey of Canada revised shell dates. Geological Survey of Canada Open File 5019, p. 530.

Miller, G., 1973. Late Quaternary glacial and climatic history of northern Cumberland Peninsula, Baffin Island, NWT, Canada. Quaternary Research 3, 561-583.

Miller, G., 1979. Radiocarbon date list IV, Baffin Island, NWT, Canada. University of Colorado, Institute of Arctic and Alpine Research Occasional Paper, 29, p. 61.

Miller, K.G., Mountain, G.S. , Wright, J.D., Browning, J.V., 2011. A 180-million-year record of sea level and ice volume variations from continental margin and deep-sea isotopic records. Oceanography 24, 40-53.

Moore, J., Hughen, K., Miller, G., Overpeck, J., 2001. Little Ice Age recorded in summer temperature reconstruction from vared sediments of Donard Lake, Baffin Island, Canada. Journal of Paleolimnology 25, 503-517.

Reimer, P.J., Baillie, M.G.L., Bard, E., Bayliss, A., Beck, J.W., Blackwell, P.G., Ramsey, C.B., Buck, C.E., Burr, G.S., Edwards, R.L., Friedrich, M., Grootes, P.M., Guilderson, T.P., Hajdas, I., Heaton, T.J., Hogg, A.G., Hughen, K.A., Kaiser, K.F., Kromer, B., McCormac, F.G., Manning, S.W., Reimer, R.W., Richards, D.A., Southon, J.R., Talamo, S., Turney, C.S.M., van der Plicht, J., Weyhenmeyer, C.E., 2009. IntCal09 and Marine09 radiocarbon age calibration curves, 0-50,000 years cal BP. Radiocarbon 51, 1111-1150.

Stuiver, M., Reimer, P.J., 1993. Extended ^{14}C data base and revised CALIB 3.0 14C age calibration program. Radiocarbon 35, 215-230.

APPENDIX A3 - Supplementary File for New Approach for Quantification of Subaerial and Subglacial Erosion Rates on High Latitude Upland Plateaus: Cumberland Peninsula, Baffin Island, Canada

A3.1 SAMPLE PREPARATION AND TCN CHEMISTRY DATA

Samples were cleaned of lichen and other organic material using a wire brush before crushing in a jaw crusher and grinding with a plate pulverizer. The grain size fraction of 355-500 μm, separated by dry sieving, was used for quartz purification, which included a combination of physical (magnetic separation, sand abrasion, isostatic) and chemical (aqua regia, HF etching, and multiple cycles of dilute HF ultrasonication) procedures (Kohl and Nishiizumi, 1992). The absence of feldspar was verified with a simple test for Al concentration in 1 g of dissolved quartz. Approximately 35 g of purified (generally Al concentration <100 ug g^{-1}) quartz were spiked with ~0.2 g of ^{10}Be carrier (Table A3.1) and dissolved in a mixture of HF and $HClO_4$. Aliquots for determining native ^{27}Al concentration in quartz were separated before and after addition of varying amounts of standard Al carrier. Native ^{27}Al concentration were measured with ICP-MS (~5% 1σ precision, MAXXXAM Inc., Halifax) and, for a few samples, ICP-OES (<2% 1σ precision, Dalhousie Geochronology Centre (DGC)). Be- and Al-cations were extracted by a combination of ion chromatography and pH-controlled precipitations of Be- and Al- hydroxides, followed by evaporation and ignition using a Bunsen burner. For AMS analysis, the Be- and Al-oxides were mixed with niobium and silver (1:1 by volume), respectively, and loaded into target holders. At the Center for Accelerator Mass Spectrometry at Lawrence Livermore National Laboratory (CAMS-LLNL), the process blanks and targets were measured against standards 07KNSTD3110 with a ^{10}Be/^{9}Be ratio

of 2.85 x 10^{-12} (Nishiizumi et al., 2007) and KNSTD10650 with a $^{26}Al/^{27}Al$ ratio of 1.065 x 10^{-11} (Nishiizumi, 2004). Process blanks for ^{10}Be and ^{26}Al were analysed with each batch of seven to twelve samples, and their measured ratios was used for background correction of the measured sample ratios (generally <1%, few low concentration samples <4%). Process blank $^{10}Be/^{9}Be$ and $^{26}Al/^{27}Al$ ranged between 7.6 x 10^{-15} to 3.6 x 10^{-14} and 1.6 x 10^{-15} to 6.1 x 10^{-15} respectively. The elevated ratios for the $^{10}Be/^{9}Be$ have been positively correlated with high isobaric boron levels in the BeO targets, owing to contamination of ^{10}B in the DGC cosmogenic nuclide lab during building renovations (e.g., installation of pink fibreglass insulation, poor HVAC filtration, and other issues that have been resolved since). Stated total analytical errors of calculated concentrations at 1σ confidence include AMS ratio measurement uncertainty (Poisson counting precision), blank correction error, an additional 2% uncertainty for sample chemistry and uncertainty in the Be concentration of the carrier, and, for ^{26}Al only, native Al concentration measurement error (from ICP.MS or ICP-OES, Table A3.1).

Three samples with initially high native Al concentrations yielded relatively large Al-AMS measurements errors (Table A3.1). We re-submitted these samples for renewed Al-AMS analysis following further quartz purification. However, the calculated ^{26}Al and ^{10}Be concentrations are lower compared to other surfaces of similar weathering degree sampled at the same site (6 & 12, Table 4.2, Fig. 4.5). We suspect that the initial Be-AMS analysis could also be affected by the high concentration of impurities in the quartz (evident from the high native Al concentration), and we have therefore purified quartz of the 250-355 μm size fraction for renewed Be- and Al-extraction and AMS analysis.

Lab ID	Sample ID	Mass of quartz dissolved	Mass of Be carrier	Mass of Al carrier	Native Al concentration	$^{10}Be/^{9}Be$ AMS	$^{26}Al/^{27}Al$ AMS	^{10}Be age [a]	^{26}Al age [a]	^{10}Be erosion rate [b]	^{26}Al erosion rate [b]	Min. exposure age [c]			Min. burial age [c]			Min. total exposure age [c]		
		(g)	(g)	(g)		(-) (-)	(-) (-)	(ka)	(ka)	(mm ka^{-1})	(mm ka^{-1})	(ka)	(-ka)	(+ka)	(ka)	(-ka)	(+ka)	(ka)	(-ka)	(+ka)
2534	10SRB-E065A-01	35.5655	0.1923	1.7293	158 ± 8	1.39E-11 ± 8.76E-14	6.21E-12 ± 1.35E-13	646 ± 83	690 ± 160	1.2 ± 0.0	1.0 ± 0.1	500	9	-1	0	-2	26	500	7	25
2535	10SRB-E066A-01	35.1074	0.1795	0.5160	255 ± 13	1.10E-11 ± 1.08E-13	3.61E-12 ± 7.10E-14	426 ± 46	370 ± 61	1.8 ± 0.0	1.8 ± 0.1	382	12	37	52	19	151	434	31	188
2533	10SRB-E064A-01	35.4837	0.1813	1.8031	393 ± 20	1.89E-12 ± 3.50E-14	3.99E-13 ± 1.64E-14	115 ± 11	100 ± 14	7.3 ± 0.2	8.0 ± 0.5	109	5	12	89	40	196	198	45	208
2532	10SRB-E042A-01	35.2063	0.1861	1.7340	855 ± 43	1.93E-12 ± 3.58E-14	1.99E-13 ± 7.95E-15	99 ± 9	82 ± 11	8.1 ± 0.2	9.2 ± 0.6	101	7	11	184	98	174	284	105	184
2536	10SRB-E074A-01	30.4142	0.1810	0.0000	2218 ± 37	2.07E-11 ± 1.85E-13	8.58E-13 ± 2.59E-14	1010 ± 170	690 ± 150	0.8 ± 0.0	0.9 ± 0.0	500	2	0	0	nd	6	500	nd	6
2526	09SRB-E222A-01	35.0116	0.1915	1.7429	77 ± 4	6.14E-12 ± 6.75E-14	4.09E-12 ± 1.10E-13	252 ± 27	190 ± 30	3.2 ± 0.1	3.8 ± 0.2	240	16	22	248	111	137	487	126	159
2527	09SRB-E222A-02	35.4640	0.1892	1.7297	14 ± 1	9.33E-13 ± 1.66E-14	7.95E-13 ± 2.25E-14	28.5 ± 2.4	15 ± 1.7	24.7 ± 0.7	45.3 ± 2.1	50	4	4	1249	122	123	1299	125	128
2528	09SRB-E222A-03	35.1831	0.1898	1.7442	77 ± 4	4.82E-12 ± 3.96E-14	3.20E-12 ± 6.28E-14	182 ± 18	146 ± 21	4.3 ± 0.1	4.9 ± 0.3	179	11	15	211	102	134	390	113	149
2529	09SRB-E222A-04	35.0160	0.1834	1.7420	31 ± 2	1.35E-12 ± 2.51E-14	1.01E-12 ± 4.26E-14	42.1 ± 3.7	24.7 ± 2.9	17.0 ± 0.5	27.9 ± 1.5	65	5	6	948	124	143	1012	128	149
2530	09SRB-E222A-05	34.7466	0.1794	1.7469	62 ± 3	5.97E-12 ± 5.08E-14	4.36E-12 ± 8.55E-14	225 ± 23	183 ± 27	3.5 ± 0.1	4.0 ± 0.2	211	12	18	173	90	135	384	102	154
2531	09SRB-E222A-06	35.0731	0.1886	0.5117	364 ± 2	5.65E-13 ± 1.05E-14	1.12E-13 ± 7.86E-15	17.1 ± 1.4	11.5 ± 1.5	40.9 ± 1.1	59.2 ± 4.3	23	2	3	745	166	227	768	168	229
2393	09SRB-A346A-01	35.1319	0.2003	2.4810	77 ± 4	3.81E-12 ± 8.56E-14	2.41E-12 ± 6.84E-14	155 ± 15	120 ± 17	4.9 ± 0.1	5.9 ± 0.4	164	12	17	290	124	146	455	136	163
2394	09SRB-A348A-01	35.3062	0.1913	2.8054	84 ± 4	2.85E-12 ± 5.30E-14	1.75E-12 ± 4.50E-14	105 ± 9.7	90 ± 12	7.0 ± 0.2	7.7 ± 0.5	107	6	10	124	67	159	230	73	169
2396	09SRB-A347A-02 [d]	38.0854	0.1946	0.5114	956 ± 48	1.37E-12 ± 2.56E-14	8.39E-14 ± 1.10E-14	44.8 ± 3.9		16.0 ± 0.4										
2395	09SRB-A347A-01	30.0465		0.0000	80 ± 1		1.48E-12 ± 5.76E-14		35 ± 4		19.9 ± 0.9	53	3	4	356	108	126	409	111	130
2384	09SRB-E304A-01	35.1661	0.1992	0.5170	147 ± 7	3.71E-12 ± 7.50E-14	2.17E-12 ± 7.27E-14	189 ± 19	143 ± 21	4.3 ± 0.1	5.2 ± 0.3	192	14	20	295	125	150	487	139	169
2588	10SRB-E020A-01	35.1812	0.1915	1.2460	68 ± 3	6.60E-12 ± 1.21E-13	5.04E-12 ± 9.74E-14	286 ± 33	200 ± 30	2.9 ± 0.1	3.7 ± 0.2	288	20	27	395	116	130	683	136	157
2589	10SRB-E021A-01	35.5590	0.1865	0.4842	67 ± 3	8.18E-12 ± 5.72E-14	7.44E-12 ± 2.12E-13	376 ± 47	233 ± 38	2.4 ± 0.1	3.2 ± 0.2	366	24	33	477	115	131	843	139	164
2590	10SRB-E022A-01	35.2522	0.1865	1.7386	101 ± 5	3.88E-12 ± 6.35E-14	2.37E-12 ± 7.37E-14	119 ± 11	81 ± 11	6.0 ± 0.2	8.3 ± 0.5	150	11	14	541	129	146	691	140	161
2391	09SRB-A355A-01	35.2918	0.1910	2.4794	92 ± 5	4.34E-12 ± 6.97E-14	2.40E-12 ± 5.46E-14	247 ± 27	191 ± 29	3.5 ± 0.1	4.1 ± 0.2	229	16	21	239	110	135	468	126	157
2392	09SRB-A356A-01	35.1482	0.1933	2.4174	87 ± 4	1.57E-12 ± 3.57E-14	1.01E-12 ± 4.08E-14	75.3 ± 6.8	64.5 ± 8.5	10.2 ± 0.3	11.4 ± 0.8	77	5	9	139	73	188	216	77	197
2386	09SRB-A186A-01	35.3395	0.2022	1.7356	107 ± 5	3.55E-12 ± 8.44E-14	2.12E-12 ± 4.89E-14	169 ± 17	124 ± 17	4.7 ± 0.1	5.9 ± 0.3	182	14	18	368	126	140	551	140	158
2387	09SRB-A188A-01	36.6153	0.1923	2.4731	95 ± 5	5.06E-12 ± 7.72E-14	2.49E-12 ± 6.00E-14	238 ± 25	164 ± 24	3.5 ± 0.1	4.5 ± 0.3	250	17	23	426	119	134	676	136	157
2390	09SRB-A187A-01	35.0101	0.2050	2.4867	105 ± 5	3.16E-12 ± 5.10E-14	1.88E-12 ± 4.26E-14	152 ± 15	123 ± 17	5.2 ± 0.1	5.9 ± 0.3	152	10	14	205	103	141	357	114	155
2381	09SRB-E221A-01 [d]	35.4572	0.1921	0.5175	872 ± 44	1.96E-12 ± 4.44E-14	2.67E-13 ± 1.86E-14	80.5 ± 7.3		9.4 ± 0.3										
2381	09SRB-E221A-01	30.0074		0.0000	456 ± 23		2.20E-13 ± 1.12E-14		57.4 ± 7.1		12.5 ± 0.7	97	7	9	488	124	139	586	131	149
2382	09SRB-E221A-02 [d]	35.6641	0.1946	0.5139	755 ± 4	3.46E-12 ± 6.38E-14	8.65E-13 ± 6.34E-14	157 ± 15		5.1 ± 0.1										
2382	09SRB-E221A-02	30.1661		0.0000	528 ± 1		4.86E-13 ± 1.41E-14		93 ± 11		7.8 ± 0.3	202	12	15	738	87	90	940	100	105
2383	09SRB-E221A-03	35.2509	0.1953	1.7299	101 ± 5	2.61E-12 ± 5.28E-14	1.76E-12 ± 3.60E-14	114 ± 11	97 ± 13	6.8 ± 0.2	7.5 ± 0.4	114	7	11	146	79	151	259	85	162

[a] CRONUS KU online calculator, 1σ error includes uncertainty in nuclide concentrations, production rates and decay constants

[b] following Lal(1991) assuming seqular equilibrium, error only includes nuclide concentration uncertainty (AMS measurement error, blank correction, 2% procedural uncertainty, and, for ^{26}Al, native Al measurement (5% ICP-MS and 2% ICP-OES)

[c] 1σ error is estimated from probability density functions based on weighted χ^2 value

[d] Initial AMS analysis using quartz with high native Al concentration and potentially additional impurities

nd = not determined

Table A3.1 Sample chemistry and AMS data: Apparent ^{10}Be and ^{26}Al exposure ages are calculated using the online CRONUS KU calculator Version 1.0 July, 26-27, 2014. Erosion rates are calculated following Lal (1991) assuming samples have reached saturation. For samples with low concentrations, these erosion rates should be interpreted as maxima. Minimum durations of exposure and burial are determined for a simple burial history of an initial continuous exposure interval followed by a single continuous burial interval (Granger and Smith, 2000).

A3.2 ADDITIONAL TCN RESULTS AND FIELD PICTURES

Apparent exposure ages are calculated using the new CRONUS KU online calculator version 1.0 (http://web1.ittc.ku.edu:8888/). For all sampled tor sites, topographic shielding is negligible, and shielding by snow is assumed to be insignificant as the majority of surfaces are on tor tops, metres above the surrounding ground, on wind-swept summits. Rock density is set to 2.65 g cm^{-3} and a subaerial erosion rate of 1 mm ka^{-1} is assumed. Low subaerial erosion rates are supported by three samples that had been continuously exposed (no or insignificant complex exposure histories, see section 4.7.1, main text) and whose nuclide concentrations can be interpreted as steady state subaerial erosion rates ranging between 0.8 – 1.6 mm ka^{-1} (Table A3.1, sites 1 and 4). These low rates are corroborated by the MC method that generally limits subaerial erosion rates at <2 mm ka^{-1} (Table 4.3, Fig. 4.8). For most samples, measured $^{26}Al/^{10}Be$ ratios are below the surface production ratio of 6.75, indicating a complex exposure history and/or plucking. Minimum estimates for exposure and burial durations are obtained assuming a continuous initial exposure interval followed by a single continuous burial episode (Granger and Smith, 2000; Granger and Muzikar, 2001; Granger, 2006). Uncertainties of these estimates are determined from probability density functions that are based on weighted χ^2 statistics (Table A3.1, Taylor, 1997). Compared with the cyclic ice cover model outlined in section 4.6.1, the calculated minimum estimates of total exposure plus burial age are only about half the value determined with the new approach (section 4.7.1, Table 4.3, Fig. A3.1).

For these calculations, a sea-level, high-latitude reference production rate of 4.0 atoms g^{-1} a^{-1} was used for ^{10}Be (Borcher et al., subm.) with a spallogenic $^{26}Al/^{10}Be$

production ratio of 6.75 (Nishiizumi et al., 1989; Balco et al., 2008). Scaling factors for spallogenic production are calculated with the time-dependent scaling scheme by Lifton et al. (2014), which is based on modelled analytical fits to measured cosmic-ray spectra (Sato 2006 and 2008). Muon production parameters are also calculated according to Lifton et al. (2014) following Heisinger et al. (2002a-b). Compared to the previously used ^{10}Be spallogenic production rate at SLHL of 4.48 atoms g^{-1} a^{-1} (Stone, 2000, recalibrated according to Nishiizumi et al., 2007) and scaled to the sample site with a time-invariant scaling scheme (Stone, 2000, after Lal, 1991), the calculated apparent exposure ages increase by approximately 11-12%.

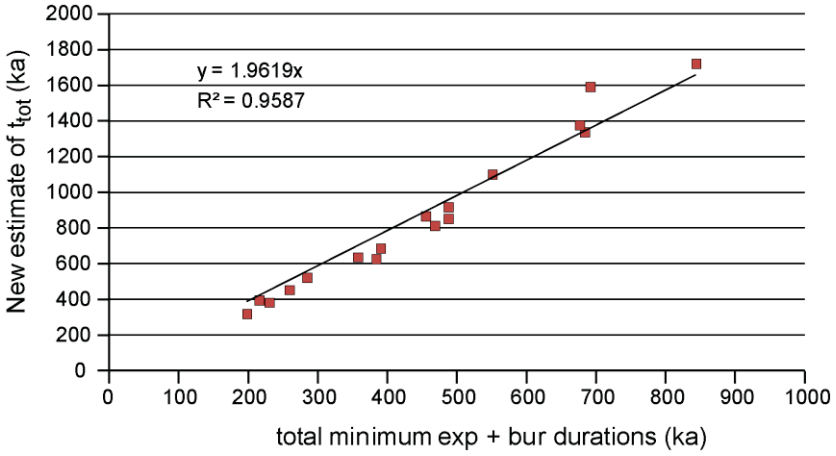

Fig. A3.1 Comparison of estimates of total complex history derived using a simplified period ice cover history (section 4.6.1) and the sum of minimum duration of a single exposure interval followed by single burial interval.

Fig. A3.2 Supplementary field photos: **A & B:** Site 11 – stage 2-3 tor: samples A188 (top of one of the blocks shown in A), A187 (on top of ridge in B), and A186 (from the extensive slab in front of the ridge shown in B). Large tor blocks in A withstood plucking, while smaller blocks in B at the same location had been plucked more frequently and more recently. **C.** Site 9 – stage 2 tor: Preservation of mushroom tors at a summit top. **D.** Aerial view of site 10 – stage 3-4 tor: Located at the edge of a plateau, sample A355 (weathered surface) was collected at the highest and centre part of the tor; sample A356 (fresher surface) was collected a few metres upslope from the high tor, on the plinth-like surface to the left. **E & F.** Site 7 – stage 3-4 tor: Sample E346 (weathered surface) collected on block 3 m to the left of person shown in E. Sample E348 (fresher bedrock surface) shown in F. **G.** Site 4: White erratic cobble. **H & I**. Site 5: Erratic blocks: Sub-rounded block with distinctive phenocrysts (train of white blobs on front side) shown in H (sample E222A-02), fresh large block shown in I (sample E222A-06).

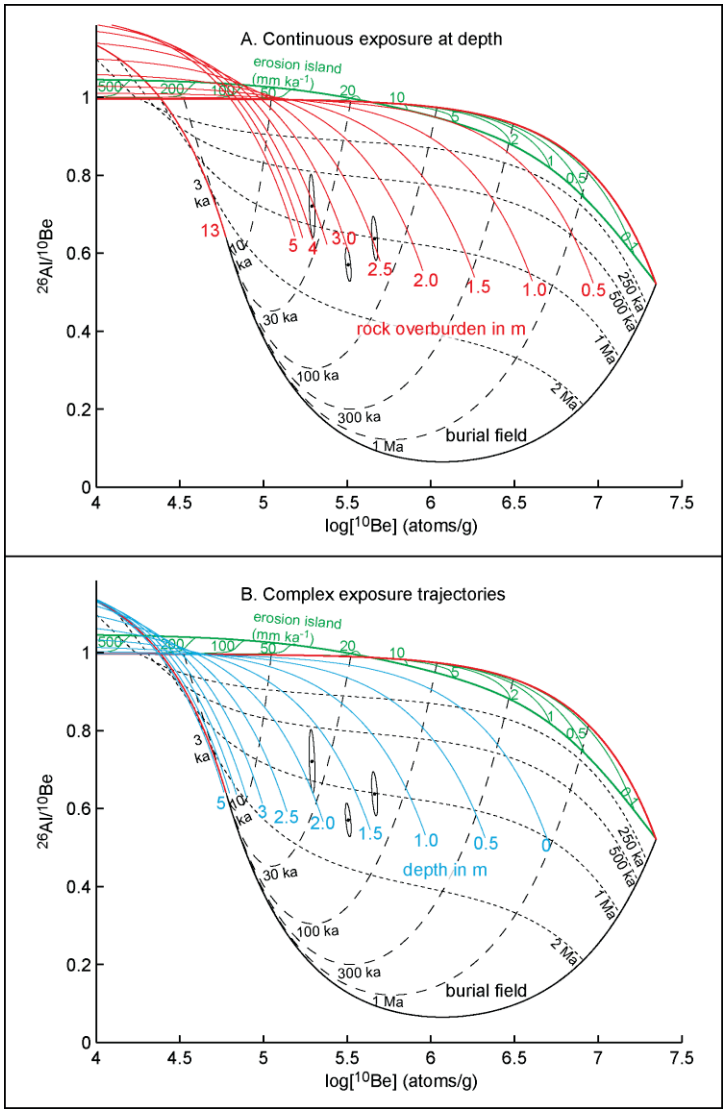

Fig. A3.3 Two ways to interpret the measured TCN concentrations of the erratic blocks on site 5 (Table 4.2, Fig. A3.2 h-i). Burial plot is shown for site-specific latitude, longitude and altitude. Production ratio of ^{26}Al to ^{10}Be is normalised by dividing the ratio by the surface production ratio of 6.75, and the burial plot is shown for an average ice thickness of 50 m occupying the site for 74.2% of the time (based on average ice-free time of 25.8% derived from three bedrock samples collected at the site). Exposure isolines are sub-vertical black dashed lines (longer dashes), burial isolines are sub-horizontal black dashed lines (smaller dashes), and constant erosion island is shown in green. **A.** Continuous exposure at depth: Additional to the red line for a continuously exposed surfaces (Fig. 4.3), lines for surfaces continuously shielded by rock of density 2.65 g cm^{-3} are shown in 0.5 m increments up to 5 m (assuming no erosion) and for the depth of continuous burial beneath the equivalent of 13 m of rock (for calculation of depth of continuous burial see caption of Fig. 4.3). **B.** Complex exposure trajectories are shown for a cyclic ice cover history with 1 ka long glacial-interglacial cycles, 25.8% ice-free time and no subaerial constant erosion at depth from 0 - 5 m in 0.5 m intervals.

For both, the simple cyclic ice cover history as well as the Monte Carlo method based on the global benthic oxygen isotope record (Lisiecki and Raymo, 2005), we assume that deglaciation of the weathered plateaus occurred sometime after the last glacial maximum. Timing of deglaciation (15 ka) is inferred from exposure ages of boulders collected on moraines in adjacent valleys (*Chapter 3*) and previous TCN data from the region (Marsella et al., 2000; Kaplan et al., 2001). To test this assumption, we have calculated the TCN concentrations that would have been measured in the sampled bedrock surfaces prior to an ice-free interval since the start of oxygen isotope stage 3 (OIS-3, 60 ka, black ellipses with points coloured according to ellipses of measured TCN concentrations, Fig. A3.4). Some of the sampled surfaces would have required long periods (>1 Ma) of burial (by 35 m of ice or 13 m of rock). This scenario is unlikely considering the periodic swings between colder and warmer climate during the Quaternary. Therefore, our assumption of ice cover during OIS-2 is justified, which is also supported by the LR04 record used in the MC method.

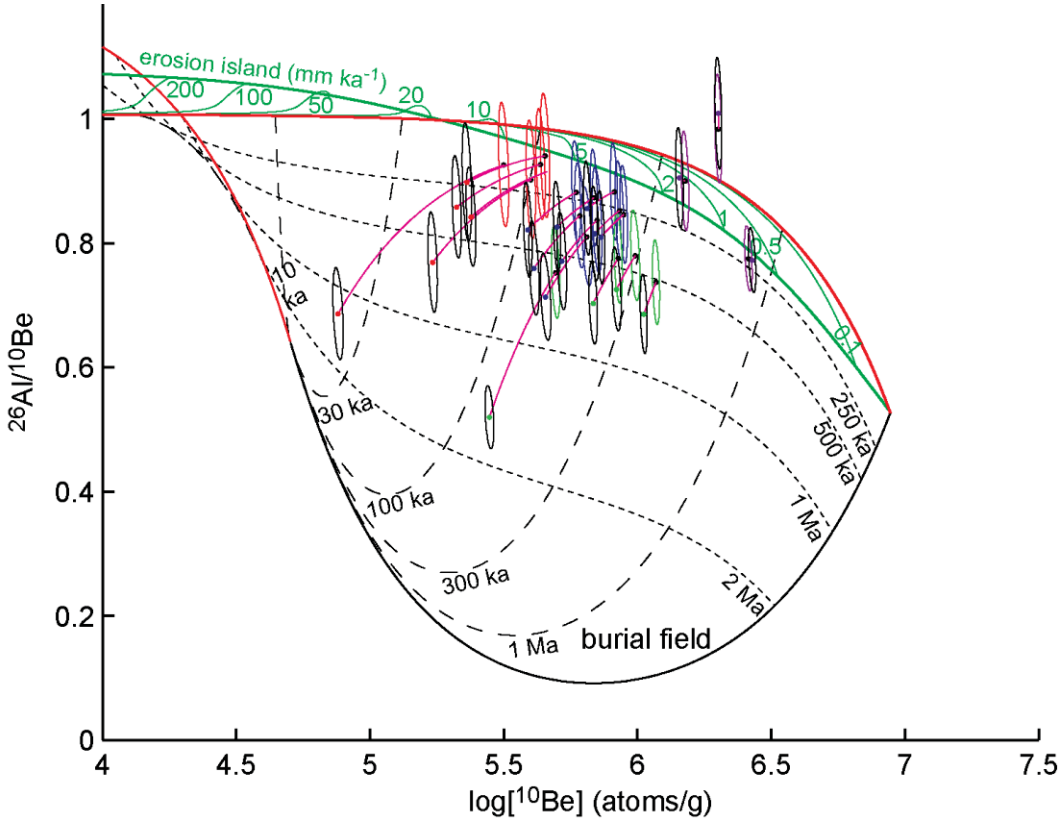

Fig. A3.4 Burial plot showing bedrock surfaces (purple ellipses: stage 1 tors, green ellipses: stage 2 tors and most weathered surface at the stage 2-3 tor; blue ellipses: stage 3 tors, weathered surface at stage 3-4 tors, and fresher surface at the stage 2-3 tor; red ellipses: stage 4-5 tors and fresher surfaces at stage 3-4 tors) and concentrations (coloured dots and black ellipses) of samples, if the sites remained ice-free for the last 60 ka (since OIS-3, increase in concentration shown by pink trajectories).

A3.3 THREE APPROACHES TO DETERMINE LAST GLACIAL PLUCKING

On Cumberland Peninsula, we have observed that stacks of weathered bedrock blocks (tor tops), whose surfaces are affected by granular disintegration, are juxtaposed with less intensely weathered solid bedrock surfaces (tor plinths). Because these surfaces experienced the same complex exposure history, sampling both a fresher and more weathered surface allows us to constrain the timing of last glacial plucking of an overlying bedrock block from the fresher surface. The measurement of two radionuclides

and their ratios in two differentially weathered surfaces reduces the degrees of freedom to constrain the complex exposure history including occasional plucking of weathered bedrock blocks.

We have derived three different approaches to constrain the timing of last glacial plucking. Two approaches (A3.3.1 and A3.3.2) are based on the differences in TCN concentration measured in the two differentially weathered surfaces. The third approach (A3.3.3) outlines how the time of last glacial plucking can be estimated for any sampled surface once the complex exposure history is constrained by multiple paired samples in the region.

A3.3.1 Pairs of Differentially Weathered Tor Surfaces – Approach 1

The strong attenuation of cosmic ray flux through mass (section 4.6.1) and the higher production ratio of $^{26}Al/^{10}Be$ from deeply penetrating muons than from fast neutrons, causes a recently plucked (less weathered) surface to have a lower TCN concentration but a higher $^{26}Al/^{10}Be$ than a non-plucked (more weathered) surface. The differences in measured concentrations and ratios are related to the timing of last plucking of the fresher surface. The close proximity of the twins or triplets of samples precludes differences in their ice cover histories, simplifying the modeling to solve for the timing of last plucking event.

In the case of continuous exposure without intermittent burial intervals, the TCN concentration measured in both surfaces can be expressed as an inherited concentration at the time of plucking and nuclide production since plucking:

$$N_{wth} = Inh_{wth} * e^{-\lambda' * t_{sp}} + \frac{P_i}{\lambda'} * \left(1 - e^{-\lambda' * t_{sp}}\right) \quad eq(A3.1)$$

$$N_{frh} = Inh_{frh} * e^{-\lambda' * t_{sp}} + \frac{P_i}{\lambda'} * \left(1 - e^{-\lambda' * t_{sp}}\right) \quad eq(A3.2)$$

$$\lambda' = \lambda + \frac{\varepsilon * \rho_r}{\Lambda_i} \quad eq(A3.3)$$

with N_{wth} and N_{frh} (atoms g^{-1}) the measured TCN concentrations of the weathered and fresher surface, Inh_{wth} and Inh_{frh} (atoms g^{-1}) the inherited concentration from prior to the plucking event, and t_{sp} the time since plucking. P_i (atoms g^{-1} a^{-1}) is the surface production rate and Λ_i (g cm^{-2}) is the attenuation length for fast neutrons, or fast or negative muons, λ (a^{-1}) is the decay constant, ε (cm a^{-1}) is a constant subaerial erosion rate, and ρ_r (g cm^{-3}) is the bulk rock density.

At the time of plucking, the inherited concentration of the fresh surface is the same as the inherited concentration of the weathered surface at a depth equal to the thickness of removed bedrock block:

$$Inh_{frh} = Inh_{wth} * e^{\frac{-z_r * \rho_r}{\Lambda_i}} \quad eq(A3.4)$$

where z_r is the thickness of removed bedrock block.

The inherited concentration of the fresh surface strongly depends on the thickness of the plucked bedrock block. Production since plucking is strongly diminished if the site has occasionally been buried by ice. For recurring cold-based (weakly erosive) ice cover, 'time-integrated' nuclide production over multiple burial intervals can be calculated using the cyclic ice cover history outlined in section 4.6.1 with glacial-interglacial cycles reduced to 1 ka durations (*eqs(1-3)* with t_c = 1 ka, Fig. 4.3a). The time-integrated

increase in concentrations and decrease in ratios can be calculated for any depth below surface using *eqs(4-5)*, so that concentration and ratio depth profiles can be obtained for different times of complex history (Fig. A3.5).

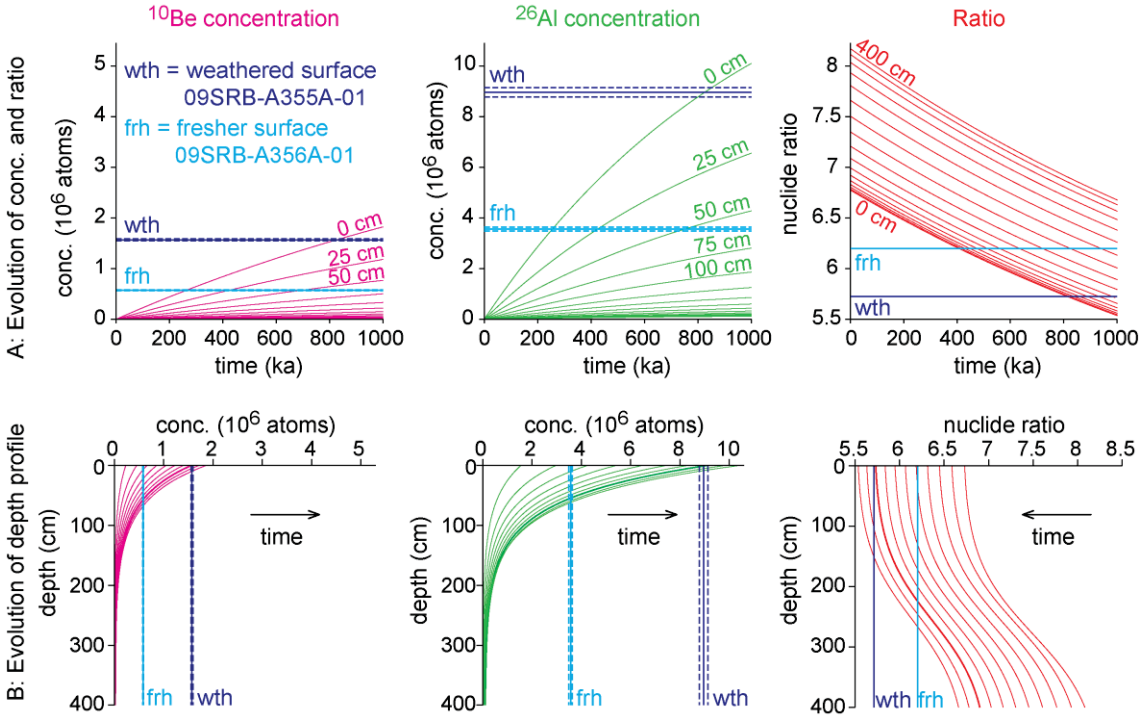

Fig. A3.5 **A.** Time-integrated increase in concentrations and decrease in ratio over multiple glacial-interglacial cycles (for ice-free time f = 20%, zero subaerial erosion, and 1 Ma duration) is calculated at various depths (25 cm intervals up to 4 m depth). TCN concentrations and ratios measured in a weathered surface (sample A355, Table 4.2, Fig. 4.2a, dark blue) and a fresher surface (sample A356, Table 4.2, Fig. 4.2b, light blue) are shown as horizontal lines. **B.** Same data as in A, but shown as depth profiles at 100 ka time intervals of complex history (10 time slices shown).

In a first approximation, we use the depth profile with a surface concentration and ratio (z_r = 0 cm) equivalent to the measured values of the weathered surface (assuming plucking occurred very recently) to derive the inherited concentration of the fresher surface at the time of plucking (Fig. A3.6). To obtain the depth profile below the weathered surface, we **first** have to determine the values of average ice-free time f (for an

assumed subaerial erosion rate ε) and total duration of complex history t_{tot} of the weathered surface (section 4.6.1, Fig. 4.3d, Table 4.3). **Second**, we calculate the depth profile at time t_{tot} using *eqs(1-5)* with t_c = 1 ka (going through as many glacial-interglacial cycles required to reach t_{tot}) and, **third**, for different block thicknesses z_r, we determine the time since plucking t_{sp}, which is the time required to reach the measured concentration of the fresher surface using *eqs(1-3)* with the same values of f and ε (Fig. A3.6). With this value of t_{sp}, we obtain a new depth profile at time t_{tot} - t_{sp} to derive an improved estimate of t_{sp} repeating the procedure until the value of t_{sp} converges.

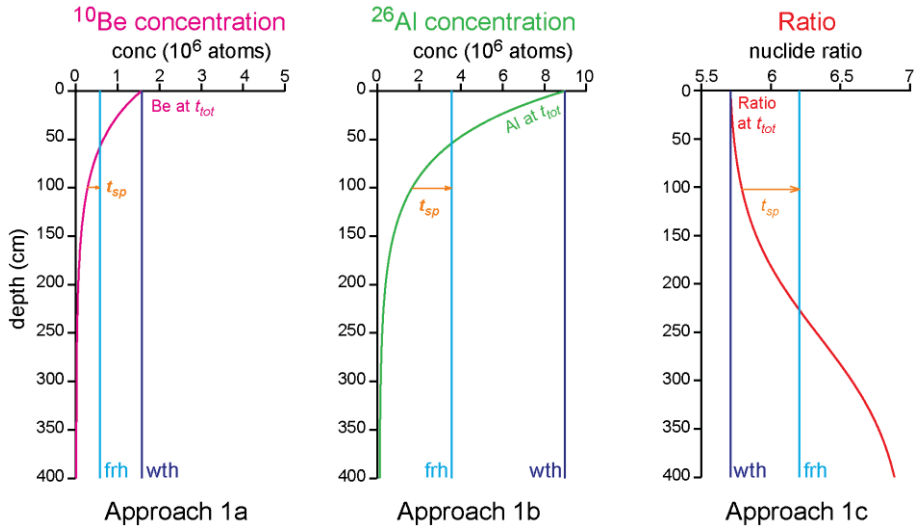

Fig. A3.6 Approaches 1a - c: TCN concentration and ratio depth profiles at time t_{tot} determined for the weathered surface using the appropriate value of f for an assumed subaerial erosion rate ε (section 4.6.1, Fig. 4.3d, Table 4.3). At any depth z_r, the time since plucking t_{sp} is equivalent to the time required to reach the measured TCN concentration or ratio of the fresher surface through a cyclic ice cover history (*eqs(1-3)*). Measured TCN concentrations and ratios for the weathered and fresher surfaces are indicated by dark and light blue lines, respectively.

This approach can be applied to both measured concentrations of ^{10}Be and ^{26}Al (Approaches 1a & b) as well as the ^{26}Al/^{10}Be (Approach 1c) to provide an average of three estimates of t_{sp} for a pair of tor surfaces. If the plucked block thickness z_r is

known (i.e., difference in height between weathered and fresher surface), t_{sp} can be solved uniquely. A range of t_{sp} can be computed for different thicknesses, when fracture density varies with depth.

A3.3.2 Pairs of Differentially Weathered Tor Surfaces – Approach 2

TCN production following the plucking event is the same for both surfaces, since they share the same ice cover history. Therefore, the inherited concentration of the fresher surface at the time of plucking (of a block with thickness z_r) is a function of the difference between the TCN concentrations measured in both surfaces.

$$Inh_{frh} = \frac{N_{wth} - N_{frh}}{e^{-\lambda' * t_{sp}} * [1 - e^{\frac{-z_r * \rho_r}{\Lambda_i}}]} \qquad eq(S5)$$

The ratio of inherited concentrations can be written as:

$$R_{inh} = \frac{Inh_{Al}}{Inh_{Be}} = \frac{([Al]_{wth} - [Al]_{frh}) * e^{-\lambda'_{Be} * t_{sp}}}{([Be]_{wth} - [Be]_{frh}) * e^{-\lambda'_{Al} * t_{sp}}} \qquad eq(S6)$$

This equation is then solved for t_{sp}:

$$t_{sp} = \frac{1}{\lambda'_{Al} - \lambda'_{Be}} * ln \frac{R_{inh} * ([Be]_{wth} - [Be]_{frh})}{([Al]_{wth} - [Al]_{frh})} \qquad eq(S7)$$

This equation allows the calculation of the time since plucking for a particular block thickness z_r, if the inherited ratio at the time of plucking can be estimated. As with Approach 1 (section A3.3.1), the first estimate of inherited ratio is derived from the ratio depth profile below the weathered surface (right profile in Fig. A3.6). Once t_{sp} has been estimated, a new depth profile is obtained at time t_{tot} - t_{sp} to calculate an improved estimate of t_{sp} until the solution for t_{sp} converges (generally after four iterations).

A3.3.3 Any Sampled Surface – Approach 3

When the average glacial conditions (estimates of f for an assumed ε, section 4.6.1, Table 4.3) of a region can be constrained from several samples collected at different locations (including pairs of differentially weathered surfaces at the same site), it is possible to determine a minimum estimate of time since plucking for any sampled surface. Without evidence for common glacial conditions, only the method using twin samples from a tor can constrain the time since plucking. If the assumption is justified that subaerial erosion rates and duration of ice cover are consistent for the same lithology within the same geographical territory (considering elevation and surface area of plateaus to support a glacier), then samples collected from different locations are expected to plot along the same complex exposure trajectory in a burial plot (section 4.6.1, Fig. 4.5, Table 4.3). If a sampled surface had been plucked very recently, then the measured TCN concentrations would plot on a complex exposure trajectory further to the left (i.e., corresponding to shielding by z_r rock overburden, Fig. 4.3c). However, subsequent to the plucking event, the TCN concentrations of the freshly exposed surface quickly follow a sub-horizontal trajectory that reaches towards the trajectory of an exposed surface (dark blue trajectory, Fig. 4.3c). Therefore, the value of average ice-free time f obtained by fitting a trajectory through the sample point represents a minimum estimate. Agreement of estimated values of f between different samples of the same region thus suggests that plucking on any sampled surface had occurred long enough ago, so that the measured TCN concentrations approximate glacial conditions for an exposed surface (i.e., the sample has reach the trajectory of an exposed surface following plucking).

Assuming that the sampled surface has reached the trajectory of an exposed surface, a minimum estimate of the time since plucking can be calculated for different plucked block thicknesses z_r (Fig. A3.7). **First**, a trajectory is fitted through the sample point (providing an estimate f for an assumed ε for that sample) and additional trajectories at various depth are calculated (Fig. A3.7, trajectory for z_r = 50 cm is shown). **Second**, for each block thickness, trajectories for plucking occurring at different times are calculated (dark blue, sub-horizontal convex lines in Fig. A3.7) each merging asymptotically with the trajectory fitted through the sample point. **Third**, the plucking trajectory requiring the shortest time to intersect with the measured concentration (crossing the error ellipse) gives a minimum estimate for t_{sp} for that particular block thickness (note: plucking could have occurred much earlier). This procedure thus renders a function of minimum time since plucking vs. block thicknesses.

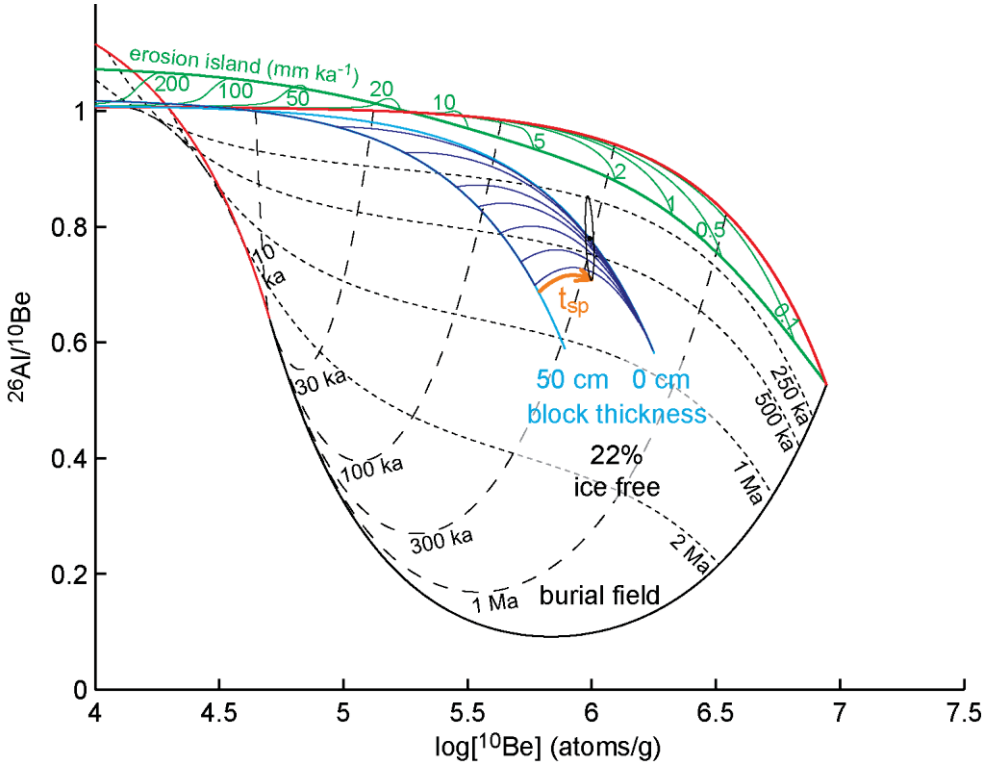

Fig. A3.7 Approach 3: Estimation of time since plucking for any surface. For an assumed subaerial erosion rate ε (here 0 mm ka^{-1}), a complex exposure trajectory is fitted through the sample point (measured nuclide concentrations) determining the percent ice-free time f at the site (section 4.6.1, Fig. 4.3d). For a particular block thickness (z_r = 50 cm is shown), plucking is assumed to occur at different times and complex exposure trajectories for the exhumed surface are calculated (dark blue, sub-horizontal convex curves), which asymptotically reach the trajectory fitted through the sample point. The trajectory requiring the shortest time to intersect the error ellipse of the sample point yields the minimum estimate for time since plucking t_{sp} (i.e., the lowest sub-horizontal trajectory intersecting the error ellipse, orange arrow).

A3.4 TIME SINCE LAST GLACIAL PLUCKING DETERMINED FROM THE THREE APPROACHES

A3.4.1 Approach 1 – Pairs of Differentially Weathered Tor Surfaces

For all four pairs of samples (two of the pairs constitute a set of three samples collected at the same site (11, Table 4.2)), the timing of last plucking determined by approach 1a-c agree closely, so that an average estimate can be calculated (red lines in Fig. A3.8). This estimate depends on the chosen values of subaerial erosion rate ε and ice-free time f. Increasing ε leads to earlier last plucking for the same block thickness, while increasing f results in more recent last plucking.

A3.4.2 Approach 2 – Pairs of Differentially Weathered Tor Surfaces

Approach 2 yields a differently shaped curve for timing of plucking with depth (green lines in Fig. A3.8) mimicking the ratio depth profile (turned by 90° counter-clockwise). As for approach 1, the time since last plucking depends on values of ε and f but in different ways. Increasing both ε and f results in earlier last plucking. Additionally, for one sample pair (A346 & A348) only three iterations could be successfully completed. A reason for this behaviour could be the relatively small difference in TCN concentrations and ratios between the weathered (A346) and fresher surface (A348).

For three of the four sample pairs, the estimate of time since last plucking derived with approach 2 is always larger than the estimate determined by approaches 1a-c (Fig. A3.8). The discrepancy between the estimates from both approaches is likely related to the values of ε and f used in the calculations. Increasing the subaerial erosion rate ε and decreasing ice-free time f would draw the estimates of timing of last glacial plucking

towards each other for three of the sample pairs. Opposite shifts in values of ε and f would be required for the fourth sample pair (A188-186).

Comparison of the timing of last plucking based on sample pairs (approaches 1a-c and 2, red and green lines in Fig. A3.8) with the estimate derived based on the fresher surface only (approach 3, using the same values of ε and f than in approaches 1 & 2, blue lines in Fig. A3.8) indicates closer similarities between approaches 3 and 1 than 2. Although the different approaches do not completely agree, approach 3 seems to yield tentatively similar results (i.e., more recent plucking for sample A356 than for sample A186). This conformity suggest that approach 3 can provide reliable estimates of timing since last plucking for any sampled surfaces, if the sampled tor sites experienced similar ice cover histories (roughly agreeing estimates of ε and f).

A3.4.3 Approach 3 – Any Sampled Surface

The timing of last plucking (Fig. A3.9) determined for all samples plotting closely to the complex exposure trajectory for a cyclic ice cover history (Fig. 4.5, section 4.6.1) varies systematically according to the weathering degree of the sampled surfaces and classification of glacial modification of the tor sites (Table 4.2, section 4.6.1). Sites with only slight glacial modification (stage 2 tors, and weathered surface on the stage 2-3 tor; green curves in Fig. A3.9) have been last plucked much earlier than sites that have been modified more strongly (stage 3 tors, weathered surface on stage 3-4 tors, and fresher surfaces on the stage 2-3 tor; blue lines in Fig. A3.9). Most recently, plucking (red lines in Fig. A3.9) occurred on the most intensely modified tors (stage 4-5) or on the fresher surface of intermediately modified sites (stage 3-4 tors). This agreement between timing of last glacial plucking determined from measured TCN concentrations and geomorphic

observations (weathering degree and degree of glacial modification) suggests that our approaches yield reasonable results, despite the multitude of assumptions and simplification required.

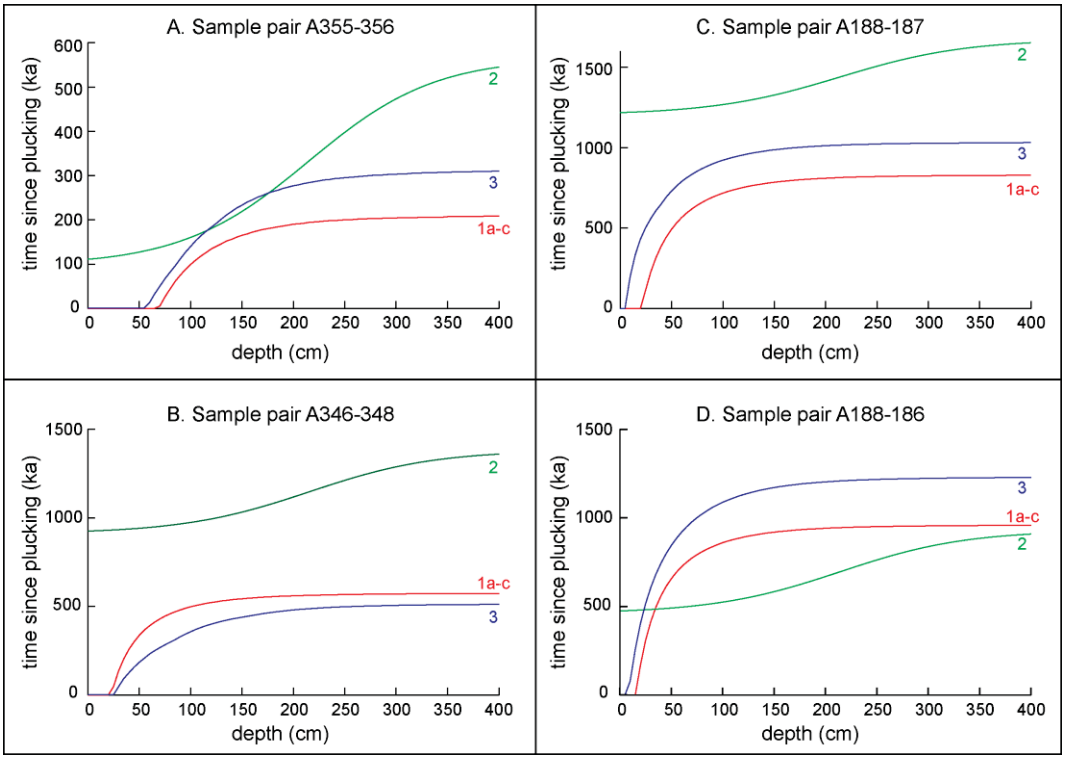

Fig A3.8 Different estimates of time since last glacial plucking determined for the fresher surface of a pair of samples collected from differentially weathered bedrock surfaces at four tor sites (Approaches 1a-c red lines, Approach 2 green curves, and Approach 3 dark blue lines). **A.** Sample pair A355 (weathered surface) and A356 (fresher surface) collected at site 10 (Table 4.2, Fig. 4.2 a-b). **B.** Sample pair A346 (weathered surface) and A348 (fresher surface) from site 6 (Fig. A3.2 e-f). **C.** Sample pair A188 (weathered surface) and A187 (fresher surface) from site 11 (Fig. A3.2a sample A188, Fig. A3.2b sample A187 is taken from top of tor ridge). **D.** Sample pair A188 (weathered surface) and A186 (fresher surface) from same site as in C (A186 collected from extensive slab in foreground of Fig. A3.2b).

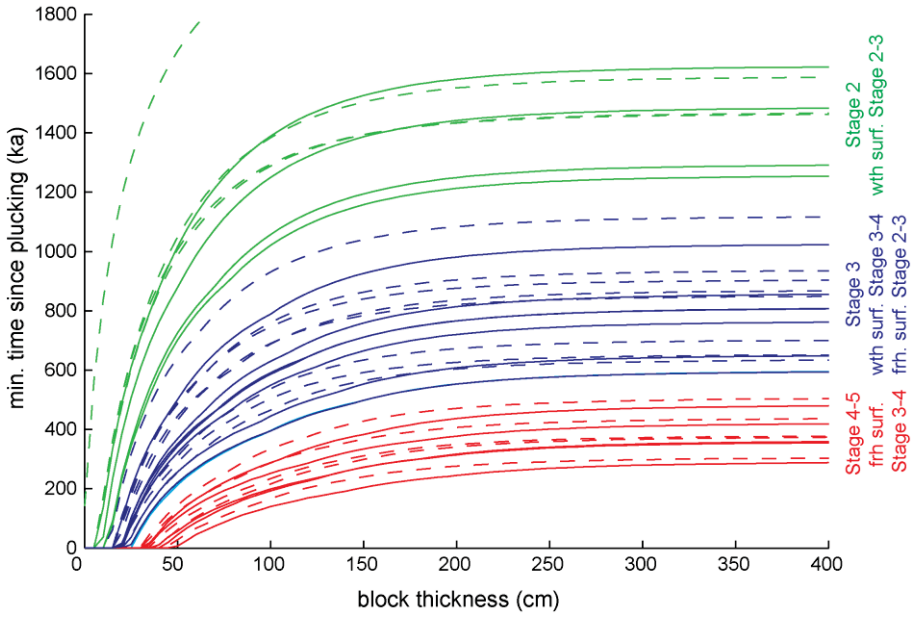

Fig. A3.9 Time since plucking calculated for any surface. Solid lines: no erosion, dashed lines 1mm ka^{-1} subaerial erosion. Green: stage 2 tors and most weathered surface (wth surf.) on the stage 2-3 tor, blue: stage 3 tors, weathered surfaces on stage 3-4 tors, and fresher surfaces on the stage 2-3 tor; and red: stage 4-5 tors and fresher surfaces of stage 3-4 tors.

A3.5 DETAILS OF MONTE CARLO METHOD

The Monte Carlo approach is based on the stacked benthic oxygen istotope record (LR04, Lisiecki and Raymo, 2005) that represents global ice volume changes. Comparing the representation of the last 1.2 Ma of LR04 in the burial plot (light blue irregular saw-tooth line in Fig. A3.10) with the trajectory of a simple cyclic ice cover history (light blue smooth line in Fig. A3.10) indicates that exposure intervals derived from LR04 are too long during the early Pleistocene, but that LR04 concurs closely with the cyclic ice cover history for the last 800 ka (inset, Fig. A3.10). The most recent complex exposure history has the largest effect on the measured TCN concentrations suggesting that the cyclic ice cover history is a valuable approximation for LR04 for the middle to late Pleistocene.

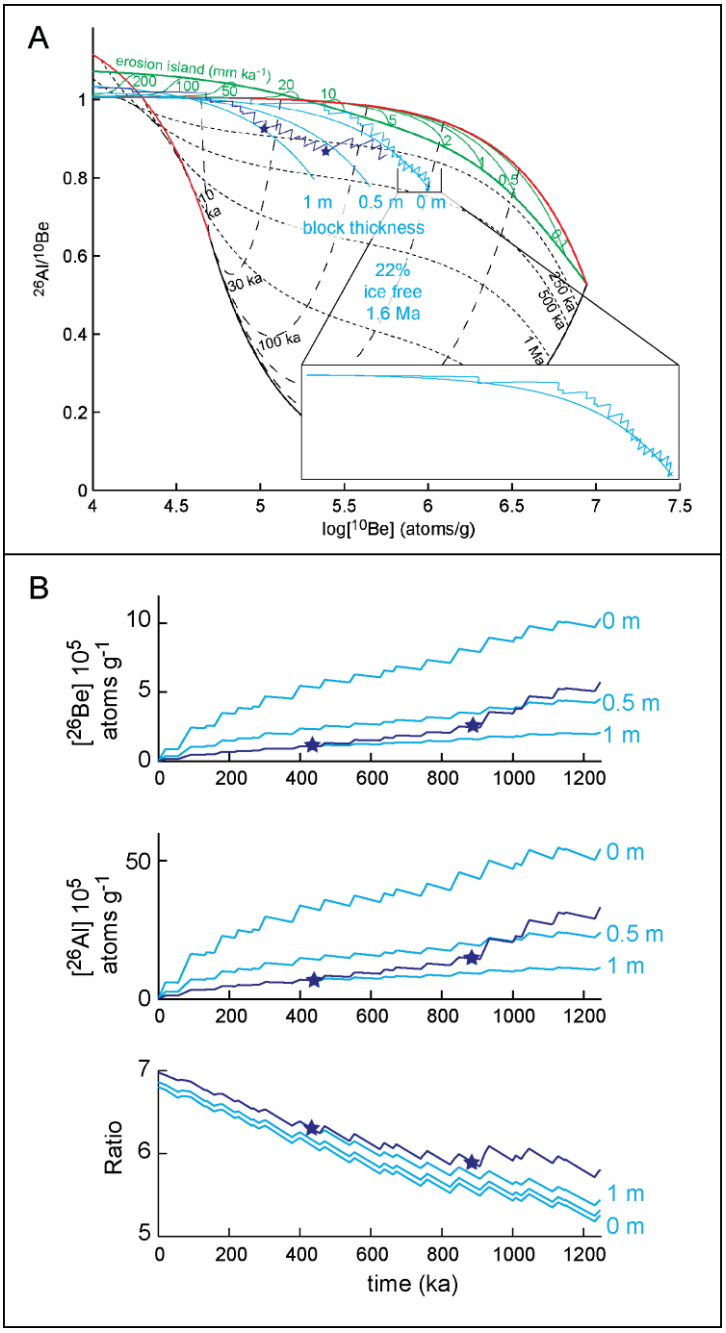

Fig. A3.10 **A.** Comparison of LR04 record ($\delta^{18}O$ = 3.8 permil dividing the record into ice-free and ice-cover intervals for the last 1250 ka (20 burial intervals; light blue, irregular saw-tooth trajectory) and cyclic ice cover history (1 ka glacial-interglacial cycles for 1.6 Ma; light blue lines shown for 0 cm, 50 cm, and 100 cm rock thicknesses). Inset displays both ice cover models for an exposed surface. Dark blue trajectory shows the same LR04 history but with two plucking events occurring during the 8th and 15th burial interval each removing 50 cm of rock (marked by dark blue stars). **B.** Increase in concentrations and decrease of ratio based on the last 1250 ka of the LR04 record (as in A) for 0, 50, and 100 cm rock thicknesses (light blue lines) and including two plucking events (dark blue line, plucking marked by blue stars).

The MC method results can be further evaluated by plotting different input parameters and calculated variables of all accepted solutions against each other (solutions are accepted if the calculated TCN concentrations are within the 1σ uncertainty ranges of the measured concentrations, Fig. A3.11 – A3.12). In these scatter plots, the size of the circles represents the χ^2 values obtained for a particular pair of variables (larger circles indicating lower χ^2 values). Plotting subaerial erosion rate against the values of $\delta^{18}O$ used to divide the LR04 record in ice-free and ice-cover intervals reveals that longer ice-free time (i.e., higher $\delta^{18}O$ values) is required for higher subaerial erosion rates (Fig. A3.11). The same relationship between subaerial erosion rates and ice-free time has already been observed for the simplified cyclic ice cover history (section 4.6.1, Fig. 4.3).

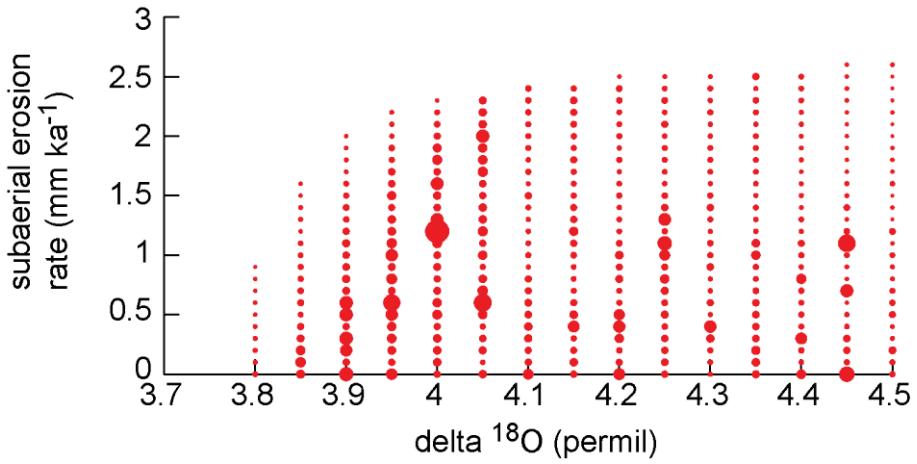

Fig. A3.11 Relationship between subaerial erosion rate and value of $\delta^{18}O$ that divides LR04 into ice-free and ice-cover intervals (shown for sample pair A355-356 (site 10, Table 4.2, Fig. 4.2 a-b) and 10,000 accepted solutions): Scatterplot is shown for all accepted solutions (calculated TCN concentrations are within 1σ of the measured concentrations) where the size of the circle is inversely proportional to the χ^2 value obtained for a specific set of erosion rate and $\delta^{18}O$. Likewise the cyclic ice cover model, larger $\delta^{18}O$ values (i.e., longer exposure intervals) are required for larger subaerial erosion rates that reach a maximum value of ~2.5 mm ka^{-1} (input range is 0 – 4 mm ka^{-1}).

Although the MC method yields more recent timing of last plucking for fresher surfaces than more weathered surfaces, the range of timing increases considerably for more weathered surfaces (Fig. 4.7). Plotting various variables against the timing of last plucking for one sample pair from site 10 (A355 weathered surface, Fig. 4.2a; A356 fresher surface, Fig. 4.2b), reveals that more recent plucking is favoured by longer ice-fee intervals (higher $\delta^{18}O$ value, Fig. A3.12a), lower erosion rates (Fig. A3.12b), and smaller block thicknesses removed during the plucking event (Fig. A3.12c). Interestingly, the range of episodic erosion rate is largest for the most probable timing of last plucking (Table 4.3, Fig. 4.8), decreases for more recent plucking events, and is smallest for the earliest plucking events (Fig. A3.12d).

The probability density distribution and hence values of the episodic erosion rate determined with the MC method is mainly a function of the measured TCN concentration. Low TCN concentrations yield a higher episodic erosion rate than higher concentrations. This dependency is similar to the variation of basin-wide denudation rates, which yield higher estimates for lower TCN concentrations (i.e., following deep-seated mass wasting events) and lower values for higher concentrations {i.e. steady background denudation, Niemi et al., 2005; Antinao Rojas, 2009). To check this relationship between estimates of episodic erosion rate and measured TCN concentrations, we adjusted the TCN concentration of the fresher surface of a sample pair to a value that would have been measured prior to plucking of a 50 cm thick bedrock block at the end of the last glaciation (i.e., the timing of deglaciation 15 ka, Fig. A3.13). The episodic erosion rate calculated for the adjusted (higher) TCN concentration has a mode of 3.25 mm ka^{-1} ($^{-1.1}/_{+5.8}$ mm ka^{-1}, 1σ error range), which is considerably lower than

calculated for the measured (lower) TCN concentration (mode 7.25 mm ka^{-1}, 1σ error range $^{-3.0}/_{+8.3}$ mm ka^{-1}). In addition, the timing of last plucking event (prior to removal of 50 cm of rock at 15 ka) is earlier (300 $^{-92}/_{+243}$ ka) than for the measured TCN concentrations (200 $^{-162}/_{+22}$ ka), indicating that our calculations are reasonable.

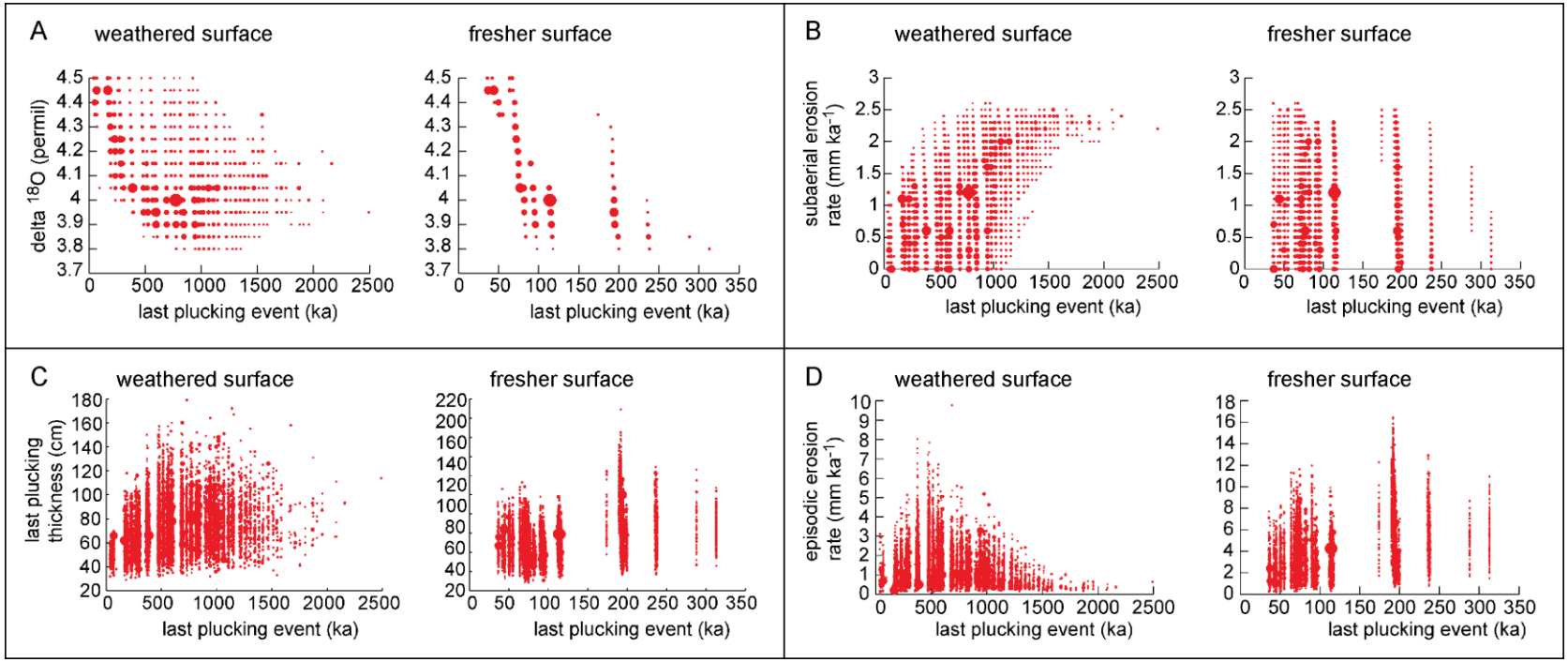

Fig. A3.12 Variation of timing of last plucking event (plotted on horizontal axis) with **A.** $\delta^{18}O$ value, **B.** Subaerial erosion rate, **C.** Thickness of removed bedrock block, and **D.** Episodic erosion rate. In each panel, the left figure shows the timing of last plucking for the weathered surface (here sample A255, site 10, Table 4.2, Fig. 4.2a) and the right figure displays the timing of last plucking of the fresher surface (sample A356, Fig. 4.2b).

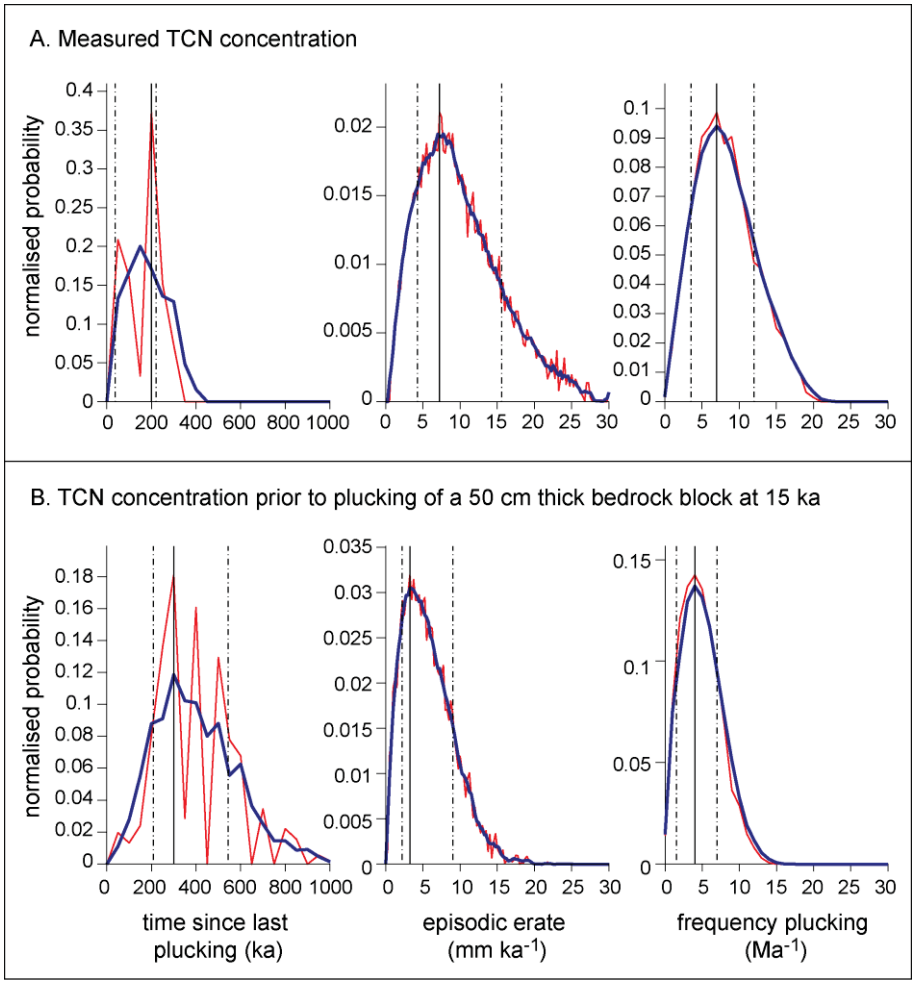

Fig. A3.13 Comparison of normalised probability distributions determined with the Monte Carlo approach for sample A356 (fresh surface site 10, Table 4.2, Fig. 4.2b) using the **A.** measured TCN concentration, and **B.** a hypothetical TCN concentration prior to plucking of a 50 cm thick bedrock block at the end of the last glaciation (i.e., timing of deglaciation 15 ka). Red lines are calculated probabilities, blue lines are smoothed probabilities, black solid line is the mode, and dashed lines the 1σ error ranges.

A3.6 REFERENCES FOR A3

Antinao Rojas, J.L., 2009. Quaternary landscape evolution of the southern Central Andes of Chile quantified using landslide inventories, beryllium-10 and chloride-36 cosmogenic isotopes and uranium-thorium/helium thermochronology. Earth Sciences, PhD Thesis. Dalhousie University, Halifax, p. 253.

Balco, G., Stone, J.O., Lifton, N.A., Dunai, T.J., 2008. A complete and easily accessible means of calculating surface exposure ages or erosion rates from ^{10}Be and ^{26}Al measurements. Quaternary Geochronology 3, 174-195.

Borcher, B., Marrero, S., Balco, G., Caffee, M., Goehring, B., Gosse, J., Lifton, N., Nishiizumi, K., Phillips, F., Schaefer, J., Stone, J.O.H., in press. Geological calibration of spallation production rates for terrestrial cosmogenic nuclides in the CRONUS-Earth Project. Quaternary Geochronology.

Granger, D.E., Smith, A.L., 2000. Dating buried sediments using radioactive decay and muogenic production of ^{26}Al and ^{10}Be. Nuclear Instruments and Methods in Physics Research Section B: Beam Interactions with Materials and Atoms 172, 822-826.

Granger, D.E., Muzikar, P.F., 2001. Dating sediment burial with in situ-produced cosmogenic nuclides: theory, techniques, and limitations. Earth and Planetary Science Letters 188, 269-281.

Granger, D.E., 2006. A review of burial dating methods using ^{26}Al and ^{10}Be, In: Siame, L.L., Bourles, D.L., Brown, E.T. (Eds.), In situ-produced cosmogenic nuclides and quantification of geological processes. Geological Society of America Special Paper, p. 1-16.

Heisinger, B., Lal, D., Jull, A., Kubik, P., Ivy-Ochs, S., Knie, K., Nolte, E., 2002a. Production of selected cosmogenic radionuclides by muons: 2. Capture of negative muons. Earth and Planetary Science Letters 200, 357-369.

Heisinger, B., Lal, D., Jull, A., Kubik, P., Ivy-Ochs, S., Neumaier, S., Knie, K., Lazarev, V., Nolte, E., 2002b. Production of selected cosmogenic radionuclides by muons:: 1. Fast muons. Earth and Planetary Science Letters 200, 345-355.

Kaplan, M., Miller, G., Steig, E., 2001. Low-gradient outlet glaciers (ice streams?) drained the Laurentide ice sheet. Geology 29, 343-346.

Kohl, C., Nishiizumi, K., 1992. Chemical isolation of quartz for measurement of in-situ-produced cosmogenic nuclides. Geochimica et Cosmochimica Acta 56, 3583-3587.

Lal, D., 1991. Cosmic ray labeling of erosion surfaces: in situ nuclide production rates and erosion models. Earth and Planetary Science Letters 104, 424-439.

Lifton, N., Sato, T., Dunai, T.J., 2014. Scaling in situ cosmogenic nuclide production rates using analytical approximations to atmospheric cosmic-ray fluxes. Earth and Planetary Science Letters 386, 149-160.

Lisiecki, L.E., Raymo, M.E., 2005. A Plio-Pleistocene stack of 57 globally distributed benthic ^{18}O records. Paleoceanography 20, 522–533.

Margreth, A., 2015. Geochronological approaches for quantification of polythermal glacier dynamics and subglacial episodic erosion on high-latitude highland plateaus, Cumberland Peninsula, Baffin Island, Nunavut. Earth Sciences, PhD. Dalhousie University, Halifax.

Marsella, K., Bierman, P., Davis, P., Caffee, M., 2000. Cosmogenic ^{10}Be and ^{26}Al ages for the last glacial maximum, eastern Baffin Island, Arctic Canada. Geological Society of America Bulletin 112, 1296-1312.

Niemi, N.A., Oskin, M., Burbank, D.W., Heimsath, A.M., Gabet, E.J., 2005. Effects of bedrock landslides on cosmogenically determined erosion rates. Earth and Planetary Science Letters 237, 480-498.

Nishiizumi, K., Winterer, E.L., Kohl, C.P., Klein, J., Middleton, R., Lal, D., Arnold, J.R., 1989. Cosmic ray production rates of ^{10}Be and ^{26}Al in quartz from glacially polished rocks. Journal of Geophysical Research: Solid Earth 94, 17907-17915.

Nishiizumi, K., 2004. Preparation of ^{26}Al AMS standards. Nuclear Instruments and Methods in Physics Research Section B: Beam Interactions with Materials and Atoms 223–224, 388-392.

Nishiizumi, K., Imamura, M., Caffee, M.W., Southon, J.R., Finkel, R.C., McAninch, J., 2007. Absolute calibration of ^{10}Be AMS standards. Nuclear Instruments and Methods in Physics Research Section B: Beam Interactions with Materials and Atoms 258, 403-413.

Stone, J.O., 2000. Air pressure and cosmogenic isotope production. Journal of Geophysical Research 105, 23753-23759.

Taylor, J., 1997. Introduction to error analysis: the study of uncertainties in physical measurements, 2nd ed. Univ. Sci. Books, Mill Valley, Calif.

APPENDIX A4 – MATLAB® Codes

A4.1 INTRODUCTION

This appendix contains all Matlab codes required for the calculations used in this thesis, with the exception of the codes for scaling production rates to site-specific locations (LSD code adapted from Lifton et al., 2014) and for plotting error ellipses (Balco et al., 2008). In order to use the LSC-scaling scheme, the 'consts' matrix has first to be loaded into the workspace. For plotting error ellipses in the burialplot, the code 'ellipse' from Balco et al. (2008) is used with slight modifiations.

All calculations are completed with the measured TCN concentrations and by scaling production rates to site- specific locations (Table A4.1). For the burialplot, TCN concentrations had to be normalized to a common location, which I have chosen to be an average location at sea level on Cumberland Peninsula (66.50°N, 65.20°W, 0 m, Table A4.2). For displaying the LR04 record in the burialplot and modelling of complex exposure histories with the Monte Carlo method, two tables containing the duration of individual exposure and burial intervals over the last 3 Ma for different $\delta^{18}O$ values (from 3.5 to 4.5 ppm, in 0.5 ppm steps) are loaded within the functions (Table A4.3 - A4.4, Lisiecki and Raymo, 2005).

Additional Matlab functions not included in this appendix:

Tor_ellipse.m	Balco et al. (2008)
LSD scaling code	Lifton et al. (2014)

A4.2 MATLAB INPUT FILES

A4.2.1 Tor Data

%Latitude %(dd.dd)	%Longitude %(dd.dd)	Elevation %(m)	%^{10}Be conc %(atoms)	%^{10}Be conc error %(atoms)	%^{26}Al conc %(atoms)	%^{26}Al conc error %(atoms)	%Field ID
66.00	-65.54	830	707233.008004766	21388.9652549905	3702246.99841709	203488.065131778	%09SRB-E221A-01
66.00	-65.54	830	1261068.500776760	34299.7703158381	5714146.27385362	201711.802239546	%09SRB-E221A-02
66.00	-65.54	830	965575.616362466	27466.1704624778	5908791.07591388	340352.127008785	%09SRB-E221A-03
66.28	-65.80	765	1406032.417437360	39954.1570756381	7873971.04346606	499150.355963401	%09SRB-E304A-01
66.11	-65.55	827	1358838.999638550	42177.2281107367	7363454.54665450	431382.859060069	%09SRB-A186A-01
66.11	-65.55	825	1777415.127541430	44714.4256420841	9220354.56007183	543794.530125116	%09SRB-A188A-01
66.11	-65.55	825	1237443.252984090	31801.1439332702	7300062.62081135	426644.726285042	%09SRB-A187A-01
66.12	-65.54	671	1570080.934969070	40276.0147626650	8965389.26575768	523954.263575652	%09SRB-A355A-01
66.12	-65.54	662	575024.825807452	17429.9628796701	3567266.11523864	240270.895602845	%09SRB-A356A-01
66.30	-65.71	975	1451819.809952160	43679.9101821799	8183575.73375743	498342.964122876	%09SRB-A346A-01
66.30	-65.71	971.7	1032604.161197980	28195.9370889393	6391546.53583253	381425.284009397	%09SRB-A348A-01
66.30	-65.71	971	466858.307691387	12787.2868714846	2625741.96594254	123415.371017464	%09SRB-A347A-01
66.36	-65.70	1038	2234964.318683340	51111.41069495320	12618353.94785590	758937.1027641590	%09SRB-E222A-01
66.36	-65.70	1038	321170.082362767	9193.74139652006	1236122.48117690	56483.2006451662	%09SRB-E222A-02
66.36	-65.70	1038	1729484.531925900	37527.67197367810	10080411.84066610	577725.0430864910	%09SRB-E222A-03
66.36	-65.70	1038	462419.397281416	13035.91436203780	1988669.59852398	104903.9315300410	%09SRB-E222A-04
67.28	-63.08	570	670667.551960581	18575.64561475100	4058001.78031583	271920.3473808540	%10SRB-E042A-01
67.60	-63.93	373	634914.537402504	17588.27417713200	4014123.53981184	272190.2059062080	%10SRB-E064A-01
67.67	-64.26	1030	5014765.597208140	105215.11643003800	32935198.62271320	1913619.7822870800	%10SRB-E065A-01
66.30	-65.81	1004	2397325.226729280	65117.61423973280	12480221.883680900	714002.6256494060	%10SRB-E020A-01
66.30	-65.81	1001	2862743.705688480	60653.32503750440	14085997.628263600	857833.8970928510	%10SRB-E021A-01
66.29	-65.75	1150	1366673.425950430	35315.42475430580	6855840.891227190	426297.6242438630	%10SRB-E022A-01
66.36	-65.70	1038	2056897.590791780	44702.40921591360	12117097.808859800	694521.3294170630	%09SRB-E222A-05
66.36	-65.70	1038	195102.628461243	5329.23728827139	949041.327747847	69437.5508509174	%09SRB-E222A-06
66.70	-61.66	1314	8232030.129133410	180299.82441555700	42473623.629146500	1690867.6533258700	%10SRB-E074A-01
67.67	-64.26	1026	3751164.665796110	83554.00877300120	22537220.713773500	1291972.2527047900	%10SRB-E066A-01

Table A4.1 Input data for all tor sites (measured values).

%Latitude %(dd.dd)	%Longitude %(dd.dd)	Elevation %(m)	%^{10}Be conc %(atoms)	%^{10}Be conc error %(atoms)	%^{26}Al conc %(atoms)	%^{26}Al conc error %(atoms)	%Field ID
66.50	-65.20	0	335987.170000000	10161.3160000000	1774374.40000000	97525.641000000	%09SRB-E221A-01
66.50	-65.20	0	599099.350000000	16294.8880000000	2738616.50000000	96674.333000000	%09SRB-E221A-02
66.50	-65.20	0	458718.720000000	13048.4310000000	2831903.90000000	163120.420000000	%09SRB-E221A-03
66.50	-65.20	0	706654.340000000	20080.4610000000	3989621.40000000	252911.900000000	%09SRB-E304A-01
66.50	-65.20	0	647221.280000000	20089.2080000000	3538120.00000000	207278.300000000	%09SRB-A186A-01
66.50	-65.20	0	848054.920000000	21334.5140000000	4437924.10000000	261738.190000000	%09SRB-A188A-01
66.50	-65.20	0	590419.100000000	15173.2230000000	3513652.70000000	205351.860000000	%09SRB-A187A-01
66.50	-65.20	0	856575.950000000	21973.0490000000	4926202.80000000	287896.580000000	%09SRB-A355A-01
66.50	-65.20	0	316197.640000000	9584.4785000000	1975448.90000000	133055.080000000	%09SRB-A356A-01
66.50	-65.20	0	609086.320000000	18325.1640000000	3468795.90000000	211234.070000000	%09SRB-A346A-01
66.50	-65.20	0	434430.480000000	11862.4110000000	2716734.30000000	162125.260000000	%09SRB-A348A-01
66.50	-65.20	0	196530.700000000	5382.9919000000	1116732.20000000	52488.752000000	%09SRB-A347A-01
66.50	-65.20	0	888825.920000000	20326.56500000000	5073392.70000000	305141.7000000000	%09SRB-E222A-01
66.50	-65.20	0	127726.550000000	3656.27120000000	497001.02000000	22709.8920000000	%09SRB-E222A-02
66.50	-65.20	0	687800.990000000	14924.43000000000	4052976.20000000	232282.7600000000	%09SRB-E222A-03
66.50	-65.20	0	183900.180000000	5184.27000000000	799573.53000000	42178.1510000000	%09SRB-E222A-04
66.50	-65.20	0	399933.270000000	11077.05100000000	2434612.40000000	163139.5600000000	%10SRB-E042A-01
66.50	-65.20	0	451423.930000000	12505.25500000000	2865416.50000000	194298.5300000000	%10SRB-E064A-01
66.50	-65.20	0	2007875.400000000	42127.36100000000	13330932.00000000	774561.4700000000	%10SRB-E065A-01
66.50	-65.20	0	981265.390000000	26653.73100000000	5162742.400000000	295364.2700000000	%10SRB-E020A-01
66.50	-65.20	0	1174757.300000000	24889.73600000000	5841690.800000000	355757.5800000000	%10SRB-E021A-01
66.50	-65.20	0	494641.640000000	12781.75100000000	2511489.400000000	156164.9400000000	%10SRB-E022A-01
66.50	-65.20	0	818010.320000000	17777.76000000000	4871855.400000000	279242.4000000000	%09SRB-E222A-05
66.50	-65.20	0	77590.622000000	2119.39140000000	381575.870000000	27918.3770000000	%09SRB-E222A-06
66.50	-65.20	0	2600430.600000000	56955.23000000000	13602558.000000000	541515.4800000000	%10SRB-E074A-01
66.50	-65.20	0	1507035.100000000	33567.92800000000	9152799.800000000	524694.8400000000	%10SRB-E066A-01

Table A4.2 Input data for all tor sites (normalized to sea level high latitude).

A4.2.2 LR04 Exposure and Burial Intervals

%3.5	%3.55	%3.6	%3.65	%3.7	%3.75	%3.8	%3.85	%3.9	%3.95	%4	%4.05	%4.1	%4.15	%4.2	%4.25	%4.3	%4.35	%4.4	%4.45	%4.5
%(ka)	%(ka)	%(ka)	%(ka)	%(ka)	%(ka)	%(ka)	%(ka)	%(ka)	%(ka)	%(ka)	%(ka)	%(ka)	%(ka)	%(ka)	%(ka)	%(ka)	%(ka)	%(ka)	%(ka)	%(ka)
10	11	11	11	12	12	12	12	13	13	13	13	14	14	14	14	15	15	15	15	15
10	11	11	12	13	14	2	3	4	6	6	2	58	13	60	62	62	1	3	1	3
3	1	3	4	5	7	16	7	11	13	15	7	30	43	30	31	32	1	7	14	18
11	2	2	9	9	11	22	17	18	19	20	17	2	30	2	19	20	63	63	1	2
18	4	4	6	7	8	8	23	27	28	28	21	13	12	14	14	60	2	4	66	67
2	13	5	15	1	5	26	10	10	10	11	29	10	9	12	41	52	32	34	1	3
4	19	14	21	16	17	25	2	4	5	6	12	37	37	39	50	1	23	25	5	13
8	2	20	4	22	23	10	27	28	28	29	7	44	2	48	57	58	61	65	6	65
12	4	2	6	5	7	7	26	28	2	37	3	33	40	34	24	1	56	62	63	2
12	2	5	6	8	9	9	20	21	31	24	31	20	27	20	36	26	2	66	2	10
6	4	6	6	8	10	12	10	2	24	13	38	20	1	24	34	37	60	70	2	69
18	6	4	10	10	10	14	16	10	6	17	26	34	18	35	16	36	70	40	1	2
18	10	8	18	12	12	14	16	3	3	6	17	32	18	34	30	16	38	18	67	65
2.5	14	4	14	20	22	22	16	16	11	18	18	6	32	12	54	32	18	36	63	73
7.5	16	10	16	14	18	18	24	16	5	22	28	26	28	28	16	56	32	60	70	6
7.5	6	12	12	4	2	4	20	18	18	20	24	52	2	54	34	18	58	30	1	74
10	2	14	18	18	6	10	6	24	20	8	20	14	24	16	66	34	22	38	71	44
12.5	22	4	2	14	20	22	12	20	18	34	52	32	52	32	74	68	34	72	40	22
5	18	16	10	18	18	4	24	8	4	24	6	16	10	16	64	80	68	84	20	38
17.5	7.5	10	10	6	10	36	6	4	4	12	26	14	28	16	40	66	82	1872	36	62
12.5	12.5	6	24	6	18	20	38	14	24	8	12	22	14	26	36	48	68	NAN	60	38
10	2.5	22	22	12	8	10	2	24	22	18	10	38	10	64	120	283	335.5	NAN	32	2076
20	15	20	5	16	8	12	22	6	8	32	18	16	20	62	42	1457.5	1460	NAN	40	NAN
15	15	7.5	12.5	26	14	14	14	40	6	10	34	54	38	38	40	NAN	NAN	NAN	2034	NAN
15	17.5	5	7.5	22	18	20	12	30	14	50	14	36	14	32	35	NAN	NAN	NAN	NAN	NAN
15	10	2.5	7.5	5	26	28	18	18	28	30	52	32	54	120	1455	NAN	NAN	NAN	NAN	NAN
5	5	2.5	5	5	22	24	22	16	10	28	32	44	32	42	NAN	NAN	NAN	NAN	NAN	NAN
17.5	20	17.5	2.5	12.5	12.5	12.5	32	18	46	22	30	34	32	36	NAN	NAN	NAN	NAN	NAN	NAN
20	15	5	20	2.5	5	17.5	26	22	30	22	26	34	2	30	NAN	NAN	NAN	NAN	NAN	NAN
12.5	2.5	5	7.5	10	10	25	15	34	4	26	24	40	34	30	NAN	NAN	NAN	NAN	NAN	NAN
22.5	12.5	5	17.5	15	5	5	20	26	20	38	28	36	28	75	NAN	NAN	NAN	NAN	NAN	NAN
25	20	15	5	7.5	17.5	12.5	30	17.5	16	26	38	25	30	412.5	NAN	NAN	NAN	NAN	NAN	NAN
22.5	17.5	17.5	2.5	7.5	5	25	25	20	22	20	28	30	38	77.5	NAN	NAN	NAN	NAN	NAN	NAN
30	20	17.5	17.5	22.5	12.5	27.5	25	60	26	25	22.5	72.5	30	845	NAN	NAN	NAN	NAN	NAN	NAN
70	27.5	10	27.5	7.5	17.5	30	30	30	36	62.5	25	87.5	22.5	NAN	NAN	NAN	NAN	NAN	NAN	NAN
105	20	7.5	25	32.5	7.5	12.5	32.5	32.5	26	32.5	67.5	317.5	25	NAN	NAN	NAN	NAN	NAN	NAN	NAN
75	20	20	5	12.5	7.5	37.5	57.5	35	17.5	35	35	75	67.5	NAN	NAN	NAN	NAN	NAN	NAN	NAN
NAN	12.5	17.5	27.5	25	25	22.5	25	60	22.5	40	37.5	842.5	37.5	NAN	NAN	NAN	NAN	NAN	NAN	NAN
NAN	55	25	22.5	30	12.5	30	32.5	27.5	62.5	65	110	NAN	40	NAN	NAN	NAN	NAN	NAN	NAN	NAN
NAN	25	25	20	32.5	35	37.5	45	37.5	30	75	77.5	NAN	115	NAN	NAN	NAN	NAN	NAN	NAN	NAN
NAN	35	20	30	7.5	17.5	52.5	55	107.5	32.5	110	112.5	NAN	80	NAN	NAN	NAN	NAN	NAN	NAN	NAN
NAN	72.5	2.5	25	55	27.5	57.5	60	62.5	37.5	67.5	70	NAN	117.5	NAN	NAN	NAN	NAN	NAN	NAN	NAN
NAN	182.5	20	22.5	22.5	35	30	72.5	75	62.5	270	270	NAN	70	NAN	NAN	NAN	NAN	NAN	NAN	NAN
NAN	NAN	30	30	30	35	35	37.5	115	32.5	42.5	77.5	NAN	275	NAN	NAN	NAN	NAN	NAN	NAN	NAN
NAN	NAN	20	55	25	10	32.5	72.5	70	40	27.5	472.5	NAN	82.5	NAN	NAN	NAN	NAN	NAN	NAN	NAN
NAN	NAN	22.5	25	25	57.5	70	67.5	37.5	110	470	NAN	NAN	477.5	NAN	NAN	NAN	NAN	NAN	NAN	NAN
NAN	NAN	15	17.5	30	25	65	32.5	25	67.5	NAN	NAN	NAN	NAN	NAN	NAN	NAN	NAN	NAN	NAN	NAN
NAN	NAN	57.5	57.5	60	32.5	32.5	22.5	467.5	267.5	NAN	NAN	NAN	NAN	NAN	NAN	NAN	NAN	NAN	NAN	NAN
NAN	NAN	27.5	30	27.5	30	22.5	67.5	NAN	37.5	NAN	NAN	NAN	NAN	NAN	NAN	NAN	NAN	NAN	NAN	NAN
NAN	NAN	35	35	20	67.5	65	395	NAN	27.5	NAN	NAN	NAN	NAN	NAN	NAN	NAN	NAN	NAN	NAN	NAN
NAN	NAN	10	15	57.5	62.5	107.5	NAN	NAN	470	NAN	NAN	NAN	NAN	NAN	NAN	NAN	NAN	NAN	NAN	NAN
NAN	NAN	75	75	32.5	27.5	280	NAN	NAN	NAN	NAN	NAN	NAN	NAN	NAN	NAN	NAN	NAN	NAN	NAN	NAN
NAN	NAN	185	187.5	60	20	NAN	NAN	NAN	NAN	NAN	NAN	NAN	NAN	NAN	NAN	NAN	NAN	NAN	NAN	NAN
NAN	NAN	NAN	NAN	80	62.5	NAN	NAN	NAN	NAN	NAN	NAN	NAN	NAN	NAN	NAN	NAN	NAN	NAN	NAN	NAN
NAN	NAN	NAN	NAN	190	35	NAN	NAN	NAN	NAN	NAN	NAN	NAN	NAN	NAN	NAN	NAN	NAN	NAN	NAN	NAN
NAN	NAN	NAN	NAN	NAN	60	NAN	NAN	NAN	NAN	NAN	NAN	NAN	NAN	NAN	NAN	NAN	NAN	NAN	NAN	NAN
NAN	NAN	NAN	NAN	NAN	2.5	NAN	NAN	NAN	NAN	NAN	NAN	NAN	NAN	NAN	NAN	NAN	NAN	NAN	NAN	NAN
NAN	NAN	NAN	NAN	NAN	82.5	NAN	NAN	NAN	NAN	NAN	NAN	NAN	NAN	NAN	NAN	NAN	NAN	NAN	NAN	NAN
NAN	NAN	NAN	NAN	NAN	192.5	NAN	NAN	NAN	NAN	NAN	NAN	NAN	NAN	NAN	NAN	NAN	NAN	NAN	NAN	NAN

Table A4.3 Durations of exposure intervals (in ka) for different $\delta^{18}O$ (indicated in first row) for the last 3 Ma derived from LR04. The most recent exposure duration is listed at the top going further back in time downwards in the table. The values for the last ice-free period are overwritten with the timing of deglaciation determined for the region (see *Chapter 4*).

%3.5	%3.55	%3.6	%3.65	%3.7	%3.75	%3.8	%3.85	%3.9	%3.95	%4	%4.05	%4.1	%4.15	%4.2	%4.25	%4.3	%4.35	%4.4	%4.45	%4.5
%(ka)	%(ka)	%(ka)	%(ka)	%(ka)	%(ka)	%(ka)	%(ka)	%(ka)	%(ka)	%(ka)	%(ka)	%(ka)	%(ka)	%(ka)	%(ka)	%(ka)	%(ka)	%(ka)	%(ka)	%(ka)
3.5	3.55	3.6	3.65	3.7	3.75	3.8	3.85	3.9	3.95	4	4.05	4.1	4.15	4.2	4.25	4.3	4.35	4.4	4.45	4.5
108	106	106	105	104	103	83	69	68	67	67	62	60	60	59	57	56	36	30	22	21
110	72	72	71	70	69	18	10	9	7	6	2	59	2	58	58	57	3	2	6	3
82	14	7	6	5	3	66	13	9	7	5	5	7	59	7	5	4	14	13	6	4
65	20	2	18	18	16	16	65	61	60	60	3	2	12	2	33	33	41	40	3	1
159	81	19	78	72	69	67	15	14	14	13	60	36	37	34	4	35	14	12	33	33
278	63	79	62	3	1	59	41	39	39	39	12	9	9	7	37	45	3	1	5	2
90	73	62	71	61	61	65	22	21	20	18	37	44	45	39	53	5	30	25	1	1
108	83	73	81	70	68	1	59	58	52	51	12	54	1	54	24	20	31	26	2	4
152	33	83	30	79	78	69	63	62	2	59	2	2	57	1	3	2	45	43	5	3
110	166	30	78	30	27	25	67	18	60	12	49	29	1	25	58	1	2	18	6	1
74	72	80	78	74	74	72	23	46	13	33	58	5	4	4	14	56	19	52	3	13
22	86	78	58	74	74	70	70	14	39	11	8	60	31	58	18	14	54	10	4	8
112.5	108	62	80	56	56	56	68	6	2	3	31	16	8	16	22	16	10	14	24	38
165	148	2	108	80	76	76	52	70	13	68	10	30	62	22	34	20	16	16	40	2
150	108	82	78	64	18	16	74	66	3	60	68	24	20	22	10	32	20	20	7	3
42.5	40	108	54	38	40	38	16	52	68	28	58	36	34	34	6	10	28	6	8	48
35	30	86	36	76	38	36	34	74	64	8	26	12	24	12	14	6	8	2	52	8
62.5	20	58	68	54	74	22	36	14	30	68	40	8	38	8	10	6	6	2	10	10
25	110	106	34	34	2	40	18	14	10	12	20	4	16	2	12	8	6	4	12	14
32.5	157.5	36	24	28	38	36	40	16	4	10	12	8	10	4	6	6	6	NAN	16	14
32.5	52.5	28	18	32	32	30	28	34	72	12	8	26	8	22	2	2	4	NAN	18	2
20	92.5	20	70.5	26	26	24	4	18	14	30	12	2	10	12	2	7.5	2.5	NAN	4	NAN
22.5	35	108	30	22	30	28	26	38	12	10	30	22	28	16	2	NAN	NAN	NAN	2	NAN
25	30	25	22.5	18	24	24	22	26	16	28	6	20	4	8	2	NAN	NAN	NAN	NAN	NAN
25	57.5	45	40	28	22	18	26	22	32	24	24	8	22	4	10	NAN	NAN	NAN	NAN	NAN
5	5	35	30	37.5	18	18	20	20	14	12	22	4	22	2	NAN	NAN	NAN	NAN	NAN	NAN
7.5	10	40	15	30	23	21	16	24	30	18	12	2	10	4	NAN	NAN	NAN	NAN	NAN	NAN
30	32.5	50	20	12.5	25	25	14	20	26	18	14	4	6	9	NAN	NAN	NAN	NAN	NAN	NAN
22.5	20	5	27.5	5	2.5	17.5	18.5	14	12	16	16	6	4	10	NAN	NAN	NAN	NAN	NAN	NAN
32.5	7.5	7.5	12.5	35	17.5	7.5	22.5	14	4	8	14	4	8	2.5	NAN	NAN	NAN	NAN	NAN	NAN
5	17.5	67.5	7.5	27.5	2.5	5	15	18.5	20	14	6	11.5	10	5	NAN	NAN	NAN	NAN	NAN	NAN
20	20	32.5	32.5	10	7.5	30	2.5	20	22	16	12	12.5	6	5	NAN	NAN	NAN	NAN	NAN	NAN
15	22.5	30	30	17.5	5	17.5	30	15	16	17.5	16	2.5	12	2.5	NAN	NAN	NAN	NAN	NAN	NAN
47.5	22.5	57.5	30	25	32.5	12.5	17.5	25	10	10	15	10	14	NAN	NAN	NAN	NAN	NAN	NAN	NAN
17.5	5	5	20	12.5	25	20	10	12.5	14	22.5	7.5	2.5	15	NAN	NAN	NAN	NAN	NAN	NAN	NAN
2.5	27.5	7.5	10	25	10	5	15	10	18.5	10	20	10	7.5	NAN	NAN	NAN	NAN	NAN	NAN	NAN
NAN	22.5	30	35	20	15	17.5	15	10	20	7.5	7.5	5	17.5	NAN	NAN	NAN	NAN	NAN	NAN	NAN
NAN	32.5	17.5	2.5	25	22.5	12.5	10	12.5	10	5	5	NAN	5	NAN	NAN	NAN	NAN	NAN	NAN	NAN
NAN	17.5	15	27.5	12.5	7.5	22.5	15	7.5	25	7.5	5	NAN	2.5	NAN	NAN	NAN	NAN	NAN	NAN	NAN
NAN	10	17.5	15	10	20	7.5	5	10	12.5	10	7.5	NAN	2.5	NAN	NAN	NAN	NAN	NAN	NAN	NAN
NAN	45	12.5	12.5	32.5	17.5	27.5	25	22.5	7.5	17.5	15	NAN	2.5	NAN	NAN	NAN	NAN	NAN	NAN	NAN
NAN	15	5	15	25	22.5	20	20	17.5	10	12.5	12.5	NAN	12.5	NAN	NAN	NAN	NAN	NAN	NAN	NAN
NAN	NAN	20	10	12.5	10	7.5	5	2.5	7.5	10	7.5	NAN	10	NAN	NAN	NAN	NAN	NAN	NAN	NAN
NAN	NAN	5	20	12.5	5	5	2.5	2.5	2.5	5	10	NAN	2.5	NAN	NAN	NAN	NAN	NAN	NAN	NAN
NAN	NAN	27.5	25	15	30	7.5	5	17.5	10	12.5	NAN	NAN	2.5	NAN	NAN	NAN	NAN	NAN	NAN	NAN
NAN	NAN	17.5	17.5	7.5	22.5	10	20	5	17.5	NAN	NAN	NAN	NAN	NAN	NAN	NAN	NAN	NAN	NAN	NAN
NAN	NAN	30	27.5	17.5	10	20	10	17.5	15	NAN	NAN	NAN	NAN	NAN	NAN	NAN	NAN	NAN	NAN	NAN
NAN	NAN	15	15	22.5	10	10	20	NAN	15	NAN	NAN	NAN	NAN	NAN	NAN	NAN	NAN	NAN	NAN	NAN
NAN	NAN	10	7.5	12.5	10	20	2.5	NAN	5	NAN	NAN	NAN	NAN	NAN	NAN	NAN	NAN	NAN	NAN	NAN
NAN	NAN	7.5	5	27.5	12.5	7.5	NAN	NAN	12.5	NAN	NAN	NAN	NAN	NAN	NAN	NAN	NAN	NAN	NAN	NAN
NAN	NAN	25	22.5	12.5	22.5	5	NAN	NAN	NAN	NAN	NAN	NAN	NAN	NAN	NAN	NAN	NAN	NAN	NAN	NAN
NAN	NAN	12.5	10	5	12.5	NAN	NAN	NAN	NAN	NAN	NAN	NAN	NAN	NAN	NAN	NAN	NAN	NAN	NAN	NAN
NAN	NAN	NAN	NAN	17.5	25	NAN	NAN	NAN	NAN	NAN	NAN	NAN	NAN	NAN	NAN	NAN	NAN	NAN	NAN	NAN
NAN	NAN	NAN	NAN	5	10	NAN	NAN	NAN	NAN	NAN	NAN	NAN	NAN	NAN	NAN	NAN	NAN	NAN	NAN	NAN
NAN	NAN	NAN	NAN	NAN	2.5	NAN	NAN	NAN	NAN	NAN	NAN	NAN	NAN	NAN	NAN	NAN	NAN	NAN	NAN	NAN
NAN	NAN	NAN	NAN	NAN	2.5	NAN	NAN	NAN	NAN	NAN	NAN	NAN	NAN	NAN	NAN	NAN	NAN	NAN	NAN	NAN
NAN	NAN	NAN	NAN	NAN	10	NAN	NAN	NAN	NAN	NAN	NAN	NAN	NAN	NAN	NAN	NAN	NAN	NAN	NAN	NAN
NAN	NAN	NAN	NAN	NAN	2.5	NAN	NAN	NAN	NAN	NAN	NAN	NAN	NAN	NAN	NAN	NAN	NAN	NAN	NAN	NAN

Table A4.3 Durations of burial intervals (in ka) for different $\delta^{18}O$ (indicated in first row) for the last 3 Ma derived from LR04. The third row restates the values of $\delta^{18}O$, which are read by the Matlab code to choose the right coloum number to retrieve burial and exposure durations, respectively. The most recent burial duration is listed at the top of the table going further back in time downwards in the table.

A4.3 MONTE CARLO METHOD FOR EPISODIC EROSION RATES

```
function out = CP_MCsim_LR04 (tordata, expdata, burdata, sample,
minbur, maxbur, expdur, averate, deglac, icethick, acc_sigma, acc_res,
maxnoresults, usewaitbar, consts)
%example:> CP_MCsim_LR04('CP_alltor.txt', 'exp_LR04.txt',
'bur_LR04.txt', [7 8], 11, 16, 0, [0 4], 15, 5000, 1, 100000, 500,
true, consts)

%INPUTS:
%tordata = name of ascii file with columns of data (e.g. 'data.txt'):
%   column 1 is the decimal latitude of each sample;
%   column 2 is the decimal longitute of each sample;
%   column 3 is the elevation of each sample; (m)
%   column 4 is measured [10Be]; (atoms/g)
%   column 5 is the measured 1 sigma error in [10Be]; (atoms/g)
%   column 6 is the measured [26Al]; (atoms/g)
%   column 7 is the measured 1 sigma error in [26Al]; (atoms/g)

%expdata = name of ascii file with coloumns of exposure intervals for
different cutoff values
%burdata = name of ascii file with coloumns of burial intervals for
different cutoff values

%sample = the row numbers of the samples you wish to model

%minbur = min number of ice ages required to model complex exposure
history

%maxbur = max number of ice ages required to model complex exposure
history

%expdur = best guess for average duration of ice-free intervals in
percentage of the total glacial cycle (i.e. 0.185 for 18.5ka of 100ka
glacial cycle); if 0 use LR04

%averate = best guess for average steady state erosion rate during
interglacials; (mm/ka = m/Ma = 1e-1 cm/ka = 1e-4 cm/a)

%deglac = estimated time of last deglaciation of tor sites (ideally
based on data); (ka)

%icethick = average ice thickness covering sample site during each
burial episode; (cm)

%acc_sigma = range for calculated concentrations to be accepted as
valuable simulations (not directly chi2)

%acc_res = min number of successful iterations (for both surfaces)

%maxnoresults = max number of attempts to find solution for one sample
%before moving to a different set of expdur and burnumb
```

```
%usewaitbar = optional, if 'true' will display the progress of the
simulation

%consts = a matlab structure containing constants used in the LSD
scaling model. This structure is loaded in the startup.m file

%A.Margreth, 2012 - 2014.
%Based on burialplot code of Alan Hidy, support from Paul Mattern and
%discussion with Lawrence Plug. LSD scaling scheme adapted from A.Hidy.
%%%%%%%%%%%%%%%%%%%%%%%%%%%%%%%%%%%%%%%%%%%%%%%%%%%%%%%%%%%%%%%%%%%%%%%%

%load data
burial_data = load(tordata);
lats = burial_data(:,1);
longs = burial_data(:,2);
elevs = burial_data(:,3);
Be_concs = burial_data(:,4);
Be_errs = burial_data(:,5);
Al_concs = burial_data(:,6);
Al_errs = burial_data(:,7);

if expdur == 0
    exp_data = load(expdata);
    bur_data = load(burdata);
    bur_int = size(bur_data);
    maxbur = bur_int(1); %set total lenghts of bur_data as maxbur
    cutoff = bur_data(1,:); %3.5:0.05:4.5;
    [r_cutoff, c_cutoff] = size(cutoff);
end

%set stepsize for normally distributed parameters and values for
lognormal-distribution
% stdexpdur = 0.03;
% stderate = 0.25;
% avthick = 60;
% stdthick = 10;
% a_beta = 6;
% b_beta = 6;
mu_plkth = 2; %mean of normal distribution of log(plkthick)
sigma_plkth = 0.25; %std of normal distribution of log(plkthick)
% min_plkth = 10;
% max_plkth = 200;
%densities used for buildup (g/cc)
r_density = 2.65;
ice_density = 0.9;

%Because muonproduction function requires massdepth as input ->
transform any depth to rock-equivalent depth, which can then be
multiplied by rock density
depth_ice = icethick*ice_density/r_density;
%recalculate ice thickness to a rock-equivalent thickenss

%decay constants (1/s)
Be10_lambda = log(2)/1378000;
%Chmeleff et al. (2010), Korschinek et al. (2010)
Al26_lambda = log(2)/720000; %Nishiizumi (2004)
```

```
%neutron attenuation length (g/cm^2)
neutron_atten = 150;
%Follows Balco et al. (2008); see Gosse and Phillips (2001)

%reference spallogenic production (atoms/g/a)
refspalprod = 4.0;%New prod rate, Brocher et al. (subm.);
ratio_init = 6.75; %Nishiizumi et al. (1989); Balco et al. (2008);
6.1/1.106 to reflect recalibration of Nishiizumi et al. (2007)

%scaling production to site of interest (spallogenic and muogenic)
%Pre-calculation of muonic production for ice-free intervals and for
%average ice-thickness covering site during burial intervals (requires
%initially a bit of time to calculate)
muon_depth = 0:1:round(maxbur*100);
fmuon_prod = nan(4,numel(muon_depth));
nmuon_prod = nan(4,numel(muon_depth));

%Get LSD scaling factors for last ice free interval since deglaciation
maxage_dgl = deglac * 1000;
%age over which to integrate production rates
LSD10 =
LSD(lats(sample(1)),longs(sample(1)),elevs(sample(1)),1,maxage_dgl,-
1,10);
LSD26 =
LSD(lats(sample(1)),longs(sample(1)),elevs(sample(1)),1,maxage_dgl,-
1,26);
agegrid = 0:1:maxage_dgl;
%average cutoff rigidity (RC) and solar modulation (SPhi)over age range
meanRC = mean(interpolate(LSD10.tv,LSD10.Rc,agegrid));
meanSPhi = mean(interpolate(LSD10.tv,LSD10.SPhi,agegrid));
%average spallogenic surface production rate over age range
Be10_spprod =
mean(refspalprod.*interpolate(LSD10.tv,LSD10.Be,agegrid));
Al26_spprod =
mean(refspalprod.*ratio_init.*interpolate(LSD26.tv,LSD26.Al,agegrid));
[Be10_fmuprod, Be10_nmuprod] = CP_P_mu_totalLSD(0 *
r_density,LSD10.pressure,meanRC,meanSPhi,consts,10,'no');
[Al26_fmuprod, Al26_nmuprod] = CP_P_mu_totalLSD(0 *
r_density,LSD10.pressure,meanRC,meanSPhi,consts,26,'no');

%Get LSD scaling factors for previous exp and bur intervals (integrated
over 100ka)
maxage = 100000; %age over which to integrate production rates
LSD10 =
LSD(lats(sample(1)),longs(sample(1)),elevs(sample(1)),1,maxage,-1,10);
LSD26 =
LSD(lats(sample(1)),longs(sample(1)),elevs(sample(1)),1,maxage,-1,26);
agegrid = 0:1:maxage;
%average cutoff rigidity (RC) and solar modulation (SPhi)over age range
meanRC = mean(interpolate(LSD10.tv,LSD10.Rc,agegrid));
meanSPhi = mean(interpolate(LSD10.tv,LSD10.SPhi,agegrid));
%average spallogenic surface production rate over age range
Be10_spalprodrate =
mean(refspalprod.*interpolate(LSD10.tv,LSD10.Be,agegrid));
```

```
Al26_spalprodrate =
mean(refspalprod.*ratio_init.*interpolate(LSD26.tv,LSD26.Al,agegrid));
%average total muogenic surface production rate over age range
for i_muon = 1:numel(muon_depth)
    [fmuon_prod(1,i_muon), nmuon_prod(1,i_muon)] =
CP_P_mu_totalLSD(muon_depth(i_muon) *
r_density,LSD10.pressure,meanRC,meanSPhi,consts,10,'no');
    [fmuon_prod(2,i_muon), nmuon_prod(2,i_muon)] =
CP_P_mu_totalLSD(muon_depth(i_muon) *
r_density,LSD10.pressure,meanRC,meanSPhi,consts,26,'no');
    [fmuon_prod(3,i_muon), nmuon_prod(3,i_muon)] =
CP_P_mu_totalLSD((muon_depth(i_muon)+depth_ice) *
r_density,LSD10.pressure,meanRC,meanSPhi,consts,10,'no');
    [fmuon_prod(4,i_muon), nmuon_prod(4,i_muon)] =
CP_P_mu_totalLSD((muon_depth(i_muon)+depth_ice) *
r_density,LSD10.pressure,meanRC,meanSPhi,consts,26,'no');
end

%**********************************************************************
%**********************************************************************
%Model of complex exposure histories to fit measured nuclide
concentrations to determine timing of last plucking event and derive
probability density functions of episodic erosion rate and other
variables

%Define vectors and matrices for saving results of individual runs and
for successful runs for all samples
nsample = numel(sample);

res_sumchi2 = nan(acc_res, 2+2*nsample); %coloums: sum_chi2,
counter_exp, chi2(nsample), numb_runs(nsample), (indexing over i_acc)
res_exp = nan(1000000, 3); %coloums: exp_part, burnumb, erate

for i_sample = 1:nsample
    res_acc.(sprintf('sample%d', i_sample)) = struct('values',
nan(acc_res, 10), 'lowering', nan(acc_res, 7), 'events', nan(acc_res,
maxbur), 'thickn', nan(acc_res, maxbur+1));
%res.(sprintf('sample%d', i_sample)) = struct('acc', false(1000000,1),
'values', nan(1000000, 7), 'events', nan(1000000, maxbur), 'thickn',
nan(1000000, maxbur+1));
end

if expdur == 0
    frac = cutoff;
else
    frac = expdur(1):0.01:expdur(2);
end
esa = averate(1):0.1:averate(2);
ttot = 0:0.1:3; %make vector starting at 0Ma to 3Ma with spacing 100ka
chi2exp_sum = zeros(numel(frac), numel(esa), numel(ttot));
chi2exp_num = zeros(numel(frac), numel(esa), numel(ttot));
chi2exp_max = zeros(numel(frac), numel(esa), numel(ttot));

tsp = 0:50:3000; %make vector starting at 0 to 3000ka with spacing 50ka
eep = 0:0.25:30;
freq = 0:1:30;
```

```
for i_sample = 1:nsample
    chi2_res.(sprintf('sample%d', i_sample)) = struct('sum',
zeros(numel(tsp),numel(eep),numel(freq)), 'num',
zeros(numel(tsp),numel(eep),numel(freq)));
end

%=========================================================================
%outer loop with calculation of environmental variables, which have to
be valid for all samples, and an inner loop where additional
variations, which are individual for each sample, are performed
rand('state', sum(100*clock));
%rng('shuffle');
min_chi2(1:nsample) = 0;
numb_runs(1:nsample) = 0;
counter_exp = 0;
% numb_res(1:nsample) = 0;
numb_exp = 0;
save_res(1:nsample) = 0;
save_exp = 0;

if usewaitbar
    fprintf('\n starting simulation')
    fprintf('%7d/%7d', 0, acc_res)
end

%-------------------------------------------------------------------------
%start outer loop which runs until n = acc_res solutions are found
for i_acc = 1:acc_res
    new_att = true;

    while new_att % outer loop with environmental factors
        counter_exp = counter_exp + 1;
        save_exp = save_exp + 1;
        min_chi2(:) = nan;

%Define total duration of complex exposure history and duration of
exposure interval compared to burial interval in one glacial cycle
        if expdur == 0
            rand_cutoff = randperm(c_cutoff);
            exp_part = cutoff(rand_cutoff(1));
            exp_dur = exp_data(:,rand_cutoff(1));
            bur_dur = bur_data(2:end,rand_cutoff(1));
            exptimes = exp_dur(~isnan(exp_dur));
            burtimes = bur_dur(~isnan(bur_dur));
            exp_times = flipud(exptimes)' * 1000;
            bur_times = flipud(burtimes)' * 1000;
            [r_burtimes, c_burtimes] = size(bur_times);
            maxbur = c_burtimes; %set total lenghts of bur_times as
maxbur (bur_times for each cutoff value different)
        else
%exp_part = ceil(1000*(expdur + stdexpdur*randn))/1000; %%%normal
distribution of exp_part with average expdur and stdev stdexpdur
            exp_part = expdur(1) + (floor(rand(1,1) * (expdur(2)*100 -
expdur(1)*100 +1)))/100;
            if exp_part <= 0; exp_part = 0; end
            exp_dur = nan(maxbur+1, 1);
```

```
            bur_dur = nan(maxbur, 1);
            for i_exp = 1:maxbur+1-9
                exp_dur(i_exp) = exp_part * 41;
            end
            for i_exp = maxbur+1-8:maxbur+1
                exp_dur(i_exp) = exp_part * 100;
            end
            for i_bur = 1:maxbur-9
                bur_dur(i_bur) = (1 - exp_part) * 41;
            end
            for i_bur = maxbur-8:maxbur
                bur_dur(i_bur) = (1 - exp_part) * 100;
            end
            exp_times = exp_dur' * 1000;
            bur_times = bur_dur' * 1000;
        end
        exp_times(1,end) = deglac * 1000; %%%%comment if no different
last deglaciation should be used

        burnumb = minbur + floor(rand(1,1) * (maxbur - minbur+1));
        bur_index = maxbur+1 - burnumb;
        burev = bur_index:maxbur;

        %radom variation of erosion rate
        erate = averate(1) + (floor(rand(1,1) * 10*(averate(2) -
averate(1))))/10;
        eros = erate/10000; %convert to cm/a from m/Ma
%         eros = ceil(10*(averate + stderate*randn)) / 100000;
%         if eros < 0; eros = 0; end

%define new lambda term for accounting for erosion during exposure
intervals
        elambda = nan(1,6);
        elambda(1) = Be10_lambda + eros*r_density/neutron_atten;
%spallogenic 10Be
        elambda(2) = Al26_lambda + eros*r_density/neutron_atten;
%spallogenic 26Al
        elambda(3) = Be10_lambda + eros*r_density/1500;
%negative muogenic 10Be
        elambda(4) = Al26_lambda + eros*r_density/1500;
%negative muogenic 26Al
        elambda(5) = Be10_lambda + eros*r_density/4320;
%fast muogenic 10Be
        elambda(6) = Al26_lambda + eros*r_density/4320;
%fast muogenic 26Al

%save environmental data (indexing over counter_exp)
        res_exp(save_exp,1:3) = [exp_part burnumb eros*10000];

        if mod(counter_exp,1000000) == 0
            numb_exp = numb_exp + 1;
            file_exp = sprintf('res_exp_%i.mat', numb_exp);
            save(file_exp, 'res_exp');
            save_exp = 0;
            res_exp(:) = nan;
        end
```

```
%-----------------------------------------------------------------
%Random variation of plucking thickness, number of plucking events and
plucking events for each individual sample
        for i_sample = 1:nsample
            strname = sprintf('sample%i', i_sample);

            noresult = true;
            resultmaxnoresult = false;
            counter_att = 0;
            if usewaitbar
                fprintf('\b\b\b\b\b\b\b\b\b\b\b\b\b\b\b\b\b\b\b%7d/%7d', i_acc-
1, acc_res)
            end

            while noresult && counter_att < maxnoresults
                counter_att = counter_att + 1;
                numb_runs(i_sample) = numb_runs(i_sample) + 1;
                save_res(i_sample) = save_res(i_sample) + 1;

                rand_numbplkev = randperm(burnumb);
                numb_plkev = rand_numbplkev(1);
                rand_burev = burev(randperm(numel(burev)));
                plk_events = sort(rand_burev(1:numb_plkev));
%plk_thick = ceil(avthick + stdthick*randn(1,numb_plkev));
%plk_thick = ceil(betarnd(a_beta,b_beta,1,numb_plkev)*100);
                plk_thick =
ceil(10*(lognrnd(mu_plkth,sigma_plkth,1,numb_plkev)));
%plk_thick = min_plkth + floor(rand(1,numb_plkev) * (max_plkth+1 -
min_plkth));

                cum_plk = [0, cumsum(plk_thick)];
                depth_index = find(cum_plk(end) == muon_depth);

                burbe = 0;
                bural = 0;

%.................................................................
%calculate alternating exposure and burial intervals, incl. decay of
previous accumulated isotopes (corrected for erosion during exposure
intervals)
                for k = bur_index:1:maxbur
%muon_depth(depth_index)
%Be10_totprod = Be10_spalprodrate*exp(-
muon_depth(depth_index)*r_density/neutron_atten) +
fmuon_prod(1,depth_index) + nmuon_prod(1,depth_index);
%Al26_totpord = Al26_spalprodrate*exp(-
muon_depth(depth_index)*r_density/neutron_atten) +
fmuon_prod(2,depth_index) + nmuon_prod(2,depth_index);
%Be10_elambda = (Be10_spalprodrate*exp(-
muon_depth(depth_index)*r_density/neutron_atten))/Be10_totprod*elambda(
1) + fmuon_prod(1,depth_index)/Be10_totprod*elambda(5) +
nmuon_prod(1,depth_index)/Be10_totprod*elambda(3);
%Al26_elambda = (Al26_spalprodrate*exp(-
muon_depth(depth_index)*r_density/neutron_atten))/Al26_totpord*elambda(
```

```
2) + fmuon_prod(2,depth_index)/Al26_totpord*elambda(6) +
nmuon_prod(2,depth_index)/Al26_totpord*elambda(4);
                    Be10_elambda = elambda(1);
                    Al26_elambda = elambda(2);
                    expbe = burbe*exp(-Be10_elambda*exp_times(k)) +
(Be10_spalprodrate/elambda(1))*(1-exp(-elambda(1)*exp_times(k)))*exp(-
muon_depth(depth_index)*r_density/neutron_atten) +
(fmuon_prod(1,depth_index)/elambda(5))*(1-exp(-
elambda(5)*exp_times(k))) + (nmuon_prod(1,depth_index)/elambda(3))*(1-
exp(-elambda(3)*exp_times(k)));
                    expal = bural*exp(-Al26_elambda*exp_times(k)) +
(Al26_spalprodrate/elambda(2))*(1-exp(-elambda(2)*exp_times(k)))*exp(-
muon_depth(depth_index)*r_density/neutron_atten) +
(fmuon_prod(2,depth_index)/elambda(6))*(1-exp(-
elambda(6)*exp_times(k))) + (nmuon_prod(2,depth_index)/elambda(4))*(1-
exp(-elambda(4)*exp_times(k)));

                    burbe = expbe*exp(Be10_lambda*bur_times(k)) +
(Be10_spalprodrate/Be10_lambda)*(1-exp(-
Be10_lambda*bur_times(k)))*exp(-
(muon_depth(depth_index)+depth_ice)*r_density/neutron_atten) +
(fmuon_prod(3,depth_index)/Be10_lambda)*(1-exp(-
Be10_lambda*bur_times(k))) +
(nmuon_prod(3,depth_index)/Be10_lambda)*(1-exp(-
Be10_lambda*bur_times(k)));
                    bural = expal*exp(Al26_lambda*bur_times(k)) +
(Al26_spalprodrate/Al26_lambda)*(1-exp(-
Al26_lambda*bur_times(k)))*exp(-
(muon_depth(depth_index)+depth_ice)*r_density/neutron_atten) +
(fmuon_prod(4,depth_index)/Al26_lambda)*(1-exp(-
Al26_lambda*bur_times(k))) +
(nmuon_prod(4,depth_index)/Be10_lambda)*(1-exp(-
Be10_lambda*bur_times(k)));

                    %check if plucking occurs during this burial event
                    for i_plk = 1:numb_plkev
                        if k == plk_events(i_plk)
                            depth_index = find(cum_plk(end-i_plk) ==
muon_depth);
                        end
                    end

                end %end of for k = 1:maxbur loop

%calculate last exposure interval since deglaciation of site
%Be10_totprod = Be10_spprod*exp(-
muon_depth(depth_index)*r_density/neutron_atten) +
fmuon_prod(1,depth_index) + nmuon_prod(1,depth_index);
%Al26_totpord = Al26_spprod*exp(-
muon_depth(depth_index)*r_density/neutron_atten) +
fmuon_prod(2,depth_index) + nmuon_prod(2,depth_index);
%Be10_elambda = (Be10_spprod*exp(-
muon_depth(depth_index)*r_density/neutron_atten))/Be10_totprod*elambda(
1) + fmuon_prod(1,depth_index)/Be10_totprod*elambda(5) +
nmuon_prod(1,depth_index)/Be10_totprod*elambda(3);
```

```
%Al26_elambda = (Al26_spprod*exp(-
muon_depth(depth_index)*r_density/neutron_atten))/Al26_totpord*elambda(
2) + fmuon_prod(2,depth_index)/Al26_totpord*elambda(6) +
nmuon_prod(2,depth_index)/Al26_totpord*elambda(4);
                    Be10_elambda = elambda(1);
                    Al26_elambda = elambda(2);
                    expbe = burbe*exp(-
Be10_elambda*exp_times(maxbur+1)) + (Be10_spprod/elambda(1))*(1-exp(-
elambda(1)*exp_times(maxbur+1)))*exp(-
muon_depth(depth_index)*r_density/neutron_atten) +
(Be10_fmuprod/elambda(5))*(1-exp(-elambda(5)*exp_times(maxbur+1))) +
(Be10_nmuprod/elambda(3))*(1-exp(-elambda(3)*exp_times(maxbur+1)));
                    expal = bural*exp(-
Al26_elambda*exp_times(maxbur+1)) + (Al26_spprod/elambda(2))*(1-exp(-
elambda(2)*exp_times(maxbur+1)))*exp(-
muon_depth(depth_index)*r_density/neutron_atten) +
(Al26_fmuprod/elambda(6))*(1-exp(-elambda(6)*exp_times(maxbur+1))) +
(Al26_nmuprod/elambda(4))*(1-exp(-elambda(4)*exp_times(maxbur+1)));

%saving all simulated results:
                chi2 = ((expbe - Be_concs(sample(i_sample))) /
Be_errs(sample(i_sample)))^2 + ((expal - Al_concs(sample(i_sample))) /
Al_errs(sample(i_sample)))^2;
                min_chi2(i_sample) = min(min(min_chi2(i_sample)),
chi2);
%res.(strname).values(save_res(i_sample), 1) = chi2;
%res.(strname).values(save_res(i_sample), 2:3) = [expbe expal];
%res.(strname).values(save_res(i_sample), 4:7) = [numb_plkev,
plk_events(end), cum_plk(2), counter_exp];
%res.(strname).events(save_res(i_sample), 1:numb_plkev) =
plk_events(end:-1:1);
%res.(strname).thickn(save_res(i_sample), 1:numb_plkev+1) = cum_plk;
%from sim ann (1:numb_plkev+1);

%weight results by chi-squared value
                if expdur == 0
                    tot_hist =
(sum(exp_times(bur_index:end))+sum(bur_times(bur_index:end)))/10^6; %Ma
                    last_plkev = (sum(bur_times(plk_events(end):end)) +
sum(exp_times(plk_events(end)+1:end)))/10^3; %in ka, starting from
following exposure interval, but not including burial interval of
plucking event
                    av_exp = (sum(exp_times(bur_index:end))*10^-
6)/tot_hist; %calculates %exp for this run
                else
                    tot_hist = (burnumb-9)*0.041 + 0.9; %in Ma
                    last_plkev = (sum(bur_times(plk_events(end):end)) +
sum(exp_times(plk_events(end)+1:end)))/10^3; %in ka, starting from
following exposure interval, but not including burial interval of
plucking event
                    av_exp = exp_part;
                end

                w_chi2 = exp(-chi2./2);
                [dump, xind] = min(abs(tsp-last_plkev));
```

```
                [dump, yind] = min(abs(eep-
(sum(plk_thick)/100))/tot_hist);
                [dump, zind] = min(abs(freq-numb_plkev/tot_hist));
                chi2_res.(strname).sum(xind,yind,zind) =
max(chi2_res.(strname).sum(xind,yind,zind),w_chi2);
%chi2_res.(strname).sum(xind,yind,zind) + w_chi2;
                chi2_res.(strname).num(xind,yind,zind) =
chi2_res.(strname).num(xind,yind,zind) + 1;

%check if final nuclide concentration is within acceptable range of
uncertainty from measured concentration, then save accepted results
                if (Be_concs(sample(i_sample)) -
acc_sigma*Be_errs(sample(i_sample)) <= expbe) && (expbe <=
Be_concs(sample(i_sample)) + acc_sigma*Be_errs(sample(i_sample)))
                    if (Al_concs(sample(i_sample)) -
acc_sigma*Al_errs(sample(i_sample)) <= expal) && (expal <=
Al_concs(sample(i_sample)) + acc_sigma*Al_errs(sample(i_sample)))
                        noresult = false;
                        res_acc.(strname).values(i_acc, 1:10) = [chi2,
counter_exp, exp_part, burnumb, maxbur, eros*10000,
numb_runs(i_sample), numb_plkev, plk_events(end), cum_plk(2)];
                        res_acc.(strname).events(i_acc, 1:numb_plkev) =
plk_events(end:-1:1);
                        res_acc.(strname).thickn(i_acc, 1:numb_plkev) =
plk_thick; %res_acc.(strname).thickn(i_acc, 1:numb_plkev+1) = cum_plk;
                        res_acc.(strname).lowering(i_acc, 1) =
numb_plkev/tot_hist;
                        res_acc.(strname).lowering(i_acc, 2) =
(sum(plk_thick)/100)/tot_hist; %lowering rate in m Ma-1
                        res_acc.(strname).lowering(i_acc, 3:7) =
[(sum(plk_thick)/100)/numb_plkev, sum(plk_thick)/100, tot_hist,
av_exp*100, last_plkev];
                        res.(strname).acc(save_res(i_sample),1) = true;
                        if counter_att == maxnoresults
                            resultmaxnoresult = true;
                        end
                    end
                end

%save structure for sample if full and empty
%if mod(numb_runs(i_sample),1000000) == 0
%numb_res(i_sample) = numb_res(i_sample) + 1;
%file_res = sprintf('res_sample%i_%i.mat', i_sample,
numb_res(i_sample));
%save(file_res, '-struct', 'res', strname);
%save_res(i_sample) = 0;
%res.(strname).acc(:) = false;
%res.(strname).values(:) = nan;
%res.(strname).events(:) = nan;
%res.(strname).thickn(:) = nan;
%end

            end %while noresult

            if ~resultmaxnoresult
                if counter_att == maxnoresults
```

```
                    min_chi2(isnan(min_chi2)) = 0;
                    sumchi2 = sum(min_chi2(:));
                    wexp_chi2 = exp(-sumchi2./2);
                    [dump, xind] = min(abs(frac-exp_part));
                    [dump, yind] = min(abs(esa-eros*10000));
                    [dump, zind] = min(abs(ttot-tot_hist));
                    chi2exp_sum(xind,yind,zind) =
chi2exp_sum(xind,yind,zind) + wexp_chi2;
                    chi2exp_num(xind,yind,zind) =
chi2exp_num(xind,yind,zind) + 1;
                    chi2exp_max (xind,yind,zind) =
max(chi2exp_max(xind,yind,zind),wexp_chi2);

                    break  %exit for i_sample = 1:nsample loop
                end
            end

            if i_sample == nsample
                new_att = false;
            end

        end %for i_sample = 1:nsamle
    end %while new_att

    res_sumchi2(i_acc,1:2) = [sum(min_chi2(:)), counter_exp];
    res_sumchi2(i_acc,3:1:2+nsample) = min_chi2(:);
    res_sumchi2(i_acc,3+nsample:1:end) = numb_runs(:);

    wexp_chi2 = exp(-res_sumchi2(i_acc,1)./2);
    [dump, xind] = min(abs(frac-exp_part));
    [dump, yind] = min(abs(esa-eros*10000));
    [dump, zind] = min(abs(ttot-tot_hist));
    chi2exp_sum(xind,yind,zind) = chi2exp_sum(xind,yind,zind) +
wexp_chi2;
    chi2exp_num(xind,yind,zind) = chi2exp_num(xind,yind,zind) + 1;
    chi2exp_max (xind,yind,zind) =
max(chi2exp_max(xind,yind,zind),wexp_chi2);

end %for i_runs

%-------------------------------------------------------------------------
%generate probability density functions for environmental and sample
%specific parameters
valid = chi2exp_num > 0;
chi2exp_sum(valid) = chi2exp_sum(valid)./chi2exp_num(valid);
probs_exp = cell(2,3);
maxs_exp  = cell(2,3);
cums_exp  = cell(2,3);
probmax_exp  = nan(2,3);
sigma1minus_exp  = zeros(2,3);
sigma1plus_exp  = zeros(2,3);
sigma2minus_exp  = zeros(2,3);
sigma2plus_exp  = zeros(2,3);
```

```
probs_exp{1,1} = sum(sum(chi2exp_sum,2),3);
probs_exp{1,1} = probs_exp {1,1}./sum(probs_exp {1,1});
maxs_exp{1,1} = max(max(chi2exp_sum,[],2),[],3);
cums_exp{1,1} = cumsum(probs_exp{1,1})/sum(probs_exp{1,1});
[b_1,i_1] = unique(cums_exp{1,1});
probmax_exp(1,1) = frac(max(probs_exp{1,1}) == probs_exp{1,1});
sigma1minus_exp(1,1) = interp1(b_1,frac(i_1),0.15865);
sigma1plus_exp(1,1) = interp1(b_1,frac(i_1),0.84135);
sigma2minus_exp(1,1) = interp1(b_1,frac(i_1),0.023);
sigma2plus_exp(1,1) = interp1(b_1,frac(i_1),0.977);

probs_exp{1,2} = sum(sum(chi2exp_sum,1),3);
probs_exp{1,2} = probs_exp{1,2}./sum(probs_exp{1,2});
maxs_exp{1,2} = max(max(chi2exp_sum,[],1),[],3);
cums_exp{1,2} = cumsum(probs_exp{1,2})/sum(probs_exp{1,2});
[b_2,i_2] = unique(cums_exp{1,2});
probmax_exp(1,2) = esa(max(probs_exp{1,2}) == probs_exp{1,2});
sigma1minus_exp(1,2) = interp1(b_2,esa(i_2),0.15865);
sigma1plus_exp(1,2) = interp1(b_2,esa(i_2),0.84135);
sigma2minus_exp(1,2) = interp1(b_2,esa(i_2),0.023);
sigma2plus_exp(1,2) = interp1(b_2,esa(i_2),0.977);

ph = nan(1,3);
ph(:) = sum(sum(chi2exp_sum,1),2);
probs_exp{1,3} = ph;
probs_exp{1,3} = probs_exp{1,3}./sum(probs_exp{1,3});
maxs_exp{1,3} = max(max(chi2exp_sum,[],1),[],2);
cums_exp{1,3} = cumsum(probs_exp{1,3})/sum(probs_exp{1,3});
[b_3,i_3] = unique(cums_exp{1,3});
probmax_exp(1,3) = ttot(max(probs_exp{1,3}) == probs_exp{1,3});
sigma1minus_exp(1,3) = interp1(b_3,ttot(i_3),0.15865);
sigma1plus_exp(1,3) = interp1(b_3,ttot(i_3),0.84135);
sigma2minus_exp(1,3) = interp1(b_3,ttot(i_3),0.023);
sigma2plus_exp(1,3) = interp1(b_3,ttot(i_3),0.977);

probs_exp{2,1} = sum(sum(chi2exp_max,2),3);
probs_exp{2,1} = probs_exp {2,1}./sum(probs_exp {2,1});
maxs_exp{2,1} = max(max(chi2exp_sum,[],2),[],3);
cums_exp{2,1} = cumsum(probs_exp{2,1})/sum(probs_exp{2,1});
[b_1,i_1] = unique(cums_exp{2,1});
probmax_exp(2,1) = frac(max(probs_exp{2,1}) == probs_exp{2,1});
sigma1minus_exp(2,1) = interp1(b_1,frac(i_1),0.15865);
sigma1plus_exp(2,1) = interp1(b_1,frac(i_1),0.84135);
sigma2minus_exp(2,1) = interp1(b_1,frac(i_1),0.023);
sigma2plus_exp(2,1) = interp1(b_1,frac(i_1),0.977);

probs_exp{2,2} = sum(sum(chi2exp_max,1),3);
probs_exp{2,2} = probs_exp{2,2}./sum(probs_exp{2,2});
maxs_exp{2,2} = max(max(chi2exp_sum,[],1),[],3);
cums_exp{2,2} = cumsum(probs_exp{1,2})/sum(probs_exp{2,2});
[b_2,i_2] = unique(cums_exp{2,2});
probmax_exp(2,2) = esa(max(probs_exp{2,2}) == probs_exp{2,2});
sigma1minus_exp(2,2) = interp1(b_2,esa(i_2),0.15865);
sigma1plus_exp(2,2) = interp1(b_2,esa(i_2),0.84135);
sigma2minus_exp(2,2) = interp1(b_2,esa(i_2),0.023);
```

```
sigma2plus_exp(2,2) = interp1(b_2,esa(i_2),0.977);

ph(:) = sum(sum(chi2exp_max,1),2);
probs_exp{2,3} = ph;
probs_exp{2,3} = probs_exp{2,3}./sum(probs_exp{2,3});
maxs_exp{2,3} = max(max(chi2exp_sum,[],1),[],2);
cums_exp{2,3} = cumsum(probs_exp{2,3})/sum(probs_exp{2,3});
[b_3,i_3] = unique(cums_exp{2,3});
probmax_exp(2,3) = ttot(max(probs_exp{2,3}) == probs_exp{2,3});
sigma1minus_exp(2,3) = interp1(b_3,ttot(i_3),0.15865);
sigma1plus_exp(2,3) = interp1(b_3,ttot(i_3),0.84135);
sigma2minus_exp(2,3) = interp1(b_3,ttot(i_3),0.023);
sigma2plus_exp(2,3) = interp1(b_3,ttot(i_3),0.977);

probs = cell(nsample,3);
maxs = cell(nsample,3);
cums = cell(nsample,3);
probmax = nan(nsample,3);
sigma1minus = zeros(nsample,3);
sigma1plus = zeros(nsample,3);
sigma2minus = zeros(nsample,3);
sigma2plus = zeros(nsample,3);

for i_sample = 1:nsample
    strname = sprintf('sample%i', i_sample);
%valid = chi2_res.(strname).num > 0;
%chi2_res.(strname).sum(valid) =
chi2_res.(strname).sum(valid)./chi2_res.(strname).num(valid);
    probs{i_sample,1} = sum(sum(chi2_res.(strname).sum,2),3);
    probs{i_sample,1} = probs{i_sample,1}./sum(probs{i_sample,1});
    maxs{i_sample,1} = max(max(chi2_res.(strname).sum,[],2),[],3);
    cums{i_sample,1} =
cumsum(probs{i_sample,1})/sum(probs{i_sample,1});
    [b_1,i_1] = unique(cums{i_sample,1});
    probmax(i_sample,1) = tsp(max(probs{i_sample,1}) ==
probs{i_sample,1});
    sigma1minus(i_sample,1) = interp1(b_1,tsp(i_1),0.15865);
    sigma1plus(i_sample,1) = interp1(b_1,tsp(i_1),0.84135);
    sigma2minus(i_sample,1) = interp1(b_1,tsp(i_1),0.023);
    sigma2plus(i_sample,1) = interp1(b_1,tsp(i_1),0.977);

    probs{i_sample,2} = sum(sum(chi2_res.(strname).sum,1),3);
    probs{i_sample,2} = probs{i_sample,2}./sum(probs{i_sample,2});
    maxs{i_sample,2} = max(max(chi2_res.(strname).sum,[],1),[],3);
    cums{i_sample,2} =
cumsum(probs{i_sample,2})/sum(probs{i_sample,2});
    [b_2,i_2] = unique(cums{i_sample,2});
    probmax(i_sample,2) = eep(max(probs{i_sample,2}) ==
probs{i_sample,2});
    sigma1minus(i_sample,2) = interp1(b_2,eep(i_2),0.15865);
    sigma1plus(i_sample,2) = interp1(b_2,eep(i_2),0.84135);
    sigma2minus(i_sample,2) = interp1(b_2,eep(i_2),0.023);
    sigma2plus(i_sample,2) = interp1(b_2,eep(i_2),0.977);

    ph(:) = sum(sum(chi2_res.(strname).sum,1),2);
    probs{i_sample,3} = ph;
```

```
    probs{i_sample,3} = probs{i_sample,3}./sum(probs{i_sample,3});
    maxs{i_sample,3} = max(max(chi2_res.(strname).sum,[],1),[],2);
    cums{i_sample,3} =
cumsum(probs{i_sample,3})/sum(probs{i_sample,3});
    [b_3,i_3] = unique(cums{i_sample,3});
    probmax(i_sample,3) = freq(max(probs{i_sample,3}) ==
probs{i_sample,3});
    sigma1minus(i_sample,3) = interp1(b_3,freq(i_3),0.15865);
    sigma1plus(i_sample,3) = interp1(b_3,freq(i_3),0.84135);
    sigma2minus(i_sample,3) = interp1(b_3,freq(i_3),0.023);
    sigma2plus(i_sample,3) = interp1(b_3,freq(i_3),0.977);
end

%=========================================================================
%Export all data and display results
res_exp = res_exp(1:counter_exp-numb_exp*1000000,:);
file = sprintf('res_exp_%i.mat', numb_exp+1);
save(file, 'res_exp');
save res_sumchi2.mat res_sumchi2

save res_chi2exp.mat probmax_exp  sigma1minus_exp  sigma1plus_exp
sigma2minus_exp  sigma2plus_exp  probs_exp  maxs_exp  cums_exp
chi2exp_sum chi2exp_num chi2exp_max
save res_chi2samples.mat probmax sigma1minus sigma1plus sigma2minus
sigma2plus probs maxs cums
for i_sample = 1:nsample
%res.(sprintf('sample%d', i_sample)).acc = res.(sprintf('sample%d',
i_sample)).acc(1:numb_runs(i_sample)-numb_res*1000000,:); %coloums:
chi2, conc_be, conc_al, numbplkev, lastplkev(contol),
lastplkth(control), counter_exp, att_inner, numb_runs(i))
%res.(sprintf('sample%d', i_sample)).values = res.(sprintf('sample%d',
i_sample)).values(1:numb_runs(i_sample)-numb_res*1000000,:);
%res.(sprintf('sample%d', i_sample)).events = res.(sprintf('sample%d',
i_sample)).events(1:numb_runs(i_sample)-numb_res*1000000,:);
%res.(sprintf('sample%d', i_sample)).thickn = res.(sprintf('sample%d',
i_sample)).thickn(1:numb_runs(i_sample)-numb_res*1000000,:);
%file_res = sprintf('res_sample%d_%d.mat', i_sample,
numb_res(i_sample)+1);
%save(file_res, '-struct', 'res', sprintf('sample%d', i_sample));
    file_res_acc = sprintf('res_acc_sample%d.mat', i_sample);
    save(file_res_acc, '-struct', 'res_acc', sprintf('sample%d',
i_sample));
    file_chi2_res = sprintf('res_chi2_sample%d', i_sample);
    save(file_chi2_res, '-struct', 'chi2_res', sprintf('sample%d',
i_sample));
end

out = [numb_runs acc_res counter_exp];
run_input = [sample minbur maxbur expdur averate deglac icethick
depth_ice acc_sigma acc_res maxnoresults];
save res_runsettings.mat out run_input
sprod = [Be10_spalprodrate Al26_spalprodrate
Al26_spalprodrate/Be10_spalprodrate];
save prod_int.mat sprod fmuon_prod nmuon_prod muon_depth exp_dur
bur_dur
```

```
if usewaitbar
    fprintf('\n all solutions found')
    fprintf('%7d/%7d', i_acc, acc_res)
    sumchi2 = min(res_sumchi2(:,1));
    index = find(res_sumchi2(:,1) == sumchi2);
    i_environ = res_sumchi2(index,2);
    if i_environ <= 100000
        environ = res_exp(i_environ,1:3);
    else
        environ = nan(1:3);
    end
    fprintf('\n optimal solution')
    fprintf('\n sumchi2: %e', sumchi2)
    fprintf('\n')
    disp([' exp_part: ' num2str(environ(1))]);
    disp([' burnumb: ' num2str(environ(2))]);
    disp([' erate: ' num2str(environ(3))]);
    sample_chi2 = res_sumchi2(index,3:1:2+nsample)
    sample_numbrun = res_sumchi2(index,3+nsample:1:end)
end

save res_output.mat sumchi2 sample_chi2 sample_numbrun environ

%-------------------------------------------------------------------------
%generate pdf's for weighted chi2 values
maxp_frac = max(probs_exp{1,1}./sum(probs_exp{1,1}));
maxp_esp = max(probs_exp{1,2}./sum(probs_exp{1,2}));
maxp_ttot = max(probs_exp{1,3}./sum(probs_exp{1,3}));
maxp_frac1 = max(probs_exp{2,1}./sum(probs_exp{2,1}));
maxp_esp1 = max(probs_exp{2,2}./sum(probs_exp{2,2}));
maxp_ttot1 = max(probs_exp{2,3}./sum(probs_exp{2,3}));

figure
subplot(2,3,1)
hold on
axis([3.5 4.5 0 1.1*maxp_frac])
plot(frac, probs_exp{1,1}./sum(probs_exp{1,1}), 'r-');
plot(frac,
smooth(frac,probs_exp{1,1})./(sum(smooth(frac,probs_exp{1,1}))), 'b-',
'linewidth', 2);
line([probmax_exp(1,1), probmax_exp(1,1)], [0 0.5], 'linestyle', '-',
'color', 'k')
line([sigma1minus_exp(1,1), sigma1minus_exp(1,1)], [0 0.5],
'linestyle', '-.', 'color', 'k')
line([sigma1plus_exp(1,1), sigma1plus_exp(1,1)], [0 0.5], 'linestyle',
'-.', 'color', 'k')
xlabel('d18O value (ppm)')
ylabel('normalised probability')
subplot(2,3,2)
hold on
axis([0 4 0 1.1*maxp_esp])
plot(esa, probs_exp{1,2}./sum(probs_exp{1,2}), 'r-');
plot(esa,
smooth(esa,probs_exp{1,2})./(sum(smooth(esa,probs_exp{1,2}))), 'b-',
'linewidth', 2);
```

```
line([probmax_exp(1,2) probmax_exp(1,2)], [0 0.5], 'linestyle', '-',
'color', 'k')
line([sigma1minus_exp(1,2), sigma1minus_exp(1,2)], [0 0.5],
'linestyle', '-.', 'color', 'k')
line([sigma1plus_exp(1,2), sigma1plus_exp(1,2)], [0 0.5], 'linestyle',
'-.', 'color', 'k')
xlabel('subaerial erate (mm ka-1)')
ylabel('normalised probability')
subplot(2,3,3)
hold on
axis([0 3000 0 1.1*maxp_ttot])
% plot(ttot, probs_exp{1,3}./sum(probs_exp{1,3}), 'r-');
plot(ttot,
smooth(ttot,probs_exp{1,3})./(sum(smooth(ttot,probs_exp{1,3}))), 'b-',
'linewidth', 2);
line([probmax_exp(1,3), probmax_exp(1,3)], [0 0.5], 'linestyle', '-',
'color', 'k')
line([sigma1minus_exp(1,3), sigma1minus_exp(1,3)], [0 0.5],
'linestyle', '-.', 'color', 'k')
line([sigma1plus_exp(1,3), sigma1plus_exp(1,3)], [0 0.5], 'linestyle',
'-.', 'color', 'k')
xlabel('tot history (Ma)')
ylabel('normalised probability')

subplot(2,3,4)
hold on
axis([3.5 4.5 0 1.1*maxp_frac1])
plot(frac, probs_exp{2,1}./sum(probs_exp{2,1}), 'r-');
plot(frac,
smooth(frac,probs_exp{2,1})./(sum(smooth(frac,probs_exp{2,1}))), 'b-',
'linewidth', 2);
line([probmax_exp(2,1), probmax_exp(2,1)], [0 0.5], 'linestyle', '-',
'color', 'k')
line([sigma1minus_exp(2,1), sigma1minus_exp(2,1)], [0 0.5],
'linestyle', '-.', 'color', 'k')
line([sigma1plus_exp(2,1), sigma1plus_exp(2,1)], [0 0.5], 'linestyle',
'-.', 'color', 'k')
xlabel('d18O value (ppm)')
ylabel('normalised probability')
subplot(2,3,5)
hold on
axis([0 4 0 1.1*maxp_esp1])
plot(esa, probs_exp{2,2}./sum(probs_exp{2,2}), 'r-');
plot(esa,
smooth(esa,probs_exp{2,2})./(sum(smooth(esa,probs_exp{2,2}))), 'b-',
'linewidth', 2);
line([probmax_exp(2,2) probmax_exp(2,2)], [0 0.5], 'linestyle', '-',
'color', 'k')
line([sigma1minus_exp(2,2), sigma1minus_exp(2,2)], [0 0.5],
'linestyle', '-.', 'color', 'k')
line([sigma1plus_exp(2,2), sigma1plus_exp(2,2)], [0 0.5], 'linestyle',
'-.', 'color', 'k')
xlabel('subaerial erate (mm ka-1)')
ylabel('normalised probability')
subplot(2,3,6)
hold on
axis([0 3000 0 1.1*maxp_ttot1])
```

```
% plot(ttot, probs_exp{2,3}./sum(probs_exp{2,3}), 'r-');
plot(ttot,
smooth(ttot,probs_exp{2,3})./(sum(smooth(ttot,probs_exp{2,3}))), 'b-',
'linewidth', 2);
line([probmax_exp(2,3), probmax_exp(2,3)], [0 0.5], 'linestyle', '-',
'color', 'k')
line([sigma1minus_exp(2,3), sigma1minus_exp(2,3)], [0 0.5],
'linestyle', '-.', 'color', 'k')
line([sigma1plus_exp(2,3), sigma1plus_exp(2,3)], [0 0.5], 'linestyle',
'-.', 'color', 'k')
xlabel('tot history (Ma)')
ylabel('normalised probability')

for i_sample = 1:nsample
    max_tsp = max(probs{i_sample,1}./sum(probs{i_sample,1}));
    max_eep = max(probs{i_sample,2}./sum(probs{i_sample,2}));
    max_frec = max(probs{i_sample,3}./sum(probs{i_sample,3}));

    figure
    subplot(1,3,1)
    hold on
    axis([0 3000 0 1.1*max_tsp])
    plot(tsp, probs{i_sample,1}./sum(probs{i_sample,1}), 'r-');
    plot(tsp,
smooth(tsp,probs{i_sample,1}).(sum(smooth(tsp,probs{i_sample,1}))),
'b-', 'linewidth', 2);
    line([probmax(i_sample,1), probmax(i_sample,1)], [0 0.1],
'linestyle', '-', 'color', 'k')
    line([sigma1minus(i_sample,1), sigma1minus(i_sample,1)], [0 0.1],
'linestyle', '-.', 'color', 'k')
    line([sigma1plus(i_sample,1), sigma1plus(i_sample,1)], [0 0.1],
'linestyle', '-.', 'color', 'k')
    xlabel('time since last plucking (ka)')
    ylabel('normalised probability')
    subplot(1,3,2)
    hold on
    axis([0 15 0 1.1*max_eep])
    plot(eep, probs{i_sample,2}./sum(probs{i_sample,2}), 'r-');
    plot(eep,
smooth(eep,probs{i_sample,2}).(sum(smooth(eep,probs{i_sample,2}))),
'b-', 'linewidth', 2);
    line([probmax(i_sample,2), probmax(i_sample,2)], [0 0.05],
'linestyle', '-', 'color', 'k')
    line([sigma1minus(i_sample,2), sigma1minus(i_sample,2)], [0 0.05],
'linestyle', '-.', 'color', 'k')
    line([sigma1plus(i_sample,2), sigma1plus(i_sample,2)], [0 0.05],
'linestyle', '-.', 'color', 'k')
    xlabel('episodic erate (mm ka-1)')
    ylabel('normalised probability')
    subplot(1,3,3)
    hold on
    axis([0 15 0 1.1*max_frec])
    % plot(freq, probs{i_sample,3}./sum(probs{i_sample,3}), 'r-');
    plot(freq,
smooth(freq,probs{i_sample,3}).(sum(smooth(freq,probs{i_sample,3}))),
'b-', 'linewidth', 2);
```

```
    line([probmax(i_sample,3), probmax(i_sample,3)], [0 0.18],
'linestyle', '-', 'color', 'k')
    line([sigma1minus(i_sample,3), sigma1minus(i_sample,3)], [0 0.18],
'linestyle', '-.', 'color', 'k')
    line([sigma1plus(i_sample,3), sigma1plus(i_sample,3)], [0 0.18],
'linestyle', '-.', 'color', 'k')
    xlabel('frequency plucking (Ma-1)')
    ylabel('normalised probability')
end

%-------------------------------------------------------------------------
%Display results: histogramms of weighted chi-square values for the
%distribution of burial events for each plucking event

%plot histograms for all results and compare to acc. reuslts of
occurance of last plucking event
for i_sample = 1:nsample
    strname = sprintf('sample%i', i_sample);
    min_lplkev = min(res_acc.(strname).values(:,5)-
res_acc.(strname).values(:,9));
    max_lplkev = max(res_acc.(strname).values(:,5)-
res_acc.(strname).values(:,9));
    min_nplkev = min(res_acc.(strname).values(:,8));
    max_nplkev = max(res_acc.(strname).values(:,8));
    min_lplkth = floor(min(res_acc.(strname).values(:,10))/10)*10;
    max_lplkth = ceil(max(res_acc.(strname).values(:,10))/10)*10;

    r_lplkev = min_lplkev:1:max_lplkev;
    b_lplkev = numel(r_lplkev);
    r_nplkev = min_nplkev:1:max_nplkev;
    b_nplkev = numel(r_nplkev);
    r_lplkth = min_lplkth:10:max_lplkth;
    b_lplkth = numel(r_lplkth);

    figure
    subplot(3,3,1)
    hold on
    box on
    axis([0.9*min_lplkev 1.1*max_lplkev 0 acc_res]);
    hist(res_acc.(strname).values(:,5)-res_acc.(strname).values(:,9),
b_lplkev)
    title('last plucking event')
    xlabel('burial episode')
    ylabel('frequency')
    legend(sprintf('sample %d', i_sample))
    subplot(3,3,2)
    hold on
    box on
    axis([0.9*min_nplkev 1.1*max_nplkev 0 acc_res]);
    hist(res_acc.(strname).values(:,8), b_nplkev)
    title('number plucking event')
    xlabel('number')
    ylabel('frequency')
    legend(sprintf('sample %d', i_sample))
    subplot(3,3,3)
    hold on
```

```
    box on
    axis([0.9*min_lplkth 1.1*max_lplkth 0 acc_res]);
    hist(res_acc.(strname).values(:,10), b_lplkth)
    title('last plucking thickness')
    xlabel('block thickness')
    ylabel('frequency')
    legend(sprintf('sample %d', i_sample))
    subplot(3,3,4)
    hold on
    box on
    plot(res_acc.(strname).values(:,1), res_acc.(strname).values(:,5)-
res_acc.(strname).values(:,9), 'b.')
    title('last plucking event')
    xlabel('chi2')
    ylabel('burial episode')
    legend(sprintf('sample %d', i_sample))
    subplot(3,3,5)
    hold on
    box on
    plot(res_acc.(strname).values(:,1), res_acc.(strname).values(:,8),
'b.')
    title('number plucking event')
    xlabel('chi2')
    ylabel('number')
    legend(sprintf('sample %d', i_sample))
    subplot(3,3,6)
    hold on
    box on
    plot(res_acc.(strname).values(:,1), res_acc.(strname).values(:,10),
'b.')
    title('last plucking thickness')
    xlabel('chi2')
    ylabel('block thickness')
    legend(sprintf('sample %d', i_sample))
    subplot(3,3,7)
    hold on
    box on
    plot(res_sumchi2(:,1), res_acc.(strname).values(:,5)-
res_acc.(strname).values(:,9), 'r.')
    title('last plucking event')
    xlabel('sum chi2')
    ylabel('burial episode')
    legend(sprintf('sample %d', i_sample))
    subplot(3,3,8)
    hold on
    box on
    plot(res_sumchi2(:,1), res_acc.(strname).values(:,8), 'r.')
    title('number plucking event')
    xlabel('sum chi2')
    ylabel('number')
    legend(sprintf('sample %d', i_sample))
    subplot(3,3,9)
    hold on
    box on
    plot(res_sumchi2(:,1), res_acc.(strname).values(:,10), 'r.')
    title('last plucking thickness')
    xlabel('sum chi2')
```

```
    ylabel('block thickness')
    legend(sprintf('sample %d', i_sample))
end

for i_sample = 1:nsample
    strname = sprintf('sample%i', i_sample);
    min_lastev = floor(min(res_acc.(strname).lowering(:,7))/100)*100;
    max_lastev = ceil(max(res_acc.(strname).lowering(:,7))/100)*100;
    min_rate = floor(min(res_acc.(strname).lowering(:,2)));
    max_rate = ceil(max(res_acc.(strname).lowering(:,2)));
    min_events = floor(min(res_acc.(strname).lowering(:,1)));
    max_events = ceil(max(res_acc.(strname).lowering(:,1)));

    range_lastev = min_lastev:50:max_lastev;
    rate_range = min_rate:0.25:max_rate;
    event_range = min_events:1:max_events;

    figure
    subplot(3,3,1)
    hold on
    box on
    axis([min_lastev max_lastev 0 acc_res]);
    hist(res_acc.(strname).lowering(:,7),  range_lastev)
    title('last plucking event')
    xlabel('ka')
    ylabel('frequency')
    legend(sprintf('sample %d', sample(i_sample)))
    subplot(3,3,2)
    hold on
    box on
    axis([min_rate max_rate 0 acc_res]);
    hist(res_acc.(strname).lowering(:,2), rate_range)
    title('episodic erosion rate')
    xlabel('erosion rate (m Ma-1)')
    ylabel('frequency')
    legend(sprintf('sample %d', sample(i_sample)))
    subplot(3,3,3)
    hold on
    box on
    axis([min_events max_events 0 acc_res]);
    hist(res_acc.(strname).lowering(:,1),  event_range)
    title('frequency of events')
    xlabel('number of events (Ma-1)')
    ylabel('frequency')
    legend(sprintf('sample %d', sample(i_sample)))
    subplot(3,3,4)
    hold on
    box on
    plot(res_acc.(strname).values(:,1),
res_acc.(strname).lowering(:,7), 'b.')
    title('last plucking event')
    xlabel('chi2')
    ylabel('ka')
    legend(sprintf('sample %d', i_sample))
    subplot(3,3,5)
    hold on
```

```
    box on
    plot(res_acc.(strname).values(:,1),
res_acc.(strname).lowering(:,2), 'b.')
    title('episodic erosion rate')
    xlabel('chi2')
    ylabel('erosion rate (m Ma-1)')
    legend(sprintf('sample %d', i_sample))
    subplot(3,3,6)
    hold on
    box on
    plot(res_acc.(strname).values(:,1),
res_acc.(strname).lowering(:,1), 'b.')
    title('frequency of events')
    xlabel('chi2')
    ylabel('number of events (Ma-1)')
    legend(sprintf('sample %d', i_sample))
    subplot(3,3,7)
    hold on
    box on
    plot(res_sumchi2(:,1), res_acc.(strname).lowering(:,7), 'r.')
    title('last plucking event')
    xlabel('chi2')
    ylabel('ka')
    legend(sprintf('sample %d', i_sample))
    subplot(3,3,8)
    hold on
    box on
    plot(res_sumchi2(:,1), res_acc.(strname).lowering(:,2), 'r.')
    title('episodic erosion rate')
    xlabel('chi2')
    ylabel('erosion rate (m Ma-1)')
    legend(sprintf('sample %d', i_sample))
    subplot(3,3,9)
    hold on
    box on
    plot(res_sumchi2(:,1), res_acc.(strname).lowering(:,1), 'r.')
    title('frequency of events')
    xlabel('chi2')
    ylabel('number of events (Ma-1)')
    legend(sprintf('sample %d', i_sample))
end

strname = sprintf('sample%i', 1);
min_frac = floor(min(res_acc.(strname).lowering(:,6))/10)*10; %in ka
max_frac = ceil(max(res_acc.(strname).lowering(:,6))/10)*10; %in ka
min_hist = floor(min(res_acc.(strname).lowering(:,5)));
max_hist = ceil(max(res_acc.(strname).lowering(:,5)));
min_suberate = floor(min(res_acc.(strname).values(:,6)));
max_suberate = ceil(max(res_acc.(strname).values(:,6)));

range_frac = min_frac:1:max_frac;
range_hist = min_hist:0.1:max_hist;
range_suberate = min_suberate:0.25:max_suberate;

figure
subplot(3,3,1)
```

```
hold on
box on
axis([min_frac max_frac 0 acc_res]);
hist(res_acc.(strname).lowering(:,6),  range_frac)
title('ice free time')
xlabel('percent')
ylabel('frequency')
subplot(3,3,2)
hold on
box on
axis([min_hist max_hist 0 acc_res]);
hist(res_acc.(strname).lowering(:,5), range_hist)
title('total exposure history')
xlabel('Ma')
ylabel('frequency')
subplot(3,3,3)
hold on
box on
axis([min_suberate max_suberate 0 acc_res]);
hist(res_acc.(strname).values(:,6),  range_suberate)
title('subaerial erosion rate')
xlabel('m Ma-1')
ylabel('frequency')
subplot(3,3,4)
hold on
box on
plot(res_acc.(strname).values(:,1), res_acc.(strname).lowering(:,6),
'b.')
title('ice free time')
xlabel('chi2')
ylabel('percent')
subplot(3,3,5)
hold on
box on
plot(res_acc.(strname).values(:,1), res_acc.(strname).lowering(:,5),
'b.')
title('total exposure history')
xlabel('chi2')
ylabel('Ma')
subplot(3,3,6)
hold on
box on
plot(res_acc.(strname).values(:,1), res_acc.(strname).values(:,6),
'b.')
title('subaerial erosion rate')
xlabel('chi2')
ylabel('m Ma-1')
subplot(3,3,7)
hold on
box on
plot(res_sumchi2(:,1), res_acc.(strname).lowering(:,6), 'r.')
title('ice free time')
xlabel('chi2')
ylabel('percent')
subplot(3,3,8)
hold on
box on
```

```
plot(res_sumchi2(:,1), res_acc.(strname).lowering(:,5), 'r.')
title('total exposure history')
xlabel('chi2')
ylabel('Ma')
subplot(3,3,9)
hold on
box on
plot(res_sumchi2(:,1), res_acc.(strname).values(:,6), 'r.')
title('subaerial erosion rate')
xlabel('chi2')
ylabel('m Ma-1')

end %end of function
```

A4.4 BURIAL PLOT INCLUDING COMPLEX EXPOSURE HISTORIES

```
function CP_burialplot_cmplxexp(tordata, samples, durglac, avexpdur,
averate, glerate, icethick, consts, sigma, plotbanana)
%example:> CP_burialplot_cmplxexp('CP_alltor.txt', 10, 100, 0.2, 1.0,
5.0, 5000, consts, 1, true)

%This function creates a muon inclusive burial plot for either SLHL
normalized samples or a sample-specific location assuming ice of
constant thickness covering the site for a pre-defined fraction of
time. In addition, it plots plausible complex exposure histories for
tors with alternate exposure intervals (glacial-interglacial cycles).
Scaling based on Lifton et al. (2014) using individual production rates
for fast and negative muons and their respective attenuation lengths.

%INPUTS:
%tordata = name of ascii file with 7 columns of data (e.g. 'data.txt'):
%   column 1 is the decimal latitude of each sample;
%   column 2 is the decimal longitute of each sample;
%   column 3 is the elevation of each sample; (m)
%   column 4 is measured [10Be]; (atoms/g)
%   column 5 is the measured 1 sigma error in [10Be]; (atoms/g)
%   column 6 is the measured [26Al]; (atoms/g)
%   column 7 is the measured 1 sigma error in [26Al]; (atoms/g)

%sample = the row number of the sample you wish to model;

%durglac = average duration of one glacial cycle; (ka)

%avexpdur = best guess for average duration of ice-free intervals in
%percentage of the total glacial cycle; (i.e. 0.185 for 18.5ka of 100ka
%glacial cycle)

%averate = best guess for average constant erosion rate during
%interglacials in mm ka-1; (mm/ka = m/Ma = 1e-1 cm/ka = 1e-4 cm/a)

%glerate = best guess for average constant erosion rate during glacials
%in mm ka-1; (mm/ka = m/Ma = 1e-1 cm/ka = 1e-4 cm/a)
```

```
%icethick = average ice thickness covering sample site during each
burial episode; (cm)

%consts = a matlab structure containing constants used in the LSD
scaling %model. This structure is loaded in the startup.m file.

%sigma = specifies the sigma confidence for the error ellipse

%plotbananna = if true, will also plot the banana window

%A.Margreth - March 2014, adapted from A. Hidy's burialplot (incl. LSD)
%%%%%%%%%%%%%%%%%%%%%%%%%%%%%%%%%%%%%%%%%%%%%%%%%%%%%%%%%%%%%%%%%%%%%%%%%%%%

%load data
burial_data = load(tordata);
lats = burial_data(:,1);
longs = burial_data(:,2);
elevs = burial_data(:,3);
Be_concs = burial_data(:,4);
Be_errs = burial_data(:,5);
Al_concs = burial_data(:,6);
Al_errs = burial_data(:,7);

sample = samples(1);

norm = 6.75;  %1 or 6.75; for normalization of burialplot

%densities used for buildup (g/cc)
r_density = 2.65;
ice_density = 0.9;

%re-calculate ice thickness to rock-equivalent thickness for burial
events
surf_depth = 0;
%used in buildup functions to draw isoexp and -bur lines
depth_ice = icethick*ice_density/r_density;
t_glac = durglac * 1000;
frac = avexpdur; %redundent assignment
eros = averate / 10000; %convert to cm a-1
gl_eros = glerate / 10000; %convert to cm a-1
bur_depth = (depth_ice * (1-frac) * t_glac) / t_glac;
%calculate average burial depth

%decay constants (1/s)
Be10_lambda = log(2)/1378000;
%Chmeleff et al. (2010), Korschinek et al. (2010)
Al26_lambda = log(2)/720000; %Nishiizumi (2004)

%neutron attenuation length (g/cm^2)
neutron_atten = 150; %Follows Balco et al. (2008); see Gosse and
Phillips (2001)
```

```
%spallogenic production (atoms/g/a)
refspalprod = 4; %New prod rate, Brocher et al. (subm.);
ratio_init = 6.75; %Nishiizumi et al. (1989); Balco et al. (2008);
6.1/1.106 to reflect recalibration of Nishiizumi et al. (2007)

%Get  surface production rates
%Get LSD scaling factors
maxage = 100000; %age over which to integrate production rates
LSD10 = LSD(lats(sample),longs(sample),elevs(sample),1,maxage,-1,10);
LSD26 = LSD(lats(sample),longs(sample),elevs(sample),1,maxage,-1,26);
agegrid = 0:1:maxage;
%average cutoff rigidity (RC) and solar modulation (SPhi)over age range
meanRC = mean(interpolate(LSD10.tv,LSD10.Rc,agegrid));
meanSPhi = mean(interpolate(LSD10.tv,LSD10.SPhi,agegrid));
%average spallogenic surface production rate over age range
Be10_spalprodrate =
mean(refspalprod.*interpolate(LSD10.tv,LSD10.Be,agegrid));
Al26_spalprodrate =
mean(refspalprod.*ratio_init.*interpolate(LSD26.tv,LSD26.Al,agegrid));
%average total muogenic surface production rate over age range
[Be10_fmusurf, Be10_nmusurf] = CP_P_mu_totalLSD(surf_depth *
r_density,LSD10.pressure,meanRC,meanSPhi,consts,10,'no');
[Al26_fmusurf, Al26_nmusurf] = CP_P_mu_totalLSD(surf_depth *
r_density,LSD10.pressure,meanRC,meanSPhi,consts,26,'no');
[Be10_fmudepth, Be10_nmudepth] = CP_P_mu_totalLSD(bur_depth *
r_density,LSD10.pressure,meanRC,meanSPhi,consts,10,'no');
[Al26_fmudepth, Al26_nmudepth] = CP_P_mu_totalLSD(bur_depth *
r_density,LSD10.pressure,meanRC,meanSPhi,consts,26,'no');
Be10_musurf = Be10_fmusurf + Be10_nmusurf;
Al26_musurf = Al26_fmusurf + Al26_nmusurf;
Be10_mudepth = Be10_fmudepth + Be10_nmudepth;
Al26_mudepth = Al26_fmudepth + Al26_nmudepth;

%=========================================================================
%definition of functions to calculate production of isotopes

%simple buildup model with no erosion
    %buildup due to exposure at surface; assumes no inheritance
    function Be10_conc_buildup_surf = Be10_buildup_surf(t_exposure)
        Be10spall_buildup = (Be10_spalprodrate/Be10_lambda)*(1-exp(-
Be10_lambda*t_exposure));
        Be10muon_buildup = (Be10_musurf/Be10_lambda)*(1-exp(-
Be10_lambda*t_exposure));
        Be10_conc_buildup_surf = Be10spall_buildup + Be10muon_buildup;
    end

    function Al26_conc_buildup_surf = Al26_buildup_surf(t_exposure)
        Al26spall_buildup = (Al26_spalprodrate/Al26_lambda)*(1-exp(-
Al26_lambda*t_exposure));
        Al26muon_buildup = (Al26_musurf/Al26_lambda)*(1-exp(-
Al26_lambda*t_exposure));
        Al26_conc_buildup_surf = Al26spall_buildup + Al26muon_buildup;
    end

    %burial production; assume buildup is inheritance
```

```
    function Be10_conc_burial_surf = Be10_burial_surf(t_exposure,
t_burial)
        Be10spall_burial = (Be10_spalprodrate/Be10_lambda)*exp(-
bur_depth*r_density/neutron_atten)*(1-exp(-Be10_lambda*t_burial));
        Be10muon_burial = (Be10_mudepth/Be10_lambda)*(1-exp(-
Be10_lambda*t_burial));
        Be10inheritance = Be10_buildup_surf(t_exposure)*exp(-
Be10_lambda*t_burial);
        Be10_conc_burial_surf = Be10spall_burial + Be10muon_burial +
Be10inheritance;
    end

    function Al26_conc_burial_surf = Al26_burial_surf(t_exposure,
t_burial)
        Al26spall_burial = (Al26_spalprodrate/Al26_lambda)*exp(-
bur_depth*r_density/neutron_atten)*(1-exp(-Al26_lambda*t_burial));
        Al26muon_burial = (Al26_mudepth/Al26_lambda)*(1-exp(-
Al26_lambda*t_burial));
        Al26inheritance = Al26_buildup_surf(t_exposure)*exp(-
Al26_lambda*t_burial);
        Al26_conc_burial_surf = Al26spall_burial + Al26muon_burial +
Al26inheritance;
    end

    %buildup due to exposure at depth; assumes no inheritance
    function Be10_conc_buildup_depth = Be10_buildup_depth(t_exposure)
        Be10spall_buildup = (Be10_spalprodrate/Be10_lambda)*(1-exp(-
Be10_lambda*t_exposure))*exp(-bur_depth*r_density/neutron_atten);
        Be10muon_buildup = (Be10_mudepth/Be10_lambda)*(1-exp(-
Be10_lambda*t_exposure));
        Be10_conc_buildup_depth = Be10spall_buildup + Be10muon_buildup;
    end

    function Al26_conc_buildup_depth = Al26_buildup_depth(t_exposure)
        Al26spall_buildup = (Al26_spalprodrate/Al26_lambda)*(1-exp(-
Al26_lambda*t_exposure))*exp(-bur_depth*r_density/neutron_atten);
        Al26muon_buildup = (Al26_mudepth/Al26_lambda)*(1-exp(-
Al26_lambda*t_exposure));
        Al26_conc_buildup_depth = Al26spall_buildup + Al26muon_buildup;
    end

%simple buildup model with erosion
    %new lambda term spallation
     function Be10lambda = Be10_elambda(erate)
        Be10lambda = Be10_lambda + erate*r_density/neutron_atten;
    end

    function Al26lambda = Al26_elambda(erate)
        Al26lambda = Al26_lambda + erate*r_density/neutron_atten;
    end

    function Be10lambdamun = Be10n_elambdamu(erate)
        Be10lambdamun = Be10_lambda + erate*r_density/1500;
    end

    function Al26lambdamun = Al26n_elambdamu(erate)
```

```
        Al26lambdamun = Al26_lambda + erate*r_density/1500;
    end

    function Be10lambdamuf = Be10f_elambdamu(erate)
        Be10lambdamuf = Be10_lambda + erate*r_density/4320;
    end

    function Al26lambdamuf = Al26f_elambdamu(erate)
        Al26lambdamuf = Al26_lambda + erate*r_density/4320;
    end

    %buildup due to exposure at surface; assumes no inheritance
    function eBe10_conc_buildup = eBe10_buildup(t_exposure, erate)
        Be10spall_buildup =
(Be10_spalprodrate./Be10_elambda(erate)).*(1-exp(-
Be10_elambda(erate).*t_exposure));
        Be10muon_buildup = Be10_fmusurf./Be10f_elambdamu(erate).*(1-
exp(-Be10f_elambdamu(erate).*t_exposure)) +
Be10_nmusurf./Be10n_elambdamu(erate).*(1-exp(-
Be10n_elambdamu(erate).*t_exposure));
        eBe10_conc_buildup = Be10spall_buildup + Be10muon_buildup;
    end

    function eAl26_conc_buildup = eAl26_buildup(t_exposure, erate)
        Al26spall_buildup =
(Al26_spalprodrate./Al26_elambda(erate)).*(1-exp(-
Al26_elambda(erate).*t_exposure));
        Al26muon_buildup = Al26_fmusurf./Al26f_elambdamu(erate).*(1-
exp(-Al26f_elambdamu(erate).*t_exposure)) +
Al26_nmusurf./Al26n_elambdamu(erate).*(1-exp(-
Al26n_elambdamu(erate).*t_exposure));
        eAl26_conc_buildup = Al26spall_buildup + Al26muon_buildup;
    end

%-------------------------------------------------------------------------
%Build burial plot with additional complex exposure pathways
%define axis for plot
plot_axis = [4 7.5 0 8/norm];

%Define locations of contours on burial plot, unit years
n1 = [250000 500000 1000000 2000000]; %burial contours
n2 = [3000 10000 30000 100000 300000 1000000]; %exposure contours
n3 = [100 50 20 10 5 2 1 0.5 0.2 0.1 0.05 0.01]/1000;
%erosion rate contours, cm/a (inside [ ] erosion rate in cm/ka)

%Create grids for plot contours
texp = 1:1000:20000000; %max 20 Ma
tbur = 1:1000:20000000; %max 10 Ma
eeros = 0:0.001/1000:500/1000; %erosion endpoints ranging from 0-500
cm/ka

figure %burial plot
hold on
axis(plot_axis);
xlabel('log[^{10}Be] (atoms g^{-1})');
ylabel('^{26}Al/^{10}Be');
```

```
title('Burial Plot');

%plot samples points and ellipses
for i_sample = 1:numel(samples)
Tor_ellipse(Be_concs(samples(i_sample)),Be_errs(samples(i_sample)),Al_c
oncs(samples(i_sample))./norm,Al_errs(samples(i_sample))./norm,sigma);
plot(log10(Be_concs(samples(i_sample))),(Al_concs(samples(i_sample))./
Be_concs(samples(i_sample)))./norm,'k.');
end

%plot burial contours and exposure contours
for k = 1:numel(n1)
plot(log10(Be10_burial_surf(texp,n1(k))),(Al26_burial_surf(texp,n1(k)).
/Be10_burial_surf(texp,n1(k)))./norm,'b-');
end

for k = 1:numel(n2)
plot(log10(Be10_burial_surf(n2(k),tbur)),(Al26_burial_surf(n2(k),tbur).
/Be10_burial_surf(n2(k),tbur))./norm,'k--');
end

%plot continuous exposure line
plot(log10(Be10_burial_surf(texp,0)),(Al26_burial_surf(texp,0)./Be10_bu
rial_surf(texp,0))./norm,'r-','linewidth',2);

%plot continuous expsure curve for bur_depth, which is the left
boundary of allowable ratio vs. concentration pairs
plot(log10(Be10_buildup_depth(texp)),(Al26_buildup_depth(texp)./Be10_bu
ildup_depth(texp))./norm,'r-','linewidth',2);
plot(log10(Be10_burial_surf(100000000,tbur)),(Al26_burial_surf(10000000
0,tbur)./Be10_burial_surf(100000000,tbur))./norm,'k-','linewidth',2);

%=========================================================================
%-----------comment if not required to calculate inherted concentration
%%% use for calculation of concentration produced during last ice-free
interval

% no_ice = 15000; %ice free interval in years
% elambda = nan(1,6);
% elambda(1) = Be10_lambda + eros*r_density/neutron_atten;
%spallogenic 10Be
% elambda(2) = Al26_lambda + eros*r_density/neutron_atten;
%spallogenic 26Al
% elambda(3) = Be10_lambda + eros*r_density/1500; %muogenic 10Be
% elambda(4) = Al26_lambda + eros*r_density/1500; %muogenic 26Al
% elambda(5) = Be10_lambda + eros*r_density/4320; %muogenic 10Be
% elambda(6) = Al26_lambda + eros*r_density/4320; %muogenic 26Al
%
% inh = nan(numel(samples),6);
% prod_inh = nan(numel(samples),6);
%
% for i_sample = 1:numel(samples)
%     %Get LSD scaling factors
%     maxage = no_ice; %age over which to integrate production rates
%     LSD10 = LSD(lats(sample),longs(sample),elevs(sample),1,maxage,-
1,10);
```

```
%     LSD26 = LSD(lats(sample),longs(sample),elevs(sample),1,maxage,-
1,26);
%     agegrid = 0:1:maxage;
%     %average cutoff rigidity (RC) and solar modulation (SPhi)over age
range
%     meanRC = mean(interpolate(LSD10.tv,LSD10.Rc,agegrid));
%     meanSPhi = mean(interpolate(LSD10.tv,LSD10.SPhi,agegrid));
%     %average spallogenic surface production rate over age range
%     Be10_spprd_noice =
mean(refspalprod.*interpolate(LSD10.tv,LSD10.Be,agegrid));
%     Al26_spprd_noice =
mean(refspalprod.*ratio_init.*interpolate(LSD26.tv,LSD26.Al,agegrid));
%     [Be10_fmuprod_noice, Be10_nmuprod_noice] =
CP_P_mu_totalLSD(surf_depth *
r_density,LSD10.pressure,meanRC,meanSPhi,consts,10,'no');
%     [Al26_fmuprod_noice, Al26_nmuprod_noice] =
CP_P_mu_totalLSD(surf_depth *
r_density,LSD10.pressure,meanRC,meanSPhi,consts,26,'no');

%     Be_concs_noice = (Be10_spprd_noice/Be10_lambda)*(1-exp(-
Be10_lambda*no_ice)) + (Be10_fmuprod_noice/Be10_lambda)*(1-exp(-
Be10_lambda*no_ice)) + (Be10_nmuprod_noice/Be10_lambda)*(1-exp(-
Be10_lambda*no_ice));
%     Al_concs_noice = (Al26_spprd_noice/Al26_lambda)*(1-exp(-
Al26_lambda*no_ice)) + (Al26_fmuprod_noice/Al26_lambda)*(1-exp(-
Al26_lambda*no_ice)) + (Al26_nmuprod_noice/Al26_lambda)*(1-exp(-
Al26_lambda*no_ice));
%
%     e_Be_concs_noice = (Be10_spprd_noice/elambda(1))*(1-exp(-
elambda(1)*no_ice)) + (Be10_fmuprod_noice/elambda(5))*(1-exp(-
elambda(5)*no_ice)) + (Be10_nmuprod_noice/elambda(3))*(1-exp(-
elambda(3)*no_ice));
%     e_Al_concs_noice = (Al26_spprd_noice/elambda(2))*(1-exp(-
elambda(2)*no_ice)) + (Al26_fmuprod_noice/elambda(6))*(1-exp(-
elambda(6)*no_ice)) + (Al26_nmuprod_noice/elambda(4))*(1-exp(-
elambda(4)*no_ice));

%     prod_inh(samples(i_sample),1) = Be_concs_noice;
%     prod_inh(samples(i_sample),2) = Al_concs_noice;
%     prod_inh(samples(i_sample),3) = e_Be_concs_noice;
%     prod_inh(samples(i_sample),4) = e_Al_concs_noice;
%     prod_inh(samples(i_sample),5) = Be10_spalprodrate + Be10_musurf;
%     prod_inh(samples(i_sample),6) = Al26_spalprodrate + Al26_musurf;
%
%     eBe_lambda = Be10_spalprodrate/(Be10_spalprodrate + Be10_fmusurf
+ Be10_nmusurf)*elambda(1) + Be10_fmusurf/(Be10_spalprodrate +
Be10_fmusurf + Be10_nmusurf)*elambda(5) +
Be10_nmusurf/(Be10_spalprodrate + Be10_fmusurf +
Be10_nmusurf)*elambda(3);
%     eAl_lambda = Al26_spalprodrate/(Al26_spalprodrate + Al26_fmusurf
+ Al26_nmusurf)*elambda(2) + Al26_fmusurf/(Al26_spalprodrate +
Al26_fmusurf + Al26_nmusurf)*elambda(6) +
Al26_nmusurf/(Al26_spalprodrate + Al26_fmusurf +
Al26_nmusurf)*elambda(4);

%     Be_inh = (Be_concs(samples(i_sample)) - Be_concs_noice)/exp(-
Be10_lambda*no_ice);
```

```
%     Al_inh= (Al_concs(samples(i_sample)) - Al_concs_noice)/exp(-
Al26_lambda*no_ice);
%     e_Be_inh = (Be_concs(samples(i_sample)) - e_Be_concs_noice)/exp(-
eBe_lambda*no_ice);
%     e_Al_inh = (Al_concs(samples(i_sample)) - e_Al_concs_noice)/exp(-
eAl_lambda*no_ice);

%     inh(samples(i_sample),1) = Be_inh;
%     inh(samples(i_sample),2) = Al_inh;
%     inh(samples(i_sample),3) = Al_inh./Be_inh;
%     inh(samples(i_sample),4) = e_Be_inh;
%     inh(samples(i_sample),5) = e_Al_inh;
%     inh(samples(i_sample),6) = e_Al_inh./e_Be_inh;
% end
%
% save inh.txt inh -ascii
% save prod_inh.txt prod_inh -ascii
%
% %%%plot all sample points (inherited with/without erosion)
% for i_sample = 1:numel(samples)
%     Tor_ellipse(inh(samples(i_sample),1),
inh(samples(i_sample),1)*(Be_errs(samples(i_sample))/Be_concs(samples(i
_sample))),inh(samples(i_sample),2)./norm,
(inh(samples(i_sample),2)*(Al_errs(samples(i_sample))/Al_concs(samples(
i_sample)))./norm,sigma);
%     Tor_ellipse(inh(samples(i_sample),4),
inh(samples(i_sample),4)*(Be_errs(samples(i_sample))/Be_concs(samples(i
_sample))),inh(samples(i_sample),5)./norm,
(inh(samples(i_sample),5)*(Al_errs(samples(i_sample))/Al_concs(samples(
i_sample)))./norm,sigma);
%     plot(log10(inh(samples(i_sample),1)),
inh(samples(i_sample),3)./norm, 'm.', log10(inh(samples(i_sample),4)),
inh(samples(i_sample),6)./norm, 'g.')
% end
%
% %%%plot last longer ice-free trajectory with/without erosion
% expose_noice = 0:no_ice;
% for i_sample = 1:numel(samples)
%     Be_noice = inh(samples(i_sample),1) .* exp(-
Be10_lambda.*expose_noice) + (Be10_spprd_noice/Be10_lambda)*(1-exp(-
Be10_lambda.*expose_noice)) + (Be10_fmuprod_noice/Be10_lambda)*(1-exp(-
Be10_lambda.*expose_noice)) + (Be10_nmuprod_noice/Be10_lambda)*(1-exp(-
Be10_lambda.*expose_noice));
%     Al_noice = inh(samples(i_sample),2) .* exp(-
Al26_lambda.*expose_noice) + (Al26_spprd_noice/Al26_lambda)*(1-exp(-
Al26_lambda.*expose_noice)) + (Al26_fmuprod_noice/Al26_lambda)*(1-exp(-
Al26_lambda.*expose_noice)) + (Al26_nmuprod_noice/Al26_lambda)*(1-exp(-
Al26_lambda.*expose_noice));
%     Be_e_noice = inh(samples(i_sample),4) .* exp(-
eBe_lambda.*expose_noice) + (Be10_spprd_noice/elambda(1))*(1-exp(-
elambda(1).*expose_noice)) + (Be10_fmuprod_noice/elambda(5))*(1-exp(-
elambda(5).*expose_noice)) + (Be10_nmuprod_noice/elambda(3))*(1-exp(-
elambda(3).*expose_noice));
%     Al_e_noice = inh(samples(i_sample),5) .* exp(-
eAl_lambda.*expose_noice) + (Al26_spprd_noice/elambda(2))*(1-exp(-
elambda(2).*expose_noice)) + (Al26_fmuprod_noice/elambda(6))*(1-exp(-
```

```
elambda(6).*expose_noice)) + (Al26_nmuprod_noice/elambda(4))*(1-exp(-
elambda(4).*expose_noice));
%     plot(log10(Be_noice),(Al_noice./Be_noice)./norm, 'm-',
log10(Be_e_noice),(Al_e_noice./Be_e_noice)./norm, 'g-')
% end
%-------------------------------------------------------end of comments

%construct complex exposure trajectories at depth
thickn = 0:50:100; %choose numbers and depth of add. lines

k_max = 20*10^6/t_glac;
%define maximum duration of cyclic ice cover history (in a)
exposet = 0:100:frac*t_glac;
burialt = 0:100:(1-frac)*t_glac;

elambda = nan(1,6);
elambda(1) = Be10_lambda + eros*r_density/neutron_atten;
%spallogenic 10Be
elambda(2) = Al26_lambda + eros*r_density/neutron_atten;
%spallogenic 26Al
elambda(3) = Be10_lambda + eros*r_density/1500; %muogenic 10Be
elambda(4) = Al26_lambda + eros*r_density/1500; %muogenic 26Al
elambda(5) = Be10_lambda + eros*r_density/4320; %muogenic 10Be
elambda(6) = Al26_lambda + eros*r_density/4320; %muogenic 26Al

gl_elambda = nan(1,6);
gl_elambda(1) = Be10_lambda + gl_eros*r_density/neutron_atten;
%spallogenic 10Be
gl_elambda(2) = Al26_lambda + gl_eros*r_density/neutron_atten;
%spallogenic 26Al
gl_elambda(3) = Be10_lambda + gl_eros*r_density/1500; %muogenic 10Be
gl_elambda(4) = Al26_lambda + gl_eros*r_density/1500; %muogenic 26Al
gl_elambda(5) = Be10_lambda + gl_eros*r_density/4320; %muogenic 10Be
gl_elambda(6) = Al26_lambda + gl_eros*r_density/4320; %muogenic 26Al

%no erosion during decay intervals
decbeexp = exp(-Be10_lambda.*exposet);
decbebur = exp(-Be10_lambda.*burialt);
decalexp = exp(-Al26_lambda.*exposet);
decalbur = exp(-Al26_lambda.*burialt);

fmuon = nan(4,numel(thickn));
nmuon = nan(4,numel(thickn));
tot_prod = nan(4,numel(thickn));
spalprod = nan(4,numel(thickn));
dec_elambda = nan(4,numel(thickn));

for t = 1:numel(thickn)
    %--------------------can be commented if no inheritence calculated
    %%%Get LSD scaling factors
%     maxage = 100000; %age over which to integrate production rates
%     LSD10 = LSD(lats(sample),longs(sample),elevs(sample),1,maxage,-
1,10);
%     LSD26 = LSD(lats(sample),longs(sample),elevs(sample),1,maxage,-
1,26);
%     agegrid = 0:1:maxage;
```

```
%     %average cutoff rigidity (RC) and solar modulation (SPhi)over age
range
%     meanRC = mean(interpolate(LSD10.tv,LSD10.Rc,agegrid));
%     meanSPhi = mean(interpolate(LSD10.tv,LSD10.SPhi,agegrid));
    %-------------------------------------------------end commenting

    [fmuon(1,t), nmuon(1,t)] = CP_P_mu_totalLSD((surf_depth +
thickn(t)) * r_density,LSD10.pressure,meanRC,meanSPhi,consts,10,'no');
    [fmuon(2,t), nmuon(2,t)] = CP_P_mu_totalLSD((surf_depth +
thickn(t)) * r_density,LSD10.pressure,meanRC,meanSPhi,consts,26,'no');
    [fmuon(3,t), nmuon(3,t)] = CP_P_mu_totalLSD((depth_ice + thickn(t))
* r_density,LSD10.pressure,meanRC,meanSPhi,consts,10,'no');
    [fmuon(4,t), nmuon(4,t)] = CP_P_mu_totalLSD((depth_ice +
thickn(t))* r_density,LSD10.pressure,meanRC,meanSPhi,consts,26,'no');

    spalprod(1,t) = Be10_spalprodrate*exp(-(surf_depth +
thickn(t))*r_density/neutron_atten);
    spalprod(2,t) = Al26_spalprodrate*exp(-(surf_depth +
thickn(t))*r_density/neutron_atten);
    spalprod(3,t) = Be10_spalprodrate*exp(-(depth_ice +
thickn(t))*r_density/neutron_atten);
    spalprod(4,t) = Al26_spalprodrate*exp(-(depth_ice +
thickn(t))*r_density/neutron_atten);

    %%%new decay terms including indvdual terms for neg. & fast muons
    tot_prod(1,t) = Be10_spalprodrate*exp(-(surf_depth +
thickn(t))*r_density/neutron_atten) + fmuon(1,t) + nmuon(1,t);
    tot_prod(2,t) = Al26_spalprodrate*exp(-(surf_depth +
thickn(t))*r_density/neutron_atten) + fmuon(2,t) + nmuon(2,t);
    tot_prod(3,t) = Be10_spalprodrate*exp(-(surf_depth +
thickn(t))*r_density/neutron_atten) + fmuon(3,t) + nmuon(3,t);
    tot_prod(4,t) = Al26_spalprodrate*exp(-(surf_depth +
thickn(t))*r_density/neutron_atten) + fmuon(4,t) + nmuon(4,t);

    dec_elambda(1,t) = (Be10_spalprodrate*exp(-(surf_depth +
thickn(t))*r_density/neutron_atten))/tot_prod(1,t) * elambda(1) +
fmuon(1,t)/tot_prod(1,t)*elambda(5) +
nmuon(1,t)/tot_prod(1,t)*elambda(3);
    dec_elambda(2,t) = (Al26_spalprodrate*exp(-(surf_depth +
thickn(t))*r_density/neutron_atten))/tot_prod(2,t) * elambda(2) +
fmuon(2,t)/tot_prod(2,t)*elambda(6) +
nmuon(2,t)/tot_prod(2,t)*elambda(4);
    dec_elambda(4,t) = (Al26_spalprodrate*exp(-(depth_ice +
thickn(t))*r_density/neutron_atten))/tot_prod(4,t) * gl_elambda(1) +
fmuon(4,t)/tot_prod(4,t)*gl_elambda(6) +
nmuon(4,t)/tot_prod(4,t)*gl_elambda(4);
    dec_elambda(3,t) = (Be10_spalprodrate*exp(-(surf_depth +
thickn(t))*r_density/neutron_atten))/tot_prod(1,t) * gl_elambda(1) +
fmuon(1,t)/tot_prod(1,t)*gl_elambda(5) +
nmuon(1,t)/tot_prod(1,t)*gl_elambda(3);
    dec_elambda(4,t) = (Al26_spalprodrate*exp(-(surf_depth +
thickn(t))*r_density/neutron_atten))/tot_prod(2,t) * gl_elambda(2) +
fmuon(2,t)/tot_prod(2,t)*gl_elambda(6) +
nmuon(2,t)/tot_prod(2,t)*gl_elambda(4);
```

```
    %%%subaerial erosion during exp intervals
    sa_decbeexp = exp(-dec_elambda(1,t).*exposet);
    sa_decalexp = exp(-dec_elambda(2,t).*exposet);
    %%%glacial erosion during bur intervals
    gl_decbebur = exp(-dec_elambda(3,t).*burialt);
    gl_decalbur = exp(-dec_elambda(4,t).*burialt);

%     %%% to plot continous exposure lines for any depth---------------
%     expbe_anydepth = (Be10_spalprodrate/Be10_lambda)*exp(-(surf_depth
+ thickn(t))*r_density/neutron_atten)*(1-exp(-Be10_lambda*texp)) +
(fmuon(1,t)/Be10_lambda)*(1-exp(-Be10_lambda*texp)) +
(nmuon(1,t)/Be10_lambda)*(1-exp(-Be10_lambda*texp));
%     expal_anydepth = (Al26_spalprodrate/Al26_lambda)*exp(-(surf_depth
+ thickn(t))*r_density/neutron_atten)*(1-exp(-Al26_lambda*texp)) +
(fmuon(2,t)/Al26_lambda)*(1-exp(-Al26_lambda*texp)) +
(nmuon(2,t)/Al26_lambda)*(1-exp(-Al26_lambda*texp));
%     plot(log10(expbe_anydepth), expal_anydepth./expbe_anydepth./norm,
'r-', 'linewidth', 2);
%
%     e_expbe_anydepth = (Be10_spalprodrate/elambda(1))*exp(-
(surf_depth + thickn(t))*r_density/neutron_atten)*(1-exp(-
elambda(1)*texp)) + (fmuon(1,t)/elambda(5))*(1-exp(-elambda(5)*texp)) +
(nmuon(1,t)/elambda(3))*(1-exp(-elambda(3)*texp));
%     e_expal_anydepth = (Al26_spalprodrate/elambda(2))*exp(-
(surf_depth + thickn(t))*r_density/neutron_atten)*(1-exp(-
elambda(2)*texp)) + (fmuon(2,t)/elambda(6))*(1-exp(-elambda(6)*texp)) +
(nmuon(2,t)/elambda(4))*(1-exp(-elambda(4)*texp));
%     plot(log10(e_expbe_anydepth),
e_expal_anydepth./e_expbe_anydepth./norm, 'g-', 'linewidth', 2);
%     %%%end comment-------------------------------------------------

    expbe = (Be10_spalprodrate/Be10_lambda)*(1-exp(-
Be10_lambda*exposet))*exp(-(surf_depth +
thickn(t))*r_density/neutron_atten) + (fmuon(1,t)/Be10_lambda)*(1-exp(-
Be10_lambda*exposet)) + (nmuon(1,t)/Be10_lambda)*(1-exp(-
Be10_lambda*exposet));
    expal = (Al26_spalprodrate/Al26_lambda)*(1-exp(-
Al26_lambda*exposet))*exp(-(surf_depth +
thickn(t))*r_density/neutron_atten) + (fmuon(2,t)/Al26_lambda)*(1-exp(-
Al26_lambda*exposet)) + (nmuon(2,t)/Al26_lambda)*(1-exp(-
Al26_lambda*exposet));
    tmp1 = max(expbe);
    tmp2 = max(expal);

    e_expbe = (Be10_spalprodrate/elambda(1))*(1-exp(-
elambda(1)*exposet))*exp(-(surf_depth +
thickn(t))*r_density/neutron_atten) + (fmuon(1,t)/elambda(5))*(1-exp(-
elambda(5)*exposet)) + (nmuon(1,t)/elambda(3))*(1-exp(-
elambda(3)*exposet));
    e_expal = (Al26_spalprodrate/elambda(2))*(1-exp(-
elambda(2)*exposet))*exp(-(surf_depth +
thickn(t))*r_density/neutron_atten) + (fmuon(2,t)/elambda(6))*(1-exp(-
elambda(6)*exposet)) + (nmuon(2,t)/elambda(4))*(1-exp(-
elambda(4)*exposet));
    e_tmp1 = max(e_expbe);
    e_tmp2 = max(e_expal);
```

```
    gle_tmp1 = e_tmp1;
    gle_tmp2 = e_tmp2;

    burbe = (Be10_spalprodrate/Be10_lambda)*(1-exp(-
Be10_lambda*burialt))*exp(-(depth_ice +
thickn(t))*r_density/neutron_atten) + (fmuon(3,t)/Be10_lambda)*(1-exp(-
Be10_lambda*burialt)) + (nmuon(3,t)/Be10_lambda)*(1-exp(-
Be10_lambda*burialt));
    bural = (Al26_spalprodrate/Al26_lambda)*(1-exp(-
Al26_lambda*burialt))*exp(-(depth_ice +
thickn(t))*r_density/neutron_atten) + (fmuon(4,t)/Al26_lambda)*(1-exp(-
Al26_lambda*burialt)) + (nmuon(4,t)/Al26_lambda)*(1-exp(-
Al26_lambda*burialt));
    e_burbe = (Be10_spalprodrate/gl_elambda(1))*(1-exp(-
gl_elambda(1)*burialt))*exp(-(depth_ice +
thickn(t))*r_density/neutron_atten) + (fmuon(3,t)/gl_elambda(5))*(1-
exp(-gl_elambda(5)*burialt)) + (nmuon(3,t)/gl_elambda(3))*(1-exp(-
gl_elambda(3)*burialt));
    e_bural = (Al26_spalprodrate/gl_elambda(2))*(1-exp(-
gl_elambda(2)*burialt))*exp(-(depth_ice +
thickn(t))*r_density/neutron_atten) + (fmuon(4,t)/gl_elambda(6))*(1-
exp(-gl_elambda(6)*burialt)) + (nmuon(4,t)/gl_elambda(4))*(1-exp(-
gl_elambda(4)*burialt)) ;

    colormat = [0.2 0.6 0.2];
    plot(log10(expbe), expal./expbe./norm,'Color',colormat,'linewidth',
0.5);
    plot(log10(e_expbe), e_expal./e_expbe./norm,'c-','linewidth', 0.5);
    plot(log10(e_expbe), e_expal./e_expbe./norm,'m-','linewidth', 0.5);


    texp_cmplx = nan(1,k_max+1);
    tbur_cmplx = nan(1,k_max);
    Rexpbe = nan(numel(thickn),k_max+1);
    Rexpal = nan(numel(thickn),k_max+1);
    Rburbe = nan(numel(thickn),k_max);
    Rbural = nan(numel(thickn),k_max);

    Rexpbe_e = nan(numel(thickn),k_max+1);
    Rexpal_e = nan(numel(thickn),k_max+1);
    Rburbe_e = nan(numel(thickn),k_max);
    Rbural_e = nan(numel(thickn),k_max);

    Rexpbe_gle = nan(numel(thickn),k_max+1);
    Rexpal_gle = nan(numel(thickn),k_max+1);
    Rburbe_gle = nan(numel(thickn),k_max);
    Rbural_gle = nan(numel(thickn),k_max);

    for k = 1:k_max
        Rexpbe(t,k) = tmp1;
        Rexpal(t,k) = tmp2;
        Rexpbe_e(t,k) = e_tmp1;
        Rexpal_e(t,k) = e_tmp2;
        Rexpbe_gle(t,k) = gle_tmp1;
```

```
        Rexpal_gle(t,k) = gle_tmp2;
        texp_cmplx(k) = exposet(end) + (k-1)*t_glac;

        %no erosion at all!
        tburbe =  tmp1.*decbebur + burbe;
        tmp3 = tburbe(end);
        tbural = tmp2.*decalbur + bural;
        tmp4 = tbural(end);
        treexpbe = tmp3.*decbeexp + expbe;
        tmp1 = treexpbe(end);
        treexpal = tmp4.*decalexp + expal;
        tmp2 = treexpal(end);

        %subaerial erosion during exp intervals
        e_tburbe =  e_tmp1.*decbebur + burbe;
        e_tmp3 = e_tburbe(end);
        e_tbural = e_tmp2.*decalbur + bural;
        e_tmp4 = e_tbural(end);
        e_treexpbe = e_tmp3.*sa_decbeexp + e_expbe;
        e_tmp1 = e_treexpbe(end);
        e_treexpal = e_tmp4.*sa_decalexp + e_expal;
        e_tmp2 = e_treexpal(end);

        %glacial erosion during bur intervals and subaerial erosion
during exp intervals
        gle_tburbe =  gle_tmp1.*gl_decbebur + e_burbe;
        gle_tmp3 = gle_tburbe(end);
        gle_tbural = gle_tmp2.*gl_decalbur + e_bural;
        gle_tmp4 = gle_tbural(end);
        gle_treexpbe = gle_tmp3.*sa_decbeexp + e_expbe;
        gle_tmp1 = gle_treexpbe(end);
        gle_treexpal = gle_tmp4.*sa_decalexp + e_expal;
        gle_tmp2 = gle_treexpal(end);

        Rburbe(t,k) = tmp3;
        Rbural(t,k) = tmp4;
        Rburbe_e(t,k) = e_tmp3;
        Rbural_e(t,k) = e_tmp4;
        Rburbe_gle(t,k) = gle_tmp3;
        Rbural_gle(t,k) = gle_tmp4;
        tbur_cmplx(k) = k*t_glac;

     plot(log10(tburbe),(tbural./tburbe)./norm,
'Color',colormat,'linewidth', 0.5);

plot(log10(treexpbe),(treexpal./treexpbe)./norm,'Color',colormat,'linew
idth', 0.5);
        plot(log10(e_tburbe),(e_tbural./e_tburbe)./norm, 'c-
','linewidth', 0.5);
        plot(log10(e_treexpbe),(e_treexpal./e_treexpbe)./norm,'c-
','linewidth', 0.5);
        plot(log10(gle_tburbe),(gle_tbural./gle_tburbe)./norm, 'm-
','linewidth', 0.5);
        plot(log10(gle_treexpbe),(gle_treexpal./gle_treexpbe)./norm,'m-
','linewidth', 0.5);
    end
```

```
    Rexpbe(t,k_max+1) = tmp1;
    Rexpal(t,k_max+1) = tmp2;
    Rexpbe_e(t,k_max+1) = e_tmp1;
    Rexpal_e(t,k_max+1) = e_tmp2;
    Rexpbe_gle(t,k_max+1) = gle_tmp1;
    Rexpal_gle(t,k_max+1) = gle_tmp2;
    texp_cmplx(k) = exposet(end) + (k-1)*t_glac;

    %%%plot lines through interglacial endpoints
    plot(log10(Rexpbe'), (Rexpal./Rexpbe)'./norm, 'Color',
colormat,'linewidth', 0.5)
    plot(log10(Rexpbe_e'), (Rexpal_e./Rexpbe_e)'./norm, 'c-
','linewidth', 0.5)
    plot(log10(Rexpbe_gle'), (Rexpal_gle./Rexpbe_gle)'./norm, 'm-
','linewidth', 0.5)

    %%%plot glacial/interglacial endpoints
    plot(log10(Rexpbe'), (Rexpal./Rexpbe)'./norm, 'k.')
    plot(log10(Rburbe'), (Rbural./Rburbe)'./norm, 'k.')
    plot(log10(Rexpbe_e'), (Rexpal_e./Rexpbe_e)'./norm, 'k.')
    plot(log10(Rexpbe_gle'), (Rexpal_gle./Rexpbe_gle)'./norm, 'k.')
    plot(log10(Rburbe_e'), (Rbural_e./Rburbe_e)'./norm, 'k.')
    plot(log10(Rburbe_gle'), (Rbural_gle./Rburbe_gle)'./norm, 'k.')
end

%%%-------------------------------------------------------------------------
%%%complex exposure trajectory including plucking
numb_plkev = numel(thickn)-1;
depth_index = numel(thickn);
plkev = [2 5];

%%%subaerial erosion during exp intervals
sa_decbeexp = exp(-dec_elambda(1,depth_index).*exposet);
sa_decalexp = exp(-dec_elambda(2,depth_index).*exposet);
%%%glacial erosion during bur intervals
gl_decbebur = exp(-dec_elambda(3,depth_index).*burialt);
gl_decalbur = exp(-dec_elambda(4,depth_index).*burialt);

expbe = (Be10_spalprodrate/Be10_lambda)*(1-exp(-
Be10_lambda*exposet))*exp(-(surf_depth +
thickn(depth_index))*r_density/neutron_atten) +
(fmuon(1,depth_index)/Be10_lambda)*(1-exp(-Be10_lambda*exposet)) +
(nmuon(1,depth_index)/Be10_lambda)*(1-exp(-Be10_lambda*exposet));
tmp1 = max(expbe);
expal = (Al26_spalprodrate/Al26_lambda)*(1-exp(-
Al26_lambda*exposet))*exp(-(surf_depth +
thickn(depth_index))*r_density/neutron_atten) +
(fmuon(2,depth_index)/Al26_lambda)*(1-exp(-Al26_lambda*exposet)) +
(nmuon(2,depth_index)/Al26_lambda)*(1-exp(-Al26_lambda*exposet));
tmp2 = max(expal);

e_expbe = (Be10_spalprodrate/elambda(1))*(1-exp(-
elambda(1)*exposet))*exp(-(surf_depth +
thickn(depth_index))*r_density/neutron_atten) +
```

```
(fmuon(1,depth_index)/elambda(5))*(1-exp(-elambda(5)*exposet)) +
(nmuon(1,depth_index)/elambda(3))*(1-exp(-elambda(3)*exposet));
e_expal = (Al26_spalprodrate/elambda(2))*(1-exp(-
elambda(2)*exposet))*exp(-(surf_depth +
thickn(depth_index))*r_density/neutron_atten) +
(fmuon(2,depth_index)/elambda(6))*(1-exp(-elambda(6)*exposet)) +
(nmuon(2,depth_index)/elambda(4))*(1-exp(-elambda(4)*exposet));
e_tmp1 = max(e_expbe);
e_tmp2 = max(e_expal);

gle_tmp1 = e_tmp1;
gle_tmp2 = e_tmp2;

burbe = (Be10_spalprodrate/Be10_lambda)*(1-exp(-
Be10_lambda*burialt))*exp(-(depth_ice +
thickn(depth_index))*r_density/neutron_atten) +
(fmuon(3,depth_index)/Be10_lambda)*(1-exp(-Be10_lambda*burialt)) +
(nmuon(3,depth_index)/Be10_lambda)*(1-exp(-Be10_lambda*burialt));
bural = (Al26_spalprodrate/Al26_lambda)*(1-exp(-
Al26_lambda*burialt))*exp(-(depth_ice +
thickn(depth_index))*r_density/neutron_atten) +
(fmuon(4,depth_index)/Al26_lambda)*(1-exp(-Al26_lambda*burialt)) +
(nmuon(4,depth_index)/Al26_lambda)*(1-exp(-Al26_lambda*burialt));

e_burbe = (Be10_spalprodrate/gl_elambda(1))*(1-exp(-
gl_elambda(1)*burialt))*exp(-(depth_ice +
thickn(depth_index))*r_density/neutron_atten) +
(fmuon(3,depth_index)/gl_elambda(5))*(1-exp(-gl_elambda(5)*burialt)) +
(nmuon(3,depth_index)/gl_elambda(3))*(1-exp(-gl_elambda(3)*burialt));
e_bural = (Al26_spalprodrate/gl_elambda(2))*(1-exp(-
gl_elambda(2)*burialt))*exp(-(depth_ice +
thickn(depth_index))*r_density/neutron_atten) +
(fmuon(4,depth_index)/gl_elambda(6))*(1-exp(-gl_elambda(6)*burialt)) +
(nmuon(4,depth_index)/gl_elambda(4))*(1-exp(-gl_elambda(4)*burialt));

colormat = [0.2 0.6 0.2];
plot(log10(expbe), expal./expbe./norm, 'Color',colormat,'linewidth',
0.5);
plot(log10(e_expbe), e_expal./e_expbe./norm, 'c-','linewidth', 0.5);
plot(log10(e_expbe), e_expal./e_expbe./norm, 'm-','linewidth', 0.5);

Rexpbe_plk = nan(1,k_max+1);
Rexpal_plk = nan(1,k_max+1);
Rburbe_plk = nan(1,k_max);
Rbural_plk = nan(1,k_max);

Rexpbe_plk_e = nan(1,k_max+1);
Rexpal_plk_e = nan(1,k_max+1);
Rburbe_plk_e = nan(1,k_max);
Rbural_plk_e = nan(1,k_max);

Rexpbe_plk_gle = nan(1,k_max+1);
Rexpal_plk_gle = nan(1,k_max+1);
Rburbe_plk_gle = nan(1,k_max);
Rbural_plk_gle = nan(1,k_max);
```

```
for k = 1:k_max
    Rexpbe_plk(k) = tmp1;
    Rexpal_plk(k) = tmp2;
    Rexpbe_plk_e(k) = e_tmp1;
    Rexpal_plk_e(k) = e_tmp2;
    Rexpbe_plk_gle(k) = gle_tmp1;
    Rexpal_plk_gle(k) = gle_tmp2;

    %no erosion at all!
    tburbe =  tmp1.*decbebur + burbe;
    tmp3 = tburbe(end);
    tbural = tmp2.*decalbur + bural;
    tmp4 = tbural(end);

    %subaerial erosion during exp intervals
    e_tburbe =  e_tmp1.*decbebur + burbe;
    e_tmp3 = e_tburbe(end);
    e_tbural = e_tmp2.*decalbur + bural;
    e_tmp4 = e_tbural(end);

    %glacial erosion during bur intervals and subaerial erosion during
exp intervals
    gle_tburbe =  gle_tmp1.*gl_decbebur + e_burbe;
    gle_tmp3 = gle_tburbe(end);
    gle_tbural = gle_tmp2.*gl_decalbur + e_bural;
    gle_tmp4 = gle_tbural(end);

    for i_plk = 1:numb_plkev
        if k == plkev(i_plk) %i_plk*0.05*k_max
            depth_index = depth_index - 1;
            %%%subaerial erosion during exp intervals
            sa_decbeexp = exp(-dec_elambda(1,depth_index).*exposet);
            sa_decalexp = exp(-dec_elambda(2,depth_index).*exposet);
            %%%glacial erosion during bur intervals
            gl_decbebur = exp(-dec_elambda(3,depth_index).*burialt);
            gl_decalbur = exp(-dec_elambda(4,depth_index).*burialt);

            expbe = (Be10_spalprodrate/Be10_lambda)*(1-exp(-
Be10_lambda*exposet))*exp(-(surf_depth +
thickn(depth_index))*r_density/neutron_atten) +
(fmuon(1,depth_index)/Be10_lambda)*(1-exp(-Be10_lambda*exposet)) +
(nmuon(1,depth_index)/Be10_lambda)*(1-exp(-Be10_lambda*exposet));
            expal = (Al26_spalprodrate/Al26_lambda)*(1-exp(-
Al26_lambda*exposet))*exp(-(surf_depth +
thickn(depth_index))*r_density/neutron_atten) +
(fmuon(2,depth_index)/Al26_lambda)*(1-exp(-Al26_lambda*exposet)) +
(nmuon(2,depth_index)/Al26_lambda)*(1-exp(-Al26_lambda*exposet));

            e_expbe = (Be10_spalprodrate/elambda(1))*(1-exp(-
elambda(1)*exposet))*exp(-(surf_depth +
thickn(depth_index))*r_density/neutron_atten) +
(fmuon(1,depth_index)/elambda(5))*(1-exp(-elambda(5)*exposet)) +
(nmuon(1,depth_index)/elambda(3))*(1-exp(-elambda(3)*exposet));
            e_expal = (Al26_spalprodrate/elambda(2))*(1-exp(-
elambda(2)*exposet))*exp(-(surf_depth +
```

```
thickn(depth_index))*r_density/neutron_atten) +
(fmuon(2,depth_index)/elambda(6))*(1-exp(-elambda(6)*exposet)) +
(nmuon(2,depth_index)/elambda(4))*(1-exp(-elambda(4)*exposet));

            burbe = (Be10_spalprodrate/Be10_lambda)*(1-exp(-
Be10_lambda*burialt))*exp(-(depth_ice +
thickn(depth_index))*r_density/neutron_atten) +
(fmuon(3,depth_index)/Be10_lambda)*(1-exp(-Be10_lambda*burialt)) +
(nmuon(3,depth_index)/Be10_lambda)*(1-exp(-Be10_lambda*burialt));
            bural = (Al26_spalprodrate/Al26_lambda)*(1-exp(-
Al26_lambda*burialt))*exp(-(depth_ice +
thickn(depth_index))*r_density/neutron_atten) +
(fmuon(4,depth_index)/Al26_lambda)*(1-exp(-Al26_lambda*burialt)) +
(nmuon(4,depth_index)/Al26_lambda)*(1-exp(-Al26_lambda*burialt));

            e_burbe = (Be10_spalprodrate/gl_elambda(1))*(1-exp(-
gl_elambda(1)*burialt))*exp(-(depth_ice +
thickn(depth_index))*r_density/neutron_atten) +
(fmuon(3,depth_index)/gl_elambda(5))*(1-exp(-gl_elambda(5)*burialt)) +
(nmuon(3,depth_index)/gl_elambda(3))*(1-exp(-gl_elambda(3)*burialt));
            e_bural = (Al26_spalprodrate/gl_elambda(2))*(1-exp(-
gl_elambda(2)*burialt))*exp(-(depth_ice +
thickn(depth_index))*r_density/neutron_atten) +
(fmuon(4,depth_index)/gl_elambda(6))*(1-exp(-gl_elambda(6)*burialt)) +
(nmuon(4,depth_index)/gl_elambda(4))*(1-exp(-gl_elambda(4)*burialt));

        end
    end

    %no erosion at all!
    treexpbe = tmp3.*decbeexp + expbe;
    tmp1 = treexpbe(end);
    treexpal = tmp4.*decalexp + expal;
    tmp2 = treexpal(end);

    %subaerial erosion during exp intervals
    e_treexpbe = e_tmp3.*sa_decbeexp + e_expbe;
    e_tmp1 = e_treexpbe(end);
    e_treexpal = e_tmp4.*sa_decalexp + e_expal;
    e_tmp2 = e_treexpal(end);

    %glacial erosion during bur intervals and subaerial erosion during
exp intervals
    gle_treexpbe = gle_tmp3.*sa_decbeexp + e_expbe;
    gle_tmp1 = gle_treexpbe(end);
    gle_treexpal = gle_tmp4.*sa_decalexp + e_expal;
    gle_tmp2 = gle_treexpal(end);

    Rburbe_plk(k) = tmp3;
    Rbural_plk(k) = tmp4;
    Rburbe_plk_e(k) = e_tmp3;
    Rbural_plk_e(k) = e_tmp4;
    Rburbe_plk_gle(k) = gle_tmp3;
    Rbural_plk_gle(k) = gle_tmp4;
```

```
    plot(log10(tburbe),(tbural./tburbe)./norm,
'Color',colormat,'linewidth', 0.5);
    plot(log10(treexpbe),(treexpal./treexpbe)./norm,
'Color',colormat,'linewidth', 0.5);
    plot(log10(e_tburbe),(e_tbural./e_tburbe)./norm, 'c-','linewidth',
0.5);
    plot(log10(e_treexpbe),(e_treexpal./e_treexpbe)./norm,'c-
','linewidth', 0.5);
    plot(log10(gle_tburbe),(gle_tbural./gle_tburbe)./norm, 'm-
','linewidth', 0.5);
    plot(log10(gle_treexpbe),(gle_treexpal./gle_treexpbe)./norm, 'm-
','linewidth', 0.5);
end

Rexpbe_plk(k_max+1) = tmp1;
Rexpal_plk(k_max+1) = tmp2;
Rexpbe_plk_e(k_max+1) = e_tmp1;
Rexpal_plk_e(k_max+1) = e_tmp2;
Rexpbe_plk_gle(k_max+1) = gle_tmp1;
Rexpal_plk_gle(k_max+1) = gle_tmp2;

plot(log10(Rexpbe_plk'),
(Rexpal_plk./Rexpbe_plk)'./norm,'Color',colormat, 'linewidth', 1)
plot(log10(Rexpbe_plk_e'), (Rexpal_plk_e./Rexpbe_plk_e)'./norm,'c-
','linewidth', 1)
plot(log10(Rexpbe_plk_gle'),
(Rexpal_plk_gle./Rexpbe_plk_gle)'./norm,'b-','linewidth', 1)

%-------------------------------------------------------------------------
%complex exposure trajectory including plucking of blocks (example)
numb_plkev = numel(thickn)-1;
depth_index = numel(thickn);
maxbur = 25;
plk_events = [12 18];

d18O = 3.8; %for LR04
exp_data = load('expdata_long.txt');
bur_data = load('burdata_long.txt');
cutoff = find(bur_data(1,:) == d18O);
exp_dur = exp_data(:,cutoff);
bur_dur = bur_data(2:end,cutoff);
exptimes = exp_dur(~isnan(exp_dur));
burtimes = bur_dur(~isnan(bur_dur));
exp_times = flipud(exptimes(1:maxbur+1))' * 1000;
bur_times = flipud(burtimes(1:maxbur))' * 1000;
exp_times(1,end) = 15 * 1000;

% exp_dur = nan(maxbur+1, 1);
% bur_dur = nan(maxbur, 1);
% for i_exp = 1:maxbur+1-9
%     exp_dur(i_exp) = frac * 41;
% end
% for i_exp = maxbur+1-8:maxbur+1
%     exp_dur(i_exp) = frac * 100;
% end
% for i_bur = 1:maxbur-9
```

```
%     bur_dur(i_bur) = (1 - frac) * 41;
% end
% for i_bur = maxbur-8:maxbur
%     bur_dur(i_bur) = (1 - frac) * 100;
% end
% exp_times = exp_dur' * 1000;
% bur_times = bur_dur' * 1000;
% exp_times(1,end) = 15 * 1000;

Rexpbe = nan(1,k_max+1);
Rexpal = nan(1,k_max+1);
Rburbe = nan(1,k_max);
Rbural = nan(1,k_max);
Rexpbe_e = nan(1,k_max+1);
Rexpal_e = nan(1,k_max+1);
Rburbe_e = nan(1,k_max);
Rbural_e = nan(1,k_max);
Rexpbe_gle = nan(1,k_max+1);
Rexpal_gle = nan(1,k_max+1);
Rburbe_gle = nan(1,k_max);
Rbural_gle = nan(1,k_max);

tmp3 = 0;
tmp4 = 0;
e_tmp3 = 0;
e_tmp4 = 0;
gle_tmp3 = 0;
gle_tmp4 = 0;

for k = 1:maxbur
    exposet = 0:exp_times(k);
    reexpbe = tmp3 .* exp(-Be10_lambda.*exposet) +
(Be10_spalprodrate/Be10_lambda)*(1-exp(-Be10_lambda*exposet))*exp(-
thickn(depth_index)*r_density/neutron_atten) +
(fmuon(1,depth_index)/Be10_lambda)*(1-exp(-Be10_lambda*exposet)) +
(nmuon(1,depth_index)/Be10_lambda)*(1-exp(-Be10_lambda*exposet));
    tmp1 = reexpbe(end);
    reexpal = tmp4 .* exp(-Al26_lambda.*exposet) +
(Al26_spalprodrate/Al26_lambda)*(1-exp(-Al26_lambda*exposet))*exp(-
thickn(depth_index)*r_density/neutron_atten) +
(fmuon(2,depth_index)/Al26_lambda)*(1-exp(-Al26_lambda*exposet)) +
(nmuon(2,depth_index)/Al26_lambda)*(1-exp(-Al26_lambda*exposet));
    tmp2 = reexpal(end);

    e_reexpbe = e_tmp3 .* exp(-dec_elambda(1,depth_index).*exposet) +
(Be10_spalprodrate/elambda(1))*(1-exp(-elambda(1).*exposet))*exp(-
thickn(depth_index)*r_density/neutron_atten) +
(fmuon(1,depth_index)/elambda(5))*(1-exp(-elambda(5).*exposet)) +
(nmuon(1,depth_index)/elambda(3))*(1-exp(-elambda(3).*exposet));
    e_reexpal = e_tmp4 .* exp(-dec_elambda(2,depth_index).*exposet) +
(Al26_spalprodrate/elambda(2))*(1-exp(-elambda(2).*exposet))*exp(-
thickn(depth_index)*r_density/neutron_atten) +
(fmuon(2,depth_index)/elambda(6))*(1-exp(-elambda(6).*exposet)) +
(nmuon(2,depth_index)/elambda(4))*(1-exp(-elambda(4).*exposet));
    e_tmp1 = e_reexpbe(end);
    e_tmp2 = e_reexpal(end);
```

```
    gle_reexpbe = gle_tmp3 .* exp(-dec_elambda(1,depth_index).*exposet)
+ (Be10_spalprodrate/elambda(1))*(1-exp(-elambda(1).*exposet))*exp(-
thickn(depth_index)*r_density/neutron_atten) +
(fmuon(1,depth_index)/elambda(5))*(1-exp(-elambda(5).*exposet)) +
(nmuon(1,depth_index)/elambda(3))*(1-exp(-elambda(3).*exposet));
    gle_reexpal = gle_tmp4 .* exp(-dec_elambda(2,depth_index).*exposet)
+ (Al26_spalprodrate/elambda(2))*(1-exp(-elambda(2).*exposet))*exp(-
thickn(depth_index)*r_density/neutron_atten) +
(fmuon(2,depth_index)/elambda(6))*(1-exp(-elambda(6).*exposet)) +
(nmuon(2,depth_index)/elambda(4))*(1-exp(-elambda(4).*exposet));
    gle_tmp1 = gle_reexpbe(end);
    gle_tmp2 = gle_reexpal(end);

    burialt = 0:bur_times(k);
    burbe =  tmp1.*exp(-Be10_lambda.*burialt) +
(Be10_spalprodrate/Be10_lambda)*(1-exp(-Be10_lambda*burialt))*exp(-
(thickn(depth_index)+depth_ice)*r_density/neutron_atten) +
(fmuon(3,depth_index)/Be10_lambda)*(1-exp(-Be10_lambda*burialt)) +
(nmuon(3,depth_index)/Be10_lambda)*(1-exp(-Be10_lambda*burialt));
    tmp3 = burbe(end);
    bural = tmp2.*exp(-Al26_lambda.*burialt) +
(Al26_spalprodrate/Al26_lambda)*(1-exp(-Al26_lambda*burialt))*exp(-
(thickn(depth_index)+depth_ice)*r_density/neutron_atten) +
(fmuon(4,depth_index)/Al26_lambda)*(1-exp(-Al26_lambda*burialt)) +
(nmuon(4,depth_index)/Al26_lambda)*(1-exp(-Al26_lambda*burialt));
    tmp4 = bural(end);

    e_burbe = e_tmp1.*exp(-Be10_lambda.*burialt) +
(Be10_spalprodrate/Be10_lambda)*(1-exp(-Be10_lambda*burialt))*exp(-
(thickn(depth_index)+depth_ice)*r_density/neutron_atten) +
(fmuon(3,depth_index)/Be10_lambda)*(1-exp(-Be10_lambda*burialt)) +
(nmuon(3,depth_index)/Be10_lambda)*(1-exp(-Be10_lambda*burialt));
    e_bural = e_tmp2.*exp(-Al26_lambda.*burialt) +
(Al26_spalprodrate/Al26_lambda)*(1-exp(-Al26_lambda*burialt))*exp(-
(thickn(depth_index)+depth_ice)*r_density/neutron_atten) +
(fmuon(4,depth_index)/Al26_lambda)*(1-exp(-Al26_lambda*burialt)) +
(nmuon(4,depth_index)/Al26_lambda)*(1-exp(-Al26_lambda*burialt));
    e_tmp3 = e_burbe(end);
    e_tmp4 = e_bural(end);

    gle_burbe = gle_tmp1.*exp(-dec_elambda(3,depth_index).*burialt) +
(Be10_spalprodrate/gl_elambda(1))*(1-exp(-gl_elambda(1)*burialt))*exp(-
(thickn(depth_index)+depth_ice)*r_density/neutron_atten) +
(fmuon(3,depth_index)/gl_elambda(5))*(1-exp(-gl_elambda(5)*burialt)) +
(nmuon(3,depth_index)/gl_elambda(3))*(1-exp(-gl_elambda(3)*burialt));
    gle_bural = gle_tmp2.*exp(-dec_elambda(4,depth_index).*burialt) +
(Al26_spalprodrate/gl_elambda(2))*(1-exp(-gl_elambda(2)*burialt))*exp(-
(thickn(depth_index)+depth_ice)*r_density/neutron_atten) +
(fmuon(4,depth_index)/gl_elambda(6))*(1-exp(-gl_elambda(6)*burialt)) +
(nmuon(4,depth_index)/gl_elambda(4))*(1-exp(-gl_elambda(4)*burialt));
    gle_tmp3 = gle_burbe(end);
    gle_tmp4 = gle_bural(end);

    for i_plk = 1:numb_plkev
        if k == plk_events(i_plk)
```

```
            depth_index = depth_index-1;
        end
    end

    Rexpbe(k) = tmp1;
    Rexpal(k) = tmp2;
    Rexpbe_e(k) = e_tmp1;
    Rexpal_e(k) = e_tmp2;
    Rexpbe_gle(k) = gle_tmp1;
    Rexpal_gle(k) = gle_tmp2;
    Rburbe(k) = tmp3;
    Rbural(k) = tmp4;
    Rburbe_e(k) = e_tmp3;
    Rbural_e(k) = e_tmp4;
    Rburbe_gle(k) = gle_tmp3;
    Rbural_gle(k) = gle_tmp4;

    colormat = [0.2 0.6 0.2];
plot(log10(reexpbe),(reexpal./reexpbe)./norm,'Color',colormat,'linewidt
h', 0.5);
    plot(log10(burbe),(bural./burbe)./norm,
'Color',colormat,'linewidth', 0.5);
    plot(log10(e_reexpbe),(e_reexpal./e_reexpbe)./norm,'c-
','linewidth', 0.5);
    plot(log10(e_burbe),(e_bural./e_burbe)./norm, 'c-','linewidth',
0.5);
    plot(log10(gle_reexpbe),(gle_reexpal./gle_reexpbe)./norm,'m-
','linewidth', 0.5);
    plot(log10(gle_burbe),(gle_bural./gle_burbe)./norm, 'm-
','linewidth', 0.5);
end

exposet = 0:exp_times(k+1);
reexpbe = tmp3 .* exp(-Be10_lambda.*exposet) +
(Be10_spalprodrate/Be10_lambda)*(1-exp(-Be10_lambda*exposet))*exp(-
thickn(depth_index)*r_density/neutron_atten) +
(fmuon(1,depth_index)/Be10_lambda)*(1-exp(-Be10_lambda*exposet)) +
(nmuon(1,depth_index)/Be10_lambda)*(1-exp(-Be10_lambda*exposet));
reexpal = tmp4 .* exp(-Al26_lambda.*exposet) +
(Al26_spalprodrate/Al26_lambda)*(1-exp(-Al26_lambda*exposet))*exp(-
thickn(depth_index)*r_density/neutron_atten) +
(fmuon(2,depth_index)/Al26_lambda)*(1-exp(-Al26_lambda*exposet)) +
(nmuon(2,depth_index)/Al26_lambda)*(1-exp(-Al26_lambda*exposet));

e_reexpbe = e_tmp3 .* exp(-dec_elambda(1,depth_index).*exposet) +
(Be10_spalprodrate/elambda(1))*(1-exp(-elambda(1)*exposet))*exp(-
thickn(depth_index)*r_density/neutron_atten) +
(fmuon(1,depth_index)/elambda(5))*(1-exp(-elambda(5)*exposet)) +
(nmuon(1,depth_index)/elambda(3))*(1-exp(-elambda(3)*exposet));
e_reexpal = e_tmp4 .* exp(-dec_elambda(2,depth_index).*exposet) +
(Al26_spalprodrate/elambda(2))*(1-exp(-elambda(2)*exposet))*exp(-
thickn(depth_index)*r_density/neutron_atten) +
(fmuon(2,depth_index)/elambda(6))*(1-exp(-elambda(6)*exposet)) +
(nmuon(2,depth_index)/elambda(4))*(1-exp(-elambda(4)*exposet));
```

```
gle_reexpbe = gle_tmp3 .* exp(-dec_elambda(1,depth_index).*exposet) +
(Be10_spalprodrate/elambda(1))*(1-exp(-elambda(1)*exposet))*exp(-
thickn(depth_index)*r_density/neutron_atten) +
(fmuon(1,depth_index)/elambda(5))*(1-exp(-elambda(5)*exposet)) +
(nmuon(1,depth_index)/elambda(3))*(1-exp(-elambda(3)*exposet));
gle_reexpal = gle_tmp4 .* exp(-dec_elambda(2,depth_index).*exposet) +
(Al26_spalprodrate/elambda(2))*(1-exp(-elambda(2)*exposet))*exp(-
thickn(depth_index)*r_density/neutron_atten) +
(fmuon(2,depth_index)/elambda(6))*(1-exp(-elambda(6)*exposet)) +
(nmuon(2,depth_index)/elambda(4))*(1-exp(-elambda(4)*exposet));

plot(log10(reexpbe),(reexpal./reexpbe)./norm,'Color',colormat,'linewidt
h', 0.5);
plot(log10(e_reexpbe),(e_reexpal./e_reexpbe)./norm,'c-','linewidth',
0.5);
plot(log10(gle_reexpbe),(gle_reexpal./gle_reexpbe)./norm,'m-
','linewidth', 0.5);

Rexpbe(k_max+1) = tmp1;
Rexpal(k_max+1) = tmp2;
Rexpbe_e(k_max+1) = e_tmp1;
Rexpal_e(k_max+1) = e_tmp2;
Rexpbe_gle(k_max+1) = gle_tmp1;
Rexpal_gle(k_max+1) = gle_tmp2;

plot(log10(Rexpbe'),
(Rexpal./Rexpbe)'./norm,'Color',colormat,'linewidth', 0.5)
plot(log10(Rexpbe_e'), (Rexpal_e./Rexpbe_e)'./norm,'c-','linewidth',
0.5)
plot(log10(Rexpbe_gle'), (Rexpal_gle./Rexpbe_gle)'./norm,'m-
','linewidth', 0.5)

%++++++++++++++++++++++++++++++++++++++++++++++++++++++++++++++++++++++++
%plot erosion banana if requested
if plotbanana  %nargin > 6
    for k = 1:numel(n3)
        plot(log10(eBe10_buildup(texp,n3(k))),
(eAl26_buildup(texp,n3(k))./eBe10_buildup(texp,n3(k)))./norm,'g');
    end

plot(log10(eBe10_buildup(10000000,eeros)),(eAl26_buildup(10000000,eeros
)./eBe10_buildup(10000000,eeros))./norm, 'g', 'linewidth', 2);
end

plot(log10(Be10_burial_surf(texp,0)),(Al26_burial_surf(texp,0)./Be10_bu
rial_surf(texp,0))./norm,'r-','linewidth',2);

end %end of function
```

A4.5 ESTIMATION OF ICE-FREE TIME AND TOTAL COMPLEX HISTORIES

```
function out = CP_exphist_values(tordata, samples, durglac, expdur,
averate, icethick, consts)
%example:> CP_exphist_values('CP_alltor.txt', 10, 1, 0.001:0.001:1, 1,
5000, consts)

%This function derives estimates of fraction of ice-free time (f) and
total complex history (ttot) from fiting a trajectory for a simple
periodic ice cover model. Scaling based on Lifton et al. (2014) using
individual production rates for fast and negative muons and their
respective attenuation lengths.

%INPUTS:
%tordata = name of ascii file with 12 columns of data (e.g.
'data.txt'):
%   column 1 is the decimal latitude of each sample;
%   column 2 is the decimal longitute of each sample;
%   column 3 is the elevation of each sample; (m)
%   column 4 is measured [10Be]; (atoms/g)
%   column 5 is the measured 1 sigma error in [10Be]; (atoms/g)
%   column 6 is the measured [26Al]; (atoms/g)
%   column 7 is the measured 1 sigma error in [26Al]; (atoms/g)

%samples = the row number of the sample you wish to model;

%durglac = average duration of one glacial cycle; (ka)

%expdur = range of values for average duration of ice-free intervals in
%percentage of the total glacial cycle (i.e. 0.185 for 18.5ka of 100ka
%glacial cycle)

%averate = best guess for average steady state erosion rate during
%interglacials; (m Ma-1) (m/Ma = mm/ka = 1e-1 cm/ka = 1e-4 cm/a)

%icethick = average ice thickness covering sample site during each
burial
%episode; (cm)

%consts = a matlab structure containing constants used in the LSD
scaling
%model. This structure is loaded in the startup.m file.

%A.Margreth - April 2014, LSD scaling scheme adapted from A.Hidy
%%%%%%%%%%%%%%%%%%%%%%%%%%%%%%%%%%%%%%%%%%%%%%%%%%%%%%%%%%%%%%%%%%%%%%%

%load data
burial_data = load(tordata);
lats = burial_data(:,1);
longs = burial_data(:,2);
elevs = burial_data(:,3);
Be_concs = burial_data(:,4);
Be_errs = burial_data(:,5);
```

```
Al_concs = burial_data(:,6);
Al_errs = burial_data(:,7);

sample = samples(1);

%densities used for buildup (g/cc)
r_density = 2.65;
ice_density = 0.9;

%recalculate ice thickness to rock-equivalent thickness for burial
events
depth_ice = icethick * ice_density / r_density;
t_glac = durglac * 1000; %convert to a
eros = averate / 10000; %convert to cm a-1

%decay constants (1/s)
Be10_lambda = log(2)/1378000;
%Chmeleff et al. (2010), Korschinek et al. (2010)
Al26_lambda = log(2)/720000; %Nishiizumi (2004)

%neutron attenuation length (g/cm^2)
neutron_atten = 150;
%Follows Balco et al. (2008); see Gosse and Phillips (2001)

%define new lambda terms to account for surface erosion
elambda = nan(1,6);
elambda(1) = Be10_lambda + eros*r_density/neutron_atten;
%spallogenic 10Be
elambda(2) = Al26_lambda + eros*r_density/neutron_atten;
%spallogenic 26Al
elambda(3) = Be10_lambda + eros*r_density/1500; %muogenic 10Be
elambda(4) = Al26_lambda + eros*r_density/1500; %muogenic 26Al
elambda(5) = Be10_lambda + eros*r_density/4320; %muogenic 10Be
elambda(6) = Al26_lambda + eros*r_density/4320; %muogenic 26Al

%reference spallogenic production (atoms/g/a)
refspalprod = 4.0; %New prod rate, Brocher et al. (subm.);
ratio_init = 6.75; %Nishiizumi et al. (1989); Balco et al. (2008);
6.1/1.106 to reflect recalibration of Nishiizumi et al. (2007)

%scaling production to site of interest (spallogenic and muogenic)
%Get LSD scaling factors
maxage = 100000; %age over which to integrate production rates
LSD10 = LSD(lats(sample),longs(sample),elevs(sample),1,maxage,-1,10);
LSD26 = LSD(lats(sample),longs(sample),elevs(sample),1,maxage,-1,26);
agegrid = 0:1:maxage;
%average cutoff rigidity (RC) and solar modulation (SPhi)over age range
meanRC = mean(interpolate(LSD10.tv,LSD10.Rc,agegrid));
meanSPhi = mean(interpolate(LSD10.tv,LSD10.SPhi,agegrid));

%average spallogenic surface production rate over age range
Be10_spalprodrate =
mean(refspalprod.*interpolate(LSD10.tv,LSD10.Be,agegrid));
Al26_spalprodrate =
mean(refspalprod.*ratio_init.*interpolate(LSD26.tv,LSD26.Al,agegrid));
```

```
%average total muogenic surface production rate over age range
[mBe_fexp, mBe_nexp] = CP_P_mu_totalLSD(0 *
r_density,LSD10.pressure,meanRC,meanSPhi,consts,10,'no');
[mAl_fexp, mAl_nexp] = CP_P_mu_totalLSD(0 *
r_density,LSD10.pressure,meanRC,meanSPhi,consts,26,'no');
[mBe_fbur, mBe_nbur] = CP_P_mu_totalLSD(depth_ice *
r_density,LSD10.pressure,meanRC,meanSPhi,consts,10,'no');
[mAl_fbur, mAl_nbur] = CP_P_mu_totalLSD(depth_ice *
r_density,LSD10.pressure,meanRC,meanSPhi,consts,26,'no');

%=========================================================================
%%% calculation of time-integrated production rate of complex exposure
%%% trajectory and comparison with trajectory including erosion
k_max = round(50*10^6/t_glac);
%max amount of glacial cycles till saturation (in a)

% P_expbe = nan(k_max+1,numel(expdur));
% P_expal = nan(k_max+1,numel(expdur));
% P_burbe = nan(k_max,numel(expdur));
% P_bural = nan(k_max,numel(expdur));
Pe_expbe = nan(k_max+1,numel(expdur));
Pe_expal = nan(k_max+1,numel(expdur));
Pe_burbe = nan(k_max,numel(expdur));
Pe_bural = nan(k_max,numel(expdur));
texp = nan(k_max+1,1);
tbur = nan(k_max,1);
% chi2_tot = nan(k_max,numel(expdur));
chi2_etot = nan(k_max,numel(expdur));
prob_values = nan(1,12); %Coloumns: median_frac, mode_frac, min1s_frac,
max1s_frac, min2s_frac, max2s_frac, median_ttot, mode_ttot, min1s_ttot
max1s_ttot, min2s_frac, max2s_ttot
% prob_values = nan(2,12); %rows: no erosion/erosion. Coloumns:
median_frac, mode_frac, min1s_frac, max1s_frac, min2s_frac, max2s_frac,
median_ttot, mode_ttot, min1s_ttot max1s_ttot, min2s_frac, max2s_ttot

for f = 1:numel(expdur)
    exposet = expdur(f)*t_glac;
    burialt = (1-expdur(f))*t_glac; %no erosion during burial intervals

    Be10_elamba = Be10_spalprodrate/(Be10_spalprodrate + mBe_fexp +
mBe_nexp)*elambda(1) + mBe_fexp/(Be10_spalprodrate + mBe_fexp +
mBe_nexp)*elambda(5) + mBe_nexp/(Be10_spalprodrate + mBe_fexp +
mBe_nexp)*elambda(3);
    Al26_elamba = Al26_spalprodrate/(Al26_spalprodrate + mAl_fexp +
mAl_nexp)*elambda(2) + mAl_fexp/(Al26_spalprodrate + mAl_fexp +
mAl_nexp)*elambda(6) + mAl_nexp/(Al26_spalprodrate + mAl_fexp +
mAl_nexp)*elambda(4);
    e_decbeexp = exp(-Be10_elamba.*exposet);
    e_decbebur = exp(-Be10_lambda.*burialt);
%could be used in case of subglacial constant eriosion rate
    e_decalexp = exp(-Al26_elamba.*exposet);
    e_decalbur = exp(-Al26_lambda.*burialt);
%could be used in case of subglacial constant eriosion rate
```

```
%     expbe = (Be10_spalprodrate/Be10_lambda)*(1-exp(-
Be10_lambda*exposet)) + (mBe_fexp/Be10_lambda)*(1-exp(-
Be10_lambda*exposet)) + (mBe_nexp/Be10_lambda)*(1-exp(-
Be10_lambda*exposet));
%     expal = (Al26_spalprodrate/Al26_lambda)*(1-exp(-
Al26_lambda*exposet)) + (mAl_fexp/Al26_lambda)*(1-exp(-
Al26_lambda*exposet)) + (mAl_nexp/Al26_lambda)*(1-exp(-
Al26_lambda*exposet));
    e_expbe = (Be10_spalprodrate/elambda(1))*(1-exp(-
elambda(1)*exposet)) + (mBe_fexp/elambda(5))*(1-exp(-
elambda(5)*exposet)) + (mBe_nexp/elambda(3))*(1-exp(-
elambda(3)*exposet));
    e_expal = (Al26_spalprodrate/elambda(2))*(1-exp(-
elambda(2)*exposet)) + (mAl_fexp/elambda(6))*(1-exp(-
elambda(6)*exposet)) + (mAl_nexp/elambda(4))*(1-exp(-
elambda(4)*exposet));

%     burbe = (Be10_spalprodrate/Be10_lambda)*(1-exp(-
Be10_lambda*burialt))*exp(-depth_ice*r_density/neutron_atten) +
(mBe_fbur/Be10_lambda)*(1-exp(-Be10_lambda*burialt)) +
(mBe_nbur/Be10_lambda)*(1-exp(-Be10_lambda*burialt));
%     bural = (Al26_spalprodrate/Al26_lambda)*(1-exp(-
Al26_lambda*burialt))*exp(-depth_ice*r_density/neutron_atten) +
(mAl_fbur/Al26_lambda)*(1-exp(-Al26_lambda*burialt)) +
(mAl_nbur/Al26_lambda)*(1-exp(-Al26_lambda*burialt));
    burbe = (Be10_spalprodrate/Be10_lambda)*(1-exp(-
Be10_lambda*burialt))*exp(-depth_ice*r_density/neutron_atten) +
(mBe_fbur/Be10_lambda)*(1-exp(-Be10_lambda*burialt)) +
(mBe_nbur/Be10_lambda)*(1-exp(-Be10_lambda*burialt));
    bural = (Al26_spalprodrate/Al26_lambda)*(1-exp(-
Al26_lambda*burialt))*exp(-depth_ice*r_density/neutron_atten) +
(mAl_fbur/Al26_lambda)*(1-exp(-Al26_lambda*burialt)) +
(mAl_nbur/Al26_lambda)*(1-exp(-Al26_lambda*burialt));

%     treexpbe = expbe;
%     treexpal = expal;
    e_treexpbe = e_expbe;
    e_treexpal = e_expal;

    for k = 1:k_max
%       P_expbe(k,f) = treexpbe;
%       P_expal(k,f) = treexpal;
        Pe_expbe(k,f) = e_treexpbe;
        Pe_expal(k,f) = e_treexpal;
        texp(k,1) = exposet + (k-1)*t_glac;
%       chi2_tot(k,f) = ((treexpbe - Be_concs(sample)) ./
Be_errs(sample))^2 + ((treexpal - Al_concs(sample)) ./
Al_errs(sample))^2;
        chi2_etot(k,f) = ((e_treexpbe - Be_concs(sample)) ./
Be_errs(sample))^2 + ((e_treexpal - Al_concs(sample)) ./
Al_errs(sample))^2;

%       tburbe = treexpbe.*decbebur + burbe;
%       tbural = treexpal.*decalbur + bural;
        e_tburbe = e_treexpbe.*e_decbebur + burbe;
        e_tbural = e_treexpal.*e_decalbur + bural;
```

```
%         treexpbe = tburbe.*decbeexp + expbe;
%         treexpal = tbural.*decalexp + expal;
        e_treexpbe = e_tburbe.*e_decbeexp + e_expbe;
        e_treexpal = e_tbural.*e_decalexp + e_expal;

%         P_burbe(k,f) = tburbe;
%         P_bural(k,f) = tbural;
        Pe_burbe(k,f) = e_tburbe;
        Pe_bural(k,f) = e_tbural;
        tbur(k,1) = k*t_glac;
    end

%     P_expbe(k_max+1,f) = treexpbe;
%     P_expal(k_max+1,f) = treexpal;
    Pe_expbe(k_max+1,f) = e_treexpbe;
    Pe_expal(k_max+1,f) = e_treexpal;
    texp(k_max+1,1) = exposet + (k_max)*t_glac;
%     chi2_tot(k_max+1,f) = ((treexpbe - Be_concs(sample)) ./
Be_errs(sample))^2 + ((treexpal - Al_concs(sample)) ./
Al_errs(sample))^2;
    chi2_etot(k_max+1,f) = ((e_treexpbe - Be_concs(sample)) ./
Be_errs(sample))^2 + ((e_treexpal - Al_concs(sample)) ./
Al_errs(sample))^2;
end

%%% save results_expdur.mat P_expbe P_expal P_burbe P_bural Pe_expbe
Pe_expal Pe_burbe Pe_bural texp tbur

%-------------------------------------------------------------------------
%%%chi2-statistics & continuous probability density function
%%%convert chi2 value (calculated for each expdur and texp) to
probability using likelihood function;
%%%for each possible value of expdur and texp find highest probability
value (one-dimensional vectors)
%%%normalize these probability values to generate probability density
funtion for expdur (=f) and texp (=ttot)

% prob = exp(-chi2_tot./2);
% frac_maxprob = max(prob);
%maximum value of probability for each expdur (coloums)
% pdf_frac = frac_maxprob./sum(frac_maxprob);
%norm probability for each expdur
% cdf_frac = cumsum(pdf_frac);
% [b_frac,i_frac] = unique(cdf_frac);
% ttot_maxprob = max(prob, [], 2);
%maximum value of probability for each texp (rows)
% pdf_ttot = ttot_maxprob./sum(ttot_maxprob);
%norm probability for each texp
% cdf_ttot = cumsum(pdf_ttot);
% [b_ttot,i_ttot] = unique(cdf_ttot);

e_prob = exp(-chi2_etot./2);
frac_emaxprob = max(e_prob);
%maximum value of probability for each expdur (coloums)
pdf_efrac = frac_emaxprob./sum(frac_emaxprob);
```

```
%norm probability for each expdur
cdf_efrac = cumsum(pdf_efrac);
[b_efrac,i_efrac] = unique(cdf_efrac);
ttot_emaxprob = max(e_prob, [], 2);
%maximum value of probability for each texp (rows)
pdf_ettot = ttot_emaxprob./sum(ttot_emaxprob);
%norm probability for each texp
cdf_ettot = cumsum(pdf_ettot);
[b_ettot,i_ettot] = unique(cdf_ettot);

%%%find mode and 1- & 2-sigma error ranges for each expdur (=f) and
texp (=ttot)
% best_frac = expdur(pdf_frac == max(pdf_frac));
%find value of expdur for max value of pdf
% med_frac = interp1(b_frac,expdur(i_frac),0.5);
% min_1s_frac = interp1(b_frac,expdur(i_frac),0.15865);
% max_1s_frac = interp1(b_frac,expdur(i_frac),0.84135);
% min_2s_frac = interp1(b_frac,expdur(i_frac),0.023);
% max_2s_frac = interp1(b_frac,expdur(i_frac),0.977);
% prob_values(1,1:6) = [med_frac*100, best_frac*100, min_1s_frac*100,
max_1s_frac*100, min_2s_frac*100, max_2s_frac*100]; %convert to %exp

% best_ttot = texp(pdf_ttot == max(pdf_ttot));
%find value of expdur for max value of pdf
% med_ttot = interp1(b_ttot,texp(i_ttot),0.5);
% min_1s_ttot = interp1(b_ttot,texp(i_ttot),0.15865);
% max_1s_ttot= interp1(b_ttot,texp(i_ttot),0.84135);
% min_2s_ttot = interp1(b_ttot,texp(i_ttot),0.023);
% max_2s_ttot = interp1(b_ttot,texp(i_ttot),0.977);
% prob_values(1,7:12) = [med_ttot./10^3, best_ttot./10^3,
min_1s_ttot./10^3, max_1s_ttot./10^3, min_2s_ttot./10^3,
max_2s_ttot./10^3];

best_efrac = expdur(pdf_efrac == max(pdf_efrac));
%find value of expdur for max value of pdf
med_efrac = interp1(b_efrac,expdur(i_efrac),0.5);
min_1s_efrac = interp1(b_efrac,expdur(i_efrac),0.15865);
max_1s_efrac = interp1(b_efrac,expdur(i_efrac),0.84135);
min_2s_efrac = interp1(b_efrac,expdur(i_efrac),0.023);
max_2s_efrac = interp1(b_efrac,expdur(i_efrac),0.977);
best_ettot = texp(pdf_ettot == max(pdf_ettot));
%find value of expdur for max value of pdf
med_ettot = interp1(b_ettot,texp(i_ettot),0.5);
min_1s_ettot = interp1(b_ettot,texp(i_ettot),0.15865);
max_1s_ettot= interp1(b_ettot,texp(i_ettot),0.84135);
min_2s_ettot = interp1(b_ettot,texp(i_ettot),0.023);
max_2s_ettot = interp1(b_ettot,texp(i_ettot),0.977);
prob_values(1,1:6) = [med_efrac*100, best_efrac*100, min_1s_efrac*100,
max_1s_efrac*100, min_2s_efrac*100, max_2s_efrac*100];
prob_values(1,7:12) =  [med_ettot./10^3, best_ettot(1)./10^3,
min_1s_ettot./10^3, max_1s_ettot./10^3, min_2s_ettot./10^3,
max_2s_ettot./10^3];
% prob_values(2,1:6) = [med_efrac*100, best_efrac*100,
min_1s_efrac*100, max_1s_efrac*100, min_2s_efrac*100,
max_2s_efrac*100];
```

```
% prob_values(2,7:12) =  [med_ettot./10^3, best_ettot(1)./10^3,
min_1s_ettot./10^3, max_1s_ettot./10^3, min_2s_ettot./10^3,
max_2s_ettot./10^3];

format long
out = prob_values;
save frac_ttot.mat prob_values
save pdf_frac_ttot.mat pdf_efrac pdf_ettot cdf_efrac cdf_ettot
%pdf_frac pdf_ttot

%%%plot probability density function with error margins
figure
subplot(2,1,1)
hold on
box on
axis([0 1.5*best_efrac+max_2s_efrac 0 1.2*max(pdf_efrac)])
% plot(expdur, pdf_frac, 'b-', 'linewidth', 1)
% line([min_1s_frac, min_1s_frac], [0 1], 'linestyle', '-.', 'color',
'k')
% line([max_1s_frac, max_1s_frac], [0 1], 'linestyle', '-.', 'color',
'k')
% line([min_2s_frac, min_2s_frac], [0 1], 'linestyle', '--', 'color',
'k')
% line([max_2s_frac, max_2s_frac], [0 1], 'linestyle', '--', 'color',
'k')
plot(expdur, pdf_efrac, 'g-', 'linewidth', 1)
line([min_1s_efrac, min_1s_efrac], [0 1], 'linestyle', '-.', 'color',
'r')
line([max_1s_efrac, max_1s_efrac], [0 1], 'linestyle', '-.', 'color',
'r')
line([min_2s_efrac, min_2s_efrac], [0 1], 'linestyle', '--', 'color',
'r')
line([max_2s_efrac, max_2s_efrac], [0 1], 'linestyle', '--', 'color',
'r')
xlabel('fraction exposure')
ylabel('normaliyed probability');
subplot(2,1,2)
hold on
box on
axis([ 0 (1.5*best_ettot+max_2s_ettot)./10^3  0 1.2*max(pdf_ettot)])
% plot(texp./10^3, pdf_ttot, 'b-', 'linewidth', 1)
% line([min_1s_ttot./10^3, min_1s_ttot./10^6], [0 1], 'linestyle', '-
.', 'color', 'k')
% line([max_1s_ttot./10^3, max_1s_ttot./10^6], [0 1], 'linestyle', '-
.', 'color', 'k')
% line([min_2s_ttot./10^3, min_2s_ttot./10^6], [0 1], 'linestyle', '--
', 'color', 'k')
% line([max_2s_ttot./10^3, max_2s_ttot./10^6], [0 1], 'linestyle', '--
', 'color', 'k')
plot(texp./10^3, pdf_ettot, 'g-', 'linewidth', 1)
line([min_1s_ettot./10^3 , min_1s_ettot./10^6 ], [0 1], 'linestyle', '-
.', 'color', 'r')
line([max_1s_ettot./10^3 , max_1s_ettot./10^6 ], [0 1], 'linestyle', '-
.', 'color', 'r')
line([min_2s_ettot./10^3 , min_2s_ettot./10^6 ], [0 1], 'linestyle', '-
-', 'color', 'r')
```

```
line([max_2s_ettot./10^3 , max_2s_ettot./10^6 ], [0 1], 'linestyle', '-
-', 'color', 'r')
xlabel('exposure duration (Ma)')
ylabel('normaliyed probability');

%%%plot concentration increase and ratio decrease over time for
best_frac
figure
subplot(1,2,1)
hold on
% plot(tbur, P_burbe(:,expdur==best_frac), 'g:', tbur,
P_bural(:,expdur==best_frac), 'm:')
% plot(texp, P_expbe(:,expdur==best_frac), 'g-', texp,
P_expal(:,expdur==best_frac), 'm-')
plot(tbur, Pe_burbe(:,expdur==best_efrac), 'y:', tbur,
Pe_bural(:,expdur==best_efrac), 'c:')
plot(texp, Pe_expbe(:,expdur==best_efrac), 'y-', texp,
Pe_expal(:,expdur==best_efrac), 'c-')
plot(texp, ones(size(texp))*Be_concs(sample), 'k-')
plot(texp, ones(size(texp))*(Be_concs(sample)-Be_errs(sample)), 'k:')
plot(texp, ones(size(texp))*(Be_concs(sample)+Be_errs(sample)), 'k:')
plot(texp, ones(size(texp))*Al_concs(sample), 'k-')
plot(texp, ones(size(texp))*(Al_concs(sample)-Al_errs(sample)), 'k:')
plot(texp, ones(size(texp))*(Al_concs(sample)+Al_errs(sample)), 'k:')
xlabel('time (years)');
ylabel('concentration (atmos)');
subplot(1,2,2)
hold on
% plot(tbur,
P_bural(:,expdur==best_frac)./P_burbe(:,expdur==best_frac), 'r:');
% plot(texp,
P_expal(:,expdur==best_frac)./P_expbe(:,expdur==best_frac), 'r-');
plot(tbur,
Pe_bural(:,expdur==best_efrac)./Pe_burbe(:,expdur==best_efrac), 'y:');
plot(texp,
Pe_expal(:,expdur==best_efrac)./Pe_expbe(:,expdur==best_efrac), 'y-');
plot(texp, ones(size(texp))*Al_concs(sample)/Be_concs(sample), 'k-')
plot(texp, ones(size(texp))*(Al_concs(sample)/Be_concs(sample)-
Al_concs(sample)/Be_concs(sample)*((Al_errs(sample)/Al_concs(sample))^2
+ (Be_errs(sample)/Be_concs(sample))^2)^0.5), 'k:');
plot(texp,
ones(size(texp))*(Al_concs(sample)/Be_concs(sample)+Al_concs(sample)/Be
_concs(sample)*((Al_errs(sample)/Al_concs(sample))^2 +
(Be_errs(sample)/Be_concs(sample))^2)^0.5), 'k:');
xlabel('time (years)');
ylabel('nuclide ratio');

end %end of function
```

A4.6 CALCULATION OF TIME SINCE PLUCKING FOR PAIRED SAMPLES

A4.6.1 Common Code for All Approaches

```
function out = CP_exphist_tplk(tordata, samples, durglac, avexpdur,
averate, icethick, consts)
%example:> CP_exphist_tplk('CP_alltor.txt', [10 11], 1, 0.27, 1, 5000,
consts)

%INPUTS:
%tordata = name of ascii file with 12 columns of data (e.g.
'data.txt'):
%   column 1 is the decimal latitude of each sample;
%   column 2 is the decimal longitute of each sample;
%   column 3 is the elevation of each sample; (m)
%   column 4 is measured [10Be]; (atoms/g)
%   column 5 is the measured 1 sigma error in [10Be]; (atoms/g)
%   column 6 is the measured [26Al]; (atoms/g)
%   column 7 is the measured 1 sigma error in [26Al]; (atoms/g)

%sample = the row number of the sample you wish to model;

%durglac = average duration of one glacial cycle; (ka)

%avexpdur = best value for average exposure at the specific site
determined with previous code

%averate = best guess for average steady state erosion rate during
interglacials; (m/Ma = mm/ka = 1e-1 cm/ka = 1e-4 cm/a)

%icethick = average ice thickness covering sample site during each
burial episode; (cm)

%consts = a matlab structure containing constants used in the LSD
scaling model. This structure is loaded in the startup.m file.

%A.Margreth - April 2014, LSD scaling scheme adapted from A.Hidy
%%%%%%%%%%%%%%%%%%%%%%%%%%%%%%%%%%%%%%%%%%%%%%%%%%%%%%%%%%%%%%%%%%%%%%%%%%%

%load data
burial_data = load(tordata);
lats = burial_data(:,1);
longs = burial_data(:,2);
elevs = burial_data(:,3);
Be_concs = burial_data(:,4);
Be_errs = burial_data(:,5);
Al_concs = burial_data(:,6);
Al_errs = burial_data(:,7);

sample = samples(1);

%densities used for buildup (g/cc)
r_density = 2.65;
ice_density = 0.9;
```

```
%recalculate ice thickness to rock-equivalent thickness for burial
events
depth_ice = icethick * ice_density / r_density;
t_glac = durglac * 1000; %convert to a
frac = avexpdur;
eros = averate / 10000; %convert to cm a-1

%decay constants (1/s)
Be10_lambda = log(2)/1378000;
%Chmeleff et al. (2010), Korschinek et al. (2010)
Al26_lambda = log(2)/720000; %Nishiizumi (2004)

%neutron attenuation length (g/cm^2)
neutron_atten = 150;
%Follows Balco et al. (2008); see Gosse and Phillips (2001)

%define new lambda terms to account for surface erosion
elambda = nan(1,6);
elambda(1) = Be10_lambda + eros*r_density/neutron_atten;
%spallogenic 10Be
elambda(2) = Al26_lambda + eros*r_density/neutron_atten;
%spallogenic 26Al
elambda(3) = Be10_lambda + eros*r_density/1500; %muogenic 10Be
elambda(4) = Al26_lambda + eros*r_density/1500; %muogenic 26Al
elambda(5) = Be10_lambda + eros*r_density/4320; %muogenic 10Be
elambda(6) = Al26_lambda + eros*r_density/4320; %muogenic 26Al

%reference spallogenic production (atoms/g/a)
refspalprod = 4.0;  %New prod rate, Brocher et al. (subm.);
ratio_init = 6.75; %Nishiizumi et al. (1989); Balco et al. (2008);
6.1/1.106 to reflect recalibration of Nishiizumi et al. (2007)

%scaling production to site of interest and at depth (spallogenic and
muogenic)
muon_depth = 0:5:400; %cm, max 10m
fmuon_prod = nan(4,numel(muon_depth));
nmuon_prod = nan(4,numel(muon_depth));
spall_prod = nan(4,numel(muon_depth));
dec_elambda = nan(2,numel(muon_depth));

%Get LSD scaling factors
maxage = 100000; %age over which to integrate production rates
LSD10 = LSD(lats(sample),longs(sample),elevs(sample),1,maxage,-1,10);
LSD26 = LSD(lats(sample),longs(sample),elevs(sample),1,maxage,-1,26);
agegrid = 0:1:maxage;
%average cutoff rigidity (RC) and solar modulation (SPhi)over age range
meanRC = mean(interpolate(LSD10.tv,LSD10.Rc,agegrid));
meanSPhi = mean(interpolate(LSD10.tv,LSD10.SPhi,agegrid));

%average spallogenic surface production rate over age range
Be10_spalprodrate =
mean(refspalprod.*interpolate(LSD10.tv,LSD10.Be,agegrid));
Al26_spalprodrate =
mean(refspalprod.*ratio_init.*interpolate(LSD26.tv,LSD26.Al,agegrid));
```

```
spall_prod(1,:) = Be10_spalprodrate .* exp(- muon_depth .* r_density ./
neutron_atten);
spall_prod(2,:) = Al26_spalprodrate .* exp(- muon_depth .* r_density ./
neutron_atten);
spall_prod(3,:) = Be10_spalprodrate .* exp(- (muon_depth + depth_ice)
.* r_density ./ neutron_atten);
spall_prod(4,:) = Al26_spalprodrate .* exp(- (muon_depth + depth_ice)
.* r_density ./ neutron_atten);

%average total muogenic surface production rate over age range
for i_muon = 1:numel(muon_depth)
    [fmuon_prod(1,i_muon), nmuon_prod(1,i_muon)] =
CP_P_mu_totalLSD(muon_depth(i_muon) *
r_density,LSD10.pressure,meanRC,meanSPhi,consts,10,'no');
    [fmuon_prod(2,i_muon), nmuon_prod(2,i_muon)] =
CP_P_mu_totalLSD(muon_depth(i_muon) *
r_density,LSD10.pressure,meanRC,meanSPhi,consts,26,'no');
    [fmuon_prod(3,i_muon), nmuon_prod(3,i_muon)] =
CP_P_mu_totalLSD((muon_depth(i_muon)+depth_ice) *
r_density,LSD10.pressure,meanRC,meanSPhi,consts,10,'no');
    [fmuon_prod(4,i_muon), nmuon_prod(4,i_muon)] =
CP_P_mu_totalLSD((muon_depth(i_muon)+depth_ice) *
r_density,LSD10.pressure,meanRC,meanSPhi,consts,26,'no');
end

tot_prod = nmuon_prod + fmuon_prod + spall_prod;
dec_elambda(1,:) = spall_prod(1,:)/tot_prod(1,:)*elambda(1) +
fmuon_prod(1,:)/tot_prod(1,:)*elambda(5) +
nmuon_prod(1,:)/tot_prod(1,:)*elambda(3);
dec_elambda(2,:) = spall_prod(2,:)/tot_prod(2,:)*elambda(2) +
fmuon_prod(2,:)/tot_prod(2,:)*elambda(6) +
nmuon_prod(2,:)/tot_prod(2,:)*elambda(4);

%%%-----------------------------------------------comment if not required
%%% use for calculation of concentration produced during last ice-free
%%% interval
no_ice = 15000; %ice free interval in a, or use durglac*100*1000
(conversion to ka in 100ka glacial cycles then to a)

%Get LSD scaling factors
maxage = no_ice; %age over which to integrate production rates
LSD10 = LSD(lats(sample),longs(sample),elevs(sample),1,maxage,-1,10);
LSD26 = LSD(lats(sample),longs(sample),elevs(sample),1,maxage,-1,26);
agegrid = 0:1:maxage;
%average cutoff rigidity (RC) and solar modulation (SPhi)over age range
meanRC = mean(interpolate(LSD10.tv,LSD10.Rc,agegrid));
meanSPhi = mean(interpolate(LSD10.tv,LSD10.SPhi,agegrid));

%average spallogenic surface production rate over age range
Be10_spprd_noice =
mean(refspalprod.*interpolate(LSD10.tv,LSD10.Be,agegrid));
Al26_spprd_noice =
mean(refspalprod.*ratio_init.*interpolate(LSD26.tv,LSD26.Al,agegrid));

%average total muogenic surface production rate over age range
```

```
[Be10_fmuprod_noice, Be10_nmuprod_noice] = CP_P_mu_totalLSD(0 *
r_density,LSD10.pressure,meanRC,meanSPhi,consts,10,'no');
[Al26_fmuprod_noice, Al26_nmuprod_noice] = CP_P_mu_totalLSD(0 *
r_density,LSD10.pressure,meanRC,meanSPhi,consts,26,'no');

Be10_elambda = Be10_spprd_noice/(Be10_spprd_noice + Be10_fmuprod_noice
+ Be10_nmuprod_noice)*elambda(1) + Be10_fmuprod_noice/(Be10_spprd_noice
+ Be10_fmuprod_noice + Be10_nmuprod_noice)*elambda(5) +
Be10_nmuprod_noice/(Be10_spprd_noice + Be10_fmuprod_noice +
Be10_nmuprod_noice)*elambda(3);
Al26_elambda = Al26_spprd_noice/(Al26_spprd_noice + Al26_fmuprod_noice
+ Al26_nmuprod_noice)*elambda(2) + Al26_fmuprod_noice/(Al26_spprd_noice
+ Al26_fmuprod_noice + Al26_nmuprod_noice)*elambda(6) +
Al26_nmuprod_noice/(Al26_spprd_noice + Al26_fmuprod_noice +
Al26_nmuprod_noice)*elambda(4);
e_Be_concs_noice = (Be10_spprd_noice/elambda(1))*(1-exp(-
elambda(1)*no_ice)) + (Be10_nmuprod_noice/elambda(3))*(1-exp(-
elambda(3)*no_ice)) + (Be10_fmuprod_noice/elambda(5))*(1-exp(-
elambda(5)*no_ice));
e_Al_concs_noice = (Al26_spprd_noice/elambda(2))*(1-exp(-
elambda(2)*no_ice)) + (Al26_nmuprod_noice/elambda(4))*(1-exp(-
elambda(4)*no_ice)) + (Al26_fmuprod_noice/elambda(6))*(1-exp(-
elambda(6)*no_ice));

for i_sample = 1:numel(samples)
    e_Be_inh(i_sample) = (Be_concs(samples(i_sample)) -
e_Be_concs_noice)/exp(-Be10_elambda*no_ice);
    e_Al_inh(i_sample) = (Al_concs(samples(i_sample)) -
e_Al_concs_noice)/exp(-Al26_elambda*no_ice);
    Be_concs(samples(i_sample)) = e_Be_inh(i_sample);
    Al_concs(samples(i_sample)) = e_Al_inh(i_sample);
end
%%%%-----------------------------------------------------------end comment

%++++++++++++++++++++++++++++++++++++++++++++++++++++++++++++++++++++++++
%Complex exposure trajectories for different depth below surface - use
%muonproduction terms from above
k_max = round(20*10^6/t_glac);
%max amount of glacial cycles till saturation (in a)

P_expbe_z = nan(k_max+1,numel(muon_depth));
P_expal_z = nan(k_max+1,numel(muon_depth));
P_burbe_z = nan(k_max,numel(muon_depth));
P_bural_z = nan(k_max,numel(muon_depth));
chi2_exp_wth = nan(k_max+1,numel(muon_depth));
chi2_bur_wth = nan(k_max,numel(muon_depth));
chi2_exp_frh = nan(k_max+1,numel(muon_depth));
chi2_bur_frh = nan(k_max,numel(muon_depth));
texp = nan(k_max+1,1);
tbur = nan(k_max,1);

exposet = frac*t_glac;
burialt = (1-frac)*t_glac;
decbebur = exp(-Be10_lambda.*burialt);
decalbur = exp(-Al26_lambda.*burialt);
```

```
for z = 1:numel(muon_depth)
    e_decbeexp = exp(-dec_elambda(1,z).*exposet);
    e_decalexp = exp(-dec_elambda(2,z).*exposet);

    expbe = (spall_prod(1,z)/elambda(1))*(1-exp(-elambda(1)*exposet)) +
(fmuon_prod(1,z)/elambda(5))*(1-exp(-elambda(5)*exposet)) +
(nmuon_prod(1,z)/elambda(3))*(1-exp(-elambda(3)*exposet));
    expal = (spall_prod(2,z)/elambda(2))*(1-exp(-elambda(2)*exposet)) +
(fmuon_prod(2,z)/elambda(6))*(1-exp(-elambda(6)*exposet)) +
(nmuon_prod(2,z)/elambda(4))*(1-exp(-elambda(4)*exposet));
    burbe = (spall_prod(3,z)/Be10_lambda)*(1-exp(-Be10_lambda*burialt))
+ (fmuon_prod(3,z)/Be10_lambda)*(1-exp(-Be10_lambda*burialt)) +
(nmuon_prod(3,z)/Be10_lambda)*(1-exp(-Be10_lambda*burialt));
    bural = (spall_prod(4,z)/Al26_lambda)*(1-exp(-Al26_lambda*burialt))
+ (fmuon_prod(4,z)/Al26_lambda)*(1-exp(-Al26_lambda*burialt)) +
(nmuon_prod(4,z)/Al26_lambda)*(1-exp(-Al26_lambda*burialt));

    treexpbe = expbe;
    treexpal = expal;

    for k = 1:k_max
        P_expbe_z(k,z) = treexpbe;
        P_expal_z(k,z) = treexpal;
        chi2_exp_wth(k,z) = ((treexpbe -
Be_concs(samples(1)))./Be_errs(samples(1)))^2 + ((treexpal -
Al_concs(samples(1)))./Al_errs(samples(1)))^2;
        chi2_exp_frh(k,z) = ((treexpbe -
Be_concs(samples(2)))./Be_errs(samples(2)))^2 + ((treexpal -
Al_concs(samples(2)))./Al_errs(samples(2)))^2;

        tburbe =  treexpbe.*decbebur + burbe;
        tbural = treexpal.*decalbur + bural;

        treexpbe = tburbe.*e_decbeexp + expbe;
        treexpal = tbural.*e_decalexp + expal;

        P_burbe_z(k,z) = tburbe;
        P_bural_z(k,z) = tbural;
        chi2_bur_wth(k,z) = ((treexpbe -
Be_concs(samples(1)))./Be_errs(samples(1)))^2 + ((treexpal -
Al_concs(samples(1)))./Al_errs(samples(1)))^2;
        chi2_bur_frh(k,z) = ((treexpbe -
Be_concs(samples(2)))./Be_errs(samples(2)))^2 + ((treexpal -
Al_concs(samples(2)))./Al_errs(samples(2)))^2;
        texp(k,1) = exposet + (k-1)*t_glac;
        tbur(k,1) = k*t_glac;
    end

    P_expbe_z(k_max+1,z) = treexpbe;
    P_expal_z(k_max+1,z) = treexpal;
    chi2_exp_wth(k_max+1,z) = ((treexpbe -
Be_concs(samples(1)))./Be_errs(samples(1)))^2 + ((treexpal -
Al_concs(samples(1)))./Al_errs(samples(1)))^2;
    chi2_exp_frh(k_max+1,z) = ((treexpbe -
Be_concs(samples(2)))./Be_errs(samples(2)))^2 + ((treexpal -
Al_concs(samples(2)))./Al_errs(samples(2)))^2;
```

```
    texp(k_max+1,1) = exposet + (k_max)*t_glac;
end

%re-define surface exposure accumulation terms
expbe_surf = (spall_prod(1,1)/elambda(1))*(1-exp(-elambda(1)*exposet))
+ (fmuon_prod(1,1)/elambda(5))*(1-exp(-elambda(5)*exposet)) +
(nmuon_prod(1,1)/elambda(3))*(1-exp(-elambda(3)*exposet));
expal_surf = (spall_prod(2,1)/elambda(2))*(1-exp(-elambda(2)*exposet))
+ (fmuon_prod(2,1)/elambda(6))*(1-exp(-elambda(6)*exposet)) +
(nmuon_prod(2,1)/elambda(4))*(1-exp(-elambda(4)*exposet));
burbe_surf = (spall_prod(3,1)/Be10_lambda)*(1-exp(-
Be10_lambda*burialt)) + (fmuon_prod(3,1)/Be10_lambda)*(1-exp(-
Be10_lambda*burialt)) + (fmuon_prod(3,1)/Be10_lambda)*(1-exp(-
Be10_lambda*burialt));
bural_surf = (spall_prod(4,1)/Al26_lambda)*(1-exp(-
Al26_lambda*burialt)) + (fmuon_prod(4,1)/Al26_lambda)*(1-exp(-
Al26_lambda*burialt)) + (fmuon_prod(4,1)/Al26_lambda)*(1-exp(-
Al26_lambda*burialt));

e_decbeexp = exp(-dec_elambda(1,1).*exposet);
e_decalexp = exp(-dec_elambda(2,1).*exposet);

%//////////////////////////////////////////////////////////////////////
%%% find best ttot for ratio
R_surf = P_expal_z(:,1)./P_expbe_z(:,1);
delta_R_surf_wth = abs(R_surf -
Al_concs(samples(1))./Be_concs(samples(1)));
ind_R_wth = find(delta_R_surf_wth == min(delta_R_surf_wth));
R_ttot_wth = texp(ind_R_wth);
delta_R_surf_frh = abs(R_surf-
Al_concs(samples(2))./Be_concs(samples(2)));
R_ttot_frh = texp(delta_R_surf_frh == min(delta_R_surf_frh));

prob_wth = (exp(-chi2_exp_wth./2));
[prob_ttot_wth, ind_ttot_wth] = max(prob_wth(:,1));
ttot_wth = texp(ind_ttot_wth);
prob_frh = (exp(-chi2_exp_frh./2));
[prob_ttot_frh, ind_ttot_frh] = max(prob_frh(:,1));
ttot_frh = texp(ind_ttot_frh);
out = [ttot_wth, R_ttot_wth, ttot_frh, R_ttot_frh];

R_prof_ttot_wth = P_bural_z(ind_R_wth,:)./P_burbe_z(ind_R_wth,:);
Al_prof_ttot_wth = P_bural_z(ind_R_wth,:);
Be_prof_ttot_wth = P_burbe_z(ind_R_wth,:);

Rprob_prof_ttot_wth =
P_bural_z(ind_ttot_wth,:)./P_burbe_z(ind_ttot_wth,:);
Alprob_prof_ttot_wth = P_bural_z(ind_ttot_wth,:);
Beprob_prof_ttot_wth = P_burbe_z(ind_ttot_wth,:);
```

A4.6.2 Specific Code for Approach 1

Concentration depth profiles (^{10}Be and ^{26}Al)

```
%*********************************************************************
%%% find time since plucking according Method 1a & b using only
concentrations separatly starting with concentration beneath weathered
surface as inhertance for fresher surface since plukcing
P_expbe_plk = nan(k_max+1,numel(muon_depth));
P_expal_plk = nan(k_max+1,numel(muon_depth));
P_burbe_plk = nan(k_max,numel(muon_depth));
P_bural_plk = nan(k_max,numel(muon_depth));
delta_Be_plk_frh = nan(k_max+1,numel(muon_depth));
delta_Al_plk_frh = nan(k_max+1,numel(muon_depth));
Be_tsp_frh = nan(1,numel(muon_depth));
Al_tsp_frh = nan(1,numel(muon_depth));

for z_plk = 1:numel(muon_depth) %for each possible plucking thickness
%     be_inh = Be_prof_ttot_wth(z_plk);
%     al_inh = Al_prof_ttot_wth(z_plk);
    be_inh = Beprob_prof_ttot_wth(z_plk);
    al_inh = Alprob_prof_ttot_wth(z_plk);

    treexpbe_plk = be_inh.*e_decbeexp + expbe_surf;
    treexpal_plk = al_inh.*e_decalexp + expal_surf;

    for k = 1:k_max
        P_expbe_plk(k,z_plk) = treexpbe_plk;
        P_expal_plk(k,z_plk) = treexpal_plk;

        tburbe_plk = treexpbe_plk.*decbebur + burbe_surf;
        tbural_plk = treexpal_plk.*decalbur + bural_surf;

        treexpbe_plk = tburbe_plk.*e_decbeexp + expbe_surf;
        treexpal_plk = tbural_plk.*e_decalexp + expal_surf;

        P_burbe_plk(k,z_plk) = tburbe_plk;
        P_bural_plk(k,z_plk) = tbural_plk;
     end

    P_expbe_plk(k_max+1,z_plk) = treexpbe_plk;
    P_expal_plk(k_max+1,z_plk) = treexpal_plk;

    delta_Be_plk_frh (:,z_plk) = abs(P_expbe_plk(:,z_plk) -
Be_concs(samples(2)));
    delta_Al_plk_frh (:,z_plk) = abs(P_expal_plk(:,z_plk) -
Al_concs(samples(2)));

    Be_tsp_frh(1,z_plk) = texp(delta_Be_plk_frh(:,z_plk) ==
min(delta_Be_plk_frh(:,z_plk)));
    Al_tsp_frh(1,z_plk) = texp(delta_Al_plk_frh(:,z_plk) ==
min(delta_Al_plk_frh(:,z_plk)));
End
```

```
%-------------------------------------------------------------------------
%%% second iteration
P_expbe_plk_1 = nan(k_max+1,numel(muon_depth));
P_expal_plk_1 = nan(k_max+1,numel(muon_depth));
P_burbe_plk_1 = nan(k_max,numel(muon_depth));
P_bural_plk_1 = nan(k_max,numel(muon_depth));

delta_Be_plk_frh_1 = nan(k_max+1,numel(muon_depth));
delta_Al_plk_frh_1 = nan(k_max+1,numel(muon_depth));
Be_tsp_frh_1 = nan(1,numel(muon_depth));
Al_tsp_frh_1 = nan(1,numel(muon_depth));

for z_plk = 1:numel(muon_depth) %for each possible plucking thickness
%     new_ttot_wth_plk_exact_Be = R_ttot_wth  - Be_tsp_frh(z_plk);
%     new_ttot_wth_plk_exact_Al = R_ttot_wth  - Al_tsp_frh(z_plk);
    new_ttot_wth_plk_exact_Be = ttot_wth  - Be_tsp_frh(z_plk);
    new_ttot_wth_plk_est_Be =
t_glac*round(new_ttot_wth_plk_exact_Be/t_glac) + frac*t_glac;

    new_ttot_wth_plk_exact_Al = ttot_wth  - Al_tsp_frh(z_plk);
    new_ttot_wth_plk_est_Al =
t_glac*round(new_ttot_wth_plk_exact_Al/t_glac) + frac*t_glac;

    Be_prof_ttot_wth_1 = P_expbe_z(texp == new_ttot_wth_plk_est_Be,:);
    Al_prof_ttot_wth_1 = P_expal_z(texp == new_ttot_wth_plk_est_Al,:);

    be_inh_1 = Be_prof_ttot_wth_1(z_plk);
    al_inh_1 = Al_prof_ttot_wth_1(z_plk);

    treexpbe_plk_1 = be_inh_1.*e_decbeexp  + expbe_surf;
    treexpal_plk_1 = al_inh_1.*e_decalexp  + expal_surf;

    for k = 1:k_max
        P_expbe_plk_1(k,z_plk) = treexpbe_plk_1;
        P_expal_plk_1(k,z_plk) = treexpal_plk_1;

        tburbe_plk_1 = treexpbe_plk_1.*decbebur + burbe_surf;
        tbural_plk_1 = treexpal_plk_1.*decalbur + bural_surf;

        treexpbe_plk_1 = tburbe_plk_1.*e_decbeexp + expbe_surf;
        treexpal_plk_1 = tbural_plk_1.*e_decalexp + expal_surf;

        P_burbe_plk_1(k,z_plk) = tburbe_plk_1;
        P_bural_plk_1(k,z_plk) = tbural_plk_1;

     end

    P_expbe_plk_1(k_max+1,z_plk) = treexpbe_plk_1;
    P_expal_plk_1(k_max+1,z_plk) = treexpal_plk_1;

    delta_Be_plk_frh_1 (:,z_plk) = abs(P_expbe_plk_1(:,z_plk) -
Be_concs(samples(2)));
    Be_tsp_frh_1(1,z_plk) = texp(delta_Be_plk_frh_1(:,z_plk) ==
min(delta_Be_plk_frh_1(:,z_plk)));
```

```
    delta_Al_plk_frh_1 (:,z_plk) = abs(P_expal_plk_1(:,z_plk) -
Al_concs(samples(2)));
    Al_tsp_frh_1(1,z_plk) = texp(delta_Al_plk_frh_1(:,z_plk) ==
min(delta_Al_plk_frh_1(:,z_plk)));
end

%-------------------------------------------------------------------------
%%% third iteration
P_expbe_plk_2 = nan(k_max+1,numel(muon_depth));
P_expal_plk_2 = nan(k_max+1,numel(muon_depth));
P_burbe_plk_2 = nan(k_max,numel(muon_depth));
P_bural_plk_2 = nan(k_max,numel(muon_depth));
delta_Be_plk_frh_2 = nan(k_max+1,numel(muon_depth));
delta_Al_plk_frh_2 = nan(k_max+1,numel(muon_depth));
Be_tsp_frh_2 = nan(1,numel(muon_depth));
Al_tsp_frh_2 = nan(1,numel(muon_depth));

for z_plk = 1:numel(muon_depth) %for each possible plucking thickness
%     new_ttot_wth_plk_exact_Be = R_ttot_wth  - Be_tsp_frh_1(z_plk);
%     new_ttot_wth_plk_exact_Al = R_ttot_wth  - Al_tsp_frh_1(z_plk);
    new_ttot_wth_plk_exact_Be = ttot_wth  - Be_tsp_frh_1(z_plk);
    new_ttot_wth_plk_est_Be =
t_glac*round(new_ttot_wth_plk_exact_Be/t_glac) + frac*t_glac;

    new_ttot_wth_plk_exact_Al = ttot_wth  - Al_tsp_frh_1(z_plk);
    new_ttot_wth_plk_est_Al =
t_glac*round(new_ttot_wth_plk_exact_Al/t_glac) + frac*t_glac;

    Be_prof_ttot_wth_2 = P_expbe_z(texp == new_ttot_wth_plk_est_Be,:);
    Al_prof_ttot_wth_2 = P_expal_z(texp == new_ttot_wth_plk_est_Al,:);

    be_inh_2 = Be_prof_ttot_wth_2(z_plk);
    al_inh_2 = Al_prof_ttot_wth_2(z_plk);

    treexpbe_plk_2 = be_inh_2.*e_decbeexp  + expbe_surf;
    treexpal_plk_2 = al_inh_2.*e_decalexp  + expal_surf;

    for k = 1:k_max
        P_expbe_plk_2(k,z_plk) = treexpbe_plk_2;
        P_expal_plk_2(k,z_plk) = treexpal_plk_2;

        tburbe_plk_2 = treexpbe_plk_2.*decbebur + burbe_surf;
        tbural_plk_2 = treexpal_plk_2.*decalbur + bural_surf;

        treexpbe_plk_2 = tburbe_plk_2.*e_decbeexp + expbe_surf;
        treexpal_plk_2 = tbural_plk_2.*e_decalexp + expal_surf;

        P_burbe_plk_2(k,z_plk) = tburbe_plk_2;
        P_bural_plk_2(k,z_plk) = tbural_plk_2;
     end

    P_expbe_plk_2(k_max+1,z_plk) = treexpbe_plk_2;
    P_expal_plk_2(k_max+1,z_plk) = treexpal_plk_2;
```

```
    delta_Be_plk_frh_2 (:,z_plk) = abs(P_expbe_plk_2(:,z_plk) -
Be_concs(samples(2)));
    Be_tsp_frh_2(1,z_plk) = texp(delta_Be_plk_frh_2(:,z_plk) ==
min(delta_Be_plk_frh_2(:,z_plk)));
    delta_Al_plk_frh_2 (:,z_plk) = abs(P_expal_plk_2(:,z_plk) -
Al_concs(samples(2)));
    Al_tsp_frh_2(1,z_plk) = texp(delta_Be_plk_frh_2(:,z_plk) ==
min(delta_Be_plk_frh_2(:,z_plk)));
end

%-------------------------------------------------------------------------
%%% fourth iteration
P_expbe_plk_3 = nan(k_max+1,numel(muon_depth));
P_expal_plk_3 = nan(k_max+1,numel(muon_depth));
P_burbe_plk_3 = nan(k_max,numel(muon_depth));
P_bural_plk_3 = nan(k_max,numel(muon_depth));
delta_Be_plk_frh_3 = nan(k_max+1,numel(muon_depth));
delta_Al_plk_frh_3 = nan(k_max+1,numel(muon_depth));
Be_tsp_frh_3 = nan(1,numel(muon_depth));
Al_tsp_frh_3 = nan(1,numel(muon_depth));

for z_plk = 1:numel(muon_depth) %for each possible plucking thickness
%     new_ttot_wth_plk_exact_Be = R_ttot_wth  - Be_tsp_frh_2(z_plk);
%     new_ttot_wth_plk_exact_Al = R_ttot_wth  - Al_tsp_frh_2(z_plk);
    new_ttot_wth_plk_exact_Be = ttot_wth  - Be_tsp_frh_2(z_plk);
    new_ttot_wth_plk_est_Be =
t_glac*round(new_ttot_wth_plk_exact_Be/t_glac) + frac*t_glac;

    new_ttot_wth_plk_exact_Al = ttot_wth  - Al_tsp_frh_2(z_plk);
    new_ttot_wth_plk_est_Al =
t_glac*round(new_ttot_wth_plk_exact_Al/t_glac) + frac*t_glac;

    Be_prof_ttot_wth_3 = P_expbe_z(texp == new_ttot_wth_plk_est_Be,:);
    Al_prof_ttot_wth_3 = P_expal_z(texp == new_ttot_wth_plk_est_Al,:);

    be_inh_3 = Be_prof_ttot_wth_3(z_plk);
    al_inh_3 = Al_prof_ttot_wth_3(z_plk);

    treexpbe_plk_3 = be_inh_3.*e_decbeexp  + expbe_surf;
    treexpal_plk_3 = al_inh_3.*e_decalexp  + expal_surf;

    for k = 1:k_max
        P_expbe_plk_3(k,z_plk) = treexpbe_plk_3;
        P_expal_plk_3(k,z_plk) = treexpal_plk_3;

        tburbe_plk_3 = treexpbe_plk_3.*decbebur + burbe_surf;
        tbural_plk_3 = treexpal_plk_3.*decalbur + bural_surf;

        treexpbe_plk_3 = tburbe_plk_3.*e_decbeexp + expbe_surf;
        treexpal_plk_3 = tbural_plk_3.*e_decalexp + expal_surf;

        P_burbe_plk_3(k,z_plk) = tburbe_plk_3;
        P_bural_plk_3(k,z_plk) = tbural_plk_3;
     end
```

```
    P_expbe_plk_3(k_max+1,z_plk) = treexpbe_plk_3;
    P_expal_plk_3(k_max+1,z_plk) = treexpal_plk_3;

    delta_Be_plk_frh_3 (:,z_plk) = abs(P_expbe_plk_3(:,z_plk) -
Be_concs(samples(2)));
    Be_tsp_frh_3(1,z_plk) = texp(delta_Be_plk_frh_3(:,z_plk) ==
min(delta_Be_plk_frh_3(:,z_plk)));
    delta_Al_plk_frh_3 (:,z_plk) = abs(P_expal_plk_3(:,z_plk) -
Al_concs(samples(2)));
    Al_tsp_frh_3(1,z_plk) = texp(delta_Al_plk_frh_3(:,z_plk) ==
min(delta_Al_plk_frh_3(:,z_plk)));
end

save tsp_Mth1_conc Be_tsp_frh Al_tsp_frh Be_tsp_frh_1 Al_tsp_frh_1
Be_tsp_frh_2 Al_tsp_frh_2 Be_tsp_frh_3 Al_tsp_frh_3

%%%display resutls of concentration depth profiles and time since
plucking for all iterations
figure
subplot(1,2,1)
hold on
figure
subplot(1,2,1)
hold on
plot(muon_depth, Be_prof_ttot_wth_3, 'g--', muon_depth,
Al_prof_ttot_wth_3, 'm--')
plot(muon_depth, Be_prof_ttot_wth_2, 'g-.', muon_depth,
Al_prof_ttot_wth_2, 'm-.')
plot(muon_depth, Be_prof_ttot_wth_1, 'g:', muon_depth,
Al_prof_ttot_wth_1, 'm:')
plot(muon_depth, Be_prof_ttot_wth, 'g-', muon_depth, Al_prof_ttot_wth,
'm-')
plot(muon_depth, Beprob_prof_ttot_wth, 'y:', muon_depth,
Al_prof_ttot_wth, 'y:')
plot(muon_depth, ones(size(muon_depth))*Al_concs(samples(1)),
'k:',muon_depth, ones(size(muon_depth))*Be_concs(samples(1)), 'k-')
plot(muon_depth, ones(size(muon_depth))*Al_concs(samples(2)), 'b:',
muon_depth, ones(size(muon_depth))*Be_concs(samples(2)),'b-')
xlabel('depth (cm)')
ylabel('Concentration')
subplot(1,2,2)
hold on
plot(muon_depth, Be_tsp_frh, 'g-', muon_depth, Al_tsp_frh, 'm-')
plot(muon_depth, Be_tsp_frh_1, 'g:', muon_depth, Al_tsp_frh_1, 'm:')
plot(muon_depth, Be_tsp_frh_2, 'g-.', muon_depth, Al_tsp_frh_2, 'm-.')
plot(muon_depth, Be_tsp_frh_3, 'g--', muon_depth, Al_tsp_frh_3, 'm--')
xlabel('depth (cm)');
ylabel('time since plucking (a)')
```

Ratio depth profile ($^{26}Al/^{10}Be$)

```
%*********************************************************************
%%% find tsp using Approach 1c starting with nuclide concentration at a
certin depth below the weathered surface, do the time integrated
complex exposure trajectory and find tsp for which R calc = R meas frh

P_expbe_plk = nan(k_max+1,numel(muon_depth));
P_expal_plk = nan(k_max+1,numel(muon_depth));
P_burbe_plk = nan(k_max,numel(muon_depth));
P_bural_plk = nan(k_max,numel(muon_depth));
R_tsp_frh = zeros(1,numel(muon_depth));

for z_plk = 1:numel(muon_depth) %for each plucking thickness
    t_sp_z = nan(1, 100);
    counter = 0;

%     be_inh = Be_prof_ttot_wth(z_plk);
%     al_inh = Al_prof_ttot_wth(z_plk);
    be_inh = Beprob_prof_ttot_wth(z_plk);
    al_inh = Alprob_prof_ttot_wth(z_plk);

    treexpbe_plk = be_inh.*decbeexp + expbe_surf;
    treexpal_plk = al_inh.*decalexp + expal_surf;

    for k = 1:k_max
        P_expbe_plk(k,z_plk) = treexpbe_plk;
        P_expal_plk(k,z_plk) = treexpal_plk;

        tburbe_plk = treexpbe_plk.*decbebur + burbe_surf;
        tbural_plk = treexpal_plk.*decalbur + bural_surf;

        treexpbe_plk = tburbe_plk.*decbeexp + expbe_surf;
        treexpal_plk = tbural_plk.*decalexp + expal_surf;

        P_burbe_plk(k,z_plk) = tburbe_plk;
        P_bural_plk(k,z_plk) = tbural_plk;

        if (treexpbe_plk >= (Be_concs(samples(2)) -
1*Be_errs(samples(2)))) && (treexpbe_plk <= (Be_concs(samples(2)) +
1*Be_errs(samples(2))))
            if (treexpal_plk >= (Al_concs(samples(2)) -
1*Al_errs(samples(2)))) && (treexpal_plk <= (Al_concs(samples(2)) +
1*Al_errs(samples(2))))
                counter = counter + 1;
                t_sp_z(1,counter) = texp(k);
            end
        end
     end

    P_expbe_plk(k_max+1,z_plk) = treexpbe_plk;
    P_expal_plk(k_max+1,z_plk) = treexpal_plk;
    R_tsp_frh(1,z_plk) = min(min(t_sp_z));
end
```

```
%-------------------------------------------------------------------------
bndr = 15;
%%% second iteration
P_expbe_plk_1 = nan(k_max+1,numel(muon_depth));
P_expal_plk_1 = nan(k_max+1,numel(muon_depth));
P_burbe_plk_1 = nan(k_max,numel(muon_depth));
P_bural_plk_1 = nan(k_max,numel(muon_depth));
R_tsp_frh_1 = zeros(1,numel(muon_depth));

for z_plk = bndr:numel(muon_depth) %for each plucking thickness
%     new_ttot_wth_plk_exact = R_ttot_wth  - R_tsp_frh(z_plk);
    new_ttot_wth_plk_exact = ttot_wth  - R_tsp_frh(z_plk);
    new_ttot_wth_plk_est = t_glac*round(new_ttot_wth_plk_exact/t_glac)
+ frac*t_glac;
    ind_R_ttot_wth_1 = find(texp == new_ttot_wth_plk_est);

    Be_prof_ttot_wth_1 = P_expbe_z(ind_R_ttot_wth_1,:);
    Al_prof_ttot_wth_1 = P_expal_z(ind_R_ttot_wth_1,:);
    be_inh_1 = Be_prof_ttot_wth_1(z_plk);
    al_inh_1 = Al_prof_ttot_wth_1(z_plk);

    t_sp_z = nan(1, 100);
    counter = 0;

    treexpbe_plk_1 = be_inh_1.*decbeexp  + expbe_surf;
    treexpal_plk_1 = al_inh_1.*decalexp  + expal_surf;

    for k = 1:k_max
        P_expbe_plk_1(k,z_plk) = treexpbe_plk_1;
        P_expal_plk_1(k,z_plk) = treexpal_plk_1;

        tburbe_plk_1 = treexpbe_plk_1.*decbebur + burbe_surf;
        tbural_plk_1 = treexpal_plk_1.*decalbur + bural_surf;

        treexpbe_plk_1 = tburbe_plk_1.*decbeexp + expbe_surf;
        treexpal_plk_1 = tbural_plk_1.*decalexp + expal_surf;

        P_burbe_plk_1(k,z_plk) = tburbe_plk_1;
        P_bural_plk_1(k,z_plk) = tbural_plk_1;

        if (treexpbe_plk_1 >= (Be_concs(samples(2)) -
1*Be_errs(samples(2)))) && (treexpbe_plk_1 <= (Be_concs(samples(2)) +
1*Be_errs(samples(2))))
            if (treexpal_plk_1 >= (Al_concs(samples(2)) -
1*Al_errs(samples(2)))) && (treexpal_plk_1 <= (Al_concs(samples(2)) +
1*Al_errs(samples(2))))
                counter = counter + 1;
                t_sp_z(1,counter) = texp(k);
            end
        end
     end

    P_expbe_plk_1(k_max+1,z_plk) = treexpbe_plk_1;
    P_expal_plk_1(k_max+1,z_plk) = treexpal_plk_1;
    R_tsp_frh_1(1,z_plk) = min(min(t_sp_z));
end
```

```
%-------------------------------------------------------------------------
%%% third iteration
P_expbe_plk_2 = nan(k_max+1,numel(muon_depth));
P_expal_plk_2 = nan(k_max+1,numel(muon_depth));
P_burbe_plk_2 = nan(k_max,numel(muon_depth));
P_bural_plk_2 = nan(k_max,numel(muon_depth));
R_tsp_frh_2 = zeros(1,numel(muon_depth));

for z_plk = bndr:numel(muon_depth) %for each plucking thickness
%       new_ttot_wth_plk_exact = R_ttot_wth  - R_tsp_frh_1(z_plk);
    new_ttot_wth_plk_exact = ttot_wth  - R_tsp_frh_1(z_plk);
    new_ttot_wth_plk_est = t_glac*round(new_ttot_wth_plk_exact/t_glac)
+ frac*t_glac;
    ind_R_ttot_wth_2 = find(texp == new_ttot_wth_plk_est);

    Be_prof_ttot_wth_2 = P_expbe_z(ind_R_ttot_wth_2,:);
    Al_prof_ttot_wth_2 = P_expal_z(ind_R_ttot_wth_2,:);

    be_inh_2 = Be_prof_ttot_wth_2(z_plk);
    al_inh_2 = Al_prof_ttot_wth_2(z_plk);

    t_sp_z = nan(1, 100);
    counter = 0;

    treexpbe_plk_2 = be_inh_2.*decbeexp  + expbe_surf;
    treexpal_plk_2 = al_inh_2.*decalexp  + expal_surf;

    for k = 1:k_max
        P_expbe_plk_2(k,z_plk) = treexpbe_plk_2;
        P_expal_plk_2(k,z_plk) = treexpal_plk_2;

        tburbe_plk_2 = treexpbe_plk_2.*decbebur + burbe_surf;
        tbural_plk_2 = treexpal_plk_2.*decalbur + bural_surf;

        treexpbe_plk_2 = tburbe_plk_2.*decbeexp + expbe_surf;
        treexpal_plk_2 = tbural_plk_2.*decalexp + expal_surf;

        P_burbe_plk_2(k,z_plk) = tburbe_plk_2;
        P_bural_plk_2(k,z_plk) = tbural_plk_2;

        if (treexpbe_plk_2 >= (Be_concs(samples(2)) -
1*Be_errs(samples(2)))) && (treexpbe_plk_2 <= (Be_concs(samples(2)) +
1*Be_errs(samples(2))))
            if (treexpal_plk_2 >= (Al_concs(samples(2)) -
1*Al_errs(samples(2)))) && (treexpal_plk_2 <= (Al_concs(samples(2)) +
1*Al_errs(samples(2))))
                counter = counter + 1;
                t_sp_z(1,counter) = texp(k);
            end
        end
     end

    P_expbe_plk_2(k_max+1,z_plk) = treexpbe_plk_2;
    P_expal_plk_2(k_max+1,z_plk) = treexpal_plk_2;
    R_tsp_frh_2(1,z_plk) = min(min(t_sp_z));
end
```

```
%-------------------------------------------------------------------------
%%% fourth iteration
P_expbe_plk_3 = nan(k_max+1,numel(muon_depth));
P_expal_plk_3 = nan(k_max+1,numel(muon_depth));
P_burbe_plk_3 = nan(k_max,numel(muon_depth));
P_bural_plk_3 = nan(k_max,numel(muon_depth));
R_tsp_frh_3 = zeros(1,numel(muon_depth));

for z_plk = bndr:numel(muon_depth) %for each plucking thickness
%     new_ttot_wth_plk_exact = R_ttot_wth  - R_tsp_frh_2(z_plk);
    new_ttot_wth_plk_exact = ttot_wth  - R_tsp_frh_2(z_plk);
    new_ttot_wth_plk_est = t_glac*round(new_ttot_wth_plk_exact/t_glac)
+ frac*t_glac;
    ind_R_ttot_wth_3 = find(texp == new_ttot_wth_plk_est);

    Be_prof_ttot_wth_3 = P_expbe_z(ind_R_ttot_wth_3,:);
    Al_prof_ttot_wth_3 = P_expal_z(ind_R_ttot_wth_3,:);

    be_inh_3 = Be_prof_ttot_wth_3(z_plk);
    al_inh_3 = Al_prof_ttot_wth_3(z_plk);

    t_sp_z = nan(1, 100);
    counter = 0;

    treexpbe_plk_3 = be_inh_3.*decbeexp  + expbe_surf;
    treexpal_plk_3 = al_inh_3.*decalexp  + expal_surf;

    for k = 1:k_max
        P_expbe_plk_3(k,z_plk) = treexpbe_plk_3;
        P_expal_plk_3(k,z_plk) = treexpal_plk_3;

        tburbe_plk_3 = treexpbe_plk_3.*decbebur + burbe_surf;
        tbural_plk_3 = treexpal_plk_3.*decalbur + bural_surf;

        treexpbe_plk_3 = tburbe_plk_3.*decbeexp + expbe_surf;
        treexpal_plk_3 = tbural_plk_3.*decalexp + expal_surf;

        P_burbe_plk_3(k,z_plk) = tburbe_plk_3;
        P_bural_plk_3(k,z_plk) = tbural_plk_3;

        if (treexpbe_plk_3 >= (Be_concs(samples(2)) -
1*Be_errs(samples(2)))) && (treexpbe_plk_3 <= (Be_concs(samples(2)) +
1*Be_errs(samples(2))))
            if (treexpal_plk_3 >= (Al_concs(samples(2)) -
1*Al_errs(samples(2)))) && (treexpal_plk_3 <= (Al_concs(samples(2)) +
1*Al_errs(samples(2))))
                counter = counter + 1;
                t_sp_z(1,counter) = texp(k);
            end
        end
     end

    P_expbe_plk_3(k_max+1,z_plk) = treexpbe_plk_3;
    P_expal_plk_3(k_max+1,z_plk) = treexpal_plk_3;
    R_tsp_frh_3(1,z_plk) = min(min(t_sp_z));
end
```

```
save tsp_Mth1_R R_tsp_frh R_tsp_frh_1 R_tsp_frh_2 R_tsp_frh_3

figure
subplot(1,3,1)
hold on
plot(muon_depth, Be_prof_ttot_wth_3, 'b-', muon_depth,
Be_prof_ttot_wth_2, 'g-')
plot(muon_depth, Be_prof_ttot_wth_1, 'y-', muon_depth,
Be_prof_ttot_wth, 'm-')
plot(muon_depth, ones(size(muon_depth))*Be_concs(samples(1)), 'k-')
plot(muon_depth, ones(size(muon_depth))*(Be_concs(samples(1))-
Be_errs(samples(1))), 'k:')
plot(muon_depth,
ones(size(muon_depth))*(Be_concs(samples(1))+Be_errs(samples(1))),
'k:')
plot(muon_depth, ones(size(muon_depth))*Be_concs(samples(2)), 'b-')
plot(muon_depth, ones(size(muon_depth))*(Be_concs(samples(2))-
Be_errs(samples(2))), 'b:')
plot(muon_depth,
ones(size(muon_depth))*(Be_concs(samples(2))+Be_errs(samples(2))),
'b:')
xlabel('depth (cm)')
ylabel('Be concentration')
subplot(1,3,2)
hold on
plot(muon_depth, Al_prof_ttot_wth_3, 'b-', muon_depth,
Al_prof_ttot_wth_2, 'g-')
plot(muon_depth, Al_prof_ttot_wth_1, 'y-', muon_depth,
Al_prof_ttot_wth, 'm-')
plot(muon_depth, ones(size(muon_depth))*Al_concs(samples(1)), 'k-')
plot(muon_depth, ones(size(muon_depth))*(Al_concs(samples(1))-
Al_errs(samples(1))), 'k:')
plot(muon_depth,
ones(size(muon_depth))*(Al_concs(samples(1))+Al_errs(samples(1))),
'k:')
plot(muon_depth, ones(size(muon_depth))*Al_concs(samples(2)), 'b-')
plot(muon_depth, ones(size(muon_depth))*(Al_concs(samples(2))-
Al_errs(samples(2))), 'b:')
plot(muon_depth,
ones(size(muon_depth))*(Al_concs(samples(2))+Al_errs(samples(2))),
'b:')
xlabel('depth (cm)')
ylabel('Al concentration')
subplot(1,3,3)
hold on
plot(muon_depth, R_tsp_frh, 'm-')
plot(muon_depth, R_tsp_frh_1, 'y-')
plot(muon_depth, R_tsp_frh_2, 'g-')
plot(muon_depth, R_tsp_frh_3, 'b-')
xlabel('depth (cm)');
ylabel('time since plucking (a)')
```

A4.6.3 Specific Code for Approach 2

```
%*********************************************************************
%%% find time since plucking using equation
new_Be10_lambda = (1-frac)*Be10_lambda + frac*dec_elambda(1,1);
new_Al26_lambda = (1-frac)*Al26_lambda + frac*dec_elambda(2,1);

tsp_eq = 1/(new_Al26_lambda - new_Be10_lambda) *
log(Rprob_prof_ttot_wth*(Be_concs(samples(1))-
Be_concs(samples(2)))/(Al_concs(samples(1))-Al_concs(samples(2))));

%  new_ttot_wth_exact = R_ttot_wth  - tsp_z_eq1(1);
 new_ttot_wth_exact = ttot_wth  - tsp_eq(1);
 new_ttot_wth_est = t_glac*round(new_ttot_wth_exact/t_glac) +
frac*t_glac;
 ind_R_wth_1 = find(texp == new_ttot_wth_est);
 R_prof_ttot_wth_1 =
P_expal_z(ind_R_wth_1,:)./P_expbe_z(ind_R_wth_1,:);
 tsp_eq_1 = 1/(new_Al26_lambda - new_Be10_lambda) * log(
R_prof_ttot_wth_1 *(Be_concs(samples(1))-
Be_concs(samples(2)))/(Al_concs(samples(1))-Al_concs(samples(2))));

%  new_ttot_wth_exact_1 = R_ttot_wth  - tsp_z_eq1_1(1);
 new_ttot_wth_exact_1 = ttot_wth  - tsp_eq_1(1);
 new_ttot_wth_est_1 = t_glac*round(new_ttot_wth_exact_1/t_glac) +
frac*t_glac;
 ind_R_wth_2 = find(texp == new_ttot_wth_est_1);
 R_prof_ttot_wth_2 =
P_expal_z(ind_R_wth_2,:)./P_expbe_z(ind_R_wth_2,:);
 tsp_eq_2 = 1/(new_Al26_lambda - new_Be10_lambda) * log(
R_prof_ttot_wth_2 *(Be_concs(samples(1))-
Be_concs(samples(2)))/(Al_concs(samples(1))-Al_concs(samples(2))));

%  new_ttot_wth_exact_2 = R_ttot_wth  - tsp_z_eq1_2(1);
 new_ttot_wth_exact_2 = ttot_wth  - tsp_eq_2(1);
 new_ttot_wth_est_2 = t_glac*round(new_ttot_wth_exact_2/t_glac) +
frac*t_glac;
 ind_R_wth_3 = find(texp == new_ttot_wth_est_2);
 R_prof_ttot_wth_3 =
P_expal_z(ind_R_wth_3,:)./P_expbe_z(ind_R_wth_3,:);
 tsp_eq_3 = 1/(new_Al26_lambda - new_Be10_lambda) * log(
R_prof_ttot_wth_3 *(Be_concs(samples(1))-
Be_concs(samples(2)))/(Al_concs(samples(1))-Al_concs(samples(2))));

 save tsp_eq tsp_eq tsp_eq_1 tsp_eq_2 tsp_eq_3

figure
subplot(2,1,1)
hold on
plot(muon_depth, R_prof_ttot_wth', 'm-')
plot(muon_depth, R_prof_ttot_wth_1', 'y-')
plot(muon_depth, R_prof_ttot_wth_2', 'g-', 'linewidth', 2)
plot(muon_depth, R_prof_ttot_wth_3', 'b-')
```

```
plot(muon_depth,
ones(size(muon_depth))*Al_concs(samples(1))/Be_concs(samples(1)), 'k-
');
plot(muon_depth,
ones(size(muon_depth))*(Al_concs(samples(1))/Be_concs(samples(1))-
((Al_errs(samples(1))/Al_concs(samples(1)))^2 +
(Be_errs(samples(1))/Be_concs(samples(1)))^2)^0.5), 'k:')
plot(muon_depth,
ones(size(muon_depth))*(Al_concs(samples(1))/Be_concs(samples(1))+((Al_
errs(samples(1))/Al_concs(samples(1)))^2 +
(Be_errs(samples(1))/Be_concs(samples(1)))^2)^0.5), 'k:')
plot(muon_depth,
ones(size(muon_prod(1,:)))*Al_concs(samples(2))/Be_concs(samples(2)),'b
-');
plot(muon_depth,
ones(size(muon_depth))*(Al_concs(samples(2))/Be_concs(samples(2))-
((Al_errs(samples(2))/Al_concs(samples(2)))^2 +
(Be_errs(samples(2))/Be_concs(samples(2)))^2)^0.5), 'b:')
plot(muon_depth,
ones(size(muon_depth))*(Al_concs(samples(2))/Be_concs(samples(2))+((Al_
errs(samples(2))/Al_concs(samples(2)))^2 +
(Be_errs(samples(2))/Be_concs(samples(2)))^2)^0.5), 'b:')
xlabel('depth (cm)')
ylabel('Ratio')
legend('1st', '2nd', '3rd', '4th')
subplot(2,1,2)
hold on
plot(muon_depth, tsp_eq, 'm-')
plot(muon_depth, tsp_eq_1, 'y-')
plot(muon_depth, tsp_eq_2, 'g-', 'linewidth', 2)
plot(muon_depth, tsp_eq_3, 'b-')
xlabel('depth (cm)')
ylabel('Time since plucking (a)')
legend('1st', '2nd', '3rd', '4th')
```

A4.6.4 Specific Code for Approach 3

```
%*********************************************************************
%%% find min time since plucking for any depth below surface
%%% define range of texp for starting points of reexposure after
plucking
ind_inh = 1:10:k_max/10; %maybe need to refine this interval 1:k_max

pdf_inh = nan(numel(muon_depth),numel(ind_inh));
tsp_prob = nan(numel(muon_depth), 3);
t_sp = nan(numel(muon_depth), 2);

for z = 1:numel(muon_depth)
    P_reexpbe = nan(k_max+1,numel(ind_inh));
    P_reexpal = nan(k_max+1,numel(ind_inh));
    P_reburbe = nan(k_max,numel(ind_inh));
    P_rebural = nan(k_max,numel(ind_inh));
    t_sp_z = nan(numel(ind_inh),1000);
    chi2_plk = nan(k_max+1, numel(ind_inh));
```

```
    for i_inh = 1:numel(ind_inh)
        counter = 0;
        e_counter = 0;
        P_reexpbe(1:ind_inh(i_inh), i_inh) =
P_expbe_z(1:ind_inh(i_inh), z);
        P_reexpal(1:ind_inh(i_inh), i_inh) =
P_expal_z(1:ind_inh(i_inh), z);
        P_reburbe(1:ind_inh(i_inh), i_inh) =
P_burbe_z(1:ind_inh(i_inh), z);
        P_rebural(1:ind_inh(i_inh), i_inh) =
P_bural_z(1:ind_inh(i_inh), z);

        be_inh = P_burbe_z(ind_inh(i_inh),z);
        al_inh = P_bural_z(ind_inh(i_inh),z);

        treexpbe = be_inh.*decbeexp + expbe;
        treexpal = al_inh.*decalexp + expal;

        for k = ind_inh(i_inh)+1:k_max
            P_reexpbe(k,i_inh) = treexpbe;
            P_reexpal(k,i_inh) = treexpal;

            chi2_plk(k,i_inh) = ((treexpbe - Be_concs(sample)) ./
Be_errs(sample))^2 + ((treexpal - Al_concs(sample)) ./
Al_errs(sample))^2;

            treburbe = treexpbe.*decbebur + burbe;
            trebural = treexpal.*decalbur + bural;

            treexpbe = treburbe.*decbeexp + expbe;
            treexpal = trebural.*decalexp + expal;

            if (treexpbe >= (Be_concs(sample) - Be_errs(sample))) &&
(treexpbe <= (Be_concs(sample) + Be_errs(sample)))
                if (treexpal >= (Al_concs(sample) - Al_errs(sample)))
&& (treexpal <= (Al_concs(sample) + Al_errs(sample)))
                    counter = counter + 1;
                    k_tsp = k - ind_inh(i_inh);
                    t_sp_z(i_inh,counter) = k_tsp*t_glac + exposet;
                end
            end

            P_reburbe(k,i_inh) = treburbe;
            P_rebural(k,i_inh) = trebural;
        end

        P_reexpbe(k_max+1,i_inh) = treexpbe;
        P_reexpal(k_max+1,i_inh) = treexpal;

        chi2_plk(k_max+1,i_inh) = ((treexpbe - Be_concs(sample)) ./
Be_errs(sample))^2 + ((treexpal - Al_concs(sample)) ./
Al_errs(sample))^2;
    end %i_inh
```

```
    prob_plk = exp(-chi2_plk./2);
    [inh_maxprob, index_inhmaxprob] = max(prob_plk);    ind_tspinh =
index_inhmaxprob - ind_inh;
    min_tspinh = min(ind_tspinh)*t_glac + exposet;
    max_tspinh = max(ind_tspinh)*t_glac + exposet;
    [tsp_inhmaxprob, ind_inhbesttsp] = max(inh_maxprob);
    best_tspinh = ind_tspinh(1,ind_inhbesttsp)*t_glac + exposet;
tsp_prob(z,:) = [best_tspinh min_tspinh max_tspinh];
    pdf_inh(z,:) = inh_maxprob./sum(inh_maxprob);

    t_sp(z,1) = min(min(t_sp_z));
    t_sp(z,2) = max(max(t_sp_z));
end %z

out = [t_sp te_sp];
save t_sp.mat t_sp te_sp

figure
hold on
plot(muon_depth, tsp_prob(:,1), 'r*', muon_depth, tsp_prob, 'r-')
plot(muon_depth, t_sp, 'c*', muon_depth, t_sp, 'b-')
xlabel('plucking thickness (cm)')
ylabel('min time since plucking (a)')
```

A4.7 BURIAL AGE CALCULATION

A4.7.1 Primary code to calculate multiple burial and exposure ages

```
function output = CP_burial_ages(tordata, muontype, samples, avexpdur,
averate, icethick, sigma, binres, consts, makeplot, plotbanana)
%example:> output = CP_burial_ages('CP_alltor.txt', 1, [1:26], 0.222,
1, 5000, 1, 2000, consts, false, false)

%This function runs the CP_burialage script for each sample included in
%samples vector. See that script for details for the inputs and output
file.

%obtain ages for each sample
output = nan(numel(samples),7);
allexpages = nan(numel(samples),11);
allburages = nan(numel(samples),11);
for k = 1:numel(samples)
    [X, Y, e_X, e_Y] = CP_burialage(tordata, muontype, samples(k),
avexpdur, averate, icethick, sigma, binres, consts, makeplot,
plotbanana);
    allexpages(k,1) = samples(k);
    allburages(k,1) = samples(k);
    allexpages(k,2:6) = X;
    allburages(k,2:6) = Y;
    allexpages(k,7:11) = e_X;
    allburages(k,7:11) = e_Y;
end
```

```
output(:,1:4) = allexpages(:,1:4);
output(:,5:7) = allburages(:,2:4);

%output concatenated pdfs (pre-convolution) with age bin (x-axis) to
file for later use
save expages.txt allexpages -ascii
save burages.txt allburages -ascii
save expburages.txt output -ascii

end
```

A4.7.2 Secondary code for individual burial and exposure ages

```
function [expages, burages, e_expages, e_burages] =
CP_burialage(tordata, muontype, sample, avexpdur, averate, icethick,
sigma, binres, consts, makeplot, plotbanana)
%example:> out = CP_burialage('CP_alltor.txt', 1, 10, 0.222, 1, 5000,
1, 2000, consts, true, true)

%This function determines the burial age that best fits concentrations
of Be-10 and Al-26 given a simple surface buildup and burial history.
Muon production based on Lifton et al. 2014 (LSD scaling scheme) is
included both during the buildup period and the burial period.

%Burial age and error is determined using a systematic parameter search
and chi-squared statistic to create a continuous probability density
function.

%Note: inputing a multi-line data file will plot all data on one burial
plot, but only the 'sample' you select will be analyzed numerically.
See 'CP_burial_ages.m' (above) to analyze multiple burial ages at once.

%INPUTS:
%tordata = name of ascii file with  columns of data (e.g. 'data.txt'):
%   column 1 is the decimal latitude of each sample;
%   column 2 is the decimal longitute of each sample;
%   column 3 is the elevation of each sample; (m)
%   column 4 is measured [10Be]; (atoms/g)
%   column 5 is the measured 1 sigma error in [10Be]; (atoms/g)
%   column 6 is the measured [26Al]; (atoms/g)
%   column 7 is the measured 1 sigma error in [26Al]; (atoms/g)

%muontype = deep muon scheme to use; surface buildup model uses Lifton
et al. (2014), but this  parameter refers to the scheme used at depth.
If = 0, there is no deep muon production; if = 1 Lifton (2013) is used
at depth (estimate from J. Stone, pers. comm.); if = 2 Heisinger (2002)
is used at depth.

%sample = the row number of the sample you wish to plot; all samples
will plot regardless, however, because of muons, the plot is
structurally different at different depths and will therefore only be
```

```
accurate for the sample specified here unless 1) all sample depths are
identical or 2) muon production is not included (muontype = 0)

%avexpdur = best guess for average duration of ice-free intervals in
percentage of the total %glacial cycle; (i.e. 0.185 for 18.5ka of 100ka
glacial cycle)

%averate = best guess for average constant erosion rate during
interglacials in mm ka-1; (mm/ka = m/Ma = 1e-1 cm/ka = 1e-4 cm/a)

%icethick = average ice thickness covering sample site during each
burial episode; (cm)

%sigma = specifies the sigma confidence for the error ellipse

%binres = the bin resolution used to calculate pdf (note: increasing
this constant geometrically increases calculation time. A value of
around 2000 is usually sufficient, which generates a pdf curve using
2000 points over the age range

%consts = a matlab structure containing constants used in the LSD
scaling model. This structure is loaded in the startup.m file.

%makeplot = if true, will output individual plots for each sample. It
is useful to suppress this if goal is to just creat pdfs for age.

%plotbananna = if true, will also plot the banana window

%OUTPUT:

%Running this program also writes a .mat file to your working
directory. The name format is the name of your data input file plus the
sample row number. This file contains a data structure called
"burialoutput" with the following results of the age calculation:
sample row number, bur/expmaxage (the most probable age as determined
from the probability density function), bur/expsigma1plus and
bur/expsigma1minus (the +/- 1sigma errors in bur/expmaxage),
bur/expsigma2plus and bur/expsigma2minus (the +/- 2sigma errors in
bur/expmaxage), burial_sim, exposure_sim and pdf_bur, pdf_exp (matrices
containing vectors for incremental time and probability--basically to
allow reconstruction of the pdf.

%A.Margreth, based on A. Hidy's burialage code (25.03.2014) adapted to
tor data on Cumberland Peninsula
%%%%%%%%%%%%%%%%%%%%%%%%%%%%%%%%%%%%%%%%%%%%%%%%%%%%%%%%%%%%%%%%%%%%%%%

%load data
burial_data = load(tordata);
lats = burial_data(:,1);
longs = burial_data(:,2);
elevs = burial_data(:,3);
Be_concs = burial_data(:,4);
Be_errs = burial_data(:,5);
Al_concs = burial_data(:,6);
Al_errs = burial_data(:,7);
```

```
ratios = Al_concs./Be_concs;

%densities used for buildup (g/cc)
r_density = 2.65;
ice_density = 0.9;

%Because muonproduction function requires massdepth as input ->
transform any depth to rock-equivalent depth, which can then be
multiplied by rock density
surf_depth = 0;
%used in buildup functions to draw isoexp and -bur lines
depth_ice = icethick*ice_density/r_density;
%recalculate ice thickness to a rock-equivalent thickenss
frac = avexpdur; %redundent assignment
bur_depth = (depth_ice * (1-frac) * 100) / 100;
eros = averate / 10000; %convert to cm a-1

%decay constants (1/s)
Be10_lambda = log(2)/1387000;
%Chmeleff et al. (2010), Korschinek et al. (2010)
Al26_lambda = log(2)/705000; %Nishiizumi (2004)

%neutron attenuation length (g/cm^2)
neutron_atten = 150;
%Follows Balco et al. (2008); see Gosse and Phillips (2001)

%spallogenic production (atoms/g/a)
refspalprod = 4.0;   %New prod rate, Brocher et al. (subm.);
ratio_init = 6.75; %Nishiizumi et al. (1989); Balco et al. (2008);
6.1/1.106 to reflect recalibration of Nishiizumi et al. (2007)

%Get LSD scaling factors
maxage = 100000; %age over which to integrate production rates
LSD10 = LSD(lats(sample),longs(sample),elevs(sample),1,maxage,-1,10);
LSD26 = LSD(lats(sample),longs(sample),elevs(sample),1,maxage,-1,26);
agegrid = 0:1:maxage;
%average cutoff rigidity (RC) and solar modulation (SPhi)over age range
meanRC = mean(interpolate(LSD10.tv,LSD10.Rc,agegrid));
meanSPhi = mean(interpolate(LSD10.tv,LSD10.SPhi,agegrid));

%average spallogenic surface production rate over age range
Be10_spalsurf =
mean(refspalprod.*interpolate(LSD10.tv,LSD10.Be,agegrid));
Al26_spalsurf =
mean(refspalprod.*ratio_init.*interpolate(LSD26.tv,LSD26.Al,agegrid));
[Be10_fmusurf, Be10_nmusurf] = CP_P_mu_totalLSD(0 *
r_density,LSD10.pressure,meanRC,meanSPhi,consts,10,'no');
[Al26_fmusurf, Al26_nmusurf] = CP_P_mu_totalLSD(0 *
r_density,LSD10.pressure,meanRC,meanSPhi,consts,26,'no');

%muonic production at depth
if muontype == 0 %no muon production
    Be10_mudepth = 0;
    Al26_mudepth = 0;
else if muontype == 1 %Use LSD rates based on
```

```
        Be10_mudepth = P_mu_totalLSD(bur_depth *
r_density,LSD10.pressure,meanRC,meanSPhi,consts,10,'no');
        Al26_mudepth = P_mu_totalLSD(bur_depth *
r_density,LSD10.pressure,meanRC,meanSPhi,consts,26,'no');
    else if muontype == 2
            Be10_mudepth = muonproduction_heisinger(bur_depth *
r_density,elevs,1);
            Al26_mudepth = muonproduction_heisinger(bur_depth *
r_density,elevs,0);
        end
    end
end

%override buildup production rates here (for example, to assume basin-
wide production rate for source)
Be10_spalbuildup = Be10_spalsurf;
Al26_spalbuildup = Al26_spalsurf;

Be10_mubuildup = Be10_fmusurf + Be10_nmusurf ;
Al26_mubuildup = Al26_fmusurf + Al26_nmusurf;

%simple buildup model with no erosion
%buildup due to exposure at surface; assumes no inheritance
    function Be10_conc_buildup = Be10_buildup(t_exposure)
        Be10spall_buildup = (Be10_spalbuildup/Be10_lambda)*(1-exp(-
Be10_lambda*t_exposure));
        Be10muon_buildup = (Be10_mubuildup/Be10_lambda)*(1-exp(-
Be10_lambda*t_exposure));
        Be10_conc_buildup = Be10spall_buildup + Be10muon_buildup;
    end

    function Al26_conc_buildup = Al26_buildup(t_exposure)
        Al26spall_buildup = (Al26_spalbuildup/Al26_lambda)*(1-exp(-
Al26_lambda*t_exposure));
        Al26muon_buildup = (Al26_mubuildup/Al26_lambda)*(1-exp(-
Al26_lambda*t_exposure));
        Al26_conc_buildup = Al26spall_buildup + Al26muon_buildup;
    end

%burial production; assume buildup is inheritance
    function Be10_conc_burial = Be10_burial(t_exposure, t_burial)
        Be10spall_burial = (Be10_spalsurf/Be10_lambda)*exp(-
bur_depth*r_density/neutron_atten)*(1-exp(-Be10_lambda*t_burial));
        Be10muon_burial = (Be10_mudepth/Be10_lambda)*(1-exp(-
Be10_lambda*t_burial));
        Be10inheritance = Be10_buildup(t_exposure)*exp(-
Be10_lambda*t_burial);
        Be10_conc_burial = Be10spall_burial + Be10muon_burial +
Be10inheritance;
    end

    function Al26_conc_burial = Al26_burial(t_exposure, t_burial)
        Al26spall_burial = (Al26_spalsurf/Al26_lambda)*exp(-
bur_depth*r_density/neutron_atten)*(1-exp(-Al26_lambda*t_burial));
        Al26muon_burial = (Al26_mudepth/Al26_lambda)*(1-exp(-
Al26_lambda*t_burial));
```

```
        Al26inheritance = Al26_buildup(t_exposure)*exp(-
Al26_lambda*t_burial);
        Al26_conc_burial = Al26spall_burial + Al26muon_burial +
Al26inheritance;
    end

%simple buildup model with erosion
%new lambda term spallation
    function Be10lambda = Be10_elambda(erate)
        Be10lambda = Be10_lambda + erate*r_density/neutron_atten;
    end

    function Al26lambda = Al26_elambda(erate)
        Al26lambda = Al26_lambda + erate*r_density/neutron_atten;
    end

    function Be10lambdamun = Be10n_elambdamu(erate)
        Be10lambdamun = Be10_lambda + erate*r_density/1500;
    end

    function Al26lambdamun = Al26n_elambdamu(erate)
        Al26lambdamun = Al26_lambda + erate*r_density/1500;
    end

    function Be10lambdamuf = Be10f_elambdamu(erate)
        Be10lambdamuf = Be10_lambda + erate*r_density/4350;
    end

    function Al26lambdamuf = Al26f_elambdamu(erate)
        Al26lambdamuf = Al26_lambda + erate*r_density/4350;
    end

    function eBe10_conc_buildup = eBe10_buildup(t_exposure, erate)
        Be10spall_buildup = (Be10_spalsurf./Be10_elambda(erate)).*(1-
exp(-Be10_elambda(erate).*t_exposure));
        Be10muon_buildup = Be10_fmusurf./Be10f_elambdamu(erate).*(1-
exp(-Be10f_elambdamu(erate).*t_exposure)) +
Be10_nmusurf./Be10n_elambdamu(erate).*(1-exp(-
Be10n_elambdamu(erate).*t_exposure));
        eBe10_conc_buildup = Be10spall_buildup + Be10muon_buildup;
    end

    function eAl26_conc_buildup = eAl26_buildup(t_exposure, erate)
        Al26spall_buildup = (Al26_spalsurf./Al26_elambda(erate)).*(1-
exp(-Al26_elambda(erate).*t_exposure));
        Al26muon_buildup = Al26_fmusurf./Al26f_elambdamu(erate).*(1-
exp(-Al26f_elambdamu(erate).*t_exposure)) +
Al26_nmusurf./Al26n_elambdamu(erate).*(1-exp(-
Al26n_elambdamu(erate).*t_exposure));
        eAl26_conc_buildup = Al26spall_buildup + Al26muon_buildup;
    end

%burial production; assume buildup is inheritance
    function eBe10_conc_burial = eBe10_burial(t_exposure, t_burial,
erate)
```

```
        Be10spall_burial = (Be10_spalsurf/Be10_lambda)*exp(-
bur_depth*r_density/neutron_atten)*(1-exp(-Be10_lambda*t_burial));
        Be10muon_burial = (Be10_mudepth/Be10_lambda)*(1-exp(-
Be10_lambda*t_burial));
        Be10inheritance = eBe10_buildup(t_exposure, erate)*exp(-
Be10_lambda*t_burial);
        eBe10_conc_burial = Be10spall_burial + Be10muon_burial +
Be10inheritance;
    end

    function eAl26_conc_burial = eAl26_burial(t_exposure, t_burial,
erate)
        Al26spall_burial = (Al26_spalsurf/Al26_lambda)*exp(-
bur_depth*r_density/neutron_atten)*(1-exp(-Al26_lambda*t_burial));
        Al26muon_burial = (Al26_mudepth/Al26_lambda)*(1-exp(-
Al26_lambda*t_burial));
        Al26inheritance = eAl26_buildup(t_exposure, erate)*exp(-
Al26_lambda*t_burial);
        eAl26_conc_burial = Al26spall_burial + Al26muon_burial +
Al26inheritance;
    end

%%%%%%%%%%%%%%%%%%%%%%%%%%%%%%%%%%%%%%%%%%%%%%%%%%%%%%%%%%%%%%%%%%%%%%%%%%%%
%Generate probability density function
%pdf grid resulution
pdfres = binres;

%create burial and exposure grids
burial_sim = linspace(0,1500000,pdfres);
% exposure_sim = logspace(0,7.2,pdfres);
exposure_sim = linspace(0, 500000, pdfres);

%initialize matrices
Be10_matrix = zeros(numel(exposure_sim),numel(burial_sim));
Al26_matrix = zeros(numel(exposure_sim),numel(burial_sim));
eBe10_matrix = zeros(numel(exposure_sim),numel(burial_sim));
eAl26_matrix = zeros(numel(exposure_sim),numel(burial_sim));

for i = 1:numel(exposure_sim)
    for j = 1:numel(burial_sim)
        Be10_matrix(i,j) = Be10_burial(exposure_sim(i),burial_sim(j));
%burial ages in columns, exposure ages in rows
        Al26_matrix(i,j) = Al26_burial(exposure_sim(i),burial_sim(j));
%burial ages in columns, exposure ages in rows
        eBe10_matrix(i,j) = eBe10_burial(exposure_sim(i),burial_sim(j),
eros); %burial ages in columns, exposure ages in rows
        eAl26_matrix(i,j) = eAl26_burial(exposure_sim(i),burial_sim(j),
eros); %burial ages in columns, exposure ages in rows
    end
end

%use grid values to compute modeled results at each point and compare
with measured concentrations to generate chi-squared grid
chi2be_matrix = abs(((Be10_matrix -
Be_concs(sample))./Be_errs(sample))).^2);
```

```
chi2al_matrix = abs((((Al26_matrix -
Al_concs(sample))./Al_errs(sample))).^2);
chi2total_matrix = chi2be_matrix + chi2al_matrix;

echi2be_matrix = abs((((eBe10_matrix -
Be_concs(sample))./Be_errs(sample))).^2);
echi2al_matrix = abs((((eAl26_matrix -
Al_concs(sample))./Al_errs(sample))).^2);
echi2total_matrix = echi2be_matrix + echi2al_matrix;

%convert chi-squared to probability using liklihood function
prob2total_matrix = exp(-chi2total_matrix./2);
eprob2total_matrix = exp(-echi2total_matrix./2);

burial_max = max(prob2total_matrix);
burial_emax = max(eprob2total_matrix);
%construct pdf normalized so area under curve=1
pdf_bur = burial_max./sum(burial_max);
cdf_bur = cumsum(pdf_bur);
[b_bur,i_bur] = unique(cdf_bur);

pdf_ebur = burial_emax./sum(burial_emax);
cdf_ebur = cumsum(pdf_ebur);
[b_ebur,i_ebur] = unique(cdf_ebur);

exposure_max = max(prob2total_matrix, [], 2);
pdf_exp = exposure_max./sum(exposure_max);
cdf_exp = cumsum(pdf_exp);
[b_exp,i_exp] = unique(cdf_exp);

exposure_emax = max(eprob2total_matrix, [], 2);
pdf_eexp = exposure_emax./sum(exposure_emax);
cdf_eexp = cumsum(pdf_eexp);
[b_eexp,i_eexp] = unique(cdf_eexp);

burialoutput.sampleID = sample;
burialoutput.burmaxage = burial_sim(pdf_bur == max(pdf_bur))/10^3;
%burial age in ka
burialoutput.bursigma1plus =
interp1(b_bur,burial_sim(i_bur),0.84135)/10^3; %del burial age in ka
burialoutput.bursigma1minus =
interp1(b_bur,burial_sim(i_bur),0.15865)/10^3; %del burial age in ka
burialoutput.bursigma2plus =
interp1(b_bur,burial_sim(i_bur),0.977)/10^3; %del burial age in ka
burialoutput.bursigma2minus =
interp1(b_bur,burial_sim(i_bur),0.023)/10^3; %del burial age in ka
burialoutput.burial_sim = burial_sim;
burialoutput.pdf_bur = pdf_bur;
burialoutput.expmaxage = exposure_sim(pdf_exp == max(pdf_exp))/10^3;
%burial age in ka
burialoutput.expsigma1plus =
interp1(b_exp,exposure_sim(i_exp),0.84135)/10^3; %del burial age in ka
burialoutput.expsigma1minus =
interp1(b_exp,exposure_sim(i_exp),0.15865)/10^3; %del burial age in ka
burialoutput.expsigma2plus =
interp1(b_exp,exposure_sim(i_exp),0.977)/10^3; %del burial age in ka
```

```
burialoutput.expsigma2minus =
interp1(b_exp,exposure_sim(i_exp),0.023)/10^3; %del burial age in ka
burialoutput.exposure_sim = exposure_sim;
burialoutput.pdf_exp = pdf_exp;

burages = [burialoutput.burmaxage burialoutput.bursigma1plus
burialoutput.bursigma1minus burialoutput.bursigma2plus
burialoutput.bursigma2minus];
expages = [burialoutput.expmaxage burialoutput.expsigma1plus
burialoutput.expsigma1minus burialoutput.expsigma2plus
burialoutput.expsigma2minus];

e_burialoutput.sampleID = sample;
e_burialoutput.burmaxage = burial_sim(pdf_ebur == max(pdf_ebur))/10^3;
%burial age in ka
e_burialoutput.bursigma1plus =
interp1(b_ebur,burial_sim(i_ebur),0.84135)/10^3; %del burial age in ka
e_burialoutput.bursigma1minus =
interp1(b_ebur,burial_sim(i_ebur),0.15865)/10^3; %del burial age in ka
e_burialoutput.bursigma2plus =
interp1(b_ebur,burial_sim(i_ebur),0.977)/10^3; %del burial age in ka
e_burialoutput.bursigma2minus =
interp1(b_ebur,burial_sim(i_ebur),0.023)/10^3; %del burial age in ka
e_burialoutput.burial_sim = burial_sim;
e_burialoutput.pdf_bur = pdf_ebur;
e_burialoutput.expmaxage = exposure_sim(pdf_eexp ==
max(pdf_eexp))/10^3; %burial age in ka
e_burialoutput.expsigma1plus =
interp1(b_eexp,exposure_sim(i_eexp),0.84135)/10^3; %del burial age in
ka
e_burialoutput.expsigma1minus =
interp1(b_eexp,exposure_sim(i_eexp),0.15865)/10^3; %del burial age in
ka
e_burialoutput.expsigma2plus =
interp1(b_eexp,exposure_sim(i_eexp),0.977)/10^3; %del burial age in ka
e_burialoutput.expsigma2minus =
interp1(b_eexp,exposure_sim(i_eexp),0.023)/10^3; %del burial age in ka
e_burialoutput.exposure_sim = exposure_sim;
e_burialoutput.pdf_exp = pdf_exp;

e_burages = [e_burialoutput.burmaxage e_burialoutput.bursigma1plus
e_burialoutput.bursigma1minus e_burialoutput.bursigma2plus
e_burialoutput.bursigma2minus];
e_expages = [e_burialoutput.expmaxage e_burialoutput.expsigma1plus
e_burialoutput.expsigma1minus e_burialoutput.expsigma2plus
e_burialoutput.expsigma2minus];

burages;
expages;
e_burages;
e_expages;

%write output file to workspace
name = strcat(mat2str(sample));
save(name,'burialoutput', 'e_burialoutput');
```

```
%%%%%%%%%%%%%%%%%%%%%%%%%%%%%%%%%%%%%%%%%%%%%%%%%%%%%%%%%%%%%%%%%%%%%%%%%%%%
%Plotting parameters
if ~makeplot %supress all burial plots?
    return
end

%pdf plot
pdfbur_axis = [0 1.5*burialoutput.bursigma2plus 0 1.2*max(pdf_bur)];
error2bur_high = (burialoutput.bursigma2plus);
error2bur_low = (burialoutput.bursigma2minus);
error1bur_high = (burialoutput.bursigma1plus);
error1bur_low = (burialoutput.bursigma1minus);
pdfexp_axis = [0 1.5*burialoutput.expsigma2plus 0 1.2*max(pdf_exp)];
error2exp_high = (burialoutput.expsigma2plus);
error2exp_low = (burialoutput.expsigma2minus);
error1exp_high = (burialoutput.expsigma1plus);
error1exp_low = (burialoutput.expsigma1minus);

pdfbur_eaxis = [0 1.5*e_burialoutput.bursigma2plus 0
1.2*max(pdf_ebur)];
error2bur_ehigh = (e_burialoutput.bursigma2plus);
error2bur_elow = (e_burialoutput.bursigma2minus);
error1bur_ehigh = (e_burialoutput.bursigma1plus);
error1bur_elow = (e_burialoutput.bursigma1minus);
pdfexp_eaxis = [0 1.5*e_burialoutput.expsigma2plus 0
1.2*max(pdf_eexp)];
error2exp_ehigh = (e_burialoutput.expsigma2plus);
error2exp_elow = (e_burialoutput.expsigma2minus);
error1exp_ehigh = (e_burialoutput.expsigma1plus);
error1exp_elow = (e_burialoutput.expsigma1minus);

figure
hold on
box on
subplot(2,2,1)
axis(pdfbur_axis)
xlabel('Burial Age (ka)');
ylabel('normalized probability');
title(strcat({'PDF: sample '},{name}));
plot(burial_sim./10^3,pdf_bur,'b-', 'linewidth', 2)
line([error2bur_high error2bur_high], [0 1], 'linestyle','-.', 'color',
'k')
line([error2bur_low error2bur_low], [0 1], 'linestyle','-.', 'color',
'k')
line([error1bur_high error1bur_high], [0 1], 'linestyle','-.', 'color',
'r')
line([error1bur_low error1bur_low], [0 1], 'linestyle','-.', 'color',
'r')
subplot(2,2,2)
axis(pdfexp_axis)
xlabel('Exposure Age (ka)');
ylabel('normalized probability');
title(strcat({'PDF: sample '},{name}));
plot(exposure_sim./10^3,pdf_exp,'b-', 'linewidth', 2)
line([error2exp_high error2exp_high], [0 1], 'linestyle','-.', 'color',
'k')
```

```
line([error2exp_low error2exp_low], [0 1], 'linestyle','-.', 'color',
'k')
line([error1exp_high error1exp_high], [0 1], 'linestyle','-.', 'color',
'r')
line([error1exp_low error1exp_low], [0 1], 'linestyle','-.', 'color',
'r')
subplot(2,2,3)
axis(pdfbur_eaxis)
xlabel('Burial Age (ka)');
ylabel('normalized probability');
title(strcat({'PDF: sample '},{name}));
plot(burial_sim./10^3,pdf_ebur,'b-', 'linewidth', 2)
line([error2bur_ehigh error2bur_ehigh], [0 1], 'linestyle','-.',
'color', 'k')
line([error2bur_elow error2bur_elow], [0 1], 'linestyle','-.', 'color',
'k')
line([error1bur_ehigh error1bur_ehigh], [0 1], 'linestyle','-.',
'color', 'r')
line([error1bur_elow error1bur_elow], [0 1], 'linestyle','-.', 'color',
'r')
subplot(2,2,4)
axis(pdfexp_eaxis)
xlabel('Exposure Age (ka)');
ylabel('normalized probability');
title(strcat({'PDF: sample '},{name}));
plot(exposure_sim./10^3,pdf_eexp,'b-', 'linewidth', 2)
line([error2exp_ehigh error2exp_ehigh], [0 1], 'linestyle','-.',
'color', 'k')
line([error2exp_elow error2exp_elow], [0 1], 'linestyle','-.', 'color',
'k')
line([error1exp_ehigh error1exp_ehigh], [0 1], 'linestyle','-.',
'color', 'r')
line([error1exp_elow error1exp_elow], [0 1], 'linestyle','-.', 'color',
'r')

%burial plot
%define axis for plot
plot_axis = [4 7.5 0 8]; %x-axis, y-axis

%Define locations of contours on burial plot, in years
n1 = [250000 500000 1000000 2000000 3000000 4000000 8000000];
%burial contours
n2 = [1000 10000 30000 100000 300000 1000000]; %exposure contours
n3 = [100 50 10 5 2 1 0.5 0.1 0.05 0.01]/1000;
%erosion rate contours for erosion banana, cm/a, [cm/ka]

%Create grids for plot contours
texp = 1:100:20000000;
tbur = 1:100:20000000;
eeros = 0:0.001/1000:500/1000;

figure
hold on
box on
axis(plot_axis);
xlabel('log[^{10}Be] (atoms g^{-1})');
```

```
ylabel('^{26}Al/^{10}Be');
title(strcat({'Burial Plot: sample '},{name}));

%Plot error ellipses and mean values for sample concentrations
plot(log10(Be_concs(sample)),ratios(sample),'k.');
Tor_ellipse(Be_concs(sample),Be_errs(sample),Al_concs(sample),Al_errs(s
ample),sigma);

%burial contours
for k = 1:numel(n1)
plot(log10(Be10_burial(texp,n1(k))),Al26_burial(texp,n1(k))./Be10_buria
l(texp,n1(k)),'b:');
end

%exposure contours
for k = 1:numel(n2)
plot(log10(Be10_burial(n2(k),tbur)),Al26_burial(n2(k),tbur)./Be10_buria
l(n2(k),tbur),'k--');
end

%surface curve for zero erosion
plot(log10(Be10_burial(texp,0)),Al26_burial(texp,0)./Be10_burial(texp,0
),'r-','linewidth',2);

%burial path starting at zero-erosion surface saturation (lower plot
%boundary)
plot(log10(Be10_burial(100000000,tbur)),Al26_burial(100000000,tbur)./Be
10_burial(100000000,tbur),'k-','linewidth',2);

%include erosion banana?
if ~plotbanana
    return
end

for k = 1:numel(n3)
    plot(log10(eBe10_buildup(texp,n3(k))),
eAl26_buildup(texp,n3(k))./eBe10_buildup(texp,n3(k)),'g-');
end
plot(log10(eBe10_buildup(10000000,eeros)),
eAl26_buildup(10000000,eeros)./eBe10_buildup(10000000,eeros),'g-
','linewidth',2);
plot(log10(Be10_burial(texp,0)),Al26_burial(texp,0)./Be10_burial(texp,0
),'r-','linewidth',2);

%depth curve for zero erosion
    function Be10_conc_buildupA = Be10_buildupA(t_exposure)
        Be10spall_buildup = (Be10_spalsurf/Be10_lambda)*(1-exp(-
Be10_lambda*t_exposure))*exp(-bur_depth*r_density/neutron_atten);
        Be10muon_buildup = (Be10_mudepth/Be10_lambda)*(1-exp(-
Be10_lambda*t_exposure));
        Be10_conc_buildupA = Be10spall_buildup + Be10muon_buildup;
    end

    function Al26_conc_buildupA = Al26_buildupA(t_exposure)
```

```
        Al26spall_buildup = (Al26_spalsurf/Al26_lambda)*(1-exp(-
Al26_lambda*t_exposure))*exp(-bur_depth*r_density/neutron_atten);
        Al26muon_buildup = (Al26_mudepth/Al26_lambda)*(1-exp(-
Al26_lambda*t_exposure));
        Al26_conc_buildupA = Al26spall_buildup + Al26muon_buildup;
    end

plot(log10(Be10_buildupA(texp)),Al26_buildupA(texp)./Be10_buildupA(texp
),'r-','linewidth',2);

end
```

A4.8 REFERENCES FOR A4

Balco, G., Stone, J.O., Lifton, N.A., Dunai, T.J., 2008. A complete and easily accessible means of calculating surface exposure ages or erosion rates from ^{10}Be and ^{26}Al measurements. Quaternary Geochronology 3, 174-195.

Lifton, N., Sato, T., Dunai, T.J., 2014. Scaling in situ cosmogenic nuclide production rates using analytical approximations to atmospheric cosmic-ray fluxes. Earth and Planetary Science Letters 386, 149-160.

Lisiecki, L.E., Raymo, M.E., 2005. A Plio-Pleistocene stack of 57 globally distributed benthic ^{18}O records. Paleoceanography 20, 522–533.

APPENDIX A5 – Chemistry Data

This appendix contains all the information necessary to re-calculate exposure ages as production rates, isotope half-lives or other parameters may change over time. In the first section, the input tables are given, which were used to calculate exposure ages with the CRONUS KU online calculator, version 1.0 (http://web1.ittc.ku.edu:8888/), together with the tables used to calculate concentrations of native Al from ICP-MS and –OES analyses. In the second section, the chemistry worksheets are included for all TCN samples (boulders, bedrock, and depth profiles).

A5.1 INPUT TABLES FOR CRONUS KU CALCULATOR AND NATIVE ALUMINUM DATA CALCULATIONS

	Sample Name	Scaling	Latitude	Longitude	Elevation	Pressure	Atmospheric Pressure or Elevation	Sample Thickness	Bulk Density	Shielding Factor	Erosion Rate	^{10}Be concen-tration	^{10}Be standar-dization	^{27}Al concen-tration	^{27}Al standar-dization	Atten-uation length	Depth to Top of Sample
			(d.d)	(d.d)	(m asl)	(hPa)		(cm)	(g cm^{-3})		(mm ka^{-1})	(atoms g^{-1})		(atoms g^{-1})		(g cm^{-2})	(g cm^{-2})
'central Valley'	09SRB-E027A-01	SA	65.1987	-64.3370	207.34		Elevation	3.5	2.60	1.00	1.00	75359	07KNSTD	0	KNSTD	150	0
	09SRB-E039A-01	SA	65.6974	-64.5085	290.02		Elevation	2.50	2.60	1.00	1.00	116848	07KNSTD	0	KNSTD	150	0
	09SRB-E040A-01	SA	65.6971	-64.5092	294.92		Elevation	3.5	2.60	1.00	1.00	0	07KNSTD	0	KNSTD	150	0
	09SRB-E092A-01	SA	66.2549	-63.6963	763.70		Elevation	1	2.60	1.00	1.00	185860	07KNSTD	0	KNSTD	150	0
	09SRB-E025A-01	SA	65.1987	-64.3375	199.44		Elevation	3	2.60	1.00	1.00	0	07KNSTD	0	KNSTD	150	0
	09SRB-E026A-01	SA	65.1988	-64.3376	203.84		Elevation	3	2.60	1.00	1.00	72817	07KNSTD	0	KNSTD	150	0
	09SRB-E041A-01	SA	65.8421	-64.4733	554.61		Elevation	2.5	2.60	1.00	1.00	211074	07KNSTD	0	KNSTD	150	0
	09SRB-E003A-01	SA	66.1722	-63.8479	551.80		Elevation	1.5	2.60	0.99	1.00	75843	07KNSTD	0	KNSTD	150	0
	09SRB-E004A-01	SA	66.1722	-63.8477	558.40		Elevation	1	2.60	0.99	1.00	72125	07KNSTD	0	KNSTD	150	0
	09SRB-E052A-01	SA	65.8190	-64.4484	391.51		Elevation	0.5	2.60	1.00	1.00	121460	07KNSTD	0	KNSTD	150	0
	09SRB-E059A-01	SA	65.7145	-64.4940	318.12		Elevation	1	2.60	1.00	1.00	136236	07KNSTD	0	KNSTD	150	0
	09SRB-E060A-01	SA	65.7119	-64.4906	297.82		Elevation	0.5	2.60	1.00	1.00	68205	07KNSTD	0	KNSTD	150	0
	09SRB-E002A-01	SA	66.1708	-63.8574	538.70		Elevation	0.50	2.60	1.00	1.00	0	07KNSTD	0	KNSTD	150	0
	09SRB-A167A-01	SA	-65.3095	-65.3095	472.40		Elevation	3.00	2.60	1.00	1.00	87152	07KNSTD	0	KNSTD	150	0
	09SRB-A167A-02	SA	-65.3095	-65.3095	472.40		Elevation	2.50	2.60	1.00	1.00	103433	07KNSTD	0	KNSTD	150	0
	09SRB-A167A-03	SA	-65.3095	-65.3095	472.40		Elevation	2.50	2.60	1.00	1.00	148691	07KNSTD	0	KNSTD	150	0
Moon Valley	09SRB-E223A-01	SA	66.3434	-65.7391	558.89		Elevation	3.50	2.60	1.00	0.00	106454	07KNSTD	0	KNSTD	150	0
	09SRB-E223A-03	SA	66.3434	-65.7391	558.89		Elevation	3.50	2.60	1.00	0.00	78538	07KNSTD	0	KNSTD	150	0
	09SRB-E223A-02	SA	66.3434	-65.7391	558.89		Elevation	3.5	2.60	1.00	0.00	0	07KNSTD	0	KNSTD	150	0
	09SRB-E224A-01	SA	66.3443	-65.7266	563.19		Elevation	3.5	2.60	1.00	0.00	136983	07KNSTD	0	KNSTD	150	0
	09SRB-E224A-02	SA	66.3443	-65.7266	563.19		Elevation	3.5	2.60	1.00	0.00	63938	07KNSTD	0	KNSTD	150	0
	09SRB-E224A-03	SA	66.3443	-65.7266	563.19		Elevation	3	2.60	1.00	0.00	250896	07KNSTD	0	KNSTD	150	0
	09SRB-E283A-01	SA	66.3455	-65.7248	578.49		Elevation	2.00	2.60	1.00	0.00	170871	07KNSTD	0	KNSTD	150	0
	09SRB-E284A-01	SA	66.3377	-65.8245	481.89		Elevation	3.00	2.60	1.00	0.00	76455	07KNSTD	0	KNSTD	150	0
	09SRB-E284A-02	SA	66.3377	-65.8245	481.89		Elevation	2.00	2.60	1.00	0.00	77710	07KNSTD	0	KNSTD	150	0
	09SRB-E284A-03	SA	66.3377	-65.8245	481.89		Elevation	2.50	2.60	1.00	0.00	106825	07KNSTD	0	KNSTD	150	0
	09SRB-A351A-01	SA	66.3097	-65.6150	477.19		Elevation	2.5	2.60	1.00	0.00	69012	07KNSTD	0	KNSTD	150	0
	09SRB-A352A-01	SA	66.3091	-65.6137	469.99		Elevation	3	2.60	1.00	0.00	71500	07KNSTD	0	KNSTD	150	0
	09SRB-A353A-01	SA	66.3110	-65.6132	469.89		Elevation	3	2.60	1.00	0.00	68754	07KNSTD	0	KNSTD	150	0
Tor - batch 1	09SRB-E221A-01	SA	66.0008	-65.5427	830.21		Elevation	3.00	2.65	1.00	1.00	707233	07KNSTD	3702247	KNSTD	150	0
	09SRB-E221A-02	SA	66.0008	-65.5427	830.21		Elevation	3.50	2.65	1.00	1.00	1261069	07KNSTD	5714146	KNSTD	150	0
	09SRB-E221A-03	SA	66.0008	-65.5427	830.21		Elevation	3.00	2.65	1.00	1.00	965576	07KNSTD	5908791	KNSTD	150	0
	09SRB-E304A-01	SA	66.2793	-65.8015	765.40		Elevation	1.50	2.65	1.00	1.00	1406032	07KNSTD	7873971	KNSTD	150	0
	09SRB-A186A-01	SA	66.1144	-65.5495	826.50		Elevation	2.00	2.65	1.00	1.00	1358839	07KNSTD	7363455	KNSTD	150	0
	09SRB-A188A-01	SA	66.1142	-65.5496	824.50		Elevation	2.00	2.65	1.00	1.00	1777415	07KNSTD	9220355	KNSTD	150	0
	09SRB-A187A-01	SA	66.1145	-65.5495	825.00		Elevation	2.00	2.65	1.00	1.00	1237443	07KNSTD	7300063	KNSTD	150	0
	09SRB-A355A-01	SA	66.1235	-65.5422	670.70		Elevation	2.50	2.65	1.00	1.00	1570081	07KNSTD	8965389	KNSTD	150	0
	09SRB-A356A-01	SA	66.1232	-65.5415	661.90		Elevation	1.50	2.65	1.00	1.00	575025	07KNSTD	3567266	KNSTD	150	0
	09SRB-A346A-01	SA	66.2989	-65.7141	975.30		Elevation	2.00	2.65	1.00	1.00	1451820	07KNSTD	8183576	KNSTD	150	0
	09SRB-A348A-01	SA	66.2977	-65.7134	971.70		Elevation	2.00	2.65	1.00	1.00	1032604	07KNSTD	6391547	KNSTD	150	0
	09SRB-A347A-01	SA	66.2987	-65.7138	971.00		Elevation	3.00	2.65	1.00	1.00	466858	07KNSTD	2625742	KNSTD	150	0
Tor - batch 2	09SRB-E222A-01	SA	66.3620	-65.7029	1038.29		Elevation	3.20	2.65	1.00	1.00	2234964	07KNSTD	12618354	KNSTD	150	0
	09SRB-E222A-02	SA	66.3620	-65.7029	1038.29		Elevation	3.10	2.65	1.00	1.00	321170	07KNSTD	1236122	KNSTD	150	0
	09SRB-E222A-03	SA	66.3620	-65.7029	1038.29		Elevation	3.60	2.65	1.00	1.00	1729485	07KNSTD	10080412	KNSTD	150	0
	09SRB-E222A-04	SA	66.3620	-65.7029	1038.29		Elevation	4.30	2.65	1.00	1.00	462419	07KNSTD	1988670	KNSTD	150	0
	10SRB-E042A-01	SA	67.2824	-63.0773	569.76		Elevation	2.00	2.65	1.00	1.00	670668	07KNSTD	4058002	KNSTD	150	0
	10SRB-E064A-01	SA	67.5961	-63.9257	373.05		Elevation	1.50	2.65	1.00	1.00	634915	07KNSTD	4014124	KNSTD	150	0
	10SRB-E065A-01	SA	67.6691	-64.2629	1029.54		Elevation	1.50	2.65	1.00	1.00	5014766	07KNSTD	32935199	KNSTD	150	0
Tor - batch 3	10SRB-E020A-01	SA	66.3010	-65.8060	1004.20		Elevation	2.00	2.65	1.00	1.00	2397325	07KNSTD	12480222	KNSTD	150	0
	10SRB-E021A-01	SA	66.3010	-65.8061	1001.20		Elevation	2.50	2.65	1.00	1.00	2862744	07KNSTD	14085998	KNSTD	150	0
	10SRB-E022A-01	SA	66.2901	-65.7524	1150.20		Elevation	1.50	2.65	1.00	1.00	1366673	07KNSTD	6855841	KNSTD	150	0
	09SRB-E222A-05	SA	66.3620	-65.7029	1038.29		Elevation	3.00	2.65	1.00	1.00	2056898	07KNSTD	12117098	KNSTD	150	0
	09SRB-E222A-06	SA	66.3620	-65.7029	1038.29		Elevation	3.50	2.65	1.00	1.00	195103	07KNSTD	949041	KNSTD	150	0
	10SRB-E074A-01	SA	66.6973	-61.6606	1314.08		Elevation	2.00	2.65	1.00	1.00	8232030	07KNSTD	42473624	KNSTD	150	0
	10SRB-E066A-01	SA	67.6693	-64.2631	1026.34		Elevation	2.00	2.65	1.00	1.00	3751165	07KNSTD	22537221	KNSTD	150	0

Table A5.1 Input data for CRONUS KU calculator.

	Sample Name	Year collected	Latitude uncer-tainty	Longitude uncer-tainty	Elevation uncert-ainty	Pressure uncer-tainty	Sample thickness uncer-tainty	Bulk density uncer-tainty	Shielding factor uncer-tainty	Erosion rate uncer-tainty	^{10}Be concen-tration uncer-tainty	^{10}Al concen-tration uncer-tainty	Atten-uation length unce-rtainty	Depth to rop of sample uncer-tainty	Year collec-ted unc-ertainty
		(AD)	(d.d)	(d.d)	(m asl)	(hPa)	(cm)	(g cm^{-3})		(mm ka^{-1})	(atoms g^{-1})	(atoms g^{-1})	(g cm^{-2})	(g cm^{-2})	(AD)
'central Valley'	09SRB-E027A-01	2009	0	0	0	0	0	0	0	0	3368	0	0	0	0
	09SRB-E039A-01	2009	0	0	0	0	0	0	0	0	3566	0	0	0	0
	09SRB-E040A-01	2009	0	0	0	0	0	0	0	0	0	0	0	0	0
	09SRB-E092A-01	2009	0	0	0	0	0	0	0	0	5113	0	0	0	0
	09SRB-E025A-01	2009	0	0	0	0	0	0	0	0	0	0	0	0	0
	09SRB-E026A-01	2009	0	0	0	0	0	0	0	0	1999	0	0	0	0
	09SRB-E041A-01	2009	0	0	0	0	0	0	0	0	19808	0	0	0	0
	09SRB-E003A-01	2009	0	0	0	0	0	0	0	0	2805	0	0	0	0
	09SRB-E004A-01	2009	0	0	0	0	0	0	0	0	2163	0	0	0	0
	09SRB-E052A-01	2009	0	0	0	0	0	0	0	0	8703	0	0	0	0
	09SRB-E059A-01	2009	0	0	0	0	0	0	0	0	3770	0	0	0	0
	09SRB-E060A-01	2009	0	0	0	0	0	0	0	0	1979	0	0	0	0
	09SRB-E002A-01	2009	0	0	0	0	0	0	0	0	0	0	0	0	0
	09SRB-A167A-01	2009	0	0	0	0	0	0	0	0	2649	0	0	0	0
	09SRB-A167A-02	2009	0	0	0	0	0	0	0	0	3189	0	0	0	0
	09SRB-A167A-03	2009	0	0	0	0	0	0	0	0	4517	0	0	0	0
Moon Valley	09SRB-E223A-01	2009	0	0	0	0	0	0	0	0	3235	0	0	0	0
	09SRB-E223A-03	2009	0	0	0	0	0	0	0	0	2209	0	0	0	0
	09SRB-E223A-02	2009	0	0	0	0	0	0	0	0	0	0	0	0	0
	09SRB-E224A-01	2009	0	0	0	0	0	0	0	0	3908	0	0	0	0
	09SRB-E224A-02	2009	0	0	0	0	0	0	0	0	2317	0	0	0	0
	09SRB-E224A-03	2009	0	0	0	0	0	0	0	0	7162	0	0	0	0
	09SRB-E283A-01	2009	0	0	0	0	0	0	0	0	5663	0	0	0	0
	09SRB-E284A-01	2009	0	0	0	0	0	0	0	0	2432	0	0	0	0
	09SRB-E284A-02	2009	0	0	0	0	0	0	0	0	2064	0	0	0	0
	09SRB-E284A-03	2009	0	0	0	0	0	0	0	0	3246	0	0	0	0
	09SRB-A351A-01	2009	0	0	0	0	0	0	0	0	2241	0	0	0	0
	09SRB-A352A-01	2009	0	0	0	0	0	0	0	0	2658	0	0	0	0
	09SRB-A353A-01	2009	0	0	0	0	0	0	0	0	2120	0	0	0	0
Tor - batch 1	09SRB-E221A-01	2009	0	0	0	0	0	0	0	0	21389	203488	0	0	0
	09SRB-E221A-02	2009	0	0	0	0	0	0	0	0	34300	201712	0	0	0
	09SRB-E221A-03	2009	0	0	0	0	0	0	0	0	27466	340352	0	0	0
	09SRB-E304A-01	2009	0	0	0	0	0	0	0	0	39954	499150	0	0	0
	09SRB-A186A-01	2009	0	0	0	0	0	0	0	0	42177	431383	0	0	0
	09SRB-A188A-01	2009	0	0	0	0	0	0	0	0	44714	543795	0	0	0
	09SRB-A187A-01	2009	0	0	0	0	0	0	0	0	31801	426645	0	0	0
	09SRB-A355A-01	2009	0	0	0	0	0	0	0	0	40276	523954	0	0	0
	09SRB-A356A-01	2009	0	0	0	0	0	0	0	0	17430	240271	0	0	0
	09SRB-A346A-01	2009	0	0	0	0	0	0	0	0	43680	498343	0	0	0
	09SRB-A348A-01	2009	0	0	0	0	0	0	0	0	28196	381425	0	0	0
	09SRB-A347A-01	2009	0	0	0	0	0	0	0	0	12787	123415	0	0	0
Tor - batch 2	09SRB-E222A-01	2009	0	0	0	0	0	0	0	0	51111	758937	0	0	0
	09SRB-E222A-02	2009	0	0	0	0	0	0	0	0	9194	56483	0	0	0
	09SRB-E222A-03	2009	0	0	0	0	0	0	0	0	37528	577725	0	0	0
	09SRB-E222A-04	2009	0	0	0	0	0	0	0	0	13036	104904	0	0	0
	10SRB-E042A-01	2010	0	0	0	0	0	0	0	0	18576	271920	0	0	0
	10SRB-E064A-01	2010	0	0	0	0	0	0	0	0	17588	272190	0	0	0
	10SRB-E065A-01	2010	0	0	0	0	0	0	0	0	105215	1913620	0	0	0
Tor - batch 3	10SRB-E020A-01	2010	0	0	0	0	0	0	0	0	65118	714003	0	0	0
	10SRB-E021A-01	2010	0	0	0	0	0	0	0	0	60653	857834	0	0	0
	10SRB-E022A-01	2010	0	0	0	0	0	0	0	0	35315	426298	0	0	0
	09SRB-E222A-05	2009	0	0	0	0	0	0	0	0	44702	694521	0	0	0
	09SRB-E222A-06	2009	0	0	0	0	0	0	0	0	5329	69438	0	0	0
	10SRB-E074A-01	2010	0	0	0	0	0	0	0	0	180300	1690868	0	0	0
	10SRB-E066A-01	2010	0	0	0	0	0	0	0	0	83554	1291972	0	0	0

Table A5.1 (*continued*) Input data for CRONUS KU calculator.

CNEF ID	Sample ID	Qtz Mass	Al Carrier Mass	Al Carrier ID	Al Carrier Conc	Al Carrier Density	27Al added	Mass of 100ml-glass flask	Mass of glass flask plus initial solution	Initial Mass of Solution (2% HCl)	Mass of aliquot vial A	Mass of glass flask plus remaining volume of solution
		(g)	(g)	(txt)	(µg/mL)	(g/mL)	(µg 27Al)		2% HCl	in 100 ml	2% HCl	in 95 ml
		40.0000	0.2000	Al carrier	1000	1.01		(g)	(g)	(g)	(g)	(g)
JG2313	blank	0.0000	2.8454	ICP-013-5 Lot H	1000	1.010	2817.23	67.7944	168.6174	100.8230	4.7501	11-Jun-00
JG2383	09SRB-E221A-03	35.2509	1.7299	ICP-013-5 Lot H	1000	1.010	1712.77	67.0047	167.8276	100.8229	4.7471	163.0680
JG2384	09SRB-E304A-01	35.1661	0.5170	ICP-013-5 Lot H	1000	1.010	511.88	67.1405	168.1019	100.9614	4.8147	163.2742
JG2386	09SRB-A186A-01	35.3395	1.7356	ICP-013-5 Lot H	1000	1.010	1718.42	67.4187	168.3115	100.8928	4.6943	163.5924
JG2387	09SRB-A188A-01	36.6153	2.4731	ICP-013-5 Lot H	1000	1.010	2448.61	66.9348	167.8929	100.9581	4.8211	163.0584
JG2390	09SRB-A187A-01	35.0101	2.4867	ICP-013-5 Lot H	1000	1.010	2462.08	66.4917	167.4246	100.9329	4.7652	162.6525
JG2391	09SRB-A355A-01	35.2918	2.4794	ICP-013-5 Lot H	1000	1.010	2454.85	66.8741	169.5705	102.6964	4.8891	164.6722
JG2392	09SRB-A356A-01	35.1482	2.4174	ICP-013-5 Lot H	1000	1.010	2393.47	66.3080	167.2512	100.9432	4.6577	162.5800
JG2393	09SRB-A346A-01	35.1319	2.4810	ICP-013-5 Lot H	1000	1.010	2456.44	66.5908	167.3973	100.8065	4.7696	162.6152
JG2394	09SRB-A348A-01	35.3062	2.8054	ICP-013-5 Lot H	1000	1.010	2777.62	65.2036	166.0705	100.8669	4.8618	161.1953

Values needed to account for dilutions; some repeated from above, some are from dilution before MAXXAM	Dilution before ICP analysis	Mass of aliquot vial A	Mass of aliquot vial A	Fraction of vial A transferred to vial AA	Vial AA diluted	Mass of aliquot vial B	Mass of aliquot vial B	Fraction of vial B transferred to vial BB	Vial BB diluted	Calculation of Al-concentration in vial B based on known mass of carrier added
	CNEF ID	2% HCl	2% HNO3	0.1 ml	10 ml	2% HCl	2% HNO3	0.1 ml	10 ml	
		(g)	(g)	(g)	(g)	(g)	(g)	(g)	(g)	
	JG2313	4.7501	11.3265	0.1222	10.4742	4.4763	11-Jan-00	0.1199	10.2373	
	JG2383	4.7471	11.3336	0.1097	10.2547	4.5242	10.5363	0.1403	10.3396	
	JG2384	4.8147	10.5770	0.1021	10.4419	4.9225	10.8407	0.1158	10.3378	
	JG2386	4.6943	10.8495	0.1070	10.3214	4.8800	11.4118	0.1024	10.1329	
	JG2387	4.8211	10.8917	0.1203	10.9025	4.9094	10.8535	0.1053	10.8819	
	JG2390	4.7652	10.7439	0.1208	10.9166	4.7677	11.4573	0.1276	10.3196	
	JG2391	4.8891	11.0301	0.1360	10.6606	4.8693	11.7301	0.1350	10.0579	
	JG2392	4.6577	11.2797	0.1144	10.2664	4.4109	10.5987	0.1099	10.0393	
	JG2393	4.7696	10.8118	0.1073	10.6289	4.6498	10.9282	0.1329	10.7528	
	JG2394	4.8618	11.1960	0.1231	10.5453	5.0300	10.7612	0.1209	10.4191	

Calculation of Al-concnetration or -mass in solution based on MAXXAM results	ICP-MS Al-calculations	Al conc. in aliquot A (measured MAXXAM)	Al conc. in aliquot A (not diluted)	Mass of Al in aliquot A	Mass of Al in initial solution	Concentration of Al in quartz	Mass of Al in 95 ml solution before addition of carrier (by mass solution)	Mass of Al in 95 ml solution before addition of carrier (by mass Al)	Mass of Al in 95 ml solution after addition of carrier	Mass of Al in target solution (by mass Al taken out in aliquot B)	Mass of Al in target solution (by mass of solution)	Al conc. in aliquot B (measured MAXXAM)
	CNEF ID	(µg/L)	(µg/mL)	(µg Al)	(µg Al)	(µg Al / g)	(µg Al)	(µg Al)	(µg Al)	(µg Al)	(µg Al)	(µg/L)
	JG2313	ND	#VALUE!	#VALUE!	#VALUE!	-	#VALUE!	#VALUE!	2817	2690	2689	140
	JG2381	1400	308	1402	30917	872	29498	29515	30027	28547	28541	1500
	JG2382	800	163	714	16273	456	15551	15559	16068	15297	15294	840
	JG2383	160	36	168	3565	101	3396	3397	5110	4873	4872	300
	JG2384	230	52	246	5165	147	4918	4919	5431	5154	5153	290
	JG2386	170	38	176	3786	107	3609	3610	5328	5063	5062	230
	JG2387	170	35	166	3479	95	3313	3313	5762	5475	5474	260
	JG2390	180	37	173	3665	105	3492	3492	5954	5666	5665	300
	JG2391	180	32	154	3237	92	3082	3083	5537	5269	5266	320
	JG2392	140	30	140	3041	87	2900	2901	5294	5057	5057	250
	JG2393	120	27	127	2689	77	2562	2562	5019	4782	4780	280
	JG2394	150	30	142	2955	84	2812	2813	5590	5306	5304	300
	JG2395	1700	363	1844	36426	956	34578	34582	35088	33474	33468	1700

Table A5.2 Native aluminum data calculation for bedrock samples – batch 1, part 1.

CNEF ID	Sample ID	Mass of remaining volume of solution	Difference between calculated and measured mass of remaining volume of solution	Mass of carrier added to 95 ml solution	Mass of glass flask plus remaining volume of solution incl. carrier	Check weighing of carrier	Mass of aliquot vial B	Mass of glass flask plus remaining volume of solution (with carrier)	Mass of emaining volume of solution (with carrier)	Difference between calculated and measured mass of remaining volume of solution	Ratio of mass between target solution and initioal solution	27Al atoms in target solution (calc. from vial B)
		in 95 ml	in 95 ml		in 95 ml		2% HCl	in 90 ml	in 90 ml	in 80 ml		into target
		(g)	(%)	(g)	(g)	(%)	(g)	(g)	(g)	(%)	(-)	(atoms 27Al)
JG2313	blank	96.0634	0.01%	2.8454	166.6812	0.77%	4.4763	162.1963	94.4019	0.04%	0.9363	6.31E+19
JG2383	09SRB-E221A-03	96.0633	0.01%	1.7299	164.7979	0.00%	4.5242	160.2514	93.2467	0.04%	0.9249	1.06E+20
JG2384	09SRB-E304A-01	96.1337	0.01%	0.5170	163.7912	0.00%	4.9225	158.8497	91.7092	0.03%	0.9084	1.16E+20
JG2386	09SRB-A186A-01	96.1737	0.03%	1.7356	165.3281	0.01%	4.8800	160.4295	93.0108	0.05%	0.9219	1.09E+20
JG2387	09SRB-A188A-01	96.1236	0.01%	2.4731	165.5252	0.25%	4.9094	160.6071	93.6723	0.03%	0.9278	1.23E+20
JG2390	09SRB-A187A-01	96.1608	0.01%	2.4867	165.1279	0.45%	4.7677	160.3527	93.8610	0.03%	0.9299	1.21E+20
JG2391	09SRB-A355A-01	97.7981	0.01%	2.4794	167.1169	1.40%	4.8693	162.237	95.3628	0.06%	0.9286	1.21E+20
JG2392	09SRB-A356A-01	96.2720	0.01%	2.4174	164.9936	0.16%	4.4109	160.572	94.2641	0.03%	0.9338	1.14E+20
JG2393	09SRB-A346A-01	96.0244	0.01%	2.4810	165.0883	0.32%	4.6498	160.414	93.8227	0.05%	0.9307	1.10E+20
JG2394	09SRB-A348A-01	95.9917	0.01%	2.8054	163.9858	0.53%	5.0300	158.938	93.7348	0.05%	0.9293	1.15E+20

Values needed to account for dilutions; some repeated from above, some are from dilution before MAXXAM

Dilution before ICP analysis CNEF ID	Calculated conc. of Al in 95 ml solution added with (µg/mL)	Calculated conc. of Al in vial B (not diluted) added (µg/mL)	Calculated conc. of Al in vial B from meas. Al-conc. (µg/mL)	Difference between measured Al-conc. and (%)
JG2313	29	29	#VALUE!	#VALUE!
JG2383	18	18	53	4%
JG2384	5	5	57	0%
JG2386	18	18	56	5%
JG2387	25	25	60	1%
JG2390	25	25	62	6%
JG2391	25	25	57	2%
JG2392	24	24	55	0%
JG2393	25	25	52	2%
JG2394	28	28	58	5%

Calculation of Al-concnetration or -mass in solution based on MAXXAM results

Estimation of mass of Al in target solution from conc. of vial A plus addition of Al through carrier

ICP-MS Al-calculations CNEF ID	Al conc. in aliquot B (not diluted) (µg/mL)	Mass of Al in aliquot B (µg Al)	Mass of Al in target solution (µg Al)	Mass of Al in target solution of carrier (corrected for mass Al taken out in aliquot B) (µg Al)	Difference between both estimates of mass of Al in target solution (%)	Estimated error MAXXAM meausrement (µg/L)	%
JG2313	30	134	2828	2689	5%	#VALUE!	5.0
JG2381	314	1493	28784	6.00E+19	1%	70	5.0
JG2382	178	822	16317	by mass sol	6%	40	5.0
JG2383	51	231	4754		3%	8	5.0
JG2384	57	278	5177	2690	0%	11.5	5.0
JG2386	53	257	4901	6.00E+19	3%	8.5	5.0
JG2387	59	289	5509	by mass Al in aliquot B	1%	8.5	5.0
JG2390	58	275	5418		5%	9	5.0
JG2391	57	277	5423		3%	9	5.0
JG2392	55	240	5121		1%	7	5.0
JG2393	53	245	4946		3%	6	5.0
JG2394	55	275	5133		3%	75	5.0
JG2395	365	1607	33310		0%	85	5.0

Table A5.2 (*continued*) Native aluminum data calculation for bedrock samples – batch 1, part 1.

CNEF ID	Sample ID	27Al atoms in target solution (calc. from vial A)	27Al atoms in target solution (calc. from average of vial B and vial A)	Difference between values calc. from vial B and vial A	Difference between values calc. from vial B and average of vial B and vial A)	Standard deviation for average of 27Al atoms in target solution		Standard deviation of the mean for 27Al atoms in target solution	ICP measurement error for estimate of 27Al atoms in target solution
		into target (atoms 27Al)	into target (atoms 27Al)	(%)	(%)	into target (atoms 27Al)		into target (atoms 27Al)	(%)
JG2313	blank	6.00E+19	6.16E+19	4.9%	2.4%	2.18E+18	3.54%	1.54E+18	2.5%
JG2383	09SRB-E221A-03	1.09E+20	1.07E+20	2.5%	1.3%	1.89E+18	1.76%	1.33E+18	1.2%
JG2384	09SRB-E304A-01	1.15E+20	1.15E+20	0.4%	0.2%	3.57E+17	0.31%	2.53E+17	0.2%
JG2386	09SRB-A186A-01	1.13E+20	1.11E+20	3.3%	1.6%	2.55E+18	2.29%	1.80E+18	1.6%
JG2387	09SRB-A188A-01	1.22E+20	1.23E+20	0.6%	0.3%	5.42E+17	0.44%	3.83E+17	0.3%
JG2390	09SRB-A187A-01	1.26E+20	1.24E+20	4.6%	2.3%	3.91E+18	3.16%	2.77E+18	2.2%
JG2391	09SRB-A355A-01	1.18E+20	1.19E+20	2.8%	1.4%	2.43E+18	2.04%	1.72E+18	1.4%
JG2392	09SRB-A356A-01	1.13E+20	1.14E+20	1.3%	0.6%	1.01E+18	0.89%	7.15E+17	0.6%
JG2393	09SRB-A346A-01	1.07E+20	1.09E+20	3.3%	1.7%	2.59E+18	2.39%	1.83E+18	1.7%
JG2394	09SRB-A348A-01	1.18E+20	1.16E+20	3.4%	1.7%	2.72E+18	2.34%	1.92E+18	1.7%

Values needed to account for dilutions; some repeated from above, some are from dilution before MAXXAM

Dilution before ICP analysis
CNEF ID
JG2313
JG2383
JG2384
JG2386
JG2387
JG2390
JG2391
JG2392
JG2393
JG2394

Calculation of Al-concnetration or -mass in solution based on MAXXAM results

ICP-MS Al-calculations
CNEF ID
JG2313
JG2381
JG2382
JG2383
JG2384
JG2386
JG2387
JG2390
JG2391
JG2392
JG2393
JG2394
JG2395

Table A5.2 (*continued*) Native aluminum data calculation for bedrock samples – batch 1, part 1.

CNEF ID	Sample ID	Qtz Mass	Al Carrier Mass	Al Carrier ID	Al Carrier Conc	Al Carrier Density	27Al added	Mass of 100ml-glass flask	Mass of glass flask plus initial solution	Initial Mass of Solution	Mass of aliquot vial A	Mass of aliquot vial B	Mass of aliquot vial B with 2 drops carrier	Mass of aliquot vial B diluted
		(g)	(g)	(txt)	(µg/mL)	(g/mL)	(µg 27Al)	[g]	[g]	in 100 ml	in 10 ml	in 5 ml	in 5 ml	in 10 ml
		40.0000	0.2000	Al carrier	1000.00	1.013				(g)	(g)	(g)	(g)	(g)
2381	09SRB-E221A-01	30.0074	0.0000	Lot# 03-16108B	1000	1.010	0.00	66.5890	167.9451	101.3561	9.9958	4.9931	5.0201	10.0188
2382	09SRB-E221A-02	30.1661	0.0000	Lot# 03-16108B	1000	1.010	0.00	66.4903	167.7223	101.2320	10.0092	4.9971	5.0263	10.0270
2395	09SRB-A347A-01	30.0465	0.0000	Lot# 03-16108B	1000	1.010	0.00	67.7306	168.9780	101.2474	10.0219	5.0106	5.0367	10.0233

Re-measurement of Al concentraion in quartz by ICP-MS at DGC on May 15, 2013 - Al in target calculation based on second AMS measurements

CNEF ID	ICP-MS Al-calculations	Al conc. in qtz (ppm)	Mass of Al in qtz dissolved for AMS analysis	Concentration of Al in solution before addition of carrier	Mass of Al in 85 ml solution before addition of carrier (by mass solution)	Mass of Al in 85 ml solution before addition of carrier (reduced for mass Al lost in aliquots A and B)	Concentration of Al in target solution	Total mass of Al in target solution (by mass solution)	Total mass of Al in target solution (reduced for mass Al lost in aliquot C)	Difference between calc. Mass of Al in target solution	2010_Tor1_2 27Al atoms in target solution	2010_Tor1_2 27Al atoms in target solution	2010_Tor1_2 Average of 27Al atoms in target solution
		(µg Al/g)	(µg Al)	(µg Al/g)	(µg Al)	(µg Al)	(µg Al/g)	(µg Al)	(µg Al)	%	(atoms 27Al)	(atoms 27Al)	(atoms 27Al)
	2381-B	755	22651	223	19299	19301	223	18181	18184	0.02%	4.06E+20	4.06E+20	4.06E+20
	2382-B	528	15917	157	13555	13557	157	12768	12770	0.02%	2.85E+20	2.85E+20	2.85E+20
	2395C/X	79	2387	24	2032	2033	24	1914	1915	0.01%	4.27E+19	4.27E+19	4.27E+19

Table A5.3 Native aluminum data calculation for bedrock samples – batch 1, part 2.

CNEF ID	Sample ID	Mass of glass flask plus remaining volume of solution	Mass of remaining volume of solution	Difference between calculated and measured mass of remaining volume of solution	Mass of carrier added to 85 ml solution	Mass of aliquot vial C	Mass of aliquot vial C diluted	Mass of glass flask plus remaining volume of solution (with carrier)	Mass of emaining volume of solution (with carrier)	Difference between calculated and measured mass of remaining volume of solution	Ratio of mass between target solution and initial solution
		in 85 ml	in 85 ml	in 85 ml		in 5 ml	in 10 ml	in 80 ml	in 80 ml	in 80 ml	
		(g)	(g)	(%)	(g)	(g)	(g)	(g)	(g)	(%)	(-)
2381	09SRB-E221A-01	152.9454	86.3564	0.01%	0.0000	4.9975	10.0145	147.945	81.3555	0.02%	0.8027
2382	09SRB-E221A-02	152.7047	86.2144	0.01%	0.0000	5.0053	10.0194	147.697	81.2070	0.02%	0.8022
2395	09SRB-A347A-01	153.9375	86.2069	0.01%	0.0000	5.0059	10.0168	148.927	81.1967	0.02%	0.8020

Re-measurement of Al concentraion in quartz by ICP-MS at DGC on May 15, 2013 - Al in target calculation based on second AMS measurements

CNEF ID	ICP-MS Al-calculations	Standard deviation for average of 27Al atoms in target solution	Standard deviation of the mean for 27Al atoms in target solution	ICP measurement error for estimate of 27Al atoms in target solution	ICP measurement error should be calculated differently: average of two different measurements (i.e. average of two wavelengts -> error)	STDEV / Average
				(%)	(%)	(%)
	2381-B	4.79E+16	3.39E+16	0.01%	0.59%	0.83%
	2382-B	3.16E+16	2.24E+16	0.01%	0.26%	0.36%
	2395C/X	4.40E+15	3.11E+15	0.01%	1.73%	5.98%

Table A5.3 (*continued*) Native aluminum data calculation for bedrock samples – batch 1, part 2.

CNEF ID	SAMPLE ID	Qtz Mass	Al Carrier Mass	Al Carrier ID	Al Carrier Conc	Al Carrier Density	27Al added	Mass of 100ml- glass flask	Mass of glass flask plus initial solution	Initial Mass of Solution	Mass of aliquot vial A	Mass of aliquot vial B
(txt)	(txt)	(g)	(g)	(txt)	(µg/mL)	(g/mL)	(µg 27Al)	[g]	[g]	in 100 ml	in 10 ml	in 5 ml
JG1234	09SRB-E222A-01	40.00	0.20	Al carrier	1000	1.01				(g)	(g)	(g)
JG2420		0.0000	2.9683	LOT # 94-096673J	1000	1.010	2938.91	66.8429	168.0166	101.1737	9.9121	5.0035
JG2526	09SRB-E222A-01	35.0116	1.7429	LOT # 94-096673J	1000	1.010	1725.64	66.3035	167.6248	101.3213	9.9080	5.0097
JG2527	09SRB-E222A-02	35.4640	1.7297	LOT # 94-096673J	1000	1.010	1712.57	68.8753	170.1347	101.2594	9.9173	5.0080
JG2528	09SRB-E222A-03	35.1831	1.7442	LOT # 94-096673J	1000	1.010	1726.93	67.0102	168.4677	101.4575	9.8653	5.0479
JG2529	09SRB-E222A-04	35.0160	1.7420	LOT # 94-096673J	1000	1.010	1724.75	67.7324	169.2417	101.5093	9.9067	5.0267
JG2532	10SRB-E042A-01	35.2063	1.7340	LOT # 94-096673J	1000	1.010	1716.83	66.5889	168.1836	101.5947	9.9587	5.0483
JG2533	10SRB-E064A-01	35.4837	1.8031	LOT # 94-096673J	1000	1.010	1785.25	66.4889	167.9088	101.4199	9.9022	5.0104
JG2534	10SRB-E065A-01	35.5655	2.4867	LOT # 94-096673J	1000	1.010	2462.08	66.7040	168.0902	101.3862	9.9024	5.0203

Re-measurement of Al concentraion in quartz by ICP-MS

ICP-MS Al-calculations	Quartz mass to disolve	Dried, disolve in 10 ml	take about 0.1 ml out	bring up to 10 ml to ICP	ICP MS Al conc. result (ppb)	Al conc. in ICP solution (ppm)	Mass of Al in ICP solution	Mass of Al in inital solution	Al conc. in qtz (ppm)	Mass of Al in qtz dissolved for AMS analysis	Concentration of Al in solution before addition of carrier
CNEF ID	(g)	(g)	(g)	(g)	(µg/L)	(µg/mL)	(µg Al)	(µg Al)	(µg Al/g)	(µg Al)	(µg Al/g)
2420											
2526	1.0493	10.0657	0.2108	10.0825	177	0.177	1.77	84	80	2815	28
2527	1.0713	10.0690	0.2004	10.0324	174	0.174	1.73	87	81	2875	28
2528	1.0180	10.0064	0.2005	10.0235	172	0.172	1.71	85	84	2944	29
2529	1.0665	10.0224	0.1988	9.9981	186	0.186	1.84	93	87	3048	30
2532	1.0332	10.1161	0.1111	9.9968	980	0.980	9.70	883	855	30095	296
2533	0.9991	10.0277	0.1805	9.9966	714	0.714	7.07	393	393	13944	137
2534	1.1503	10.0132	0.1933	10.0928	350	0.350	3.50	181	158	5602	55

Re-measurement of Al concentraion in quartz by ICP-MS at DGC on Feb 6, 2014

ICP-MS Al-calculations	Al conc. in qtz (ppm)	Mass of Al in qtz dissolved for AMS analysis	Concentration of Al in solution before addition of carrier	Mass of Al in 85 ml solution before addition of carrier (by mass solution)	Mass of Al in 85 ml solution before addition of carrier (reduced for mass Al lost in aliquots A and B)	Concentration of Al in target solution	Total mass of Al in target solution (by mass solution)	Total mass of Al in target solution (reduced for mass Al lost in aliquot C)	Difference between calc. Mass of Al in target solution		2010_Tor1_2 27Al atoms in target solution
CNEF ID	(µg Al/g)	(µg Al)	(µg Al/g)	(µg Al)	(µg Al)	(µg Al/g)	(mg Al)	(mg Al)	%		(atoms 27Al)
2527	14	487	5	416	416	24	2007	2007	0.01%		4.48E+19
2529	31	1072	11	914	914	30	2488	2489	0.02%		5.55E+19

Table A5.4 Native aluminum data calculation for bedrock samples – batch 2.

CNEF ID	SAMPLE ID	Mass of aliquot vial B with 2 drops carrier	Mass of aliquot vial B diluted	Mass of glass flask plus remaining volume of solution	Mass of remaining volume of solution	Difference between calculated and measured mass of remaining volume of solution	Mass of carrier added to 95 ml solution	Mass of aliquot vial C	Mass of aliquot vial C diluted	Mass of glass flask plus remaining volume of solution (with carrier)	Mass of remaining volume of solution (with carrier)
(txt) JG1234	(txt) 09SRB-E222A-01	in 5 ml (g)	in 10 ml (g)	in 85 ml (g)	in 85 ml (g)	in 85 ml (%)	(g)	in 5 ml (g)	in 10 ml (g)	in 80 ml (g)	in 80 ml (g)
JG2420		5.0349	10.1181	153.0874	86.2445	0.02%	2.9683	5.0052	10.1571	151.0382	84.1953
JG2526	09SRB-E222A-01	5.0436	10.1648	152.6938	86.3903	0.02%	1.7429	5.0131	10.1863	149.4197	83.1162
JG2527	09SRB-E222A-02	5.0389	10.1040	155.1942	86.3189	0.02%	1.7297	5.0139	10.1150	151.9035	83.0282
JG2528	09SRB-E222A-03	5.0798	10.1496	153.5407	86.5305	0.02%	1.7442	5.0806	10.1489	150.2085	83.1983
JG2529	09SRB-E222A-04	5.0555	10.0839	154.2865	86.5541	0.03%	1.7420	5.0216	10.1396	151.0011	83.2687
JG2532	10SRB-E042A-01	5.0789	10.1488	152.7854	86.1965	0.45%	1.7340	5.0134	10.1172	149.8733	83.2844
JG2533	10SRB-E064A-01	5.0390	10.1832	152.9680	86.4791	0.03%	1.8031	5.0066	10.0983	149.7551	83.2662
JG2534	10SRB-E065A-01	5.0521	10.1324	153.1353	86.4313	0.04%	2.4867	5.0013	10.1289	149.8577	83.1537

Re-measurement of Al concentraion in quartz by ICP-MS

ICP-MS Al-calculations	Mass of Al in 85 ml solution before addition of carrier (by mass solution)	Mass of Al in 85 ml solution before addition of carrier (reduced for mass Al lost in aliquots A and B)	Concentration of Al in target solution	Total mass of Al in target solution (by mass solution)	Total mass of Al in target solution (reduced for mass Al lost in aliquot C)
CNEF ID	(µg Al)	(µg Al)	(µg Al/g)	(µg Al)	(µg Al)
2420			33	2774	2774
2526	2400	2400	47	3891	3891
2527	2451	2451	47	3927	3927
2528	2510	2510	48	3994	3993
2529	2599	2600	49	4078	4079
2532	25662	25668	311	25938	25823
2533	11830	11884	155	12892	12894
2534	4776	4778	81	6771	6833

Re-measurement of Al concentraion in quartz by ICP-MS at DGC on Feb 6, 2014

ICP-MS Al-calculations	2010_Tor1_2 27Al atoms in target solution	2010_Tor1_2 Average of 27Al atoms in target solution	Standard deviation for average of 27Al atoms in target solution	Standard deviation of the mean for 27Al atoms in target solution	ICP measurement error for estimate of 27Al atoms in target solution	ICP measurement error should be calculated differently: average of two different measurements (i.e. average of two wavelengts -> error)	STDEV / Average
CNEF ID	(atoms 27Al)	(atoms 27Al)			(%)	(%)	(%)
2527	4.48E+19	4.48E+19	3.57E+15	2.52E+15	0.01%	10.23%	2.95%
2529	5.55E+19	5.55E+19	6.16E+15	4.36E+15	0.01%	8.56%	2.47%

Table A5.4 (*continued*) Native aluminum data calculation for bedrock samples – batch 2.

CNEF ID	SAMPLE ID	Difference between calculated and measured mass of remaining volume of solution	Ratio of mass between target solution and initial solution	2010_Tor1_2 27Al atoms in target solution	2010_Tor1_2 27Al atoms in target solution	2010_Tor1_2 Average of 27Al atoms in target solution	Standard deviation for average of 27Al atoms in target solution	Standard deviation of the mean for 27Al atoms in target solution	ICP measurement error for estimate of 27Al atoms in target solution
(txt) JG1234	(txt) 09SRB-E222A-01	in 80 ml (%)	(-)	into target (atoms 27Al)	into target (atoms 27Al)	into target (atoms 27Al)	into target (atoms 27Al)	into target (atoms 27Al)	into target (%)
								!Change N!	
JG2420		0.03%	0.83	6.19E+19	6.19E+19	6.19E+19	6.39E+15	4.52E+15	0.0%
JG2526	09SRB-E222A-01	0.02%	0.82	8.68E+19	8.68E+19	8.68E+19	2.88E+15	2.04E+15	0.0%
JG2527	09SRB-E222A-02	0.03%	0.82	~~8.76E+19~~	~~8.76E+19~~	~~8.76E+19~~	~~4.85E+15~~	~~3.43E+15~~	~~0.0%~~
JG2528	09SRB-E222A-03	0.01%	0.82	8.91E+19	8.91E+19	8.91E+19	3.18E+15	2.25E+15	0.0%
JG2529	09SRB-E222A-04	0.03%	0.82	~~9.10E+19~~	~~9.10E+19~~	~~9.10E+19~~	~~4.48E+15~~	~~3.17E+15~~	~~0.0%~~
JG2532	10SRB-E042A-01	0.03%	0.82	5.79E+20	5.76E+20	5.78E+20	1.81E+18	1.28E+18	0.2%
JG2533	10SRB-E064A-01	0.05%	0.82	2.88E+20	2.88E+20	2.88E+20	2.30E+16	1.62E+16	0.0%
JG2534	10SRB-E065A-01	0.96%	0.82	1.51E+20	1.53E+20	1.52E+20	9.80E+17	6.93E+17	0.5%

too low ICP error, but no uncertainty stated my MAXXAM

Re-measurement of Al concentraion in quartz by ICP-MS

ICP-MS Al-calculations

CNEF ID
2420
2526
2527
2528
2529
2532
2533
2534

Re-measurement of Al concentraion in quartz by ICP-MS at DGC on Feb 6, 2014

ICP-MS Al-calculations

CNEF ID
2527
2529

Table A5.4 (*continued*) Native aluminum data calculation for bedrock samples – batch 2.

CNEF ID	Sample ID	Qtz Mass	Al Carrier Mass	Al Carrier ID	Al Carrier Conc	Al Carrier Density	27Al added	Mass of 100ml- glass flask	Mass of glass flask plus initial solution	Initial Mass of Solution	Mass of aliquot vial A	Mass of aliquot vial B	Mass of aliquot vial B with 2 drops carrier	Mass of aliquot vial B diluted	Mass of glass flask plus remaining volume of solution	Mass of remaining volume of solution	Difference between calculated and measured mass of remaining volume of solution
		(g)	(g)	(txt)	(µg/mL)	(g/mL)	(µg 27Al)	[g]	[g]	in 100 ml (g)	in 10 ml (g)	in 5 ml (g)	in 5 ml (g)	in 10 ml (g)	in 85 ml (g)	in 85 ml (g)	in 85 ml (%)
		40.0000	0.2000	Al carrier	1000	1.013											
2423	blank	0.0000	2.9705	Lot# 03-16108B	1000	1.010	2941.09	66.8411	167.9061	101.0650	10.0168	5.0026	5.0292	10.0347	152.8754	86.0343	0.01%
2588	10SRB-E020A-01	35.1812	1.2460	Lot# 03-16108B	1000	1.010	1233.66	67.1376	168.2867	101.1491	10.0035	5.0225	5.0484	10.0278	153.2503	86.1127	0.01%
2589	10SRB-E021A-01	35.5590	0.4842	Lot# 03-16108B	1000	1.010	479.41	68.8721	169.9443	101.0722	10.0189	5.0300	5.0471	9.9927	154.8824	86.0103	0.02%
2590	10SRB-E022A-01	35.2522	1.7386	Lot# 03-16108B	1000	1.010	1721.39	67.4181	168.6731	101.2550	10.0074	5.0054	5.0332	10.0195	153.6480	86.2299	0.01%
2530	09SRB-E222A-05	34.7466	1.7469	Lot# 03-16108B	1000	1.010	1729.60	67.1808	168.3829	101.2021	10.0525	5.0143	5.0416	10.0079	153.3037	86.1229	0.01%
2531	09SRB-E222A-06	35.0731	0.5117	Lot# 03-16108B	1000	1.010	506.63	66.3006	167.5321	101.2315	9.9953	5.0104	5.0355	10.0003	152.5151	86.2145	0.01%
2536	10SRB-E074A-01	30.4142	0.0000	Lot# 03-16108B	1000	1.010	0.00	67.3498	168.6547	101.3049	10.0037	5.0005	5.0256	10.0170	153.6404	86.2906	0.01%
2535	10SRB-E066A-01	35.1074	0.5160	Lot# 03-16108B	1000	1.010	510.89	66.7016	167.8980	101.1964	10.0221	5.0068	5.0338	10.0046	152.6808	85.9792	0.22%

Values needed to account for dilutions; some repeated from above, some are from dilution before MAXXAM

CNEF ID	Dilution before ICP analysis	Mass of aliquot vial A	Fraction of vial A transferred to vial AA	Vial AA diluted	Mass of aliquot vial B with 2 drops carrier	Mass of aliquot vial B diluted	Fraction of vial B transferred to vial BB	Vial BB diluted	Mass of aliquot vial C	Mass of aliquot vial C diluted	Fraction of vial C transferred to vial CC	Vial CC diluted
		in 10 ml (g)	0.5 ml (g)	10 ml (g)	in 5 ml (g)	in 10 ml (g)	0.2 ml (g)	10 ml (g)	in 5 ml (g)	in 10 ml (g)	0.1 ml (g)	10 ml (g)
2423		10.0168	0.5121	10.0776	5.0292	10.0347	0.2101	10.1537	5.0003	10.0188	0.0993	10.3764
2588		10.0035	0.5139	10.2592	5.0484	10.0278	0.2125	10.3465	5.0580	10.0152	0.1058	10.0772
2589		10.0189	0.5032	10.1484	5.0471	9.9927	0.2111	10.2388	5.0128	10.0191	0.1078	10.1177
2590		10.0074	0.5188	10.1055	5.0332	10.0195	0.1983	10.0671	5.0518	9.9992	0.1061	10.1031
2530		10.0525	0.5095	10.1305	5.0416	10.0079	0.2053	10.2857	5.0622	10.0400	0.1067	10.0340
2531		9.9953	0.5086	10.0905	5.0355	10.0003	0.2067	10.1283	5.0236	10.0175	0.1047	10.0490
2536		10.0037	0.5104	10.0989	5.0256	10.0170	0.2058	10.0415	5.0255	10.0299	0.1071	10.0213
2535		10.0221	0.5049	10.0352	5.0338	10.0046	0.2038	10.0275	5.0432	10.1945	0.1066	10.1712
2381		9.9958	0.5084	10.0673	5.0201	10.0188	0.2081	10.1797	4.9975	10.0145	0.1125	10.7846
2382		10.0092	0.5106	10.3520	5.0263	10.0270	0.2080	10.9312	5.0053	10.0194	0.1084	10.2792
2395		10.0219	0.5047	10.0609	5.0367	10.0233	0.2023	10.1865	5.0059	10.0168	0.1065	10.3884

Estimation of mass of Al in target solution from conc. of vial A plus addition of Al through carrier

Estimation of n

CNEF ID	Calculation of Al-concnetration or -mass in solution based on MAXXAM results	Al conc. in aliquot A (measured MAXXAM)	Al conc. in aliquot A (not diluted)	Mass of Al in aliquot A	Mass of Al in initial solution	Concentration of Al in quartz	Mass of Al in 85 ml solution before addition of carrier (by mass	Mass of Al in 85 ml solution before addition of carrier (by mass Al)	Mass of Al in 85 ml solution after addition of carrier (by mass solution)	Mass of Al in 85 ml solution after addition of carrier (by mass Al)	Mass of Al in target solution (by mass of solution)	Mass of Al in target solution (by mass Al taken out in aliquot C)	Al conc. in aliquot B (measured MAXXAM)	Al conc. in aliquot B (not diluted)	Mass of Al in aliquot B	Mass of Al in aliquot B before addition of two drops of carrier	Mass of Al in 85 ml solution before addition of carrier (by mass
		(µg/L)	(µg/mL)	(µg Al)	(µg Al)	(µg Al / g)	(µg Al)	(µg Al)	(µg Al)	(µg Al)	(µg Al)	(µg Al)	(µg/L)	(µg/mL)	(µg Al)	(µg Al)	(µg Al)
2423		ND	#VALUE!	#VALUE!	#VALUE!	-	#VALUE!	#VALUE!	2941	2941	2776	2776	58	6	28	2	28
2588		1190	24	235	2379	68	2025	2026	3259	3259	3070	3071	312	30	151	125	2146
2589		1180	24	236	2381	67	2027	2027	2506	2506	2361	2361	293	28	141	124	2115
2590		1830	36	353	3574	101	3043	3044	4765	4765	4491	4491	311	31	157	129	2224
2530		1090	22	216	2172	62	1848	1848	3578	3578	3371	3372	285	28	141	114	1966
2531		7800	155	1531	15510	442	13210	13211	13716	13718	12921	12923	1380	134	670	645	11093
2536		21200	419	4155	42073	1383	35838	35842	35838	35842	33752	33755	3750	365	1815	1790	30886
2535		4500	89	888	8961	255	7614	7631	8125	8141	7682	7667	906	89	442	415	7124

Re-measurement of Al concentraion in quartz by ICP-MS at DGC on May 15, 2013

CNEF ID	ICP-MS Al-calculations	Al conc. in qtz (ppm)	Mass of Al in qtz dissolved for AMS analysis	Concentration of Al in solution before addition of carrier	Mass of Al in 85 ml solution before addition of carrier (by mass solution)	Mass of Al in 85 ml solution before addition of carrier (reduced for mass Al lost in aliquots A and B)	Concentration of Al in target solution	Total mass of Al in target solution (by mass solution)	Total mass of Al in target solution (reduced for mass Al lost in aliquot C)	Difference between calc. Mass of Al in target solution	2010_Tor1_2 27Al atoms in target solution	2010_Tor1_2 27Al atoms in target solution	2010_Tor1_2 Average of 27Al atoms in target solution	Standard deviation for average of 27Al atoms in target solution	Standard deviation of the mean for 27Al atoms in target solution	ICP measurement error for estimate of 27Al atoms in target solution
		(µg Al/g)	(µg Al)	(µg Al/g)	(µg Al)	(µg Al)	(µg Al/g)	(mg Al)	(mg Al)	%	(atoms 27Al)	(atoms 27Al)	(atoms 27Al)	(atoms 27Al)	(atoms 27Al)	(%)
2531-B		364	12765	126	10871	10873	131	10717	10720	0.03%	2.39E+20	2.39E+20	2.39E+20	4.60E+16	3.25E+16	0.01%
2536-B		2218	67462	666	57463	57470	666	54113	54123	0.02%	1.21E+21	1.21E+21	1.21E+21	1.57E+17	1.11E+17	0.01%

Table A5.5 Native aluminum data calculation for bedrock samples – batch 3.

CNEF ID	Sample ID	Mass of carrier added to 85 ml solution	Mass of aliquot vial C	Mass of aliquot vial C diluted	Mass of glass flask plus remaining volume of solution (with carrier)	Mass of emaining volume of solution (with carrier)	Difference between calculated and measured mass of remaining volume of solution	Ratio of mass between target solution and initial solution	27Al atoms in target solution (calc. from vial A)	27Al atoms in target solution (calc. from vial B)	27Al atoms in target solution (calc. from vial C)	27Al atoms in target solution (calc. from average of all vials)	Standard deviation for average of 27Al atoms in target solution	Standard deviation of the mean for 27Al atoms in target solution	ICP measurement error for estimate of 27Al atoms in target solution
			in 5 ml	in 10 ml	in 80 ml	in 80 ml	in 80 ml		into target	into target	into target	into target	into target	into target	into target
		(g)	(g)	(g)	(g)	(g)	(%)	(-)	(atoms 27Al)	(atoms 27Al)	(atoms 27Al)	(atoms 27Al)	(atoms 27Al)	(atoms 27Al)	(%)
														lChange NI	
2423	blank	2.9705	5.0003	10.0188	150.8357	83.9946	0.03%	0.8311	6.20E+19	6.25E+19	6.41E+19	6.29E+19	1.12E+18	6.48E+17	1.0%
2588	10SRB-E020A-01	1.2460	5.0580	10.0152	149.4246	82.2870	0.03%	0.8135	6.85E+19	7.11E+19	7.00E+19	6.99E+19	1.27E+18	7.34E+17	1.1%
2589	10SRB-E021A-01	0.4842	5.0128	10.0191	150.3426	81.4705	0.03%	0.8061	5.27E+19	5.45E+19	5.47E+19	5.40E+19	1.12E+18	6.45E+17	1.2%
2590	10SRB-E022A-01	1.7386	5.0518	9.9992	150.3217	82.9036	0.03%	0.8188	1.00E+20	8.30E+19	8.08E+19	8.19E+19	1.56E+18	1.10E+18	1.3%
2530	09SRB-E222A-05	1.7469	5.0622	10.0400	149.9754	82.7946	0.03%	0.8181	7.53E+19	7.77E+19	7.95E+19	7.75E+19	2.14E+18	1.23E+18	1.6%
2531	09SRB-E222A-06	0.5117	5.0236	10.0175	147.9912	81.6906	0.03%	0.8070	~~2.88E+20~~	~~2.44E+20~~	~~2.52E+20~~	~~2.48E+20~~	~~5.39E+18~~	~~2.81E+18~~	~~1.5%~~
2536	10SRB-E074A-01	0.0000	5.0255	10.0299	148.6095	81.2597	0.02%	0.8021	~~7.53E+20~~	~~6.49E+20~~	~~6.30E+20~~	~~6.40E+20~~	~~1.33E+19~~	~~9.38E+18~~	~~1.5%~~
2535	10SRB-E066A-01	0.5160	5.0432	10.1945	148.3189	81.6173	0.03%	0.8065	1.71E+20	1.60E+20	1.80E+20	1.76E+20	6.42E+18	4.54E+18	2.6%

red values excluded from average and std dev

Values needed to account for dilutions; some repeated from above, some are from dilution before MAXXAM

CNEF ID	Dilution before ICP analysis
2423	
2588	
2589	
2590	
2530	
2531	
2536	
2535	
2381	
2382	
2395	

ass of Al in target solution from conc. of vial B plus addition of Al through carrier

Calculation of Al-concnetration or -mass in solution based on MAXXAM results	Mass of Al in 85 ml solution after addition of carrier	Mass of Al in target solution (by mass Al taken out in aliquot C)	Mass of Al in target solution (by mass of solution)	Al conc. in aliquot C (measured MAXXAM)	Al conc. in aliquot C (not diluted)	Mass of Al in aliquot C	Mass of Al in target solution	Mass of Al in target solution of carrier (corrected for mass Al taken out in aliquot	Difference between both estimates of mass of Al in target solution from	Difference between both estimates of mass of Al in target solution from
CNEF ID	(µg Al)	(µg Al)	(µg Al)	(µg/L)	(µg/mL)	(µg Al)	(µg Al)	(µg Al)		(%)
2423	2969	2802	2802	165	35	171	2873	2776	3%	2%
2588	3380	3184	3184	204	38	193	3135	6.19E+19	2%	2%
2589	2594	2444	2443	162	30	151	2451	by mass sol	4%	0%
2590	3945	3719	3718	234	44	221	3620		24%	3%
2530	3695	3483	3482	233	43	218	3562	2776	5%	2%
2531	11600	10928	10926	728	139	693	11269	6.20E+19	15%	3%
2536	30886	29087	29085	1880	351	1747	28246	by mass Al in	20%	3%
2535	7635	7189	7204	518	100	499	8074	aliquot C	5%	11%

Re-measurement of Al concentraion in quartz by ICP-MS at DGC on May 15, 2013

ICP-MS Al-calculations	ICP measurement error should be calculated differently: average of two different measurements (i.e. average of two wavelengts -> error)	STDEV / Average
CNEF ID	(%)	(%)
2531-B	0.42%	0.59%
2536-B	1.66%	2.34%

Table A5.5 (*continued*) Native aluminum data calculation for bedrock samples – batch 3.

A5.2 CHEMISTRY WORKSHEETS

A5.2.1 Boulder Data for Chapter 3

Chemistry worksheets of boulders from 'central valley'

WS4_QtzDissolution p1

This worksheet outlines the steps for dissolving quartz and adding Be carrier.

Chemist: AM/GY **Date:** 02/02/2010

	1	2	3	4	5	6	7	8
CNEF ID	2396	2397	2398	2400	2402	2403	2404	
Sample ID	09SRB-E027A-01	09SRB-E039A-01	09SRB-E040A-01	09SRB-E092A-01	09SRB-E025A-01	09SRB-E026A-01	09SRB-E041A-01	
300 ml vessel ID	B2	B3	B5	B6	B8	B9	B10	
Beryl Carrier ID	Be Carrier Bottle 2							
Al Carrier ID	N/A..No Al data needed							
Mass 300 ml vessel	10.4058	10.1035	10.1965	10.1222	10.4041	10.4134	10.4240	
Mass 40g quartz	35.5406	36.0183	36.2254	35.3615	35.0693	35.8344	35.4114	
Mass Be carrier	0.1932	0.1932	0.2046	0.1975	0.2129	0.1939	0.1933	
Mass Al Carrier	NO Al data for this group							

1. Add 20 ml conc. HF and 2 ml HClO4 per 5 g of quartz
2. Add 5 ml Aqua Regia
3. Heat at 100-125o C until quartz dissolves, add HF if needed
4. Raise to 200o C and evaporate to dryness
5. Add 5 ml HClO4 and evaporate to dryness
6. Add 8 to 10 ml conc. HNO3, swirl, and evaporate to dryness
7. Dissolved dried sample in 20 ml of 2% HCl

Comments

B17: 45ml HF + 50ml AR + 8ml HClO4; B23: 110ml HF + 50ml AR + 8ml HClO4;
all other plus blank: 140ml HF + 50ml AR + 8 HClO4
Feb 03 9:15 am, all dissolved, open lid, to dry at 200°C, not much residue
Feb 04 8:30 am, 5ml HClO4, rinse with dionized water
3:40 pm, add 8-10ml HNO3, down to 110°C -> to dry
B14 white, large, full bottom of jar; B15 small, brown; B3 small brown; B6 small white/brown;
B5 small brown; B2 small, dark brown; B21 small, light brown; B17 small, light brown;
B9 small, white; B23 small, brown; B31 clean, tiny; B30 small, light brown; B10 small, brown;
B8 large, white, full bottom

WS4_QtzDissolution p2

This worksheet outlines the steps for dissolving quartz and adding Be carrier.

Chemist: AM/GY **Date:** 02/02/2010

	1	2	3	4	5	6	7	8
CNEF ID	2406	2407	2408	2409	2410	2412	2415	
Sample ID	09SRB-E003A-01	09SRB-E004A-01	09SRB-E052A-01	09SRB-E059A-01	09SRB-E060A-01	09SRB-E002A-01	Blank	
300 ml vessel ID	B14	B15	B17	B21	B23	B30	B31	
Beryl Carrier ID	Be Carrier bottle 2							
Al Carrier ID	N/A							
Mass 300 ml vessel	10.6022	10.1103	10.1881	10.2695	10.4052	10.3925	150.1907	
Mass 40g quartz	35.7158	35.4866	11.1915	36.1225	27.2192	35.0875	0.0000	
Mass Be carrier	0.2003	0.1906	0.1821	0.2014	0.1938	0.2023	0.1990	
Mass Al Carrier	Add Al carrier next step. With Aliquot, Nov 2009							

1. Add 20 ml conc. HF and 2 ml HClO4 per 5 g of quartz
2. Add 5 ml Aqua Regia
3. Heat at 100-125o C until quartz dissolves, add HF if needed
4. Raise to 200o C and evaporate to dryness
5. Add 5 ml HClO4 and evaporate to dryness
6. Add 8 to 10 ml conc. HNO3, swirl, and evaporate to dryness
7. Dissolved dried sample in 20 ml of 2% HCl

Comments

B17: 45ml HF + 50ml AR + 8ml HClO4; B23: 110ml HF + 50ml AR + 8ml HClO4;
all other plus blank: 140ml HF + 50ml AR + 8 HClO4
Feb 03 9:15 am, all dissolved, open lid, to dry at 200°C, not much residue
Feb 04 8:30 am, 5ml HClO4, rinse with dionized water
3:40 pm, add 8-10ml HNO3, down to 110°C -> to dry
B14 white, large, full bottom of jar; B15 small, brown; B3 small brown; B6 small white/brown;
B5 small brown; B2 small, dark brown; B21 small, light brown; B17 small, light brown;
B9 small, white; B23 small, brown; B31 clean, tiny; B30 small, light brown; B10 small, brown;
B8 large, white, full bottom

WS6_Anion Column Chemistry p1

This worksheet outlines the steps for the Anion Column Chemistry (2ml size small column)

Chemist: GY/AM **Date:** 02/09/2010

---

1. Evaporate 20 ml to dryness at 100-120°C (will take at least 3 hrs)
2. Dissolve in 10 ml 9 N HCl (let stand for several hours)
3. Transfer to 15 ml centrifuge tubes, rinse digestion vessels with 9 N HCl to bring volume in tube to 10 ml
4. Centrifuge at 1500 rpm or higher for minimum of 10 minutes
5. Allow any 9 N HCl in columns to drain out; discard

Column ID	1	2	3	4	5	6	7	8
Vessel	B2	B3	B5	B6	B8	B9	B10	
CNEF ID	2396	2397	2398	2400	2402	2403	2404	
Sample ID	09SRB-E027A-01	09SRB-E039A-01	09SRB-E040A-01	09SRB-E092A-01	09SRB-E025A-01	09SRB-E026A-01	09SRB-E041A-01	

6. With stopcock closed, pipet sample (avoid residue) onto 2ml size columns.
7. Collect sample in same 300 ml teflon vessel.
8. Elute with 10 ml 9 N HCl, and collect that, close stopcock
9. 5 ml 4.5 N HCl, collect Anion Supernate in labeled 100 ml bottle
10. 10 ml 1 N HCl, collect Anion Supernate
11. 50 ml deionized water. Discard.
12. CONDITION ANION COLUMN
    - (bottle A1) 10 ml 1N HCl, discard
    - (bottle A2) 10 ml 4.5 N HCl, discard
    - (bottle A3) 10 ml 9 N HCl, discard, but retain acid approx. 2 mm above resin

Comments

Feb 09	B5 large redbrown residue; B8 large transparent 'foamy' residue; B9 very small white residue
Feb 09	Run 14 Anion columns. 6 columns have been used once (Alan's) B3-B10; 8 new columns with new resin B2, B14-B31
Feb 10	B14 large white to transparent 'foamy' residue; B15/B17/B21 red-brown residue; B23 red-brown residue, large

WS6_Anion Column Chemistry p2

This worksheet outlines the steps for the Anion Column Chemistry (2ml size small column)

Chemist: GY/AM **Date:** 02/09/2010

---

1. Evaporate 20 ml to dryness at 100-120°C (will take at least 3 hrs)
2. Dissolve in 10 ml 9 N HCl (let stand for several hours)
3. Transfer to 15 ml centrifuge tubes, rinse digestion vessels with 9 N HCl to bring volume in tube to 10 ml
4. Centrifuge at 1500 rpm or higher for minimum of 10 minutes
5. Allow any 9 N HCl in columns to drain out; discard

Column ID	1	2	3	4	5	6	7	8
Vessel	B14	B15	B17	B21	B23	B30	B31	
CNEF ID	2406	2407	2408	2409	2410	2412	2415	
Sample ID	09SRB-E003A-01	09SRB-E004A-01	09SRB-E052A-01	09SRB-E059A-01	09SRB-E060A-01	09SRB-E002A-01	Blank	

6. With stopcock closed, pipet sample (avoid residue) onto 2ml size columns.
7. Collect sample in same 300 ml teflon vessel.
8. Elute with 10 ml 9 N HCl, and collect that, close stopcock
9. 5 ml 4.5 N HCl, collect Anion Supernate in labeled 100 ml bottle
10. 10 ml 1 N HCl, collect Anion Supernate
11. 50 ml deionized water. Discard.
12. CONDITION ANION COLUMN
    - (bottle A1) 10 ml 1 N HCl, discard
    - (bottle A2) 10 ml 4.5 N HCl, discard
    - (bottle A3) 10 ml 9 N HCl, discard, but retain acid approx. 2 mm above resin

Comments

Feb 09	B5 large redbrown residue; B8 large transparent 'foamy' residue; B9 very small white residue
Feb 09	Run 14 Anion columns. 6 columns have been used once (Alan's) B3-B10; 8 new columns with new resin B2, B14-B31
Feb 10	B14 large white to transparent 'foamy' residue; B15/B17/B21 red-brown residue; B23 red-brown residue, large

WS7_Controlled Precipitate p1

This worksheet outlines the steps for the controlled precipitation chemistry

Chemist: GY/AM **Date:** 02/10/2010

---

1 Evaporate "anion" elute to dryness at 125°C
2 Dissolve in 10 ml of a 1:1 solution of 0.5 N HCl and 2% NH_4Cl
3 Transfer to 15 ml centrifuge, centrifuge for 10 minutes
4 Decant into clean test tube, heat in water bath at 60°C
5 Add drops of 1:1 NH_4OH:H_2O to pH=9.2 (5 drops first then single)
6 Centrifuge for 15 minutes
7 Check pH of liquid, if less than pH=7, redo step 5
8 Decant, save with Anion Supernate
9 Wash with deionized water, vortex, centrifuge, decant
10 Wash with deionized water, vortex, centrifuge, decant
11 Wash with deionized water, vortex, centrifuge, decant

CNEF ID	2396	2397	2398	2400	2402	2403	2404	
Vessel	B2	B3	B5	B6	B8	B9	B10	
Sample ID	09SRB-E027A-01	09SRB-E039A-01	09SRB-E040A-01	09SRB-E092A-01	09SRB-E025A-01	09SRB-E026A-01	09SRB-E041A-01	
Approx. vol. Ptte	0.2	0.3	0.5	0.4	0.5	0.3	0.3	

Comments

Residue B8 white; B14 white; B31 blank, brown gel color (new resin, black before disolving)
All other gels are light brown color (new resin for anion columns)

WS7_Controlled Precipitate p2

This worksheet outlines the steps for the controlled precipitation chemistry

Chemist: GY/AM **Date:** 02/10/2010

---

1 Evaporate "anion" elute to dryness at 125°C
2 Dissolve in 10 ml of a 1:1 solution of 0.5 N HCl and 2% NH_4Cl
3 Transfer to 15 ml centrifuge, centrifuge for 10 minutes
4 Decant into clean test tube, heat in water bath at 60°C
5 Add drops of 1:1 NH_4OH:H_2O to pH=9.2 (5 drops first then single)
6 Centrifuge for 15 minutes
7 Check pH of liquid, if less than pH=7, redo step 5
8 Decant, save with Anion Supernate
9 Wash with deionized water, vortex, centrifuge, decant
10 Wash with deionized water, vortex, centrifuge, decant
11 Wash with deionized water, vortex, centrifuge, decant

CNEF ID	2406	2407	2408	2409	2410	2412	2415	
Vessel	B14	B15	B17	B21	B23	B30	B31	
Sample ID	09SRB-E003A-01	09SRB-E004A-01	09SRB-E052A-01	09SRB-E059A-01	09SRB-E060A-01	09SRB-E002A-01	Blank	
Approx. vol. Ptte	3.5	0.5	0.3	0.8	0.5	0.3	0.2	

Comments

Residue B8 white; B14 white; B31 blank, brown gel color (new resin, black before disolving)
All other gels are light brown color (new resin for anion columns)

WS8_Cation Column Chemistry p1

This worksheet outlines the steps for the Cation Column Chemistry

Chemist: GY/AM **Date:** **02/11/2010**
morning

1. Dissolve in 5 ml conc. HCl and evaporate to dryness at 125°C
2. Redissolve in 2.5 ml 1 N HCl and 2.5 ml 0.5 N HCl
3. Transfer to centrifuge tube, rinse with 1 ml 0.5 N, and centrifuge

Column ID	1	2	3	4	5	6	7	8
Vessel	B2	B3	B5	B6	B8	B9	B10	
CNEF ID	2396	2397	2398	2400	2402	2403	2404	
Sample ID	09SRB-E027A-01	09SRB-E039A-01	09SRB-E040A-01	09SRB-E092A-01	09SRB-E025A-01	09SRB-E026A-01	09SRB-E041A-01	

4. Pipette all of the sample into designated conditioned cation column, 17ml
5. Discard the eluant. Add 285 ml 0.5 N HCL (Bottle C6)
6. Drain the column, discard the first 300 ml of eluant
7. Add 60 ml of 0.5 N HCl, (Bottle C7), Collect eluant as Cation Supernate
8. Add 65 ml of 0.5 N HCl, (Bottle C8), Save it as Be-Sample
9. Add 120 ml 1N HCl (bottle C9)
10. Save this as Be-sample as well.
11. Add 80 ml 4.5 N HCl (bottle C10), save the eluant as Al sample.
12. CONDITION CATION COLUMN

(bottle C1) 100 ml 9 N HCl
(bottle C2) 50 ml 4.5 N HCl
(bottle C3) 50 ml 1 N HCl
(bottle C4) 50 ml water
(bottle C5) 100 ml 0.5 N HCl

* 17 ml Column

WS8_Cation Column Chemistry p2

This worksheet outlines the steps for the Cation Column Chemistry

Chemist: GY/AM **Date:** **02/11/2010**
afternoon

1. Dissolve in 5 ml conc. HCl and evaporate to dryness at 125°C
2. Redissolve in 2.5 ml 1 N HCl and 2.5 ml 0.5 N HCl
3. Transfer to centrifuge tube, rinse with 1 ml 0.5 N, and centrifuge

Column ID	1	2	3	4	5	6	7	8
Vessel	B14	B15	B17	B21	B23	B30	B31	
CNEF ID	2406	2407	2408	2409	2410	2412	2415	
Sample ID	09SRB-E003A-01	09SRB-E004A-01	09SRB-E052A-01	09SRB-E059A-01	09SRB-E060A-01	09SRB-E002A-01	Blank	

4. Pipette all of the sample into designated conditioned cation column, 17ml
5. Discard the eluant. Add 285 ml 0.5 N HCL (Bottle C6)
6. Drain the column, discard the first 300 ml of eluant
7. Add 60 ml of 0.5 N HCl, (Bottle C7), Collect eluant as Cation Supernate
8. Add 65 ml of 0.5 N HCl, (Bottle C8), Save it as Be-Sample
9. Add 120 ml 1N HCl (bottle C9)
10. Save this as Be-sample as well.
11. Add 80 ml 4.5 N HCl (bottle C10), save the eluant as Al sample.
12. CONDITION CATION COLUMN

(bottle C1) 100 ml 9 N HCl
(bottle C2) 50 ml 4.5 N HCl
(bottle C3) 50 ml 1 N HCl
(bottle C4) 50 ml water
(bottle C5) 100 ml 0.5 N HCl

* 17 ml Column

WS9_Be Sample Chemistry p1

This worksheet outlines the steps to prepare the BeO sample

Chemist: GY/AM **Date:** 02/12/2010

---

1. Evaporate Be Sample from column in wiped digestion vessels at 125°C
2. Add 2-5 ml 20% perchloric and evaporate at 200oC
3. Again, add 2-5 ml 20% perchloric and evaporate at 200°C
4. Dissolve sample in 10 ml of 0.5 N HCl (optima grade)
5. Transfer to 15 ml centrifuge tube
6. Centrifuge and decant into clean centrifuge tube
7. Heat centrifuge tubes in water bath at 60°C
8. Precipitate $Be(OH)_2$ using Matheson ultimate grade ammonia gas
   Gently bubble NH_3 with clean pipet tip on hose
   for ca.15 bubbles, or ca. 8-12 sec until ptte forms
   Optimum pH=9.2; 1N HCl may be added
9. Centrifuge 15 min., decant (save and redo $\square_8$ if pH of liquid is < 8)
10. Wash with water, vortex, centrifuge for 10 min, and decant
11. Record mass quartz vials, label, and place them in furnace holder

CNEF ID	2396	2397	2398	2400	2402	2403	2404	
Vessel	B2	B3	B5	B6	B8	B9	B10	
Sample ID	09SRB-E027A-01	09SRB-E039A-01	09SRB-E040A-01	09SRB-E092A-01	09SRB-E025A-01	09SRB-E026A-01	09SRB-E041A-01	
Mass Qtz Vial	2.6393	2.5921	2.5430	2.5664	2.5438	2.6947	2.4426	
Mass Vial+Spl	2.6404	2.5924	2.5434	2.5661	2.5435	2.6948	2.4414	
Mass Spl	0.0011	0.0003	0.0004	-0.0003	-0.0003	0.0001	-0.0012	

12. Add 1 small drop of water with micropipet, slurry precipitate
13. Transfer sample into quartz vial, cover with quartz lid
14. Turn on Bunsen Burner, dry the gel carefully.
15. Burn the Be(OH)2 gel on bunsen burner at least 2 mins, at blue flame.
16. Convert to BeO
17. Determine mass of vial + sample

WS9_Be Sample Chemistry p2

This worksheet outlines the steps to prepare the BeO sample

Chemist: GY/AM **Date:** 02/12/2010

---

1. Evaporate Be Sample from column in wiped digestion vessels at 125°C
2. Add 2-5 ml 20% perchloric and evaporate at 200oC
3. Again, add 2-5 ml 20% perchloric and evaporate at 200°C
4. Dissolve sample in 10 ml of 0.5 N HCl (optima grade)
5. Transfer to 15 ml centrifuge tube
6. Centrifuge and decant into clean centrifuge tube
7. Heat centrifuge tubes in water bath at 60°C
8. Precipitate $Be(OH)_2$ using Matheson ultimate grade ammonia gas
   Gently bubble NH_3 with clean pipet tip on hose
   for ca.15 bubbles, or ca. 8-12 sec until ptte forms
   Optimum pH=9.2; 1N HCl may be added
9. Centrifuge 15 min., decant (save and redo 8 if pH of liquid is < 8)
10. Wash with water, vortex, centrifuge for 10 min, and decant
11. Record mass quartz vials, label, and place them in furnace holder

CNEF ID	2406	2407	2408	2409	2410	2412	2415	
Vessel	B14	B15	B17	B21	B23	B30	B31	
Sample ID	09SRB-E003A-01	09SRB-E004A-01	09SRB-E052A-01	09SRB-E059A-01	09SRB-E060A-01	09SRB-E002A-01	Blank	
Mass Qtz Vial	2.6548	2.6043	2.4908	2.7072	2.6052	2.5822	2.5394	
Mass Vial+Spl	2.6559	2.6038	2.4900	2.7064	2.6058	2.5827	2.5390	
Mass Spl	0.0011	-0.0005	-0.0008	-0.0008	0.0006	0.0005	-0.0004	

12. Add 1 small drop of water with micropipet, slurry precipitate
13. Transfer sample into quartz vial, cover with quartz lid
14. Turn on Bunsen Burner, dry the gel carefully.
15. Burn the Be(OH)2 gel on bunsen burner at least 2 mins, at blue flame.
16. Convert to BeO
17. Determine mass of vial + sample

WS4_QtzDissolution p1

This worksheet outlines the steps for dissolving quartz and adding Be carrier.

Chemist: GY **Date:** 01/01/2010

	1	2	3	4	5	6	7	8
CNEF ID	2375	2376	2377	2378	2379	2380	2371	2372
Sample ID	09SRB-E223A-01	09SRB-E223A-03	09SRB-E223A-02	09SRB-E224A-01	09SRB-E224A-02	09SRB-E224A-03	09SRB-E283A-01	09SRB-E284A-01
300 ml vessel ID	B1	B3	B6	B8	B11	B12	B14	B20
Beryl Carrier ID	Be Carrier Bottle 2							
Al Carrier ID	N/A..No Al data needed							
Mass 300 ml vessel	10.4296	10.4327	10.4156	10.4113	10.4303	10.1189	10.1435	10.4324
Mass 40g quartz	36.2755	37.6230	37.0617	37.3268	37.5235	36.5319	38.3565	36.7188
Mass Be carrier	0.2037	0.1994	0.2025	0.1938	0.2005	0.2047	0.2011	0.2055
Mass Al Carrier	NO Al data for this group							

1. Add 20 ml conc. HF and 2 ml HClO4 per 5 g of quartz
2. Add 5 ml Aqua Regia
3. Heat at 100-125°C until quartz dissolves, add HF if needed
4. Raise to 200°C and evaporate to dryness
5. Add 5 ml HClO4 and evaporate to dryness
6. Add 8 to 10 ml conc. HNO3, swirl, and evaporate to dryness
7. Dissolved dried sample in 20 ml of 2% HCl

Comments

Omini trace HF, HNO3, HCl, HClO4
Jan 04 140ml HF, 50ml AR, 8ml HClO4
Jan 05 All dissolved, 200°C 9:00 am, no crust, clean
Rinse all tubes, pipete with 2% HNO3
Jan 06 2:00 pm, Add ~3-5ml HClO4. Rinse with dionized water, 200°C to dry
B30 large, thin, yellow; B23 small, yellow; B27 small, yellow; B31 large, needleshape: white/yellow;
B32 blank - tiny; B21 large; B14 small yellow; B6 small; B1 small; B20 small; B12 small; B11 small;
Jan 07 8:30 am. Add 8ml conc. HNO3 -> 110°C to dry
Jan 08 2% HCl -> back to jar -> dry

WS4_QtzDissolution p2

This worksheet outlines the steps for dissolving quartz and adding Be carrier.

Chemist: GY **Date:** 01/01/2010

	1	2	3	4	5	6	7	8
CNEF ID	2373	2374	2385	2388	2389	2312		
Sample ID	09SRB-E284A-02	09SRB-E284A-03	09SRB-A167A-01	09SRB-A167A-02	09SRB-A167A-03	Blank		
300 ml vessel ID	B21	B23	B27	B30	B31	B32		
Beryl Carrier ID	Be carrier Bottle 2							
Al Carrier ID	No Al data needed							
Mass 300 ml vessel	10.1259	10.1367	10.1475	10.4267	10.4212	150.2453		
Mass 40g quartz	37.1511	36.6987	40.5384	37.1910	36.6939	0.0000		
Mass Be carrier	0.2015	0.1970	0.1924	0.1909	0.1964	0.1928		
Mass Al Carrier	Add Al carrier next step. With Aliquot, Nov 2009							

1. Add 20 ml conc. HF and 2 ml HClO4 per 5 g of quartz
2. Add 5 ml Aqua Regia
3. Heat at 100-125°C until quartz dissolves, add HF if needed
4. Raise to 200°C and evaporate to dryness
5. Add 5 ml HClO4 and evaporate to dryness
6. Add 8 to 10 ml conc. HNO3, swirl, and evaporate to dryness
7. Dissolved dried sample in 20 ml of 2% HCl

Comments

Omini trace HF, HNO3, HCl, HClO4
Jan 04 140ml HF, 50ml AR, 8ml HClO4
Jan 05 All dissolved, 200°C 9:00 am, no crust, clean
Rinse all tubes, pipete with 2% HNO3
Jan 06 2:00 pm, Add ~3-5ml HClO4. Rinse with dionized water, 200°C to dry
B30 large, thin, yellow; B23 small, yellow; B27 small, yellow; B31 large, needleshape: white/yellow;
B32 blank - tiny; B21 large; B14 small yellow; B6 small; B1 small; B20 small; B12 small; B11 small;
Jan 07 8:30 am. Add 8ml conc. HNO3 -> 110°C to dry
Jan 08 2% HCl -> back to jar -> dry

WS6_Anion Column Chemistry p1

This worksheet outlines the steps for the Anion Column Chemistry (2ml size small column)

Chemist: GY/AM **Date:** 01/11/2010

---

1. Evaporate 20 ml to dryness at 100-120°C (will take at least 3 hrs)
2. Dissolve in 10 ml 9 N HCl (let stand for several hours)
3. Transfer to 15 ml centrifuge tubes, rinse digestion vessels with 9 N HCl to bring volume in tube to 10 ml
4. Centrifuge at 1500 rpm or higher for minimum of 10 minutes
5. Allow any 9 N HCl in columns to drain out; discard

Column ID	1	2	3	4	5	6	7	8
Vessel	B1	B3	B6	B8	B11	B12	B14	B20
CNEF ID	2375	2376	2377	2378	2379	2380	2371	2372
Sample ID	09SRB-E223A-01	09SRB-E223A-03	09SRB-E223A-02	09SRB-E224A-01	09SRB-E224A-02	09SRB-E224A-03	09SRB-E283A-01	09SRB-E284A-01

6. With stopcock closed, pipet sample (avoid residue) onto 2ml size columns.
7. Collect sample in same 300 ml teflon vessel.
8. Elute with 10 ml 9 N HCl, and collect that, close stopcock
9. 5 ml 4.5 N HCl, collect Anion Supernate in labeled 100 ml bottle
10. 10 ml 1 N HCl, collect Anion Supernate
11. 50 ml deionized water. Discard.
12. CONDITION ANION COLUMN
    - (bottle A1) 10 ml 1 N HCl, discard
    - (bottle A2) 10 ml 4.5 N HCl, discard
    - (bottle A3) 10 ml 9 N HCl, discard, but retain acid approx. 2 mm above resin

Comments

Column has been used 2 times before, everything fine.

WS6_Anion Column Chemistry p2

This worksheet outlines the steps for the Anion Column Chemistry (2ml size small column)

Chemist: GY/AM **Date:** 01/12/2010

---

1. Evaporate 20 ml to dryness at 100-120°C (will take at least 3 hrs)
2. Dissolve in 10 ml 9 N HCl (let stand for several hours)
3. Transfer to 15 ml centrifuge tubes, rinse digestion vessels with 9 N HCl to bring volume in tube to 10 ml
4. Centrifuge at 1500 rpm or higher for minimum of 10 minutes
5. Allow any 9 N HCl in columns to drain out; discard

Column ID	1	2	3	4	5	6	7	8
Vessel	B21	B23	B27	B30	B31	B32		
CNEF ID	2373	2374	2385	2388	2389	2312		
Sample ID	09SRB-E284A-02	09SRB-E284A-03	09SRB-A167A-01	09SRB-A167A-02	09SRB-A167A-03	Blank		

6. With stopcock closed, pipet sample (avoid residue) onto 2ml size columns.
7. Collect sample in same 300 ml teflon vessel.
8. Elute with 10 ml 9 N HCl, and collect that, close stopcock
9. 5 ml 4.5 N HCl, collect Anion Supernate in labeled 100 ml bottle
10. 10 ml 1 N HCl, collect Anion Supernate
11. 50 ml deionized water. Discard.
12. CONDITION ANION COLUMN
    - (bottle A1) 10 ml 1 N HCl, discard
    - (bottle A2) 10 ml 4.5 N HCl, discard
    - (bottle A3) 10 ml 9 N HCl, discard, but retain acid approx. 2 mm above resin

Comments

4th time for anion column, good.

WS7_Controlled Precipitate p1

This worksheet outlines the steps for the controlled precipitation chemistry

Chemist: GY/AM **Date:** 01/13/2010

---

1. Evaporate "anion" elute to dryness at 125°C
2. Dissolve in 10 ml of a 1:1 solution of 0.5 N HCl and 2% NH_4Cl
3. Transfer to 15 ml centrifuge, centrifuge for 10 minutes
4. Decant into clean test tube, heat in water bath at 60°C
5. Add drops of 1:1 NH_4OH:H_2O to pH=9.2 (5 drops first then single)
6. Centrifuge for 15 minutes
7. Check pH of liquid, if less than pH=7, redo step 5
8. Decant, save with Anion Supernate
9. Wash with deionized water, vortex, centrifuge, decant
10. Wash with deionized water, vortex, centrifuge, decant
11. Wash with deionized water, vortex, centrifuge, decant

CNEF ID	2375	2376	2377	2378	2379	2380	2371	2372
Vessel	B1	B3	B6	B8	B11	B12	B14	B20
Sample ID	09SRB-E223A-01	09SRB-E223A-03	09SRB-E223A-02	09SRB-E224A-01	09SRB-E224A-02	09SRB-E224A-03	09SRB-E283A-01	09SRB-E284A-01
Approx. vol. Ptte	0.5	0.7	0.9	2.5	0.8	0.9	1.5	0.9

Comments

WS7_Controlled Precipitate p2

This worksheet outlines the steps for the controlled precipitation chemistry

Chemist: GY/AM **Date:** 01/13/2010

---

1 Evaporate "anion" elute to dryness at 125°C
2 Dissolve in 10 ml of a 1:1 solution of 0.5 N HCl and 2% NH_4Cl
3 Transfer to 15 ml centrifuge, centrifuge for 10 minutes
4 Decant into clean test tube, heat in water bath at 60°C
5 Add drops of 1:1 NH_4OH:H_2O to pH=9.2 (5 drops first then single)
6 Centrifuge for 15 minutes
7 Check pH of liquid, if less than pH=7, redo step 5
8 Decant, save with Anion Supernate
9 Wash with deionized water, vortex, centrifuge, decant
10 Wash with deionized water, vortex, centrifuge, decant
11 Wash with deionized water, vortex, centrifuge, decant

CNEF ID	2373	2374	2385	2388	2389	2312		
Vessel	B21	B23	B27	B30	B31	B32		
Sample ID	09SRB-E284A-02	09SRB-E284A-03	09SRB-A167A-01	09SRB-A167A-02	09SRB-A167A-03	Blank		
Approx. vol. Ptte	0.7	0.5	0.9	1.0	0.1			

Comments

WS8_Cation Column Chemistry p1

This worksheet outlines the steps for the Cation Column Chemistry

Chemist: GY/AM **Date:** **01/14/2010**

morning

1. Dissolve in 5 ml conc. HCl and evaporate to dryness at 125°C
2. Redissolve in 2.5 ml 1 N HCl and 2.5 ml 0.5 N HCl
3. Transfer to centrifuge tube, rinse with 1 ml 0.5 N, and centrifuge

Column ID	1	2	3	4	5	6	7	8
Vessel	B1	B3	B6	B8	B11	B12	B14	B20
CNEF ID	2375	2376	2377	2378	2379	2380	2371	2372
Sample ID	09SRB-E223A-01	09SRB-E223A-03	09SRB-E223A-02	09SRB-E224A-01	09SRB-E224A-02	09SRB-E224A-03	09SRB-E283A-01	09SRB-E284A-01

4. Pipette all of the sample into designated conditioned cation column, 17 ml
5. Discard the eluant. Add 285 ml 0.5 N HCL (Bottle C6)
6. Drain the column, discard the first 300ml of eluant
7. Add 60 ml of 0.5N HCl, (Bottle C7), Collect eluant as Cation Supernate
8. Add 65 ml of 0.5N HCl, (Bottle C8), Save it as Be-Sample
9. Add 120 ml 1N HCl (bottle C9)
10. Save this as Be-sample as well.
11. Add 80 ml 4.5 N HCl (bottle C10) , save the eluant as Al sample.
12. CONDITION CATION COLUMN

(bottle C1) 100 ml 9 N HCl

(bottle C2) 50 ml 4.5 N HCl

(bottle C3) 50 ml 1 N HCl

(bottle C4) 50 ml water

(bottle C5) 100 ml 0.5 N HCl

* 17 ml Column

WS8_Cation Column Chemistry p2

This worksheet outlines the steps for the Cation Column Chemistry

Chemist: GY/AM **Date:** **01/14/2010**
afternoon

1. Dissolve in 5 ml conc. HCl and evaporate to dryness at 125°C
2. Redissolve in 2.5 ml 1 N HCl and 2.5 ml 0.5 N HCl
3. Transfer to centrifuge tube, rinse with 1 ml 0.5 N, and centrifuge

Column ID	1	2	3	4	5	6	7	8
Vessel	B21	B23	B27	B30	B31	B32		
CNEF ID	2373	2374	2385	2388	2389	2312		
Sample ID	09SRB-E284A-02	09SRB-E284A-03	09SRB-A167A-01	09SRB-A167A-02	09SRB-A167A-03	Blank		

4. Pipette all of the sample into designated conditioned cation column, 17ml
5. Discard the eluant. Add 285 ml 0.5 N HCL (Bottle C6)
6. Drain the column, discard the first 300 ml of eluant
7. Add 60 ml of 0.5 N HCl, (Bottle C7), Collect eluant as Cation Supernate
8. Add 65 ml of 0.5 N HCl, (Bottle C8), Save it as Be-Sample
9. Add 120 ml 1N HCl (bottle C9)
10. Save this as Be-sample as well.
11. Add 80 ml 4.5 N HCl (bottle C10), save the eluant as Al sample.
12. CONDITION CATION COLUMN

(bottle C1) 100 ml 9 N HCl
(bottle C2) 50 ml 4.5 N HCl
(bottle C3) 50 ml 1 N HCl
(bottle C4) 50 ml water
(bottle C5) 100 ml 0.5 N HCl

* 17 ml Column

WS9_Be Sample Chemistry p1

This worksheet outlines the steps to prepare the BeO sample

Chemist: GY/AM **Date:** **01/15/2010**
01/18-19/2010

☐1 Evaporate Be Sample from column in wiped digestion vessels at 125°C
☐2 Add 2-5 ml 20% perchloric and evaporate at 200oC
☐3 Again, add 2-5 ml 20% perchloric and evaporate at 200°C
☐4 Dissolve sample in 10 ml of 0.5 N HCl (optima grade)
☐5 Transfer to 15 ml centrifuge tube
☐6 Centrifuge and decant into clean centrifuge tube
☐7 Heat centrifuge tubes in water bath at 60°C
☐8 Precipitate $Be(OH)_2$ using Matheson ultimate grade ammonia gas
Gently bubble NH_3 with clean pipet tip on hose
for ca.15 bubbles, or ca. 8-12 sec until ptte forms
Optimum pH=9.2; 1N HCl may be added
☐9 Centrifuge 15 min., decant (save and redo ☐8 if pH of liquid is < 8)
☐10 Wash with water, vortex, centrifuge for 10 min, and decant
☐11 Record mass quartz vials, label, and place them in furnace holder

CNEF ID	2-Jul-06	2376	2377	2378	2379	2380	2371	2372
Vessel	B1	B3	B6	B8	B11	B12	B14	B20
Sample ID	09SRB-E223A-01	09SRB-E223A-03	09SRB-E223A-02	09SRB-E224A-01	09SRB-E224A-02	09SRB-E224A-03	09SRB-E283A-01	09SRB-E284A-01
Mass Qtz Vial	2.2145	2.6144	2.5807	2.5067	2.5405	2.5916	2.5744	2.5672
Mass Vial+Spl	2.2153	2.6157	2.5831	2.5080	2.5419	2.5950	2.5758	2.5705
Mass Spl	0.0008	0.0013	0.0024	0.0013	0.0014	0.0034	0.0014	0.0033

☐12 Add 1 small drop of water with micropipet, slurry precipitate
☐13 Transfer sample into quartz vial, cover with quartz lid
☐14 Turn on Bunsen Burner, dry the gel carefully.
☐15 Burn the Be(OH)2 gel on bunsen burner at least 2 mins, at blue flame.
☐16 Convert to BeO
☐17 Determine mass of vial + sample

WS9_Be Sample Chemistry p2

This worksheet outlines the steps to prepare the BeO sample

Chemist: GY/AM **Date:** **01/15/2010**
01/18-19/2010

- ☐1 Evaporate Be Sample from column in wiped digestion vessels at 125°C
- ☐2 Add 2-5 ml 20% perchloric and evaporate at 200oC
- ☐3 Again, add 2-5 ml 20% perchloric and evaporate at 200°C
- ☐4 Dissolve sample in 10 ml of 0.5 N HCl (optima grade)
- ☐5 Transfer to 15 ml centrifuge tube
- ☐6 Centrifuge and decant into clean centrifuge tube
- ☐7 Heat centrifuge tubes in water bath at 60°C
- ☐8 Precipitate $Be(OH)_2$ using Matheson ultimate grade ammonia gas
  Gently bubble NH_3 with clean pipet tip on hose
  for ca.15 bubbles, or ca. 8-12 sec until ptte forms
  Optimum pH=9.2; 1N HCl may be added
- ☐9 Centrifuge 15 min., decant (save and redo ☐8 if pH of liquid is < 8)
- ☐10 Wash with water, vortex, centrifuge for 10 min, and decant
- ☐11 Record mass quartz vials, label, and place them in furnace holder

CNEF ID	2373	2374	2385	2388	2389	2312		
Vessel	B21	B23	B27	B30	B31	B32		
Sample ID	09SRB-E284A-02	09SRB-E284A-03	09SRB-A167A-01	09SRB-A167A-02	09SRB-A167A-03	Blank		
Mass Qtz Vial	2.6034	2.5976	2.5180	2.6340	2.5830	2.5920		
Mass Vial+Spl	2.6064	2.6004	2.5207	2.6381	2.5846	2.5928		
Mass Spl	0.0030	0.0028	0.0027	0.0041	0.0016	0.0008		

- ☐12 Add 1 small drop of water with micropipet, slurry precipitate
- ☐13 Transfer sample into quartz vial, cover with quartz lid
- ☐14 Turn on Bunsen Burner, dry the gel carefully.
- ☐15 Burn the Be(OH)2 gel on bunsen burner at least 2 mins, at blue flame.
- ☐16 Convert to BeO
- ☐17 Determine mass of vial + sample

A5.2.2 Depth Profile Data for Chapter 3

Depth profile in 'central valley'

WS4_QtzDissolution

This worksheet outlines the steps for dissolving quartz and adding Be carrier.

Chemist: AM **Date:** 03/11/11

	1	2	3	4	5	6	7	8
CNEF ID	2547	2548	2549	2550	2551	2424		
Sample ID	10SRB-E140A-02	10SRB-E140A-03	10SRB-E140A-04	10SRB-E140A-05	10SRB-E140A-06	blank		
500 ml vessel ID	A2	A5	A14	A16	A18	-		
300 ml vessel ID	B23	B26	B28	B31	B32	B99		
Beryl Carrier ID	Fe3-Carrier, 1015 ppm Be, r = 1.013 g ml-1, Dec 10 2001, JCG, Bottle 2							
Al Carrier ID								
Mass 300 ml vessel	-	-	-	-	-	150.2540		
Mass 40g quartz	150.0810	150.1752	150.0270	130.8439	97.3646	-		
Mass Be carrier	0.1884	0.1886	0.1797	0.1854	0.1941	0.1907		
Mass Al Carrier								
Residue	large white spongy	med. yellow to white spongy	(med.)-large white spongy	med. yellow to white	small-med. yellow to white	small white (little dot)		

1 Add 20 ml conc. HF and 2 ml HClO4 per 5 g of quartz
2 Add 5 ml Aqua Regia
3 Heat at 100-125o C until quartz dissolves, add HF if needed
4 Raise to 200o C and evaporate to dryness
5 Add 5 ml HClO4 and evaporate to dryness
6 Add 8 to 10 ml conc. HNO3, swirl, and evaporate to dryness
7 Dissolved dried sample in 20 ml of 2% HCl

Comments

March 11:	add 300ml HF, 50ml AR, 10ml HClO4 to each sample add 140ml HF, 50ml AR, 10ml HClO4 to blank put on hotplate for dissolution at 17:00 at 125 °C
March 17:	9:00 open lid, increase T = 200 °C for partial evaporation, A5 (2548) and A16 (2550) precipitate on lid -> scratch carefully from lid using sterile tools (white "crunchy" crystalls), all samples floading precipitate 17:30 add 160ml HF to blank to increase total amount of adic added to 300ml HF
March 18:	8:30 add 150ml HF to all samples and blank for further dissolution of sample, less floating precipitation 14:00 close lid, reduce heat to 125 °C for further dissolution (protection from sandabrastion)
March 19:	12:30 add 80ml HF, 20ml HNO3 to all samples and blank, A5 (2548) lots of precipitation on lid and walls, scratch carefulluy from lid using sterile tool 17:45 increase T = 200 °C, open lid, further evaporation, 2 samples dissolved, 3 samples <20g left, blank remains on other hotplate T = 125 °C because otherwize far earlier evaporized
March 20:	11:30 most samples dissolved, only A2 (2547) few grains and A14 (2549) few more grains left, include blank for evaporation on this hotplate T = 200 °C 17:30 transfer A18 to B32, rinse 3 times with deionized water, everything transferred
March 21:	8:30 transfer A16 to B31 and A5 to B26, rinse 3 times with deionized water, everything transf.; in A5 (2548) jar some white sticky grains on bottom, add 20ml HNO3, scratch floor until everything dissolved, transfer to B26, rinse with deionized water; blank completely dry (note residue); A2 (2547) and A14 (2549) still some undissolved material, add 20ml HNO3, swirl 12:00 transfer A14 to B28, few Qz-grains left (~1g), transfer everything, rinse several times with deionized water, add 20ml HF, close lid, decrease T = 150 °C for final dissolution transfer A2 to B23, some white crystalls ("crunchy"; solid, larger than Qz-grains, no shape visible), add 20ml HNO3 to A2, scratch floor carefully until everything dissolved, transfer to B23, add 20ml HF to B23, close lid, decrease T = 150 °C for final dissolution 16:30 B23 and B28 seem to be clear, no solid particles visible, open lid for final evaporation Note: from now on 18 samples on 2 hotplates)
March 22:	all samples almost dryed, tap carefully, record residue (large for 4 samples!) 19:00 Remove samples from hotplate, close lid, set aside until hotplate available for evaporation of HClO4 to be added
March 23:	10:30 Add 10 ml HClO4, swirl and put back on hotplate at T=200°C 15:00 tap jar and lids, <1ml HClO4 left, put back on hotplate
March 24:	7:15 add ~12ml HNO3, reduce T=125°C (slightly increased amount of acid due to large amount of residue) 14:00 nearly dry, tap jar and lids
March 25:	14:00 add ~8-12 ml 2% HCl, talk to John about large volume of residue (pictures) -> change procedure, add again 5ml HClO4 to each sample and put back on hotplate at first T=125°C, later T=200°C in order to evaporate as much as possible (esp. Boron)
March 26:	samples not completely dry, tap twice and put back on hotplate
March 27:	samples dry, still large white crust (pictures) 15:15 add ~5-10ml 2% HCl, let stand for complete dissolution -> large residue after centrifuge B23 (2547): 2times 2ml residue (white with black dots); B26 (2548): 1.5ml + 0.3ml residue (dense white, layered); B28 (2549): 2ml + 1ml redidue (white with black dots); B31 (2550): 2times ~3mm residue (dense white, layered); B32 (2551): <1mm residue (white)

WS6_Anion Column Chemistry

This worksheet outlines the steps for the Anion Column Chemistry (2ml size small column)

Chemist: AM **Date:** 03/28/11

---

1. Evaporate 20 ml to dryness at 100-120°C (will take at least 3 hrs)
2. Dissolve in 10 ml 9 N HCl (let stand for several hours)
3. Transfer to 15 ml centrifuge tubes, rinse digestion vessels with 9 N HCl to bring volume in tube to 10 ml
4. Centrifuge at 1500 rpm or higher for minimum of 10 minutes
5. Allow any 9 N HCl in columns to drain out; discard

Column ID	1	2	3	4	5	6	7	8
Vessel	B23	B26	B28	B31	B32	B99		
CNEF ID	2547	2548	2549	2550	2551	2424		
Sample ID	10SRB-E140A-02	10SRB-E140A-03	10SRB-E140A-04	10SRB-E140A-05	10SRB-E140A-06	blank		
Residue (after 2%)	large yellow	large yellow	large yellow	large (spread) yellow	small yellow	white		
Residue in tubes	0.5 ml white	0.1 ml white	0.3 ml white	<0.05 ml white	<1 mm white	-		

6. With stopcock closed, pipet sample (avoid residue) onto 2ml size columns.
7. Collect sample in same 300 ml teflon vessel.
8. Elute with 10 ml 9 N HCl, and collect that, close stopcock
9. 5 ml 4.5 N HCl, collect Anion Supernate in labeled 100 ml bottle
10. 10 ml 1 N HCl, collect Anion Supernate
11. 50 ml deionized water. Discard.
12. CONDITION ANION COLUMN
    - (bottle A1) 10 ml 1N HCl, discard
    - (bottle A2) 10 ml 4.5 N HCl, discard
    - (bottle A3) 10 ml 9 N HCl, discard, but retain acid approx. 2 mm above resin

Comments

March 28: Due to still large residue transfer liquid to clean centrifuge tube, vortex residue with additional 3ml 9N HCl and centrifuge, add liquid to clean tubes

WS7_Controlled Precipitate

This worksheet outlines the steps for the controlled precipitation chemistry

Chemist: AM **Date:** 03/29/11

---

1 Evaporate "anion" elute to dryness at 125°C
2 Dissolve in 10 ml of a 1:1 solution of 0.5 N HCl and 2% NH_4Cl
3 Transfer to 15 ml centrifuge, centrifuge for 10 minutes
4 Decant into clean test tube, heat in water bath at 60°C
5 Add drops of 1:1 NH_4OH:H_2O to pH=9.2 (5 drops first then single)
6 Centrifuge for 15 minutes
7 Check pH of liquid, if less than pH=7, redo step 5
8 Decant, save with Anion Supernate
9 Wash with deionized water, vortex, centrifuge, decant
10 Wash with deionized water, vortex, centrifuge, decant
11 Wash with deionized water, vortex, centrifuge, decant

CNEF ID	2547	2548	2549	2550	2551	2424		
Vessel	B23	B26	B28	B31	B32	B99		
Sample ID	10SRB-E140A-02	10SRB-E140A-03	10SRB-E140A-04	10SRB-E140A-05	10SRB-E140A-06	blank		
Approx. vol. Ptte	3.5 ml lowest 0.25ml dense	3.5 ml ~1.5ml dense	3.5ml ~0.5ml dense	3.5 ml ~0.2ml yellow to white, ~1.5ml dense	1.5ml gel	0.1ml brown transparent		

Comments

WS8_Cation Column Chemistry - 1

For Samples with high Al, need two runs to get better Be

Chemist: AM **Date:** 03/30/11

---

1 Dissolve in 5 ml conc. HCl and evaporate to dryness at 125°C
2 Redissolve in 2.5 ml 1 N HCl and 2.5 ml 0.5 N HCl
3 Transfer to centrifuge tube, rinse with 1 ml 0.5 N, and centrifuge

Column ID	1	2	3	4	5	6	7	8
Vessel	B23	B26	B28	B31	B32	B99		
CNEF ID	2547	2548	2549	2550	2551	2424		
Sample ID	10SRB-E140A-02	10SRB-E140A-03	10SRB-E140A-04	10SRB-E140A-05	10SRB-E140A-06	blank		

4 Pipette all of the sample into designated conditioned cation column, 17 ml
5 Discard the eluant.
6 Add 250 ml 0.5 N HCL (Bottle C6)
7 Drain the column, discard the 250ml of eluant
8 Add 250 ml 1.0 HCl, (Bottle 7), Collect eluent as Be-sample
9 Add 100 ml 4.5 N HCl (bottle 10) , save the eluant as Al sample.

10 CONDITION CATION COLUMN

(bottle C1) 100 ml 9 N HCl
(bottle C2) 50 ml 4.5 N HCl
(bottle C3) 50 ml 1 N HCl
(bottle C4) 50 ml water
(bottle C5) 100 ml 0.5 N HCl

* 17 ml Column

WS8_Cation Column Chemistry - 2

This worksheet outlines the steps for the Cation Column Chemistry

Chemist: GY/AM **Date:** **04/01/11**

---

1. Dissolve in 5 ml conc. HCl and evaporate to dryness at 125°C
2. Redissolve in 2.5 ml 1 N HCl and 2.5 ml 0.5 N HCl
3. Transfer to centrifuge tube, rinse with 1 ml 0.5 N, and centrifuge

Column ID	1	2	3	4	5	6	7	8
Vessel	B23	B26	B28	B31	B32	B99		
CNEF ID	2547	2548	2549	2550	2551	2424		
Sample ID	10SRB-E140A-02	10SRB-E140A-03	10SRB-E140A-04	10SRB-E140A-05	10SRB-E140A-06	blank		
Residue after first additional cation column	large-med. white solid	med. yellow to white solid	large-med. white solid	med. yellow to white transp.	med. yellow transp.	white trasnp.		

4. Pipette all of the sample into designated conditioned cation column, 17ml
5. Discard the eluant. Add 285 ml 0.5 N HCL (Bottle C6)
6. Drain the column, discard the first 300 ml of eluant
7. Add 60 ml of 0.5 N HCl, (Bottle C7), Collect eluant as Cation Supernate
8. Add 65 ml of 0.5 N HCl, (Bottle C8), Save it as Be-Sample
9. Add 120 ml 1N HCl (bottle C9)
10. Save this as Be-sample as well.
11. Add 80 ml 4.5 N HCl (bottle C10), save the eluant as Al sample.
12. CONDITION CATION COLUMN

(bottle C1) 100 ml 9 N HCl

(bottle C2) 50 ml 4.5 N HCl

(bottle C3) 50 ml 1 N HCl

(bottle C4) 50 ml water

(bottle C5) 100 ml 0.5 N HCl

* 17 ml Column

WS9_Be Sample Chemistry

This worksheet outlines the steps to prepare the BeO sample

Chemist: AM **Date:** **04/02/11 - 04/06/11**

☐1 Evaporate Be Sample from column in wiped digestion vessels at 125°C
☐2 Add 2-5 ml 20% perchloric and evaporate at 200oC
☐3 Again, add 2-5 ml 20% perchloric and evaporate at 200°C
☐4 Dissolve sample in 10 ml of 0.5 N HCl (optima grade)
☐5 Transfer to 15 ml centrifuge tube
☐6 Centrifuge and decant into clean centrifuge tube
☐7 Heat centrifuge tubes in water bath at 60°C
☐8 Precipitate $Be(OH)_2$ using Matheson ultimate grade ammonia gas
Gently bubble NH_3 with clean pipet tip on hose
for ca.15 bubbles, or ca. 8-12 sec until ptte forms
Optimum pH=9.2; 1N HCl may be added
☐9 Centrifuge 15 min., decant (save and redo ☐8 if pH of liquid is < 8)
☐10 Wash with water, vortex, centrifuge for 10 min, and decant
☐11 Record mass quartz vials, label, and place them in furnace holder

CNEF ID	2547	2548	2549	2550	2551	2424		
Vessel	B23	B26	B28	B31	B32	B99		
Sample ID	10SRB-E140A-02	10SRB-E140A-03	10SRB-E140A-04	10SRB-E140A-05	10SRB-E140A-06	blank		
Mass Qtz Vial	2.5278	2.4328	2.4254	2.4279	2.1604	2.3295		
Mass Vial+Spl	2.5273	2.4333	2.4253	2.4276	2.1609	2.3289		
Mass Spl	-0.0005	0.0005	-0.0001	-0.0003	0.0005	-0.0006		

☐12 Add 1 small drop of water with micropipet, slurry precipitate
☐13 Transfer sample into quartz vial, cover with quartz lid
☐14 Turn on Bunsen Burner, dry the gel carefully.
☐15 Burn the Be(OH)2 gel on bunsen burner at least 2 mins, at blue flame.
☐16 Convert to BeO
☐17 Determine mass of vial + sample

WS4_QtzDissolution p1

This worksheet outlines the steps for dissolving quartz and adding Be carrier.

Chemist: GY/AM **Date:** 10/30/2009

	1	2	3	4	5	6	7	8
CNEF ID	2358	2359	2360	2361	2362	2363	2364	2365
Sample ID	09SRB-E282A-01	09SRB-E282A-02	09SRB-E282A-03	09SRB-E282A-04	09SRB-E282A-05	09SRB-A351A-01	09SRB-A352A-01	09SRB-A353A-01
300 ml vessel ID	B3	B11	B21	B31	B32	B1	B6	B12
Beryl Carrier ID	BE Carrier bottle 2							
Al Carrier ID	no data needed							
Mass 300 ml vessel	18.1869	18.1575	18.2272	18.0741	18.0537	150.2614	18.1616	18.0838
Mass 40g quartz	130.7309	135.7612	130.1105	130.3569	112.4853	35.3900	35.0260	36.2615
Mass Be carrier	0.2085	0.2048	0.2030	0.2086	0.2136	0.2087	0.2040	0.2274
Mass Al Carrier	NO Al data for this group							

1. Add 20 ml conc. HF and 2 ml $HClO_4$ per 5 g of quartz
2. Add 5 ml Aqua Regia
3. Heat at 100-125°C until quartz dissolves, add HF if needed
4. Raise to 200°C and evaporate to dryness
5. Add 5 ml $HClO_4$ and evaporate to dryness
6. Add 8 to 10 ml conc. HNO_3, swirl, and evaporate to dryness
7. Dissolved dried sample in 20 ml of 2% HCl

Comments

If we need Al-26 data, we should add Al carrier at WS5B_ Add Al Carrier sheet. Try not add Al at beginning bacause it will cause high blank for Be…

Oct. 10	E2-E6: add 450ml HF, 100ml AR, 10ml $HClO_4$
	E8: add 400ml HF, 100ml AR, 10ml $HClO_4$
	B1, B6, B12: add 140ml HF, 40ml AR, 5ml $HClO_4$
Nov 03	transfer from 1000ml vessels (E) to 300ml vessels (B), rinse with H_2O
	E2 -> B3, E4 -> B11, E5 -> B21, E6 -> B31, E8 -> B32
Nov 04	still 3 not dry yet, add 15ml HNO_2 since they are large samples, reduce heat to 110°C,
	add 8-10ml HNO_3 to each sample

WS4_QtzDissolution p2

This worksheet outlines the steps for dissolving quartz and adding Be carrier.

Chemist: GY/AM **Date:** 10/30/2009

	1	2	3	4	5	6	7	8
CNEF ID	2311							
Sample ID	blank							
300 ml vessel ID	B27							
Beryl Carrier ID	BE Carrier bottle 2							
Al Carrier ID								
Mass 300 ml vessel	10.1259							
Mass 40g quartz	37.1511							
Mass Be carrier	0.2015							
Mass Al Carrier	NO Al data for this group							

- ☐ 1 Add 20 ml conc. HF and 2 ml HClO4 per 5 g of quartz
- ☐ 2 Add 5 ml Aqua Regia
- ☐ 3 Heat at 100-125°C until quartz dissolves, add HF if needed
- ☐ 4 Raise to 200°C and evaporate to dryness
- ☐ 5 Add 5 ml HClO4 and evaporate to dryness
- ☐ 6 Add 8 to 10 ml conc. HNO3, swirl, and evaporate to dryness
- ☐ 7 Dissolved dried sample in 20 ml of 2% HCl

Comments

If we need Al-26 data, we should add Al carrier at WS5B_ Add Al Carrier sheet. Try not add Al at beginning bacause it will cause high blank for Be…

Oct. 10	E2-E6: add 450ml HF, 100ml AR, 10ml HClO4
	E8: add 400ml HF, 100ml AR, 10ml HClO4
	B1, B6, B12: add 140ml HF, 40ml AR, 5ml HClO4
Nov 03	transfer from 1000ml vessels (E) to 300ml vessels (B), rinse with H2O
	E2 -> B3, E4 -> B11, E5 -> B21, E6 -> B31, E8 -> B32
Nov 04	still 3 not dry yet, add 15ml HNO2 since they are large samples, reduce heat to 110°C,
	add 8-10ml HNO3 to each sample

WS6_Anion Column Chemistry p1

This worksheet outlines the steps for the Anion Column Chemistry (2ml size small column)

Chemist: GY/AM **Date:** 11/06/2009

---

1. Evaporate 20 ml to dryness at 100-120°C (will take at least 3 hrs)
2. Dissolve in 10 ml 9 N HCl (let stand for several hours)
3. Transfer to 15 ml centrifuge tubes, rinse digestion vessels with 9 N HCl to bring volume in tube to 10 ml
4. Centrifuge at 1500 rpm or higher for minimum of 10 minutes
5. Allow any 9 N HCl in columns to drain out; discard

Column ID	1	2	3	4	5	6	7	8
Vessel	B3	B11	B21	B31	B32	B1	B6	B12
CNEF ID	2358	2359	2360	2361	2362	2363	2364	2365
Sample ID	09SRB-E282A-01	09SRB-E282A-02	09SRB-E282A-03	09SRB-E282A-04	09SRB-E282A-05	09SRB-A351A-01	09SRB-A352A-01	09SRB-A353A-01

6. With stopcock closed, pipet sample (avoid residue) onto 2ml size columns.
7. Collect sample in same 300 ml teflon vessel.
8. Elute with 10 ml 9 N HCl, and collect that, close stopcock
9. 5 ml 4.5 N HCl, collect Anion Supernate in labeled 100 ml bottle
10. 10 ml 1 N HCl, collect Anion Supernate
11. 50 ml deionized water. Discard.
12. CONDITION ANION COLUMN
    - (bottle A1) 10 ml 1 N HCl, discard
    - (bottle A2) 10 ml 4.5 N HCl, discard
    - (bottle A3) 10 ml 9 N HCl, discard, but retain acid approx. 2 mm above resin

Comments

Sample 2358 - 2362 are dark yellow color, but clear.
Sample 2363 - 2365 are light yellow.
Anion column from before work fine.
300 ml vessels are back to hotplate.

WS6_Anion Column Chemistry p2

This worksheet outlines the steps for the Anion Column Chemistry (2ml size small column)

Chemist: GY/AM **Date:** 11/06/2009

---

1. Evaporate 20 ml to dryness at 100-120°C (will take at least 3 hrs)
2. Dissolve in 10 ml 9 N HCl (let stand for several hours)
3. Transfer to 15 ml centrifuge tubes, rinse digestion vessels with 9 N HCl to bring volume in tube to 10 ml
4. Centrifuge at 1500 rpm or higher for minimum of 10 minutes
5. Allow any 9 N HCl in columns to drain out; discard

Column ID	1	2	3	4	5	6	7	8
Vessel	B27							
CNEF ID	2311							
Sample ID	blank							

6. With stopcock closed, pipet sample (avoid residue) onto 2ml size columns.
7. Collect sample in same 300 ml teflon vessel.
8. Elute with 10 ml 9 N HCl, and collect that, close stopcock
9. 5 ml 4.5 N HCl, collect Anion Supernate in labeled 100 ml bottle
10. 10 ml 1 N HCl, collect Anion Supernate
11. 50 ml deionized water. Discard.
12. CONDITION ANION COLUMN
    - (bottle A1) 10 ml 1 N HCl, discard
    - (bottle A2) 10 ml 4.5 N HCl, discard
    - (bottle A3) 10 ml 9 N HCl, discard, but retain acid approx. 2 mm above resin

Comments

Sample 2358 - 2362 are dark yellow color, but clear.
Sample 2363 - 2365 are light yellow.
Anion column from before work fine.
300 ml vessels are back to hotplate.

WS7_Controlled Precipitate p1

This worksheet outlines the steps for the controlled precipitation chemistry

Chemist: GY/AM **Date:** 11/09/2009

---

1. Evaporate "anion" elute to dryness at 125°C
2. Dissolve in 10 ml of a 1:1 solution of 0.5 N HCl and 2% NH_4Cl
3. Transfer to 15 ml centrifuge, centrifuge for 10 minutes
4. Decant into clean test tube, heat in water bath at 60°C
5. Add drops of 1:1 NH_4OH:H_2O to pH=9.2 (5 drops first then single)
6. Centrifuge for 15 minutes
7. Check pH of liquid, if less than pH=7, redo step 5
8. Decant, save with Anion Supernate
9. Wash with deionized water, vortex, centrifuge, decant
10. Wash with deionized water, vortex, centrifuge, decant
11. Wash with deionized water, vortex, centrifuge, decant

CNEF ID	2-Jul-06	2376	2377	2378	2379	2380	2371	2372
Vessel	B3	B11	B21	B31	B32	B1	B6	B12
Sample ID	09SRB-E282A-01	09SRB-E282A-02	09SRB-E282A-03	09SRB-E282A-04	09SRB-E282A-05	09SRB-A351A-01	09SRB-A352A-01	09SRB-A353A-01
Approx. vol. Ptte	2.5 ml	1.5 ml	2 ml	1.5 ml	1.5 ml	0.6 ml	0.6 ml	0.8 ml

Comments

Sample 2358 - 2365: white color gel, not solid white
Sample 2363 - 2365: light brown coloured gel, not solid
Sample 2311: light brown coloured gel, not solid

WS7_Controlled Precipitate p2

This worksheet outlines the steps for the controlled precipitation chemistry

Chemist: GY/AM **Date:** 11/09/2009

- ☐ 1 Evaporate "anion" elute to dryness at 125°C
- ☐ 2 Dissolve in 10 ml of a 1:1 solution of 0.5 N HCl and 2% NH_4Cl
- ☐ 3 Transfer to 15 ml centrifuge, centrifuge for 10 minutes
- ☐ 4 Decant into clean test tube, heat in water bath at 60°C
- ☐ 5 Add drops of 1:1 NH_4OH:H_2O to pH=9.2 (5 drops first then single)
- ☐ 6 Centrifuge for 15 minutes
- ☐ 7 Check pH of liquid, if less than pH=7, redo step ☐ 5
- ☐ 8 Decant, save with Anion Supernate
- ☐ 9 Wash with deionized water, vortex, centrifuge, decant
- ☐ 10 Wash with deionized water, vortex, centrifuge, decant
- ☐ 11 Wash with deionized water, vortex, centrifuge, decant

CNEF ID	2311							
Vessel	B27							
Sample ID	blank							
Approx. vol. Ptte	0.1 ml							

Comments

Sample 2358 - 2365: white color gel, not solid white
Sample 2363 - 2365: light brown coloured gel, not solid
Sample 2311: light brown coloured gel, not solid

WS8_Cation Column Chemistry p1

This worksheet outlines the steps for the Cation Column Chemistry

Chemist: GY/AM **Date:** 11/10/2009

---

1 Dissolve in 5 ml conc. HCl and evaporate to dryness at 125°C
2 Redissolve in 2.5 ml 1 N HCl and 2.5 ml 0.5 N HCl
3 Transfer to centrifuge tube, rinse with 1 ml 0.5 N, and centrifuge

Column ID	1	2	3	4	5	6	7	8
Vessel	B3	B11	B21	B31	B32	B1	B6	B12
CNEF ID	2358	2359	2360	2361	2362	2363	2364	2365
Sample ID	09SRB-E282A-01	09SRB-E282A-02	09SRB-E282A-03	09SRB-E282A-04	09SRB-E282A-05	09SRB-A351A-01	09SRB-A352A-01	09SRB-A353A-01

4 Pipette all of the sample into designated conditioned cation column, 17 ml
5 Discard the eluant. Add 285 ml 0.5 N HCL (Bottle C6)
6 Drain the column, discard the first 300ml of eluant
7 Add 60 ml of 0.5N HCl, (Bottle C7), Collect eluant as Cation Supernate
8 Add 65 ml of 0.5N HCl, (Bottle C8), Save it as Be-Sample
9 Add 120 ml 1N HCl (bottle C9)
10 Save this as Be-sample as well.
11 Add 80 ml 4.5 N HCl (bottle C10) , save the eluant as Al sample.
12 CONDITION CATION COLUMN

(bottle C1) 100 ml 9 N HCl
(bottle C2) 50 ml 4.5 N HCl
(bottle C3) 50 ml 1 N HCl
(bottle C4) 50 ml water
(bottle C5) 100 ml 0.5 N HCl

* 17 ml Column

WS8_Cation Column Chemistry p2

This worksheet outlines the steps for the Cation Column Chemistry

Chemist: GY/AM **Date:** 11/10/2009

---

1 Dissolve in 5 ml conc. HCl and evaporate to dryness at 125°C
2 Redissolve in 2.5 ml 1 N HCl and 2.5 ml 0.5 N HCl
3 Transfer to centrifuge tube, rinse with 1 ml 0.5 N, and centrifuge

Column ID	1	2	3	4	5	6	7	8
Vessel	B27							
CNEF ID	2311							
Sample ID	blank							

4 Pipette all of the sample into designated conditioned cation column, 17ml
5 Discard the eluant. Add 285 ml 0.5 N HCL (Bottle C6)
6 Drain the column, discard the first 300 ml of eluant
7 Add 60 ml of 0.5 N HCl, (Bottle C7), Collect eluant as Cation Supernate
8 Add 65 ml of 0.5 N HCl, (Bottle C8), Save it as Be-Sample
9 Add 120 ml 1N HCl (bottle C9)
10 Save this as Be-sample as well.
11 Add 80 ml 4.5 N HCl (bottle C10), save the eluant as Al sample.
12 CONDITION CATION COLUMN

(bottle C1) 100 ml 9 N HCl
(bottle C2) 50 ml 4.5 N HCl
(bottle C3) 50 ml 1 N HCl
(bottle C4) 50 ml water
(bottle C5) 100 ml 0.5 N HCl

* 17 ml Column

WS9_Be Sample Chemistry p1

This worksheet outlines the steps to prepare the BeO sample

Chemist: GY/AM **Date:** **11/11/2009**
11/13/2009

---

1. Evaporate Be Sample from column in wiped digestion vessels at 125°C
2. Add 2-5 ml 20% perchloric and evaporate at 200oC
3. Again, add 2-5 ml 20% perchloric and evaporate at 200°C
4. Dissolve sample in 10 ml of 0.5 N HCl (optima grade)
5. Transfer to 15 ml centrifuge tube
6. Centrifuge and decant into clean centrifuge tube
7. Heat centrifuge tubes in water bath at 60°C
8. Precipitate $Be(OH)_2$ using Matheson ultimate grade ammonia gas
   Gently bubble NH_3 with clean pipet tip on hose
   for ca.15 bubbles, or ca. 8-12 sec until ptte forms
   Optimum pH=9.2; 1N HCl may be added
9. Centrifuge 15 min., decant (save and redo 8 if pH of liquid is < 8)
10. Wash with water, vortex, centrifuge for 10 min, and decant
11. Record mass quartz vials, label, and place them in furnace holder

CNEF ID	2358	2359	2360	2361	2362	2363	2364	2365
Vessel	B3	B11	B21	B31	B32	B1	B6	B12
Sample ID	09SRB-E282A-01	09SRB-E282A-02	09SRB-E282A-03	09SRB-E282A-04	09SRB-E282A-05	09SRB-A351A-01	09SRB-A352A-01	09SRB-A353A-01
Mass Qtz Vial	2.6347	2.5141	2.6313	2.5503	2.5108	2.5304	2.6013	2.5298
Mass Vial+Spl	2.6365	2.5161	2.6337	2.5534	2.5196	2.5332	2.6029	2.5315
Mass Spl	0.0018	0.0020	0.0024	0.0031	0.0088	0.0028	0.0016	0.0017

12. Add 1 small drop of water with micropipet, slurry precipitate
13. Transfer sample into quartz vial, cover with quartz lid
14. Turn on Bunsen Burner, dry the gel carefully.
15. Burn the Be(OH)2 gel on bunsen burner at least 2 mins, at blue flame.
16. Convert to BeO
17. Determine mass of vial + sample

WS9_Be Sample Chemistry p2

This worksheet outlines the steps to prepare the BeO sample

Chemist: GY/AM **Date:** **11/11/2009**
11/13/2009

☐1 Evaporate Be Sample from column in wiped digestion vessels at 125°C
☐2 Add 2-5 ml 20% perchloric and evaporate at 200oC
☐3 Again, add 2-5 ml 20% perchloric and evaporate at 200°C
☐4 Dissolve sample in 10 ml of 0.5 N HCl (optima grade)
☐5 Transfer to 15 ml centrifuge tube
☐6 Centrifuge and decant into clean centrifuge tube
☐7 Heat centrifuge tubes in water bath at 60°C
☐8 Precipitate $Be(OH)_2$ using Matheson ultimate grade ammonia gas
Gently bubble NH_3 with clean pipet tip on hose
for ca.15 bubbles, or ca. 8-12 sec until ptte forms
Optimum pH=9.2; 1N HCl may be added
☐9 Centrifuge 15 min., decant (save and redo ☐8 if pH of liquid is < 8)
☐10 Wash with water, vortex, centrifuge for 10 min, and decant
☐11 Record mass quartz vials, label, and place them in furnace holder

CNEF ID	2311							
Vessel	B27							
Sample ID	blank							
Mass Qtz Vial	2.6698							
Mass Vial+Spl	2.6703							
Mass Spl	0.0005							

☐12 Add 1 small drop of water with micropipet, slurry precipitate
☐13 Transfer sample into quartz vial, cover with quartz lid
☐14 Turn on Bunsen Burner, dry the gel carefully.
☐15 Burn the Be(OH)2 gel on bunsen burner at least 2 mins, at blue flame.
☐16 Convert to BeO
☐17 Determine mass of vial + sample

A5.2.3 Bedrock Data for Chapter 4

Bedrock surfaces – batch 1

WS4_QtzDissolution p1

This worksheet outlines the steps for dissolving quartz and adding Be carrier.

Chemist: AM/GY **Date:** 20/01/2010

	1	2	3	4	5	6	7	8
CNEF ID	2381	2382	2383	2384	2386	2387	2390	
Sample ID	09SRB-E221A-01	09SRB-E221A-02	09SRB-E221A-03	09SRB-E304A-01	09SRB-A186-01	09SRB-A188A-01	09SRB-A187A-01	
300 ml vessel ID	B99	B4	B7	B16	B18	B19	B22	
Beryl Carrier ID	Be Carrier bottle 2							
Al Carrier ID								
Mass 300 ml vessel	10.1156	10.4280	10.3508	10.0888	10.6777	10.5270	10.3410	
Mass 40g quartz	35.4572	35.6641	35.2509	35.1661	35.3395	36.6153	35.0101	
Mass Be carrier	0.1921	0.1946	0.1953	0.1992	0.2022	0.1923	0.2050	
Mass Al Carrier	Add Al carrier next step. With Aliquot, Nov 2009							

1. Add 20 ml conc. HF and 2 ml HClO4 per 5 g of quartz
2. Add 5 ml Aqua Regia
3. Heat at 100-125o C until quartz dissolves, add HF if needed
4. Raise to 200o C and evaporate to dryness
5. Add 5 ml HClO4 and evaporate to dryness
6. Add 8 to 10 ml conc. HNO3, swirl, and evaporate to dryness
7. Dissolved dried sample in 20 ml of 2% HCl

Comments

All Acids used here are omniTrace level.
Tor Site, Be+Al data
Jan 20, 2010: 140ml HF+50ml Aqua Regia+8ml HClO4
Jan 21: All disolved. Open lids, to dry.
Jan 22: 5ml HClO4 and DI water to rinse.
Jan 22: 1:25pm Add 8ml HNO3 to each one. 110°C to dry over night
Jan23: Turn off hotplate
Jan25: 2%HCl : B29 lots of residue ~0.5ml white

WS4_QtzDissolution p2

This worksheet outlines the steps for dissolving quartz and adding Be carrier.

Chemist: AM/GY **Date:** 20/01/2010

	1	2	3	4	5	6	7	8
CNEF ID	2391	2392	2393	2394	2395	2313		
Sample ID	09SRB-A355A-01	09SRB-A356A-01	09SRB-A346A-01	09SRB-A348A-01	09SRB-A347-01	Blank		
300 ml vessel ID	B24	B25	B26	B28	B29	B13		
Beryl Carrier ID	Be Carrier Bottle 2							
Al Carrier ID								
Mass 300 ml vessel	10.0752	10.0699	10.4894	10.0615	10.6142	154.7955		
Mass 40g quartz	35.2918	35.1482	35.1319	35.3062	38.0854	0.0000		
Mass Be carrier	0.1910	0.1933	0.2003	0.1913	0.1946	0.1904		
Mass Al Carrier	Add Al carrier next step. With Aliquot, Nov 2009							

1. Add 20 ml conc. HF and 2 ml HClO4 per 5 g of quartz
2. Add 5 ml Aqua Regia
3. Heat at 100-125°C until quartz dissolves, add HF if needed
4. Raise to 200°C and evaporate to dryness
5. Add 5 ml HClO4 and evaporate to dryness
6. Add 8 to 10 ml conc. HNO3, swirl, and evaporate to dryness
7. Dissolved dried sample in 20 ml of 2% HCl

Comments

All Acids used here are omniTrace level.
Tor Site, Be+Al data
Jan 20, 2010: 140ml HF+50ml Aqua Regia+8ml HClO4
Jan 21: All disolved. Open lids, to dry.
Jan 22: 5ml HClO4 and DI water to rinse.
Jan 22: 1:25pm Add 8ml HNO3 to each one. 110oC to dry over night
Jan23: Turn off hotplate
Jan25: 2%HCl : B29 lots of residue ~0.5ml white

WS5B_ICP Aliquot and Al spiking p1

This worksheet outlines the steps for collecting ICP aliquots and adding Al carrier.

Chemist: AM/GY **Date:** 01/25/2010

---

1. Label one 100 ml volumetric flasks per sample
2. Label one ICP vial with CNEF ID per sample

Vessel ID	B99	B4	B7	B16	B18	B19	B22	0
CNEF ID	2381	2382	2383	2384	2386	2387	2390	
Sample ID	09SRB-E221A-01	09SRB-E221A-02	09SRB-E221A-03	09SRB-E304A-01	09SRB-A186-01	09SRB-A188A-01	09SRB-A187A-01	
Al carrier ID	ICP-013-5 Lot H00551 Ultra Scientific							
Quant-EM est. Al in qtz	50	50	25	50	25	10	10	
Mass100 ml volumetric	67.1840	67.3487	67.0047	67.1405	67.4187	66.9348	66.4917	
100ml volumetric + sample + 2%HCl	168.5842	168.3658	167.8276	168.1019	168.3115	167.8929	167.4246	
Mass 5 ml sample pipetted to vol A	4.5973	4.4314	4.7471	4.8147	4.6943	4.8211	4.7652	
95ml Solution +Volumetric	163.9315	163.8827	163.0680	163.2742	163.5924	163.0584	162.6525	
After Al Carrier Added to Solution	164.4490	164.3966	164.7979	163.7912	165.3281	165.5252	165.1279	
Al carrier Mass	0.5175	0.5139	1.7299	0.5170	1.7356	2.4731	2.4867	
Mass 5 ml Sample to Vial B	4.7950	4.6540	4.5242	4.9225	4.8800	4.9094	4.7677	
Final Mass of 100 ml vol and smple	159.6341	159.7220	160.2514	158.8497	160.4295	160.6071	160.3527	
A, dried, bring back with HNO3								
B, Dried, bring back with HNO3								

---

3. Get digestion vessel and cover ready, Do not wipe now.
4. Transfer the 90 ml sample back into vessel
5.
6. Transfer contents volumetrics to ICP vials with same number

---

WS5B_ICP Aliquot and Al spiking p2

This worksheet outlines the steps for collecting ICP aliquots and adding Al carrier.

Chemist: AM/GY **Date:** 01/25/2010

---

1. Label one 100 ml volumetric flasks per sample
2. Label one ICP vial with CNEF ID per sample

Vessel ID	B24	B25	B26	B28	B29	B13		
CNEF ID	2391	2392.00	2393	2394	2395	2313		
Sample ID	09SRB-A355A-01	09SRB-A356A-01	09SRB-A346A-01	09SRB-A348A-01	09SRB-A347-01	Blank		
Al carrier ID	ICP-013-5 1000ug/ml, Lot: H00551							
Quant-EM est. Al in qtz	10	50	10	10	50	0		
Mass100 ml volumetric	66.8741	66.3080	66.5908	65.2036	67.7314	67.7944		
100ml volumetric + sample + 2%HCl	169.5705	167.2512	167.3973	166.0705	168.9515	168.6174		
Mass 5 ml sample pipetted to vol A	4.8891	4.6577	4.7696	4.8618	5.1245	4.7501		
95ml Solution +Volumetric	164.6722	162.5800	162.6152	161.1953	163.8162	163.8578		
After Al Carrier Added to Solution	167.1169	164.9936	165.0883	163.9858	164.3216	168.6812		
Al carrier Mass	2.4794	2.4174	2.4810	2.8054	0.5114	2.8454		
Mass 5 ml Sample to Vial B	4.8693	4.4109	4.6498	5.0300	4.4436	4.4763		
Final Mass of 100 ml vol and smple	162.2369	160.5721	160.4135	158.9384	159.8679	162.1963		
A, dried, bring back with HNO3								
B, Dried, bring back with HNO3								

---

3. Get digestion vessel and cover ready, Do not wipe now.
4. Transfer the 90 ml sample back into vessel
5.
6. Transfer contents volumetrics to ICP vials with same number

---

WS6_Anion Column Chemistry p1

This worksheet outlines the steps for the Anion Column Chemistry (2ml size small column)

Chemist: GY/AM **Date:** **01/26/2010**
afternoon

---

1. Evaporate 20 ml to dryness at 100-120°C (will take at least 3 hrs)
2. Dissolve in 10 ml 9 N HCl (let stand for several hours)
3. Transfer to 15 ml centrifuge tubes, rinse digestion vessels with 9 N HCl to bring volume in tube to 10 ml
4. Centrifuge at 1500 rpm or higher for minimum of 10 minutes
5. Allow any 9 N HCl in columns to drain out; discard

Column ID	1	2	3	4	5	6	7	8
Vessel	B99	B4	B7	B16	B18	B19	B22	
CNEF ID	2381	2382	2383	2384	2386	2387	2390	
Sample ID	09SRB-E221A-01	09SRB-E221A-02	09SRB-E221A-03	09SRB-E304A-01	09SRB-A186-01	09SRB-A188A-01	09SRB-A187A-01	

6. With stopcock closed, pipet sample (avoid residue) onto 2ml size columns.
7. Collect sample in same 300 ml teflon vessel.
8. Elute with 10 ml 9 N HCl, and collect that, close stopcock
9. 5 ml 4.5 N HCl, collect Anion Supernate in labeled 100 ml bottle
10. 10 ml 1 N HCl, collect Anion Supernate
11. 50 ml deionized water. Discard.
12. CONDITION ANION COLUMN
    - (bottle A1) 10 ml 1N HCl, discard
    - (bottle A2) 10 ml 4.5 N HCl, discard
    - (bottle A3) 10 ml 9 N HCl, discard, but retain acid approx. 2 mm above resin

Comments

WS6_Anion Column Chemistry p2

This worksheet outlines the steps for the Anion Column Chemistry (2ml size small column)

Chemist: GY/AM **Date:** **01/26/2010**
morning

1. Evaporate 20 ml to dryness at 100-120°C (will take at least 3 hrs)
2. Dissolve in 10 ml 9 N HCl (let stand for several hours)
3. Transfer to 15 ml centrifuge tubes, rinse digestion vessels with 9 N HCl to bring volume in tube to 10 ml
4. Centrifuge at 1500 rpm or higher for minimum of 10 minutes
5. Allow any 9 N HCl in columns to drain out; discard

Column ID	1	2	3	4	5	6	7	8
Vessel	B24	B25	B26	B28	B29	B13		
CNEF ID	2391	2392	2393	2394	2395	2313		
Sample ID	09SRB-A355A-01	09SRB-A356A-01	09SRB-A346A-01	09SRB-A348A-01	09SRB-A347-01	Blank		

6. With stopcock closed, pipet sample (avoid residue) onto 2ml size columns.
7. Collect sample in same 300 ml teflon vessel.
8. Elute with 10 ml 9 N HCl, and collect that, close stopcock
9. 5 ml 4.5 N HCl, collect Anion Supernate in labeled 100 ml bottle
10. 10 ml 1 N HCl, collect Anion Supernate
11. 50 ml deionized water. Discard.
12. CONDITION ANION COLUMN
    - (bottle A1) 10 ml 1 N HCl, discard
    - (bottle A2) 10 ml 4.5 N HCl, discard
    - (bottle A3) 10 ml 9 N HCl, discard, but retain acid approx. 2 mm above resin

Comments

WS7_Controlled Precipitate p1

This worksheet outlines the steps for the controlled precipitation chemistry

Chemist: GY/AM **Date:** 01/27/2010

---

1. Evaporate "anion" elute to dryness at 125°C
2. Dissolve in 10 ml of a 1:1 solution of 0.5 N HCl and 2% NH_4Cl
3. Transfer to 15 ml centrifuge, centrifuge for 10 minutes
4. Decant into clean test tube, heat in water bath at 60°C
5. Add drops of 1:1 NH_4OH:H_2O to pH=9.2 (5 drops first then single)
6. Centrifuge for 15 minutes
7. Check pH of liquid, if less than pH=7, redo step 5
8. Decant, save with Anion Supernate
9. Wash with deionized water, vortex, centrifuge, decant
10. Wash with deionized water, vortex, centrifuge, decant
11. Wash with deionized water, vortex, centrifuge, decant

CNEF ID	2381	2382	2383	2384	2386	2387	2390	
Vessel	B99	B4	B7	B16	B18	B19	B22	
Sample ID	09SRB-E221A-01	09SRB-E221A-02	09SRB-E221A-03	09SRB-E304A-01	09SRB-A186-01	09SRB-A188A-01	09SRB-A187A-01	
Approx. vol. Ptte	2.8	4.0	1.8	2.0	2.3	2.0	2.0	

1) 0.75ml solid white
2) 2.75ml -> pH ok

Comments

All, but B99 gelish

WS7_Controlled Precipitate p2

This worksheet outlines the steps for the controlled precipitation chemistry

Chemist: GY/AM **Date:** 01/27/2010

---

1. Evaporate "anion" elute to dryness at 125°C
2. Dissolve in 10 ml of a 1:1 solution of 0.5 N HCl and 2% NH_4Cl
3. Transfer to 15 ml centrifuge, centrifuge for 10 minutes
4. Decant into clean test tube, heat in water bath at 60°C
5. Add drops of 1:1 NH_4OH:H_2O to pH=9.2 (5 drops first then single)
6. Centrifuge for 15 minutes
7. Check pH of liquid, if less than pH=7, redo step 5
8. Decant, save with Anion Supernate
9. Wash with deionized water, vortex, centrifuge, decant
10. Wash with deionized water, vortex, centrifuge, decant
11. Wash with deionized water, vortex, centrifuge, decant

CNEF ID	2391	2392	2393	2394	2395	2313		
Vessel	B24	B25	B26	B28	B29	B13		
Sample ID	09SRB-A355A-01	09SRB-A356A-01	09SRB-A346A-01	09SRB-A348A-01	09SRB-A347-01	Blank		
Approx. vol. Ptte	1.8	1.5	1.5	1.5	1.75/2.25	0.5		

Comments

B29: 1) 0.25ml solid white , 2) 1.75ml still white, 3) 2.25ml gelly on top part

WS8_Cation Column Chemistry p1

This worksheet outlines the steps for the Cation Column Chemistry

Chemist: GY/AM **Date:** 01/27/2010

---

1. Dissolve in 5 ml conc. HCl and evaporate to dryness at 125°C
2. Redissolve in 2.5 ml 1 N HCl and 2.5 ml 0.5 N HCl
3. Transfer to centrifuge tube, rinse with 1 ml 0.5 N, and centrifuge

Column ID	1	2	3	4	5	6	7	8
Vessel	B99	B4	B7	B16	B18	B19	B22	
Al Vessel	C2	C3	C4	C5	C6	C7	C9	
CNEF ID	2381	2382	2383	2384	2386	2387	2390	
Sample ID	09SRB-E221A-01	09SRB-E221A-02	09SRB-E221A-03	09SRB-E304A-01	09SRB-A186-01	09SRB-A188A-01	09SRB-A187A-01	

4. Pipette all of the sample into designated conditioned cation column, 17 ml
5. Discard the eluant. Add 285 ml 0.5 N HCL (Bottle C6)
6. Drain the column, discard the first 300ml of eluant
7. Add 60 ml of 0.5N HCl, (Bottle C7), Collect eluant as Cation Supernate
8. Add 65 ml of 0.5N HCl, (Bottle C8), Save it as Be-Sample
9. Add 120 ml 1N HCl (bottle C9)
10. Save this as Be-sample as well.
11. Add 80 ml 4.5 N HCl (bottle C10) , save the eluant as Al sample.
12. CONDITION CATION COLUMN

(bottle C1) 100 ml 9 N HCl

(bottle C2) 50 ml 4.5 N HCl

(bottle C3) 50 ml 1 N HCl

(bottle C4) 50 ml water

(bottle C5) 100 ml 0.5 N HCl

* 17 ml Column

WS8_Cation Column Chemistry p2

This worksheet outlines the steps for the Cation Column Chemistry

Chemist: GY/AM **Date:** 01/28/2010

---

1. Dissolve in 5 ml conc. HCl and evaporate to dryness at 125°C
2. Redissolve in 2.5 ml 1 N HCl and 2.5 ml 0.5 N HCl
3. Transfer to centrifuge tube, rinse with 1 ml 0.5 N, and centrifuge

Column ID	1	2	3	4	5	6	7	8
Vessel	B24	B25	B26	B28	B29	B13		
Al Vessel	C9	C10	C11	C14	C17	C18		
CNEF ID	2391	2392	2393	2394	2395	2313		
Sample ID	09SRB-A355A-01	09SRB-A356A-01	09SRB-A346A-01	09SRB-A348A-01	09SRB-A347-01	Blank		

4. Pipette all of the sample into designated conditioned cation column, 17 ml
5. Discard the eluant. Add 285 ml 0.5 N HCL (Bottle C6)
6. Drain the column, discard the first 300ml of eluant
7. Add 60 ml of 0.5N HCl, (Bottle C7), Collect eluant as Cation Supernate
8. Add 65 ml of 0.5N HCl, (Bottle C8), Save it as Be-Sample
9. Add 120 ml 1N HCl (bottle C9)
10. Save this as Be-sample as well.
11. Add 80 ml 4.5 N HCl (bottle C10) , save the eluant as Al sample.
12. CONDITION CATION COLUMN

    (bottle C1) 100 ml 9 N HCl

    (bottle C2) 50 ml 4.5 N HCl

    (bottle C3) 50 ml 1 N HCl

    (bottle C4) 50 ml water

    (bottle C5) 100 ml 0.5 N HCl

* 17 ml Column

WS9_Be Sample Chemistry p1

This worksheet outlines the steps to prepare the BeO sample

Chemist: GY/AM **Date:** 02/01/2010

---

1. Evaporate Be Sample from column in wiped digestion vessels at 125°C
2. Add 2-5 ml 20% perchloric and evaporate at 200oC
3. Again, add 2-5 ml 20% perchloric and evaporate at 200°C
4. Dissolve sample in 10 ml of 0.5 N HCl (optima grade)
5. Transfer to 15 ml centrifuge tube
6. Centrifuge and decant into clean centrifuge tube
7. Heat centrifuge tubes in water bath at 60°C
8. Precipitate $Be(OH)_2$ using Matheson ultimate grade ammonia gas
   Gently bubble NH_3 with clean pipet tip on hose
   for ca.15 bubbles, or ca. 8-12 sec until ptte forms
   Optimum pH=9.2; 1N HCl may be added
9. Centrifuge 15 min., decant (save and redo 8 if pH of liquid is < 8)
10. Wash with water, vortex, centrifuge for 10 min, and decant
11. Record mass quartz vials, label, and place them in furnace holder

CNEF ID	2381	2382	2383	2384	2386	2387	2390	
Vessel	B99	B4	B7	B16	B18	B19	B22	
Sample ID	09SRB-E221A-01	09SRB-E221A-02	09SRB-E221A-03	09SRB-E304A-01	09SRB-A186-01	09SRB-A188A-01	09SRB-A187A-01	
Mass Qtz Vial	2.5284	2.5797	2.5749	2.6337	2.5957	2.5788	2.6769	
Mass Vial+Spl	2.5308	2.5804	2.5760	2.6372	2.5977	2.5807	2.6784	
Mass Spl	0.0024	0.0007	0.0011	0.0035	0.0020	0.0019	0.0015	
Residue ml	0.1000	0.0500	0.0500	0.7500	0.0500	0.0500	0.1000	
Residue	yellow	little yellow	white fluffy	white solid	white	white solid	white fluffy	

12. Add 1 small drop of water with micropipet, slurry precipitate
13. Transfer sample into quartz vial, cover with quartz lid
14. Turn on Bunsen Burner, dry the gel carefully.
15. Burn the Be(OH)2 gel on bunsen burner at least 2 mins, at blue flame.
16. Convert to BeO
17. Determine mass of vial + sample

WS9_Be Sample Chemistry p2

This worksheet outlines the steps to prepare the BeO sample

Chemist: GY/AM **Date:** 02/01/2010

- ☐1 Evaporate Be Sample from column in wiped digestion vessels at 125°C
- ☐2 Add 2-5 ml 20% perchloric and evaporate at 200oC
- ☐3 Again, add 2-5 ml 20% perchloric and evaporate at 200°C
- ☐4 Dissolve sample in 10 ml of 0.5 N HCl (optima grade)
- ☐5 Transfer to 15 ml centrifuge tube
- ☐6 Centrifuge and decant into clean centrifuge tube
- ☐7 Heat centrifuge tubes in water bath at 60°C
- ☐8 Precipitate $Be(OH)_2$ using Matheson ultimate grade ammonia gas
  Gently bubble NH_3 with clean pipet tip on hose
  for ca.15 bubbles, or ca. 8-12 sec until ptte forms
  Optimum pH=9.2; 1N HCl may be added
- ☐9 Centrifuge 15 min., decant (save and redo ☐8 if pH of liquid is < 8)
- ☐10 Wash with water, vortex, centrifuge for 10 min, and decant
- ☐11 Record mass quartz vials, label, and place them in furnace holder

CNEF ID	2391	2392	2393	2394	2395	2313		
Vessel	B24	B25	B26	B28	B29	B13		
Sample ID	09SRB-A355A-01	09SRB-A356A-01	09SRB-A346A-01	09SRB-A348A-01	09SRB-A347-01	Blank		
Mass Qtz Vial	2.5477	2.5427	2.4856	2.6656	2.4936	2.5204		
Mass Vial+Spl	2.5495	2.5443	2.4879	2.6681	2.4957	2.5211		
Mass Spl	0.0018	0.0016	0.0023	0.0025	0.0021	0.0007		
Residue ml	0.1000	0.0500	0.7500	0.1500	0.2000	0.0500		
Residue	white fluffy	little yellow	white	white	yellow!	white very fluffy		

- ☐12 Add 1 small drop of water with micropipet, slurry precipitate
- ☐13 Transfer sample into quartz vial, cover with quartz lid
- ☐14 Turn on Bunsen Burner, dry the gel carefully.
- ☐15 Burn the Be(OH)2 gel on bunsen burner at least 2 mins, at blue flame.
- ☐16 Convert to BeO
- ☐17 Determine mass of vial + sample

WS10_Al Sample Chemistry p1

This worksheet outlines the steps to prepare the Al oxide sample

Chemist: AM/GY **Date:** 01/29/2010

☐1 Evaporate Al Sample from column in wiped teflon vessel at 125°C
☐2 Dissolve sample in 10 ml of 0.5 N HCl (optima grade)
☐3 Transfer to 15 ml centrifuge tube
☐4 Centrifuge and decant into clean centrifuge tube
☐5 Heat centrifuge tubes in water bath at 60°C
☐6 Precipitate $Al(OH)_3$ using 50% NH_3OH (drops: 25, 5, 5, 3, 2…)
Optimum pH=6.3; 1N HCl may be added
☐7 Centrifuge 15 min., decant (save and redo ☐6 if pH of liquid is < 8)
☐8 Wash with water, vortex, centrifuge for 10 min, and decant
☐9 Record mass quartz vials, label, and place them in furnace holder

Vessel ID	C2	C3	C4	C5	C6	C7	C8	
CNEF ID	2381	2382	2383	2384	2386	2387	2390	
Sample ID	09SRB-E221A-01	09SRB-E221A-02	09SRB-E221A-03	09SRB-E304A-01	09SRB-A186-01	09SRB-A188A-01	09SRB-A187A-01	
Mass Qtz Vial	2.5739	2.6192	2.5267	2.6407	2.3677	2.5608	2.5221	
Mass Vial+Spl	2.6008	2.6428	2.5339	2.6490	2.3738	2.5687	2.5301	
Mass Spl	0.0269	0.0236	0.0072	0.0083	0.0061	0.0079	0.008	
Residue ml	2.25	1.75	0.4	0.4	0.4	0.4	0.5	
Residue	white							

☐10 Add 1 small drop of water with micropipet, slurry precipitate
☐11 Transfer sample into quartz vial, cover with alumina vial
☐12 Heat in oven at 120°C for 2-3 hours
☐13 Let cool and scrape sample down from walls of quartz tube
☐14 Convert to Al_2O_3 in furnace at 950°C for minimum of 1 hr
☐15 Determine mass of vial + sample

WS10_Al Sample Chemistry p2

This worksheet outlines the steps to prepare the Al oxide sample

Chemist: AM/GY **Date:** 01/29/2010

☐1 Evaporate Al Sample from column in wiped teflon vessel at 125°C
☐2 Dissolve sample in 10 ml of 0.5 N HCl (optima grade)
☐3 Transfer to 15 ml centrifuge tube
☐4 Centrifuge and decant into clean centrifuge tube
☐5 Heat centrifuge tubes in water bath at 60°C
☐6 Precipitate $Al(OH)_3$ using 50% NH_3OH (drops: 25, 5, 5, 3, 2…)
Optimum pH=6.3; 1N HCl may be added
☐7 Centrifuge 15 min., decant (save and redo ☐6 if pH of liquid is < 8)
☐8 Wash with water, vortex, centrifuge for 10 min, and decant
☐9 Record mass quartz vials, label, and place them in furnace holder

Vessel ID	C9	C10	C11	C14	C17	C18		
CNEF ID	2391	2392	2393	2394	2395	2313		
Sample ID	09SRB-A355A-01	09SRB-A356A-01	09SRB-A346A-01	09SRB-A348A-01	09SRB-A347-01	Blank		
Mass Qtz Vial	2.5648	2.5015	2.6198	2.6835	2.6446	2.5160		
Mass Vial+Spl	2.5727	2.5090	2.6283	2.6923	2.6819	2.5199		
Mass Spl	0.0079	0.0075	0.0085	0.0088	0.0373	0.0039		
Residue ml	0.4	0.5	0.5	0.5	2.5	0.2		
Residue					large amount			

☐10 Add 1 small drop of water with micropipet, slurry precipitate
☐11 Transfer sample into quartz vial, cover with alumina vial
☐12 Heat in oven at 120°C for 2-3 hours
☐13 Let cool and scrape sample down from walls of quartz tube
☐14 Convert to Al_2O_3 in furnace at 950°C for minimum of 1 hr
☐15 Determine mass of vial + sample

WS4_QtzDissolution p1

This worksheet outlines the steps for dissolving quartz and adding Be carrier.

Chemist: AM **Date:** 11/19/2010

	1	2	3	4	5	6	7	8
CNEF ID	2526	2527	2528	2529	2530	2531	2532	2533
Sample ID	09SRB-E222A-01	09SRB-E222A-02	09SRB-E222A-03	09SRB-E222A-04	09SRB-E222A-05	09SRB-E222A-06	10SRB-E042A-01	10SRB-E064A-01
300 ml vessel ID	B1	B2	B6	B7	B8	B10	B12	B15
Beryl Carrier ID	Be3-Carrier,1015 ppm Be,1.013g/ml, Dec 10 2001, JCG, Bottle 2							
Al Carrier ID								
Mass 300 ml vessel	150.2878	150.2873	150.2750	150.2903	150.2229	150.1597	155.1095	150.2883
Mass 40g quartz	35.0116	35.4640	35.1831	35.0160	35.1028	35.0759	35.2063	35.4837
Mass Be carrier	0.1915	0.1892	0.1898	0.1834	0.1861	0.1874	0.1861	0.1813
Mass Al Carrier								

1. Add 20 ml conc. HF and 2 ml HClO4 per 5 g of quartz
2. Add 5 ml Aqua Regia
3. Heat at 100-125o C until quartz dissolves, add HF if needed
4. Raise to 200o C and evaporate to dryness
5. Add 5 ml HClO4 and evaporate to dryness
6. Add 8 to 10 ml conc. HNO3, swirl, and evaporate to dryness
7. Dissolved dried sample in 20 ml of 2% HCl

Comments

19.11.2(add 140 ml HF, 50 ml Aqua Regia, 8ml HClO4, put on hotplate @ 15:00

21.11.2(all sample dissolved, except for #26 and #29 some residue, open lid @ 12:00, increse to 200 C

22.11.2(add 5 ml HClO4 @ 14:00; blank small white dot, most samples yellow or brown small precipitation; #12 some white fluffy precipitation; #8 and #10 quite some white fluffy precipitation and some large white needle/shaped crzstalls; #26 lots of white fluffy precipitation, many large white needle-shaped crystalls; #29 some brown and some white fluffy precipitation (no needle shaped crystalls); #15 very long to evaporate, add 5ml HClO4 @ 17:45

22.11.2(add 8 / 15 / 20 ml HNO3 @ 23:00, reduce heat to 110 C; almost all samples (add 8ml(yellow or brown small precipitation, #12 (add 8ml) some white solid precipitation (not fluffy anymore), #8 and #10 (add 15ml) quite some white precipitation with large needle-shaped crystalls, # 26 (add 20 ml) lots of white precipitation with large needle-shaped crystalls, #29 (add 15ml) some brown and white fluffy precipitation (no crystalls)

23.11.2(all samples but #30 (blank), #1 and #2 dry; fan of fumehood makes strange sound -> shut down fumehood ventilation during repair and samples still drying on hotplate

most samples small brown or yellow precipitation, samples #8, 10, 26 a lot of white precititation with manz smaller (0.5cm-long) needle-shaped crystalls (#26 has most precipitation); #29 some yellow and more white precipitation (no crystalls), when dissolved in 2% HNO3 especially yellow precipitation turned into a 'gel'-like mass

#8 = 25 after ultrasonic (3 rounds) some white chunks left plus some white grains (probably felspar?)
Al-test: medium-sized fluffy precipitation

#10 = 2! same as 2530, but more white grains left after ultrasonic (3 rounds)
Al-test: medium-sized fluffy precipitation

#26 = 2! after ultrasonic (5 rounds) few small white chunks left plus many white grains (probably felspar?)
Al-test: medium-sized fluffy precipitation
one of two true tor samples from ridge NW of Broughten channel (other sample 2534 no problems)

#29 = 2! after ultrasonic (5 rounds) some muscovite left plus some few white grains (fine)
Al-test: medium-sized fluffy precipitation, result 100 ppm due to Al in muscovite
Moonshine ridge sample (strained tonalite with 20% mica)

23.11.2(samples #8, #10, #26 and #29 not dissolved and a lot of residue after centrifuging for 10 min
try to bring back residue of samples #8 and #29 by spliting up sample between 4 test tubes (before and afterwards vortex) and adding 5ml of concentrated HNO3 to each tube (bring it up to 10.5ml in total), heat the test tubes in waterbath @ 100 C for up to 1 hour -> still not dissolved
take these samples out of process and do sand abrasion with left over sample, include into next batch of tor samples (4 more samples need to be crushed and purified)

24.11.2(samples #30, #1 and #2 dry @ 14:30, dissolve in 20ml 2% HNO3

WS4_QtzDissolution p2

This worksheet outlines the steps for dissolving quartz and adding Be carrier.

Chemist: AM **Date:** 11/19/2010

	1	2	3	4	5	6	7	8
CNEF ID	2534	2535	2536	2420				
Sample ID	10SRB-E065A-01	10SRB-E066A-01	10SRB-E074A-01	blank				
300 ml vessel ID	B18	B26	B29	B30				
Beryl Carrier ID	Be3-Carrier, 1015 ppm Be,1.013g/ml, Dec 10 2001, JCG, Bottle 2							
Al Carrier ID								
Mass 300 ml vessel	150.2457	150.6166	150.1950	150.2078				
Mass 40g quartz	35.5655	35.1844	35.2873					
Mass Be carrier	0.1923	0.1920	0.1913	0.1803				
Mass Al Carrier								

1. Add 20 ml conc. HF and 2 ml HClO4 per 5 g of quartz
2. Add 5 ml Aqua Regia
3. Heat at 100-125°C until quartz dissolves, add HF if needed
4. Raise to 200°C and evaporate to dryness
5. Add 5 ml HClO4 and evaporate to dryness
6. Add 8 to 10 ml conc. HNO3, swirl, and evaporate to dryness
7. Dissolved dried sample in 20 ml of 2% HCl

Comments

19.11.2010 add 140 ml HF, 50 ml Aqua Regia, 8ml HClO4, put on hotplate @ 15:00

21.11.2010 all sample dissolved, except for #26 and #29 some residue, open lid @ 12:00, increse to 200 C

22.11.2010 add 5 ml HClO4 @ 14:00; blank small white dot, most samples yellow or brown small precipitation; #12 some white fluffy precipitation; #8 and #10 quite some white fluffy precipitation and some large white needle/shaped crzstalls; #26 lots of white fluffy precipitation, many large white needle-shaped crystalls; #29 some brown and some white fluffy precipitation (no needle shaped crystalls); #15 very long to evaporate, add 5ml HClO4 @ 17:45

22.11.2010 add 8 / 15 / 20 ml HNO3 @ 23:00, reduce heat to 110 C; almost all samples (add 8ml(yellow or brown small precipitation, #12 (add 8ml) some white solid precipitation (not fluffy anymore), #8 and #10 (add 15ml) quite some white precipitation with large needle-shaped crystalls, # 26 (add 20 ml) lots of white precipitation with large needle-shaped crystalls, #29 (add 15ml) some brown and white fluffy precipitation (no crystalls)

23.11.2010 all samples but #30 (blank), #1 and #2 dry; fan of fumehood makes strange sound -> shut down fumehood ventilation during repair and samples still drying on hotplate

most samples small brown or yellow precipitation, samples #8, 10, 26 a lot of white precititation with manz smaller (0.5cm-long) needle-shaped crystalls (#26 has most precipitation); #29 some yellow and more white precipitation (no crystalls), when dissolved in 2% HNO3 especially yellow precipitation turned into a 'gel'-like mass

#8 = 2530 after ultrasonic (3 rounds) some white chunks left plus some white grains (probably felspar?)
Al-test: medium-sized fluffy precipitation

#10 = 2530 same as 2530, but more white grains left after ultrasonic (3 rounds)
Al-test: medium-sized fluffy precipitation

#26 = 2534 after ultrasonic (5 rounds) few small white chunks left plus many white grains (probably felspar?)
Al-test: medium-sized fluffy precipitation
one of two true tor samples from ridge NW of Broughten channel (other sample 2534 no problems)

#29 = 2535 after ultrasonic (5 rounds) some muscovite left plus some few white grains (fine)
Al-test: medium-sized fluffy precipitation, result 100 ppm due to Al in muscovite
Moonshine ridge sample (strained tonalite with 20% mica)

23.11.2010 samples #8, #10, #26 and #29 not dissolved and a lot of residue after centrifuging for 10 min
try to bring back residue of samples #8 and #29 by spliting up sample between 4 test tubes (before and afterwards vortex) and adding 5ml of concentrated HNO3 to each tube (bring it up to 10.5ml in total), heat the test tubes in waterbath @ 100 C for up to 1 hour -> still not dissolved
take these samples out of process and do sand abrasion with left over sample, include into next batch of tor samples (4 more samples need to be crushed and purified)

24.11.2010 samples #30, #1 and #2 dry @ 14:30, dissolve in 20ml 2% HNO3

WS5B_ICP Aliquot and Al spiking p1

This worksheet outlines the steps for collecting ICP aliquots and adding Al carrier.

Chemist: AM **Date:** 11/24/2010

1. Label one 100 ml volumetric flasks per sample
2. Label one ICP vial with CNEF ID per sample

Vessel ID	B1	B2	B6	B7	~~B8~~	~~B10~~	B12	B15
CNEF ID	2526	2527	2528	2529	~~2530~~	~~2531~~	2532	2533
Sample ID	09SRB-E222A-01	09SRB-E222A-02	09SRB-E222A-03	09SRB-E222A-04	~~09SRB-E222A-05~~	~~09SRB-E222A-06~~	10SRB-E042A-01	10SRB-E064A-01
Al carrier ID	LOT # 94-096673J							
Quant-EM est. Al in qtz	25	25	25	25			25	25
Mass 100 ml volumetric	66.3035	68.8753	67.0102	67.7324			66.5889	66.4889
100 ml volumetric + sample + 2% HNO3	167.6248	170.1347	168.4677	169.2417			168.1836	167.9088
Mass 10 ml smple to vol A (10 ml tube)	9.9080	9.9173	9.8653	9.9067			9.9587	9.9022
Mass 5 ml to volumetric B	5.0097	5.0080	5.0479	5.0267			5.0483	5.0104
Add 2 drops carrier, mass	5.0436	5.0389	5.0798	5.0555			5.0789	5.0390
Bring B to 10 ml with 2% HNO3	10.1648	10.1040	10.1496	10.0839			10.1488	10.1832
Mass8 5 ml Sample	152.6938	155.1942	153.5407	154.2865			152.7854	152.9680
Add carrier to 85ml sample	1.7429	1.7297	1.7442	1.7420			1.7340	1.8031
Mass 5 ml with carrier to Volumtric C	5.0131	5.0139	5.0806	5.0216			5.0134	5.0066
Bring C to 10 ml	10.1863	10.1150	10.1489	10.1396			10.1172	10.0983
Mass of 80 ml sample	**149.4197**	**151.9035**	**150.2085**	**151.0011**			**149.8733**	**149.7551**

Samples 2530 and 2531 not furhter processed -> require more purification

WS5B_ICP Aliquot and Al spiking p2

This worksheet outlines the steps for collecting ICP aliquots and adding Al carrier.

Chemist: AM **Date:** 11/24/2010

1. Label one 100 ml volumetric flasks per sample
2. Label one ICP vial with CNEF ID per sample

Vessel ID	**B18**	~~**B26**~~	~~**B29**~~	**B30**				
CNEF ID	**2534**	~~**2535**~~	~~**2536**~~	**2420**				
Sample ID	10SRB-E065A-01	~~10SRB-E066A-01~~	~~10SRB-E074A-01~~	blank				
Al carrier ID	LOT # 94-096673J							
Quant-EM est. Al in qtz	25			25				
Mass 100 ml volumetric	66.7040			66.8429				
100 ml volumetric + sample + 2% HNO3	168.0902			168.0166				
Mass 10 ml smple to vol A (10 ml tube)	9.9024			9.9121				
Mass 5 ml to volumetric B	5.0203			5.0035				
Add 2 drops carrier, mass	5.0521			5.0349				
Bring B to 10 ml with 2% HNO3	10.1324			10.1181				
Mass8 5 ml Sample	153.1353			153.0874				
Add carrier to 85ml sample	1.7293			2.9683				
Mass 5 ml with carrier to Volumtric C	5.0013			5.0052				
Bring C to 10 ml	10.1289			10.1571				
Mass of 80 ml sample	**149.8577**			**151.0382**				

Samples 2535 and 2536 not furhter processed -> require more purification

WS6_Anion Column Chemistry p1

This worksheet outlines the steps for the Anion Column Chemistry (2ml size small column)

Chemist: AM **Date:** 11/25/2010

☐1 Evaporate 20 ml to dryness at 100-120°C (will take at least 3 hrs)
☐2 Dissolve in 10 ml 9 N HCl (let stand for several hours)
☐3 Transfer to 15 ml centrifuge tubes, rinse digestion vessels with 9 N HCl to bring volume in tube to 10 ml
☐4 Centrifuge at 1500 rpm or higher for minimum of 10 minutes
☐5 Allow any 9 N HCl in columns to drain out; discard

Column ID	1	2	3	4	5	6	7	8
Vessel	B1	B2	B6	B7	~~B8~~	~~B10~~	B12	B15
CNEF ID	2526	2527	2528	2529	~~2530~~	~~2531~~	2532	2533
Sample ID	09SRB-E222A-01	09SRB-E222A-02	09SRB-E222A-03	09SRB-E222A-04	~~09SRB-E222A-05~~	~~09SRB-E222A-06~~	10SRB-E042A-01	10SRB-E064A-01

☐6 With stopcock closed, pipet sample (avoid residue) onto 2ml size columns.
☐7 Collect sample in same 300 ml teflon vessel.
☐8 Elute with 10 ml 9 N HCl, and collect that, close stopcock
☐9 5 ml 4.5 N HCl, collect Anion Supernate in labeled 100 ml bottle
☐10 10 ml 1 N HCl, collect Anion Supernate
☐11 50 ml deionized water. Discard.
☐12 CONDITION ANION COLUMN
(bottle A1) 10 ml 1N HCl, discard
(bottle A2) 10 ml 4.5 N HCl, discard
(bottle A3) 10 ml 9 N HCl, discard, but retain acid approx. 2 mm above resin

Comments

WS6_Anion Column Chemistry p2

This worksheet outlines the steps for the Anion Column Chemistry (2ml size small column)

Chemist: AM **Date:** 11/25/2010

☐1 Evaporate 20 ml to dryness at 100-120°C (will take at least 3 hrs)
☐2 Dissolve in 10 ml 9 N HCl (let stand for several hours)
☐3 Transfer to 15 ml centrifuge tubes, rinse digestion vessels with 9 N HCl to bring volume in tube to 10 ml
☐4 Centrifuge at 1500 rpm or higher for minimum of 10 minutes
☐5 Allow any 9 N HCl in columns to drain out; discard

Column ID	1	2	3	4	5	6	7	8
Vessel	B18	~~B26~~	~~B29~~	B30				
CNEF ID	2534	~~2535~~	~~2536~~	2420				
Sample ID	10SRB-E065A-01	~~10SRB-E066A-01~~	~~10SRB-E074A-01~~	blank				

☐6 With stopcock closed, pipet sample (avoid residue) onto 2ml size columns.
☐7 Collect sample in same 300 ml teflon vessel.
☐8 Elute with 10 ml 9 N HCl, and collect that, close stopcock
☐9 5 ml 4.5 N HCl, collect Anion Supernate in labeled 100 ml bottle
☐10 10 ml 1 N HCl, collect Anion Supernate
☐11 50 ml deionized water. Discard.
☐12 CONDITION ANION COLUMN
(bottle A1) 10 ml 1 N HCl, discard
(bottle A2) 10 ml 4.5 N HCl, discard
(bottle A3) 10 ml 9 N HCl, discard, but retain acid approx. 2 mm above resin

Comments

WS7_Controlled Precipitate p1

This worksheet outlines the steps for the controlled precipitation chemistry

Chemist: AM **Date:** 11/26/2010

---

1. Evaporate "anion" elute to dryness at 125°C
2. Dissolve in 10 ml of a 1:1 solution of 0.5 N HCl and 2% NH_4Cl
3. Transfer to 15 ml centrifuge, centrifuge for 10 minutes
4. Decant into clean test tube, heat in water bath at 60°C
5. Add drops of 1:1 NH_4OH:H_2O to pH=9.2 (5 drops first then single)
6. Centrifuge for 15 minutes
7. Check pH of liquid, if less than pH=7, redo step 5
8. Decant, save with Anion Supernate
9. Wash with deionized water, vortex, centrifuge, decant
10. Wash with deionized water, vortex, centrifuge, decant
11. Wash with deionized water, vortex, centrifuge, decant

CNEF ID	2526	2527	2528	2529	~~2530~~	~~2531~~	2532	2533
Vessel	B1	B2	B6	B7	~~B8~~	~~B10~~	B12	B15
Sample ID	09SRB-E222A-01	09SRB-E222A-02	09SRB-E222A-03	09SRB-E222A-04	~~09SRB-E222A-05~~	~~09SRB-E222A-06~~	10SRB-E042A-01	10SRB-E064A-01
Approx. vol. Ptte	0.8 ml	0.9 ml	0.7 ml	0.6 ml			2 ml	1 ml

Comments

2526 white to yellowish fluffy precipitate
2527 white fluffy precipitate
2528 white fluffy to solid precipitate
2529 white fluffy to solid precipitate
2532 bottom <0.1 ml white solid above white very fluffy precipitate
2533 white to yellowish fluffy precipitate
2543 white very fluffy precipitate
2420 white very fluffy precipitate

WS7_Controlled Precipitate p2

This worksheet outlines the steps for the controlled precipitation chemistry

Chemist: AM **Date:** 11/26/2010

- ☐ 1 Evaporate "anion" elute to dryness at 125°C
- ☐ 2 Dissolve in 10 ml of a 1:1 solution of 0.5 N HCl and 2% NH_4Cl
- ☐ 3 Transfer to 15 ml centrifuge, centrifuge for 10 minutes
- ☐ 4 Decant into clean test tube, heat in water bath at 60°C
- ☐ 5 Add drops of 1:1 NH_4OH:H_2O to pH=9.2 (5 drops first then single)
- ☐ 6 Centrifuge for 15 minutes
- ☐ 7 Check pH of liquid, if less than pH=7, redo step ☐ 5
- ☐ 8 Decant, save with Anion Supernate
- ☐ 9 Wash with deionized water, vortex, centrifuge, decant
- ☐ 10 Wash with deionized water, vortex, centrifuge, decant
- ☐ 11 Wash with deionized water, vortex, centrifuge, decant

CNEF ID	2534	~~2535~~	~~2536~~	2420				
Vessel	B18	~~B26~~	~~B29~~	B30				
Sample ID	10SRB-E065A-01	~~10SRB-E066A-01~~	~~10SRB-E074A-01~~	blank				
Approx. vol. Ptte	1.5 ml			0.35 ml				

Comments

2526 white to yellowish fluffy precipitate
2527 white fluffy precipitate
2528 white fluffy to solid precipitate
2529 white fluffy to solid precipitate
2532 bottom <0.1 ml white solid above white very fluffy precipitate
2533 white to yellowish fluffy precipitate
2543 white very fluffy precipitate
2420 white very fluffy precipitate

WS8_Cation Column Chemistry p1

This worksheet outlines the steps for the Cation Column Chemistry

Chemist: AM **Date:** 11/29/2010

---

1. Dissolve in 5 ml conc. HCl and evaporate to dryness at 125°C
2. Redissolve in 2.5 ml 1 N HCl and 2.5 ml 0.5 N HCl
3. Transfer to centrifuge tube, rinse with 1 ml 0.5 N, and centrifuge

Column ID	1	2	3	4	5	6	7	8
Vessel	B1	B2	B6	B7	~~B8~~	~~B10~~	B12	B15
CNEF ID	2526	2527	2528	2529	~~2530~~	~~2531~~	2532	2533
Sample ID	09SRB-E222A-01	09SRB-E222A-02	09SRB-E222A-03	09SRB-E222A-04	~~09SRB-E222A-05~~	~~09SRB-E222A-06~~	10SRB-E042A-01	10SRB-E064A-01

4. Pipette all of the sample into designated conditioned cation column, 17 ml
5. Discard the eluant. Add 285 ml 0.5 N HCL (Bottle C6)
6. Drain the column, discard the first 300ml of eluant
7. Add 60 ml of 0.5N HCl, (Bottle C7), Collect eluant as Cation Supernate
8. Add 65 ml of 0.5N HCl, (Bottle C8), Save it as Be-Sample
9. Add 120 ml 1N HCl (bottle C9)
10. Save this as Be-sample as well.
11. Add 80 ml 4.5 N HCl (bottle C10) , save the eluant as Al sample.
12. CONDITION CATION COLUMN

(bottle C1) 100 ml 9 N HCl

(bottle C2) 50 ml 4.5 N HCl

(bottle C3) 50 ml 1 N HCl

(bottle C4) 50 ml water

(bottle C5) 100 ml 0.5 N HCl

* 17 ml Column

WS8_Cation Column Chemistry p2

This worksheet outlines the steps for the Cation Column Chemistry

Chemist: AM **Date:** 11/29/2010

---

1. Dissolve in 5 ml conc. HCl and evaporate to dryness at 125°C
2. Redissolve in 2.5 ml 1 N HCl and 2.5 ml 0.5 N HCl
3. Transfer to centrifuge tube, rinse with 1 ml 0.5 N, and centrifuge

Column ID	1	2	3	4	5	6	7	8
Vessel	B18	~~B26~~	~~B29~~	B30				
CNEF ID	2534	~~2535~~	~~2536~~	2420				
Sample ID	10SRB-E065A-01	~~10SRB-E066A-01~~	~~10SRB-E074A-01~~	blank				

4. Pipette all of the sample into designated conditioned cation column, 17 ml
5. Discard the eluant. Add 285 ml 0.5 N HCL (Bottle C6)
6. Drain the column, discard the first 300ml of eluant
7. Add 60 ml of 0.5N HCl, (Bottle C7), Collect eluant as Cation Supernate
8. Add 65 ml of 0.5N HCl, (Bottle C8), Save it as Be-Sample
9. Add 120 ml 1N HCl (bottle C9)
10. Save this as Be-sample as well.
11. Add 80 ml 4.5 N HCl (bottle C10) , save the eluant as Al sample.
12. CONDITION CATION COLUMN

(bottle C1) 100 ml 9 N HCl

(bottle C2) 50 ml 4.5 N HCl

(bottle C3) 50 ml 1 N HCl

(bottle C4) 50 ml water

(bottle C5) 100 ml 0.5 N HCl

* 17 ml Column

WS9_Be Sample Chemistry p1

This worksheet outlines the steps to prepare the BeO sample

Chemist: AM **Date:** 12/01/2010

---

1. Evaporate Be Sample from column in wiped digestion vessels at 125°C
2. Add 2-5 ml 20% perchloric and evaporate at 200oC
3. Again, add 2-5 ml 20% perchloric and evaporate at 200°C
4. Dissolve sample in 10 ml of 0.5 N HCl (optima grade)
5. Transfer to 15 ml centrifuge tube
6. Centrifuge and decant into clean centrifuge tube
7. Heat centrifuge tubes in water bath at 60°C
8. Precipitate $Be(OH)_2$ using Matheson ultimate grade ammonia gas
   Gently bubble NH_3 with clean pipet tip on hose
   for ca.15 bubbles, or ca. 8-12 sec until ptte forms
   Optimum pH=9.2; 1N HCl may be added
9. Centrifuge 15 min., decant (save and redo ☐8 if pH of liquid is < 8)
10. Wash with water, vortex, centrifuge for 10 min, and decant
11. Record mass quartz vials, label, and place them in furnace holder

CNEF ID	2526	2527	2528	2529	~~2530~~	~~2531~~	2532	2533
Vessel	B1	B2	B6	B7	~~B8~~	~~B10~~	B12	B15
Sample ID	09SRB-E222A-01	09SRB-E222A-02	09SRB-E222A-03	09SRB-E222A-04	~~09SRB-E222A-05~~	~~09SRB-E222A-06~~	10SRB-E042A-01	10SRB-E064A-01
Mass Qtz Vial	2.6110	2.5631	2.6555	2.5395			2.6240	2.6555
Mass Vial+Spl	2.6137	2.5650	2.6560	2.5412			2.6264	2.6574
Mass Spl	0.0027	0.0019	0.0005	0.0017			0.0024	0.0019

12. Add 1 small drop of water with micropipet, slurry precipitate
13. Transfer sample into quartz vial, cover with quartz lid
14. Turn on Bunsen Burner, dry the gel carefully.
15. Burn the Be(OH)2 gel on bunsen burner at least 2 mins, at blue flame.
18. Convert to BeO
19. Determine mass of vial + sample

WS9_Be Sample Chemistry p2

This worksheet outlines the steps to prepare the BeO sample

Chemist: AM **Date:** 12/01/2010

☐1 Evaporate Be Sample from column in wiped digestion vessels at 125°C
☐2 Add 2-5 ml 20% perchloric and evaporate at 200oC
☐3 Again, add 2-5 ml 20% perchloric and evaporate at 200°C
☐4 Dissolve sample in 10 ml of 0.5 N HCl (optima grade)
☐5 Transfer to 15 ml centrifuge tube
☐6 Centrifuge and decant into clean centrifuge tube
☐7 Heat centrifuge tubes in water bath at 60°C
☐8 Precipitate $Be(OH)_2$ using Matheson ultimate grade ammonia gas
Gently bubble NH_3 with clean pipet tip on hose
for ca.15 bubbles, or ca. 8-12 sec until ptte forms
Optimum pH=9.2; 1N HCl may be added
☐9 Centrifuge 15 min., decant (save and redo ☐8 if pH of liquid is < 8)
☐10 Wash with water, vortex, centrifuge for 10 min, and decant
☐11 Record mass quartz vials, label, and place them in furnace holder

CNEF ID	2534	~~2535~~	~~2536~~	2420				
Vessel	B18	~~B26~~	~~B29~~	B30				
Sample ID	10SRB-E065A-01	~~10SRB-E066A-01~~	~~10SRB-E074A-01~~	blank				
Mass Qtz Vial	2.6298			2.6279				
Mass Vial+Spl	2.6311			2.6285				
Mass Spl	0.0013			0.0006				

☐12 Add 1 small drop of water with micropipet, slurry precipitate
☐13 Transfer sample into quartz vial, cover with quartz lid
☐14 Turn on Bunsen Burner, dry the gel carefully.
☐15 Burn the Be(OH)2 gel on bunsen burner at least 2 mins, at blue flame.
☐18 Convert to BeO
☐19 Determine mass of vial + sample

WS10_Al Sample Chemistry p1

This worksheet outlines the steps to prepare the Al oxide sample

Chemist: AM **Date:** 11/30/2010

☐1 Evaporate Al Sample from column in wiped teflon vessel at 125°C
☐2 Dissolve sample in 10 ml of 0.5 N HCl (optima grade)
☐3 Transfer to 15 ml centrifuge tube
☐4 Centrifuge and decant into clean centrifuge tube
☐5 Heat centrifuge tubes in water bath at 60°C
☐6 Precipitate $Al(OH)_3$ using 50% NH_3OH (drops: 25, 5, 5, 3, 2…)
Optimum pH=6.3; 1N HCl may be added
☐7 Centrifuge 15 min., decant (save and redo ☐6 if pH of liquid is < 8)
☐8 Wash with water, vortex, centrifuge for 10 min, and decant
☐9 Record mass quartz vials, label, and place them in furnace holder

CNEF ID	2526	2527	2528	2529	~~2530~~	~~2531~~	2532	2533
Sample ID	09SRB-E222A-01	09SRB-E222A-02	09SRB-E222A-03	09SRB-E222A-04	~~09SRB-E222A-05~~	~~09SRB-E222A-06~~	10SRB-E042A-01	10SRB-E064A-01
Mass Qtz Vial	2.5979	2.5879	2.5950	2.6506			2.6315	2.6108
Mass Vial+Spl	2.6044	2.5937	2.6022	2.6577			2.6560	2.6193
Mass Spl	0.0065	0.0058	0.0072	0.0071			0.0245	0.0085

☐10 Add 1 small drop of water with micropipet, slurry precipitate
☐11 Transfer sample into quartz vial, cover with alumina vial
☐12 Heat in oven at 120°C for 2-3 hours
☐13 Let cool and scrape sample down from walls of quartz tube
☐14 Convert to Al_2O_3 in furnace at 950°C for minimum of 1 hr
☐15 Determine mass of vial + sample

WS10_Al Sample Chemistry p2

This worksheet outlines the steps to prepare the Al oxide sample

Chemist: AM **Date:** 11/30/2010

☐1 Evaporate Al Sample from column in wiped teflon vessel at 125°C
☐2 Dissolve sample in 10 ml of 0.5 N HCl (optima grade)
☐3 Transfer to 15 ml centrifuge tube
☐4 Centrifuge and decant into clean centrifuge tube
☐5 Heat centrifuge tubes in water bath at 60°C
☐6 Precipitate $Al(OH)_3$ using 50% NH_3OH (drops: 25, 5, 5, 3, 2…)
Optimum pH=6.3; 1N HCl may be added
☐7 Centrifuge 15 min., decant (save and redo ☐6 if pH of liquid is < 8)
☐8 Wash with water, vortex, centrifuge for 10 min, and decant
☐9 Record mass quartz vials, label, and place them in furnace holder

CNEF ID	2534	~~2535~~	~~2536~~	2420				
Sample ID	10SRB-E065A-01	~~10SRB-E066A-01~~	~~10SRB-E074A-01~~	blank				
Mass Qtz Vial	2.5345			2.6458				
Mass Vial+Spl	2.5451			2.6490				
Mass Spl	0.0106			0.0032				

☐10 Add 1 small drop of water with micropipet, slurry precipitate
☐11 Transfer sample into quartz vial, cover with alumina vial
☐12 Heat in oven at 120°C for 2-3 hours
☐13 Let cool and scrape sample down from walls of quartz tube
☐14 Convert to Al_2O_3 in furnace at 950°C for minimum of 1 hr
☐15 Determine mass of vial + sample

WS4_QtzDissolution p1

This worksheet outlines the steps for dissolving quartz and adding Be carrier.

Chemist: AM **Date:** 03/11/11

	1	2	3	4	5	6	7	8
CNEF ID	2588	2589	2590	2530	2531	2536	2535	
Sample ID	10SRB-E020A-01	10SRB-E021A-01	10SRB-E022A-01	09SRB-E222-05	09SRB-E222-06	10SRB-E074A-01	10SRB-E066A-01	
300 ml vessel ID	B2	B3	B6	B7	B10	B12	B13	
Beryl Carrier ID	Be3-Carrier, 1015 ppm Be, r = 1.013 g ml-1, Dec 10 2001, JCG, Bottle 2							
Al Carrier ID								
Mass 300 ml vessel	150.2807	150.2890	150.2665	150.2766	150.1261	155.0433	154.7739	
Mass 40g quartz	35.1812	35.5590	35.2522	34.7466	35.0731	30.4142	35.1074	
Mass Be carrier	0.1915	0.1865	0.1865	0.1794	0.1886	0.1810	0.1795	
Mass Al Carrier								
Residue	med. yellow to brown	med. yellow to brown	med. yellow to brown	med. yellow to brown	med. white to yellow with holes	large-med. white with holes	med. yellow to brown	
Colo 2% HNO3:	rust brown	yellow brown	yellow cloudy	yellow to white	light yellow cloudy	white cloudy	normal transparent	
Residue in tube:	~1mm	<1mm	<1mm	<0.5mm	<1mm	~0.2ml	none	

1. Add 20 ml conc. HF and 2 ml HClO4 per 5 g of quartz
2. Add 5 ml Aqua Regia
3. Heat at 100-125o C until quartz dissolves, add HF if needed
4. Raise to 200o C and evaporate to dryness
5. Add 5 ml HClO4 and evaporate to dryness
6. Add 8 to 10 ml conc. HNO3, swirl, and evaporate to dryness
7. Dissolved dried sample in 20 ml of 2% HCl

Comments

March 11:	add 140ml HF, 50ml AR, 10ml HClO4 to each sample put on hotplate for dissolution at 17:00 at 125°C
March 15:	Samples completely dissolved, open lid, increase T = 200°C, start evaporation at 14:00
March 16:	Samples 1/2 - 3/4 evaporated, less efficient on front side -> rotate samples on hotplate
March 17:	8:30 some drops on walls and lid left, but bottom dry -> note colour and amount of residue 13:30 some drops on walls and lid left -> tap jar carefully and put back on hotplate
March 15-17:	Samples open at same time as Alan's Wounded Moose samples (high nuclide concentration)
March 18:	14:00 samples completely dry, remove from hotplate, close lid and set aside to wait for three more samples form last year to be included in this batch of samples
March 19:	Set up 3 more samples from last year (poor Al-AMS measurement, likely due to chemistry) for just Al targets; 11:00 add 140 ml HF, 50 ml AR, 10 ml HCl04 for dissolution at 125 °C
March 20:	11:30 samples 2381 / 82 / 95 completely dissolved, open lid, increase T = 200°C, start evaporation
March 21:	16:30 add 5 ml HClO4 to first group of samples plus blank, 3 other samples not completely dry 19:00 add 5 ml HClO4 to 3 other samples
March 22:	8:30 / 12:30 samples almost dry, just few drops on walls and lids left -> tap jar carefully 19:00 add 5ml conc. HNO3, swirl and evaporate, add ~3-5ml conc. HNO3 to dissolve all samples
March 23:	samples completely dry, remove from hotplate, add 2% HNO3, soak -> very colourful sonsutions, transfer to 2 centrifuge tubes, bring up to 9ml, some samples difficult to transfer, because of high surface tension of some material, makes it hard to soak everything up, after centrifuge clear or slightly yellow solutions, colour trapped into residue, pipette solution into two additional centrifuge tubes and centrifuge again -> less cloudy solutions, some small residue; clean residue with additional 2ml 2% HNO3, vortex and centrifuge, transfer clean solution to two additional tubes; little bit of residue of sample B12 lost (plopped while cleaning)
Note:	All acids used trace metal grade and micro-purified water

WS4_QtzDissolution p2

This worksheet outlines the steps for dissolving quartz and adding Be carrier.

Chemist: AM **Date:** 03/11/11

	1	2	3	4	5	6	7	8
CNEF ID	2423	2381	2382	2395				
Sample ID	blank	09SRB-E221A-01	09SRB-E221A-02	09SRB-A347A-01				
300 ml vessel ID	B16	B17	B18	B20				
Beryl Carrier ID	Be3-Carrier, 1015 ppm Be, r = 1.013 g ml-1, Dec 10 2001, JCG, Bottle 2							
Al Carrier ID								
Mass 300 ml vessel	155.8895	154.9266	150.2344	150.2993				
Mass 40g quartz	-	30.0074	30.1661	30.0465				
Mass Be carrier	0.1922	-	-	-				
Mass Al Carrier								
Residue	small white (little dot)	med. rusty brown	med. brown	med. yellow to white				
Colo 2% HNO3:	normal	yellow clear	light yellow clear	white cloudy				
Residue in tube:	none	~1mm	<1mm	~1mm				

1. Add 20 ml conc. HF and 2 ml HClO4 per 5 g of quartz
2. Add 5 ml Aqua Regia
3. Heat at 100-125°C until quartz dissolves, add HF if needed
4. Raise to 200°C and evaporate to dryness
5. Add 5 ml HClO4 and evaporate to dryness
6. Add 8 to 10 ml conc. HNO3, swirl, and evaporate to dryness
7. Dissolved dried sample in 20 ml of 2% HCl

Comments

March 11:	add 140ml HF, 50ml AR, 10ml HClO4 to each sample put on hotplate for dissolution at 17:00 at 125°C
March 15:	Samples completely dissolved, open lid, increase T = 200°C, start evaporation at 14:00
March 16:	Samples 1/2 - 3/4 evaporated, less efficient on front side -> rotate samples on hotplate
March 17:	8:30 some drops on walls and lid left, but bottom dry -> note colour and amount of residue 13:30 some drops on walls and lid left -> tap jar carefully and put back on hotplate
March 15-17:	Samples open at same time as Alan's Wounded Moose samples (high nuclide concentration)
March 18:	14:00 samples completely dry, remove from hotplate, close lid and set aside to wait for three more samples form last year to be included in this batch of samples
March 19:	Set up 3 more samples from last year (poor Al-AMS measurement, likely due to chemistry) for just Al targets; 11:00 add 140 ml HF, 50 ml AR, 10 ml HCl04 for dissolution at 125 °C
March 20:	11:30 samples 2381 / 82 / 95 completely dissolved, open lid, increase T = 200°C, start evaporation
March 21:	16:30 add 5 ml HClO4 to first group of samples plus blank, 3 other samples not completely dry 19:00 add 5 ml HClO4 to 3 other samples
March 22:	8:30 / 12:30 samples almost dry, just few drops on walls and lids left -> tap jar carefully 19:00 add 5ml conc. HNO3, swirl and evaporate, add ~3-5ml conc. HNO3 to dissolve all samples
March 23:	samples completely dry, remove from hotplate, add 2% HNO3, soak -> very colourful sonsutions, transfer to 2 centrifuge tubes, bring up to 9ml, some samples difficult to transfer, because of high surface tension of some material, makes it hard to soak everything up, after centrifuge clear or slightly yellow solutions, colour trapped into residue, pipette solution into two additional centrifuge tubes and centrifuge again -> less cloudy solutions, some small residue; clean residue with additional 2ml 2% HNO3, vortex and centrifuge, transfer clean solution to two additional tubes; little bit of residue of sample B12 lost (plopped while cleaning)
Note:	All acids used trace metal grade and micro-purified water

WS5B_ICP Aliquot and Al spiking p1

This worksheet outlines the steps for collecting ICP aliquots and adding Al carrier.

Chemist: AM **Date:** 03/23/11

---

1. Label one 100 ml volumetric flasks per sample
2. Label one ICP vial with CNEF ID per sample

Vessel ID	B2	B3	B6	B7	B10	B12	B13	
CNEF ID	2588	2589	2590	2530	2531	2536	2535	
Sample ID	10SRB-E020A-01	10SRB-E021A-01	10SRB-E022A-01	09SRB-E222-05	09SRB-E222-06	10SRB-E074A-01	09SRB-E066A-01	
Al carrier ID	Aluminium, plasma standard solution, Specpcere, A=1000µg/ml, Stock# 38727, Lot# 03-16108B, Nov. 2011							
Quant-EM est. Al in qtz	35	50	25	25	50	100	50	
Mass 100 ml volumetric	67.1376	68.8721	67.4181	67.1808	66.3006	67.3498	66.7016	
100 ml volumetric + sample + 2% HNO3	168.2867	169.9443	168.6731	168.3829	167.5321	168.6547	167.8980	
Mass 10 ml smple to vol A (10 ml tube)	10.0035	10.0189	10.0074	10.0525	9.9953	10.0037	10.0221	
Mass 5 ml to volumetric B	5.0225	5.0300	5.0054	5.0143	5.0104	5.0005	5.0068	
Add 2 drops carrier, mass	5.0484	5.0471	5.0332	5.0416	5.0355	5.0256	5.0338	
Bring B to 10 ml with 2% HNO3	10.0278	9.9927	10.0195	10.0079	10.0003	10.0170	10.0046	
Mass8 5 ml Sample	153.2503	154.8824	153.6480	153.3037	152.5151	153.6404	152.6808	
Add carrier to 85ml sample	1.2460	0.4842	1.7386	1.7469	0.5117	-	0.5160	
Mass 5 ml with carrier to Volumtric C	5.0580	5.0128	5.0518	5.0622	5.0236	5.0255	5.0432	
Bring C to 10 ml	10.0152	10.0191	9.9992	10.0400	10.0175	10.0299	10.1945	
Mass of 80 ml sample	**149.4246**	**150.3426**	**150.3217**	**149.9754**	**147.9912**	**148.6095**	**148.3189**	

---

3. Get digestion vessel and cover ready, Do not wipe now.
4. Transfer the 90 ml sample back into vessel
5.
6. Transfer contents volumetrics to ICP vials with same number

---

WS5B_ICP Aliquot and Al spiking p2

This worksheet outlines the steps for collecting ICP aliquots and adding Al carrier.

Chemist: AM **Date:** 03/24/11

---

1. Label one 100 ml volumetric flasks per sample
2. Label one ICP vial with CNEF ID per sample

Vessel ID	B16	B17	B18	B20	0			
CNEF ID	2423	2381	2382	2395	0.00			
Sample ID	blank	09SRB-E221A-01	09SRB-E221A-02	09SRB-A347A-01	0			
Al carrier ID	Aluminium, plasma standard solution, Specpcere, A=1000µg/ml, Stock# 38727, Lot# 03-16108B, Nov. 2011							
Quant-EM est. Al in qtz	0	392	194	119	ICP-measurement			
Mass 100 ml volumetric	66.8411	66.5890	66.4903	67.7306				
100 ml volumetric + sample + 2% HNO3	167.9061	167.9451	167.7223	168.9780				
Mass 10 ml smple to vol A (10 ml tube)	10.0168	9.9958	10.0092	10.0219				
Mass 5 ml to volumetric B	5.0026	4.9931	4.9971	5.0106				
Add 2 drops carrier, mass	5.0292	5.0201	5.0263	5.0367				
Bring B to 10 ml with 2% HNO3	10.0347	10.0188	10.0270	10.0233				
Mass8 5 ml Sample	152.8754	152.9454	152.7047	153.9375				
Add carrier to 85ml sample	2.9705	-	-	-				
Mass 5 ml with carrier to Volumtric C	5.0003	4.9975	5.0053	5.0059				
Bring C to 10 ml	10.0188	10.0145	10.0194	10.0168				
Mass of 80 ml sample	**150.8357**	**147.9445**	**147.6973**	**148.9273**				

---

3. Get digestion vessel and cover ready, Do not wipe now.
4. Transfer the 90 ml sample back into vessel
5.
6. Transfer contents volumetrics to ICP vials with same number

---

WS6_Anion Column Chemistry p1

This worksheet outlines the steps for the Anion Column Chemistry (2ml size small column)

Chemist: AM **Date:** 03/25/11

---

1. Evaporate 20 ml to dryness at 100-120°C (will take at least 3 hrs)
2. Dissolve in 10 ml 9 N HCl (let stand for several hours)
3. Transfer to 15 ml centrifuge tubes, rinse digestion vessels with 9 N HCl to bring volume in tube to 10 ml
4. Centrifuge at 1500 rpm or higher for minimum of 10 minutes
5. Allow any 9 N HCl in columns to drain out; discard

Column ID	1	2	3	4	5	6	7	
Vessel	B2	B3	B6	B7	B10	B12	B13	
CNEF ID	2588	2589	2590	2530	2531	2536	2535	
Sample ID	10SRB-E020A-01	10SRB-E021A-01	10SRB-E022A-01	09SRB-E222-05	09SRB-E222-06	10SRB-E074A-01	10SRB-E066A-01	
Redisue (after 2%)	small brown	small brown	small-med. brown	small white	small-med. white	small-med. white	small yellow to white	

6. With stopcock closed, pipet sample (avoid residue) onto 2ml size columns.
7. Collect sample in same 300 ml teflon vessel.
8. Elute with 10 ml 9 N HCl, and collect that, close stopcock
9. 5 ml 4.5 N HCl, collect Anion Supernate in labeled 100 ml bottle
10. 10 ml 1 N HCl, collect Anion Supernate
11. 50 ml deionized water. Discard.
12. CONDITION ANION COLUMN
    - (bottle A1) 10 ml 1N HCl, discard
    - (bottle A2) 10 ml 4.5 N HCl, discard
    - (bottle A3) 10 ml 9 N HCl, discard, but retain acid approx. 2 mm above resin

Comments

March 25: 16:30 put on hotplate T=125°C

WS6_Anion Column Chemistry p2

This worksheet outlines the steps for the Anion Column Chemistry (2ml size small column)

Chemist: AM **Date:** **03/25/11** blank

03/28/11 B17 / B18 / B20

1. Evaporate 20 ml to dryness at 100-120°C (will take at least 3 hrs)
2. Dissolve in 10 ml 9 N HCl (let stand for several hours)
3. Transfer to 15 ml centrifuge tubes, rinse digestion vessels with 9 N HCl to bring volume in tube to 10 ml
4. Centrifuge at 1500 rpm or higher for minimum of 10 minutes
5. Allow any 9 N HCl in columns to drain out; discard

Column ID	1	2	3	4	5	6	7	8
Vessel	B16	B17	B18	B20				
CNEF ID	2423	2381	2382	2395				
Redisue (after 2%)	small white	med.-large yellow	med. yellow to brown	small white				
Residue in tube		0.1 ml white	0.05-0.075 ml white	-				

6. With stopcock closed, pipet sample (avoid residue)onto 2ml size columns.
7. Collect sample in same 300 ml teflon vessel.
8. Elute with 10 ml 9 N HCl, and collect that, close stopcock
9. 5 ml 4.5 N HCl, collect Anion Supernate in labeled 100 ml bottle
10. 10 ml 1 N HCl, collect Anion Supernate
11. 50 ml deionized water. Discard.
12. CONDITION ANION COLUMN
    - (bottle A1) 10 ml 1 N HCl, discard
    - (bottle A2) 10 ml 4.5 N HCl, discard
    - (bottle A3) 10 ml 9 N HCl, discard, but retain acid approx. 2 mm above resin

Comments

March 28: B17, B18 and B20 sitting in 9n HCl since March 25, lid closed under fumehood (3 days)
B17, B18 and B20 transfer liquid to clean centrifuge tube, vortex residue with additional 3ml 9N HCl

WS7_Controlled Precipitate p1

This worksheet outlines the steps for the controlled precipitation chemistry

Chemist: AM **Date:** 03/26/11

---

1. Evaporate "anion" elute to dryness at 125°C
2. Dissolve in 10 ml of a 1:1 solution of 0.5 N HCl and 2% NH_4Cl
3. Transfer to 15 ml centrifuge, centrifuge for 10 minutes
4. Decant into clean test tube, heat in water bath at 60°C
5. Add drops of 1:1 NH_4OH:H_2O to pH=9.2 (5 drops first then single)
6. Centrifuge for 15 minutes
7. Check pH of liquid, if less than pH=7, redo step 5
8. Decant, save with Anion Supernate
9. Wash with deionized water, vortex, centrifuge, decant
10. Wash with deionized water, vortex, centrifuge, decant
11. Wash with deionized water, vortex, centrifuge, decant

CNEF ID	2588	2589	2590	2530	2531	2536	2535	
Vessel	B2	B3	B6	B7	B10	B12	B13	
Sample ID	10SRB-E020A-01	10SRB-E021A-01	10SRB-E022A-01	09SRB-E222-05	09SRB-E222-06	10SRB-E074A-01	10SRB-E066A-01	
Approx. vol. Ptte	0.7 ml white	0.7 ml white	1 ml orange to white	0.7 ml white	1 ml white dense	2.3 ml white dense	0.9 ml white dense	

Comments

WS7_Controlled Precipitate p2

This worksheet outlines the steps for the controlled precipitation chemistry

Chemist: AM **Date:** **03/26/11** blank
03/29/11 B17, B18, B20

1. Evaporate "anion" elute to dryness at 125°C
2. Dissolve in 10 ml of a 1:1 solution of 0.5 N HCl and 2% NH_4Cl
3. Transfer to 15 ml centrifuge, centrifuge for 10 minutes
4. Decant into clean test tube, heat in water bath at 60°C
5. Add drops of 1:1 NH_4OH:H_2O to pH=9.2 (5 drops first then single)
6. Centrifuge for 15 minutes
7. Check pH of liquid, if less than pH=7, redo step 5
8. Decant, save with Anion Supernate
9. Wash with deionized water, vortex, centrifuge, decant
10. Wash with deionized water, vortex, centrifuge, decant
11. Wash with deionized water, vortex, centrifuge, decant

CNEF ID	2423	2381	2382	2395				
Vessel	B16	B17	B18	B20				
Sample ID	blank	09SRB-E221A-01	09SRB-E221A-02	09SRB-A347A-01				
Approx. vol. Ptte	0.3 ml white	1.5 ml white	1.5-1.75 ml white	0.5-0.6 ml white				

Comments

WS8_Cation Column Chemistry p1

This worksheet outlines the steps for the Cation Column Chemistry

Chemist: AM **Date:** 03/27/11

☐1 Dissolve in 5 ml conc. HCl and evaporate to dryness at 125°C
☐2 Redissolve in 2.5 ml 1 N HCl and 2.5 ml 0.5 N HCl
☐3 Transfer to centrifuge tube, rinse with 1 ml 0.5 N, and centrifuge

Column ID	1	2	3	4	5	6	7	8
Vessel	B2	B3	B6	B7	B10	B12	B13	
CNEF ID	2588	2589	2590	2530	2531	2536	2535	
Sample ID	10SRB-E020A-01	10SRB-E021A-01	10SRB-E022A-01	09SRB-E222-05	09SRB-E222-06	10SRB-E074A-01	10SRB-E066A-01	
Small Vessel	C2	C3	C6	C9	C10	C11	C14	

☐4 Pipette all of the sample into designated conditioned cation column, 17 ml
☐5 Discard the eluant. Add 285 ml 0.5 N HCL (Bottle C6)
☐6 Drain the column, discard the first 300ml of eluant
☐7 Add 60 ml of 0.5N HCl, (Bottle C7), Collect eluant as Cation Supernate
☐8 Add 65 ml of 0.5N HCl, (Bottle C8), Save it as Be-Sample
☐9 Add 120 ml 1N HCl (bottle C9)
☐10 Save this as Be-sample as well.
☐11 Add 80 ml 4.5 N HCl (bottle C10) , save the eluant as Al sample.
☐12 CONDITION CATION COLUMN

(bottle C1) 100 ml 9 N HCl
(bottle C2) 50 ml 4.5 N HCl
(bottle C3) 50 ml 1 N HCl
(bottle C4) 50 ml water
(bottle C5) 100 ml 0.5 N HCl

* 17 ml Column

WS8_Cation Column Chemistry p2

This worksheet outlines the steps for the Cation Column Chemistry

Chemist: AM **Date:** **03/27/11** blank

04/01/11 B17, B18, B20

1. Dissolve in 5 ml conc. HCl and evaporate to dryness at 125°C
2. Redissolve in 2.5 ml 1 N HCl and 2.5 ml 0.5 N HCl
3. Transfer to centrifuge tube, rinse with 1 ml 0.5 N, and centrifuge

Column ID	1	2	3	4	5	6	7	8
Vessel	B16	B17	B18	B20				
CNEF ID	2423	2381	2382	2395				
Sample ID	blank	09SRB-E221A-01	09SRB-E221A-02	09SRB-A347A-01				
Small Vessel	C20	Only Al-sample, Be-sample not collected						

4. Pipette all of the sample into designated conditioned cation column, 17 ml
5. Discard the eluant. Add 285 ml 0.5 N HCL (Bottle C6)
6. Drain the column, discard the first 300ml of eluant
7. Add 60 ml of 0.5N HCl, (Bottle C7), Collect eluant as Cation Supernate
8. Add 65 ml of 0.5N HCl, (Bottle C8), Save it as Be-Sample
9. Add 120 ml 1N HCl (bottle C9)
10. Save this as Be-sample as well.
11. Add 80 ml 4.5 N HCl (bottle C10) , save the eluant as Al sample.
12. CONDITION CATION COLUMN

(bottle C1) 100 ml 9 N HCl

(bottle C2) 50 ml 4.5 N HCl

(bottle C3) 50 ml 1 N HCl

(bottle C4) 50 ml water

(bottle C5) 100 ml 0.5 N HCl

* 17 ml Column

WS9_Be Sample Chemistry p1

This worksheet outlines the steps to prepare the BeO sample

Chemist: AM **Date:** **03/29/11** - 04/04/11

☐1 Evaporate Be Sample from column in wiped digestion vessels at 125°C
☐2 Add 2-5 ml 20% perchloric and evaporate at 200oC
☐3 Again, add 2-5 ml 20% perchloric and evaporate at 200°C
☐4 Dissolve sample in 10 ml of 0.5 N HCl (optima grade)
☐5 Transfer to 15 ml centrifuge tube
☐6 Centrifuge and decant into clean centrifuge tube
☐7 Heat centrifuge tubes in water bath at 60°C
☐8 Precipitate $Be(OH)_2$ using Matheson ultimate grade ammonia gas
Gently bubble NH_3 with clean pipet tip on hose
for ca.15 bubbles, or ca. 8-12 sec until ptte forms
Optimum pH=9.2; 1N HCl may be added
☐9 Centrifuge 15 min., decant (save and redo ☐8 if pH of liquid is < 8)
☐10 Wash with water, vortex, centrifuge for 10 min, and decant
☐11 Record mass quartz vials, label, and place them in furnace holder

CNEF ID	2588	2589	2590	2530	2531	2536	2535	
Vessel	B2	B3	B6	B7	B10	B12	B13	
Sample ID	10SRB-E020A-01	10SRB-E021A-01	10SRB-E022A-01	09SRB-E222-05	09SRB-E222-06	10SRB-E074A-01	10SRB-E066A-01	
Vol. Precipitate	0.05 ml	0.05 ml	0.05 ml	0.05 ml	0.075 ml	0.1 ml	0.1 ml	
Mass Qtz Vial	2.5239	2.4475	2.5505	2.5199	2.4731	2.5688	2.4591	
Mass Vial+Spl	2.5243	2.4478	2.5513	2.5205	2.4733	2.5705	2.4617	
Mass Spl	0.0004	0.0003	0.0008	0.0006	0.0002	0.0017	0.0026	

☐12 Add 1 small drop of water with micropipet, slurry precipitate
☐13 Transfer sample into quartz vial, cover with quartz lid
☐14 Turn on Bunsen Burner, dry the gel carefully.
☐15 Burn the Be(OH)2 gel on bunsen burner at least 2 mins, at blue flame.
☐18 Convert to BeO
☐19 Determine mass of vial + sample

WS9_Be Sample Chemistry p2

This worksheet outlines the steps to prepare the BeO sample

Chemist: AM **Date:** **03/29/11** - 04/04/11

- ☐1 Evaporate Be Sample from column in wiped digestion vessels at 125°C
- ☐2 Add 2-5 ml 20% perchloric and evaporate at 200oC
- ☐3 Again, add 2-5 ml 20% perchloric and evaporate at 200°C
- ☐4 Dissolve sample in 10 ml of 0.5 N HCl (optima grade)
- ☐5 Transfer to 15 ml centrifuge tube
- ☐6 Centrifuge and decant into clean centrifuge tube
- ☐7 Heat centrifuge tubes in water bath at 60°C
- ☐8 Precipitate $Be(OH)_2$ using Matheson ultimate grade ammonia gas
  Gently bubble NH_3 with clean pipet tip on hose
  for ca.15 bubbles, or ca. 8-12 sec until ptte forms
  Optimum pH=9.2; 1N HCl may be added
- ☐9 Centrifuge 15 min., decant (save and redo ☐8 if pH of liquid is < 8)
- ☐10 Wash with water, vortex, centrifuge for 10 min, and decant
- ☐11 Record mass quartz vials, label, and place them in furnace holder

CNEF ID	2423	~~2381~~	~~2382~~	~~2395~~				
Vessel	B16	~~B17~~	~~B18~~	~~B20~~				
Sample ID	blank	~~09SRB-E221A-01~~	~~09SRB-E221A-02~~	~~09SRB-A347A-01~~				
Vol. Precipitate	0.05 ml							
Mass Qtz Vial	2.3666							
Mass Vial+Spl	2.3661							
Mass Spl	-0.0005							

- ☐12 Add 1 small drop of water with micropipet, slurry precipitate
- ☐13 Transfer sample into quartz vial, cover with quartz lid
- ☐14 Turn on Bunsen Burner, dry the gel carefully.
- ☐15 Burn the Be(OH)2 gel on bunsen burner at least 2 mins, at blue flame.
- ☐18 Convert to BeO
- ☐19 Determine mass of vial + sample

WS10_Al Sample Chemistry p1

This worksheet outlines the steps to prepare the Al oxide sample

Chemist: AM **Date:** **03/29/11** - 04/04/11

1. Evaporate Al Sample from column in wiped teflon vessel at 125°C
2. Dissolve sample in 10 ml of 0.5 N HCl (optima grade)
3. Transfer to 15 ml centrifuge tube
4. Centrifuge and decant into clean centrifuge tube
5. Heat centrifuge tubes in water bath at 60°C
6. Precipitate $Al(OH)_3$ using 50% NH_3OH (drops: 25, 5, 5, 3, 2…)
   Optimum pH=6.3; 1N HCl may be added
7. Centrifuge 15 min., decant (save and redo 6 if pH of liquid is < 8)
8. Wash with water, vortex, centrifuge for 10 min, and decant
9. Record mass quartz vials, label, and place them in furnace holder

Small Vessel	C2	C3	C6	C9	C10	C11	C14	
CNEF ID	2588	2589	2590	2530	2531	2536	2535	
Sample ID	10SRB-E020A-01	10SRB-E021A-01	10SRB-E022A-01	09SRB-E222-05	09SRB-E222-06	10SRB-E074A-01	10SRB-E066A-01	
Vol. Precipitate	0.4 ml	0.2 ml	0.4 ml	0.4 ml	1.5 ml	1 ml	0.9 ml	
Mass Qtz Vial	2.3896	2.5344	2.5730	2.4312	2.3978	2.5173	2.4555	
Mass Vial+Spl	2.3947	2.5385	2.5794	2.4376	2.4174	2.5516	2.4691	
Mass Spl	0.0051	0.0041	0.0064	0.0064	0.0196	0.0343	0.0136	

10. Add 1 small drop of water with micropipet, slurry precipitate
11. Transfer sample into quartz vial, cover with alumina vial
12. Heat in oven at 120°C for 2-3 hours
13. Let cool and scrape sample down from walls of quartz tube
14. Convert to Al_2O_3 in furnace at 950°C for minimum of 1 hr
15. Determine mass of vial + sample

WS10_Al Sample Chemistry p2

This worksheet outlines the steps to prepare the Al oxide sample

Chemist: AM **Date:** **03/29/11** - 04/04/11

☐1 Evaporate Al Sample from column in wiped teflon vessel at 125°C
☐2 Dissolve sample in 10 ml of 0.5 N HCl (optima grade)
☐3 Transfer to 15 ml centrifuge tube
☐4 Centrifuge and decant into clean centrifuge tube
☐5 Heat centrifuge tubes in water bath at 60°C
☐6 Precipitate $Al(OH)_3$ using 50% NH_3OH (drops: 25, 5, 5, 3, 2…)
Optimum pH=6.3; 1N HCl may be added
☐7 Centrifuge 15 min., decant (save and redo ☐6 if pH of liquid is < 8)
☐8 Wash with water, vortex, centrifuge for 10 min, and decant
☐9 Record mass quartz vials, label, and place them in furnace holder

Small Vessel	**C20**	**B17**	**B18**	**B20**				
CNEF ID	**2423**	**2381**	**2382**	**2395**				
Sample ID	blank	09SRB-E221A-01	09SRB-E221A-02	09SRB-A347A-01				
Vol. Precipitate	0.35 ml	1 ml	0.5 ml	0.2 ml				
Mass Qtz Vial	2.5089	2.3055	2.5570	2.4748				
Mass Vial+Spl	2.5127	2.3309	2.5783	2.4784				
Mass Spl	0.0038	0.0254	0.0213	0.0036				

☐10 Add 1 small drop of water with micropipet, slurry precipitate
☐11 Transfer sample into quartz vial, cover with alumina vial
☐12 Heat in oven at 120°C for 2-3 hours
☐13 Let cool and scrape sample down from walls of quartz tube
☐14 Convert to Al_2O_3 in furnace at 950°C for minimum of 1 hr
☐15 Determine mass of vial + sample

APPENDIX A6 – Electronic Supplementary Files

Plate 1 – Map of ice recession of alpine glaciers on Cumberland Peninsula

This map displays mapped ice margin positions and contours on a DEM of Cumberland Peninsula at a scale of 1:325,000. New geochronological control in the interior of the peninsula is combined with previous age control to infer ice extent of alpine glaciers during deglaciation from the coast to the interior: The green and light blue hand-colored ares indicate early deglacial ice extent, the purple and pink hand-colored areas indicate ice extent during the Younger Dryas cold interval, and the orange and yellow hand-colored areas indicate Cockburn-equivalent ice extent. Figures 3.7 – 3.9 presented and discussed in *Chapter 3* have been derived from this map.

The map is available in the Dalhousie Repository (DalSpace):

http://dalspace.library.dal.ca/handle/10222/10559

APPENDIX A7 - License Agreement for Manuscript 'Neoglacial Ice Expansion and Late Holocene Cold-Based Ice Cap Dynamics on Cumberland Peninsula, Baffin Island, Arctic Canada', Published in *Quaternary Science Reviews*

ELSEVIER LICENSE
TERMS AND CONDITIONS

Feb 10, 2015

This is a License Agreement between Annina Margreth ("You") and Elsevier ("Elsevier") provided by Copyright Clearance Center ("CCC"). The license consists of your order details, the terms and conditions provided by Elsevier, and the payment terms and conditions.

All payments must be made in full to CCC. For payment instructions, please see information listed at the bottom of this form.

Supplier	Elsevier Limited The Boulevard,Langford Lane Kidlington,Oxford,OX5 1GB,UK
Registered Company Number	1982084
Customer name	Annina Margreth
Customer address	Dalhousie University Halifax, NS B3H 4R2
License number	3565390061119
License date	Feb 10, 2015
Licensed content publisher	Elsevier
Licensed content publication	Quaternary Science Reviews
Licensed content title	Neoglacial ice expansion and late Holocene cold-based ice cap dynamics on Cumberland Peninsula, Baffin Island, Arctic Canada
Licensed content author	Annina Margreth,Arthur S. Dyke,John C. Gosse,Alice M. Telka
Licensed content date	1 May 2014
Licensed content volume number	91
Licensed content issue number	n/a
Number of pages	15
Start Page	242
End Page	256
Type of Use	reuse in a thesis/dissertation
Portion	full article
Format	both print and electronic
Are you the author of this Elsevier article?	Yes
Will you be translating?	No

Title of your thesis/dissertation	GEOCHRONOLOGICAL APPROACHES FOR QUANTIFICATION OF POLYTHERMAL GLACIER DYNAMICS AND SUBGLACIAL EPISODIC EROSION ON HIGH-LATITUDE HIGHLAND PLATEAUS, CUMBERLAND PENINSULA, BAFFIN ISLAND, NUNAVUT
Expected completion date	Mar 2015
Estimated size (number of pages)	300
Elsevier VAT number	GB 494 6272 12
Permissions price	0.00 CAD
VAT/Local Sales Tax	0.00 CAD / 0.00 GBP
Total	0.00 CAD
Terms and Conditions	

INTRODUCTION

1. The publisher for this copyrighted material is Elsevier. By clicking "accept" in connection with completing this licensing transaction, you agree that the following terms and conditions apply to this transaction (along with the Billing and Payment terms and conditions established by Copyright Clearance Center, Inc. ("CCC"), at the time that you opened your Rightslink account and that are available at any time at http://myaccount.copyright.com).

GENERAL TERMS

2. Elsevier hereby grants you permission to reproduce the aforementioned material subject to the terms and conditions indicated.

3. Acknowledgement: If any part of the material to be used (for example, figures) has appeared in our publication with credit or acknowledgement to another source, permission must also be sought from that source. If such permission is not obtained then that material may not be included in your publication/copies. Suitable acknowledgement to the source must be made, either as a footnote or in a reference list at the end of your publication, as follows:

"Reprinted from Publication title, Vol /edition number, Author(s), Title of article / title of chapter, Pages No., Copyright (Year), with permission from Elsevier [OR APPLICABLE SOCIETY COPYRIGHT OWNER]." Also Lancet special credit - "Reprinted from The Lancet, Vol. number, Author(s), Title of article, Pages No., Copyright (Year), with permission from Elsevier."

4. Reproduction of this material is confined to the purpose and/or media for which permission is hereby given.

5. Altering/Modifying Material: Not Permitted. However figures and illustrations may be altered/adapted minimally to serve your work. Any other abbreviations, additions, deletions and/or any other alterations shall be made only with prior written authorization of Elsevier Ltd. (Please contact Elsevier at permissions@elsevier.com)

6. If the permission fee for the requested use of our material is waived in this instance, please be advised that your future requests for Elsevier materials may attract a fee.

7. Reservation of Rights: Publisher reserves all rights not specifically granted in the combination of (i) the license details provided by you and accepted in the course of this licensing transaction, (ii) these terms and conditions and (iii) CCC's Billing and Payment terms and conditions.

8. License Contingent Upon Payment: While you may exercise the rights licensed immediately upon issuance of the license at the end of the licensing process for the transaction, provided that you have disclosed complete and accurate details of your proposed use, no license is finally effective unless and until full payment is received from you (either by publisher or by CCC) as provided in CCC's Billing and Payment terms and conditions. If full payment is not received on a timely basis, then any license preliminarily granted shall be deemed automatically revoked and shall be void as if never granted. Further, in the event that you breach any of these terms and conditions or any of CCC's Billing and Payment terms and conditions, the license is automatically revoked and shall be void as if never granted. Use of materials as described in a revoked license, as well as any use of the materials beyond the scope of an unrevoked license, may constitute copyright infringement and publisher reserves the right to take any and all action to protect its copyright in the materials.

9. Warranties: Publisher makes no representations or warranties with respect to the licensed material.

10. Indemnity: You hereby indemnify and agree to hold harmless publisher and CCC, and their respective officers, directors, employees and agents, from and against any and all claims arising out of your use of the licensed material other than as specifically authorized pursuant to this license.

11. No Transfer of License: This license is personal to you and may not be sublicensed, assigned, or transferred by you to any other person without publisher's written permission.

12. No Amendment Except in Writing: This license may not be amended except in a writing signed by both parties (or, in the case of publisher, by CCC on publisher's behalf).

13. Objection to Contrary Terms: Publisher hereby objects to any terms contained in any purchase order, acknowledgment, check endorsement or other writing prepared by you, which terms are inconsistent with these terms and conditions or CCC's Billing and Payment terms and conditions. These terms and conditions, together with CCC's Billing and Payment terms and conditions (which are incorporated herein), comprise the entire agreement between you and publisher (and CCC) concerning this licensing transaction. In the event of any conflict between your obligations established by these terms and conditions and those established by CCC's Billing and Payment terms and conditions, these terms and conditions shall control.

14. Revocation: Elsevier or Copyright Clearance Center may deny the permissions described in this License at their sole discretion, for any reason or no reason, with a full refund payable to you. Notice of such denial will be made using the contact information provided by you. Failure to receive such notice will not alter or invalidate the denial. In no event will Elsevier or Copyright Clearance Center be responsible or liable for any costs, expenses or damage incurred by you as a result of a denial of your permission request, other than a refund of the amount(s) paid by you to Elsevier and/or Copyright Clearance Center for denied permissions.

LIMITED LICENSE

The following terms and conditions apply only to specific license types:

15. **Translation**: This permission is granted for non-exclusive world **English** rights only unless your license was granted for translation rights. If you licensed translation rights you may only translate this content into the languages you requested. A professional translator must perform all translations and reproduce the content word for word preserving the integrity of the article. If this license is to re-use 1 or 2 figures then permission is granted for non-exclusive world rights in all languages.

16. **Posting licensed content on any Website**: The following terms and conditions apply as follows: Licensing material from an Elsevier journal: All content posted to the web site must maintain the copyright information line on the bottom of each image; A hyper-text must be included to the Homepage of the journal from which you are licensing athttp://www.sciencedirect.com/science/journal/xxxxx or the Elsevier homepage for books athttp://www.elsevier.com; Central Storage: This license does not include permission for a scanned version of the material to be stored in a central repository such as that provided by Heron/XanEdu.

Licensing material from an Elsevier book: A hyper-text link must be included to the Elsevier homepage at http://www.elsevier.com . All content posted to the web site must maintain the copyright information line on the bottom of each image.

Posting licensed content on Electronic reserve: In addition to the above the following clauses are applicable: The web site must be password-protected and made available only to bona fide students registered on a relevant course. This permission is granted for 1 year only. You may obtain a new license for future website posting.

17.**For journal authors:** the following clauses are applicable in addition to the above: Permission granted is limited to the author accepted manuscript version* of your paper.

***Accepted Author Manuscript (AAM) Definition:** An accepted author manuscript (AAM) is the author's version of the manuscript of an article that has been accepted for publication and which may include any author-incorporated changes suggested through

the processes of submission processing, peer review, and editor-author communications. AAMs do not include other publisher value-added contributions such as copy-editing, formatting, technical enhancements and (if relevant) pagination.

You are not allowed to download and post the published journal article (whether PDF or HTML, proof or final version), nor may you scan the printed edition to create an electronic version. A hyper-text must be included to the Homepage of the journal from which you are licensing at http://www.sciencedirect.com/science/journal/xxxxx. As part of our normal production process, you will receive an e-mail notice when your article appears on Elsevier's online service ScienceDirect (www.sciencedirect.com). That e-mail will include the article's Digital Object Identifier (DOI). This number provides the electronic link to the published article and should be included in the posting of your personal version. We ask that you wait until you receive this e-mail and have the DOI to do any posting.

18.**Posting to a repository:** Authors may post their AAM immediately to their employer's institutional repository for internal use only and may make their manuscript publically available after the journal-specific embargo period has ended.

Please also refer to Elsevier's Article Posting Policy for further information.

19. **For book authors** the following clauses are applicable in addition to the above: Authors are permitted to place a brief summary of their work online only.. You are not allowed to download and post the published electronic version of your chapter, nor may you scan the printed edition to create an electronic version. **Posting to a repository:** Authors are permitted to post a summary of their chapter only in their institution's repository.

20. **Thesis/Dissertation**: If your license is for use in a thesis/dissertation your thesis may be submitted to your institution in either print or electronic form. Should your thesis be published commercially, please reapply for permission. These requirements include permission for the Library and Archives of Canada to supply single copies, on demand, of the complete thesis and include permission for Proquest/UMI to supply single copies, on demand, of the complete thesis. Should your thesis be published commercially, please reapply for permission.

Elsevier Open Access Terms and Conditions

Elsevier publishes Open Access articles in both its Open Access journals and via its Open Access articles option in subscription journals.

Authors publishing in an Open Access journal or who choose to make their article Open Access in an Elsevier subscription journal select one of the following Creative Commons user licenses, which define how a reader may reuse their work: Creative Commons Attribution License (CC BY), Creative Commons Attribution – Non Commercial - ShareAlike (CC BY NC SA) and Creative Commons Attribution – Non Commercial – No

21. **Other Conditions**:

v1.7

Questions? customercare@copyright.com or +1-855-239-3415 (toll free in the US) or +1-978-646-2777.

Gratis licenses (referencing $0 in the Total field) are free. Please retain this printable license for your reference. No payment is required.

APPENDIX A8 - Contribution to Manuscripts in Thesis

DALHOUSIE University

Faculty of Graduate Studies

STUDENT CONTRIBUTION TO MANUSCRIPTS IN THESIS

MUST BE WORD-PROCESSED OR TYPEWRITTEN.

NAME:	ANNINA MARGRETH	**STUDENT ID #:**	B00537846
DEPARTMENT:	EARTH SCIENCES	**PROGRAMME:**	PhD
PHONE:		**E-MAIL:**	ANNINA@DAL.CA

MANUSCRIPT AUTHORS:	ANNINA MARGRETH, ARTHUR S. DYKE, JOHN C. GOSSE, ALICE M. TELKA
MANUSCRIPT TITLE:	NEOGLACIAL ICE EXPANSION AND LATE HOLOCENE COLD-BASED ICE CAP DYNAMICS ON CUMBERLAND PENINSULA, BAFFIN ISLAND, ARCTIC CANADA
JOURNAL:	QUATERNARY SCIENCE REVIEWS
STUDENT CONTRIBUTION:	I'VE COMPLETED THE INTERPRETATION OF ALL RADIOCARBON DATA AND PREPARED THE MANUSCRIPT WITH DISCUSSION AND EDITING BY ALL CO-AUTHORS.
SUPERVISOR SIGNATURE:	

MANUSCRIPT AUTHORS:	ANNINA MARGRETH, JOHN C. GOSSE, ARTHUR S. DYKE
MANUSCRIPT TITLE:	WISCONSINAN GLACIAL DYNAMICS OF CUMBERLAND PENINSULA, BAFFIN ISLAND, ARCTIC CANADA
JOURNAL:	INTENDED FOR SUBMISSION TO QUATERANRY RESEARCH
STUDENT CONTRIBUTION:	I'VE COMPLETED THE CHEMISTRY ON MANY OF THE SAMPLES, PARTICIPATED IN THE AMS ANALYSIS, AND DONE THE INTERPRETATION OF COSMOGENIC NUCLIDE EXPOSURE AND RADIOCARBON DATA AND INFERED THE ICE EXTENT MAPS AND PALEO-EQUILLIBRIUM LINE ALTITUDE RECONSTRUCTION BASED ON AN ICE MARGIN MAP PROVIDED BY ARTHUR S. DYKE. I'VE PREPARED THE MANUSCRIPT WITH DISCUSSION AND EDITING BY ALL CO-AUTHORS.
SUPERVISOR SIGNATURE:	

MANUSCRIPT AUTHORS:	ANNINA MARGRETH, JOHN C. GOSSE, ARTHUR S. DYKE
MANUSCRIPT TITLE:	NEW APPROACH FOR QUANTIFICATION OF SUBAERIAL AND SUBGLACIAL EROSION RATES ON HIGH LATITUDE UPLAND PLATEAUS: CUMBERLAND PENINSULA, BAFFIN ISLAND, CANADA
JOURNAL:	INTENDED FOR SUBMISSION TO QUATERNARY SCIENCE REVIEWS
STUDENT CONTRIBUTION:	I'VE COMPLETED THE CHEMISTRY ON MANY OF THE SAMPLES AND PARTICIPATED IN THE AMS ANALYSIS. I'VE DEVLEOPED THE CALCULATION SCHEMES USED TO INTERPRET THE COSMOGENIC NUCLIDE EXPOSURE DATA TO DERIVE PROBABILITY DENSITY FUNCTIONS OF VARIOUS VARIABLES (INCL. EPISODIC EROSION RATES). I'VE INTERPRETED THE RESULTS AND PEPARED THE MANUSCRIPT WITH DISCUSSION AND EDITING BY ALL CO-AUTHORS.
SUPERVISOR SIGNATURE:	